



**HAL**  
open science

# Active tectonics and paleoseismology of strike-slip faults of Central Iran

Mohammad Foroutan

► **To cite this version:**

Mohammad Foroutan. Active tectonics and paleoseismology of strike-slip faults of Central Iran. Earth Sciences. Université Pierre et Marie Curie - Paris VI, 2013. English. NNT: . tel-00922358

**HAL Id: tel-00922358**

**<https://theses.hal.science/tel-00922358>**

Submitted on 26 Dec 2013

**HAL** is a multi-disciplinary open access archive for the deposit and dissemination of scientific research documents, whether they are published or not. The documents may come from teaching and research institutions in France or abroad, or from public or private research centers.

L'archive ouverte pluridisciplinaire **HAL**, est destinée au dépôt et à la diffusion de documents scientifiques de niveau recherche, publiés ou non, émanant des établissements d'enseignement et de recherche français ou étrangers, des laboratoires publics ou privés.

**THÈSE DE DOCTORAT DE  
L'UNIVERSITÉ PIERRE ET MARIE CURIE**

Spécialité  
Géoscience et ressources naturelles

Présentée par  
**M. Mohammad Foroutan**

Pour obtenir grade de  
**DOCTEUR de l'UNIVERSITÉ PIERRE ET MARIE CURIE**

**Tectonique active et paléosismologie des  
décrochements de l'Iran Central**

Soutenue le 17 décembre 2013

Devant le jury composé de:

Bertrand MEYER	PR. UPMC, ISteP-Paris	Directeur de thèse
Michel SÉBRIER	DR. CNRS, ISteP-Paris	Co-directeur de thèse
Thierry CAMELBEECK	PR. ORB-Brussels	Rapporteur
Yann KLINGER	DR. CNRS, IPGP-Paris	Rapporteur
Hamid NAZARI	Chercheur, GSI-Téhéran	Examineur, responsable scientifique iranien
Olivier LACOMBE	PR. UPMC, ISteP-Paris	Examineur
Andrea WALPERSDORF	PHYS. ISterre-Grenoble	Examineur



## Résumé

Le plateau d'Iran central est caractérisé par de très faibles taux de déformation GPS et apparaît asismique pendant les derniers millénaires. Néanmoins, il est découpé par plusieurs décrochements dextres de direction N-S qui s'étendent sur plusieurs centaines de kilomètres. Le taux de glissement et le comportement sismique de trois de ces failles décrochantes (d'ouest en est: Dehshir, Anar et Nayband) ont été analysés dans cette thèse. Les études paléosismologiques sur la faille de Dehshir, longue de 380 km, démontrent l'existence d'au moins trois gros ( $M_w \approx 7$ ) séismes pendant les derniers 22 ka, l'événement le plus récent s'étant produit juste avant 2 ka. Nos observations permettent aussi de calculer un taux de glissement pour cette faille compris entre 0.9 et 1.48 mm a<sup>-1</sup> au cours des derniers 42 ka, ce taux est identique à celui déterminé antérieurement à  $1.2 \pm 0.3$  mm a<sup>-1</sup> et moyenné sur les derniers 270 ka. Cela suggère que le taux de glissement est resté constant au cours du Pléistocène supérieur et de l'Holocène. L'étude paléosismologique de la faille d'Anar, longue de 200 km, montre que trois gros séismes se sont produits à  $4.4 \pm 0.8$ ,  $6.8 \pm 1$ , et  $9.8 \pm 2$  ka. L'âge de l'événement le plus récent (compris entre 3.6 et 5.2 ka) suggère que la faille s'approche de la fin de son cycle sismique. Nos résultats confirment aussi que le taux de glissement minimum de la faille d'Anar est de  $0.8 \pm 0.1$  mm a<sup>-1</sup>, indiquant que les failles majeures les plus occidentales de l'Iran central possèdent des taux de glissement proches de 1 mm a<sup>-1</sup>. Le taux de glissement sur la faille de Nayband, longue de 290 km, est déterminé à partir de décalages datés par des mesures de <sup>36</sup>Cl ou d'OSL. Ces décalages, qui sont compris entre  $9 \pm 1$  m et  $195 \pm 15$  m avec des âges entre  $6.8 \pm 0.6$  et 100 ka, fournissent un taux de glissement de  $1.8 \pm 0.7$  mm a<sup>-1</sup>. Nos données paléosismologiques démontrent l'existence d'au moins quatre gros séismes pendant les derniers  $17.4 \pm 1.3$  ka et de deux événements plus anciens (avant 23 ka et  $70 \pm 5$  ka). Les pénultième et antépénultième séismes se sont produits entre  $6.5 \pm 0.4$  ka et  $6.7 \pm 0.4$  ka, tandis que l'événement le plus récent s'est produit il y a moins de 800 ans. Une telle succession irrégulière de séismes suggère un comportement sismique en "clustering". Bien que le séisme le plus récent sur les failles de Nayband et Dehshir se soit respectivement produit après 1200 AD et juste avant 2 ka, ces séismes n'apparaissent pas dans les chroniques historiques. Ces résultats illustrent clairement l'incomplétude des catalogues de sismicité historique pour l'Iran central, limitant toute évaluation de l'aléa sismique sans données géologiques. L'Iran central n'est pas un bloc totalement rigide, sa déformation interne modérée est néanmoins responsable d'un aléa sismique significatif. Ainsi, des séismes forts et peu fréquents caractérisent les failles décrochantes dextres à faibles taux de glissement qui découpent l'Iran central et oriental. La sommation de ces taux de glissement du Plateau iranien jusqu'à la limite avec l'Afghanistan ne semble pas en accord avec les données GPS disponibles.



## Abstract

The Central Iran plateau is experiencing very low GPS deformation rates and appears aseismic during the last few millennia. Nevertheless, it is sliced by several N-striking, right-lateral, strike-slip faults that are hundreds of kilometers long. The slip rate and seismic behavior of three of these faults (from west to east: Dehshir, Anar, and Nayband) have been investigated throughout this dissertation. The paleoseismic records along the 380-km long, Dehshir fault demonstrate the occurrence of at least three large ( $M_w \approx 7$ ) earthquakes during the last 22 ka, the most recent event occurring shortly before  $\sim 2$  ka. Additional observations yield a slip rate between 0.9 and 1.48 mm yr<sup>-1</sup> over the last 42 ka, which agrees with the previous slip rate of  $1.2 \pm 0.3$  mm yr<sup>-1</sup> averaged over the last 270 ka. This suggests that the slip rate has remained constant during the late Pleistocene and Holocene. The paleoseismic study on the 200-km long, Anar fault shows that three large earthquakes occurred at  $4.4 \pm 0.8$ ,  $6.8 \pm 1$ , and  $9.8 \pm 2$  ka. The age of the most recent event (3.6-5.2 ka) suggests the fault is approaching the end of its seismic cycle. These results confirm a previous minimum slip rate of  $0.8 \pm 0.1$  mm yr<sup>-1</sup> for the Anar fault, indicating that the westernmost prominent faults of Central Iran are characterized by slip rates close to 1 mm yr<sup>-1</sup>. The slip rate on the 290-km long, Nayband fault is determined using cosmogenic and optically stimulated luminescence dating of cumulative offsets. The offsets range between  $9 \pm 1$  m and  $195 \pm 15$  m with ages from  $6.8 \pm 0.6$  ka to  $\sim 100$  ka, yielding a slip rate of  $1.8 \pm 0.7$  mm yr<sup>-1</sup>. The first paleoseismic record demonstrates the occurrence of at least four large earthquakes during the last  $17.4 \pm 1.3$  ka and two older events (before  $\sim 23$  ka and  $70 \pm 5$  ka). Penultimate and antepenultimate events occurred between  $6.5 \pm 0.4$  and  $6.7 \pm 0.4$  ka, whereas the most recent event took place within the last 800 years. Such an irregular earthquake occurrence suggests seismic clustering. Although the most recent earthquakes on the Nayband and Dehshir faults occurred after AD 1200 and shortly before  $\sim 2$  ka, respectively, these events went unnoticed in the historical seismic records. These are marked illustrations of the incompleteness of the historical seismic catalogs in Central Iran, challenging any seismic hazard assessment without geologic information. The paleoseismic records show that Central Iran does not behave totally as a rigid block and that its moderate internal deformation is nonetheless responsible for a significant seismic hazard. Thus, large infrequent earthquakes typify the slow-slipping strike-slip faults slicing Central and Eastern Iran, which slip rates summed from the Iran Plateau up to the Afghan lowlands remain difficult to match with the available GPS data.



## چکیده

فلات ایران مرکزی امروزه آهنگ دگرشکل GPS بسیار اندکی را تجربه می‌کند، و در گذر هزاره‌های اخیر بمواره بی لرزه جلوه نموده است. این در حالی است که چندین کسل راستا لغز راست براراستی شمالی- جنوبی و درازای چند صد کیلومتر پهنا ایران مرکزی واقع می‌کنند. از این میان، رساله پیش روی، آهنگ لغزش و رفتار لرزه‌ای بروی کسل راستا لغز (به ترتیب از باختر به خاور؛ دیشیر، انار و نایند) را مورد بررسی قرار داده است. برداشت‌های پارینه لرزه‌شناختی در راستای کسل دیشیر به درازای ۳۸۰ کیلومتر، دلالت بر رخداد دست کم سه زمین لرزه بزرگ ( $M_w \approx 7$ ) در گذر ۳۲ هزار سال پیش داشته، و بیاگر رخداد آخرین رویداد لرزه‌ای، اندکی پیش از ۲- هزار سال گذشته است. بررسی‌های تکلیفی بروی کسل دیشیر، اشاره بر آهنگ لغزشی بین ۰/۱۹ تا ۱/۴۸ میلی‌متر در سال، در گذر ۴۲ هزار سال اخیر دارد. این بازه پیشنهادی همساز با آهنگ لغزش میانگینی است که بیشتر برابر با  $0/۳ \pm ۱/۲$  میلی‌متر در سال، در گذر ۲۷۰ هزار سال اخیر برآورده شده است. چنین سازگاری می‌تواند نشان از یک نواختی آهنگ لغزش در بازه زمانی پلیستوسن پامانی و هولوسن داشته باشد. پژوهش‌های پارینه لرزه‌شناختی بروی کسل انار به درازای ۲۰۰ کیلومتر، گواهی بر رخداد سه زمین لرزه بزرگ در  $0/۸ \pm ۰/۴$ ،  $۱/۸ \pm ۰/۶$ ، و  $۱/۸ \pm ۰/۲$  هزار سال پیش دارند. بازه زمانی رخداد آخرین زمین لرزه (بین ۳/۶ و ۵/۲ هزار سال) بیاگر نزدیکی کسل انار به پایان چرخه لرزه‌ای جاری خود است. این نتایج، افزون بر تایید کینه آهنگ لغزش پیشنهادی برای کسل انار برابر با  $0/۱۸ \pm ۰/۱$  میلی‌متر در سال، دلالت بر لغزش کسل‌های باختری ایران مرکزی با آهنگی نزدیک به ۱ میلی‌متر در سال دارند. آهنگ لغزش بروی کسل نایند به درازای ۲۹۰ کیلومتر، مابره‌گیری از سن نخی جابجایی‌های انباشتی به روش‌های کامپوزیتیک و لومینسانس نوری برآورده شده است. جابجایی‌های ریخت زمین‌ساختی بین  $۱ \pm ۹$  و  $۱۵ \pm ۱۹$  متر با سن یابی بین  $۰/۶ \pm ۱/۸$  و  $۰/۶ \pm ۱/۰$  هزار سال، آهنگ لغزشی برابر با  $0/۱۷ \pm ۱/۸$  میلی‌متر در سال را فراهم می‌کنند. نخستین برداشت پارینه لرزه‌شناختی در پهنه کسل نایند حاکی از رویداد دست کم چهار زمین لرزه بزرگ در گذر  $۱/۳ \pm ۱/۴$  و  $۱۷/۴$  هزار سال گذشته و دو زمین لرزه کمن‌تر (پیش از ۲۳- و  $۰/۵ \pm ۷/۰$  هزار سال) است. رویدادهای لرزه‌ای ماقبل و پیش از ماقبل آخر در کستره زمانی  $0/۴ \pm ۱/۵$  و  $۰/۴ \pm ۱/۷$  هزار سال رخ داده‌اند، در حالیکه آخرین زمین لرزه در گذر ۸۰۰ سال پیش شکل گرفته است. چنین الگوی بی‌سامان در توالی زمین لرزه‌ها، پیشنهاد دهنده رفتار لرزه‌ای نواختی است. اگرچه آخرین رویدادهای لرزه‌ای بروی کسل‌های نایند و دیشیر به ترتیب پس از سال ۱۳۰۰ میلادی و اندکی پیش از ۲- هزار سال گذشته رخ داده‌اند، بررسی‌های تکلیفی لرزه‌های تاریخی نشانی از رخداد این زمین لرزه‌ها بدست نمی‌دهد. این دو زمین لرزه نمونه‌های آشکاری بر کاستی کاتالوگ‌های لرزه‌ای تاریخی در ایران مرکزی به شمار آمده، و ارزیابی خطر زمین لرزه در نبود داده‌های زمین‌شناختی را با چالش روبرو می‌کنند. برداشت‌های پارینه لرزه‌شناختی نشان می‌دهند که ایران مرکزی به طور کامل بلوکی بی لرزه و استوار نبوده، و دگرشکل می‌تواند حاکم بر آن توان ایجاد خطر لرزه‌ای قابل توجهی را دارا است. بنابراین، تولید زمین لرزه‌های نادر و بزرگ از ویژگی‌های کسل‌های راستا لغز در ایران مرکزی و خاور ایران به شمار می‌آید، کستره‌ای که مجموع آهنگ‌های لغزش زمین‌شناختی از فلات ایران زمین تا دشت‌های بلوک افغان با داده‌های GPS در دسترس، همساز نمی‌نماید.



## Acknowledgements

This work benefited from the support of Geological Survey of Iran (GSI) and Université Pierre et Marie Curie (UPMC). GSI provided the logistic and financial assistance for the extensive field work and the OSL dating. I am grateful to the GSI president, Mohammad-Taghi Korehie, for his constant support. UPMC and INSU-CNRS provided complementary funding for the satellite imagery, field work, OSL dating, and  $^{36}\text{Cl}$  measurements.

The French Embassy in Tehran provided a 15-months scholarship grant, I acknowledge both the former and current Attaché Scientifique et Culturel, David Lambert and Pierre-André Lhôte, for their support to the cooperation between UPMC and GSI. Additional funding from Institut des Science de la Terre de Paris (ISTeP) and UPMC provided invaluable support allowing the completion of my PhD dissertation during a 27-months stay at ISTeP.

I am deeply grateful to my thesis supervisor, Bertrand Meyer. I have benefited from his excellent advice, constant and invaluable guidance, and support both in the field and at ISTeP. Bertrand fostered my intellect and allowed me to grow into an independent researcher. I am indebted to Bertrand for his encouragement and wonderful support during the last years. This work would have been impossible without the additional supervision of Michel Sébrier. Michel has been a great friend and a constant source of advice with endless patience since October 2006. In the last years, Michel has supported me not only by providing research advices, but also helped me to sort out the many administrative issues through the road to finish my thesis at UPMC. Many thanks also to Michel's family: Yolande, Lucie, Dominique, and Nick for their kindness and moral support during my stay in Paris. I got a tremendous support, even before the beginning of this work, from Hamid Nazari, my Iranian advisor and my friend from GSI. I am indebted to Hamid, my thesis project would have been impossible without his incentive collaboration.

I would like to express my sincere gratitude to the thesis committee members, Thierry Camelbeeck and Yann Klinger for their thoughtful reports and constructive comments on the dissertation, Olivier Lacombe and Andrea Walpersdorf for joining the defense committee and for thorough discussions.

I am also grateful to Andrew Murray from the Nordic Laboratory for Luminescence Dating, Aarhus University. I could not have completed my dissertation in due time without his support with the OSL measurements of the Lut region samples. Reza Sohbati and technical staff at Risø, specially Vicki Hansen, are thanked for their kindness and hospitality during my short visit at the

## Acknowledgements

---

Risø laboratory. I thank Morteza Fattahi for providing the OSL measurements along Dehshir and Anar faults.

Special thanks go to everyone who helped out with the field work: Mohammad Ali Shokri (without him, fieldwork would have been much more difficult and not nearly as much fun), Shahryar Solaymani Azad, Ali Rashidi, Kristell Le Dortz, Mojtaba Bassiri, Mohammad Javad Bolourchi, Manoochehr Ghorraishi, Morteza Talebian, Khaled Hessami, Mohammad Reza Ghassemi, Behnam Oveisi, Massoud Nazem Zadeh, Milad Ghanbari, Ahmad Agha Hosseini, Reza Tajik, Reza Darvish, Ali Nam Avar, Habib Ahmadi, Ali Samadian, and Ahmad Rassedi. I would also like to acknowledge Salman Abedini and Ali Abedini for their help during trenching on the Dehshir and Anar faults. H. Bani Assadi, M. Adhami, M. Takhtchin, M. Kord, H. Mokhtari, A. Hazratifar, R. Abdi, M. Salimian, M. Hashemloo, M. Akbari are thanked for their safe driving in the field.

I thank Robert Engdahl for giving me access to his updated EHB catalog, Ali Dehghani for providing access to the gravity field data in Central Iran and Lut block, and Bruno Vrielynck for helpful discussions on the paleogeography of Iran and adjacent areas.

I am also grateful to all the members of ISTeP, in particular to Philippe Huchon, Olivier Lacombe, Philippe Agard, Eric Barrier, Nicolas Bellahsen, Dovy Tristani, Sandrine Gay, Mari José Queyroy, Marc Bruneaux, Christophe Brunet, and Yamar Ripault; my office mates: Nico, Arnaud, and Alex; former PhD students and postdoc: Kristell, Vincent S., Vincent R., Céline, Mathieu, Hakim, Thomas F., Jeroen, Sirwan; and current students Ameen, Nafi, Leila, Dmitriy, Saya, Jordane, and Camille.

I take this opportunity to acknowledge all of the staff at “Le Service de Coopération et d’Action Culturelle” from the French Embassy in Tehran (specially Mrs. Mirbaha and Mrs. Ershadi), at CROUS de Paris (Mrs. Vanessa Szenwald and Mr. Mohamed Bouhdadi), and at Campus France (Mrs. Emilie Pollet and Ms. Mélanie Recuerda).

Finally, I would like to express my warmest gratitude to my parents-in-law and my spouse, Ailar. Her constant love, encouragement and support sustained me throughout these years.

Paris, 20 December 2013

*I dedicate this dissertation to the memory of my parents, whose unconditional love, support, and encouragement have always carried me through, and to my spouse whose love and confidence is a constant source of inspiration.*



# CONTENTS

<b>INTRODUCTION</b>	1
Dissertation Plan	7
<b>CHAPTER 1</b>	
<b>REGIONAL SETTING &amp; METHODOLOGY</b>	9
1.1. Geodynamic framework	10
1.2. Structural background and seismotectonic setting of Central Iran	16
1.3. Questions to address and methodology	27
1.3.1. Paleoseismology	28
1.3.2. OSL dating	31
1.3.2.1. Basis of the method	32
1.3.2.2. Sample collection	35
1.3.2.3. Measurements	36
<b>CHAPTER 2</b>	
<b>LARGE EARTHQUAKES ON THE DEHSHIR FAULT</b>	43
2.1. Introduction	44
2.2. First evidence for large earthquakes on the Deshir fault, Central Iran Plateau	45
Abstract	46
Introduction and geological setting	46
The trench site and the excavation	46
Trench stratigraphy	47
Seismic event identification	52
Conclusions	54
Acknowledgements	54
References	54
2.3. Refined OSL ages and implications for seismic history of the Dehshir fault	56
2.3.1. Site North	56
2.3.2. Site South	63

## CHAPTER 3

<b>LARGE EARTHQUAKES ON THE ANAR FAULT</b>	73
3.1. Introduction	74
3.2. New evidence for large earthquakes on the Central Iran plateau: palaeoseismology of the Anar fault	74
Summary	75
Introduction	75
Site selection and trench stratigraphy	77
OSL dating	79
Ages of trench units	82
Seismic event identification	83
Discussion and conclusions	86
Acknowledgments	87
References	87

## CHAPTER 4

<b>SLIP RATE &amp; PALEOSEISMOLOGY OF THE NAYBAND FAULT</b>	89
4.1. Introduction	90
4.2. Late Pleistocene-Holocene right-slip rate and paleoseismology of the Nayband fault, western margin of the Lut block, Iran	91
Abstract	92
1. Introduction	93
2. Geologic setting and seismotectonic background	95
3. Morphological offsets and slip rate estimate	100
3.1. Site North	100
3.2. Site South	104
3.3. Chronological tools: cosmic ray exposure and OSL dating	109
3.3.1. <sup>36</sup> Cl CRE dating	111
3.3.2. OSL dating	118
3.4. Interpretation and possible range of slip rate	119
4. Identification of past earthquakes on the Nayband fault	123
4.1. Geomorphic setting of the trench site	123
4.2. Trench stratigraphy	129
4.3. OSL dating and ages of stratigraphic units	133

4.4. Seismic event identification	140
5. Discussion and conclusions	151
5.1. Slip rate constraints and paleoearthquakes along the Nayband fault	151
5.2. The most recent earthquake on the Nayband fault versus the historical records	155
5.3. Implications for seismic hazard and kinematics in Central and Eastern Iran	156
Acknowledgments	159
References	159

## CHAPTER 5

<b>GENERAL DISCUSSION, CONCLUSIONS &amp; PERSPECTIVES</b>	173
5.1. Timing of latest alluvial fan emplacement and most recent incision in Central Iran	174
5.2. Late Pleistocene and Holocene slip rates of major strike-slip faults in Central Iran	176
5.3. Seismic behavior of major strike-slip faults in Central Iran	179
5.4. Historical seismic catalogs versus paleoseismic data	185
5.5. Geologic versus geodetic slip rates in Central and Eastern Iran	188
5.6. Studies in progress and perspectives	192
5.6.1. Paleoseismology of the Gowk fault	192
5.6.2. Slip rate along the Sistan fault system	195

<b>REFERENCES</b>	197
-------------------	-----

### Appendix A.1

Refining the OSL age of the last earthquake on the Dehshir fault, Central Iran

### Appendix A.2

Dating inset terraces and offset fans along the Dehshir fault (Iran) combining cosmogenic and OSL methods

### Appendix A.3

Holocene right-slip rate determined by cosmogenic and OSL dating on the Anar fault, Central Iran

# LIST OF FIGURES

## INTRODUCTION

- Figure 1:** Schematic diagrams of four models for slip accumulation along a fault. 4
- Figure 2:** Earthquake fatalities versus magnitude since 1900. 5

## CHAPTER 1

- Figure 1.1:** GTOPO30 digital topographic map of the Alpine-Himalayan orogenic belt. 11
- Figure 1.2:** Map of the major active faults in Iran. 12
- Figure 1.3:** Distribution of the ophiolitic complexes surrounding Central Iran. 13
- Figure 1.4:** GPS velocities in Eurasian-fixed reference frame with 95 per cent confidence ellipse for ZABO and YAZT sites. 15
- Figure 1.5:** LANDSAT Mosaic of the major active faults and the tectonic context of Central and Eastern Iran. 17
- Figure 1.6:** Distribution of instrumental and historical earthquakes in Central and Eastern Iran. 23
- Figure 1.7:** Fault-plane solutions of instrumentally recorded earthquakes ( $M \geq 4$ ) in Central and Eastern Iran during the period 1976 to 2013. 24
- Figure 1.8:** Schematic diagrams of common stratigraphic indicators of paleoearthquakes in strike-slip environments. 30
- Figure 1.9:** The basic principle of optically stimulated luminescence dating. 33
- Figure 1.10:** Energy-level diagram illustrating OSL process. 34
- Figure 1.11:** Schematic representation of the additive dose and regenerative methods to determine equivalent dose ( $D_e$ ). 38
- Figure 1.12:** Radial plots of measured doses from two OSL samples with different patterns of luminescence signals. 40

## CHAPTER 2

### *First evidence for large earthquakes on the Dehshir fault, Central Iran Plateau*

- Figure 1:** Simplified seismotectonic map of the Dehshir fault. 47
- Figure 2:** The excavation site. 48
- Figure 3:** 3-D perspective view of the excavation site. 49
- Figure 4:** Photo-mosaic of the southern wall of the trench, corresponding log, and simplified stratigraphiy. 51
- Figure 5:** Field photograph of the upper part of the trench and the east-facing scarp. 52
- Figure 6:** Evidence for coseismic deformations. 53

### *Refined OSL ages and implications for seismic history of the Dehshir fault*

- Figure 2.1:** SPOT satellite image along the southern part of the Dehshir fault. 59
- Figure 2.2:** Log of the southern wall of the Dehshir trench at site North and simplified stratigraphic correlation. 60
- Figure 2.3:** Geomorphic interpretation overlain on Quickbird satellite image of the Dehshir fault west of the Marvast Town. 64
- Figure 2.4:** Photomosaic and simplified log of the south wall of the Dehshir trench at site South. 66
- Figure 2.5:** Photomosaic and corresponding stratigraphic log of the deposits exposed to the east of the main fault zone in the Dehshir trench at site South. 68
- Figure 2.6:** Photomosaic (top) and interpretation (bottom) of the main fault zone exposed on the south wall of the Dehshir trench at site South. 69
- Figure 2.7:** Raw Quickbird satellite image (a) and interpretation (b) centered on the paleoseismic trench at the site South. 71

## CHAPTER 3

- Figure 1:** Landsat mosaic of the Anar fault area. 76
- Figure 2:** Field photograph of the Anar fault with emphasis on a 3-m right-lateral offset rill. 77
- Figure 3:** Quickbird imagery of the Anar fault trace centred on the palaeoseismological site. 78

<b>Figure 4:</b> Composite photomosaic of the sediments exposed in the Anar trench excavation.	79
<b>Figure 5:</b> Photomosaic of southern trench wall and corresponding log.	80
<b>Figure 6:</b> Photomosaic and interpretation of the main faulted zone.	83
<b>Figure 7:</b> Schematic view of possible restoration of trench log.	84
<b>Figure 8:</b> Evidence for the penultimate earthquake.	85
<b>Figure 9:</b> Five well-constrained OSL ages place bounds on the ages of the three palaeoearthquakes identified in the Anar trench exposure.	86

## CHAPTER 4

<b>Figure 1:</b> (a) Map of the major active faults in Central and Eastern Iran. (b) Simplified seismotectonic map of east-Central Iran and western Lut Block. (c) Raw Quickbird imagery of the Nayband fault.	94
<b>Figure 2:</b> Site North. (Left) Quickbird imagery of the Nayband fault across the Quaternary alluvial deposits and Neogene marls. (Right) Corresponding geologic map	101
<b>Figure 3:</b> (a) 3D perspective diagram of site North and surrounding area. (b) Perspective view highlights the recent offset streams 1 and 2 by the fault trace. (c-f) Field photographs of three dextral offsets.	103
<b>Figure 4:</b> Field photographs of two offset channels at the site North.	104
<b>Figure 5:</b> Site South. (a) Raw Quickbird imagery of a 100-m wide step-over along the segment NA2 of the Nayband fault. (b) Corresponding geologic map adapted from Quickbird imagery, field observations and regional geology.	105
<b>Figure 6:</b> A panoramic view of eastern part of site South (a) and corresponding interpretative sketch (b). (c) Schematic diagram highlights two beheaded wind-gaps (R1 and R2) south of the ongoing incision of active river (R0).	106
<b>Figure 7:</b> Field photograph (a) and interpretative sketch (b) of the northern stream (R0) west of the fault zone taken from R1 east of the fault zone.	107
<b>Figure 8:</b> Late Pleistocene-Holocene morphotectonic evolution of the landform of site South.	108
<b>Figure 9:</b> Plot of $^{36}\text{Cl}$ and OSL ages for alluvial surfaces at the sites North and South.	113
<b>Figure 10:</b> Distribution of in-situ $^{36}\text{Cl}$ CRE ages, modeled with no erosion and no	

inheritance, for the surface samples collected on the alluvial fan surfaces at the sites North and South, including (left panel) and discarding (right panel) outlier samples.	114
<b>Figure 11:</b> Frequency (top) and percentage (bottom) of the 88 right-lateral offsets smaller than 300 m measured along the 30-km long stretch of the segment NA2 of the Nayband fault.	120
<b>Figure 12:</b> Summary of right-slip rates deduced from geomorphic offsets combined with cosmogenic and OSL dating at the sites North and South.	122
<b>Figure 13:</b> Raw Quickbird imagery (a) and interpretation (b) of Central portion of the Nayband fault.	124
<b>Figure 14:</b> (a) Raw Quickbird imagery of a local pull-apart within releasing step-over along the Nayband fault. (b) Photograph looking south along W-facing scarp in the foreground and E-facing scarp farther south.	125
<b>Figure 15:</b> Fault trace north of the trench site.	126
<b>Figure 16:</b> Recent right-lateral offsets north of the trench site.	127
<b>Figure 17:</b> (a) Raw Quickbird satellite image of the fault trace south of the trench site. (b) High-resolution colored shaded relief map extracted from the DGPS survey of the trench site. (c) Corresponding topographic map.	128
<b>Figure 18:</b> Field photographs of the fault with clear scarps north (a) and south (b) of the pond and no discernable scarp (c) within the pond.	130
<b>Figure 19:</b> Log of the southern wall of the trench excavated across the Nayband fault.	131
<b>Figure 20:</b> Photo mosaics and corresponding stratigraphic logs of the sediments exposed in the trench excavation, with vertical positions of dated OSL samples.	137
<b>Figure 21:</b> Sedimentation rates calculated for the eastern and western stratigraphic logs.	139
<b>Figure 22:</b> Evidence for the most recent earthquake (event A).	142
<b>Figure 23:</b> Photomosaic and interpretive sketch close to the western limit of the MFZ.	143
<b>Figure 24:</b> Oblique photograph and interpretive sketch of two sandy dikes formed during event A, at the western end of the trench.	144
<b>Figure 25:</b> Liquefaction features on the southern and the northern walls in the western section of the trench exposure deposits giving evidence for event C.	146
<b>Figure 26:</b> Evidence for the penultimate and antepenultimate earthquakes.	148

<b>Figure 27:</b> Evidence for the fourth paleoearthquake (event D).	150
<b>Figure 28:</b> (Left) Distribution of the 67 measured right-lateral offsets smaller than 30 m plotted as a function of latitude along the 30-km-long stretch of the segment NA2 of the Nayband fault. (Right) Summed Gaussian probability density function of the plotted measured offset in (left).	154
<b>Figure 29:</b> Summary of late Quaternary slip rates and paleoseismic data presently available across Central Iran.	157

## CHAPTER 5

<b>Figure 5.1:</b> Probability density functions of the identified paleoearthquakes in this study along the Dehshir, Anar, and Nayband faults.	185
<b>Figure 5.2:</b> Archaeological sites with evidence of destructive earthquakes beyond the 4th century BC on the Iranian Plateau.	187
<b>Figure 5.3:</b> Summary of late Quaternary slip rates available across Central and Eastern Iran.	190
<b>Figure 5.4:</b> Simplified seismotectonic map of southwestern Lut Block.	193

# LIST OF TABLES

## CHAPTER 1

<b>Table 1.1:</b> Source parameters of the well-constrained fault-plane solutions of major instrumentally recorded earthquakes in Central and Eastern Iran.	26
---	----

## CHAPTER 2

### *First evidence for large earthquakes on the Dehshir fault, Central Iran Plateau*

<b>Table 1:</b> Description of the sedimentary units observed within the Dehshir trench.	50
--	----

<b>Table 2:</b> Optically Stimulated Luminescence ages for the Dehshir samples.	52
---	----

### *Refined OSL ages and implications for seismic history of the Dehshir fault*

<b>Table 2.1:</b> Summary of equivalent dose, annual dose rate, and OSL ages of the samples collected from two trenches at the sites North and South.	61
---	----

<b>Table 2.2:</b> Description of the sedimentary units observed within the Dehshir trench at site North.	62
--	----

<b>Table 2.3:</b> Summary of the measured fault planes and striae within the Dehshir trench at site South.	67
--	----

## CHAPTER 3

<b>Table 1:</b> Detailed description of the units observed in the trench excavated across the Anar fault.	79
---	----

<b>Table 2:</b> Calculated OSL ages on the Anar samples with their parameters.	80
--	----

## CHAPTER 4

<b>Table 1:</b> Source parameters of the well-constrained fault-plane solutions of instrumental earthquakes in east-Central Iran.	99
---	----

<b>Table 2:</b> Concentrations of <i>in-situ</i> produced $^{36}\text{Cl}$ and corresponding CRE ages.	116
<b>Table 3:</b> Chemical composition of the samples collected for $^{36}\text{Cl}$ dating.	117
<b>Table 4:</b> Summary of the OSL ages for the samples collected from the trench site and the site North along the Nayband fault.	134
<b>Table 5:</b> Detailed description of stratigraphic units in Nayband trench.	135
<b>Table A1:</b> Locations and corresponding measurements of geomorphic offsets along the second segment of the Nayband fault.	171

## CHAPTER 5

<b>Table 5.1:</b> Source parameters of the well-constrained fault-plane solutions of instrumental earthquakes in southwestern Lut Block.	194
--	-----



# INTRODUCTION

---

Active deformation in most regions of continental tectonics is typically accommodated within broad areas (e.g., *Molnar et al.*, 1973; *Jackson and McKenzie*, 1984; *Peltzer and Tapponnier*, 1988; *Avouac and Tapponnier*, 1993; *Jackson et al.*, 1995; *Peltzer and Saucier*, 1996; *England and Molnar*, 1997; *Thatcher et al.*, 1999; *King et al.*, 2004; *Wright et al.*, 2004; *Zhang et al.*, 2004; *Reilinger et al.*, 2006; *Meade*, 2007; *Devès et al.*, 2011), some authors favoring models of pervasive distributed deformation and others favoring models with localized deformation on a few major active fault systems. The question of how active fault systems accommodate regional strain in regions of active continental tectonics remains debated and there is no consensus on the type of the model to retain. Understanding how active deformations accommodate across continental lithosphere is heavily influenced by knowledge of reliable short-term (decadal) geodetic and short-term geologic ( $10^3$ - $10^5$  years) data sets along active faults.

The available comparisons of short-term geodetic and longer-term geologic rates show different degrees of consistency. Several studies have confirmed that rates of slip are consistent over geodetic and geologic timescales. As such, several studies along major plate-boundaries such as the San Andreas and the North Anatolian faults, and in the eastern California shear zone indicate a consistency between the geodetic and geologic deformation rates (*Sieh and Jahns*, 1984; *Argus and Gordon*, 2001; *Hubert-Ferrari et al.*, 2002; *Dixon et al.*, 2003; *Spinler et al.*,

2010; *Frankel et al.*, 2011; *Lindsey and Fialko*, 2013). Conversely, several other studies mostly along intracontinental faults indicate temporal slip variations through the geologic and geodetic timescales (e.g., *Friedrich et al.*, 2003; *Niemi et al.*, 2004; *Chevalier et al.*, 2005; *Dolan et al.*, 2007; *Oskin et al.*, 2008; *McGill et al.*, 2009; *Ganev et al.*, 2012; *Gold et al.*, 2013). As a result, extrapolating geodetic deformation rates over Quaternary timescales in regions where geologic slip rates are unknown is highly debated.

Resolving distribution of short-term geologic deformation across major intracontinental faults throughout late Quaternary is critical to understand how active deformation is accommodated in the continents. In addition, knowledge of the geologic slip rates is key point to assess the contribution of individual faults to the regional active deformation (e.g., *Van Der Woerd et al.*, 2000, 2002; *Frankel et al.*, 2007a). Nevertheless, well-determined offsets associated with well-constrained ages are scant on many intracontinental active faults so that a valuable quantitative piece of information, the geologic slip rate, is often missing (e.g., *Tapponnier et al.*, 2001).

Considering intracontinental strike-slip faults, several well-documented active tectonic studies suggest slip rates ranging from a few tenth of millimeter up to more than a centimeter over late Quaternary timescales. For faults with moderate to high rates of slip, more than 5 mm yr<sup>-1</sup>, one can list the following examples. *Daëron et al.* (2004) using cosmogenic <sup>36</sup>Cl dating of left-laterally offset alluvial fans at two sites along the Yammoûneh fault (Lebanon), the main strike-slip branch of the Levant fault system, proposed a slip rate of  $5.1 \pm 1.3$  mm yr<sup>-1</sup> averaged over the last 25 ka. *Wesnousky et al.* (2012) used cosmogenic <sup>10</sup>Be dating to date right-laterally offset moraines along the Boconó fault in the Mérida Andes (Venezuela), and documented a right-slip rate of  $\sim <5.5-6.5$  mm yr<sup>-1</sup> over the last 15 ka. *McGill et al.* (2009) used radiocarbon dating to date a left-laterally offset channel along the Garlock fault in California, and proposed a slip rate of 7.6 mm yr<sup>-1</sup> averaged over the Holocene. *Van Der Woerd et al.* (2002) using <sup>26</sup>Al, <sup>10</sup>Be, and <sup>14</sup>C dating of several offset risers in six sites along the Kunlun fault, in northeastern Tibet, documented left-lateral slip rates of  $11.5 \pm 2.0$  mm yr<sup>-1</sup> over the last 37 ka. *Matmon et al.* (2006) used cosmogenic <sup>10</sup>Be dating to date right-laterally offset moraines at five sites along the Denali fault in Alaska, and documented a right-slip rate of 7.8-13.8 mm yr<sup>-1</sup> averaged over the last 18 ka.

For faults with low to moderate slip rates, mostly less than  $5 \text{ mm yr}^{-1}$ , one can mention to the following examples. *Li et al.* (2009) surveyed offset terrace risers at three sites along the eastern part of the Haiyuan fault in northeastern Tibet, and using  $^{14}\text{C}$  dating of the terrace risers they proposed an average slip rate of  $4.5 \pm 1 \text{ mm yr}^{-1}$  over the Holocene. *Frankel et al.* (2007b) studied two sites along the Death Valley-Fish Lake Valley fault zone in the eastern California shear zone, and using cosmogenic  $^{10}\text{Be}$  dating of two right-laterally offset alluvial fans they estimated a right-slip rate of  $\sim 2.5\text{-}3 \text{ mm yr}^{-1}$  over the last 105 ka. *Rizza et al.* (2011b) using cosmogenic  $^{10}\text{Be}$  dating of left-laterally offset terrace risers and streams at four sites along the Bogd fault in Mongolia, proposed a slip rate of  $<1 \text{ mm yr}^{-1}$  over the past 200 ka. *Le Dortz et al.* (2011) recognized several right-laterally offset streams and terraces at two sites along the Dehshir fault in Central Iran, and using cosmogenic  $^{10}\text{Be}$ ,  $^{36}\text{Cl}$ , and optically stimulated luminescence dating they proposed a right-slip rate of  $0.9\text{-}1.5 \text{ mm yr}^{-1}$  averaged over the last 270 ka (see appendix A.2).

In general, low rates of slip along intracontinental faults considered as input favoring models with distributed deformation while high slip rates are often taken to justify models with localized deformation, where strain is mostly concentrated in a narrow zone (e.g., *Li et al.*, 2009).

The geomorphologic studies also provide essential information for assessing the regional seismic hazard. Indeed, active fault mapping, measurement of offset geomorphic features, and dating offset features, help estimating slip rates, and provide an important contribution for better understanding of the seismic behavior of active faults and of the seismic hazard they pose. Understanding the way earthquake ruptures repeat through time for a given fault is of primary interest for earthquake mechanics as well as for assessment of regional seismic hazard. Several models have been proposed to describe the spatial and temporal patterns of earthquake recurrence.

*Schwartz and Coppersmith* (1984) proposed three possible models for the patterns of coseismic slip along a fault. The first model considers variable earthquake magnitude as well as slip distribution along the fault (variable-slip model, Figure 1a). In this model, the amounts of displacement associated at any given point and position of the rupture segment vary through time and between successive earthquakes. However, due to the lack of permanent segments, the slip is distributed evenly along the fault so that the long-term slip rate at any given point remains

constant. The second model, called uniform-slip model, was introduced by *Sie*h (1981). This model suggests that a large earthquake with the same slip distribution occurs periodically along the same segment of the fault, with cumulative displacement being leveled by more frequent moderate earthquakes to achieve a constant long-term slip rate (Figure 1b). Accordingly, at any given point the coseismic slip is constant from one large earthquake to the next, although displacement can vary along strike. The third model, called characteristic earthquake model involves repetitive cycles of displacement with similar earthquake size and displacement at a given point from one earthquake to the next (Figure 1c). The coseismic displacement of the characteristic earthquake model varies along the length of the fault, hence the slip rate varies along the fault, and ruptures on adjacent fault segments may overlap (dashed line in Figure 2c) to fill the slip deficit. More recently, another model, the patch-slip model, was proposed by *Sie*h (1996) in which large earthquakes are also occurring in the characteristic earthquake type, but the variable total displacement is leveled by moderate earthquakes producing individual fault segments (patches) with limited coseismic slip (Figure 1d).

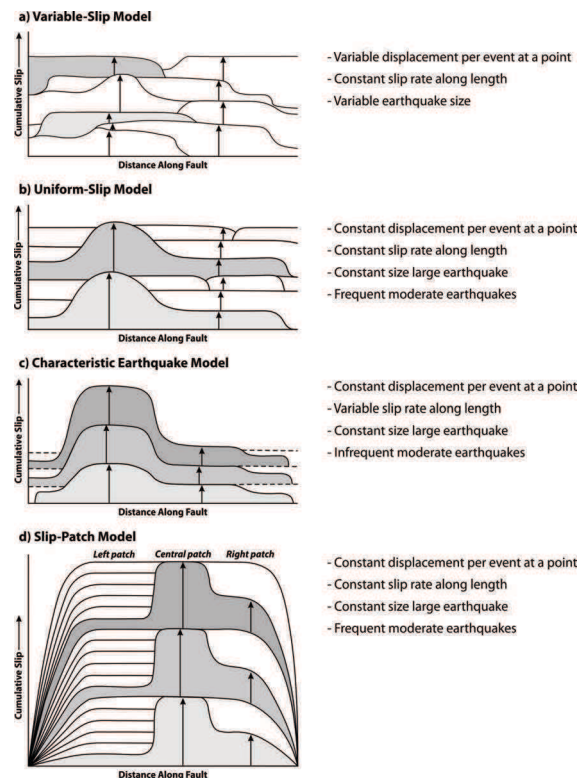


**Figure 1.** Schematic diagrams of four models for slip accumulation along a fault. Models for variable slip (a), uniform slip (b), and characteristic earthquake (c) are modified after *Schwartz and Coppersmith* (1984). The slip-patch model (d) is redrafted from Figure 7 of *Sie*h (1996).

The general agreement is that the characteristic earthquake model, often used for seismic hazard assessment, is too simplistic to depict the mechanics of earthquake ruptures. Although more sophisticated models have been proposed to design the temporal and spatial patterns of earthquake recurrence, the lack of reliable data covering several seismic cycles for a given fault make difficult to test, and hence validate any of these models. In many regions, available seismic records extend back only several centuries and many active faults have not record of destructive seismic events during historical period. Nevertheless, several recent devastating earthquakes have occurred on faults that had not generated a surface-rupturing earthquake in historical times (Figure 2).

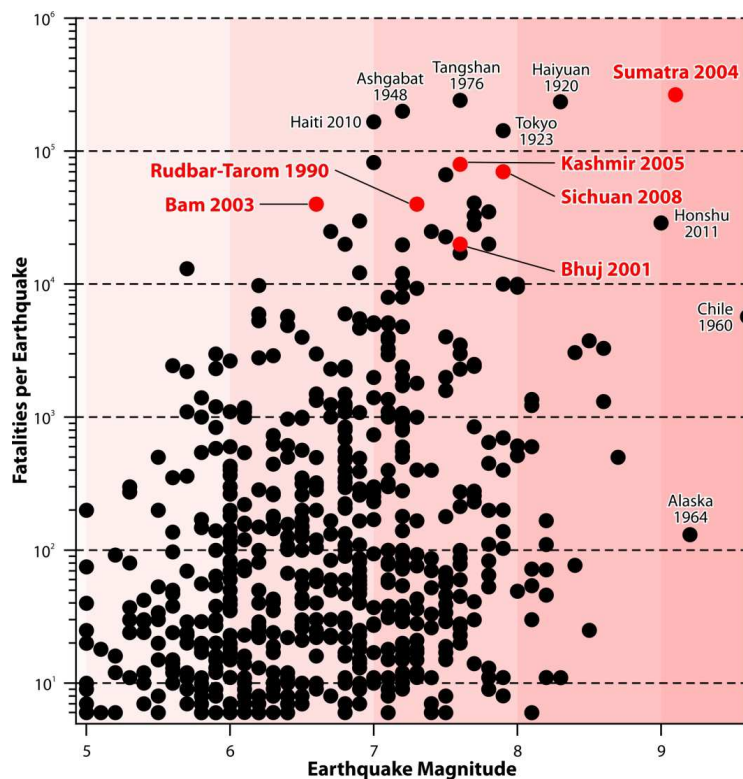


**Figure 2.** Earthquake fatalities versus magnitude since 1900. Recent destructive earthquakes without known historical surface-rupturing event are shown in red. The very largest and very high fatality earthquakes are named in black. Updated from *Bilham* (2010).

For instance, 1990,  $M_w$  7.3, Rudbar-Tarom earthquake with 40,000 dead in Iran (e.g., *Berberian et al.*, 1992); 2001,  $M_w$  7.6, Bhuj earthquake with 20,000 dead in India (e.g., *Wesnousky et al.*, 2001); 2003,  $M_w$  6.6, Bam earthquake with 40,000 dead in Iran (e.g., *Talebian et al.*, 2004; *Jackson et al.*, 2006); 2004,  $M_w > 9.0$ , Sumatra-Andaman earthquake with >250,000 dead in Indonesia (e.g., *Borrero*, 2005; *Sieh*, 2006); 2005,  $M_w$  7.6, Kashmir earthquake with

80,000 dead in Pakistan (e.g., *Avouac et al.*, 2006; *Pathier et al.*, 2006); and 2008,  $M_w$  7.9, Sichuan/Wenchuan earthquake with 69,000 dead in China (e.g., *Wang et al.*, 2009; *de Michele et al.*, 2010), all occurred on fault segments without any historical record of significant surface-rupturing earthquake.

Even in the countries with long historical seismic records lasting for several thousands of years, such as China and Iran, the available seismic catalogs might not be representative of the earthquake potential for a given region. Moreover, in regions experiencing very low, if any, seismic activity such a lack of seismicity does not rule out the possibility for occurrence a large earthquake in the future. Indeed, segments of active faults that have generated large earthquakes in the past may currently show very low/any seismic activity. Therefore, the lack of seismic records may lead to underestimate the regional seismic hazard. All the considerations above highlight the need for working out the behavior of active faults over longer periods and through several seismic cycles, hence the need for paleoseismic studies.

Indeed, paleoseismic studies extend back the seismic history of a given fault beyond the historical seismic catalogs (e.g., *Sieh*, 1978; *Yeats and Prentice*, 1996; *McCalpin*, 2009). Paleoseismic studies allow detecting past surface ruptures, and dating the identified earthquakes. This latter can be constrained by determining the respective ages of the material deposited before and after the earthquakes (see Chapter 1).

This dissertation uses geomorphic and paleoseismic approaches as well as cosmogenic exposure and optically stimulated luminescence techniques to address two fundamental aspects of active deformation in the Central Iran Plateau: slip rates and seismic behavior. Central Iran is a continental domain where distributed strike-slip faulting plays a key role in the accommodation of the regional active deformation resulting from the Arabia-Eurasia convergence. In the last years several studies have striven for describing geometry, kinematics, and slip rates of the strike-slip faults in Central Iran for a better understanding of the role of these faults to accommodate regional strain and then to refine the assessment of the regional seismic hazard (e.g., *Walker and Jackson*, 2002, 2004; *Meyer and Le Dortz*, 2007; *Walker et al.*, 2009, 2010a, 2010b; *Allen et al.*, 2011; *Le Dortz et al.*, 2011). However, the general picture is far from being complete, mostly due to the lack of Quaternary chronological dating and multiplicity of the active faults.

In addition, the lack of seismicity along the major strike-slip faults inside Central Iran and the lack of paleoseismic data make it impossible to assess the seismic behavior of the faults. The available geodetic data (*Vernant et al.*, 2004; *Masson et al.*, 2005, 2007) indicate that Central Iran is experiencing a coherent motion and limited internal deformation. This may suggest that the strike-slip faults in Central Iran accommodate relatively low rates of deformation. Therefore, performing paleoseismic studies is the only way to document the seismic behavior of these strike-slip faults which could be characterized by low rates of slip, and hence long recurrence intervals that may exceed the time span covered by historical catalogs.

## Dissertation Plan

The main subject of the five chapters presented in this dissertation is to determine the late Pleistocene-Holocene right-lateral slip rates and seismic behavior of the major strike-slip faults in Central Iran through the last seismic cycles.

**Chapter 1** provides the general geodynamic framework of Iran territory with emphasis on the structural background and the seismotectonic setting of Central Iran. A brief introduction to paleoseismology and a description of the most common stratigraphic indicators used to detect past earthquakes are also presented as well as the basic principles and general concepts of OSL dating method.

**Chapter 2** presents paleoseismic investigations along the Dehshir fault and gives evidence for the occurrence of several large earthquakes at two sites about 30 km apart. The first part of the chapter is a paper published by *Nazari et al.* (2009a) in *Terra Nova*. Six of the OSL ages that were previously published have been refined, allowing a better constraint on the age of the last earthquakes as well as on the recurrence interval. These refinements are briefly summarized at the end of the chapter.

**Chapter 3** investigates the late Pleistocene and Holocene seismic behavior of the Anar fault using paleoseismic studies along the central part of the fault. A brief introduction precedes a paper published by *Foroutan et al.* (2012) in *Geophysical Journal International*.

**Chapter 4** is a comprehensive study of the Nayband fault that has been submitted to *Journal of Geophysical Research*. The submitted manuscript investigates the right-lateral slip rate of the

fault using several geomorphic offset features at two sites dated by cosmogenic  $^{36}\text{Cl}$  and OSL techniques and its seismic behavior over the last 20 ka within a trench excavated across the fault.

**Chapter 5** summarizes briefly the main results and conclusions of this study and investigates the implications of these results on the active deformation pattern of Central Iran as well as on the regional seismic hazard in Central and Eastern Iran.

Three additional publications which are not included in the main corpus of the dissertation are given in the following appendixes.

### **Appendix A.1**

Fattahi, M., Nazari, H., Bateman, M. D., Meyer, B., Sébrier, M., Talebian, M., Le Dortz, K., Foroutan, M., Ahmadi Givi, F., Ghorashi, M. (2010), Refining the OSL age of the last earthquake of the Dhesir fault, Central Iran, *Quat. Geochronol.*, 5, 286-292, doi:10.1016/j.quageo.2009.04.005.

### **Appendix A.2**

Le Dortz, K., Meyer, B., Sébrier, M., Braucher, R., Nazari, H., Benedetti, L., Fattahi, M., Bourlès, D., Foroutan, M., Siame, L., Rashidi, A., and M. D. Bateman (2011), Dating inset terraces and offset fans along the Dehshir Fault (Iran) combining cosmogenic and OSL methods, *Geophys. J. Int.*, 185, 1147-1174.

### **Appendix A.3**

Le Dortz, K., Meyer, B., Sébrier, M., Nazari, H., Braucher, R., Fattahi, M., Benedetti, L., Foroutan, M., Siame, L., Bourlès, D., Talebian, M., Bateman, M. D., and M. Ghorashi (2009), Holocene right-slip rate determined by cosmogenic and OSL dating on the Anar fault, Central Iran, *Geophys. J. Int.*, 179, 700-710.

# CHAPTER 1

## **REGIONAL SETTING & METHODOLOGY**

---

## 1.1. Geodynamic framework

Iran territory belongs to the diffuse and widespread Alpine-Himalayan orogenic belt (Figures 1.1 and 1.2). Iran territory is made of a continental domain, roughly triangular-shaped, including several terranes bounded by three major ophiolite sutures that represent former oceanic domains between these continental terranes. Iran block, main part of the Iran territory, is bounded by an E-striking, ill-defined, Paleotethys suture to the north, which extends roughly eastward along the north of the present-day Alborz and south of the Kopeh Dagh Mountain ranges. The more continuous NW-striking Zagros suture, which parallels the Main Zagros Thrust (MZT), forms its SW boundary. The Zagros suture has been formed as a consequence of collision between the Iran block and the Arabian platform during Late Eocene-Oligocene (e.g., *Berberian and King, 1981; Agard et al., 2005; Allen and Armstrong, 2008; Karagaranbafghi et al., 2012; Mouthereau et al., 2012*), following the closure of the Neotethys Ocean. The NNW-striking Sistan suture that is localized roughly along the Sistan Fault Zone (SFZ) forms its eastern boundary. The Sistan suture has been formed as a result of the welding of the Iran and Afghan blocks by Middle Eocene (e.g., *Camp and Griffis, 1982; Tirrul et al., 1983*). There, two ophiolitic complexes of Cretaceous (Ratuk) and Eocene (Neh), remnants of the oceanic lithosphere of the Sistan Ocean, are separated from the Sefidabeh fore-arc basin to the east by a major right-lateral strike-slip fault zone, the SFZ.

This Iran block drifted northward from Gondwana during the latest Paleozoic to be subsequently welded to Eurasia by Late Triassic. The collision occurred during the Eo-Cimmerian event, which corresponds to the closure of the Paleo-Tethys Ocean as a consequence of northward subduction of the Paleo-Tethys oceanic crust under Eurasia (Turan plate) (e.g., *Boulin, 1988; Alavi, 1991; Zanchi et al., 2009*). The Eo-Cimmerian event is marked by a regional unconformity sealed by deposition of the Late Triassic-Jurassic deposits (e.g., *Stöcklin, 1974; Fürsich et al., 2009; Zanchetta et al., 2009*). Although the Iran block is composed of several terranes, paleomagnetic data indicate that these different terranes display a common drift pattern (*Besse et al., 1998; Muttoni et al., 2009*). These paleomagnetic studies indicate that the Iran block was part of Gondwana in the southern hemisphere before the latest Paleozoic. The Gondwanian affinity of the Iran block is also supported by the geological (e.g., *Stöcklin 1974*;

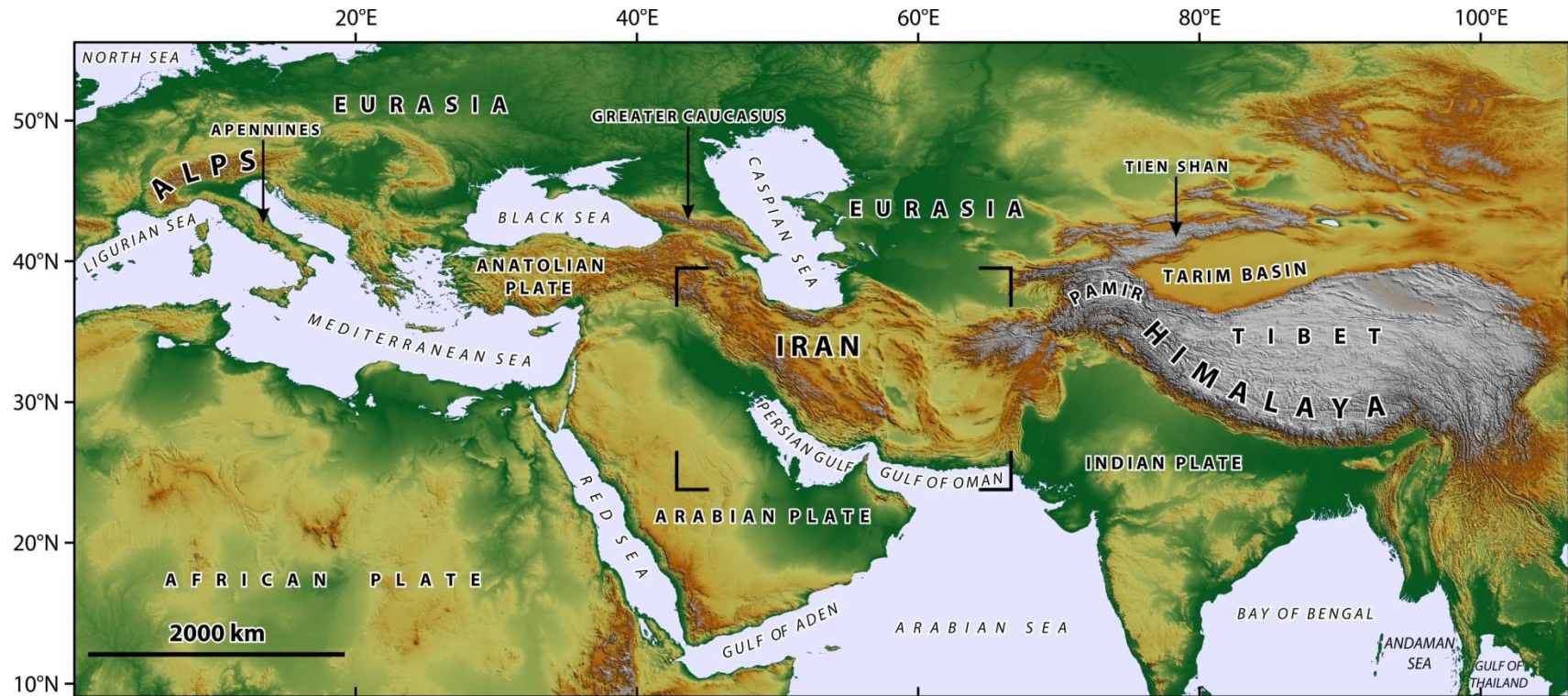


**Figure 1.1.** GTOPO30 digital topographic map of the Alpine-Himalayan orogenic belt showing the location of Iran territory in the central part of the deformation belt. Iran territory bounds the northern and southern limits of the Alpine-Himalayan deformation between the longitudes of 44°E and 62°E. The northward motion of the Arabian plate away from Africa as a result of the opening of the Red Sea and Gulf of Aden causes the Arabia-Eurasia convergence. Black corners denote the outline of Figure 1.2.

*Berberian and King, 1981*) and geochronological (*Hassanzadeh et al., 2008*) similarities of their late Neoproterozoic-Early Cambrian crystalline basements.

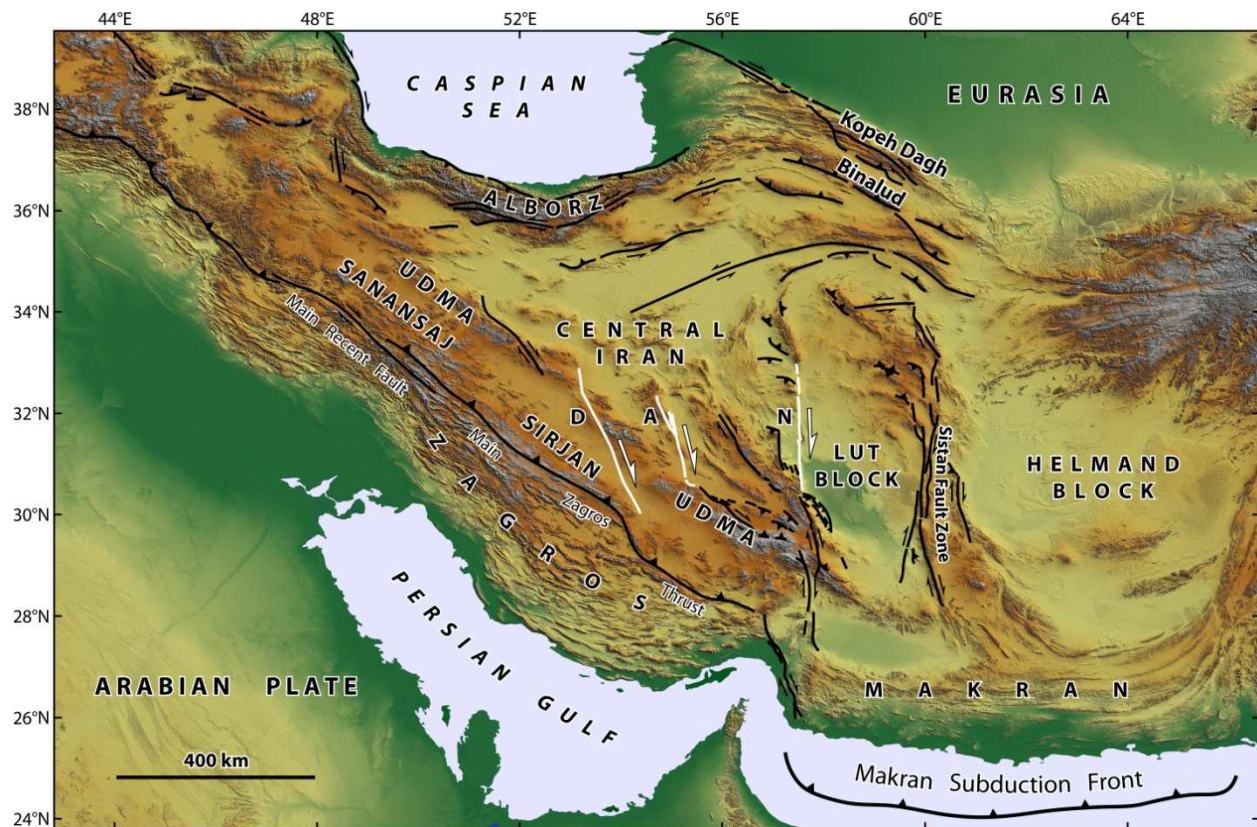


**Figure 1.2.** Map of the major active faults in Iran superimposed on the 90-m SRTM Digital Elevation Model. White lines denote active strike-slip faults slicing Central Iran, which are investigated throughout this study. A, Anar fault; D, Dehshir fault; and N, Nayband fault.

Inside this composite Iran block, two other ophiolite sutures (Sabzevar and Nain-Baft) are considered as former back-arc basins that opened and closed along the Mesozoic Eurasia margin (Figure 1.3; e.g., *Rossetti et al., 2010*; *Agard et al., 2011* and references therein). These two short-lived, back-arc basins are thought to have opened during Late Cretaceous and closed in Paleocene. These geodynamic processes are considered as a result of Jurassic-Cretaceous tectonic events such as the Neo-Cimmerian one that is well expressed by an angular unconformity between Cretaceous and older units. The Sabzevar ophiolite, a remnant of the Mesozoic oceanic crust, has been emplaced on the northern margin of the Neotethys following the NE-dipping subduction of the Sabzevar oceanic crust under the Eurasia. The NW-SE Nain-Baft ophiolite emplaced as a result of oblique eastward subduction of the Neotethys under the Iran block. The most pronounced topographic feature of the Iranian plateau, the Urumieh-

Dokhtar magmatic arc (UDMA on Figure 1.2), is made of calc-alkaline magmatic rocks paralleling the Nain-Baft ophiolite. This magmatic arc assemblage formed as a consequence of eastward subduction of the Neotethys oceanic crust under Sanandaj-Sirjan and Central Iran (e.g., *Bernerian and Berberian*, 1981). Emplacement of the UDMA mostly took place during Eocene-Oligocene, after emplacement of the Nain-Baft suture and prior to the final closure of the Neotethys, hence emplacement of the MZT suture.

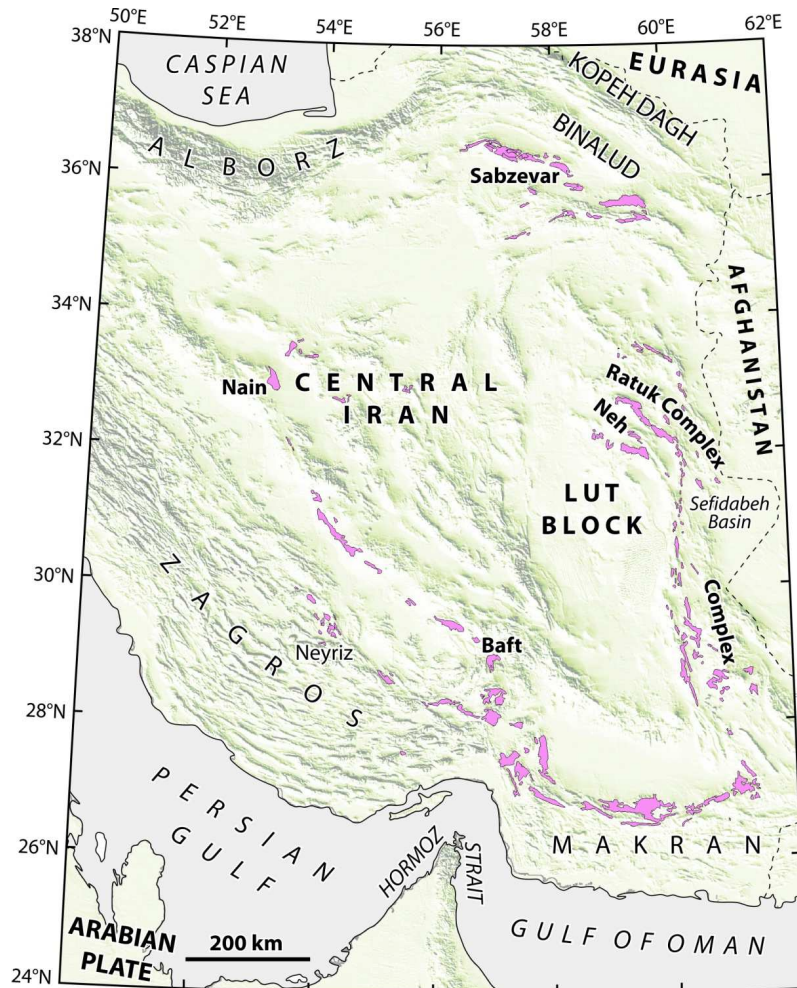


**Figure 1.3.** Distribution of the ophiolitic complexes surrounding Central Iran, after *Emami et al.* (1993).

Such a long-lasting and rather complex tectonic history that involves several opening and closure of oceanic domains, hence collision events, has been followed by a strike-slip tectonic regime now prevailing inside the Iran block. It is indeed commonly accepted that the present-day widespread strike-slip faulting represents the last stage of the Arabia-Eurasia collision in response to the northward movement of the Iran block with respect to the Eurasian

Helmand/Afghan block (e.g., *Tirrul et al.*, 1983; *McQuarrie et al.*, 2003). However, there is no consensus on the onset of the strike-slip tectonics in Iran. Some authors have proposed an age of 3-7 Ma, based on the time needed to extrapolate present-day GPS-derived slip rates to achieve the total cumulative fault displacement (e.g., *Allen et al.*, 2004; *Walker and Jackson*, 2004). *Shabanian et al.* (2009) proposed an age of  $\sim 4$  Ma, based on extrapolating Quaternary slip rates to achieve the cumulative horizontal displacements within the Kopeh Dagh Mountains. *Hollingsworth et al.* (2006) proposed an earlier date of 10 Ma, based on extrapolating present-day slip rates derived from GPS to achieve the total cumulative strike-slip offsets in NE Iran. *Agard et al.* (2011) also proposed a similar date of 10 Ma based on geodynamic reconstructions in SW Iran. *Meyer and Le Dortz* (2007) proposed a time range between 8-22 Ma by extrapolating short-term geologic (Holocene) slip rates to achieve the total cumulative fault offsets in Central and Eastern Iran.

The northward movement of Arabia respect to Eurasia and the internal deformation of the Iran territory has been pictured by two years (*Vernant et al.*, 2004) and six years (*Masson et al.*, 2007) of GPS campaigns (Figure 1.4). These data show a northward motion of the Arabian Plate relative to Eurasia at a rate of  $22 \pm 2$  mm yr<sup>-1</sup> at the longitude of 50.6°E. Since the GPS sites east of the Sistan suture (YAZT and ZABO) do not show any significant movement relative to Eurasia, *Masson et al.* (2005) conclude that the Afghan block belongs to the stable Eurasia, as already suggested by *Jackson and McKenzie* (1984) on the basis of the abrupt decrease in seismic activity east of 61°E. According to these geodetic studies, the Arabia-Eurasia convergence is mostly accommodated at the Iran block borders by the Zagros ( $6.5 \pm 2$  mm yr<sup>-1</sup>) to the southwest and the Alborz ( $8 \pm 2$  mm yr<sup>-1</sup>) to the north of the collision zone, by the Makran subduction zone ( $19.5 \pm 2$  mm yr<sup>-1</sup>) to the southeast and by the Kopeh Dagh Mountains ( $6.5 \pm 2$  mm yr<sup>-1</sup>) to the east of the collision zone (*Vernant et al.*, 2004). Accordingly, the Central Iran block is experiencing a coherent motion and a limited internal deformation, less than 2 mm yr<sup>-1</sup> (*Vernant et al.*, 2004; *Reilinger et al.*, 2006), and is often described as a rigid block (e.g., *Jackson and McKenzie*, 1984; *Jackson et al.*, 1995; *Vernant et al.*, 2004; *Walpersdorf et al.*, 2006).

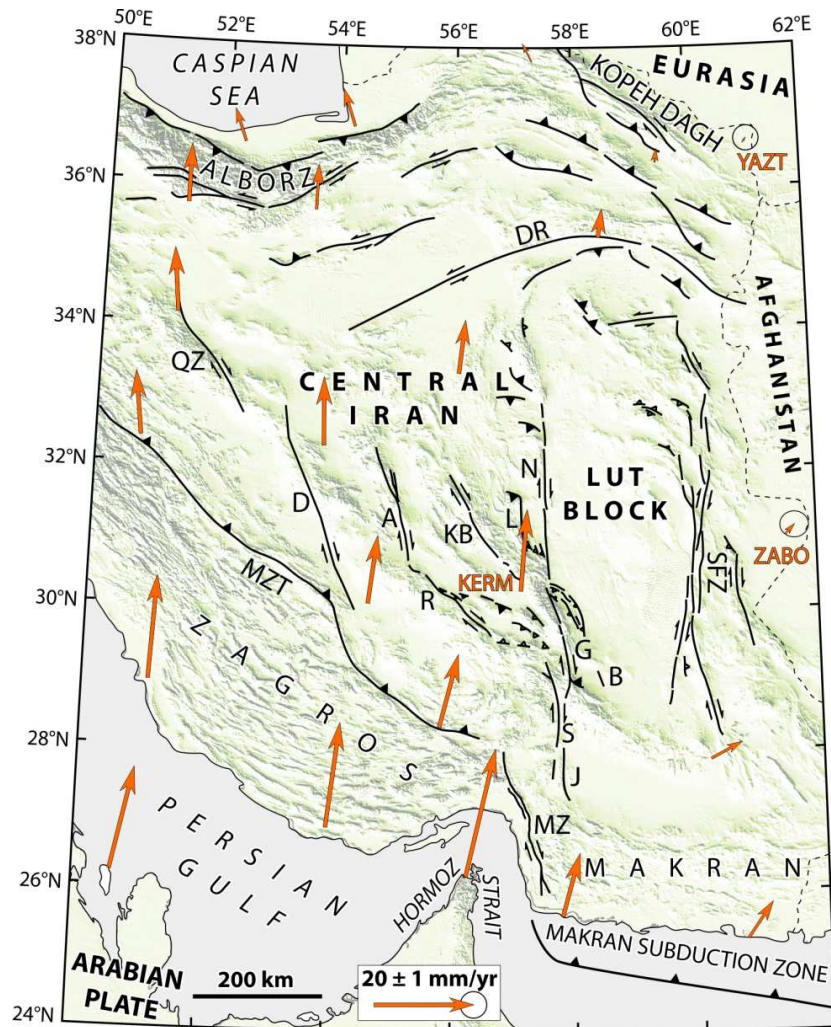


**Figure 1.4.** GPS velocities (orange arrows) in Eurasian-fixed reference frame with 95 per cent confidence ellipse for ZABO and YAZT sites from *Vernant et al. (2004)* and *Masson et al. (2007)*. The velocity of ZABO and YAZT sites does not present significant motion relative to Eurasia. A, Anar fault; B, Bam fault; D, Dehshir fault; DR, Doruneh fault; G, Gowk fault; J, Jiroft fault; KB, Kuh Banan fault; L, Lakar Kuh fault; MZ, Minab-Zendan fault system; MZT, Main Zagros Thrust fault; N, Nayband fault; QZ, Qom-Zefreh fault; R, Rafsanjani fault; S, Sabzevaran fault; and SFZ, Sistan Fault Zone.

The way the Arabia-Eurasia convergence is accounted for west (broad collision zone) and east (almost narrow subduction zone) of  $57^{\circ}\text{E}$  induces an overall differential motion between Central and Eastern Iran. This differential motion is accounted across the Lut block and amounts to  $16 \pm 2 \text{ mm yr}^{-1}$  of N-S, right-lateral shear at  $30.5^{\circ}\text{N}$  (difference between the vectors KERM and ZABO, Figure 1.4). The Lut block is bounded by the right-lateral, N-striking Sistan fault zone to the east and the Nayband fault to the west. On the basis of the GPS-derived velocity field

that is obtained from GPS campaigns between 1988 and 2005, and using seismic records, *Reilinger et al.* (2006) proposed an elastic block model that suggests a northward movement of the Lut block respect to the Eurasia at a rate of  $7 \text{ mm yr}^{-1}$ . However, neither the distribution of the dextral shear between the eastern and western faulted Lut borders, nor the along-strike evolution along a given border, is well established. By contrast, west of the Lut block, the limited internal deformation evidenced by GPS appears challenged by the slip rates of the faulting inner the Central Iran Plateau. Indeed, well-constrained late Quaternary slip-rates of the Dehshir, Anar and Rafsanjan strike-slip faults are respectively of  $1.2 \pm 0.3 \text{ mm yr}^{-1}$  (*Le Dortz et al.*, 2011),  $0.8 \pm 0.1 \text{ mm yr}^{-1}$  (*Le Dortz et al.*, 2009; *Foroutan et al.*, 2012), and  $0.4 \text{ mm yr}^{-1}$  (*Fattahi et al.*, 2011). The dextral slip-rate of the more easterly trending Kuh Banan fault is estimated between  $1\text{-}2 \text{ mm yr}^{-1}$  (*Allen et al.*, 2011; *Walker and Allen*, 2012) and, though their rates remain to establish, several active thrust faults have also been documented within the interiors of the Central Iran Plateau (*Walker et al.*, 2010a).

## 1.2. Structural background and seismotectonic setting of Central Iran

Central Iran is a wide region, generally, bounded between two belts, the prominent active Alborz Mountains to the north and the Sanandaj-Sirjan to the south, a narrow smoothed belt paralleling the MZT, and incorporated within the Iranian Plateau (Figure 1.2). The Central Iran domain sometimes referred as CIB (Central Iran Block; *Jackson et al.*, 1995; *Besse et al.*, 1998; *Vernant et al.*, 2004) is experiencing low GPS deformation rates and is dominated by intracontinental active strike-slip faulting. Several N-striking, right-lateral strike-slip faults accommodate most of the dextral shear induced by the differential accommodation of the Arabia-Eurasia convergence between the Zagros collision domain to the west and the active Makran subduction zone to the east. Such dextral faults locate within a wide zone encompassing the western Central Iran Plateau (Dehshir and Anar faults) and the Lut borders (Nayband, Gowk, West Neh, Kahurak, East Neh, Assaghi, Nosratabad and Zahedan faults, Figure 1.5). The available information on the long-term strain distribution of the major strike-slip faults inside Central and Eastern Iran is summarized in the following paragraphs.

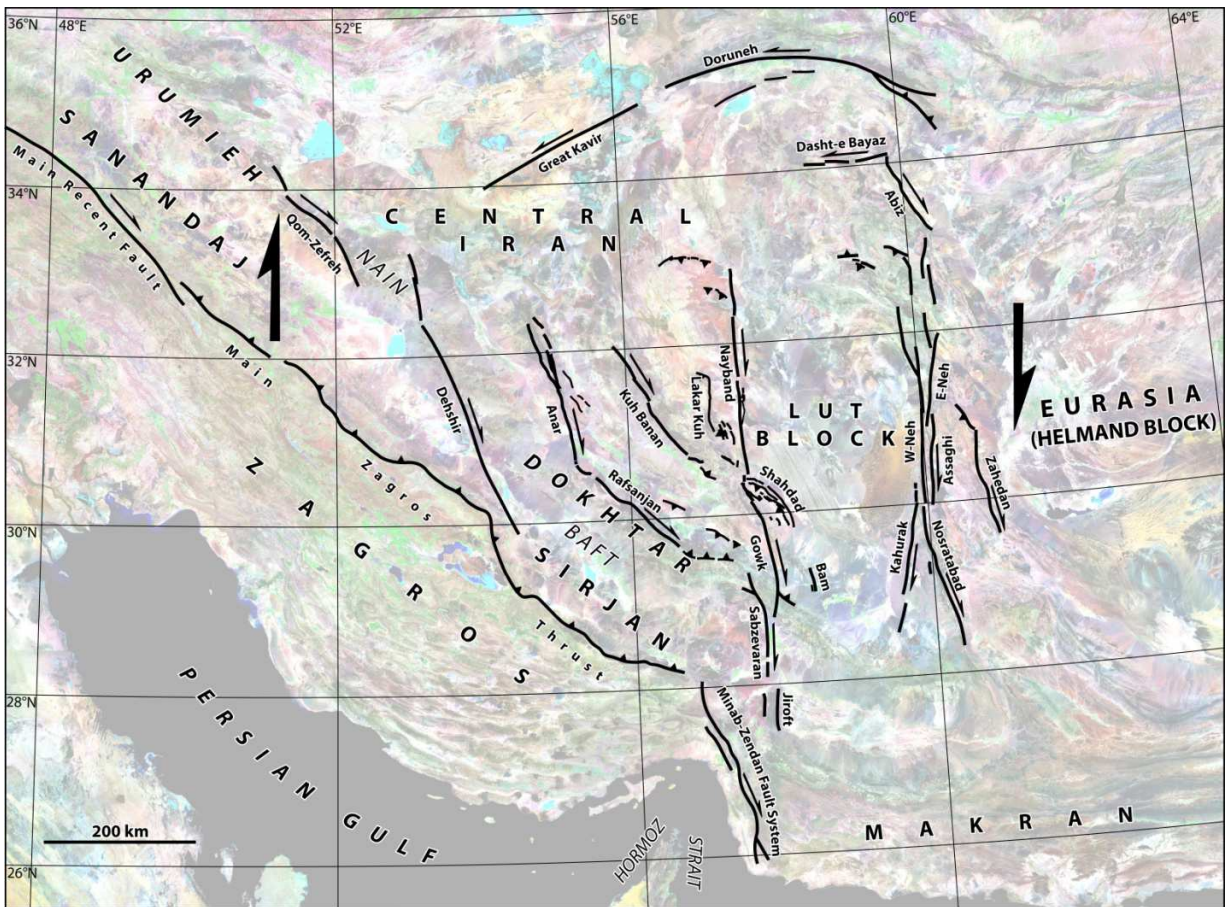


**Figure 1.5.** LANDSAT Mosaic of the major active faults and the tectonic context of Central and Eastern Iran. Black arrows show generalized dextral shear between Central Iran and Helmand block (stable Eurasia) as determined from the geodetic data (Vernant *et al.*, 2004; Masson *et al.*, 2005, 2007).

To the north, at 35°N, an E-striking, left-lateral strike-slip fault system forms the northern limit of the former N-striking, right-lateral strike-slip faults. This latter fault system is often referred as Dorouneh fault while in some recent studies (e.g., Fattahi *et al.*, 2007; Farbod *et al.*, 2011) it is divided into two major portions: the Dorouneh fault to the east and the Great Kavir fault to the west. The eastern portion (the Dorouneh fault) separates the northern margin of the Lut block from the Binalud and Kopeh Dagh Mountains. Indeed, this fault zone separates two regions with distinct tectonic regimes, N-S strike-slip faulting in Central Iran to the south and compressional tectonics to the north. The western portion (the Great Kavir fault) runs inside Central Iran and cuts through the Dasht-e Kavir depression. Overall, the Doruneh fault system has a 600-km length and is considered as the longest strike-slip fault through the Iranian plateau (e.g., Wellman, 1966; Fattahi *et al.*, 2007; Farbod *et al.*, 2011). To constrain the amount of slip

rate on the Dorouneh fault, *Fattahi et al.* (2007) interpreted a geomorphic deflected marker as a left-lateral offset of a terrace along the central segment of the fault. Combining an offset of ~25 m with infrared stimulated luminescence (IRSL) dating, they hypothesized an average slip rate of  $2.4 \pm 0.3 \text{ mm yr}^{-1}$  over the last 10 kyr. The reliability of the former geomorphic marker has been challenged by *Farbod et al.* (2011), who recently documented several offset alluvial fans and estimated a faster slip rate on the order of  $5.3 \text{ mm yr}^{-1}$  by combining offsets and cosmogenic dating (*Farbod*, 2012).

South of the Dorouneh fault system, the westernmost of the dextral strike-slip faults encountered in Central Iran is the Qom-Zefreh fault. It locates some 200-km farther west from the western termination of the Great Kavir fault. The Qom-Zefreh fault zone is made of several NW- to NNW-striking, right-lateral strike-slip segments and accommodates part of the dextral shear taking place between the Zagros and the Alborz Mountains (e.g., *Nabavi*, 1977; *Jamali et al.*, 2011). The Qom-Zefreh fault zone, with a total length of ~200 km, is running along the northeastern boundary of the UDMA almost up to the north of the city of Natanz, around  $33.5^{\circ}\text{N}$ . To the south of  $33.5^{\circ}\text{N}$ , the fault veers southwards and cuts through the UDMA. *Jamali et al.* (2011) recognized several cumulative right-lateral geomorphic offsets along one of the fault segment to the north, the Kashan segment. They proposed a minimum right-slip rate along the Kashan segment on the order of  $2.2 \text{ mm yr}^{-1}$ . Their estimate is based on the cumulative offset of  $11 \pm 1 \text{ m}$  of displaced Qanats (underground water channels, traceable at the surface by aligned and closely spaced access shafts), and an inferred maximum age of 5 ka for the Qanats construction.

Some 70-km farther east, the Dehshir fault is the major N-striking, right-lateral strike-slip fault slicing Central Iran, the UDMA, and the Nain-Baft suture (Figure 1.5). Both the Nain-Baft suture and the UDMA are dextrally displaced by the Dehshir fault (e.g., *Amidi*, 1975; *Huber*, 1977; *Tirrul et al.*, 1983; *Walker and Jackson*, 2004), and this offset is considered as the total cumulative geological offset across the fault ( $65 \pm 15 \text{ km}$ , *Meyer et al.*, 2006). *Meyer et al.* (2006) documented cumulative dextral offsets ranging between 25 and 900 m along the southern part of the fault and postulated the smallest cumulative offsets record fault motion since the last regional incision in the area. Postulating that incision relates to the onset of the Holocene ( $12 \pm 2 \text{ ka}$ ), they ended with an estimated average slip rate of about  $2 \text{ mm yr}^{-1}$ . Recently, *Le Dortz et al.*

(2011) recognized several morphological dextral offsets along the Dehshir fault ranging from 10 to 400 m. Combining the measured offsets with corresponding  $^{10}\text{Be}$  and  $^{36}\text{Cl}$  cosmic ray exposure (CRE) and optically stimulated luminescence (OSL) ages, they proposed a right-slip rate of  $1.2 \pm 0.3 \text{ mm yr}^{-1}$  averaged over the last 270 kyr.

Some 100-km farther east, another N-striking right-lateral fault, the Anar fault, with 200-km long cutting across Central Iran and terminates southward to the north of the UDMA. The Anar fault is the shortest of N-striking dextral faults slicing Central Iran. The total cumulative right-lateral offset along the fault is determined by correlation of Lower Cretaceous sandstones across the central part of the fault and amounts to  $25 \pm 5 \text{ km}$  (Nabavi, 1970; Walker and Jackson, 2004; Le Dortz et al., 2009). Le Dortz et al. (2009) recognized cumulative right-lateral offset riser of  $7.5 \pm 0.5 \text{ m}$  along the southern part of the fault. Combining this offset with corresponding  $^{10}\text{Be}$  cosmic ray exposure (CRE) and optically stimulated luminescence (OSL) ages, they proposed a minimum slip rate of  $0.8 \text{ mm yr}^{-1}$  over the Holocene.

Farther south, the NW-striking, ~200-km-long Rafsanjan right-lateral strike-slip fault is accounted to transfer part of dextral shear to the Anar fault. Fattahi et al. (2011) recognized several cumulative offset drainage channels of  $48 \pm 4 \text{ m}$  that incised into an alluvial surface. They obtained four IRSL ages from the uppermost 1 m of the fan deposits range from 119 ka to 213 ka. Comparing the age ranges with a regional climatic transition from a glacial to interglacial environment at ~120 ka ago, they tentatively suggest that the younger bound of the IRSL ages should be considered as a proxy for the age of abandonment of the alluvial surface, hence ~120 ka. Combining the offset channels with the preferred age, they estimate an average right-slip rate of  $0.4 \text{ mm yr}^{-1}$  along the Rafsanjan fault. Fattahi and his colleagues also identified several small right-lateral offset streams of ~3 m along the eastern part of the fault, and speculate that these offset are associated with the only recorded destructive earthquake in the region, the 1923 Lalehzar earthquake.

Some 100-km farther east, the NW-striking, right lateral strike-slip Kuh Banan fault runs for ~200 km mostly at the base of a steep mountain range front (e.g., Talebian et al., 2006; Walker et al., 2010a). The Kuh Banan fault, generally, forms a series of dextral segments which are arranged in right-stepping en-echelon pattern (Berberian, 2005). A minimum total dextral offset along the fault is determined based on both correlation of the Cambrian and Jurassic outcrops

(Berberian, 2005) and length of two pull-apart basins located along the fault (Walker and Allen., 2012) and amounts to 5-7 km. Allen et al. (2011) recognized several dextral geomorphic offsets along the southern part of the fault, ranging from 10 m to ~1 km. They postulated that the smallest of the offsets are postdating the last regional incision, following the regional climate change in early Holocene. Accordingly, they proposed a right-slip rate of 1-2 mm yr<sup>-1</sup> averaged over the last 12 ± 2 kyr. The estimated low to moderate rate of deformation, though remains to establish, was responsible to produce few moderate to large seismic events in the past years. Indeed, unlike the other major active faults inside Central Iran, which have not any sign of seismicity, the Kuh Banan fault has a limited record of recent and historical seismicity over the last centuries (e.g., Ambraseys and Melville, 1982; Engdahl et al., 2006).

The eastern margin of Central Iran is bounded by a N-striking right-lateral fault, the Nayband fault, delineating the western border of the Lut block. The Nayband fault is located between two domains with contrasted topography: the relatively high (up to some 3000 m above sea level, asl) Tabas block to the west, which belongs to Central Iran, and the low subdued depression (<500 m asl) of the Lut block to the east, which belongs to eastern Iran. These two blocks differ both by their geology and crustal thickness (e.g., Kluyver et al., 1983; Dehghani and Makris, 1984), suggesting that the location of the present-day right-lateral Nayband fault is partly superimposed on some lithosphere weakness due to previous fault zone activity. Present trace of the Nayband fault dextrally offsets a river course by 3.2 km. Since the river course has incised the southern margin of Quaternary basaltic lavas, Walker et al. (2009) performed <sup>40</sup>Ar/<sup>39</sup>Ar dating on the basaltic lavas. Combining the corresponding radiometric ages of 2.15-2.31 Ma, they estimated a slip rate of 1.4 ± 0.5 mm yr<sup>-1</sup> averaged over Quaternary.

Farther south, the right-lateral strike-slip Gowk fault forms the southwestern border of the Lut block and runs southward within the UDMA up to its southern termination at the Jebal-e Barez Mountains. The Gowk fault has a 160-km length and runs along a NNW-striking valley between two elevated mountains; the Sekonj Mountains (4200 m asl) to the west and the Abbarik Mountains (2700 m asl) to the east. These mountains comprise folded Mesozoic and Cretaceous sediments. Such a structural pattern suggests that the present-day strike-slip Gowk fault is partly superimposed on some former compressional tectonics. Walker and Jackson (2002) proposed a total cumulative right-lateral offset of 12 km by hypothesizing drainage reconstructions. Several

local pull-apart depressions have formed along the fault and favored ponding of young sediments. The largest of such ponds is located south of the city of Golbaf and preserves evidence of right-lateral motions of rills incising the pond deposits. *Walker et al.* (2010b) recognized several small cumulative right-lateral offsets of  $30 \pm 5$  m. Combining these offsets with two  $^{14}\text{C}$  ages acquired from terrestrial woods trapped within the pond deposits, they proposed a minimum slip rate of  $3.8 \pm 0.7$  mm yr<sup>-1</sup> over the Holocene. Recently, *Fattahi et al.* (2013) using luminescence dating of right-laterally offset lake-bed and alluvial deposits in the center and margin of the South Golbaf basin, respectively, proposed a slip rate of 3.8-5.7 mm yr<sup>-1</sup> averaged over the Holocene.

Several NW-striking, sub parallel thrusts crop out some 20-km farther east of the Gowk fault. The thrusts emplace folded Neogene sediments over the Quaternary alluvial fans to the SW of the Lut depression. They form a narrow (<20-km wide) fold-and-thrust belt, the Shahdad fold-and-thrust belt thought to accommodate part of the active deformation between the Nayband and Gowk faults (e.g., *Berberian et al.*, 2001; *Walker and Jackson*, 2002). *Berberian et al.* (2001) suggest that a shallow-dipping thrust underlies the ridges bordering the Lut desert east of the Gowk fault. They proposed a spatial separation (slip partitioning) of the strike-slip and thrust components along the Gowk and Shahdad thrust faults, respectively. *Fielding et al.* (2004) proposed somehow a fault-related fold geometry formed above a gently ( $\sim 8^\circ$ ) SW-dipping basal décollement with several shallower fault strands splaying from the décollement and terminating upward beneath surface folds. This structural pattern is in agreement with the structural field observations across the Shahdad fold-and-thrust belt given by *Mohajjel* (2009).

South of the Gowk fault, the N-striking Sabzevaran-Jiroft and Minab-Zendan fault systems are accounting for a significant part of the dextral shear between Central and Eastern Iran. Indeed, these strike-slip fault systems contributing to transfer the dextral slip northward, along the Gowk and Nayband faults. *Regard et al.* (2005) documented geomorphic offset features along the Sabzevaran-Jiroft fault system and combining with corresponding  $^{10}\text{Be}$  CRE ages, they proposed a right-slip rate of  $5.7 \pm 1.7$  mm yr<sup>-1</sup> averaged over the late Pleistocene and Holocene. The Minab-Zendan fault system slips at a faster rate and the fault zone accommodates a transpressive tectonic regime at the transition between the E-striking Makran subduction zone to the east and the NW-striking Zagros collision domain to the west (e.g., *Regard et al.*, 2005;

*Bayer et al.*, 2006; *Regard et al.*, 2010). Using a similar methodology, *Regard et al.* (2010) estimate a right-lateral slip rate along the Minab-Zendan fault system of  $4.7 \pm 2 \text{ mm yr}^{-1}$  or  $6.3 \pm 2.3 \text{ mm yr}^{-1}$ , depending on the age attributed to the offset markers on the Zendan fault. The estimated slip rates can be even higher. Indeed, their estimations rely on negligible inherited cosmic ray exposure and negligible post-depositional erosion. While the very little amount of post-depositional erosion demonstrated a few hundreds of kilometers farther northwest, along the Dehshir and Anar faults agrees with the first assumption, the large amount of significant inheritance of the measured  $^{10}\text{Be}$  concentrations through the past  $10^4$  to several  $10^5$  years (*Le Dortz et al.*, 2009; *Le Dortz et al.*, 2011) cast doubts on the second assumption. Without depth-profile sampling, the limited sampling of surface pebbles collected on a given surface by *Regard et al.* (2005) cannot rule out a variable inheritance, hence the possibility of higher slip rates (see *Le Dortz et al.*, 2012) on the Sabzevaran-Jiroft and Minab-Zendan fault systems.

East of the Lut block, several N-striking right-lateral strike-slip faults, namely the Sistan fault zone (West Neh, East Neh, Assaghi, Kahurak, Nosratabad and Zahedan faults), cut through the eastern Iranian range, NNW-striking mountains squeezed between the Lut block to the west and the stable Eurasian Helmand block to the east (Figure 1.5). The Sistan fault zone accommodates part of the active shear following northward motion of the Iran block respect to the Eurasian Helmand block. The total cumulative right-lateral offsets along the Neh fault system and the Zahedan fault are on the order of  $\sim 60$  (*Tirrul et al.*, 1983) and 13 (*Freund*, 1970) km, respectively. *Walker and Jackson* (2004) regarding a  $\sim 70$  km of total offset across the eastern side of the Lut block, and assuming a 5 Ma for the onset of strike-slip faulting, proposed a cumulative slip rate of  $\sim 15 \text{ mm yr}^{-1}$  along the Sistan fault zone. Considering the  $16 \pm 2 \text{ mm yr}^{-1}$  of present-day dextral shear between Central Iran and the Helmand block (*Vernant et al.*, 2004) and the absence of active strike-slip faulting inside the Lut block, *Walker and Jackson's* (2004) model hence postulates a total right-lateral shear less than  $3 \text{ mm yr}^{-1}$  west of the Lut block, along the Nayband-Gowk fault system. On one hand, the average slip rate of  $\sim 1.4 \pm 0.5 \text{ mm yr}^{-1}$  estimated over the last 2.25 Myr along the Nayband fault (*Walker et al.*, 2009) agrees with the model. On the other hand, the higher minimum slip rate of  $3.8 \pm 0.7 \text{ mm yr}^{-1}$  averaged over the Holocene along the Gowk fault (*Walker et al.*, 2010b) does not match with the model prediction.

The seismicity of Iran has been pictured by instrumental and historical seismic records (Figure 1.6, *Ambraseys and Melville, 1982; Ambraseys and Jackson, 1998; Berberian and Yeats, 1999; Engdahl et al., 2006*). Both records show concentration of frequent, small- to moderate-magnitude earthquakes in the Zagros, Alborz and Kopeh Dagh Mountains and a low level of seismicity in Central Iran. Accordingly, several prominent right-lateral strike-slip faults within Central Iran remained quiescent for millennia. While the interiors of Central Iran are mostly devoid of historical and instrumental seismicity, several earthquakes have occurred close to or along its border with the Lut desert (Figure 1.7 and Table 1.1).

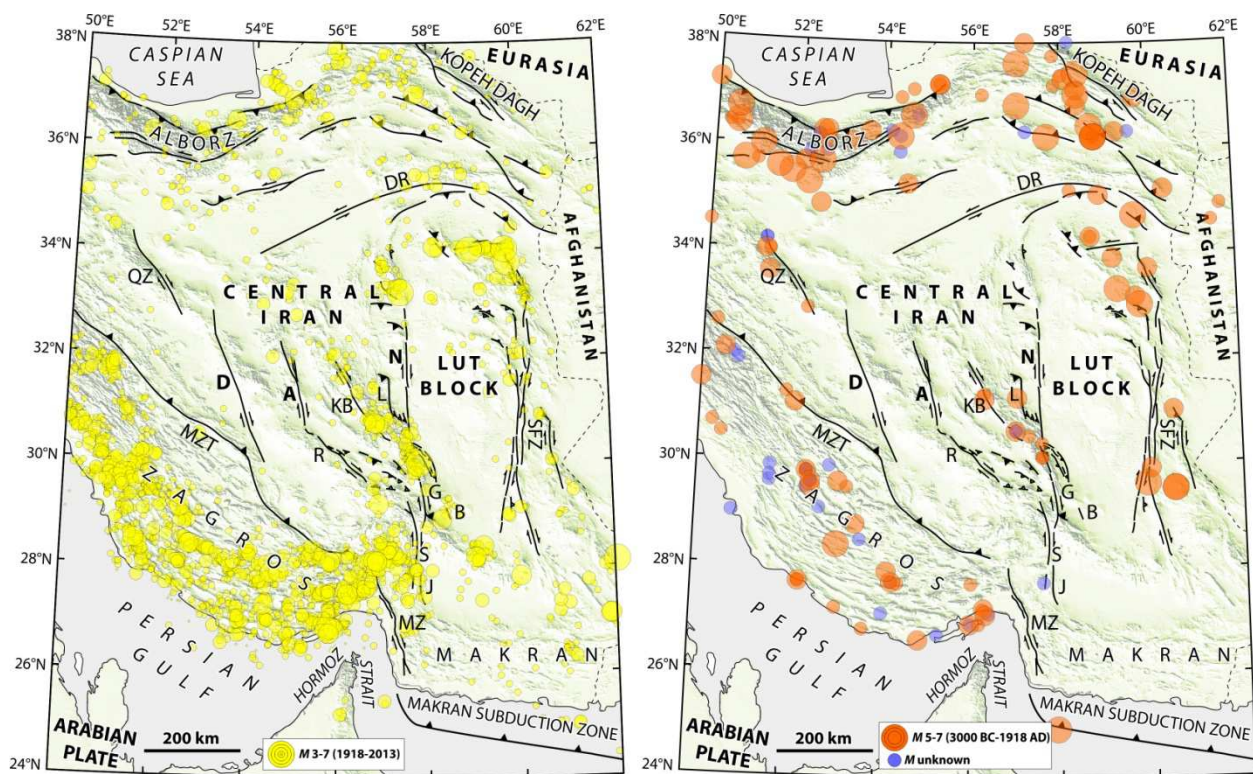


**Figure 1.6.** Distribution of instrumental (left) and historical (right) earthquakes in Central and Eastern Iran. Epicenters of the instrumental earthquakes between 1918 and 2004 are from the catalog of *Engdahl et al. (2006)* and between 2004 and 2013 from NEIC. Historical earthquakes (3000 BC to 1918 AD) are from *Ambraseys and Melville (1982)*. Note the very few epicenters in Central Iran and the lack of earthquake along the Dehshir, Anar and Nayband faults. Fault abbreviations are the same as in Figure 1.4.

The destructive Tabas earthquake of Ms 7.7 (*Berberian, 1979a,b*) is the largest earthquake recorded in Central Iran. It has remained the largest instrumentally recorded event in Iran (*Walker et al., 2003, 2013a*) until the occurrence of the recent (2013 April 16), Mw 7.8 Saravan

earthquake in the Makran. The Tabas earthquake struck a region known to have been quiescent for the last millennium and resulted in approximately 20,000 death casualties. It combined thrust

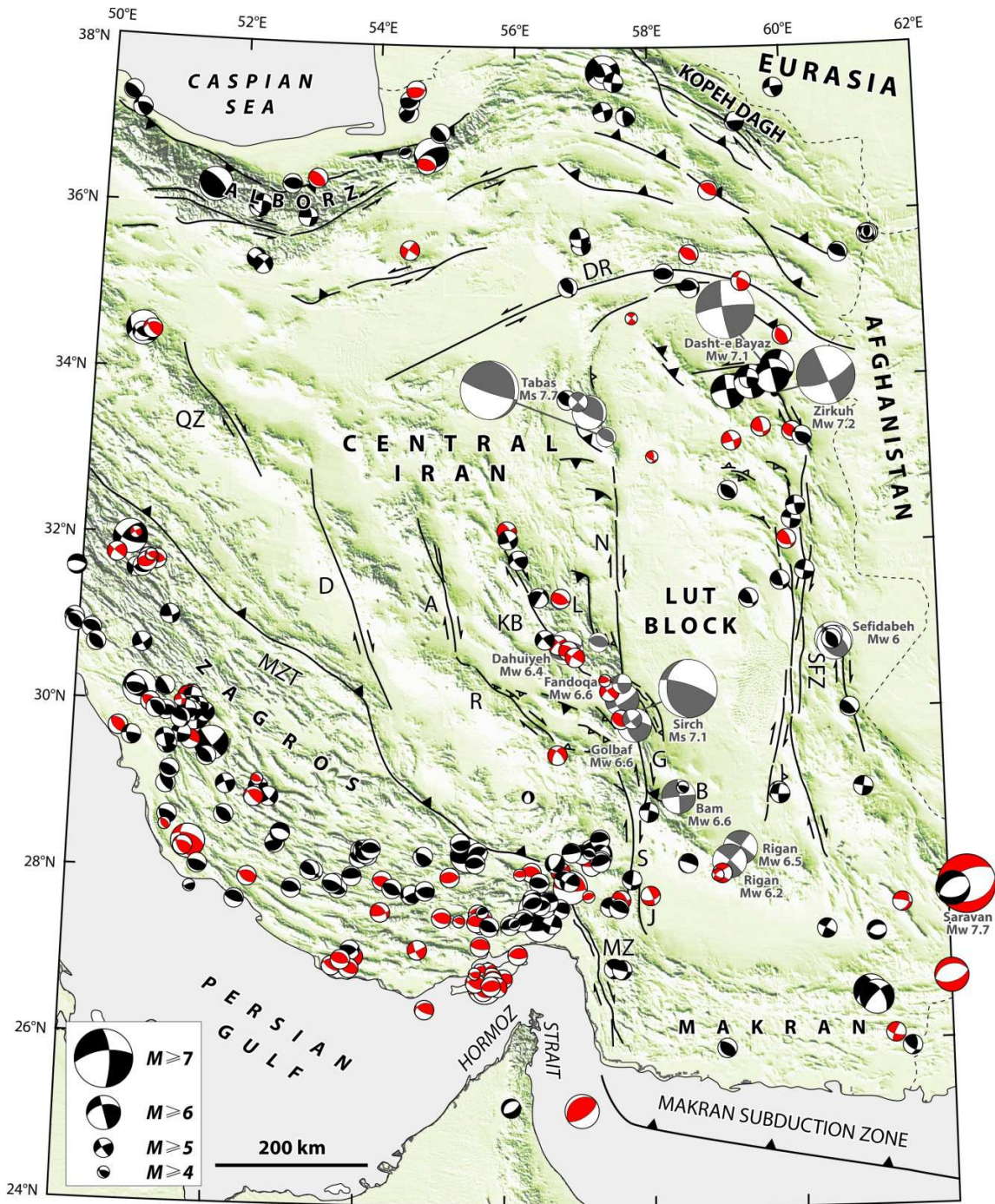


**Figure 1.7.** Fault-plane solutions of instrumentally recorded earthquakes ( $M \geq 4$ ) in Central and Eastern Iran during the period 1976 to 2013. Black solutions denote the recorded earthquakes before 2004 from the Global Centroid Moment Tensor (CMT) catalog (<http://www.globalcmt.org>) with earthquake

epicenters from the catalog of *Engdahl et al.* (2006). Red solutions denote the recorded earthquakes after 2004 from the CMT catalog. Grey solutions are from different references (see Table 1.1 for source parameters). Fault abbreviations are the same as in Figure 1.4.

and dextral motions along NNW-striking faults that may account for a transpressive tectonic regime by the northwestern termination of the N-striking Nayband fault. The Tabas earthquake has been followed in the subsequent years by moderate events with either thrust or strike-slip fault-plane solutions that also express the transpressive state of the tectonic regime.

Another famous sequence of earthquakes and associated surface breaks has taken place south of 30.5°N where NNW-SSE parallel thrust (Shahdad) and strike slip (Gowk) faults are thought to achieve slip partitioning at the southeastern tip of the Nayband fault. The Gowk fault has hosted five major earthquakes during a seventeen years period. The sequence started in 1981 with the two destructive earthquakes of Ms 6.7 (Golbaf) and Ms 7.1 (Sirch) on June 11 and July 28, respectively (*Berberian et al.*, 1984). Both ruptured the Gowk fault up to the surface with an overall 70-km-long fault break interrupted by a 10-15-km slip gap further filled during the 1998 March 14 Fandoqa earthquake. The Fandoqa earthquake of magnitude  $M_w$  6.6 is also known to have re-ruptured a significant portion of the Sirch break and to have triggered slip on the Shahdad thrusts (*Berberian et al.*, 2001; *Fielding et al.*, 2004). The Fandoqa event has been followed by a smaller ( $M_w$  5.4) event, the Chahar Farsakh earthquake, which took place on November 18 and produced minor surface cracking over 4 km. In the meantime between the 1981 and 1998 events, the south Golbaf Ms 5.7 earthquake has taken place in 1989. It has produced a 19-km-long surface break distributed on two sub-parallel fault strands (*Berberian and Qorashi*, 1994).

Five years after the last destructive earthquake (Fandoqa), a catastrophic  $M_w$  6.6 event has occurred some 45-km east of the southern termination of the Gowk fault. The Bam earthquake of 2003 December 26 resulted in approximately 40,000 death casualties and destroyed the biggest adobe citadel in the world, Arg-e Bam. The coseismic rupture induced a series of discontinuous left-stepping, en echelon surface breaks over 5 km with a maximum right-lateral offset of 20 cm (e.g., *Talebian et al.*, 2004). The event activated a right-lateral strike-slip segment with an average slip of ~2.0 m to the depth between 2-8 km (e.g., *Jackson et al.*, 2006).

Finally, an additional event with magnitude  $M_w$  6.4, the Dahuiyeh event, has occurred some 90-km NW of the Gowk fault and 100-km west of the Nayband fault, inner Central Iran Plateau. The event strokes the city of Zarand on 2005 February 22 and produced a 13 km long, E-striking thrust fault break splaying of the Kuh Banan strike-slip fault (*Talebian et al.*, 2006).

In summary, according to the instrumental and historical regional seismic records (*Ambraseys and Melville*, 1982; *Ambraseys and Jackson*, 1998; *Berberian and Yeats*, 1999; *Engdahl et al.*, 2006), there is no evidence of significant earthquake in the vicinity of the Dehshir, Anar, and Nayband faults (Figures 1.6 and 1.7). However, the lack of recent and historical seismicity along these faults does not rule out the possibility that these faults hosted seismic events in the past.

**Table 1.1.** Source parameters of the well-constrained fault-plane solutions of major instrumentally recorded earthquakes in Central and Eastern Iran. The fault-plane solutions are shown in grey color on Figure 1.7.

Event	Region	Lat. °N	Long. °E	Strike	Dip	Rake	Depth (km)	$M_w$	Fault	Reference
1978 Sept. 16	Tabas	33.25	57.38	355	16	155	9	7.28	Tabas	<i>Walker et al.</i> (2003)*
1979 Feb. 13	Tabas	33.31	57.40	327	28	116	11	5.58	Tabas	<i>Walker et al.</i> (2003)*
1979 Nov. 27	Dasht-e Bayaz	34.06	59.76	261	82	8	8	7.1	Dasht-e Bayaz	<i>Walker et al.</i> (2004)*
1980 Jan. 12	Tabas	33.55	57.23	348	20	137	14	6.0	Tabas	<i>Walker et al.</i> (2003)*
1981 Jun. 11	Golbaf	29.86	57.68	169	52	156	20	6.58	Gowk	<i>Berberian et al.</i> (2001)*
1981 Jul. 28	Sirch	29.99	57.79	177	69	184	18	6.98	Gowk	<i>Berberian et al.</i> (2001)*
1984 Aug. 6	Hur	30.80	57.17	279	35	86	11	5.3	—	<i>Baker</i> (1993)
1989 Nov. 20	South Golbaf	29.90	57.72	145	69	188	10	5.83	Gowk	<i>Berberian et al.</i> (2001)*
1990 Mar. 25	Tabas	33.34	56.99	223	90	-180	15	5.1	Tabas	Harvard CMT
1994 Feb. 23	Sefidabeh	30.80	60.57	143	29	96	7	6.05	Sefidabeh	<i>Berberian et al.</i> (2000)*
1994 Feb. 24	Sefidabeh	30.82	60.52	155	45	110	10	6.2	Sefidabeh	<i>Berberian et al.</i> (2000)*
1994 Feb. 26	Sefidabeh	30.78	60.55	146	36	107	5	5.95	Sefidabeh	<i>Berberian et al.</i> (2000)*
1997 May 10	Abiz	33.81	59.81	156	89	-160	13	7.2	Zirkuh	<i>Berberian et al.</i> (1999)
1998 Mar. 14	Fandoqa	30.08	57.58	156	54	195	5	6.57	Gowk	<i>Berberian et al.</i> (2001)*
1998 Nov. 18	Chahar Farsakh	30.32	57.53	174	55	173	15	5.34	Gowk	<i>Berberian et al.</i> (2001)*
2003 Dec. 26	Bam	29.04	58.36	355	86	-178	5.5	6.6	Bam	<i>Jackson et al.</i> (2006)
2005 Feb. 22	Dahuiyeh (Zarand)	30.77	56.73	270	60	104	7	6.4	Kuh Banan	<i>Talebian et al.</i> (2006)*
2010 Dec. 20	Rigan	28.33	59.19	213	85	173	5	6.5	Rigan	<i>Walker et al.</i> (2013b)
2011 Jan. 27	Rigan	28.17	59.04	221	87	176	9	6.2	Rigan	<i>Walker et al.</i> (2013b)

\* Epicenters from *Engdahl et al.*'s (1998) catalog and the subsequent updates.

### 1.3. Questions to address and methodology

Understanding the seismic behavior of major active intracontinental strike-slip faults that remained quiescent over the last thousands of years is a fundamental goal for assessing the earthquake hazard of Central Iran. Key aspects centre on how strains accumulate along these active faults and how they release accumulated strains through time. Furthermore, estimation of geologic slip rates along the major strike-slip faults slicing Central Iran is essential to investigate the degree of consistency between the long-term strain distribution and present-day geodetic deformation. In these terms, an appropriate description of the pattern of active deformation in Central Iran requires answering two fundamental questions: (1) how is active deformation accommodated by strike-slip faulting across Central Iran over the late Quaternary, and (2) what is the seismic history of the faults over the last seismic cycles?

The first question can be addressed by estimating right-slip rates over the late Pleistocene and the Holocene along the major N-striking, active strike-slip faults across Central Iran. This needs to consider individual datable morphologic features that first be displaced by the fault motions and then preserved over the observable displacement interval (e.g., *Sieh and Jahns, 1984; Weldon and Sieh, 1985; Peltzer et al., 1988*). The geomorphic offset features were measured along the strike-slip faults either on the Quickbird imagery (60-cm pixel size) or high-resolution topographic maps obtained by Real-Time Kinematic (RTK) survey, and where possible, by direct field measurements. Due to the scarcity of organic material in arid regions such as Central Iran, radiocarbon dating is scant, and therefore to constrain the ages of the displaced geomorphic features, cosmic ray exposure and optically stimulated luminescence dating are used instead.

The second question can be addressed by the way of paleoseismic studies. Indeed, as for areas with moderate active deformation, because large earthquakes may repeat with long recurrence intervals, longer than the time span covered by historical seismic catalogs, paleoseismology is the appropriate tool. The occurrence of several destructive earthquakes, either after a long-lasting quiescent period (Tabas earthquake) or even without any record of past earthquake (Bam case), are outstanding examples of such a situation. Another such example is given by the Nayband fault. Indeed, the Nayband fault is the only portion of the long quiescent western Lut border that has not been reactivated during the last few millenniums. While the neighboring Tabas and Gowk faults hosted recent destructive events that might enhance the

probability of triggering earthquakes on the Nayband fault, it is of importance to document both its Holocene slip-rate and its seismic history for assessing the regional seismic hazard.

### 1.3.1. Paleoseismology

Paleoseismology is an intermediate link between seismology and geology that has developed in the last decades after recognition of impressive surface faulting produced by devastating earthquakes of the 19<sup>th</sup> and the beginning of the 20<sup>th</sup> centuries in the United States (e.g., Farview Peak, 1854; Owens Valley, 1872; San Francisco, 1906; Pleasant Valley, 1915), New Zealand (e.g., Marlborough, 1888), and Japan (e.g., Nobi, 1891; Kanto, 1923). Paleoseismology as a part of the broader field of earthquake geology deals with young deformation of landforms and sediments allowing for spatial and temporal study of earthquakes over the last thousands of years (e.g., Sieh, 1978; Adams, 1980; Wallace, 1981; Weldon and Sieh, 1985; Vittori, 1991; Yeats and Prentice, 1996; Dolan *et al.*, 1997; McCalpin, 2009).

Strong earthquakes often leave some detectable evidence on the ground surface, which such a surface is referred after to an “earthquake horizon”; widely used as “event horizon” and determines most closely approximates the time of earthquake. In suitable environmental and geological conditions, these features can be preserved over  $10^3$  to  $10^4$  year timescales. Consequently, paleoseismic studies may detect and date them to permit extension of knowledge beyond the historical seismic records, and in some cases to improve their bias for strong earthquakes. The best sites for performing such studies have many distinct recent stratigraphic units that can record coseismic displacements on faults and dateable material to provide a timescale of the past earthquakes. The evidence of paleoearthquakes can be preserved in regions dominated by rather equilibrated rates between deposition, erosion and fault displacement (e.g., McCalpin, 2009). The event horizon and its related features in regions of high deposition rates would be buried rather deep, hence difficult to access the target level. Instead, low energy depositional place, such as continuous quiet-water deposition of fine sediments (e.g., sag ponds), is commonly considered as one of the best places to record and preserve evidence of paleoearthquakes. In contrast, in regions that erosion rate exceeds the fault displacement rate, evidence of paleoearthquakes would be eroded away and disappeared soon after occurrence of an earthquake (e.g., Bull, 2007).

There are two main types of evidence to identifying past earthquakes using paleoseismic studies: primary or direct evidence that is related to direct fault investigations such as those expose on the trench walls, and secondary or indirect evidence such as those reveal by dendroseismology (e.g., *Meisling and Sieh*, 1980), lichenometric analysis (e.g., *Bull*, 1996), and speleoseismology (e.g., *Forti*, 2001). Since changes in annual growth rings pattern of trees, lichens sizes and origin of broken speleothems can be also accompanied with other natural processes such as climatic variations, thus, a robust explanation for earthquake origin of such evidence can only be achieved by correlation with results of direct dating of primary evidence close to given sites (*Becker et al.*, 2006). Furthermore, in many arid and semi-arid regions due to the minimal vegetation cover, dendroseismology and lichenometry methods are not performable. In general, secondary evidence raises a critical question of how the causative fault inducing secondary deformation can be identified, as ground deformation associated with past earthquakes could have been generated by either a near-field moderate earthquake or a far-field larger one (*McCalpin*, 2009).

While there remain uncertainties and limitations using some of the indirect evidence to identifying the past earthquakes, now widely trenching in deformation zones is accepted and used in regions of different climatic settings. The paleoseismic trenches excavated perpendicular and/or parallel to the fault trace in different strategies based on the fault mechanism, site conditions and particularly goals of study. For instance, in the case of buried offset features across a strike-slip fault, to identifying the size of lateral offsets for each paleoearthquakes that is the size of slip per event, several progressive closely spaced (<1 m) trenches can perform in both sides and parallel to the fault trace (e.g., *Liu et al.*, 2004; *Rockwell et al.*, 2009). Such three-dimensional excavations permit to trace piercing lines into the fault zone; hence slip per event would be measurable by reconstruction of offset markers across the fault. However, throughout this study in Central Iran, the paleoseismic trenches were excavated within alluvial fan materials with channels difficult to trace through exposures, and 3D trenching was not used.

Several stratigraphic indicators are used to identifying event horizons, hence past earthquakes in the exposed stratigraphic sequences in trenches. Some indicators are rather common to recognize an event horizon in exposures of strike-slip faults, such as abrupt upward termination of fault displacements, angular unconformities formed by overlying undeformed strata on tilted

or folded beds, abrupt changes in vertical separation of strata across a fault strand, fissures and sand-blows (Figure 1.8).

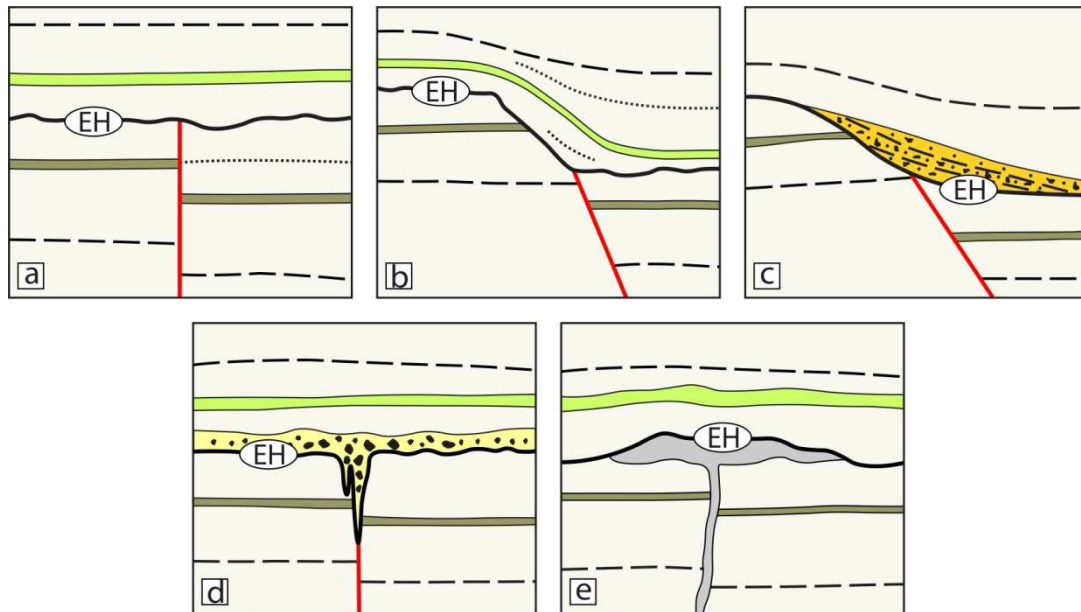


**Figure 1.8.** Schematic diagrams of common stratigraphic indicators of paleoearthquakes in strike-slip environments. In each example strata have been displaced by similar vertical amount displaying evidence for one earthquake. Black thick lines denote event horizon (EH) of each diagram. (a) Fault abruptly terminates upward and consequently sealed by younger and undisturbed strata. (b) Eroded fault scarp deposits rest unconformably on event horizon and lower strata. (c) Fault underlies a scarp-derived colluvium (orange). Base of the colluvium denotes an event horizon. (d) Fissure has been formed along a fault strand and filled by younger sediments (yellow). (e) Liquefied sandy material (Grey) injected into host layers and has covered by undisturbed strata. Top of the liquefied material denotes an event horizon. Redrafted from Figure 6-16 of *Allen* (1986).

Coseismic fissures and sand blows can be considered as reliable indicators of the stratigraphic position of an earthquake. Fissure fills, generally, are sub-vertical, downward-tapering shaped that are filled and sealed with younger sediments. In several examples of the Central Iranian sites, mostly all of these fissures were filled with fine and loose aeolian sands and silts, probably by dust storms some weeks or months after occurrence of earthquake. This coseismic feature, therefore, reveals occurrence of a paleoearthquake rather immediately before deposition of the infill sediments. The sand-blow as a kind of liquefaction features is one of the common soft-sediment deformation associated with seismic shaking that forms as a consequence of sudden increase in pore fluid pressure in the sediment matrix (e.g., *Owen*, 1987). This is made

of injected fine and loose sediments into the host materials and causes deformation in host sediments close to the liquefaction pillars which are usually placed at the centre of liquefied features.

In some cases, incorrectly interpreting non-seismic features (e.g., nonseismic-induced liquefaction features; *Holzer and Clark, 1993*) as indicator of past earthquakes may lead to an overestimation of the number of paleoearthquakes. In contrast, erosion of subtle features and/or absence of paleoseismic feature in near-surface deposits lead to an underestimation of the number of paleoearthquakes that have occurred at a site. Furthermore, large earthquakes are sometimes associated with little (e.g., 1981, Ms 6.7, Golbaf earthquake; *Berberian et al., 1984*) or no surface rupturing (e.g., 2010,  $M_w$  7.0, Haiti earthquake; *Hayes et al., 2010; Calais et al., 2010; Prentice et al., 2010*). These are intrinsic limitations of paleoseismic studies. However, problems arising from overrepresentation and underrepresentation can be reduced by applying large doses of caution when interpreting paleoseismic evidence (*McCalpin, 2009*).

Despite these uncertainties, the paleoseismic investigations are widely considered as a robust tool to reconstruct large earthquakes beyond the instrumental and historical seismic catalogs, through the past thousands to tens of thousands of years. Since geologic evidence of small and moderate seismic events is rarely created or preserved near the surface, the paleoseismic studies, typically, can reconstruct only large and great earthquakes; i.e., with magnitude  $M_w > 6.5$  (*McCalpin, 2009*). Furthermore, deformation during large younger earthquakes may obscure evidence of smaller, older ones. Thus, short-term seismicity variations during earthquake cycles could be difficult to work out using available paleoseismic approaches (e.g., *Vittori et al., 1991; McCalpin, 2009*).

### 1.3.2. OSL dating

The choice of dating method to constrain the age of past earthquakes is severely dictated by the characteristics of sediments in the exposed stratigraphic sequences across the fault zones. The most common technique used to date paleoearthquakes is to date organic materials such as charcoal, peat, wood, shell, organic lake sediment, using accelerated mass spectrometry (AMS)  $^{14}\text{C}$  procedures (e.g., *Schwartz and Coppersmith, 1984; Sieh et al., 1989; Machette et al., 1991; Grant and Sieh, 1994; Biasi et al., 2002; Klinger et al., 2003; Hartleb et al., 2006; Rockwell et*

*al.*, 2009; *Scharer et al.*, 2011; *Schwartz et al.*, 2012). The scarcity of organic materials in arid and semi-arid regions often limits the use of radiocarbon dating. Instead, quartz-rich sediments and pebbles often prevail in these regions that are suitable for optically stimulated luminescence (OSL) dating. In comparison with  $^{14}\text{C}$  technique, the age determination using OSL method can extend much further back in time (>350 ka; *Murray and Olley*, 2002) than ages based on radiocarbon analysis (~45 ka; *Walker*, 2005). Recently, OSL dating is applied in paleoseismic studies and considered as an extremely useful method, particularly in arid and semi-arid regions, to bracket the age of past earthquakes (e.g., *Lee et al.*, 2001; *Prentice et al.*, 2002; *Porat et al.*, 2009).

### **1.3.2.1. Basis of the method**

Optical dating of sediments started with the pioneering work of *Huntley et al.* (1985) using OSL signals in mineral grains. Huntley and co-workers discovered that the luminescence signal could be stimulated from sedimentary minerals by exposing them to light, instead of heat which was formerly applied in thermoluminescence (TL) method (e.g., *Aitken et al.*, 1968). Indeed, OSL dating was developed based on a physical principle that response of natural minerals such as quartz and feldspar to environmental radiation is cumulative over time (Figure 1.9). When such a quartz or feldspar grain is subjected to ionizing radiation, some electrons are ejected from their usual states of energy and partly become lodged in crystal lattice defects; that are referred to as traps. Thus, the more the exposure to nuclear radiation lasts, the greater number of electrons is trapped. Exposure to the sunlight causes a natural relaxation of each electron to its former state, resulting in the emission of luminescence (Figure 1.10) that is referred to as bleaching. The intensity of this emission is proportional to the radiation concentration in defects (e.g., *Smith et al.*, 1986; *Aitken and Smith*, 1988). Basically, in optical dating intense light by shining a beam of light onto the sample is used to eject the trapped electrons that accumulated in light-sensitive traps through time (e.g., *Godfrey-Smith et al.*, 1988).

The radiation dose accumulates during burial period and is defined as the amount of absorbed radiation energy per unit mass of the mineral; the S.I. unit is the gray, with  $1 \text{ Gy} = 1 \text{ J.kg}^{-1}$ . The natural dose rate is expressed as gray per thousand years ( $\text{Gy ka}^{-1}$ ), or as milligray per year ( $\text{mGy a}^{-1}$ ), that in the latter case is referred to as the annual dose. The term “equivalent dose”, commonly abbreviated  $D_e$  or  $D_{eq}$ , means the radiation dose obtained in the laboratory that would

produces the same population of trapped electrons as did the actual environmental radiation dose (e.g., *Duller*, 1991, 1995; *Murray et al.*, 1995; *Aitken*, 1998; *Rhodes*, 2011). Then, age of a sample will be calculated by dividing the equivalent dose value by the annual dose rate.

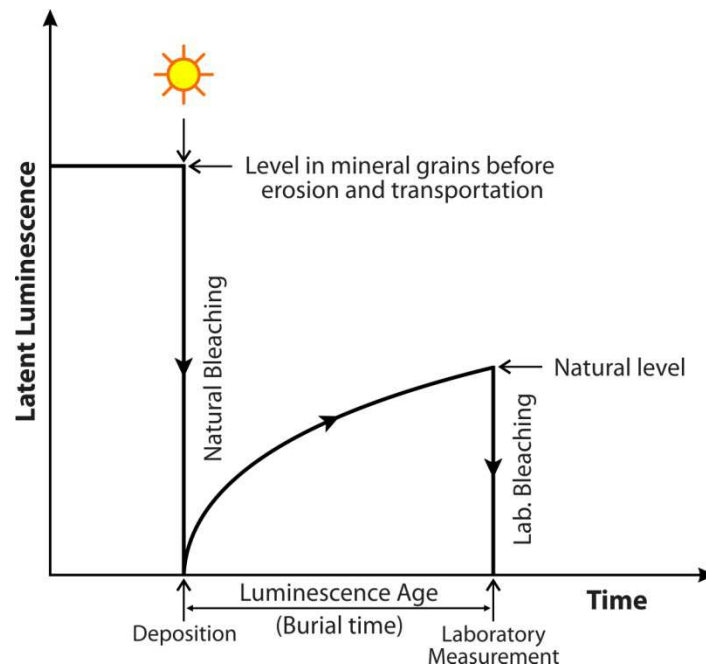


**Figure 1.9.** The basic principle of optically stimulated luminescence dating. Previously accumulated OSL signal in mineral grains is bleached by exposing to sufficient daylight during erosion and transportation. After deposition of mineral grains, when the material is sealed from sufficient daylight, the luminescence signal accumulates through time until measurement of the natural luminescence signal in the laboratory. Redrafted from Figure 1.1 of *Aitken* (1998).

The objective of OSL dating is to determine the radiation dose, and hence the time elapsed since the last exposure of sediments to sufficient sunlight either direct daylight or through clouds or water. The pioneering work of *Huntley et al.* (1985) has shown that sunlight exposures as short as ten seconds would be sufficient to empty more than 90% of the light-sensitive traps, effectively resetting the OSL dating clock. Thus, they proposed that OSL technique should be applicable to dating sediments which have received at least a short exposure to sunlight during the depositional process, before the last burial time.

If the sampled material was not exposed to sufficient sunlight before deposition, the obtained age denotes an earlier exposure event. Indeed, incomplete solar resetting (partial bleaching) of OSL

signal results in age overestimation; hence the measured equivalent dose will not give a true proxy of the elapsed time since the last deposition (e.g., *Bailey et al.*, 1997). The partial bleaching of the luminescence signal at the time of deposition could result due to the poor exposure to sunlight during sediment transport and/or the short transport distances as well as the surface coating of grains usually by iron and manganese oxides (e.g., *Berger*, 1990; *Murray and Olley*, 2002). For instance, in the case of flood deposits, the incomplete bleaching seems to result from the fact that flood sediments are only exposed to significant light levels at times of low flow, when the water level is sufficiently low to allow light to penetrate. Consequently, the grains being deposited with a heterogeneous distribution of residual trapped charge, and display a wide range of measured equivalent dose values (e.g., *Rittenour*, 2008).

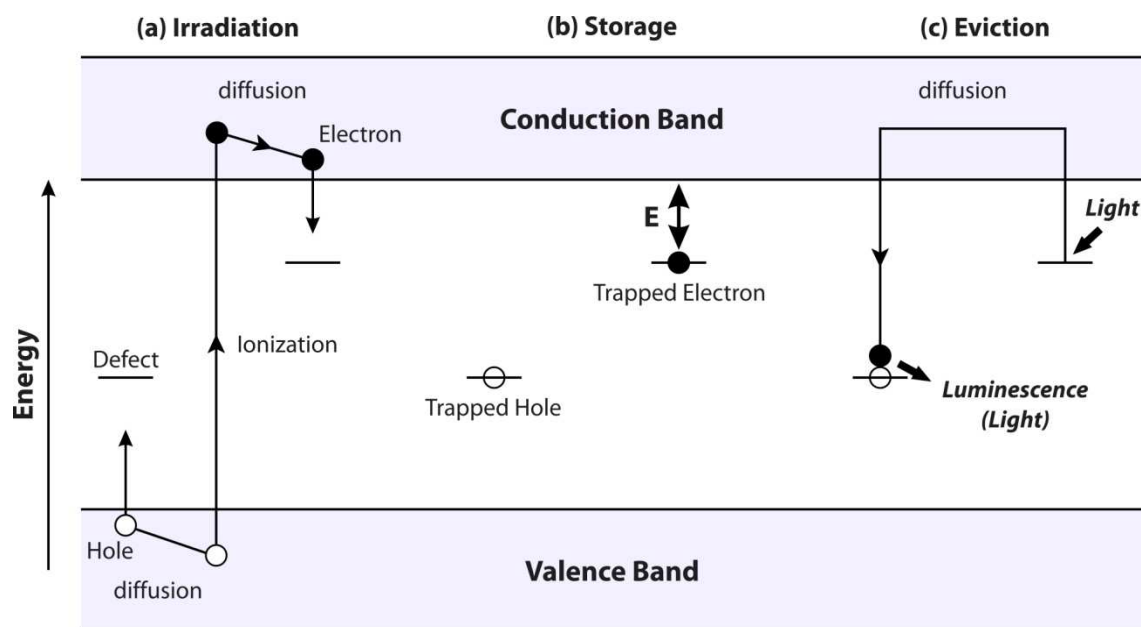


**Figure 1.10.** Energy-level diagram illustrating OSL process. (a) During burial conditions, due to exposure of crystal to the flux of nuclear radiation, ionization results in creation of electron-hole pairs. Electrons (black circle) and holes (open circle) become trapped at defects. (b) The electron is transferred to levels below the conduction band. The lifetime of the trapped electron has a direct ratio with the trap depth ( $E$ ) below the conduction band. Shallow trapped electrons are unstable, where thermal eviction is high. Thus, storage of electrons takes place in deep trapping levels, where thermal eviction is negligible. (c) Electrons are evicted from traps after excitation by intense blue-green stimulating light and the energy loss released by the emission of light (luminescence). Redrafted from Figure 1.6 of *Aitken* (1998).

A major development in OSL technique has been generated by *Murray and Wintle* (2000). Indeed, they formalized a reliable procedure for single aliquots (portions or sub-samples) of quartz that have a rapidly bleached (fast OSL component). A major advantage of decreasing sample size is the ability to identify the presence of contaminants in a bulk sample, and to exclude them from the final age determination (*Murray and Roberts*, 1997). Using single-aliquot regenerative-dose (SAR) protocol, OSL age estimates could be determined for single quartz grains, an approach now applied routinely to help overcome limitations formed by incomplete signal zeroing (partial bleaching) in environments such as caves (e.g., *Henshilwood et al.*, 2002), flood and fluvial deposits (e.g., *Murray et al.*, 1995; *Rittenour*, 2008; *Rhodes et al.*, 2010).

### **1.3.2.2. Sample collection**

Quartz and feldspar minerals are used for optical dating because of their ubiquity, ease of separation from sediments, and because they yield ample luminescence for measurement (*Huntley and Lian*, 1999). Thus, any sediment that contains quartz or feldspar and has been exposed to sufficient sunlight prior to burial is suitable for optical dating. Since sunlight, even brief, can empty some light-sensitive traps, hence during the sample extraction there must be no light exposure to the target grains that are to be measured. Sample can be collected pushing a stainless steel tube (e.g., 6 cm x 25 cm) into the sediment. In this case, just after sample extraction, both tube ends have to be sealed and covered using both aluminum foil and black tape. This allows protecting the sampled material from any sunlight contamination, and also preserves the water content of the sample before performing OSL analyses in the laboratory. For material that can be carved into a block (~1 kg), such a block can be collected in daylight, wrapped in foil and sealed. The outer mantle of the sampled block that was exposed to sunlight during sample extraction will be removed from the block in the laboratory and discarded. About 1 kg of material is usually more than adequate, and should be collected if it is available. There are occasions where 1 kg is not adequate and there are also cases where it may be possible to date as little as 1 g. If the sediment is loose then a fresh face should be exposed and the sample put into a 1 liter lined can and sealed; this is best done at night, although it can be done quickly under a black, thick cloth in the daytime.

The OSL dating also can be considered as applicable technique to constrain abandonment ages of geomorphic surfaces (e.g., *Rhodes*, 2011). In some cases, there is no suitable natural

exposure containing loose fine-grained sediments for OSL analyses. In such a consideration, sample could be extracted from the bulk of coarse sediments following a procedure described below and designed specifically for arid environments (e.g., *Rizza et al.*, 2011a, 2011b). For this, first a pit with a depth of some 1 m should be opened on the target surface (e.g., abandoned alluvial fan surface). Then, to prevent light-induced effects on the OSL signal during sample extraction, the top of the pit has to be covered with several layers of dark, thick tarpaulins. Then, in complete darkness, the targeted sampling area (~15 cm in diameter) should be cleaned by removing around 10 cm of the materials exposed to the sunlight during the digging of the pit. Then, about 1 kg of the bulk of sediment, including silts to coarse pebbles (<3 cm) should be collected from the cleaned sediment face. The sampled material might be collected in a thick, black, plastic bag, doubled by several additional black bags and wrapped with a black tape before removing the artificial darkness prevailing within the pit. This allows protecting the sampled material from any OSL signal resetting, and also preserves the water content of the sample before performing OSL analyses in the laboratory.

### ***1.3.2.3. Measurements***

The OSL dating of a collected sample requires the determination of two quantities: the equivalent radiation dose and the annual radiation dose. Dividing the value of the equivalent radiation dose by the annual radiation dose gives the age of the sample. The values of the equivalent radiation dose and the annual radiation dose can be determined based on some physical characters of minerals such as quartz and feldspar. Sunlight ejects electrons from traps in crystal lattice of minerals, and environmental radiation after burial slowly puts electrons in traps again (*Huntley et al.*, 1985). The measurements procedure is the stimulation of an irradiated sample by shining light on mineral grains extracted from the sample, and measuring the light that is emitted in response (e.g., *Smith et al.*, 1986). The intensity of this light emission is thus a measure of the number of electrons trapped since the last sunlight exposure. The luminescence emission is monitored continuously until all the traps are emptied. The emitted photons are converted to electrical pulse for each photon and counted using a sensitive detector (photomultiplier tube) (e.g., *Bøtter-Jensen*, 1997).

Two methods, generally, can be used to determine the laboratory radiation dose that produces the same population of trapped electrons as did the environmental radiation dose (equivalent

dose): additive-dose method for feldspar (e.g., *Duller, 1991*) and quartz (*Murray and Roberts, 1997*) grains, and regeneration method (e.g., *Mejdahl and Bøtter-Jensen, 1994; Murray and Wintle, 2000*). Both the additive dose and the regeneration methods can be applied using two main protocols: multiple and single-aliquot protocols. The multiple aliquot protocol gets its name from the fact that many aliquots, sometimes up to 60, are needed to determine a single equivalent dose (e.g., *Murray and Mejdahl, 1999*), while in single-aliquot protocols the equivalent radiation dose can be measured using only one aliquot of a sample (*Duller, 1991, 1995; Murray et al., 1997*). Indeed, the single-aliquot protocols allow the equivalent radiation dose to be measured on single, small aliquots and even on single grains (*Murray and Roberts, 1997*).

The additive-dose method involves characterizing the growth of the luminescence signal as a function of radiation dose added in the laboratory (e.g., *Duller, 1995*). An initial measurement is made of the luminescence signal from the aliquot when it has not been exposed to any artificial radiation dose; this is referred to as natural dose (Figure 1.11a). Then, radiation dose is added to the natural dose and the luminescence response signal would be measured. This procedure is repeated several times to characterize the response of the luminescence signal, hence to create an additive-dose growth curve. The equivalent radiation dose is then obtained by extrapolating a line fitted to the luminescence response points and its intercept with the dose axis. The additive-dose method is quite suitable when response of the luminescence signal versus dose data is approximately linear so that an accurate extrapolation can be made (*Huntley et al., 1985; Wintle, 1997*). Otherwise, a regeneration method should be seriously considered (Figure 1.11b, e.g., *Murray and Wintle, 2000*). In regenerative-dose method the zeroing of OSL signal is analogous to the zeroing that took place in nature by exposure to sunlight, and doses are subsequently given to construct an OSL response curve (growth curve) (e.g., *Wintle, 2008*). The equivalent dose is then obtained by projecting the natural OSL level onto the growth curve.

The intensity and spectrum of sunlight are highly variable. The grains may have been coated by minerals (such as calcite) or organic materials, or even the grains may have been exposed through turbid water (e.g., *Murray and Olley, 2002; Rhodes, 2011*). If the grains were not uniformly exposed to sunlight (i.e., some grains were well exposed to sunlight and others were not), it may give rise to a recognizable form of scatter in the measured luminescence signals. Another possibility to scatter the signals and age results can be considered by influence of

bioturbation as movement of sediments by flora and fauna (*Bateman et al., 2007*). *Bateman et al. (2007)* proposed that the bioturbation as a post-depositional disturbance may have a significant impact on chronologic records by rejuvenation of more ancient strata with upward or downward movements of sediments.

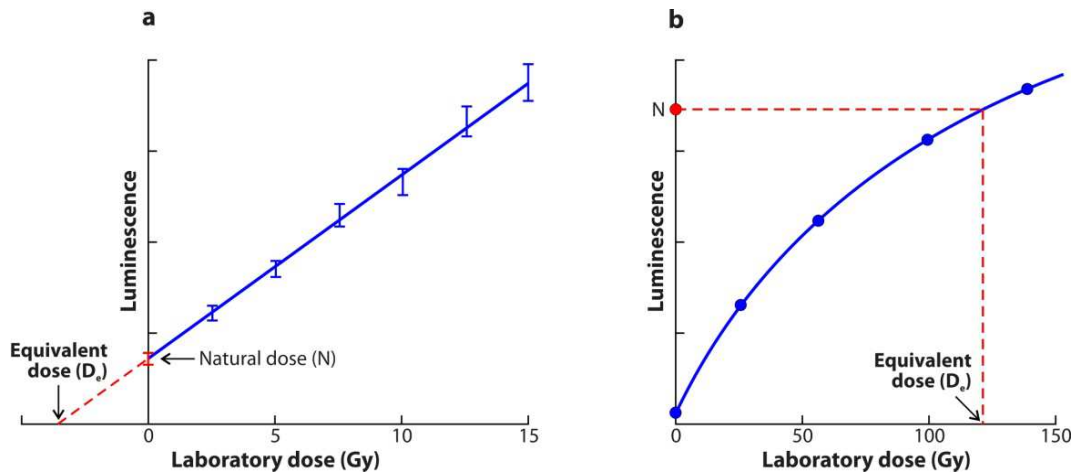


**Figure 1.11.** Schematic representation of the additive dose (a) and regenerative (b) methods to determine equivalent dose ( $D_e$ ). Each data point in (a) represents the average luminescence signal obtained from a group of aliquots. See text for explanation. Redrafted from Figures 1.4 and 1.5 of *Aitken (1998)*.

If a significant proportion of sampled grains display variation in equivalent-radiation dose, as a result of incomplete bleaching, bioturbation, or combination of these factors, a statistical age model can be used to obtain proper estimate from such spread data sets. Several statistical models can be applied to obtain meaningful dose estimation for different patterns of the luminescence signals. For the incomplete bleached buried grains that are preserved some inherited luminescence signals at the time of deposition and characterized by the skewed-dose distribution, the minimum age model (MAM) may provide a meaningful age of the sample (*Galbraith and Laslett, 1993; Galbraith et al., 1999*). The MAM may not be appropriate for samples that have undergone post-depositional disturbance such as bioturbation resulting in the intrusion of grains from younger strata. In such a case, the MAM may not yield an accurate estimate of the true burial age of the host deposit (*Olley et al., 2004*).

If all of the analyzed grains extracted from a given sample do not display a same age bound, the finite mixture model (FMM) may consider as an appropriate model to obtain a proper dose

estimation (*Galbraith and Green, 1990; Roberts et al., 2000*). This is the case when sampled grains consider as amalgamation of buried grains with different burial histories (heterogeneous bleaching). The FMM can be applied for the samples that exhibit multimodal dose distributions as a consequence of mixing proportions from well-bleached and partially-bleached grains (Figure 1.12a). *Rodnight (2008)* using the MAM and the FMM for heterogeneous-bleached samples proposed that at least 50 equivalent dose values per sample are needed to estimate a proper proxy of equivalent radiation dose for such samples. In the case of well-bleached samples, the central age model (CAM) can provide an appropriate estimate of the mean dose and associated uncertainty (Figure 1.12b, *Galbraith et al., 1999*). The CAM assumes normal distribution of the true equivalent radiation dose values, and can be applied for unimodal and non-skewed dose distributions of small aliquots (e.g., *Roberts et al., 2001*).

The value of the annual radiation dose (dose rate) can be determined both directly in the field by *in-situ* high-resolution gamma spectrometry (*Murray et al., 1987*) and in the laboratory either by laboratory gamma spectrometry or measurements of the radionuclide concentrations using ICP-MS or beta counting (*Bøtter-Jensen, 1988*). The radiation dose arises from two different sources: (1) cosmic rays contribution, and (2) radioactive decay of potassium (K), uranium (U), thorium (Th), rubidium (Rb), and their daughter products, both within the target sediment grains and from its surroundings up to ~50 cm away (e.g., *Rhodes, 2011*). Two other parameters are also needed to calculate the radiation dose rate value: the cosmic dose rate and the water content. The contribution of cosmic rays to the dose rates, generally, depends to the altitude, latitude and depth of the sampled material. The cosmic dose contributes usually as a small component (less than 10%; *Rhodes, 2011*) and can be estimated using the equations of *Prescott and Hutton (1988, 1994)*. Water in the sediment pores absorbs radiation and reduce dose rate (*Rhodes, 2011*). Based on measured water content, a single correction to each different forms of radiation (alpha, beta, and gamma) should be employed. Water is also responsible for the dissolution and re-precipitation of carbonate in sediments and this would also affect dose rate through time (*Wintle, 2008*).

Present-day water content of sampled materials can be assessed in the laboratory. For this, the light-exposed portions of the sampled sediments (e.g., about 5 cm of the collected sediments

at both ends of the steel tube) first should be weighted, dried at 110° C for 48 h and then weighted again (e.g., *Stevens et al.*, 2007).

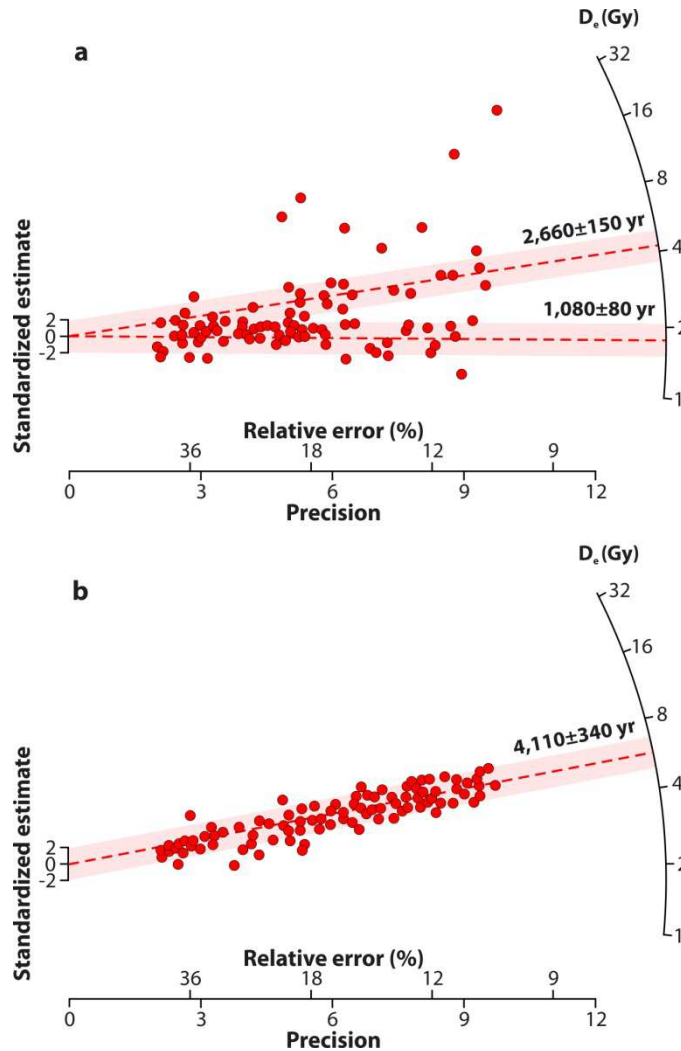


**Figure 1.12.** Radial plots of measured doses from two OSL samples with different patterns of luminescence signals. Both the samples were collected from young alluvial sediments in Australia (Redrafted from Figure 9 of *Rhodes*, 2011). (a) The sample shows multiple dose values of measured grains (red circles), and the equivalent dose is defined by the finite mixture model. Dashed red lines represent the lower two  $D_e$  component associated with uncertainties of  $2\sigma$  (light orange shading), suggesting two distinct bleached populations. (b) Well-bleached sample shows a uniform dose distribution of measured grains, and the equivalent dose is defined by central age model.

In the case of using field gamma spectrometer, first a ~30 cm hole should be dogged into the free face sediments in order to place the field gamma spectrometer. Then, sediments at the back of the hole can be scrapped into an airtight pot. Similarly, these materials would be weighted in laboratory, dried at 110° C for 48 h and then weighted again. The percentage of water content in the sediment, if there is any, should be defined as an average wetness over the entire burial period. Since estimating the water content history over the existence of the deposit can be difficult or even impossible, uncertainty of this factor is usually a fundamental limitation to reduce error limits on the age to below of  $\pm 5$  per cent (*Aitken*, 1998). However, in arid environments that have been arid at least during the last thousands of years there is no such a difficulty for young sediments.

Ultimately, having measured the radionuclide concentrations in the surrounding material, calculated the cosmic ray contribution, and the average water content percentage over the burial period the total dose rate can be calculated using the conversion factors of *Olley et al.* (1996) and *Adamiiec and Aitken* (1998).



CHAPTER 2

**LARGE EARTHQUAKES ON THE  
DEHSIR FAULT**

---

## 2.1. Introduction

Although there is no record of instrumental and historical seismicity in the vicinity of the Dehshir fault, several studies provided evidence of the fault activity during the late Quaternary (e.g., *Berberian, 1976; Walker and Jackson, 2004; Meyer et al., 2006*).

*Berberian (1976)* using aerial photos showed that the central part of the Dehshir fault cuts Quaternary alluvial deposits to the east of the Abarkuh depression, and questioned on whether the fault releases the accumulated strain by aseismic creep or it is currently locked. *Walker and Jackson (2004)* recognized an alluvial surface that is dextrally offset by 100 m along the central part of the Dehshir fault while a river channel incised into the abandoned alluvial surface does not show any offset. Assuming the incision was initiated as a result of the last regional climatic change between 5 and 9 ka (*Regard et al., 2003*), they proposed that the last earthquake on the Dehshir fault might have occurred at least before ~5000 years ago. *Meyer et al. (2006)* recognized several small rills along the southern part of the fault which are dextrally offset up to 4-5 m. They suggested that these small offsets may be associated with one seismic event, probably the most recent earthquake. However, due to the lack of geochronological data, the rate of slip and the seismic behavior of the fault were poorly known.

This chapter aims at providing the critical data used to address the previously unanswered questions about the seismic behavior of the Dehshir fault. The results of the first paleoseismic studies at two sites (sites North and South) along the southern part of the Dehshir fault are presented throughout this chapter. The paleoseismic data from a trench at the site North show evidence for occurrence of several large earthquakes during the latest Pleistocene and Holocene (section 2.2). Section 2.3 provides additional paleoseismic data that have not been included in the paper published in *Terra Nova* given in section 2.2. These additional data consist of six refined OSL ages from the site North and help to discuss more tightly the implications for the seismic behavior of the fault over the last 20 ka. These refined ages (section 2.3.1) permit to better constrain the average recurrence interval between large earthquakes. In addition, section 2.3.2 provides unpublished trench observations performed at the site South, close to the Marvast River. This trench mostly exposes sediments older than the marine isotope stage MIS-2 and provides evidence for at least two seismic events within the last 20 ka. Two OSL ages from that site are given, and their implications for the late Quaternary right-slip rate of the Dehshir fault are also discussed.

## **2.2. First evidence for large earthquakes on the Deshir fault, Central Iran Plateau**

Paper Published in *Terra Nova* by *Nazari et al.* (2009a)

My contribution to this work included collecting the geomorphologic data in the field, logging the paleoseismic trench at the site North along the southern part of the fault, collecting samples for OSL dating, and surveying local topography using differential GPS.

# First evidence for large earthquakes on the Deshir Fault, Central Iran Plateau

H. Nazari,<sup>1</sup> M. Fattahi,<sup>2,3,4</sup> B. Meyer,<sup>5,6</sup> M. Sébrier,<sup>5,6</sup> M. Talebian,<sup>1</sup> M. Foroutan,<sup>1</sup> K. Le Dortz,<sup>5,6</sup> M. D. Bateman<sup>3</sup> and M. Ghorashi<sup>1</sup>

<sup>1</sup>Institute for Earth Sciences, Geological Survey of Iran, P.O. Box: 13185-1494, Teheran, Iran; <sup>2</sup>The Institute of Geophysics, University of Teheran, Teheran, Iran; <sup>3</sup>Sheffield Centre for International Drylands Research, Department of Geography, University of Sheffield, Winter Street, Sheffield S10 2TN, UK; <sup>4</sup>Oxford University Center of Environment South Parks Road, Oxford, OX1 3QY, UK; <sup>5</sup>UPMC Univ Paris 06, ISTEP, UMR 7193, F-75005, Paris, France; <sup>6</sup>CNRS, ISTEP, UMR 7193; F-75005, Paris, France.

## ABSTRACT

Although sliced by several strike slip faults, a large part of Central Iran remained aseismic during the period of time covered by the instrumental and historical seismic records. Stating the existence of earthquakes in the Holocene is therefore important for the assessment of the regional seismic hazard. A palaeoseismic study of the Deshir fault demonstrates that Central Iran hosted large earthquakes during latest Pleistocene and Holocene. The last event corresponds to 1 m-deep fissures, which sandy infilling yielded an optically stimulated luminescence (OSL) age of  $2.8 \pm 1.4$  ka. At least two

previous events, outlined by older fissures and/or colluvial wedges, have been recorded over the last 10–30 ka. The magnitudes are difficult to assess because the actual slips per event are unknown. The size of the fissures and the significant vertical displacement associated with a colluvial wedge are nevertheless compatible with  $M \approx 7$  events along a primary strike-slip surface break.

Terra Nova, 21, 417–426, 2009

## Introduction and geological setting

The Deshir Fault is the westernmost prominent N-striking dextral strike-slip fault of a series that slice Central and Eastern Iran (e.g. Berberian, 1981; Walker and Jackson, 2004; Meyer and Le Dortz, 2007; inset, Fig. 1). The fault locates North of the Zagros, nearby  $54^\circ\text{E}$ , and cuts across an area of the Central Iran Plateau devoid of instrumental and historical seismicity (Ambraseys and Melville, 1982; Ambraseys and Jackson, 1998). Despite the lack of seismicity in its vicinity and the absence of resolvable deformation by the GPS network in Central Iran over 2 (Vernant *et al.*, 2004) and 6 (Masson *et al.*, 2007) years, the fault has long been suggested active (e.g. Berberian, 1981). There is now morphological evidence for it and right-lateral offsets document a cumulative fault-slip of  $\sim 25$  m at several sites along the fault (Meyer *et al.*, 2006). However, the Holocene time-period over which it surmised to have accumulated remains questionable. Although Meyer *et al.* (2006) suggested that small stream offsets of

4–5 m to the south of Marvast might result from coseismic slip during an earthquake of unknown age and magnitude  $\sim 7$ , the seismic behaviour of the Deshir fault is still not assessed. Trenching appears therefore appropriate to document Holocene earthquakes, if there were any, in a region that long remained quiescent according to the seismic records.

The information on the geometry and overall fault morphology is summarized from Meyer *et al.* (2006). The Deshir fault is a 380-km long straight strike-slip fault involving several portions (Fig. 1). The northern portion, located between Nain and Deshir, disrupts the western part of the Nain-Baft suture and cuts across the Urumieh Doktor magmatic arc. The southern 230-km-long portion extends between Deshir and Harat and cuts the eastern part of the Nain-Baft suture. The piercing points of the suture are difficult to pinpoint and estimates of the total dextral offset range between 50 and 80 km. South of Deshir, the fault trends N150–160 and runs obliquely across coalescent fans that merge with Quaternary salt flat depressions. Within the salt flats, the fault intersects marshes along an ill-defined scarp. Through the coalescent fans, the fault bears a clear 2–20 m high cumulative

scarp depending on the relative ages of the fans and its prevalent dextral motion is attested by deflected river courses and offsets of terrace-risers. We scrutinized the southern fault portion on SPOT imagery and in the field, searching for the favourable places to conduct palaeoseismic investigations and document the seismic history of the fault. We excavated trenches at three sites several tens of kilometres apart. Two revealed evidences of palaeoseismic events. The third revealed unsuitable and showed distributed shear across steeply-dipping neogene units without convincing evidences of deformation of the thin discontinuous aeolian sands mantling the Neogene. We report here the observations gathered at the northernmost site where the lithology allowed us to distinguish several events unambiguously.

## The trench site and the excavation

The excavation site is located north of Marvast where the fault cuts across a large intermittent stream that supplies water to the Deshir salt flat. Except for the main river flood plain where it has been eroded, the fault scarp is readily seen on the SPOT imagery and well expressed in the field (Fig. 2). The scarp is less than 2 m-high, faces to

Correspondence: H. Nazari, Institute for Earth Sciences, Geological Survey of Iran, P.O. Box: 13185-1494, Teheran, Iran. e-mail: nazari@gsi-iran.org

the east, and delineates a subtle depression or furrow associated with prevalent strike-slip motion. Tiny morphological features are well resolved on the right bank of the river where the fault cuts across an abandoned fan surface. Several ephemeral

gullies denoted by grey linear areas have incised the fan surface to join the active flood plain. The gullies have probably formed as a result of regressive erosion since the last significant incision of the network. Close to the main river flood plain, one such gully,

less than 200 m long, flows nearby and parallel to the fault. Further to the south, the fault intersects at right angle several gullies, a few tens to a few hundreds of metres long. The right-lateral offset of the two gullies to the south amounts to  $25 \pm 5$  m. In between the smallest of the gullies intersecting the fault and the upper reaches of the gully paralleling it, there is a 30–50 m long section of the scarp preserved from recent erosion (Figs 2,3a). The smooth scarp delineates a subdued, 10–20 m wide, 1.5 m deep, depression denoted by white patches on the SPOT image (Fig. 3b). These white patches outline the accumulation of a thin layer of silts and clays washed out from the scarp during episodic surface runoff. We discuss the most elucidating wall of a 25-m long, 2-m wide, 4-m deep trench excavated across this depression.

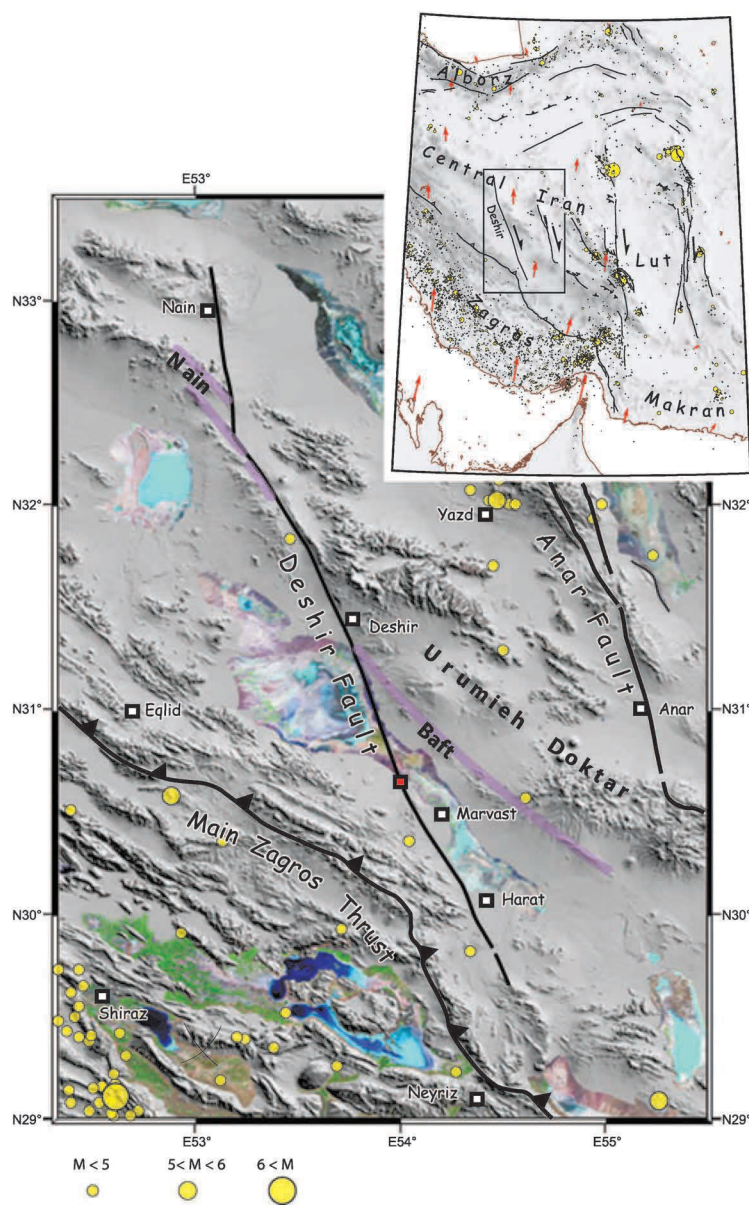


**Fig. 1** Simplified tectonic map of the Deshir fault. 1973–2008 seismicity from NEIC (<http://neic.usgs.gov/neis/epic/>). Background image is from SRTM data (<http://edcgs9.cr.usgs.gov/pub/data/srtm/>) supplemented with Landsat images for unfilled areas (mostly lakes and salt flats). Red square for location of Fig. 2. Insert locates the area within the simplified tectonic map of Iran. Red arrows are GPS velocities with respect to stable Eurasia (Vernant *et al.*, 2004; Masson *et al.*, 2007).

### Trench stratigraphy

The trench wall (Fig. 4) exhibits highly disrupted, coarse Quaternary deposits so that unit correlations across fault splays (f1 to f6) may be questionable. The overall structure of the trench corresponds to an asymmetric sag, limited to the east by the main fault zone (MFZ) and to the west by the f1 fault. The latter has controlled the development of the east-facing scarp that delineates the Deshir fault along several tens of kilometres on the satellite imagery (Figs 1, 2). The eastern part of the trench is a tilted block, which extends between the MFZ and the easternmost faults (f5, f6). The overall structure thus suggests that the most recent deposits should have been trapped in the central part of the sag between f1 and f2. Despite the difficulties correlating units across individual faults, the overall stratigraphy is made of two main bodies of units: (1) older alluvial conglomerates (blue colours, Fig. 4) and (2) younger alluviums and colluviums (non-blue colours). The units have been described separately within the different blocks (Table 1 and Fig. 4) and named accordingly with different letters (A to E) followed by a numbering order from bottom to top. Older units (A1, C1, D1, and E1) are exposed on both edges and in the lower part of the trench. They corre-

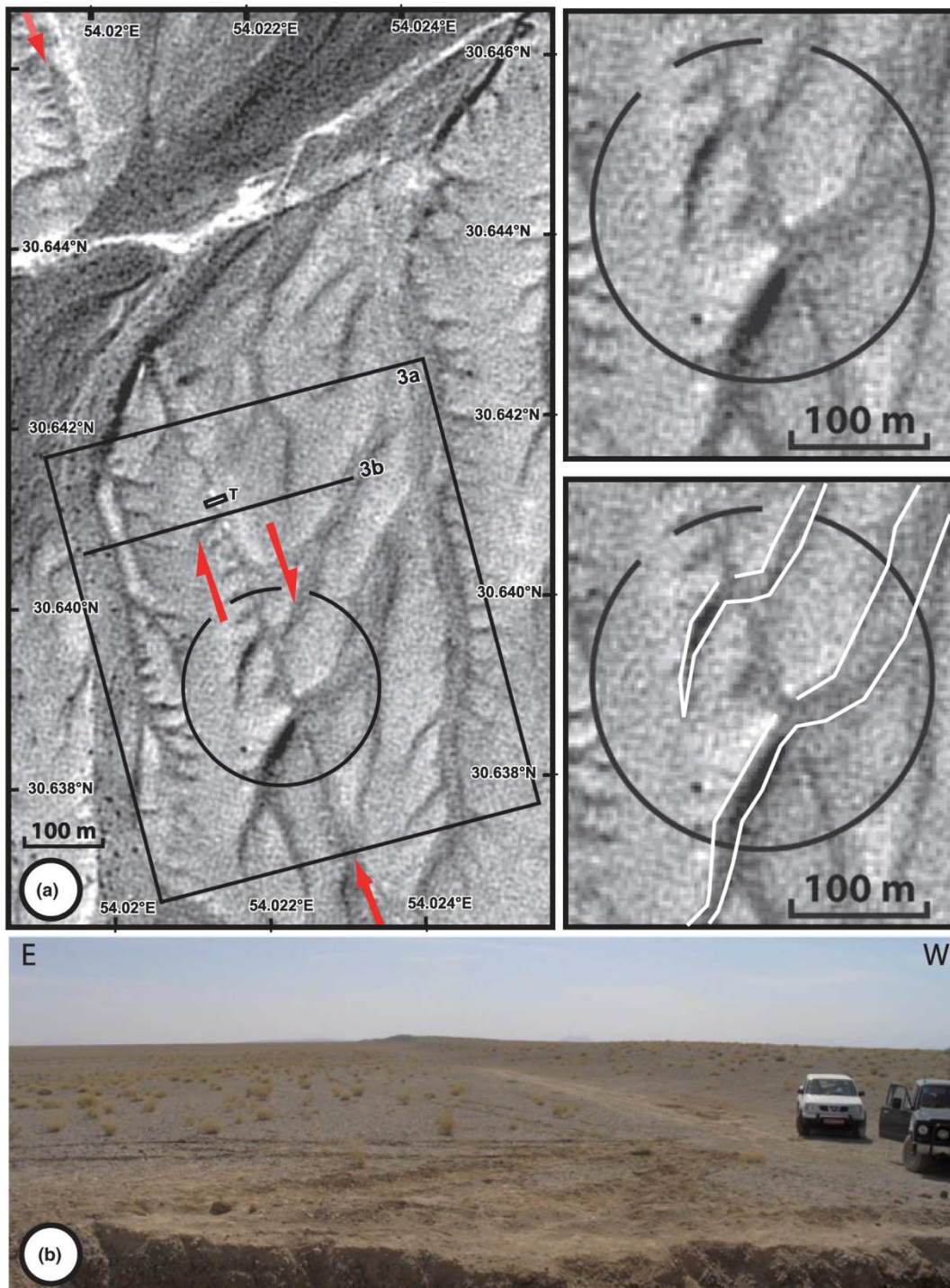


**Fig. 2** The excavation site. (a) SPOT satellite extract highlighting fault trace on both sides of a main river flood plain which tributaries have incised an abandoned fan. Right-lateral offset of two small gullies (circled area) is 20–30 m. Rectangle 3a and line 3b respectively locate 3-D enlargement and section in Fig. 3. T indicates position and approximate extent of analysed trench. Right panels show enlargements of raw (top) and interpreted (bottom) images of the offset gullies. (b) Field photograph of the N160 linear, east-facing, 2 m-high scarp. View is taken to the south from the eastern tip of the trench. Cars parked by the base of the scarp for scale.

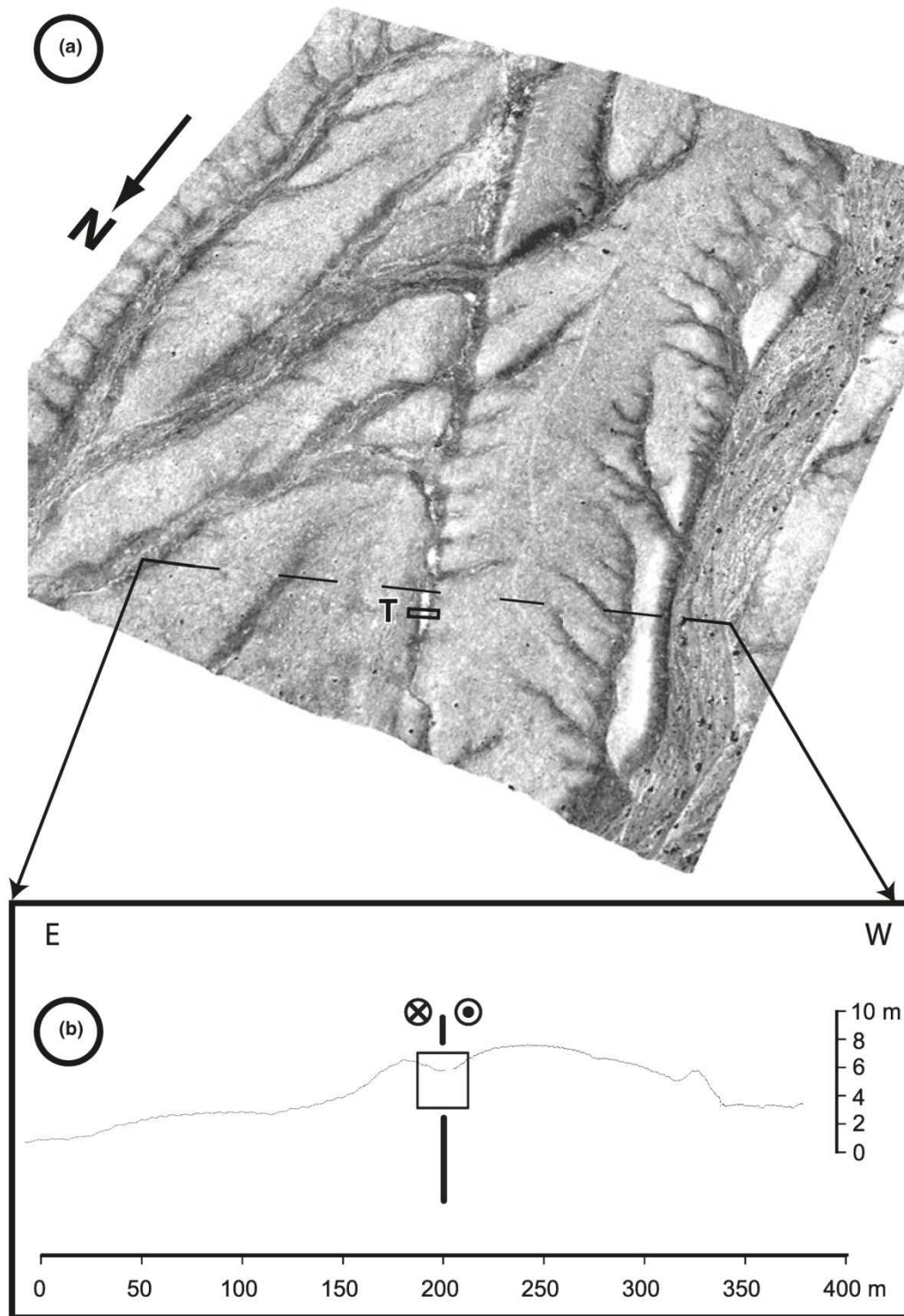


**Fig. 3** (a) 3-D perspective view of the excavation site obtained from draping a HR Quickbird image on a Digital Elevation Model worked out from a differential GPS survey. (b) Topographic profile (VE~14) across the fault zone with dots indicating the density of the GPS survey. A depression outlines the strike-slip fault and a gentle warping to the East possibly reflects blind thrusting and upper slip partitioning of a slightly transpressive motion at depth. Box is projection of the excavated area in Fig. 4.

**Table 1** Description of the sedimentary units observed within the Dehsir trench (see Fig. 4). Block names are in column headers and unit names are indicated in bold. Thin black lines are either block limits (vertical) or boundary between units (horizontal). Thick continuous black lines figure confidently determined event horizons of earthquake while thick dotted-dashed lines represent questionable event horizon.

East Block	East Tilted Zone	West Tilted Zone	Main Fault Zone	Central Sag	West Block
7. white-brown colluvial deposit - fair sorting, 2% (Ø 0.2–1 cm) clasts, sub-round to round - sandy on trench edges and silty in centre - thin run-off and aeolian deposits filling cracks within calcrete horizon	<b>D6:</b> coarse fissure fill, non-stratified, 70% (Ø 0.5–2 cm) clasts, angular - clay silt and coarse sand matrix - calcrete cementation with gypsum <b>D5:</b> brown colluvial wedge deposit - poor sorting, fair stratification - 60% (Ø 0.5–4 cm) clasts, angular - strong calcrete cementation - reworking alluvial material from the East block	<b>C2:</b> - light grey to beige colluvial deposits - fair sorting, non-stratified - 60% (Ø 0.5–4 cm) clasts, sub-round to round - silt and sand matrix - calcrete cementation with gypsum	<b>B2:</b> - red to brown alluvial-colluvial deposits - poor sorting, poor stratification, angular to sub-round - silt and sand matrix - 29.5 ± 9 OSL ka at B2 base - 20.7 ± 3.9 OSL ka in fissure fill on upper fl termination	<b>B1:</b> - light red to brown alluvial deposits - poor stratification, poor sorting - 5% (Ø 0.5–4 cm) clasts, angular to sub-round - clay silt and sand matrix, gypsum content increases upward - 26 ± 2.2 OSL ka - B1 top bracketted between 23.8 and 28.2 ka.	<b>A3b:</b> - white to brown colluvium - poor to medium sorting, non-stratified - 20% (Ø 0.5–4 cm) clasts, sub-round - silt and sand matrix - calcrete cementation with gypsum. <b>A3a:</b> - colluvial deposits, sand pebble channel with 80% clasts. - belong to the desert colluvial cover of A1 alluvial deposits.
<b>E1:</b> - distal alluvial fan deposits corresponding to uppermost terrace level above present-day streams - similar to A1 and D1 - 51.3 ± 21 OSL ka in a sand lens between I5 and I6 indicating age ranging between 30.3 and 72.3 ka	<b>D4:</b> - grey alluvial material, similar to D3b, - fair sorting, thin stratification - 80% (Ø 0.5–5 cm) clasts, sub-round - silt and sand matrix - sand lens with 21.1 ± 11.2 OSL ka <b>D3c:</b> - light brown alluvial deposits - fair sorting, fair stratification - 5% (Ø 0.5–3 cm) sub-round clasts in small lenses, clay and silt matrix <b>D3b:</b> grey alluvial material - fair sorting, poor stratification - 85% (Ø 0.5–4 cm) clasts, sub-round - silt and sand matrix - sand lens with 34.6 ± 17.5 OSL ka, indicating D3b age ranging between 17.1 and 52.1 ka. <b>D3a:</b> - brown alluvial deposits, fair sorting - 5% (Ø 0.5–2 cm) clasts, sub-round - similar to D3c.	<b>Dx:</b> light grey to beige colluviums - non-stratified fair sorting - 2% (Ø 0.2–1 cm) clasts - silt and coarse sand matrix - 41.5 ± 15.9 OSL ka - Dx age bracketed between 25.6 and 57.4 ka <b>D3:</b> - light grey colluvial deposits - poor sorting, non-stratified - 30% (Ø 0.2–2 cm) angular clasts - clay silt and coarse sand matrix - corresponds to distal runoff material reworking D1 and possibly D2 units close to fault scarp.	<b>C1:</b> - alluvial material similar to A1, D1, and E1 - (50%) clasts - unit highly sheared and disrupted showing broken clasts oriented parallel to T2–E3 zone	<b>A2:</b> - light grey to buffish alluvial material - poorly sorting, non-stratified - 25% (Ø 0.5–4 cm) clasts, sub-round - silt and clay matrix - channels with higher (35%) clay percentage - cut and fill within highest terrace (A1) - corresponds to mud flow deposits reworking A1	<b>A1:</b> - grey to brown alluvial material - poor-medium sorting, poor stratification - 80% (Ø 0.5–10 cm) clasts, sub-round to round - clay silt and sand matrix - carbonate cementation and gypsum - correspond to distal alluvial fan deposits of the uppermost terrace level observed above present-day streams.



**Table 2** Optically Stimulated Luminescence ages for the Deshir samples. Age determination requires knowledge of the equivalent ( $D_e$ ) and annual ( $D_a$ ) doses for each sample. Ages have been calculated for Quartz grains with size ranging between 90 and 250 microns.

Sample*	Unit	Equivalent Dose $D_e$ (Grays)†	depth (m)	Water (%)	$K_{\ddagger}$ (%)	$U_{\ddagger}$ (ppm)	$Th_{\ddagger}$ (ppm)	Annual Dose rate $D_a$ (Grays/ka)§	Age (ka)¶
HI/2006-I	B1	60.16 ± 4.60	1.2	0.9	1.22 ± 0.01	1.79 ± 0.05	6 ± 0.1	2.31 ± 0.06	26.0 ± 2.2
HI/2006-II	7	5.00 ± 2.37	4	1.1	0.73 ± 0.01	1.67 ± 0.05	5.5 ± 0.1	1.76 ± 0.04	2.8 ± 1.4
HI/2006-IV	B2	70.21 ± 21.24	0.8	1.2	1.2 ± 0.01	2.09 ± 0.05	6 ± 0.1	2.38 ± 0.06	29.5 ± 9.0
HI/2006-V	Dx	81.97 ± 31.23	1.3	1.0	0.98 ± 0.01	1.47 ± 0.05	5.9 ± 0.1	1.98 ± 0.05	41.5 ± 15.9
HI/2006-VI	B2	50.14 ± 9.26	1.5	1.3	1.27 ± 0.01	2.04 ± 0.05	6 ± 0.1	2.42 ± 0.06	20.7 ± 3.9
HI/2008-VII	D3b	47.00 ± 23.79	1.6	1.1	0.61 ± 0.01	1.1 ± 0.05	4.3 ± 0.1	1.36 ± 0.03	34.6 ± 17.5
HI/2008-VIII	D4	30.64 ± 23.77	0.95	0.9	0.66 ± 0.01	1.13 ± 0.05	4.6 ± 0.1	1.45 ± 0.03	21.1 ± 11.2
HI/2008-IX	E1	71.63 ± 29.22	2.8	1.2	0.66 ± 0.01	1.12 ± 0.05	4.5 ± 0.1	1.40 ± 0.03	51.3 ± 21.0

\*The samples were collected using stainless steel tubes (5 by 25 cm) and both ends were sealed and covered using both aluminium foil and black tape. Quartz was extracted from all samples using standard methods in the Sheffield Centre for International Drylands Research Centre Luminescence Laboratory (see Bateman and Catt (1996) for details).

†Luminescence measured through 7 mm Hoya U-340 filters in a Risø (Model TL/OSL-DA-15) automated TL/OSL system. The equivalent dose ( $D_e$ ) was obtained using the conventional quartz single aliquot regeneration method (Murray and Wintle, 2000).

‡Uranium, thorium and potassium concentrations were measured using inductively coupled plasma mass spectrometer (ICP-MS) at SGS laboratories Ontario, Canada.

§The annual dose ( $D_a$ ) was estimated from these data and the cosmic ray contributions as described in Fattahi et al. (2006, 2007).

¶Errors are 1 sigma.

spond to distal alluvial fan deposits that were probably shed by the Marvast River during Quaternary. Younger units of more local origin are exposed in the centre and the upper part of the trench and consist of:

- 1 alluviums (A2, D2, D3, D4) corresponding to surface runoff sediments emplaced by short streams and small channels reworking older units and flowing mainly parallel to the fault. Such a network has probably been similar to the current second-order streams (Fig. 2a);
- 2 muddy deposits corresponding to distal surface runoff material (B1, B2);
- 3 colluviums corresponding to desert cover (A3, C2, 7), colluvial wedge (D5), or fissure fills (D6, part of unit 7).

The stratigraphy has been constrained in age using Optically Stimulated Luminescence (OSL, Table 2). Although most ages have large uncertainties precluding accurate unit correlations, the ages indicate that unit 7 is Late Holocene (Marine Isotopic Stage MIS-1) while B2 and B1 are approximately coeval with MIS-2 ( $\approx 12$ –22 ka) and MIS-3 ( $\approx 22$ –59 ka) respectively. Then, D5, D6 and possibly C2 and A3 correlate with B2 (MIS2) whilst D4, D3, Dx, and possibly A2 correlate with B1 (MIS-3). Aggradation of older alluvial units A1, C1, D1 and E1

occurred partly during MIS-4 ( $\approx 59$ –80 ka). Finally, the calcrete formation should be of Early-Middle Holocene age, as the youngest deposits (unit 7,  $2.8 \pm 1.4$  ka) do not contain calcretes.

### Seismic event identification

The excavation evidences that coseismic surface ruptures have occurred repeatedly on the Deshir fault. The youngest event (ev1; Figs 4,5,6a) corresponds to open cracks and fissures filled by unit 7 and to the sealing unconformity on

the Main Fault Zone. Indeed, a western MFZ splay, sealed by unit 7 the thickness of which rapidly decreases eastward, indicates the occurrence of a small step prior to unit 7, hence a surface break coeval with ev1. The largest fissures are recognized on the two walls of the trench; they strike N170–180 obliquely to the N160 fault zone and to the slope of the scarp, as expected for dextral en echelon tension gashes. These fissures are remnants of en echelon cracks along a primary dextral tectonic break. They post-date A3 and subsequent calcrete



**Fig. 5** Field photograph showing the upper part of the trench and the east-facing scarp in the background. View to the south with 1.65 m tall geologist for scale. The smooth topography of the scarp contrasts markedly with the rugged set of fissures disrupting a calcrete and filled by recent sediments (aeolian sands and thin slope colluviums of unit 7, see also Fig. 4 and Table 1).

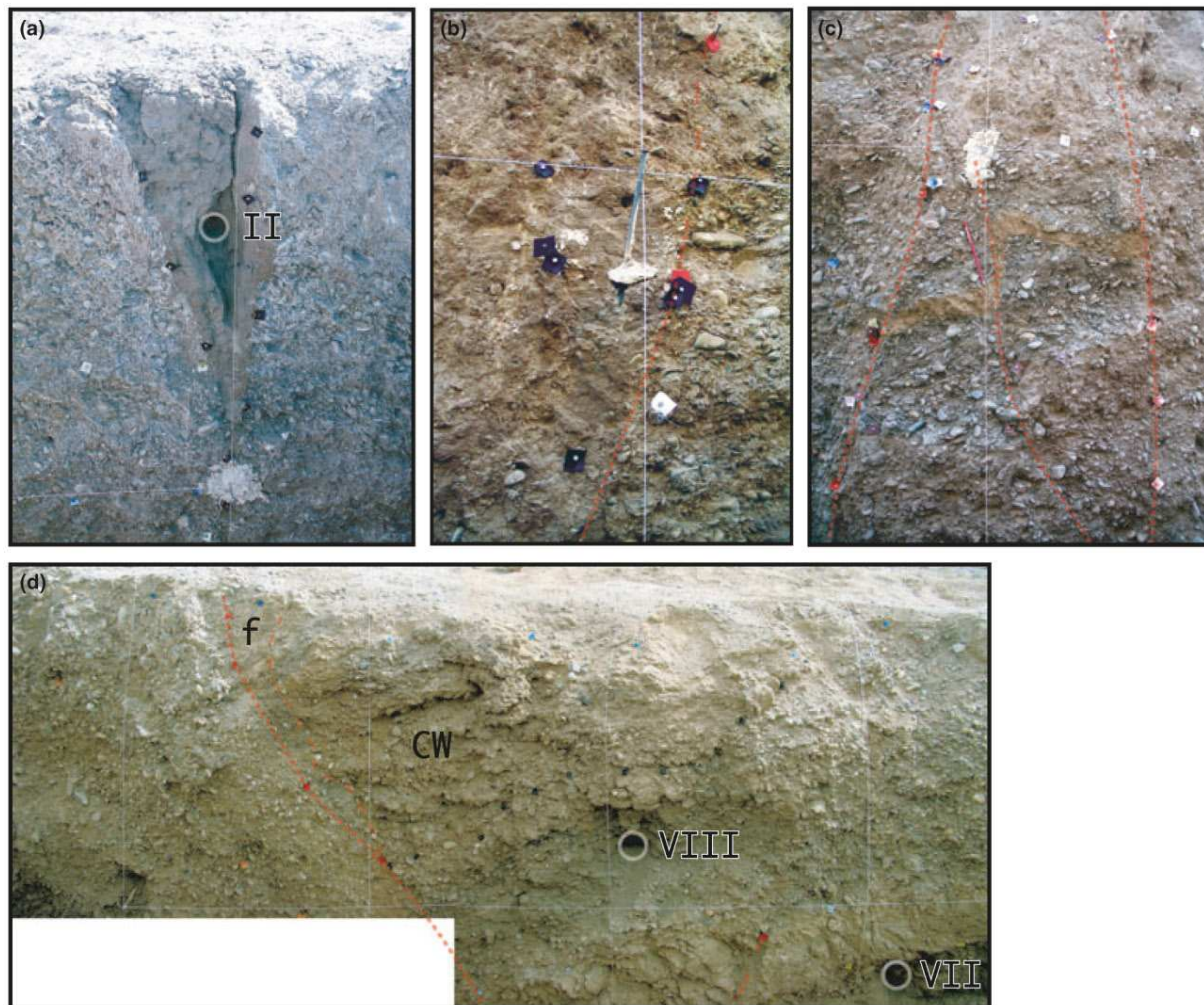


**Fig. 6** Evidence for coseismic deformations. (a) 1 m-deep fissure disrupting a gypsiferous calcrete developed from colluviums A3. The sandy-silty material of the fissure was emplaced probably during dust winter storms, shortly after the earthquake. The hole, 50 cm below ground surface, locates the OSL sample HI/2006-II. (b), fissure (dark blue flags) filled by sands abutting on f1 fault. (c), Steep faults disrupting coarse alluviums. The middle fault, disrupting an alternation of conglomeratic and sandy-silty layers (D2 unit), is sealed by a colluvium (D3 unit). (d), colluvial wedge (CW, brown horizontal layers, D5 unit) unconformable on 15–20°E dipping alluvial units tilted against a 50°W dipping fault. A fissure filled by gravelly material and coarse sands (f, D6 unit) disrupts the colluvial wedge. The fissure and the colluvial wedge have been both indurated by a calcrete pedogenesis and coated by a thin layer of sand and silt.

cementation and pre-date 7 not cemented by the calcrete. OSL dating within the infill of one of these fissures indicates that the causative seismic event occurred prior to  $2.8 \pm 1.4$  ka. As the sandy-silty material that fills the fissure has a significant aeolian component, it was probably emplaced shortly after the earthquake during winter dust storm and the OSL age of the infill provides a likely estimate of the time of the earthquake. The event horizon, pre-dating unit 7, is distinguished all along the trench. In con-

trast, older events are difficult to correlate across the entire trench. They are described in each block and identified with the letters T to Z on Fig. 4.

In the central sag and West block, west of f2, two additional event horizons may be identified below the ev1 horizon: evZ pre-dates B2 and post-dates B1 as the base of B2 is filling a fissure along the upper termination of f1 (Fig. 6b); evY pre-dates A2 and post-dates A1 as the base of A2 appears to be filling fissures within

A1. Three OSL ages indicate that evZ should have occurred between 20.5 and 28.2 ka and evY prior to 28.2 ka. Older seismic events may have occurred during B2 aggradation as this unit appears sealing f2 fault splays. However, their corresponding event horizons are not clearly identified within B2 unit.

Four additional event horizons may be identified below ev1, between f4 and f5 in the Eastern tilted zone: evV, evU, evW, and evT. EvV pre-dates D6 fissure fill and post-dates D5. As D6 is

cemented by the same calcrete to D5, evV cannot correspond to evI and therefore must post-date the calcrete. If evU pre-dates the D5 colluvial wedge (Fig. 6d) and post-dates D4, then evV and evU should correspond to surface breaks reactivating f5 between  $2.8 \pm 1.4$  ka and  $21.1 \pm 11.2$  ka.

The two older events, evW and evT, are ill-defined. evW may correspond to a small crack splaying off fault f5 and sealed by D4 unit. If this is the case then it has occurred between  $21.1 \pm 11.2$  and  $34.6 \pm 17.5$  ka. evT is extrapolated from the Western tilted zone where the D2-D3 limit is an event horizon.

Three event horizons may be identified below evI in the Western tilted zone between f3 and f4: evX pre-dates C2 and post-dates Dx. Indeed, the boundary between Dx and C2 appears as an event horizon as C2 is sealing f3 and most of the MFZ. Event evW would pre-date Dx and post-date D3, as the base of Dx appears filling a fissure along f4. evT, pre-dating D3 and post-dating D2, corresponds to the sealing unconformity of a f3 fault splay with drag fold by D3 (Fig. 6c). The OSL age of Dx indicates that evX post-dates while evW and evT pre-date  $41.5 \pm 15.9$  ka. Only two events, evI and evX, can be identified in the MFZ.

Considering available ages, there is no simple correlation for events prior to evI. Two options may be contemplated for the penultimate event that occurred between 20.5 and 28.2 ka: (1) evV could correlate with evX and evZ, also seen as the penultimate event in their respective blocks or (2) evV is not present to the west of f4 fault and then, evU, evX, and evZ may correspond to the same event. Correlations for older events are only speculative: evW is ill-defined, inaccurately dated between 9.8 and 52.1 ka, and not recognized to the west of the MFZ; evT, which pre-dates  $34.6 \pm 17.5$  and  $41.5 \pm 15.9$  ka, might correlate with evY.

## Conclusions

Palaeoseismic data give evidence for a maximum of five earthquakes on the Deshir fault during latest Pleistocene-Holocene. OSL dating constrains the late last three events to the last

$21.1 \pm 11.2$  ka, suggesting a rough return period of  $7 \pm 4$  ka. The time elapsed since the last earthquake likely ranges between 1.4 and 4.2 ka\*. The corresponding magnitudes, specifically for strike-slip earthquakes in a single trench, remain difficult to assess because the actual slip per event is not accessible. It is nonetheless possible to place loose constraints on the size of two earthquakes. For the antepenultimate event, evU, the thickness of the colluvial wedge D5 indicates significant ( $\approx 1$  m) vertical offset, hence large (several metres) horizontal displacement, along a primary strike-slip break and appears compatible with an event of magnitude  $M > 6.5$ . For the last event, the deep fissures in the trench are much larger than the small fissures observed along the tiny surface break of the 2003  $M = 6.5$  Bam earthquake (Jackson *et al.*, 2006). They rather compare with the prominent open fissures mapped along the 150 km-long portion of the North Anatolian Fault broken by the  $M_w = 7.6$  Izmit (Barka *et al.*, 2002) and  $M_w = 7.2$  Düzce (Akyüz *et al.*, 2002) earthquakes. Accordingly, the last event evidenced in the trench might have been of magnitude  $M \geq 7$  and large enough to account for the small stream offsets of 4–5 m documented by Meyer *et al.* (2006) only 30 kilometres to the South of the trench. Moreover, the gullies incised within the fan surface post-date the whole set of alluvial and colluvial units and yield a minimum slip-rate on the order of  $0.8\text{--}2.5$  mm yr<sup>-1</sup>, assuming their 25 m offset is at most  $21.1 \pm 11.2$  ka (age of D4, youngest colluviums pre-dating the abandonment of the fan surface and subsequently incised by streams flowing through the fault zone).

Although providing rough estimates on the recurrence and loose constraints on the magnitude of earthquakes, such studies are the only conceivable way for assessing seismic hazard in regions where the seismic

\*During the review process of this manuscript, a subsequent study of a small subset of the OSL data explored non-standard methods and unconventional statistical tests to narrow the error bars and has resulted in a refined likely age of  $2.0 \pm 0.2$  ka for the last earthquake (Fattahi *et al.*, 2009).

cycle spans a period of time longer than that accessible to instrumental and historical seismic records, as is the case of Central Iran. Several other faults, that are now recognized as active (e.g. Meyer and Le Dortz, 2007; Walker, 2008; Le Dortz *et al.*, 2009) but whose seismic behaviour remains unknown, require a better description of the current tectonics and an appropriate hazard assessment by trenching and application of chronological control.

## Acknowledgements

This study benefited from logistic and financial assistance from Geological Survey of Iran. UPMC Univ Paris06, INSU-CNRS, and CNES-SPOT Image (ISIS0403-622, ISIS0510-812) provided complementary funding. KL received a Ministry of Research and Education scholarship granted by the President of UPMC. We acknowledge constructive criticisms by F. Cinti, J-F. Ritz, R. Walker and an anonymous reviewer. Editor and Associate Editor, C. Doglioni and H. Pedersen, provided helpful suggestions.

## References

- Akyüz, H.S., Hartleb, R., Barka, A., Altunel, E., Sunal, G., Meyer, B., Armijo, R. and de Chabaliér, J.B., 2002. Field observations and slip distribution of the November 12, 1999 Düzce earthquake ( $M = 7.1$ ), Bolu-Turkey. *Bull Seism. Soc. Am.*, **92**, 61–66.
- Ambraseys, N.N. and Jackson, J.A., 1998. Faulting associated with historical and recent earthquakes in the Eastern Mediterranean region. *Geophys. J. Int.*, **133**, 390–406.
- Ambraseys, N. and Melville, C., 1982. *A History of Persian Earthquakes*. Cambridge University Press, Cambridge.
- Barka, A., Akyuz, H.S., Sunal, G., Cakir, Z., Dikba, A., Yerli, B., Armijo, R., Meyer, B., de Chabaliér, J.B., Rockwell, T., Dolan, J.R., Hartleb, R., Dawson, T., Christofferson, S., Tucker, A., Fumal, T., Langridge, R., Stenner, H., Lettis, W., Bachhuber, J. and Page, W., 2002. The August 17, 199 Izmit earthquake,  $M = 7.4$ , Eastern Marmara region, Turkey: study of surface rupture and slip distribution. *Bull. Seism. Soc. Am.*, **92**, 43–60.
- Bateman, M.D. and Catt, J.A., 1996. An absolute chronology for the raised beach and associated deposits at Sewerby, East Yorkshire, England. *J. Quatern. Sci.*, **11**, 389–395.
- Berberian, M., 1981. Active faulting and tectonics of Iran. In: *Zagros-Hindu*

- Kush-Himalaya Geodynamic Evolution, Geodynamic Series*, Chapter 3 (H. Gupta and F. Delany, eds), pp. 33–69. American Geophysical Union.
- Fattahi, M., Walker, R., Hollingsworth, J., Bahroudi, A., Talebian, M., Armitage, S. and Stokes, S., 2006. Holocene slip-rate on the Sabzevar thrust fault, NE Iran, determined using Optically-stimulated Luminescence (OSL). *Earth Planet. Sci. Lett.*, **245**, 673–684.
- Fattahi, M., Walker, R., Khatib, M.M., Dolati, A. and Bahroudi, J., 2007. Slip-rate estimates and past earthquakes on the Doruneh fault, eastern Iran. *Geophys. J. Int.*, **168**, 691–709.
- Fattahi, M., Nazari, H., Bateman, M.D., Meyer, B., Sébrier, M., Talebian, M., Le Dortz, K., Foroutan, M., Ahmadi Givi, F. and Ghorashi, M., 2009. Refining the OSL age of the last earthquake on the Dheshir fault, Central Iran. *Quat. Geochronology*. Doi:10.1016/j.quageo.2009.04.005. (in press).
- Jackson, J., Bouchon, M., Fielding, E., Funning, G., Ghorashi, M., Hatzfeld, D., Nazari, H., Parsons, B., Priestley, K., Talebian, M., Tatar, M., Walker, R. and Wright, T., 2006. Seismotectonic, rupture process, and earthquake-hazard aspects of the 2003 December 26 Bam, Iran, earthquake. *Geophys. J. Int.*, **166**, 1270–1292.
- Le Dortz, K., Meyer, B., Sébrier, M., Nazari, H., Braucher, R., Fattahi, M., Benedetti, L., Foroutan, M., Siame, L., Bourles, D., Talebian, M., Bateman, M.D. and Ghorashi, M., 2009. Holocene right-slip rate determined by cosmogenic and OSL dating on the Anar fault, Central Iran. *Geophys. J. Int.* Doi:10.1111/j.1365-246X.2009.04309.x. (in press).
- Masson, F., Anvari, M., Djamour, Y., Walpersdorf, A., Tavakoli, F., Daigünières, M., Nankali, H. and Van Gorp, S., 2007. Large-scale velocity field and strain tensor in Iran inferred from GPS measurements: new insight for the present-day deformation pattern within NE Iran. *Geophys. J. Int.*, **170**, 436–440. Doi:10.1111/j.1365-246X.2007.03477.x
- Meyer, B. and Le Dortz, K., 2007. Strike-slip kinematics in Central and Eastern Iran: Estimating fault slip-rates averaged over the Holocene. *Tectonics*, **26**, TC5009. Doi:10.1029/2006TC002073.
- Meyer, B., Mouthereau, F., Lacombe, O. and Agard, P., 2006. Evidence of Quaternary activity along the Deshir fault: implication for the Tertiary tectonics of Central Iran. *Geophys. J. Int.*, **164**, 192–201.
- Murray, A.S. and Wintle, A.G., 2000. Luminescence dating of quartz using an improved single-aliquot regenerative-dose protocol. *Radiat. Meas.*, **32**, 57–73.
- Vernant, Ph., Nilforoushan, F., Hatzfeld, D., Abassi, M.R., Vigny, C., Masson, F., Nankali, H., Martinod, J., Ashtiani, A., Bayer, R., Tavakoli, F. and Chery, J., 2004. Present-day crustal deformation and plate kinematics in the Middle East constrained by GPS measurements in Iran and Northern Oman. *Geophys. J. Int.*, **157**, 381–398.
- Walker, R., 2008. A remote sensing study of active folding and faulting in southern Kerman province, S.E. Iran. *J. Struct. Geol.*, **28**, 654–668.
- Walker, R. and Jackson, J., 2004. Active tectonics and late Cenozoic strain distribution in Central and Eastern Iran. *Tectonics*, **23**, TC5010. Doi:10.1029/2003TC001529.

*Received 12 September 2008; revised version accepted 15 June 2009*

### 2.3. Refined OSL ages and implications for seismic history of the Dehshir fault

#### 2.3.1. Site North

Two paleoseismic sites, sites North and South, which are about 30 km apart, have been studied along the southern part of the Dehshir fault (Figure 2.1). As seen in section 2.2, the paleoseismic data at the site North indicate that the Dehshir fault hosted at least three large-magnitude earthquakes during the last  $21.1 \pm 11.2$  kyr, yielding an average recurrence interval of  $7 \pm 4$  ka. However, due to the large uncertainties, more than 35%, associated with most of the OSL ages, the occurrence times of the identified earthquakes have been poorly constrained. Refining the analytical procedure used by *Nazari et al.* (2009a), six out of the eight OSL ages at the site North have been refined. The respective parameters are summarized in Table 2.1 (see also Appendixes A.1 and A.2). Accordingly, the uncertainties on the refined OSL ages are less than 10%. This allows to better constrain the time of the past earthquakes as well as to precise the recurrence interval of large earthquakes along the Dehshir fault.

*Fattahi et al.* (2010) have refined the age of one sample, the sample HI-II, to  $2.0 \pm 0.2$  ka by measuring 48 aliquots (9.6 mm diameter) of coarse grain quartz and using Finite Mixture Model (FMM, see Appendix A.1). Since this sample was collected from a fissure fill associated with the most recent earthquake at the site North, the refined OSL age indicates that the most recent earthquake occurred shortly before  $2.0 \pm 0.2$  ka (Figure 2.2 and Table 2.2).

The refined OSL ages also provide better constraints for the age of the third paleoearthquake at this site. To the east of the Main Fault Zone (MFZ), the base of unit 5 corresponds to the event horizon of the third earthquake (evU) within the tilted zone (Figure 2.2). Using FMM, the sample HI-VIII, which was collected below unit D5, yields an age of  $20.1 \pm 1.6$  ka. This age defines the lower bound of the third earthquake. To the west of the MFZ, two other refined OSL ages bracket an event horizon (evZ) within the central sag, which previously was considered by *Nazari et al.* (2009a) as a possible lateral equivalent of evU. These samples were collected from immediately below (sample HI-I, unit B1) and above (sample HI-VI, unit B2) the event horizon (evZ). Using Central Age Model (CAM), the age of the samples have been refined to  $26 \pm 1.0$  ka (sample HI-I) and  $20.2 \pm 0.8$  ka (sample HI-VI). These refined ages indicate that event Z (evZ, at the base of unit B2) occurred sometime between  $20.2 \pm 0.8$  and  $26 \pm 1.0$  ka. Therefore, accounting for the age of the third earthquake in the tilted zone (evU), younger than  $20.1 \pm 1.6$

ka, correlation of evU to the east of the MFZ with evZ to the west of it is very likely. In such a case, evZ in the central sag likely corresponds to the third earthquake, and the OSL age of  $20.2 \pm 0.8$  ka (sample HI-VI, within a fissure fill) defines the upper bound of this event. Thus, the age constraints on both sides of the MFZ imply that the third earthquake occurred between  $20.2 \pm 0.8$  ka (sample HI-VI) and  $20.1 \pm 1.6$  ka (sample HI-VIII). Combining these ages, the occurrence time of the third earthquake is bracketed between 19.4 and 21.7 ka.

The recurrence interval of large earthquakes at the site North can also be constrained using the refined OSL ages. The event horizons of the last three seismic events have been preserved to the east of the MFZ, at the base of units D5 (evU), D6 (evV) and 7 (ev1). The refined OSL age of the sample HI-VIII indicates that the last three earthquakes postdate  $20.1 \pm 1.6$  ka (Figure 2.2). Accounting for the occurrence of three earthquakes during 21.7 ka (maximum possible age of the sample HI-VIII) suggests an average recurrence interval of at most 7.2 ka. Alternatively, using the minimum possible age of the sample HI-VI (19.4 ka), youngest possible age of the third earthquake, one may estimate a recurrence interval of 6.5 ka. Thus, a rough estimate of the recurrence interval for the large earthquakes ranges between 6.5 and 7.2 ka. This rough estimate can be further refined by considering the occurrence of a seismic event at the base of unit D4 (evW), before  $20.1 \pm 1.6$  ka (sample HI-VIII), and accounting for the age of the most recent earthquake ( $2.0 \pm 0.2$  ka). Indeed, three seismic cycles from evW to ev1 should be bracketed by samples HI-VI and HI-II (Figure 2.2). Subtracting the age of  $2.0 \pm 0.2$  ka (sample HI-II) from  $20.2 \pm 0.8$  ka (sample HI-VI) provides a time duration of  $18.2 \pm 1.0$  kyr for the three seismic cycles. Therefore, the large uncertainty associated with the early proposed average recurrence interval of  $7 \pm 4$  ka (see section 2.2) can be significantly reduced to  $6.1 \pm 0.4$  ka.

Nevertheless, there is some evidence for the incompleteness of the stratigraphic records exposed in the trench exposure. To the east of the MFZ, the thickness of sediments between the sample HI-VIII ( $20.1 \pm 1.6$  ka) and unit 7 ( $2.0 \pm 0.2$  ka, sample HI-II) is less than 120 cm. Combining this with the time interval between the samples HI-II and HI-VIII ( $18.1 \pm 1.8$  kyr) indicates that the trench displays a discontinuous record of deposits between MIS-2 and the late Holocene. Similarly, to the west of the MFZ, near meter 9, combining the vertical thickness of sediments between the sample HI-VI ( $20.2 \pm 0.8$  ka) and unit 7 (<120 cm) with the relevant time interval of  $18.2 \pm 1.0$  kyr confirms such a gap of deposits. The lack of sediments is also discernible from the lateral correlation between evZ as penultimate event in the central sag and

evU as third event in the tilted zone. Indeed, due to the lack of sediments postdating evZ in the central sag, evidence for the penultimate event to the west of the MFZ is missing. Combining the time interval between the samples HI-VII ( $45.5 \pm 4.6$  ka) and HI-VIII ( $20.1 \pm 1.6$  ka) in the tilted zone, which ranges between 19.2 and 31.6 kyr, with the thickness of sediments between these two samples (<100 cm) indicates a prominent gap of sediments between MIS-3 and MIS-2.

In addition, another line of evidence also testifies for the lack of sediments in the trench exposure postdating the third earthquake. An intermittent stream about 200 m north of the trench cuts the lowest, hence the most recent terrace tread, and forms the youngest riser-cut (T1a/T0) at the site North (see Figure 5 in Appendix A.2). This riser-cut, which postdates the emplacement of the terrace T1a (at most 10.6 ka), is right-laterally offset by  $12 \pm 2$  m (*Le Dortz et al.*, 2011). Assuming the minimum horizontal offset of 4-5 m, previously documented by *Meyer et al.* (2006) along the southern part of the Dehshir fault, is related to a single large earthquake, the right-lateral offset of  $12 \pm 2$  m would have accumulated by two or three last large earthquakes. Thus, record of just one earthquake (ev1,  $2.0 \pm 0.2$  ka), in most of the trench length, postdating 10.6 ka may indicate that the records of at least one or two additional earthquakes during the Holocene have been missed.

The lack of sediments could result from either a prominent gap of sedimentation or significant erosion phase/s postdating the third earthquake ( $20.6 \pm 1.2$  ka). The lack of evidence for the penultimate earthquake to the west of the MFZ makes the first consideration unlikely. Rather, is more likely that the evidence of the penultimate event as well as another event/s have been removed by significant erosion phase/s along a local depression at the trench site (see Figure 3 in section 2.2).

All these considerations highlight the possibility of incomplete records of seismic events between MIS-3 and the late Holocene. This suggests that the estimated recurrence interval of  $6.1 \pm 0.4$  ka could be overestimated, and hence this interval should be considered as a maximum estimate. In other words, combining the overestimated recurrence interval of  $6.1 \pm 0.4$  ka with the elapsed time since the most recent earthquake ( $2.0 \pm 0.2$  ka) does not rule out the possibility of occurrence of the next earthquake on the southern part of the Dehshir fault in the near future.

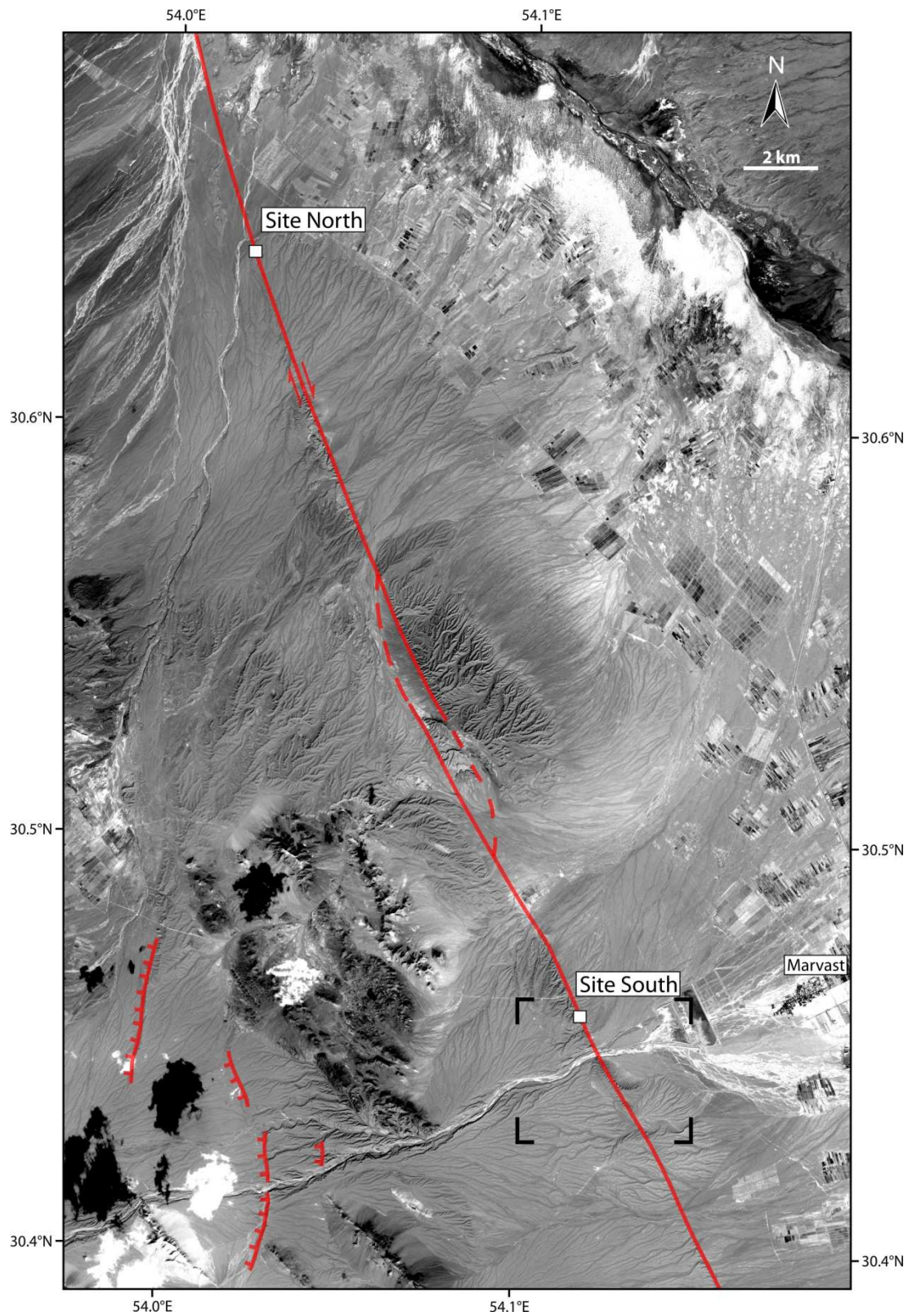


**Figure 2.1.** SPOT satellite image showing locations of two paleoseismic sites along the southern part of the Dehshir fault, near Marvast Town. Black corners delineate the outline of Figure 2.2.

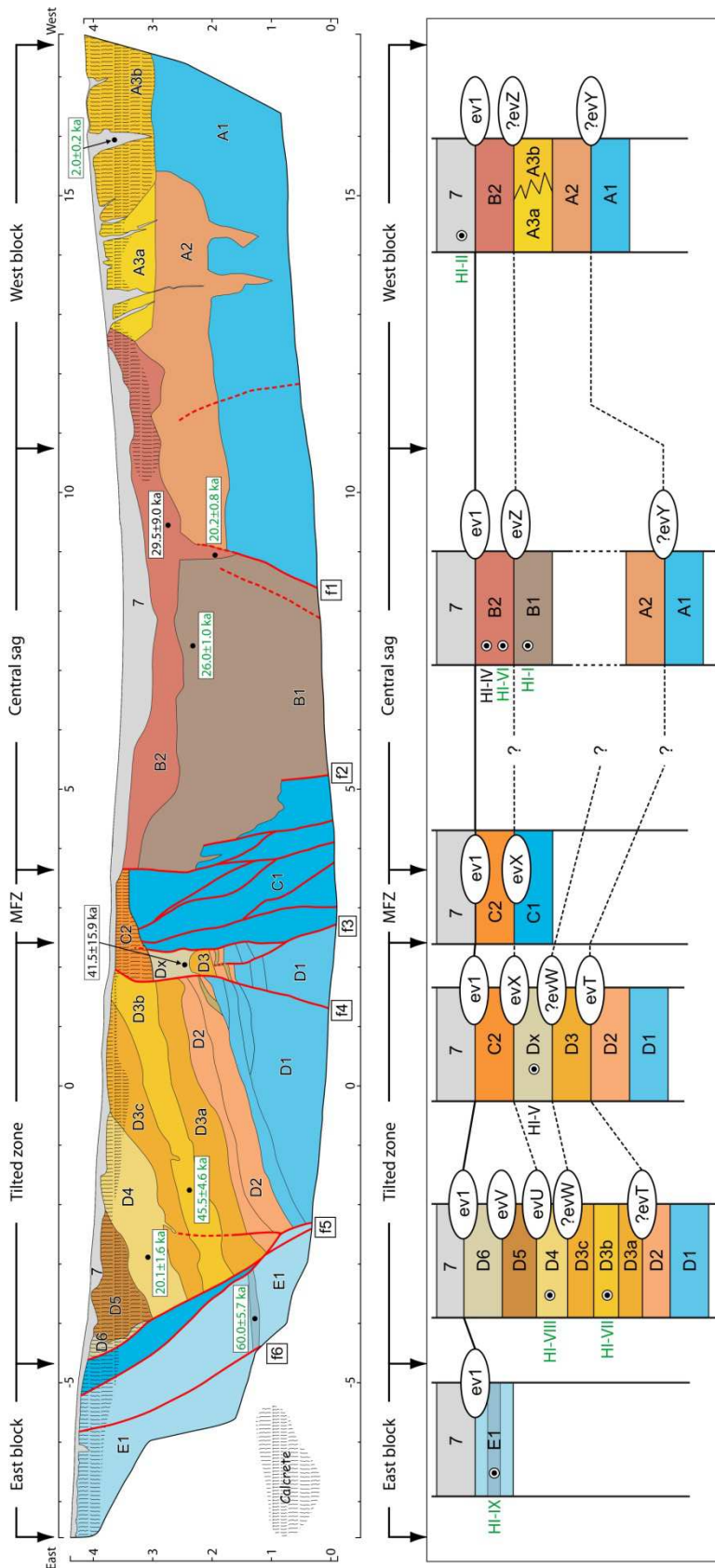


**Figure 2.2.** Log of the southern wall of the Dehshir trench at site North (top) and simplified stratigraphic correlation (bottom) redrafted from Figure 4 of Nazari *et al.* (2009a). Refined OSL ages are indicated in green.

**Table 2.1.** Summary of equivalent dose, annual dose rate, and OSL ages of the samples collected from two trenches at the sites North and South. The weighted mean OSL ages which were published by *Nazari et al.* (2009a) have been refined following the statistical analysis used by *Fattahi et al.* (2010) to account for partial bleaching (see Appendix A.1).

Sample	Latitude (°N)	Longitude (°E)	Depth (cm)	Water (percent)	K (percent)	U (percent)	Th (percent)	Equivalent dose CAM (Gy)	Equivalent dose FMM <sup>a</sup> (Gy)	Annual dose rate (Gy ka <sup>-1</sup> )	Age (ka)
<i>Site North</i>											
HI-II	30.64113	54.02119	45	1.1	0.73	1.67	5.5	6.79±0.08	3.63±0.28	1.79±0.06	2.0±0.2 <sup>b</sup>
HI-VI	30.64121	54.02127	150	1.3	1.27±0.01	2.04±0.05	6.0±0.1	48.8±0.3		2.43±0.09	20.2±0.8 <sup>c</sup>
HI-VIII	30.64123	54.02148	95	0.9	0.66±0.01	1.13±0.05	4.6±0.1	45.3±7.1	29.3±2.0	1.45±0.03	20.1±1.6 <sup>b</sup>
HI-I	30.64118	54.02131	120	0.9	1.22±0.01	1.79±0.05	6.0±0.1	60.2±0.28		2.29±0.09	26.0±1.0 <sup>c</sup>
HI-VII	30.64123	54.02145	160	1.1	0.61±0.01	1.1±0.05	4.3±0.1	62.0±6.0		1.36±0.03	45.5±4.6 <sup>c</sup>
HI-IX	30.64123	54.02150	280	1.2	0.66±0.01	1.12±0.05	4.5±0.1	83.0±7.3		1.40±0.03	60.0±5.7 <sup>c</sup>
<i>Site South</i>											
AB-I	30.45719	54.11822	90	1.1±0.2	0.86±0.01	0.86±0.01	4.2±0.1	73.3±3.7	72.9±3.8	1.83±0.05	39.7±2.6 <sup>b</sup>
AB-II	30.45719	54.11831	70	1.1±0.2	1.1±0.01	1.1±0.01	59±0.1	57.4±7.6	43.2±2.3	2.16±0.05	20.0±1.3 <sup>b</sup>

<sup>a</sup>Finite Mixture Model (*Roberts et al.*, 2000) of replicate  $D_e$  values only undertaken where  $D_e$  distributions were multimodal, skewed and/or scattered (see section 1.3.2.3 for details).

<sup>b</sup>Age based on  $D_e$  determined using Finite Mixture Model (FMM, *Roberts et al.*, 2000).

<sup>c</sup>Age based on  $D_e$  determined using Central Age Model (CAM, *Galbraith et al.*, 1999).

**Table 2.2.** Description of the sedimentary units observed within the Dehshir trench at site North (redrafted from Table 1 of Nazari *et al.*, 2009a). Refined OSL ages are indicated in bold (see Figure 2.2).

East Block	East Tilted Zone	West Tilted Zone	Main Fault Zone	Central Sag	West Block	
7: White-brown colluvial deposit -fair sorting, 2% (Ø 0.2-1 cm) clasts, sub-rounded to rounded -sandy on trench edges and silty in centre -thin run-off and aeolian deposits filling cracks within calcrete horizon, crack infill with <b>2.0±0.2 OSL ka</b>						
<p><b>E1:</b></p> <ul style="list-style-type: none"> <li>- distal alluvial fan deposits corresponding to uppermost terrace level above present-day streams</li> <li>- similar to A1 and D1</li> <li>- <b>60.0 ± 5.7 OSL ka</b> in a sand lens between f5 and f6</li> </ul>	<p><b>D6:</b> coarse fissure fill, non-stratified, 70% (Ø 0.5-2cm) clasts, angular</p> <ul style="list-style-type: none"> <li>- clay silt and coarse sand matrix</li> <li>- calcrete cementation with gypsum</li> </ul>	<p><b>C2:</b></p> <ul style="list-style-type: none"> <li>- light grey to beige colluvial deposits</li> <li>- fair sorting, non-stratified</li> <li>- 60% (Ø 0.5-4cm) clasts, sub-rounded to rounded</li> <li>- silt and sand matrix</li> <li>- calcrete cementation with gypsum</li> </ul>		<p><b>B2:</b></p> <ul style="list-style-type: none"> <li>- red to brown alluvial-colluvial deposits</li> <li>- poor sorting, poor stratification</li> <li>- 20% (Ø 0.5-2cm) clasts</li> <li>- angular to sub-rounded</li> <li>- silt and sand matrix</li> <li>- <b>20.2±0.8 OSL ka</b> at B2 base</li> <li>- <b>29.5±9.0 OSL ka</b> in fissure fill on upper fl termination</li> </ul>	<p><b>A3a:</b></p> <ul style="list-style-type: none"> <li>- white to brown colluvium</li> <li>- poor to medium sorting, non-stratified</li> <li>- 20% (Ø 0.5-4cm) clasts, sub-rounded</li> <li>- silt and sand matrix</li> <li>- calcrete cementation with gypsum</li> </ul>	<p><b>A3b:</b></p> <ul style="list-style-type: none"> <li>- colluvial deposits, sand pebble channel with 80% clasts</li> <li>- A3a and A3b cut and fill within A2</li> <li>- belong to the desert colluvial cover of A1 alluvial deposits</li> </ul>
	<p><b>D5:</b> brown colluvial wedge deposit</p> <ul style="list-style-type: none"> <li>- poor sorting, fair stratification</li> <li>- 60% (Ø 0.5-4cm) clasts, angular</li> <li>- strong calcrete cementation</li> <li>- reworking alluvial material from the East block</li> </ul>			<p><b>D4:</b></p> <ul style="list-style-type: none"> <li>- grey alluvial material, similar to D3b</li> <li>- fair sorting, thin stratification</li> <li>- 80% (Ø 0.5-5cm) clasts, sub-rounded</li> <li>- silt and sand matrix</li> <li>- sand lens with <b>20.1 ± 1.6 OSL ka</b></li> </ul>		
		<p><b>D3c:</b></p> <ul style="list-style-type: none"> <li>- light brown alluvial deposits</li> <li>- fair sorting, fair stratification</li> <li>- 5% (Ø 0.5-3cm) sub-rounded clasts in small lenses, clay and silt matrix</li> </ul>	<p><b>D3:</b></p> <ul style="list-style-type: none"> <li>- light grey colluvial deposits</li> <li>- poor sorting, non-stratified</li> <li>- 30% (Ø 0.2-2cm) angular clasts</li> <li>- clay silt and coarse sand matrix</li> <li>- corresponds to distal runoff material reworking D1 and possibly D2 units close to fault scarp</li> </ul>		<p><b>A2:</b></p> <ul style="list-style-type: none"> <li>- light grey to buffish alluvial material</li> <li>- poor sorting, non-stratified</li> <li>- 25% (Ø 0.5-4cm) clasts, sub-rounded</li> <li>- silt and clay matrix</li> <li>- channels with higher (35%) clast percentage</li> <li>- cut and fill within highest terrace (A1)</li> <li>- corresponds to mud flow deposits reworking A1</li> </ul>	
		<p><b>D3b:</b> grey alluvial material</p> <ul style="list-style-type: none"> <li>- fair sorting, poor stratification</li> <li>- 85% (Ø 0.5-4cm) clasts, sub-rounded</li> <li>- silt and sand matrix</li> <li>- sand lens with <b>45.5 ± 4.6 OSL ka</b></li> </ul>				
		<p><b>D3a:</b></p> <ul style="list-style-type: none"> <li>- brown alluvial deposits, fair sorting</li> <li>- 5% (Ø 0.5-2cm) clasts, sub-rounded</li> <li>- clay and silt matrix</li> <li>- similar to D3c</li> </ul>				
		<p><b>D2:</b> grey to light brown alluvial material, dark level for red-brown sands</p> <ul style="list-style-type: none"> <li>- fair sorting, fair stratification</li> <li>- 80% (Ø 0.2-7cm) clasts, sub-rounded to rounded</li> <li>- clay silt and sand matrix, less cemented and more layered than D1</li> <li>- overlying D1 without noticeable unconformity</li> <li>- corresponds to remnants of intermediate alluvial terrace younger than A1, D1, and E1 and emplaced approximately parallel to Dehshir fault</li> </ul>	<p><b>C1:</b></p> <ul style="list-style-type: none"> <li>- alluvial material similar to A1, D1, and E1</li> <li>- 50% clasts</li> <li>- unit highly sheared and disrupted showing broken clasts oriented parallel to f2-f3 zone</li> </ul>		<p><b>A1:</b></p> <ul style="list-style-type: none"> <li>- grey to brown alluvial material</li> <li>- poor-medium sorting, poor stratification</li> <li>- 80% (Ø 0.5-10cm) clasts, sub-rounded to rounded</li> <li>- clay silt and sand matrix</li> <li>- carbonate cementation and gypsum</li> <li>- correspond to distal alluvial fan deposits of the uppermost terrace level observed above present-day streams</li> </ul>	
	<p><b>D1:</b> alluvial deposit similar to A1 and E1</p>					

### 2.3.2. Site South

This site is located about 30 km south of the site North (Figures 2.1). There, the fault trace with an overall strike of N153°E is manifested both on the satellite imageries and in the field, where the fault cuts through the Neogene deposits, the late Pleistocene and Holocene alluvial fans and terraces as well as the active streams. The remnants of the Neogene deposits including Pliocene (?) fanglomerates and marls cropping out mostly close to the fault zone (Figure 2.3). The late Pleistocene and Holocene inset terraces are divided into several different levels (T0, T1a, T1b, T2 and T3) by *Le Dortz et al.* (2011) and dated using cosmogenic  $^{36}\text{Cl}$  and  $^{10}\text{Be}$  as well as OSL dating (see Appendix A.2). According to the dating results, the maximum possible ages of the identified levels have been constrained to 10.6 ka (T1a), 23.4 ka (T1b), 28.2 ka (T2), and 271 ka (T3). The abandoned terrace treads and alluvial fans are incised by tributary gullies and recent streams, which are dextrally offset along the fault between 4 and 400 m (*Meyer et al.*, 2006; *Le Dortz et al.* 2011).

The paleoseismic site is located some 1 km to the north of the Marvast River at 30.4572°N, 54.1183°E, and 1609 m altitude above sea level (asl, Figure 2.3). The trench site is bounded to the west by a scarp (>10 m) made of Neogene fanglomerates and marls. These Neogene deposits have been deeply (8 m) incised by an intermittent stream to the north and slightly (2.5 m) incised to the south by a narrow gully. To the east of the scarp, a thin veneer of the most recent alluvial deposits partly conceals the remnants of an older alluvial fan that is likely coeval with T2 level (yellow shading in Figure 2.3). The highest, hence oldest alluvial surface that is probably coeval with the emplacement of T3 has been preserved south of the trench site (orange shading in Figure 2.3).

Four paleoseismic trenches were excavated within the most recent alluvial material and most likely T2 surface both across and parallel to the fault. Two trenches were excavated across the fault trace, and two fault-parallel trenches were dug on both sides of the fault. Each of the fault-parallel trenches extends up to some 22 m and was excavated some 12 m away from the fault trace. These fault-parallel trenches display no potential marker to trace on both sides of the fault; hence any comparable piercing point was detected on each side of the fault. The fault-perpendicular trenches provide evidence for at least two seismic events as discussed in the next paragraphs for the northern trench.

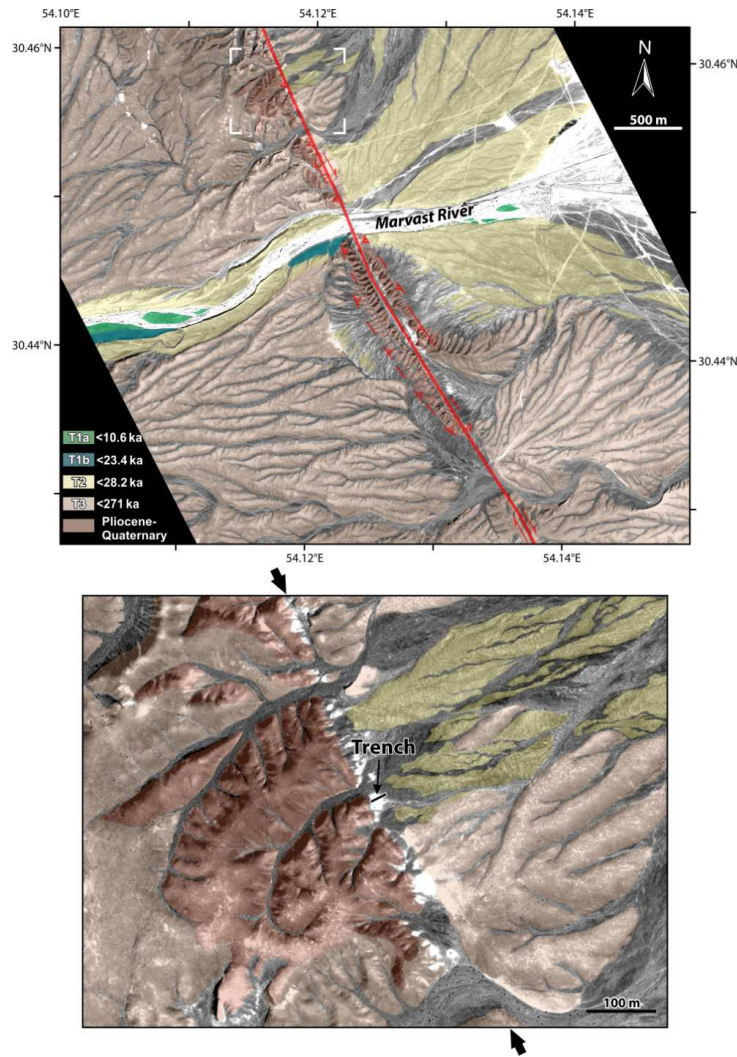


**Figure 2.3.** (top) Geomorphic interpretation overlain on Quickbird satellite image of the Dehshir fault west of the Marvast Town. Ages of terrace treads are from *Le Dortz et al.* (2011), see Appendix A.2. Terrace surfaces and abandoned fans are shaded as a function of increasing elevation and age (same code as for Figure 2 of *Le Dortz et al.*, 2011). White corners denote outline of the close up on the trench site (bottom). White patches outline thin layers of silts and clays washed out from the scarp during episodic surface runoff and consequently have been accumulated within the fault zone, between black arrows. Note mismatch of the alluvial fan surfaces with their source streams across the fault zone.

The northern trench strikes N63°E, perpendicular to the fault trace, has a length of 18 m, depth of up to 3.8 m, and width of some 3 m (Figure 2.4). This trench exposes two different types of sediments that are separated by a steep fault zone near meter 11 (Figure 2.4a). Indeed, the fault zone juxtaposes sequences of sub-horizontal, coarse-grained, alluvial sediments against the sheared marls deposits. To the west, many steep W-dipping fault strands cut through the

Neogene (Pliocene?) marls while to the east, only two fault strands cut across the late Pleistocene alluvial deposits between meters 1 and 4. The measurements of the fault planes indicate that the majority of the fault strands have an average strike of  $N145^{\circ} \pm 5^{\circ}$ , which are dominated by an average dip of  $75^{\circ} \pm 5^{\circ}$  toward southwest (Figures 2.4b-2.4e and Table 2.3). A few observed striations on the measured fault planes indicate a dominant right-lateral component, mostly with a plunge of less than 15 degrees toward northwest.

The oldest sediments recorded in the trench correspond to the Neogene (Pliocene?) marls (units 1, 2, 3, and 12), which are exposed to the east of the fault zone. The alluvial sediments exposed to the east of the fault zone (units 4-11 and 13) are mainly composed of fining-upward coarse pebbles and sparse cobbles with coarse-grained sandy matrix (Figure 2.5). The upper one meter of the sediment pile (units 14, 15, and 16) corresponds to a colluvial veneer and contains matrix-supported pebbles, which are then affected by compact carbonate cement (unit 17) in the fault zone between meters 9 and 11. The later unit is affected by a fissure that was filled by colluvial deposits (unit 18). The youngest sediments (units 19 and 20) represent a thin cover of whitish to grey fine-grained sediments washed out from the Neogene conglomerates and marls to the west and sealed older units.

The stratigraphic record exposed in the trench excavation provides evidence of at least two seismic events postdating unit 17. Many fault strands, west of meter 8, cut through all the exposed sediments up to the ground surface, testifying for the occurrence of most recent earthquake (EH-A in Figure 2.6) at the site South. A fissure near meters 10 and 11, with a maximum depth of some 1 m has affected units 3 and 17 and was subsequently filled with coarse sands and scattered coarse pebbles (5 cm) of unit 18. This indicates occurrence of penultimate event postdating units 3 and 17 and predating unit 18, hence its event horizon lies at the base of unit 18. Since this later unit as well as the western edge of the fissure fill are sealed by unit 19, a lateral equivalent of unit 20, therefore the event horizon of the penultimate earthquake (EH-B) can also be traced at the base of units 19 and 20 (Figure 2.6). A fault strand, near meter 2, terminates at the base of unit 20, indicating the occurrence of the penultimate event prior to the aggradation of unit 20. In addition, two fault strands to the west of the fissure fill cut up unit 3 and terminate below unit 18. These fault strands have been formed either during the penultimate event or by the most recent one.

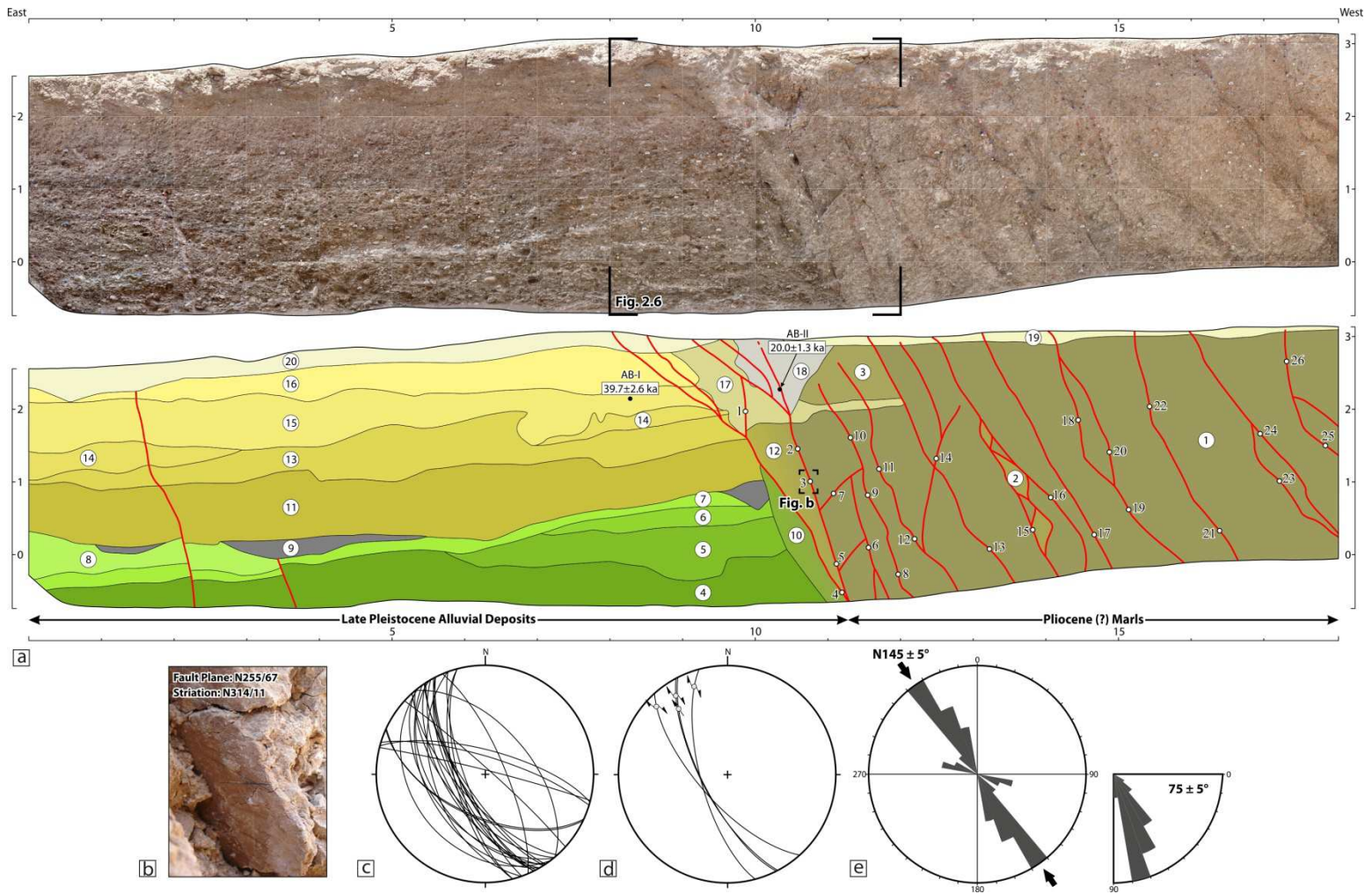


**Figure 2.4.** (a) Photomosaic (top) and simplified log (bottom) of the south wall of the Dehshir trench at site South. The older, Pliocene (?) marls to the west of the fault zone have been abutted the younger, late Pleistocene alluvial deposits to the east. (b) Oblique view of a measured fault plane and associated striae. (c) Stereoplots of the measured fault planes (see Table 2.3 for details). (d) Measured striations on the fault planes (great circles) are shown by grey dots and senses of motion are indicated by arrows. (e) Distribution rose diagram of the measured fault planes indicates an average strike of  $N145 \pm 5^\circ$  and a dominant dip of more than  $70^\circ$ .

**Table 2.3.** Summary of the measured fault planes and striae within the Dehshir trench at site South. Measurement locations are indicated by white circles in Figure 2.3.

Fault Plane No.	Dip Direction	Dip	Trend	Plunge	Fault Plane No.	Dip Direction	Dip	Trend	Plunge
1	255	67			14	67	75		
2	228	69	314	11	15	255	70	339	15
3	243	71	323	26	16	232	32		
4	240	62			17	230	62		
5	242	71	327	15	18	42	86		
6	236	74			19	15	72		
7	50	55			20	17	77		
8	243	68			21	204	58		
9	250	51			22	14	87		
10	237	60			23	235	50		
11	237	72			24	205	57		
12	239	45			25	243	66		
13	230	48			26	250	75		

Two OSL samples (AB-I and AB-II) were collected from the upper 1 m, one (sample AB-I) from the upper parts of the alluvial material (unit 15) and the another one (sample AB-II) at the base of the fissure fill (unit 18, Figure 2.4). Using FMM, the ages of these two samples are  $39.7 \pm 2.6$  ka (sample AB-I) and  $20.0 \pm 1.3$  ka (sample AB-II). The age of sample AB-II provides an extreme lower bound for the occurrence time of the most recent earthquake ( $20.0 \pm 1.3$  ka). This sample also provides an upper bound for the age of the penultimate earthquake (18.7 ka; minimum possible age of the sample AB-II). The age of sample AB-I brackets the extreme oldest possible age of the penultimate earthquake (42.3 ka; maximum possible age of the sample AB-I). Therefore, the penultimate earthquake occurred sometime between 42.3 and 18.7 ka, with a more likely age of shortly before  $20.0 \pm 1.3$  ka (sample AB-II).

Therefore, the trench exposure at the site South provides evidence of at least two seismic events within the last  $20.0 \pm 1.3$  kyr (sample AB-II). Accounting for the age of the third earthquake in the site North ( $20.6 \pm 1.2$ ), is very likely that the penultimate event in the site South is equivalent to the third earthquake at the site North. This implies that the surface rupture of the third earthquake extended at least from the site North to the site South, for some 30 km. Using the empirical relationships linking surface rupture lengths and moment magnitudes for strike-slip faults, proposed by *Wells and Coppersmith* (1994), the minimum length of the surface rupture of some 30 km would yield a magnitude of  $M_w \approx 7$  for the third earthquake. However, due to the lack of recent sediments mostly younger than 20 ka, at both sites, unraveling the

seismic history of the Dehshir fault during late MIS-2 and early-middle Holocene timescales will remain out of reach as long as additional paleoseismic studies will not be conducted.

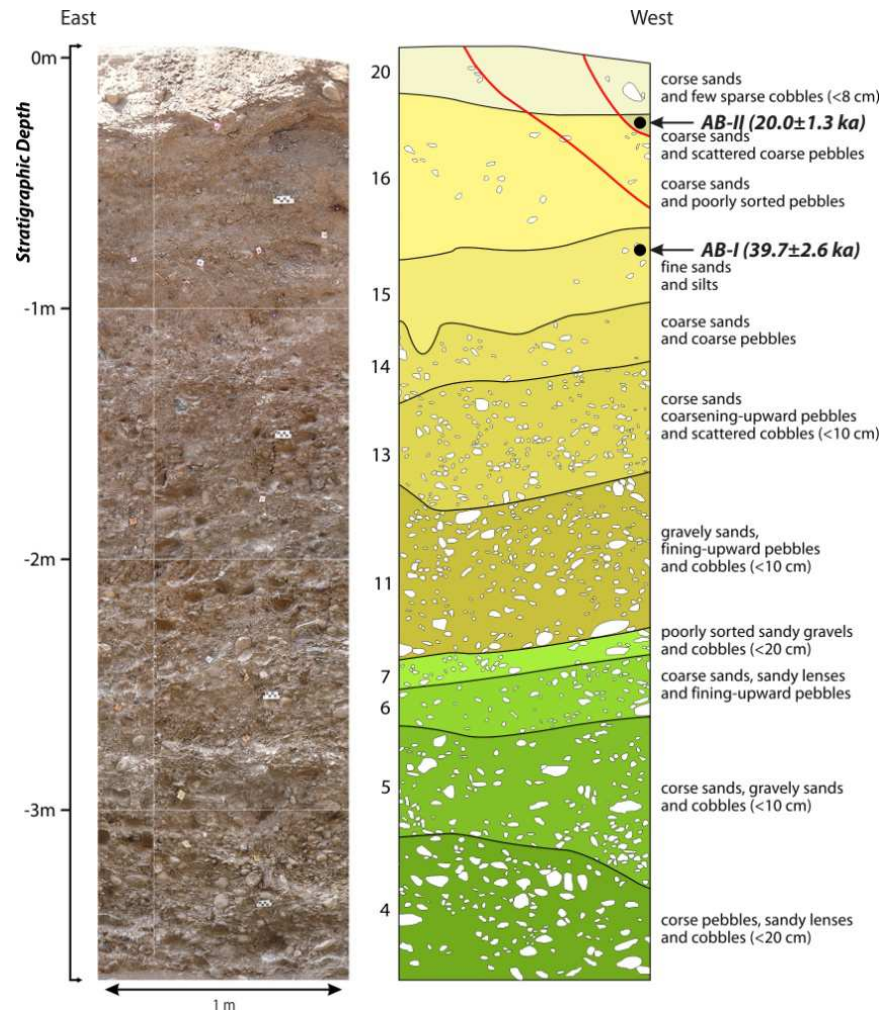


**Figure 2.5.** Photomosaic (left) and corresponding stratigraphic log (right) of the deposits exposed to the east of the main fault zone in the Dehshir trench at site South. Black dots locate the vertical positions of two refined OSL samples (see exact locations in Figure 2.4).

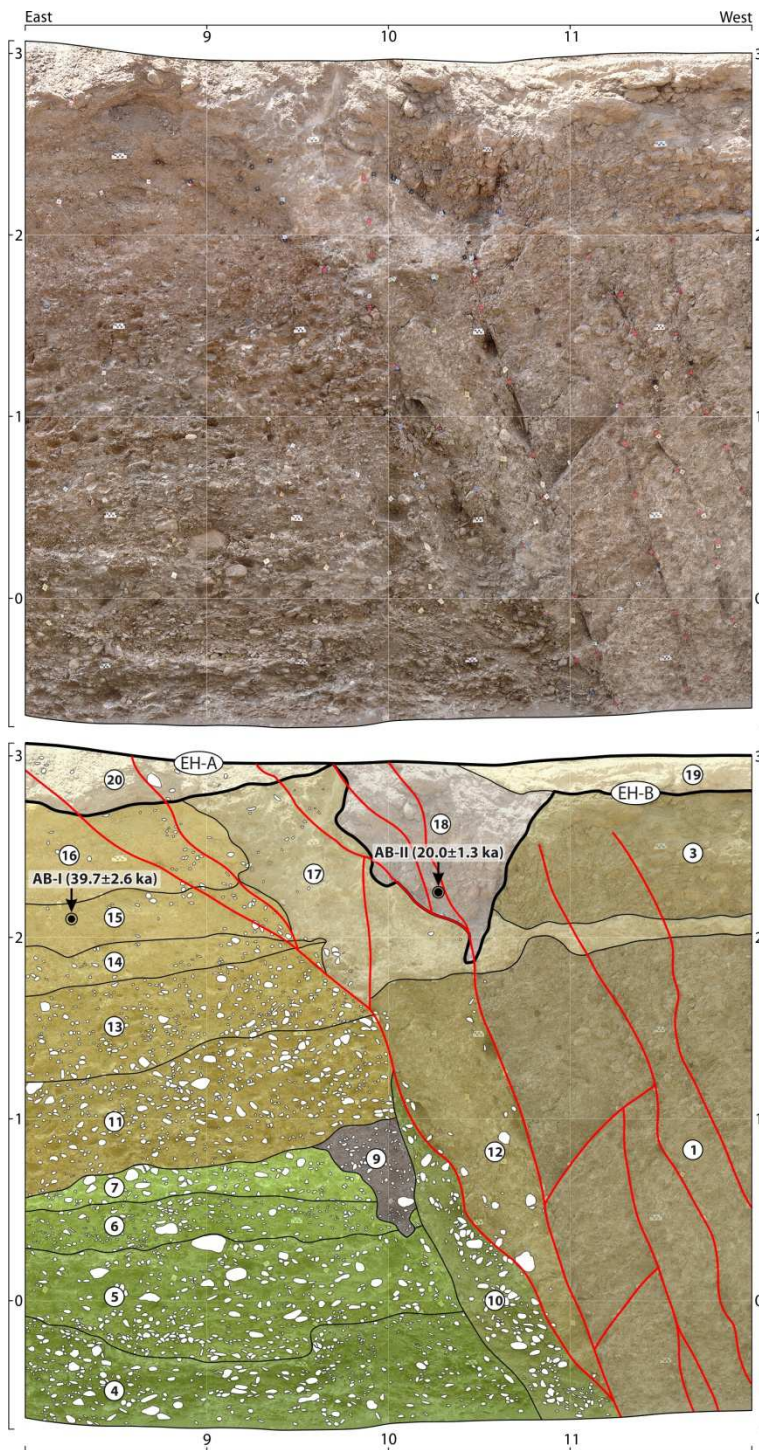


**Figure 2.6.** Photomosaic (top) and interpretation (bottom) of the main fault zone exposed on the south wall of the Dehshir trench at site South showing evidence for events A and B (see Figure 2.4 for location). Unit 18 corresponds to a fissure fill that has formed as a result of event B. The fissure fill has been covered by units 19 and 20 and subsequently faulted by event A. Location of two refined OSL samples with corresponding ages are indicated (see Table 2.1 for the OSL parameters).

The age of sample AB-I can also be considered as an oldest possible age of the abandonment of the alluvial surface at the trench site, where two abandoned alluvial surfaces (yellow shading in Figures 2.3 and 2.7) are right-laterally offset by the fault. Restoring the remnants of the offset alluvial fans to the possible source streams along the fault provides the extreme lower and upper bounds of offset on the order of 25 and 55 m (Figure 2.7). Indeed, restoring cumulative slip of 55 m realigns a north-facing slope of the alluvial fan to the east of the fault trace with a south-facing slope of the older (Pliocene?) deposits to the west of the fault. This indicates that the actual right-lateral offset of the alluvial surface should be less than 55 m, and the restoration should be considered as a maximal estimate. Consequently, combining the abandonment age of 37.1 ka (youngest possible age of the sample AB-I) with the maximum right-lateral offset of 55 m would bracket the upper bound of slip rate by  $1.48 \text{ mm yr}^{-1}$ . Alternatively, combining the oldest possible age of the sample AB-I (42.3 ka) with the minimum offset of 25 m yields a minimum slip rate of  $0.6 \text{ mm yr}^{-1}$ .

One can also assume the emplacement of the young alluvial surfaces at the trench site is coeval with the T2 level dated about one kilometer to the south by *Le Dortz et al.* (2011). In that scheme, one can retain an abandonment age younger than 28.2 ka for the young alluvial surfaces at the trench site (Figure 2.3). Hence, combining the age of 28.2 ka with the minimum right-lateral offset of 25 m provides a lower bound of slip rate of  $0.88 \text{ mm yr}^{-1}$ , in agreement with the minimum slip rate of  $0.9 \text{ mm yr}^{-1}$  estimated by *Le Dortz et al.* (2011). Combining the age of 28.2 ka with the maximum right-lateral offset of 55 m yields an upper bound of slip rate of  $1.95 \text{ mm yr}^{-1}$ . From these three upper bounds of slip rate ( $1.48$ ,  $1.5$ , and  $1.95 \text{ mm yr}^{-1}$ ) one has to retain the smallest one. Therefore, the slip rate of  $1.48 \text{ mm yr}^{-1}$  should be considered as a safe estimate of the maximum right-slip rate. Also, the largest amount of the minimum slip rates ( $0.9 \text{ mm yr}^{-1}$ ) provides a safe estimate of the minimum slip rate. Thus, all the considerations bracket the right-slip rate of the Dehshir fault by  $1.2 \pm 0.3 \text{ mm yr}^{-1}$ .

Accounting for the average slip rate of  $1.2 \text{ mm yr}^{-1}$  and considering the elapsed time since the most recent earthquake ( $2.0 \pm 0.2 \text{ ka}$ ) would imply that the southern part of the Dehshir fault is theoretically capable at present to produce a large-magnitude ( $M_w > 7$ ) earthquake with an average horizontal slip of  $\sim 2.5 \text{ m}$ .

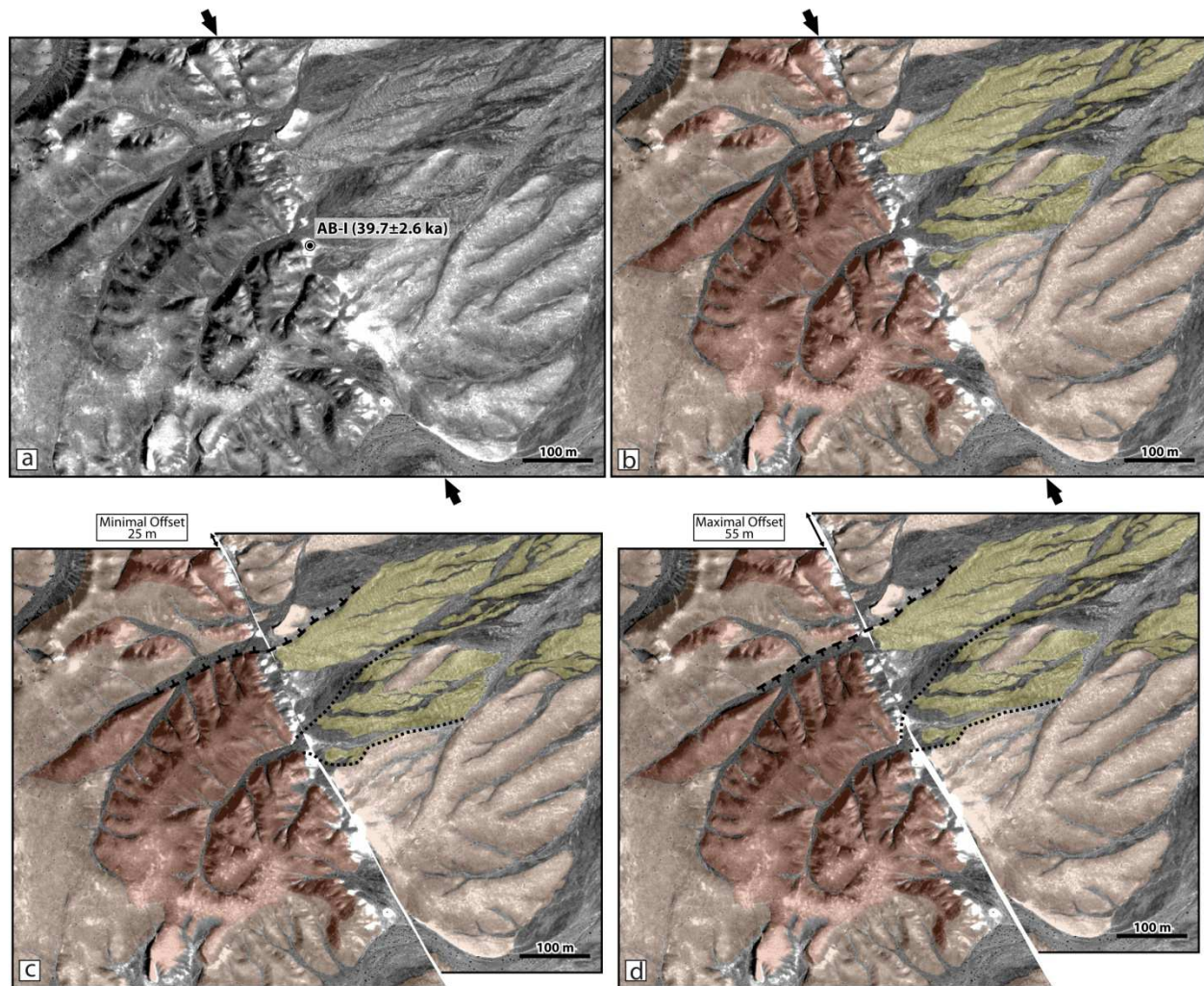


**Figure 2.7.** Raw Quickbird satellite image (a) and interpretation (b) centered on the paleoseismic trench at the site South (see Figure 2.3 for location). Location of the OSL sample AB-I is indicated. Reconstructions showing the restored alluvial fans (green shading) corresponding to the minimum (c) and maximum (d) right-lateral offsets of 25 and 55 m, respectively.



CHAPTER 3

**LARGE EARTHQUAKES**

**ON THE ANAR FAULT**

---

### **3.1. Introduction**

The 200-km-long, N-striking right-lateral Anar fault is the next active strike-slip fault to the east of the Dehshir fault. Similar to the Dehshir fault, none of the available instrumental and historical seismic catalogs provide evidence for occurrence of significant earthquake in the vicinity of the Anar fault. However, several geomorphic studies provided evidence of the fault activity during the Quaternary period (*Berberian, 1976; Walker and Jackson, 2004; Meyer and Le Dortz, 2007; Le Dortz et al., 2009*). *Le Dortz et al. (2009)* recognized cumulative right-lateral offsets of ~8 m at two sites along the fault, and using cosmogenic and luminescence dating of the offset features they estimated a minimum right-slip rate of  $0.8 \text{ mm yr}^{-1}$  over the Holocene. Such a rather low rate of slip suggests a long recurrence interval (several thousands of years) of large earthquakes along the fault, which can exceed the time span covered by the historical seismic catalogs. Therefore, performing paleoseismological investigations is essential to unravel the ambiguity in the seismic behavior of this historically silent fault.

In this chapter, the results of the first paleoseismic study conducted along the Anar fault are presented. The paleoseismic data provide direct and secondary (earthquake-induced features) evidence for the occurrence of several large and infrequent earthquakes during the latest Pleistocene and Holocene timescales. Due to the lack of organic material and the ubiquity of the quartz-rich sandy sediments in the exposed strata, the ages of the recognized paleoearthquakes are constrained using the optically stimulated luminescence (OSL) dating. In addition, three OSL samples that were previously published by *Le Dortz et al. (2009)* have been refined. The refined ages are used to examine the minimum slip rate of the fault and to constrain the age of the identified paleoearthquakes in the trench site. The data presented in this chapter have implications both on the assessment of regional seismic hazard and on the mechanisms of strain release along the slow-slipping intracontinental strike-slip faults.

### **3.2. New evidence for large earthquakes on the Central Iran plateau: palaeoseismology of the Anar fault**



## New evidence for large earthquakes on the Central Iran plateau: palaeoseismology of the Anar fault

M. Foroutan,<sup>1,2,3</sup> M. Sébrier,<sup>2,3</sup> H. Nazari,<sup>4</sup> B. Meyer,<sup>2,3</sup> M. Fattahi,<sup>5,6,7</sup> A. Rashidi,<sup>8</sup> K. Le Dortz<sup>2,3,\*</sup> and M. D. Bateman<sup>6</sup>

<sup>1</sup>Geological Survey of Iran, Azadi Square, Meraj Avenue, PO Box 13185–1494, Tehran, Iran

<sup>2</sup>UPMC (Université Pierre et Marie Curie) Université Paris 06, ISTEP UMR 7193, F-75005, Paris, France. E-mail: mohammad.foroutan@upmc.fr

<sup>3</sup>CNRS, ISTEP, UMR 7193, F-75005, Paris, France

<sup>4</sup>Research Institute for Earth Sciences, Geological Survey of Iran, PO Box 13185–1494, Tehran, Iran

<sup>5</sup>The Institute of Geophysics, University of Tehran, Tehran, Iran

<sup>6</sup>Sheffield Centre for International Dryland Research, Department of Geography, University of Sheffield, Winter Street, Sheffield S10 2TN, UK

<sup>7</sup>The School of Geography, University of Oxford, OX1 3QY, UK

<sup>8</sup>Geological Survey of Iran, Postal Code 7615736841, Kerman, Iran

Accepted 2012 January 5. Received 2011 November 24; in original form 2011 August 18

### SUMMARY

The Central Iran plateau appears aseismic during the last few millennia based on instrumental and historical seismic records. Nevertheless, it is sliced by several strike-slip faults that are hundreds of kilometres long. These faults display along-strike, horizontal offsets of intermittent gullies that suggest the occurrence of earthquakes in the Holocene. Establishing this is crucial for accurately assessing the regional seismic hazard. The first palaeoseismic study performed on the 200-km long, NS striking Anar fault shows that this right-lateral fault hosted three large ( $M_w \approx 7$ ) earthquakes during the Holocene or possibly Uppermost Pleistocene for the older one. These three seismic events are recorded within a sedimentary succession, which is not older than 15 ka, suggesting an average recurrence of at most 5 ka. The six optically stimulated luminescence ages available provide additional constraints and allow estimating that the three earthquakes have occurred within the following time intervals:  $4.4 \pm 0.8$ ,  $6.8 \pm 1$  and  $9.8 \pm 2$  ka. The preferred age of the more recent event, ranging between 3600 and 5200 yr, suggests that the fault is approaching the end of its seismic cycle and the city of Anar could be under the threat of a destructive earthquake in the near future. In addition, our results confirm a previous minimum slip rate estimate of  $0.8 \pm 0.1 \text{ mm yr}^{-1}$  for the Anar fault indicating that the westernmost prominent right-lateral faults of the Central Iran plateau are characterized by slip rates close to  $1 \text{ mm yr}^{-1}$ . These faults, which have repeatedly produced destructive earthquakes with large magnitudes and long recurrence interval of several thousands of years during the Holocene, show that the Central Iran plateau does not behave totally as a rigid block and that its moderate internal deformation is nonetheless responsible for a significant seismic hazard.

**Key words:** Geomorphology; Continental tectonics: strike-slip and transform; Tectonics and landscape evolution; Palaeoseismology; Seismicity and tectonics.

### INTRODUCTION

The Central Iran plateau is a wide region experiencing low GPS deformation rates and is commonly described as a rigid block (e.g. Jackson & McKenzie 1984; Vernant *et al.* 2004). The region (Fig. 1) is nonetheless sliced by several strike-slip faults with clear morphological traces (Walker & Jackson 2004; Meyer *et al.* 2006; Meyer & Le Dortz 2007) that contrast with the very few earthquakes recorded

in the region (Ambraseys & Jackson 1998). Destructive earthquakes have occurred close to or along the Lut faulted borders only, and according to the historical and instrumental records (Ambraseys & Melville 1982; Ambraseys & Jackson 1998), the prominent right-lateral strike-slip faults inland remained quiescent for millennia. Although the absence of historical record of earthquakes in remote and uninhabited desert does not mean an absence of earthquakes, knowledge of the behaviour of such faults and assessment of the regional seismic hazard requires palaeoseismic studies and depends on the selection of suitable trenching sites. This is the case for the region of the Dehshir and Anar faults. Although a recent

\*Now at: Laboratoire de Géologie, ENS, UMR 8538, 75231 Paris, France.

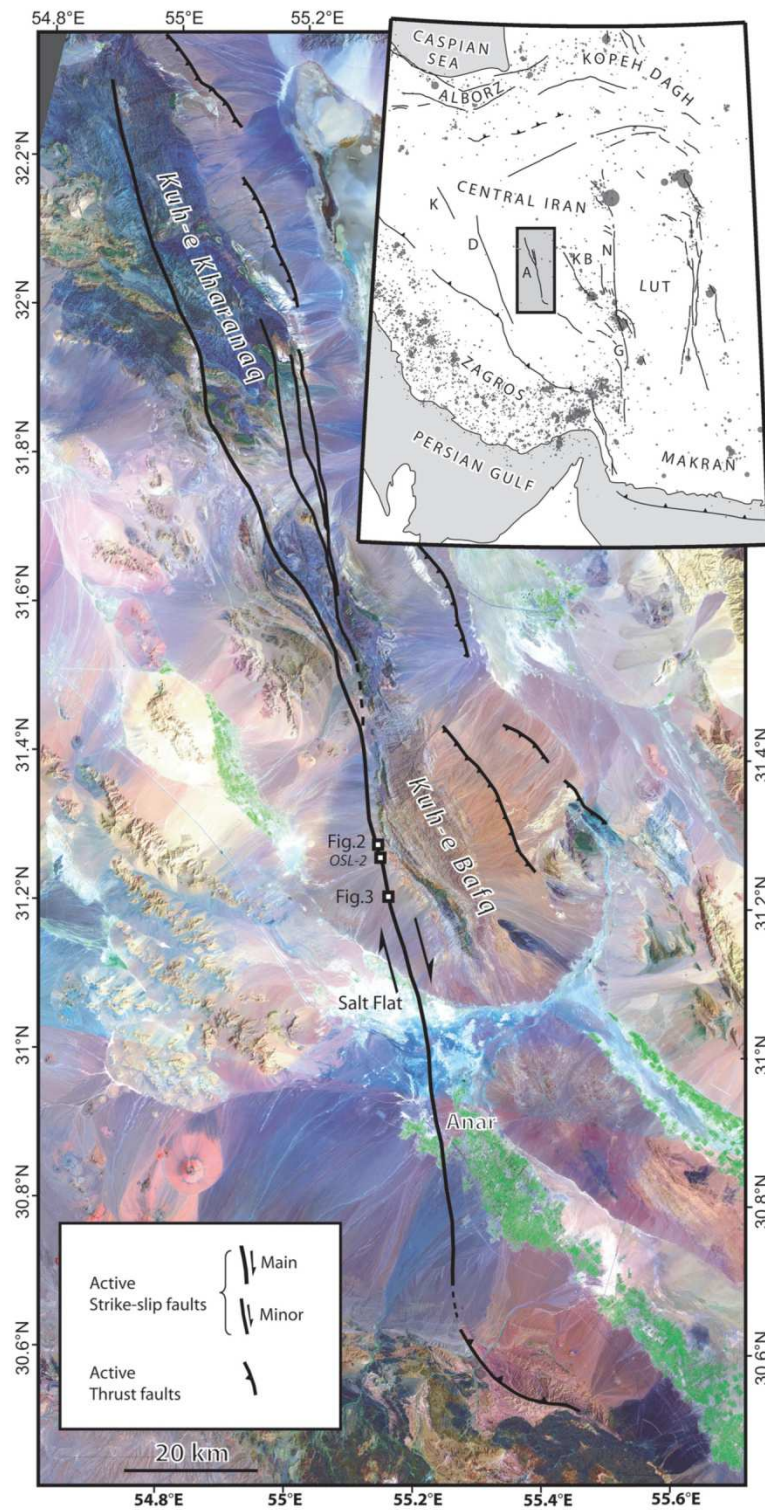


**Figure 1.** Landsat mosaic of the Anar fault area. White squares for location of photograph in Fig. 2, Quickbird extract in Fig. 3 and location of OSL-2 sampling site. Upper right-hand inset locates the area within a simplified seismotectonic map of Iran. K, D, A, KB, N and G, respectively for Kashan, Dehshir, Anar, Kuh Banan, Nayband and Gowk faults.



**Figure 2.** Field photograph of the Anar fault (vertical arrows, top panel) taken towards the north from  $31.2764^{\circ}\text{N}$  to  $55.1304^{\circ}\text{E}$  with emphasis on a 3-m right-lateral offset rill (horizontal arrow, bottom panel).

palaeoseismic study stated the occurrence of large and infrequent earthquakes on the Dehshir fault (Nazari *et al.* 2009; Fattahi *et al.* 2010), the seismic behaviour of the Anar fault is still to be assessed.

The Anar fault is a 200-km-long NS strike-slip fault located nearby  $55^{\circ}\text{E}$ , in the middle of the Central Iran plateau (Fig. 1). The northern part of the fault is located within a mountainous region where several closely spaced splays cut across the Kuh-e Kharanaq range. The southern portion of the fault runs along the Kuh-e Bafq range and cuts right across the western piedmont of the range and across the Anar salt flat. The fault goes through the populated city of Anar and further bends eastwards to reactivate a thrust fault to the south. According to  $^{10}\text{Be}$  cosmic ray exposure (CRE) and optically stimulated luminescence (OSL) dating of cumulative offset of alluvial fans, the southern portion of the fault slips at a minimum rate of  $0.8 \text{ mm yr}^{-1}$  (Le Dortz *et al.* 2009). Both the sharpness of these cumulative offsets and the absence of along fault microseismicity suggest these offsets have accrued through large and infrequent

earthquakes rather than by creeping. At a few places, the offset of small gullies that ranges between 2.5 and 3.5 m (Fig. 2) may be interpreted as the amount of coseismic slip during the last earthquake but clear evidence for a continuous and distinctive surface break is missing. Trenching appears therefore necessary to document earthquakes and access the recent seismic history of the fault.

#### SITE SELECTION AND TRENCH STRATIGRAPHY

We scrutinized the fault on Quickbird satellite imagery and in the field to select the most favourable place to conduct palaeoseismic investigations. The selected site is located 35 km north of the city of Anar along a very clear portion of the  $\text{N}175^{\circ}\text{E}$  fault trace that is highlighted by an E-facing scarp (Fig. 3). This fault scarp is readily seen cutting across numerous rills and ephemeral streams that incise a fan surface characterized by a subdued bar-and-swale

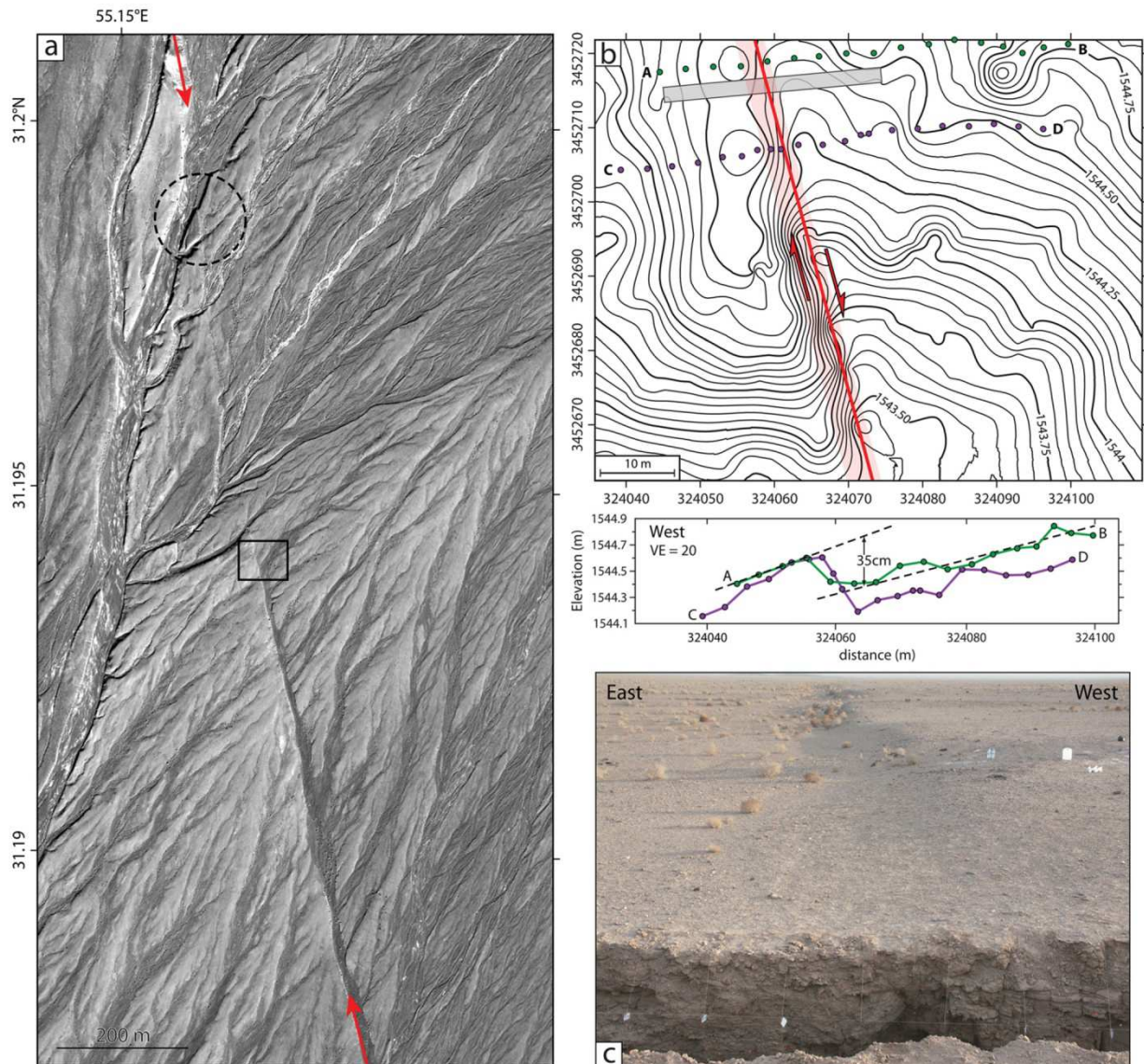


**Figure 3.** (a) Quickbird imagery of the Anar fault trace (red arrows) centred on the palaeoseismological site (rectangle). Circle indicates the  $8 \pm 0.5$  m cumulative dextral-offset riser described as site 1 in Le Dortz *et al.* (2009). (b) Topographic DGPS map (top) and profiles (bottom) of the palaeoseismological site. Contour interval is 5 cm (survey data not tied to absolute elevation). The smooth and subdued E-facing fault scarp is indicated by a red overprint and the location of the trench by a rectangle. Violet and green dots locate the DGPS data points used for the topographic profiles. (c) Field photograph, looking south, of the E-facing fault scarp. The upper part of the southern trench wall is in the foreground. Three white labels that are 1-m spaced show scale on trench wall.

morphology. The abandoned alluvial fan surface comprises a loose desert pavement of varnished clasts separated by sandy–silty material. The smooth scarp has a minimum height of 35 cm near the excavation (Fig. 3b). South of the trench site, the scarp height increases progressively to reach 1 m where small streams, which have been dammed and channelled along the fault, rejuvenate this scarp. North of the trench site, the scarp height also increases, but the streams are wider and deeper than to the south and have been able to maintain their courses to flow across the fault trace. At the trench site, the possibility of damming small intermittent streams during the emplacement of the fan material is high and the possibility of subsequent erosion low, maximizing the chances to record the earth-

quakes coeval with alluvial aggradation and subsequent colluvial deposition. The next paragraphs report the observations gathered at the selected site, where trenching allowed us to distinguish three unambiguous events.

The eastern tip of the excavated trench is located about 5 km west of the Kuh-e Bafq range at  $31.1953^{\circ}\text{N}$ ,  $55.1536^{\circ}\text{E}$  and 1544 m altitude above sea level (asl; Figs 1 and 3b). The trench strikes  $\text{N}85^{\circ}\text{E}$ , it has a length of 28 m, a depth between 4.3 and 4.7 m and a width of some 1.5 m (Figs 3–5). Trench walls expose a total deposit thickness of 5.9 m with fairly flat, 0.1- to 1-m-thick beds that correspond to medium-distal, alluvial fan facies. Trench stratigraphy is relatively straightforward as these beds are continuous and easily correlated

10 *M. Foroutan et al.*

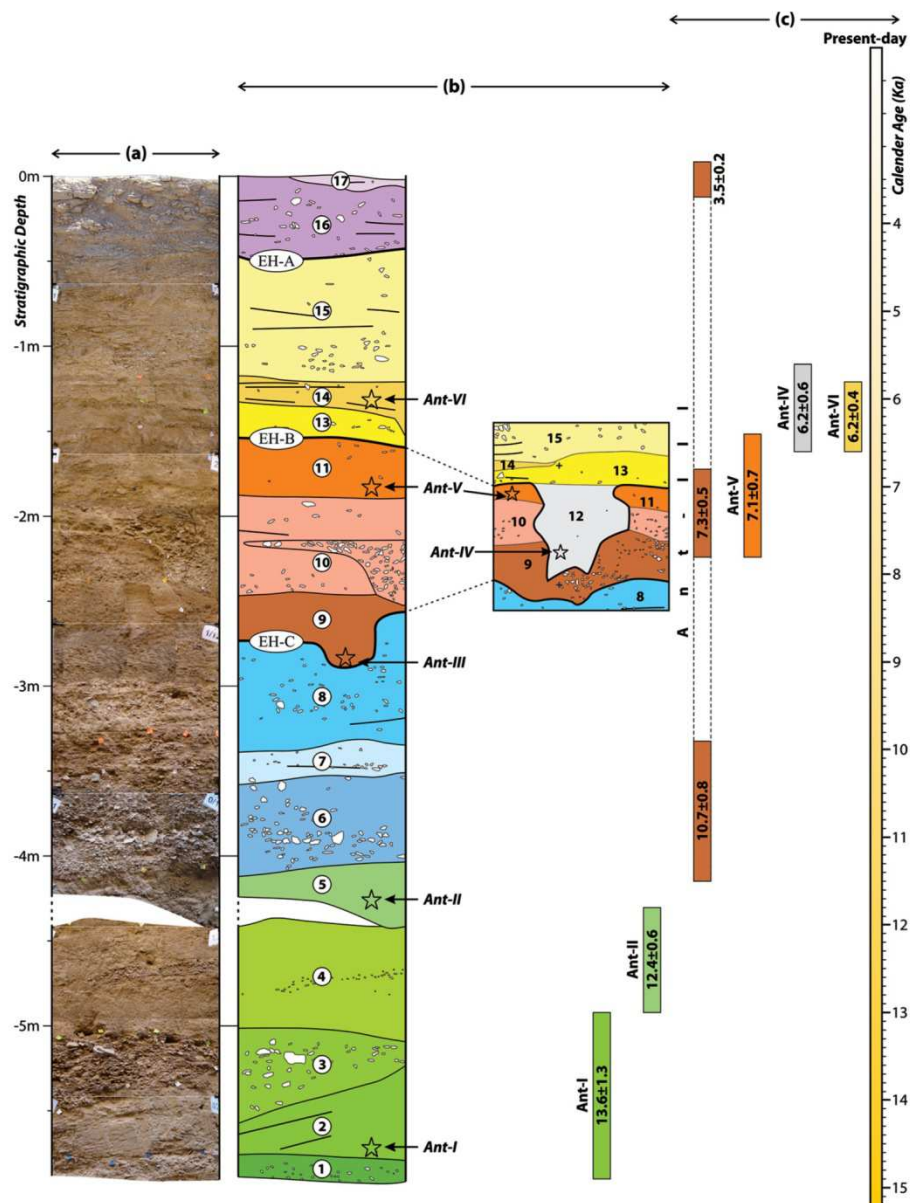


**Figure 4.** Composite photomosaic of the sediments exposed in the Anar trench excavation, (a) with top 4 m (between 11 and 12 m) east and bottom 2 m (between 19 and 20 m) west of the main fault zone, and (b) corresponding stratigraphic log of the units with vertical positions of dated samples. Numbers indicate units described in detail in Table 1. Three event horizons (EH-A, EH-B and EH-C) are shown as thick black lines (see text for discussion). (c) Stars locate the positions (see exact location in Fig. 5) of the six samples with OSL ages given.

across the fault zone located approximately in the middle of the trench (Fig. 5). Overall the beds found in the trench are composed of sands and gravels mixed with variable amounts of silt and clay, these deposits correspond mostly to a debris-flow dominated alluvial fan. Although debris flows and sheet floods appear to dominate, sediment dynamics is not easy to determine precisely for each bed due to the medium-distal deposit conditions.

A total of 17 units have been defined in the excavated trench (Table 1; Figs 4 and 5). The uppermost part of the trench, approximately the last metre, is made of the thinner units 13–17 containing smaller pebbles than the alluvial units 1–8 and an almost clay-free

matrix contrary to the units 9–11. This last metre hence is made of run-off deposits. The only evidence for a significant break in alluvial sedimentation is the  $\approx 0.15$ -m-thick, gypsiferous calcrete that is located towards the top of unit 11. This latter unit and units 9 and 10 correspond to reddish brown, mud-dominated debris flows. OSL was used to date the alluvial layers seen in the trench.

### OSL DATING

Six lenses of fine sandy silts intercalated between fanglomerates at various depths below the surface were sampled for OSL in opaque

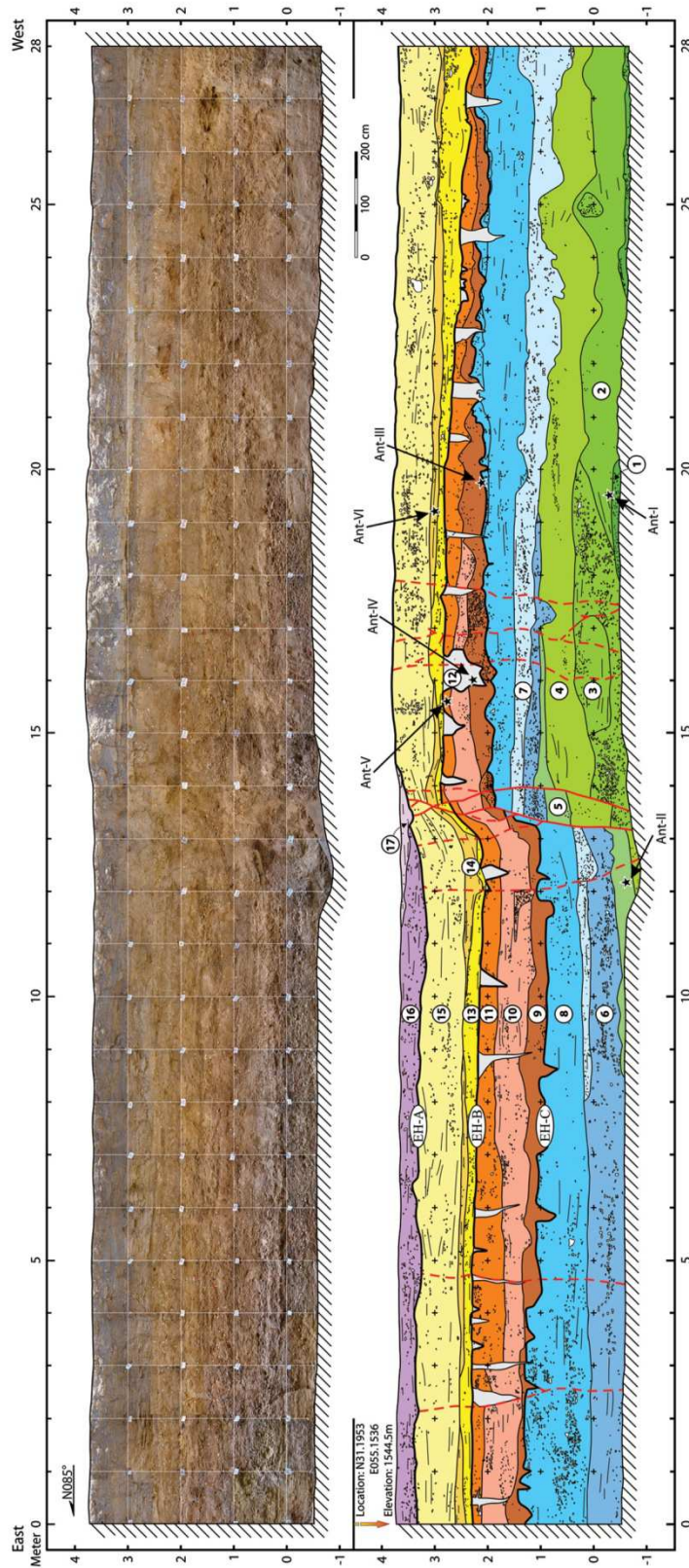


**Figure 5.** Top panel: photograph of southern trench wall (see Fig. 3 for location). Bottom panel: corresponding log, with labels marking the stratigraphic units. Faults and fractures are shown with red and dashed red lines, respectively. Short black lines represent bedding of sedimentary layers. Event horizons discussed in text are labelled as EH-A, EH-B and EH-C. Labelled black stars locate the OSL samples. Sample Ant-I, collected west of the fault zone at 4.1-m deep within unit 2, yields an age of  $13.6 \pm 1.3$  ka. Sample Ant-II, collected east of the fault zone at 4.2-m deep within unit 5, yields an age of  $12.4 \pm 0.6$  ka. Sample Ant-III, collected at 1.5-m deep in a sandy lens of unit 9, yields a poorly constrain ages between 11.5 and 3.3 ka. Sample Ant-IV, collected at 1.5-m deep at the base of a fissure filled with colian and run-off sand deposits within unit 12, yields an age of  $6.2 \pm 0.6$  ka. Sample Ant-V, collected at 1-m deep within unit 11, yields an age of  $7.1 \pm 0.7$  ka. Sample Ant-VI, collected at 0.8-m deep in a sandy lens within unit 14, yields an age of  $6.2 \pm 0.4$  ka.

12 *M. Foroutan et al.***Table 1.** Detailed description of the units observed in the trench excavated across the Anar fault, corresponding stratigraphic column and log are shown in Figs 4 and 5, respectively.

Unit	Detailed stratigraphic explanation
17	Light grey to cream, poorly stratified, silty sand with some angular gravels (20 per cent, 0.5–2 cm).
16	Light cream, fairly stratified, medium consolidated, angular gravels (60 per cent, 0.5–6 cm), with sand and silt matrix and some gypsiferous cementation.
15	Buff to light grey, well stratified, medium consolidated, angular gravels (50 per cent, 0.5–10 cm), with sand and silt matrix and some gypsiferous cementation.
14	Grey to buff grey, thinly stratified, medium consolidated sand and angular granules (0.5–4 cm) with cross-bedding.
13	Grey, well stratified, medium to well consolidated, coarse sand with angular granules and few pebbles (30 per cent, 0.2–6 cm). The unit bottom is erosive and rests both on units 12 and 11.
12	Light cream to grey, sandy fissure fills and sand-blows.
11	Brown to olive cream, roughly stratified, medium to well consolidated, silts and sands with some channels of angular gravels (40 per cent, 0.1–4 cm). The top exhibits a hard gypsiferous calcrete.
10	Cream to grey, fairly stratified, poorly consolidated, coarse sands and angular gravels (50 per cent, 0.1–3 cm) with sandy–silty matrix and some cross-bedding.
9	Reddish brown to brownish grey, non-stratified, semi-consolidated coarse sand, with clayish silt matrix, including some channels of angular gravels (90 per cent, 2–15 cm) with silt matrix.
8	Cream to brownish grey, fairly stratified, well consolidated, angular granules and pebbles (60 per cent, 0.2–3 cm), with silty sand matrix, including some small cobbles and traces of sulphate calcrete within the coarser levels.
7	Grey to brownish grey, poorly stratified, poorly sorted angular pebbles (70 per cent, 0.5–10 cm), with sandy silt matrix.
6	Cream to brown, fairly stratified, angular granules and pebbles (80 per cent, 0.2–4 cm), with silty sand matrix, including some sparse big cobbles and silty sand lenses.
5	Buff to light grey, fairly stratified, loose silt and sand.
4	Grey to light grey, poorly stratified, well sorted, silty sands with some cross-bedding and gravel lenses.
3	Grey, fairly stratified, well consolidated, medium to well sorted, coarse angular gravels (90 per cent, 0.5–10 cm) with silty sand matrix, including some sparse bigger cobbles and clayish silty sand lenses.
2	Grey, stratified, loose, silty sand, with some cross-bedding.
1	Grey, poorly stratified, well consolidated, angular pebbles (>20 per cent, 0.5–3 cm) with silty sand matrix.

tubes (Fig. 5). The Single Aliquot Regeneration (SAR) protocol (e.g. Murray & Wintle 2000) was employed for the equivalent dose (De) measurement once quartz had been extracted and cleaned from each sample. The analytical procedures employed are identical to that applied to similar samples from the neighbouring Sabzevar, Doruneh and Dehshir faults (Fattahi *et al.* 2006, 2007, 2010; Le Dortz *et al.* 2011). To make all data consistent, three samples with ages that were previously published in Le Dortz *et al.* (2009), including one sample collected approximately 8 km farther north (OSL-2 on Fig. 1 and in Table 2), have been refined in the light of procedural development outlined by Fattahi *et al.* (2010). Table 2 provides the relevant information for OSL ages in years from present (2010) with  $1\sigma$  errors.

Initial attempts to use single grains for De determination failed due to the dimness of OSL signal. As a result, De measurements were undertaken on 9.6-mm diameter aliquots containing approximately 1500–2000 grains. Although normally this might result in averaging out of any multiple dose component within a sample, here it is assumed that for these dim samples the luminescence signal from each aliquot was produced by a relatively few number of bright grains and thus may be considered as almost measuring at single grain level. Therefore, the De distribution of the single aliquot De measurements is considered to be almost a true reflection of the actual De distribution within a sample. For samples showing unimodal, apparently normally distributed De's with a low overdispersion (Ant-I and Ant-IV in Table 2), which are interpreted as having had the OSL signal reset (bleached) before burial, central age model (CAM) was employed for calculation purposes. For the remaining samples (Ant-II, Ant-III, Ant-V, Ant-VI and OSL-2 in Table 2), the depositional setting, field sedimentary logs and the scatter of the replicate aliquot De data indicated that before burial,

full resetting (bleaching) of the OSL signal had not taken place and/or that the sediments had undergone some post-depositional disturbance (Bateman *et al.* 2007). Indeed, the small size of the catchment area at the trench site, less than 20 km<sup>2</sup>, is indicative of a rapid transport before the emplacement of the fan (Le Dortz *et al.* 2009). The great majority of the Anar trench deposits come from high-discharge depositional events with limited surface exposure, which favour partial bleaching (Rittenour 2008). As a consequence, finite mixture model (FMM; Roberts *et al.* 2000) was used where samples showed skewed, scattered or multimodal distributions and the dominant De component was used for age calculations (as in Fattahi *et al.* 2010). This approach yielded ages in accordance with site stratigraphy except for sample Ant-III whose age was too young. This sample has exhibited the highest overdispersion value (51 per cent, Table 2) of all measured samples and three De component were extracted by FMM for this sample, the highest representing 30 per cent of the signal and the smallest 47 per cent. It is possible to get an age that fits with stratigraphy using the higher two De components extracted using FMM, corresponding to ages of  $7.3 \pm 0.5$  and  $10.7 \pm 0.8$  ka, respectively. However, there are no good reasons to accept components representing only 23 or 30 per cent of the data over the 47 per cent of the data incorporated into the dominant smallest FMM component. The latter cannot be ignored on the basis of partial bleaching as it has a lower De and is unlikely to represent post-depositional disturbance, as it is the dominant De component but also based on observed bedding within the unit. However, unlike most other samples studied, Ant-III was sampled actually on a stratigraphic boundary (between units 8 and 9). As the dose-rate for this sample is based only on the activity from unit 9, a difference in the gamma radiation dose received from unit 8 might help explain the apparent underestimation of age based on the lowest FFM De

**Table 2.** Calculated OSL ages on the Anar samples with their parameters. Ages have been calculated for quartz grains with size ranging between 90 and 150  $\mu\text{m}$ .

Sample	Latitude $^{\circ}\text{N}$	Longitude $^{\circ}\text{E}$	Depth (m)	Water (per cent)	K (per cent)	U (per cent)	Th (per cent)	Annual dose rate ( $\text{Gy ka}^{-1}$ )	overdispersion (per cent)	Skewness	CAM De (Gy)	FMM De (Gy)	Age (ka)
Ant-I (OSL1-b) <sup>a</sup>	31.1952	55.1534	4.1	2	0.93 $\pm$ 0.03	1.16 $\pm$ 0.05	4.0 $\pm$ 0.1	1.64 $\pm$ 0.05	24	0.69	22.3 $\pm$ 1.90	17.5 $\pm$ 0.47	13.6 $\pm$ 1.3 <sup>b</sup>
Ant-II	31.1952	55.1534	4.2	0.4	0.77 $\pm$ 0.03	0.97 $\pm$ 0.05	3.4 $\pm$ 0.1	1.42 $\pm$ 0.04	27	4.09	16.1 $\pm$ 0.90	6.1 $\pm$ 0.24	12.4 $\pm$ 0.6 <sup>c</sup>
Ant-III	31.1952	55.1534	1.7	1.1	0.97 $\pm$ 0.01	1.23 $\pm$ 0.05	4.3 $\pm$ 0.1	1.75 $\pm$ 0.04	51	2.1	9.7 $\pm$ 1.09	6.1 $\pm$ 0.24	3.5 $\pm$ 0.2 <sup>c</sup>
Ant-IV	31.1952	55.1534	1.5	0.6	0.94 $\pm$ 0.01	1.44 $\pm$ 0.05	3.7 $\pm$ 0.1	1.78 $\pm$ 0.14	20	0.01	11.0 $\pm$ 0.61	6.2 $\pm$ 0.6 <sup>b</sup>	6.2 $\pm$ 0.6 <sup>b</sup>
Ant-V	31.1952	55.1534	1.0	0.3	0.99 $\pm$ 0.01	1.72 $\pm$ 0.05	4.2 $\pm$ 0.1	1.96 $\pm$ 0.14	25	0.35	13.5 $\pm$ 0.90	13.9 $\pm$ 0.70	7.1 $\pm$ 0.7 <sup>c</sup>
Ant-VI (OSL1-a) <sup>d</sup>	31.1952	55.1534	0.8	0.6	1.21 $\pm$ 0.01	1.60 $\pm$ 0.05	5.9 $\pm$ 0.1	2.20 $\pm$ 0.05	42	0.94	11.6 $\pm$ 1.39	13.7 $\pm$ 0.56	6.2 $\pm$ 0.4 <sup>d</sup>
OSL-2	31.2697	55.1337	0.8	1.1	1.06 $\pm$ 0.01	1.33 $\pm$ 0.05	4.0 $\pm$ 0.1	1.90 $\pm$ 0.05	41	2.39	20.1 $\pm$ 2.16	19.3 $\pm$ 0.76	10.1 $\pm$ 0.6 <sup>d</sup>

<sup>a</sup> Parenthesis contains the sample label used by Le Dortz *et al.* (2009).<sup>b</sup> Age based on De determined using central age model (CAM; Galbraith *et al.* 1999).<sup>c</sup> Age based on De determined using the dominant component of finite mixture modelling (FMM; Roberts *et al.* 2000).<sup>d</sup> Age previously published, now refined using finite mixture modelling (FMM; Roberts *et al.* 2000).

component. Unfortunately, field-based gamma-spectrometer readings or material for analysing the radioactive elements within unit 8 were not available to test this and so the age of Ant-III has not been included within the subsequent site interpretation. Thus, the ages of the trench units have been constrained based on only five OSL ages (Ant-I, Ant-II, Ant-IV, Ant-V and Ant-VI).

## AGES OF TRENCH UNITS

The samples collected within the trench define a time range spanning from 5.8 to 14.9 ka. The oldest age Ant-I (13.6  $\pm$  1.3 ka) stands at the bottom of the trench and belongs to one of the oldest stratigraphic units (unit 2), it indicates that all the trench units should be younger than 15 ka. As the youngest OSL sample Ant-VI (6.2  $\pm$  0.4 ka) is located at 0.8 m below the surface (unit 14), these ages define a maximum time interval between 0 and 14.9 ka and a minimum one between 6.6 and 12.3 ka, indicating that the trench deposits aggraded during the uppermost Marine Isotopic Stage 2 (MIS-2  $\approx$  12–22 ka) and part or the entirety of MIS-1. The age of the fan surface at the trench site appears poorly constrained between 0 and 6.6 ka.

A proxy to the surface age may be obtained by estimating average sedimentation rates. Assuming this fan surface is still active, the whole 5.9 m of sedimentary units seen in the trench should have been aggraded during the last 14.9 or 12.3 ka at an overall sedimentation rate ranging between 0.4 and 0.48  $\text{mm yr}^{-1}$ . Deposit thickness above the samples Ant-I (13.6  $\pm$  1.3 ka) and Ant-II (12.4  $\pm$  0.6 ka) yield slightly lower rates ranging between 0.28 and 0.36  $\text{mm yr}^{-1}$ . Conversely, if one assumes the top of the fan surface was abandoned just after 6.6 ka, the oldest possibility for the youngest sample (Ant-VI), the sedimentation rate may have reached 1  $\text{mm yr}^{-1}$ . These two extreme hypotheses raise the problem of the abandonment age of the alluvial fan at the precise location where the trench was excavated. The refined age of OSL-2 (10.1  $\pm$  0.6 ka versus 11.8  $\pm$  6.5 ka in Le Dortz *et al.* 2009), which is sampled some 8 km north of the trench (see location on Fig. 1, see also figs 4a and 7 in Le Dortz *et al.* 2009) at 0.8 m below the surface of another fan on the riser of a  $\approx$ 4.5-m incised dry stream, suggests that its surface was abandoned some 9–10 ka ago at this site whereas the fan surface at the trench site cannot be older than 6.6 ka. These ages are in agreement with the late Pleistocene and Holocene regional climate scenario, for the central and eastern Iran, as recently proposed by Walker & Fattahi (2011). In fact, the satellite image in the vicinity of the trench site (Fig. 3a) shows this location corresponds to an area where the fan surface has been exceptionally preserved from the backward erosion of deeply incised dry streams. Therefore, the late aggradation on the fan surface at the trench site ( $\sim$ 1544 m asl), resulting from surface run-off, lasted until more recently than some 8 km farther north on a more proximal alluvial fan ( $\sim$ 1748 m asl) where Le Dortz *et al.* (2009) collected the sample OSL-2. In conclusion, the best estimate for the aggradation rate of the trench sediments is provided by the depth difference of 3.3 m between Ant-I (13.6  $\pm$  1.3 ka) and Ant-VI (6.2  $\pm$  0.4 ka) samples, this rate ranges between 0.36 and 0.58  $\text{mm yr}^{-1}$ . Interestingly, this rate is comparable to the late Pleistocene–Holocene aggradation rates derived from alluvial sediments in similar deposition settings at southwestern Nebraska, Negev desert and Central Iran plateau (Daniels *et al.* 2003; Guralnik *et al.* 2011; Schmidt *et al.* 2011). Consequently, the best averaged net sedimentation rate, if meaningful in such environment, amounts to 0.47  $\pm$  0.11  $\text{mm yr}^{-1}$  suggesting that the final aggradation of the trench units ended between 3.6 and 5.2 ka to the west of the

14 *M. Foroutan et al.*

fault zone and approximately 1000 yr later to the east of the fault zone accounting for the thickness of units 16 and 17. The abandonment age of the fan surface at the trench site ( $4.4 \pm 0.8$  ka) is comparable with late Holocene drought cycles at 4.2 ka, proposed by Staubwasser *et al.* (2003) to the southeast of the Persian Gulf.

### SEISMIC EVENT IDENTIFICATION

The surface geomorphology, particularly, the characteristics of the fault scarp, detailed geological and structural analyses of the trench walls (bed unconformities, sealed fault strands and fissure fills or sand-blows) and restoration of the trench log permit to trace three individual event horizons that correlate with three destructive past earthquakes, which ruptured the ground surface. The evidence for these three seismic events, which are labelled A, B and C from the youngest to the oldest, is presented below.

'Event A', the youngest event is responsible for the 35-cm-high, E-facing scarp, which is observed at the surface in the vicinity of the

trench (Figs 3b and c). The trench log shows this scarp is located above a nearly 1-m wide, steep faulted zone associated with an E-facing flexure of the upper trench units; that is, downthrown to the east (Fig. 5). Units 16 and 17 are neither observed west of the fault zone nor warped eastward. They rest unconformably on unit 15 dipping about  $25^\circ$  E (Fig. 6), hence indicating the faulting and flexuring deformation post-date unit 15 and pre-date units 16 and 17. As there are no significant thickness differences of the upper trench units on both sides of the fault zone, the faulting and flexuring deformation appear to result from a sudden and discrete slipping event on the fault zone instead of a continuous shear; that is, creep slip (Fig. 7, step 1). In as much as the upper trench units are seen faulted up to unit 15, the discrete slipping event should relate to an earthquake that ruptured the surface producing the scarp. The event horizon of this earthquake locates on the top boundary of unit 15, so that it stands between this latter and units 16 and 17 to the east of the fault and corresponds approximately with the present-day topographic surface to the west of the fault. This suggests that the

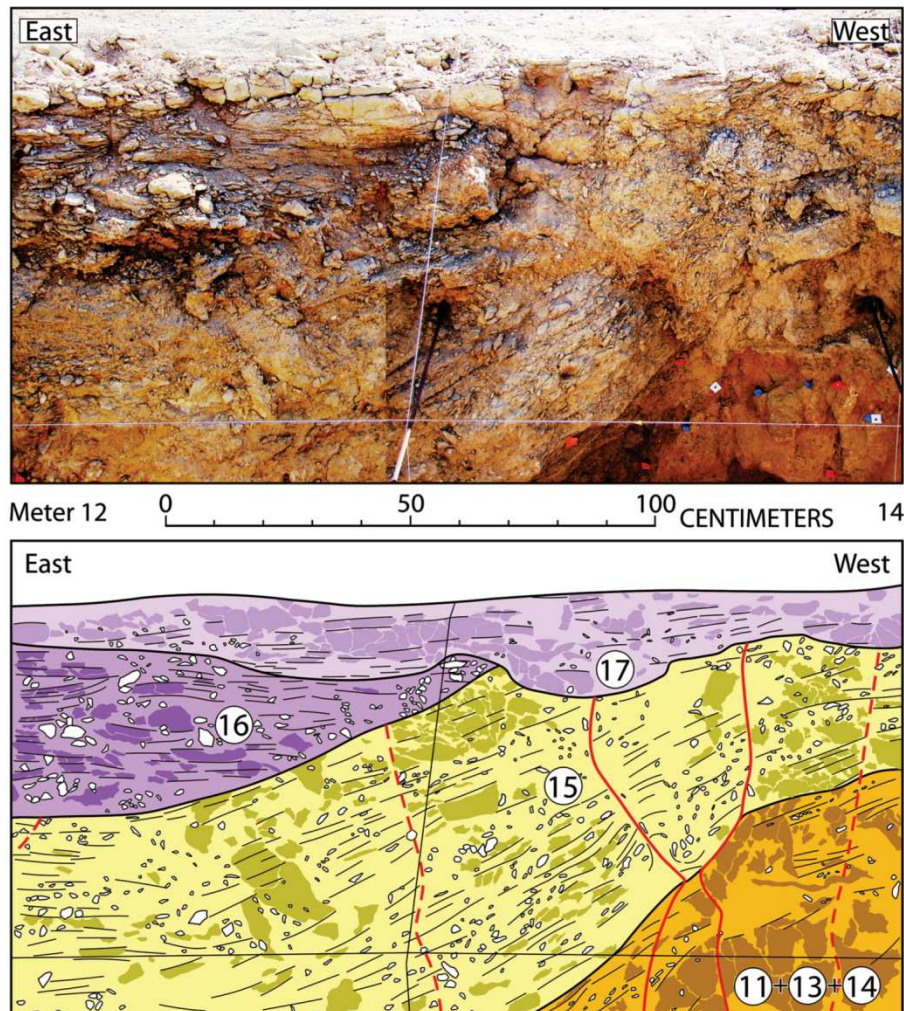


**Figure 6.** Photomosaic (top) and interpretation (bottom) of the main faulted zone showing evidence for the most recent earthquake (event A). Units 11–15, affected by faulting, are warped downward, while undeformed units 16 and 17 lie unconformably atop. Faults and tiny fractures are shown as red and dashed red lines, respectively.

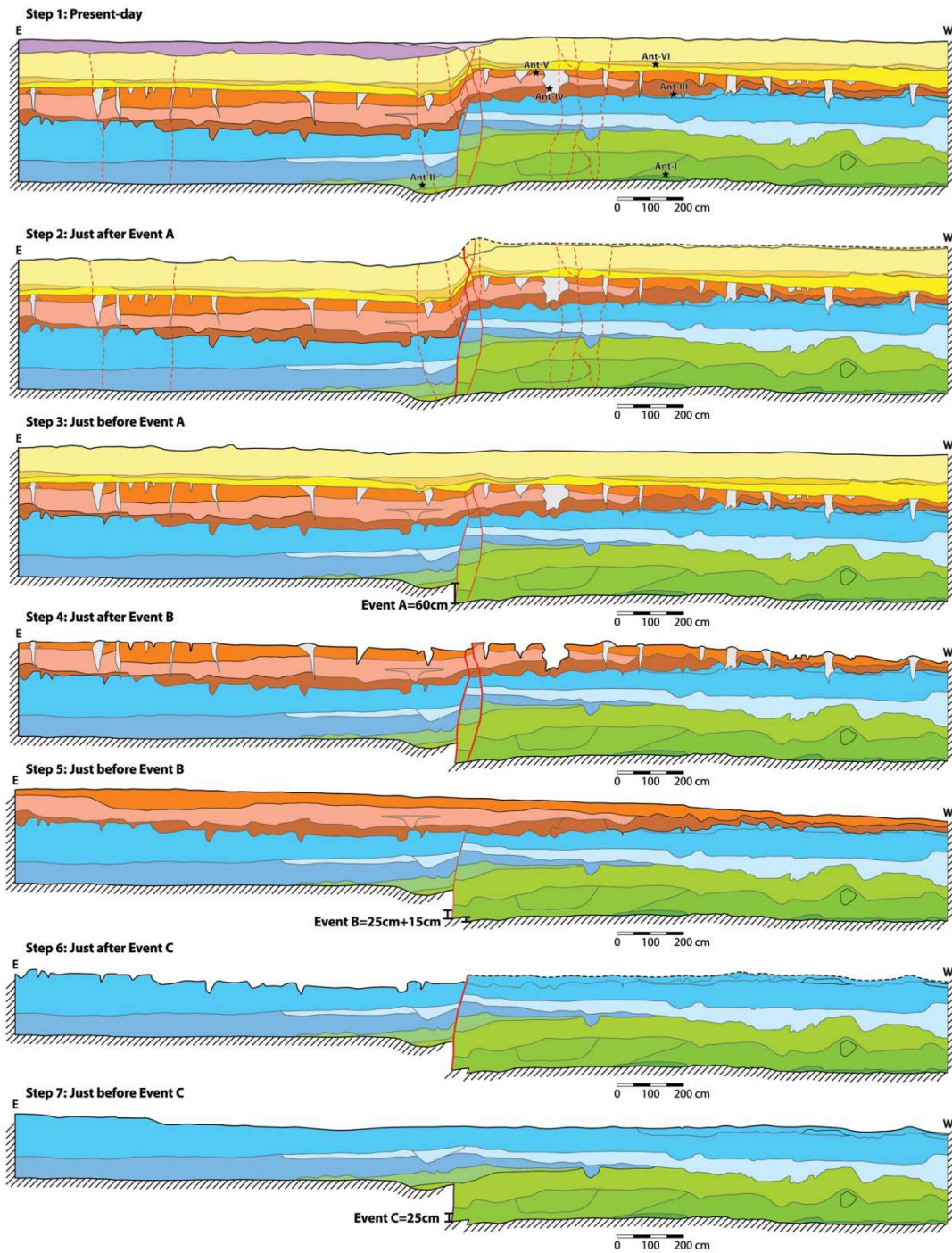


**Figure 7.** Schematic view of possible restoration of trench log showing sequence of faulting and depositional phases from present-day (step 1) to before the oldest palaeoearthquake (step 7). The trench log has been simplified for clarity. Dashed black lines show inferred ground surface before the erosion. Step (1) is present-day situation. Step (2) is E-facing fault scarp formed during the most recent earthquake. Step (3) is restoration of the ground surface to its position before event A showing a vertical displacement of about 60 cm created by faulting on the eastern branch. Step (4) is the penultimate earthquake denoted by open fissures and cracks formed near the main faulted zone. Sand-blows also emplaced in both sides and away of the main faulted zone. Step (5) is restoration of the ground surface to its position before event B showing vertical displacement created during penultimate earthquake on the eastern and western fault branches about 25 and 15 cm, respectively. Step (6) is the oldest earthquake, it has produced some surficial fissures within downthrown (eastern) block and a 25-cm-high E-facing fault scarp. Step (7) is restoration of the ground surface to its position before event C, showing a vertical displacement of about 25 cm.

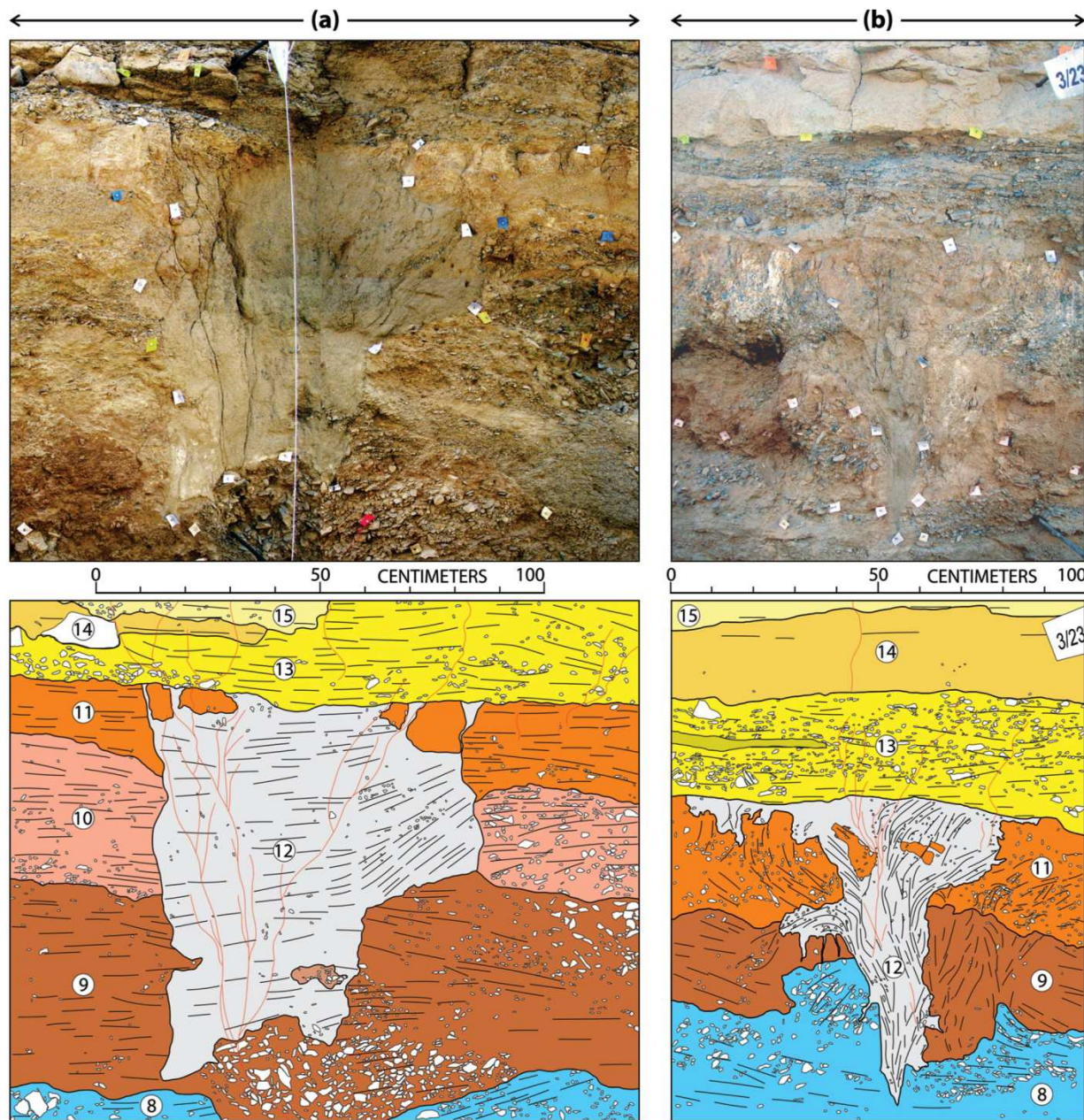


**Figure 8.** Evidence for the penultimate earthquake (event B) encountered in a fissure fill and a liquefaction feature (sand-blow) at 16 and 22 m of the trench log, respectively. Red lines correspond to tiny cracks post-dating the penultimate earthquake. (a) Photomosaic of fissure filled with eolian sands and silts and interpretative sketch. The fissure is  $\sim 85$ -cm deep and up to  $\sim 55$ -cm wide, tapering downward through unit 9. Colours denote stratigraphy as shown in Figs 4 and 5. The material at the base of the fissure includes a collapsed piece from sidewall and grades into interbedded sand and silt layers. The fissure is sealed by a grey, well-stratified, surficial run-off deposit (unit 13). (b) Photomosaic and interpretative sketch of a sand-blow (unit 12) made of sandy material of unit 8 injected into and deforming units 9 and 11. Hydraulic fractures, vertical and oblique alignments of dragged sands and gravels deform the host sediments close to the liquefaction pillar.

western block has been slightly eroded and partly concealed by units 16 and 17 so that its present-day height underestimates its original height at the time of the earthquake (Fig. 7, step 2). Then, unit 17 is a local sag pond deposit caused by event A.

Backstripping of event A suggests its vertical throw is of some 60 cm (Fig. 7, step 3), confirming that the 35-cm-high scarp at

the surface has been partly degraded. Taking into account the Anar fault is dominantly a strike-slip fault (Fig. 2), the 60 cm of vertical displacement should be associated with at least a couple of metres of right-lateral displacement. Then, the magnitude of event A should be at least on the order of  $M_w \approx 7$ . The age of event A is poorly constrained as the uppermost OSL sample (Ant-VI), which is at

0.8-m depth, comes from unit 14. This indicates only that event A is younger than 6.6 ka. Tentatively, the sediment thickness, which stands between the sample Ant-VI and the event horizon of event A, may be used to propose a rough estimate of the youngest possible age for this seismic event based on the aggradation rate between Ant-VI and Ant-I. Since aggradation of unit 15 ended between 3600 and 5200 yr (see previous section), event A should not be younger than 3600 yr and might be as old as 5200 yr. This time interval will be considered as the preferred age of event A in the following discussion.

'Event B', the penultimate event, is easily determined from analysis of the trench walls. Several filled fissures (unit 12), which post-date unit 11 and pre-date unit 13, are seen (Figs 5 and 7, step 4). A careful analysis of these filled fissures permits to conclude they correspond indeed to either open cracks or sand-blows (Figs 8a and b). It is possible to observe that these features formed suddenly as they disrupt the hard gypsiferous calcrete (e.g. Fig. 8b), which is located in the top part of unit 11. Thus, the interface between units 11 and 13 corresponds to the event horizon of event B. The backstripping analysis of the trench log (Fig. 7), removing the effects of event A and the units aggraded between events A and B, allow reconstructing the event B horizon just after the penultimate earthquake (Fig. 7, step 4). This reconstruction suggests that the rupture of event B should have occurred on two parallel fault strands of the Anar fault zone, totalling a vertical throw of some 40 cm, distributed into 25 cm on the eastern strand and 15 cm on the western one. Thus, the penultimate earthquake appears to have a vertical throw close to that of the last one, hence a magnitude lightly comparable with the one of event A. The age of event B is well constrained by three OSL ages (Ant-V, Ant-IV and Ant-VI) and bracketed between 5.8 and 7.8 ka yielding an average age of  $6.8 \pm 1$  ka for this earthquake (Fig. 9).

'Event C', the oldest seismic event, can be safely identified on the trench walls. Evidence for a third earthquake rests on the facts that lower trench units (5–8) exhibit higher vertical throws than middle ones (9–11). Different reconstructions have been tested to restore the trench lower units; the best fit is obtained when considering the interface between units 8 and 9 as the event horizon of a surface-rupturing earthquake (Fig. 7, step 6). This reconstruction favours that event C ruptured along the eastern fault strand with a vertical displacement of about 25 cm. Nevertheless, this vertical displacement is poorly constrained and higher estimates might be obtained according to the amount of erosion chosen (dashed line on Fig. 7, step 6). Even if this vertical throw is poorly determined and appears smaller than the ones of the subsequent earthquakes, this does not imply a much smaller magnitude as the amount of coseismic vertical displacement is highly variable along a strike-slip fault (e.g. Barka 1996; Barka *et al.* 2002). The age of event C is not well constrained; it occurred before the OSL age of sample Ant-V ( $7.1 \pm 0.7$  ka) and after that of Ant-II ( $12.4 \pm 0.6$  ka) so that it is bracketed within the interval between 6.4 and 13 ka, with a minimum interval of 4 ka (Fig. 9). We have investigated the possibility for a fourth event in the lowermost part of the trench (Fig. 5). However, the lowermost units (1–4) cannot be followed on the eastern side of the trench precluding the possibility to document an additional event.

## DISCUSSION AND CONCLUSIONS

Due to the reduced size of the surface sag pond, a 3-D trench exploration was not undertaken at the trench site so that the slip per event was not directly measurable for the three identified seismic events,

## Large earthquakes on the Anar fault 17

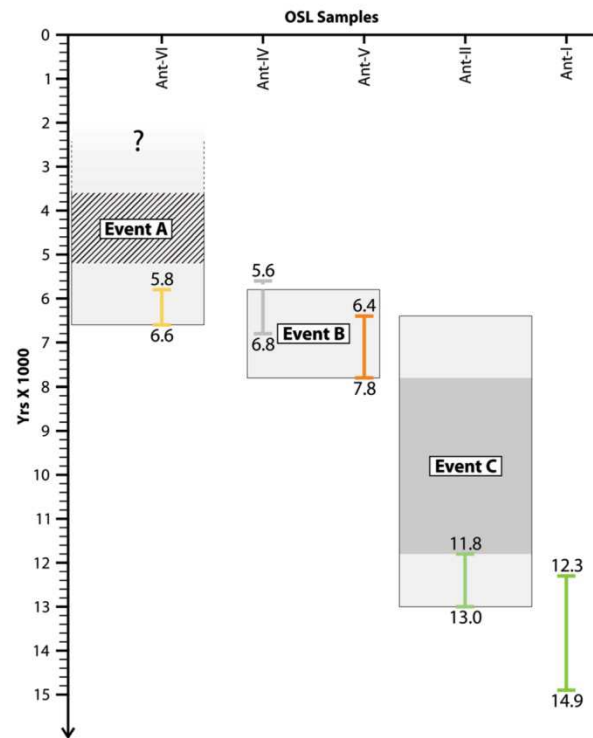


**Figure 9.** Five well-constrained OSL ages place bounds on the ages of the three palaeoearthquakes (A, B and C) identified in the Anar trench exposure. Light grey areas represent the maximum time windows for the past earthquakes, dark grey pointing the minimum time window for event C. For event A, hatched domain shows the preferred time interval of the earthquake ( $4.4 \pm 0.8$  ka). Colour codes are similar to units shown in Figs 4 and 5. Question mark illustrates the ambiguity due to the lack of ages in units post-dating the most recent earthquake (16 and 17).

A, B and C. Accounting for the lack of morphological segmentation along the Anar fault (Le Dortz *et al.* 2009) and the excavation of a single trench, there are no possibilities to calculate confidently any magnitude. The restored vertical throws per event suggest only that the related magnitudes are more likely on the order of  $M_w \approx 7$  (see previous section). The right-lateral offsets observed at the surface (Figs 2 and 3a) permit to reinforce this inference. Deeply incised intermittent streams are seen offset by  $8 \pm 0.5$  m (Le Dortz *et al.* 2009 and Fig. 3a) whereas several weakly incised small dry gullies show offsets of  $3 \pm 0.5$  m only (Fig. 2). Considering these lower offsets were more likely formed during the most recent earthquake, they provide the best estimate for the coseismic horizontal slip of event A. Such a coseismic slip at the surface agrees with a magnitude close to 7. Thus the higher offsets, which are only observed where the alluvial surface is older, should represent the cumulative horizontal slip of the last three events that are seen in the trench. Therefore, the three events, which are observed within the trench to the north of Anar city, should have had slip per event on the order of 3 m, suggesting they are of similar magnitudes.

Overall, the new data presented in this paper give evidence for at least three seismic events of similar sizes on the Anar fault (Fig. 9). OSL age of Ant-I sample indicates that the aggradation of the trench units did not started much before 14.9 ka or to the latest by 12.3 ka. Because only three events have occurred during the last 15 ka, this provides a rough estimate of at most 5 ka for the average

18 M. Foroutan et al.

maximum time interval between two earthquakes. The youngest age possibility may reduce this average time interval between two earthquakes to  $\approx 4$  ka. Considering the best estimates of average ages for the three seismic events A, B and C are:  $4.4 \pm 0.8$ ,  $6.8 \pm 1$  and  $9.7 \pm 3.3$  ka, respectively (Fig. 9), the time interval between two subsequent earthquakes is ill defined and might vary significantly. Nevertheless, the average ages for events A, B and C indicate that the intervals between two subsequent earthquakes should be 2400 and 2900 yr between events A–B and B–C, respectively. As the elapsed time since the last earthquake is 3600 yr at least and 5200 yr at most, this suggests we are getting close to the end of the seismic cycle and may anticipate a destructive earthquake for the Anar city in the near future.

Finally, the cumulative offset of  $8 \pm 0.5$  m (Le Dortz *et al.* 2009) post-dating fan aggradation and the refined age of fan abandonment given by OSL-2 sample ( $10.1 \pm 0.6$  ka) confirm a minimum slip rate estimate of  $0.8 \pm 0.1$  mm yr<sup>-1</sup> for the Anar fault. Then, the westernmost prominent right-lateral faults of the Central Iran plateau, namely the Dehshir and Anar faults, which are active though void of historical and instrumental earthquakes, are characterized by slip rates close to 1 mm yr<sup>-1</sup> (Le Dortz *et al.* 2009, 2011). Such faults have repeatedly produced destructive earthquakes with large magnitudes ( $M_w \approx 7$ ) and long recurrence interval of several thousands of years during the Holocene (Nazari *et al.* 2009; Fattahi *et al.* 2010 and this paper). This demonstrates that the Central Iran plateau does not behave totally as a rigid block and that its moderate internal deformation is nonetheless responsible for a significant seismic hazard.

#### ACKNOWLEDGMENTS

This study benefited of the logistic and financial assistance from Geological Survey of Iran. Université Pierre et Marie Curie and INSU-CNRS provided complementary funding for the fieldwork and OSL measurements. M. Foroutan acknowledges a grant from the French Embassy in Tehran for part of his PhD thesis and complementary support from UPMC-ISTeP. David Lambert, Attaché Scientifique et Culturel, is thanked for his continuing support to the cooperation between UPMC and GSI. M. Hosseini from Kerman GSI office helped with the logistics of the fieldwork. B. Oveisi, M. Nazem Zadeh, A. Agha Hosseini and M.A. Shokri are thanked for various contributions to the fieldwork, H. Bani Assadi and M. Adhami for their safe driving in the field. M. Fattahi would like to thank the research department of the Tehran University. We thank two anonymous reviewers for helpful and constructive comments.

#### REFERENCES

- Ambraseys, N.N. & Jackson, J.A., 1998. Faulting associated with historical and recent earthquakes in the Eastern Mediterranean region, *Geophys. J. Int.*, **133**, 390–406.
- Ambraseys, N. & Melville, C., 1982. *A History of Persian Earthquakes*. Cambridge University Press, Cambridge.
- Barka, A.A., 1996. Slip distribution along the North Anatolian Fault associated with the large earthquakes of the period 1939 to 1967, *Bull. seism. Soc. Am.*, **86**(5), 1238–1254.
- Barka, A.A. *et al.*, 2002. The surface rupture and slip distribution of the 17 August 1999 Izmit Earthquake (M 7.4), North Anatolian Fault, *Bull. seism. Soc. Am.*, **92**, 43–60.
- Bateman, M.D., Boulter, C.H., Carr, A.S., Frederick, C.D., Peter, D. & Wilder, M., 2007. Preserving the palaeoenvironmental record in drylands: bioturbation and its significance for luminescence derived chronologies, *Sediment. Geol.*, **195**(1–2), 5–19.
- Daniels, J.M., 2003. Floodplain aggradation and pedogenesis in a semiarid environment, *Geomorphology*, **56**, 225–242.
- Fattahi, M., Walker, R., Hollingsworth, J., Bahroudi, A., Nazari, H., Talebian, M., Armitage, S. & Stokes, S., 2006. Holocene slip-rate on the Sabzevar thrust fault, NE Iran, determined using optically-stimulated luminescence (OSL), *Earth planet. Sci. Lett.*, **245**, 673–684.
- Fattahi, M., Walker, R.T., Khatib, M.M., Dolati, A. & Bahroudi, A., 2007. Slip-rate estimate and past earthquakes on the Doruneh fault, eastern Iran, *Geophys. J. Int.*, **168**, 691–709.
- Fattahi, M. *et al.*, 2010. Refining the OSL age of the last earthquake on the Dheshir fault, Central Iran. *Quat. Geochronol.*, **5**, 286–292, doi:10.1016/j.quageo.2009.04.005.
- Galbraith, R.F., Roberts, R.G., Laslett, G.M., Yoshida, H. & Olley, J.M., 1999. Optical dating of single and multiple grains of quartz from Jinnium rock shelter, northern Australia, part 1, Experimental design and statistical models, *Archaeometry*, **41**, 339–364.
- Guralnik, B., Matmon, A., Avni, Y., Porat, N. & Fink, D., 2011. Constraining the evolution of river terraces with integrated OSL and cosmogenic nuclide data, *Quat. Geochronol.*, **6**, 22–32.
- Jackson, J. & D. McKenzie, 1984. Active tectonics of the Alpine-Himalayan Belt between western Turkey and Pakistan, *Geophys. J.R. astr. Soc.*, **77**, 185–264.
- Le Dortz, K. *et al.*, 2009. Holocene right-slip rate determined by cosmogenic and OSL dating on the Anar fault, Central Iran, *Geophys. J. Int.*, **179**, 700–710.
- Le Dortz, K. *et al.*, 2011. Dating inset terraces and offset fans along the Dehshir fault combining cosmogenic and OSL methods, *Geophys. J. Int.*, **185**, 1147–1174.
- Meyer, B. & Le Dortz, K., 2007. Strike-slip kinematics in Central and Eastern Iran: estimating fault slip-rates averaged over the Holocene, *Tectonics*, **26**, TC5009, doi:10.1029/2006TC002073.
- Meyer, B., Mouthereau, F., Lacombe, O. & Agard, P., 2006. Evidence of quaternary activity along the Deshir Fault, *Geophys. J. Int.*, **164**, 192–201.
- Murray, A.S. & Wintle, A.G., 2000. Luminescence dating of quartz using an improved single-aliquot regenerative-dose protocol, *Radiat. Meas.*, **32**, 57–73.
- Nazari, H. *et al.*, 2009. First evidence for large earthquakes on the Deshir Fault, Central Iran Plateau, *Terra Nova*, **21**, 417–426.
- Rittenour, T.M., 2008. Luminescence dating of fluvial deposits: applications to geomorphic, palaeoseismic and archaeological research, *Boreas*, **37**, 613–635.
- Roberts, R.G., Galbraith, R.F., Yoshida, H., Laslett, G.M. & Olley, J.M., 2000. Distinguishing dose populations in sediment mixtures: a test of single-grain optical dating procedures using mixtures of laboratory-dosed quartz, *Radiat. Meas.*, **32**, 459–465.
- Schmidt, A., Quigley, M., Fattahi, M., Azizi, Gh., Maghsoudi, M. & Fazeli, H., 2011. Holocene settlement shifts and palaeoenvironments on the Central Iranian Plateau: investigating linked systems, *Holocene*, **21**(4), 583–595, doi:10.1177/0959683610385961.
- Staubwasser, M., Sirocco, F., Grootes, P.M. & Segl, M., 2003. Climate change at the 4.2 ka BP termination of the Indus valley civilization and Holocene south Asian monsoon variability, *Geophys. Res. Lett.*, **30**(8), 1425, doi:10.1029/2002GL016822.
- Vernant, P. *et al.*, 2004. Present-day crustal deformation and plate kinematics in the Middle East constrained by GPS measurements in Iran and northern Oman, *Geophys. J. Int.*, **157**, 381–398.
- Walker, R. & Fattahi, M., 2011. A framework of Holocene and Late Pleistocene environmental change in eastern Iran inferred from the dating of periods of alluvial fan abandonment, river terracing, and lake deposition, *Quat. Sci. Rev.*, **30**, 1256–1271, doi:10.1016/j.quascirev.2011.03.004.
- Walker, R. & Jackson, J., 2004. Active tectonics and late Cenozoic strain distribution in central and eastern Iran, *Tectonics*, **23**, TC5010, doi:10.1029/2003TC001529.



CHAPTER 4

**SLIP RATE & PALEOSEISMOLOGY**

**OF THE NAYBAND FAULT**

---

## 4.1. Introduction

This chapter reports the very first geomorphic and paleoseismic studies of the right-lateral strike-slip Nayband fault, where none of the available instrumental and historical seismic catalogs provides evidence of a significant earthquake in the vicinity of the fault. This study adds to previous works performed on the right-lateral strike-slip faults at the transition between the Zagros collision domain and the Makran subduction zone. In addition to provide a description of the active deformations of a fault hitherto poorly studied, this chapter shed lights on the tectonic processes at work across the boundary between a young collision and a still active subduction.

The data presented in this chapter are used to determine the slip rate and the seismic behavior of this historically silent fault. The fault slip rate is determined by  $^{36}\text{Cl}$  cosmic ray exposure and optically stimulated luminescence (OSL) dating of several geomorphic offsets at two sites along the fault (section 3). The seismic history of the fault is constrained by dating of 18 OSL samples collected within a 59-m-long paleoseismic trench excavated across the fault (section 4). The paleoseismic records provide evidence for the occurrence of several large-magnitude ( $M\sim 7$ ) earthquakes during the late Pleistocene and Holocene timescales. Furthermore, despite the lack of seismicity in the vicinity of the Nayband fault during the last few millennia, the paleoseismic investigations provide evidence for a large earthquake within the last millennium.

These new results have implications both on the assessment of regional seismic hazard and on the mechanisms of continental deformation. By the end of this chapter, the slip rate constraints are compared to the paleoseismic data, and the mechanism of strain release on the Nayband fault over the last seismic cycles is discussed in section 5.1. A comparison of the paleoseismic record with the available historical seismic catalogs is provided in section 5.2. The determination of the Nayband slip rate allows comparing the short-term geologic ( $10^3$ - $10^5$  yr) deformation field to that obtained from the GPS observations. Then, the implication of these results for the distribution of strain in Central and Eastern Iran are discussed in section 5.3.

## 4.2. Late Pleistocene-Holocene right-slip rate and paleoseismology of the Nayband fault, western margin of the Lut block, Iran

Paper Submitted to *Journal of Geophysical Research*

M. Foroutan<sup>1,2,3</sup>, B. Meyer<sup>1,2</sup>, M. Sébrier<sup>1,2</sup>, H. Nazari<sup>4</sup>, A. S. Murray<sup>5</sup>, K. Le Dortz<sup>1,2</sup>, M. A. Shokri<sup>3</sup>, R. Braucher<sup>6</sup>, D. Bourlès<sup>6</sup>, S. Solaymani Azad<sup>3</sup>, and M. J. Bolourchi<sup>3</sup>

<sup>1</sup>UPMC (Université Pierre et Marie Curie) Université Paris 06, ISTEP UMR 7193, F-75005, Paris, France  
Email: [mohammad.foroutan@upmc.fr](mailto:mohammad.foroutan@upmc.fr), [bertrand.meyer@upmc.fr](mailto:bertrand.meyer@upmc.fr), [michel.sebrier@upmc.fr](mailto:michel.sebrier@upmc.fr),  
[kristell.ledortz@upmc.fr](mailto:kristell.ledortz@upmc.fr)

<sup>2</sup>CNRS, ISTEP, UMR 7193, F-75005, Paris, France

<sup>3</sup>Geological Survey of Iran, Azadi Square, Meraj Avenue, PO Box: 13185-1494, Tehran, Iran  
Email: [foroutan@gsi.ir](mailto:foroutan@gsi.ir), [m.shokri@gsi.ir](mailto:m.shokri@gsi.ir), [s.solaymani@gsi.ir](mailto:s.solaymani@gsi.ir), [mjbolourchi@gsi.ir](mailto:mjbolourchi@gsi.ir)

<sup>4</sup>Research Institute for Earth Sciences, Geological Survey of Iran, PO Box: 13185-1494, Tehran, Iran  
Email: [h.nazari@gsi.ir](mailto:h.nazari@gsi.ir)

<sup>5</sup>Nordic Laboratory for Luminescence Dating, Department of Geoscience, Aarhus University, Risø DTU, DK-4000 Roskilde, Denmark  
Email: [anmu@dtu.dk](mailto:anmu@dtu.dk)

<sup>6</sup>CEREGE, UMR 6635 CNRS-Aix Marseille Université, 13545 Aix-en-Provence, France  
Email: [braucher@cerege.fr](mailto:braucher@cerege.fr), [bourles@cerege.fr](mailto:bourles@cerege.fr)

## Abstract

The 290-km-long, Nayband strike-slip fault bounds the western margin of the Lut block and cuts across a region known to have been quiescent during the last few millennia. Cl-36 cosmic ray exposure (CRE) and optically stimulated luminescence (OSL) dating of cumulative geomorphic offsets are used to derive the long-term slip rate. The measured offsets at two sites along the fault range between  $9 \pm 1$  m and  $195 \pm 15$  m with ages from  $6.8 \pm 0.6$  ka to  $\sim 100$  ka, yielding minimum and maximum bounds of late Pleistocene and Holocene slip rates of  $1.15$  and  $2.45$  mm yr<sup>-1</sup>, respectively. This moderate slip rate of  $1.8 \pm 0.7$  mm yr<sup>-1</sup>, averaged over several earthquake cycles, is compared with the paleoseismic record retrieved from the first trench excavated across the fault. Combining the paleoseismic evidence with 18 OSL ages obtained from this trench site demonstrates the occurrence of at least four large ( $M_w \sim 7$ ) earthquakes during the last  $17.4 \pm 1.3$  ka and of two older earthquakes, one before  $\sim 23$  ka and another before  $70 \pm 5$  ka. The exposed sediment succession also indicates a significant gap at the end of MIS-2 and the beginning of MIS-1. The age of the most recent regional incision is accurately bracketed between 6.1 ka and 7.4 ka. Sediments from the last  $\sim 7$  ka contain evidence of the three younger earthquakes. Interestingly, the penultimate and antepenultimate events occurred between  $6.5 \pm 0.4$  ka and  $6.7 \pm 0.4$  ka within a time interval lasting at most 1 ka whereas the most recent earthquake occurred within the last millennium. Such an irregular earthquake occurrence suggests the seismic behavior of the Nayband fault should be characterized by clustering strain release. From this and taking into account the occurrence of the most recent earthquake within the last 800 years, the imminence of an earthquake along the Nayband fault cannot be discarded. Although the most recent surface-rupturing event seems to have occurred after AD 1200, this event went unnoticed in the historical records. This provides a marked illustration of the incompleteness of the historical seismic catalogs in Central Iran, challenging any assessment of regional seismic hazard without appropriate geologic and geochronological information. Large and infrequent earthquakes are characteristic of the seismic behavior of the slow-slipping strike-slip faults slicing Central and Eastern Iran. Also, the slip rates summed across Central and Eastern Iran from the Iran Plateau up to the Afghan lowlands remain difficult to match with the available GPS data.

## 1. Introduction

Central Iran experiences low GPS deformation rates [Vernant *et al.*, 2004; Masson *et al.*, 2005, 2007] and is commonly described as an area with a very low level of seismicity over the few millennia covered by the instrumental and historical seismic records [e.g., Ambraseys and Melville, 1982; Engdahl *et al.*, 2006]. Nevertheless, this presently aseismic block is sliced by several N-striking, right-lateral, intracontinental active faults (Figure 1a). These dextral faults are located within a wide zone extending from the western Central Iran Plateau (Dehshir and Anar faults) to the western margin of the Lut block (Nayband and Gowk faults).

Understanding the pattern of faulting and the long-term distribution of deformation across the entire region is critical to our understanding of how the deformation induced at the transition between the Zagros collision domain to the west and the Makran subduction zone to the east has been accommodated in Central Iran. Such information is essential to investigations of the degree of consistency between the long-term strain distribution and the present-day geodetic deformation. Moreover, a good knowledge of fault kinematics is a pre-requisite for paleoseismic investigations; both are essential in the assessment of the regional seismic hazard. Several geomorphological studies have been undertaken to estimate the long-term slip rates of several of the major strike-slip faults slicing Central Iran. The slip rates are known over a few tens of thousands to a few hundred thousand years for the Dehshir ( $1.2 \pm 0.3 \text{ mm yr}^{-1}$  [Le Dortz *et al.*, 2011]), Anar ( $\geq 0.8 \pm 0.1 \text{ mm yr}^{-1}$  [Le Dortz *et al.*, 2009; Foroutan *et al.*, 2012]), and Gowk ( $\geq 3.8 \pm 0.7 \text{ mm yr}^{-1}$  [Walker *et al.*, 2010b]) faults. However, the Nayband fault slip rate of  $1.4 \pm 0.5 \text{ mm yr}^{-1}$  has been averaged over the much longer timescale of the entire Quaternary [Walker *et al.*, 2009]) precluding a meaningful comparison between short-term geological ( $10^3$ - $10^5 \text{ yr}$ ) slip rates and the geodetic displacement field. Some of these studies have been complemented by paleoseismic investigations [e.g., Nazari *et al.*, 2009; Fattahi *et al.*, 2010; Foroutan *et al.*, 2012]. However, neither the late Pleistocene-Holocene slip rate nor the seismic behavior of the historically silent Nayband fault is known.

This paper aims to provide the critical data required to quantify the late Pleistocene-Holocene slip rate and seismic history of the Nayband fault. First we document cumulative geomorphic offsets and date them with  $^{36}\text{Cl}$  cosmic ray exposure (CRE) and optically stimulated luminescence (OSL) techniques. Then, the first paleoseismic investigation ever conducted along

the Nayband fault is reported. The implications of these results are then discussed both for the distribution of strain and the assessment of seismic hazard in Central and Eastern Iran.

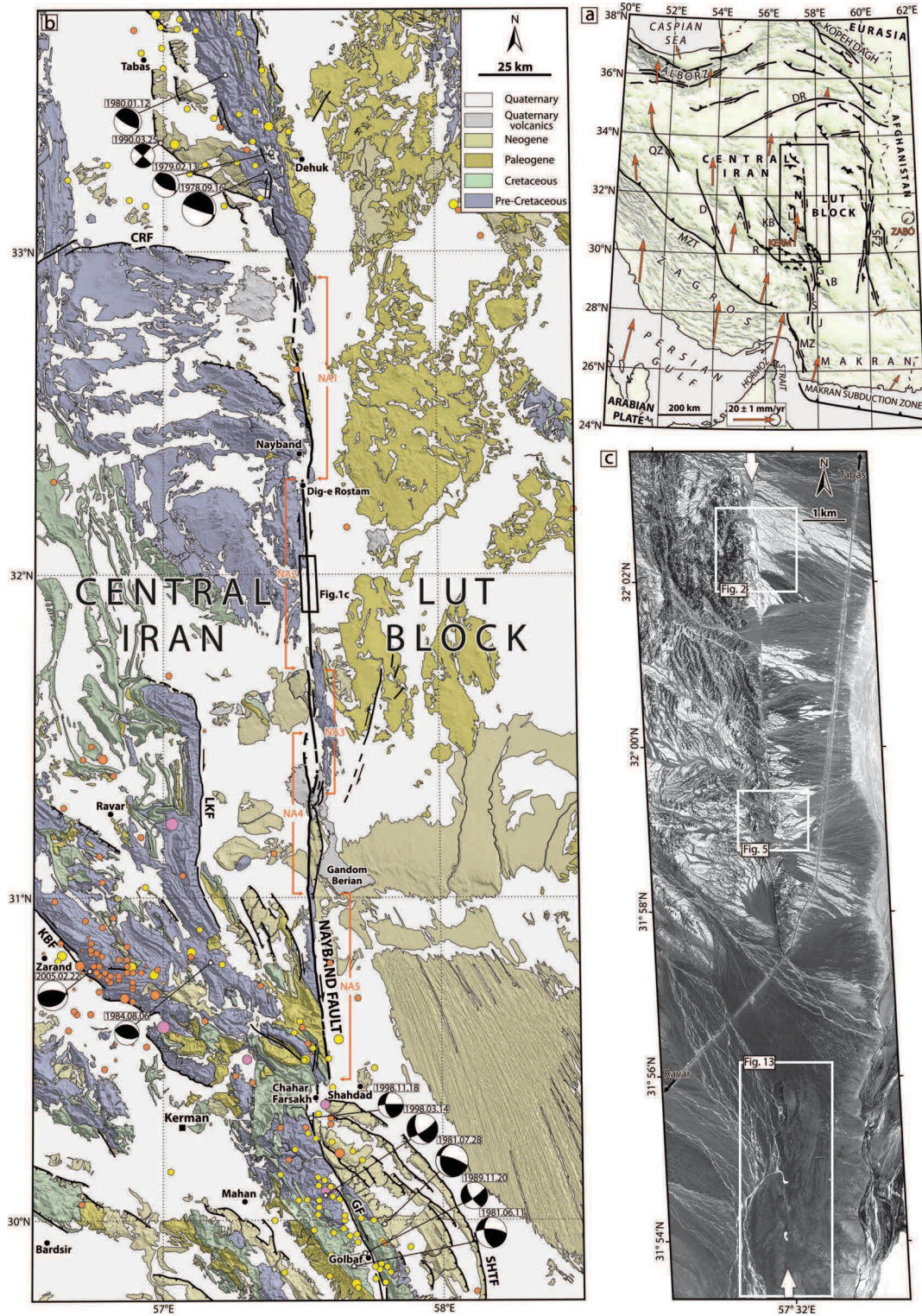


Figure 1. See next page.

**Figure 1.** (a) Map of the major active faults in Central and Eastern Iran superimposed on the shaded DEM map. A, Anar fault; B, Bam fault; D, Dehshir fault; DR, Doruneh fault; G, Gowk fault; J, Jiroft fault; KB, Kuh Banan fault; L, Lakar Kuh fault; MZ, Minab-Zendan fault system; MZT, Main Zagros Thrust fault; QZ, Qom-Zefreh fault; R, Rafsanjan fault; S, Sabzevaran fault; and SFZ, Sistan Fault Zone. GPS velocities (orange arrows) in Eurasian-fixed reference frame with 95 per cent confidence ellipse for ZABO site from *Vernant et al.* [2004] and *Masson et al.* [2007]. The velocity of ZABO site does not present significant motion relative to Eurasia. Black box shows the location of Figure 1b. (b) Simplified seismotectonic map of east-Central Iran and western Lut Block. Regional geology compiled from *Stöcklin and Nabavi* [1969], *Aghanabati* [1974, 1993], *NIOC* [1977], *Alavi-Naini and Griffis* [1981a, b], *Vahdati Daneshmand* [1992], *Sahandi* [1992], *Soheili* [1995], and *Mahdavi* [1996], overlain on shaded relief 90-m SRTM Digital Elevation Model. Active fault traces (dashed where inferred) from Landsat, SPOT, Quickbird imageries and field observations. CRF, Cheshmeh Rostam Fault; GF, Gowk Fault; KBF, Kuh Banan Fault; LKF, Lakar Kuh Fault; and SHTF, Shahdad Thrust Faults. Orange circles are epicenters of most recent (2004-2012) earthquakes ( $m_b > 3$ ) from the NEIC catalog (<http://earthquake.usgs.gov/earthquakes/eqarchives/epic/>). Yellow circles are epicenters of recent (1918-2004) earthquakes from *Engdahl et al.* [2006]. Violet circles are historical epicenters of older (before 1918) earthquakes from *Ambraseys and Melville* [1982]. Well-constrained fault-plane solutions are indicated (see Table 1 for source parameters). Note the lack of instrumental and historical seismicity in the neighborhood of the Nayband fault trace. Black box shows the location of Figure 1c. (c) Raw Quickbird imagery (pixel-size, 60 cm) showing the trace of the Nayband fault (white arrows) cutting mostly across Pleistocene-Holocene alluvial fans and Neogene marls (whitish parts). Streams and gullies incised within alluvial fans show right-lateral offsets ranging from several meters to several hundred meters. Boxes show the locations of site North (Figure 2, along single straight fault portion), site South (Figure 5, along a 100-m-wide step-over) and paleoseismic trench site (Figure 13).

## 2. Geologic Setting and Seismotectonic Background

The N-striking Nayband fault (N on Figure 1a) is located in the eastern Iran Plateau on the Iran block, a roughly triangular-shaped, continental block that is bounded by three major ophiolite sutures: (1) the E-striking, ill-defined, discontinuous Paleotethys suture to the north, which extends roughly along the south of the Kopeh Dagh and north of the Alborz, (2) the more continuous NW-striking Zagros suture to the SW, which parallels the Main Zagros Thrust (MZT), and (3) the NNW-striking Sistan suture to the east, localized roughly along the Sistan Fault Zone (SFZ). The Iran block drifted northward from Gondwana during the latest Paleozoic

to be subsequently welded to Eurasia by the Late Triassic during the Eo-Cimmerian collision event, when the Paleo-Tethys Ocean closed [e.g., *Boulin*, 1988; *Alavi*, 1991; *Zanchi et al.*, 2009]. The SW boundary of the Iran block, the Zagros suture, results from the collision that occurred between the Iran block and Arabia during Late Eocene-Oligocene [e.g., *Berberian and King*, 1981; *Agard et al.*, 2005; *Allen and Armstrong*, 2008; *Karagaranbafghi et al.*, 2012], following the closure of the Neotethys Ocean. The eastern limit of the Iran block corresponds to the Sistan suture that results from the welding of the Iran and Afghan blocks by the Middle Eocene [e.g., *Camp and Griffis*, 1982; *Tirrul et al.*, 1983]. Although this Iran block is composed of several terranes (mainly Yazd, Tabas and Lut “blocks”), paleomagnetic data indicate that these different terranes display a common drift pattern [*Besse et al.*, 1998; *Muttoni et al.*, 2009]. Moreover, the ophiolite sutures, which are observed inside this composite Iran block (Sabzevar and Nain-Baft), are considered as former back-arc basins that opened and closed along the Mesozoic Eurasia margin [e.g., *Agard et al.*, 2011 and references therein]. These geodynamic processes are related to Jurassic and/or Cretaceous tectonic events such as the Neo-Cimmerian, well expressed by an angular unconformity between Cretaceous and older units (Figure 1b).

At a detailed regional scale, the Nayband fault is located between two domains of contrasting topography: the relatively high Tabas block to the west in Central Iran, and the low subdued depression of the Lut block to the east in eastern Iran. These two blocks differ both in their geology and crustal thickness [e.g., *Kluyver et al.*, 1983; *Dehghani and Makris*, 1984], suggesting that the location of the present-day right-lateral Nayband fault is partly superimposed on some lithosphere weakness due to previous fault zone activity.

It is commonly accepted that the present-day widespread strike-slip faulting represents the last stage of the Arabia-Eurasia collision in response to the northward movement of the Iran block with respect to the Eurasian Afghan block [e.g., *McQuarrie et al.*, 2003]. However, there is continuing debate over the onset of strike-slip tectonics in Iran. Some authors have proposed a time range of 3-7 Ma, based on the time needed to extrapolate present-day GPS-derived slip rates to give the observed total cumulative fault displacement [e.g., *Allen et al.*, 2004; *Walker and Jackson*, 2004]. However, *Hollingsworth et al.* [2008] and *Agard et al.* [2011] proposed an earlier date of 10 Ma, based on extrapolating present-day slip rates derived from GPS to achieve the total cumulative strike-slip offsets in NE Iran and geodynamic reconstructions in SW Iran,

respectively. *Meyer and Le Dortz* [2007] proposed a time range between 8-22 Ma based on extrapolating short-term geologic (Holocene) slip rates to give the total cumulative fault offsets in Central and Eastern Iran. Because of the lack of clear evidence of the total cumulative displacement along the Nayband fault, inception time estimate of dextral faulting remains unknown.

While uncertainties remain about the onset of the strike-slip tectonic regime now prevailing in Central and Eastern Iran, the current regional velocity field has been well described by GPS campaigns [*Vernant et al.*, 2004; *Masson et al.*, 2005, 2007]. The overall differential motion between Central and Eastern Iran across the Lut block amounts to  $16 \pm 2 \text{ mm yr}^{-1}$  of N-S right-lateral shear at  $\sim 30.5^\circ\text{N}$  (difference between the vectors KERM and ZABO, Figure 1a). But neither the distribution of dextral shear between the eastern and western faulted Lut borders, nor the along-strike evolution along a given border, is well established. By contrast, west of the Lut, the limited internal deformation evidenced by GPS appears to be challenged by the slip rates of faulting inside the Central Iran Plateau. Indeed, well-constrained late Quaternary slip rates of the Dehshir, Anar and Rafsanjan strike-slip faults are  $1.2 \pm 0.3 \text{ mm yr}^{-1}$  [*Le Dortz et al.*, 2011],  $0.8 \pm 0.1 \text{ mm yr}^{-1}$  [*Le Dortz et al.*, 2009; *Foroutan et al.*, 2012], and  $0.4 \text{ mm yr}^{-1}$  [*Fattahi et al.*, 2011], respectively. The dextral slip rate of the more easterly trending Kuh Banan fault is estimated between 1 and 2  $\text{mm yr}^{-1}$  [*Allen et al.*, 2011; *Walker and Allen*, 2012] and several active thrust faults have also been documented within the interiors of the Central Iran Plateau [*Walker et al.*, 2010a], although their slip rates are not yet determined.

While the historical and instrumental record does not indicate significant seismicity in the interior of the Central Iran Plateau, several earthquakes have occurred close to or along the eastern border with the Lut desert (Figure 1b and Table 1). North of  $33^\circ\text{N}$ , the destructive Tabas earthquake of  $M_s$  7.7 [*Berberian*, 1979a, b] occurred in a region hitherto known to have been quiescent for the last millennium. This earthquake remained the largest instrumentally recorded event in Iran [*Walker et al.*, 2003, 2013] until the recent (2013 April 16),  $M_w$  7.8 Saravan intermediate-depth earthquake, which struck the Makran region. The Tabas earthquake, which resulted in approximately 20,000 deaths, combined thrust and dextral motions along NNW-striking faults; these may account for a transpressive tectonic regime at the northwestern termination of the N-striking Nayband fault. Over the next few years this destructive event was

followed by moderate events with either thrust or strike-slip fault-plane solutions, also expressing the transpressive state of the tectonic regime.

Another sequence of earthquakes with associated surface breaks has taken place south of 30.5°N, where NNW-striking parallel thrusts (Shahdad) and strike-slip (Gowk) faults are thought to achieve slip partitioning at the southeastern tip of the Nayband fault. The Gowk fault slips at a minimum slip rate of  $3.8 \pm 0.7 \text{ mm yr}^{-1}$  averaged over the last 8 ka [Walker *et al.*, 2010b] and has hosted five destructive earthquakes during a seventeen year of stress transfer period [Nalbant *et al.*, 2006]. The sequence started in 1981 with the two destructive earthquakes of  $M_s$  6.7 (Golbaf) and  $M_s$  7.1 (Sirch) on June 11 and July 28, respectively [Berberian *et al.*, 1984]. Both ruptured the Gowk fault to the surface with an overall 70-km-long fault break interrupted by a 10-15-km slip gap further filled during the 1998 March 14 Fandoqa earthquake. The Fandoqa earthquake of magnitude  $M_w$  6.6 is also known to have re-ruptured a significant portion of the Sirch break and to have triggered slip on the Shahdad thrusts [Berberian *et al.*, 2001; Fielding *et al.*, 2004]. The Fandoqa event was followed by a smaller ( $M_w$  5.4) event, the Chahar Farsakh earthquake, which took place on November 18 of the same year and produced minor surface cracking over 4 km. In the meantime, between the 1981 and 1998 events, the south Golbaf  $M_s$  5.7 earthquake took place in 1989. It produced a 19-km-long surface break distributed on two sub-parallel fault strands [Berberian and Qorashi, 1994].

An additional event with magnitude  $M_w$  6.4, the Dahuiyeh event, occurred some 90-km NW of the Gowk fault and 100-km west of the Nayband fault, within the Central Iran Plateau. The event struck the city of Zarand on February 22, 2005 and produced a 13-km long, thrust fault break splaying of the Kuh Banan strike-slip fault [Talebian *et al.*, 2006].

Thus, the Nayband fault seems the only portion of the long quiescent western Lut border that has not been reactivated during the last few millenniums (Figure 1b), at least according to the instrumental and historical regional seismic records [Ambraseys and Melville, 1982; Ambraseys and Jackson, 1998; Berberian and Yeats, 1999; Engdahl *et al.*, 2006]. Although the long-term slip rate of the Nayband fault averaged over the entire Quaternary is suggested to be of the order of  $1.4 \pm 0.5 \text{ mm yr}^{-1}$  [Walker *et al.*, 2009] neither its short-term slip rate nor its paleoseismic history are known. While the neighboring Tabas and Gowk faults have hosted recent destructive events that might enhance the probability of triggering earthquakes on the Nayband fault, it is

clearly of importance to document both its Holocene slip rate and its seismic history in order to assess the regional seismic hazard.

**Table 1.** Source parameters of the well-constrained fault-plane solutions of instrumental earthquakes in east-Central Iran. The fault-plane solutions are shown on Figure 1b.

Event	Region	Lat. (°N)	Long. (°E)	Strike	Dip	Rake	Depth (km)	M <sub>w</sub>	Fault	Source
1978 Sept. 16	Tabas	33.25	57.38	355	16	155	9	7.28	Tabas	<i>Walker et al. [2003]</i> *
1979 Feb. 13	Tabas	33.31	57.40	327	28	116	11	5.58	Tabas	<i>Walker et al. [2003]</i> *
1980 Jan. 12	Tabas	33.55	57.23	348	20	137	14	6.0	Tabas	<i>Walker et al. [2003]</i> *
1981 Jun. 11	Golbaf	29.86	57.68	169	52	156	20	6.58	Gowk	<i>Berberian et al. [2001]</i> *
1981 Jul. 28	Sirch	29.99	57.79	177	69	184	18	6.98	Gowk	<i>Berberian et al. [2001]</i> *
1984 Aug. 6	Hur	30.80	57.17	279	35	86	11	5.3	—	<i>Baker [1993]</i>
1989 Nov. 20	South Golbaf	29.90	57.72	145	69	188	10	5.83	Gowk	<i>Berberian et al. [2001]</i> *
1990 Mar. 25	Tabas	33.34	56.99	223	90	-180	15	5.1	Tabas	Harvard CMT
1998 Mar. 14	Fandoqa	30.08	57.58	156	54	195	5	6.57	Gowk	<i>Berberian et al. [2001]</i> *
1998 Nov. 18	Chahar Farsakh	30.32	57.53	174	55	173	15	5.34	Gowk	<i>Berberian et al. [2001]</i> *
2005 Feb. 22	Dahuieh (Zarand)	30.77	56.73	270	60	104	7	6.4	Kuh Banan	<i>Talebian et al. [2006]</i> *

\* Epicenters from *Engdahl et al. [1998]* or subsequent updates to their catalog.

The Nayband fault runs for some 290 km along the western margin of the Lut block (Figure 1). Although the overall trace of the Nayband fault is straight, five first order segments can be identified on the basis of main structural discontinuities such as bend, step over and strike variations.

The northern termination of the linear fault trace lies close to 33°N, where it splays into the Cheshmeh Rostam fault E-striking south-dipping thrust fault (CRF on Figure 1b). From that junction and up to the south of the village of Nayband, the northernmost fault segment strikes N172°E along some 78 km and cuts across Eocene volcanic rocks as well as recent deposits. Near 32.37°N, east of the Nayband village, the northern segment bends westwards and ends east of Dig-e Rostam, where the fault trace makes a right-step over. The second segment strikes ~N178°E and runs from the Dig-e Rostam hot springs 65-km to 31.7°N. There, the fault trace makes another right-step defining the boundary with a third segment which cuts through

Neogene sediments, Quaternary alluvial fans and recent playas. This segment has an average strike of N175°E and a length of about 40 km up to the north of the Gandom Berian basaltic plateau (Figure 1b); it controls the eastern edge of a 4-km wide pull-apart basin [Walker *et al.*, 2009]. The western edge of this basin is controlled by the beginning of a fourth, 50-km-long, N178°E striking segment cutting the Gandom Berian basalts along its northern portion and bounded by a parallel secondary thrust along its southern portion. Farther south, where the secondary thrust dies out at about 31°N, the main strike-slip fault veers eastwards into a fifth segment. This 65-km length southernmost segment has an average strike of N173°E and runs parallel to the mountain front up to the northeast of the Chahar Farsakh village.

The next section reports the observations collected from the second segment of the Nayband fault; geomorphic features, cosmogenic and luminescence dating are then used to determine the late Pleistocene-Holocene slip rate.

### 3. Morphological Offsets and Slip Rate Estimate

The use of morphological offsets to determine the long-term slip rate on an active fault requires datable morphologic features that were first displaced by the fault motion(s) and then preserved over the observable displacement interval [e.g., Sieh and Jahns, 1984; Weldon and Sieh, 1985; Peltzer *et al.*, 1988]. Below we document several offset features along the second segment of the Nayband fault. These offset features are alluvial fans, terraces and stream channels that have been studied in detail at two sites about 5 km apart. We then discuss the ages of the geomorphic markers using <sup>36</sup>Cl CRE and OSL dating to derive the slip rate averaged over the late Pleistocene-Holocene.

#### 3.1. Site North

Site North is located about 26 km south of the Dig-e Rostam hot springs (Figure 1c). This site was presented first by Wellman [1966] as a sketch map based on aerial photos showing several dextral offset streams along the fault (see Figure 2G of Wellman [1966]). There, smooth hills made of Triassic rocks outcropping to the west of the fault are overlain by Neogene piedmont sediments outcropping mostly east of the fault (Figure 2). The location of the fault is well constrained both on the Quickbird imagery and in the field by a clear, linear, single trace that offsets several rivers, the longest of which are more displaced than the smallest gullies

(Figures 2 and 3a). The largest hectometric dextral offsets are associated with two major rivers that incise into the Triassic shales, sandstones and limestones west of the fault. East of the fault, both rivers feed prominent alluvial fans nested within Neogene marls interbedded with conglomerate levels. The fans and the overbank surfaces display a dark hue on the Quickbird imagery highlighting the dextral along-fault offsets of the river beds (Figures 2 and 3a).

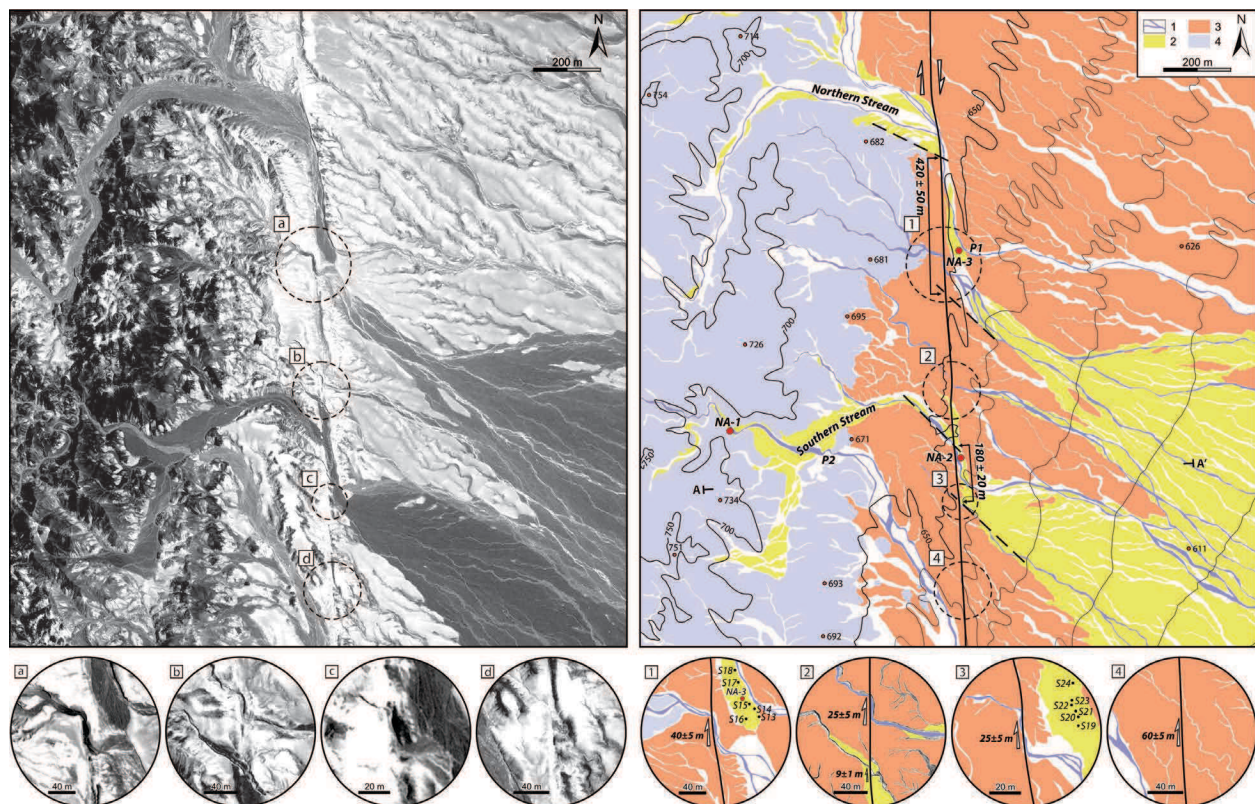


**Figure 2.** Site North. (Left) Quickbird imagery of the Nayband fault across the Quaternary alluvial deposits and Neogene marls. Dashed circles indicate recent right-lateral offset streams. (Right) Corresponding geologic map adapted from Quickbird imagery, field observations and regional geology [Alavi-Naini and Griffis, 1981a]. Contour lines and elevation points in meters, asl, derived from 1:25,000 topographic map (National Cartographic Center of Iran; Sheet No. 7554-III SW). Main contour interval is 50 m. Intermediate contours, every 10 m are represented east of the fault. Red dots locate the OSL samples collected from the abandoned alluvial fans and the most recent risers of incised stream. P1 and P2 are Recent stream piracies. 1, active channels; 2, Recent alluvial fans and terraces of Holocene and late-Pleistocene ages; 3, poorly consolidated Neogene marls and sandstones; 4, Triassic shales and sandstones. Dashed circles denote locations of raw (a, b, c, d) and interpreted (1, 2, 3, 4) Quickbird enlargements. Black dots locate the  $^{36}\text{Cl}$  samples collected on the surface of the alluvial fans (see text for discussion).

A southwards flowing tributary joins the main overbank surface of the northernmost river, and as a result the streambed widens as it approaches the fault. Because of this, the intersections of the upstream and downstream right banks between the prolongation towards the fault are the most reliable piercing points; this indicate a right-lateral offset of  $420 \pm 50$  m (Figure 2). Farther south, another prominent river has been offset by  $180 \pm 20$  m. These large rivers are no longer feeding the fans they originally emplaced so that these offsets are much older than the recent incision of the latest deposits filling the valleys. The recent incision has resulted in piracy that disconnected the alluvial fans from their upstream tributaries. The piracy P1 that disconnects the northern fan occurred east of and close to the fault trace while that of the southern fan, P2, occurred upstream and west of the fault. The abandonment of the fans is therefore coeval with the beginning of incision by the present-day drainage network of the infilling of the wide flat-floored valleys and related outlet fans. This abandonment (and so the last incision of the fans) seems rather recent since the surfaces of the fans are characterized by a subdued bar-and-swale morphology and a poorly developed desert pavement [e.g., *Frankel and Dolan, 2007*]. Such recent incision may relate to the widespread regional incision documented by *Meyer and Le Dortz [2007]* for the Central Iran Plateau and assigned to the Holocene.

Several smaller offsets of intermittent streams and channels have been preserved. There are many intermittent river-courses that collect gullies draining small catchments within the Triassic rocks; where these cross the fault they incise narrow gorges into the soft and easily erodible Neogene marls, and as a result numerous conspicuous dogleg offsets are visible along the fault. These offsets, ranging between 10 and several tens of meters, are described from the North towards the South. The northernmost is preserved along a tributary close to the outlet of the northern abandoned fan with a conspicuous dogleg dextral offset of  $40 \pm 5$  m (Figures 2, 3a, 3b and 3c). Farther south, a narrow stream is incised  $\sim 15$  m into the poorly-consolidated Neogene marls mantled by remnants of Quaternary colluviums. This intermittent stream is right-laterally offset by about  $25 \pm 5$  m (Figures 2, 3b and 3d). The smallest cumulative geomorphic offset observed along the fault occurs 50 m to the south of the former offset-stream. There, a very narrow gully is incised by  $\sim 3.3$  m into both the Neogene sediments and a thin alluvial veneer that previously fed the southern fan; this gully is right-laterally offset by  $9 \pm 1$  m (Figures 2, 3b, 3e and 3f). Farther south and a little west of the outlet of the southern alluvial fan, another  $25 \pm 5$  m right-lateral dogleg offset on an ephemeral gully is well preserved (Figures 2 and 4a). A larger

offset of  $60 \pm 5$  m on an intermittent channel incising obliquely to the fault strike is seen 250 m farther to the south (Figures 2 and 4b).

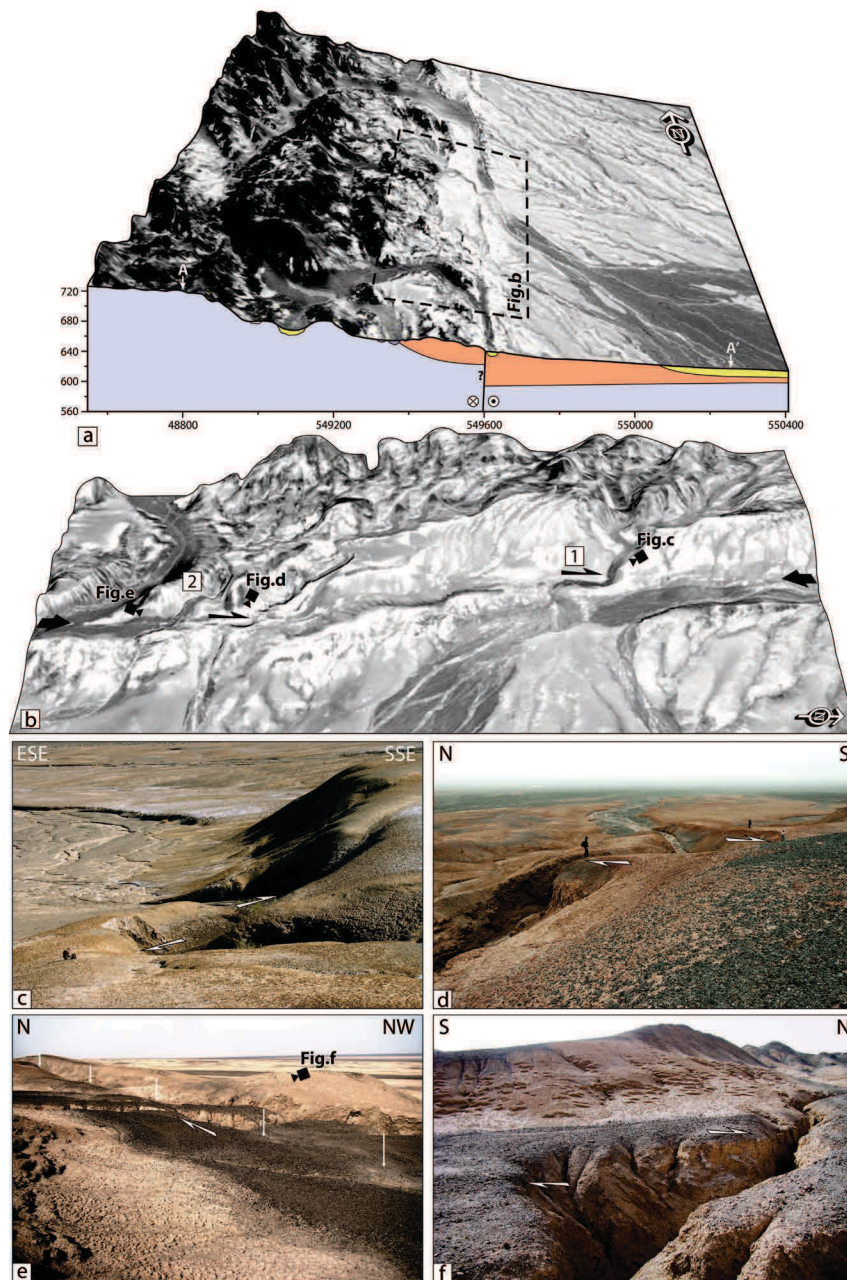


**Figure 3.** (a) 3D perspective diagram (vertical exaggeration=2) of site North and surrounding area obtained by draping the Quickbird imagery over the shaded relief Digital Elevation Model extracted from 1:25,000 topographic data. The Nayband fault trace makes the transition between Quaternary alluvial fans and Neogene piedmont deposits, east of smoothed hills made of Triassic rocks. Simplified cross-section schematizes the units relations (see Figure 2 for location). Color codes as in Figure 2. (b) Perspective

view highlights the recent offset streams 1 and 2 by the fault trace (see Figure 2 for location). (c-f) Field photographs of three dextral offsets; c: right-lateral dogleg offset of  $40 \pm 5$  m (square 1 on Figure 2); d: right-lateral offset of an incised ( $\sim 15$  m) channel by  $25 \pm 5$  m (square 2 on Figure 2); e-f: different views of  $9 \pm 1$  m offset preserved by an incised ( $\sim 3.3$  m) gully.

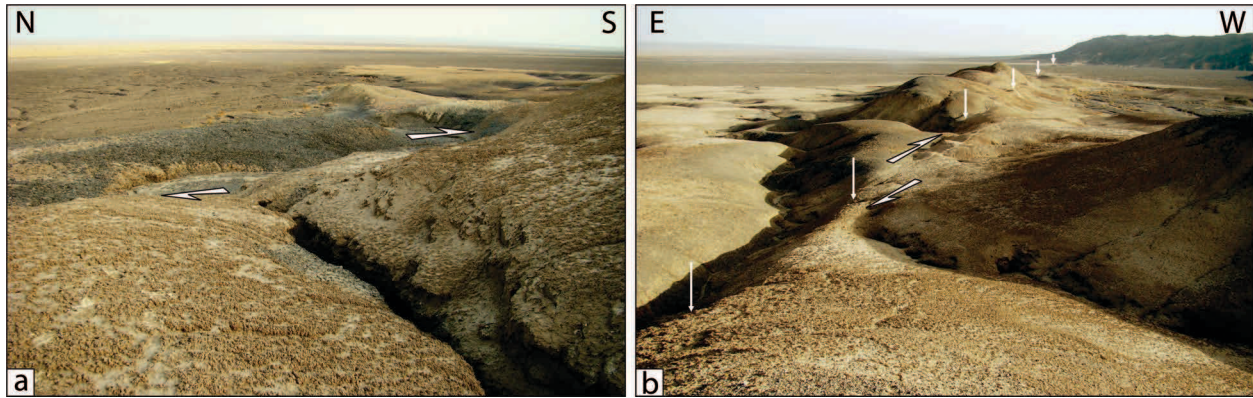


**Figure 4.** Field photographs of two offset channels at the site North (see squares 3 and 4 on Figure 2 for locations). (a) View to the east of an ephemeral gully incised into poorly consolidated Neogene marls that are partially covered by younger alluvial fan deposits. Its offset amounts to  $25 \pm 5$  m (square 3 on Figure 2). (b) View to the south of right-lateral offset of an intermittent channel by  $60 \pm 5$  m, which is incised within poorly consolidated Neogene marls (square 4 on Figure 2).

### 3.2. Site South

This site is located about 5 km south of the site North (Figure 1c and 5a). Two parallel fault strands delineate a 100-m-wide, 1-km-long releasing step-over cutting through the Neogene deposits, Pleistocene and Holocene alluvial fans, and active streams. Figure 5b shows the overall mapping based on Quickbird imagery and field observations. For most of its length, the trace of the eastern fault strand (EFS) runs more or less at the base of a  $\leq 10$ -m high west-facing steep slope between Neogene marls and Quaternary alluvial deposits. The trace of the western fault strand (WFS) runs at the base of a 30-40-m high, east-facing slope and separates Neogene marls ( $< 10^\circ$  northwest-dipping) from Quaternary deposits. While the trace of the EFS vanishes to the south, the trace of the WFS merges with that of the EFS some 250 m north of the site. The low-relief depression between these two fault strands is filled mainly with Pleistocene alluvial deposits that have been eroded by two major E-W intermittent streams.

The course of the northern stream (R0) trends N110°E upstream where it flows into a 50-m-wide valley. Nearby the fault zone, R0 is deflected to the north to flow downstream into a

narrow, N100°E, 10-20-m wide, entrenched valley. The present downstream portion of R0 is building a young alluvial fan at its eastern outlet, close to 610-m above sea level (asl) (Figures 5a and 5b). The southern stream is smaller and less powerful than R0, and flows some 500 m to the south. It does not show any discernible offset or deflection across the fault zone. A recent fan is building at the outlet of the southern river along the WFS. This recent fan merges with several overbank beds that feed a broader alluvial fan the apex of which lies ~610-m asl. Between these two major streams the topography is hilly on both sides of the fault zone, and several abandoned or intermittent channels and regressive gullies have incised the Neogene marls.

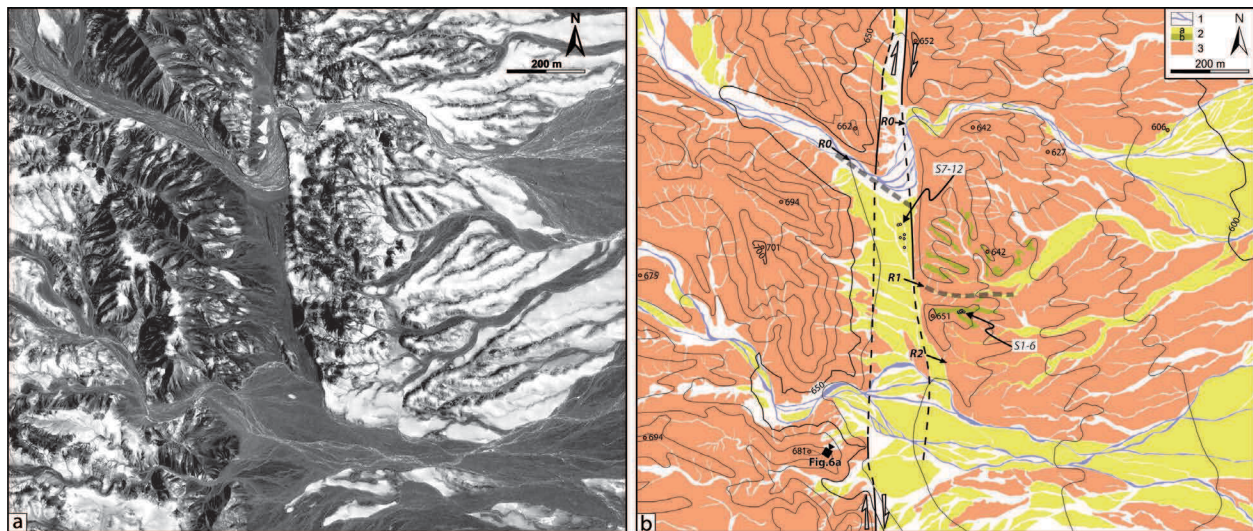


**Figure 5.** Site South. (a) Raw Quickbird imagery of a 100-m wide step-over along the segment NA2 of the Nayband fault. (b) Corresponding geologic map adapted from Quickbird imagery, field observations and regional geology [Alavi-Naini and Griffis, 1981b]. 1, active channels; 2, Recent alluvial fans and terraces of (2a) Holocene, and (2b) late-Pleistocene ages; 3, poorly consolidated Neogene marls and sandstones. Contour interval from 1:25,000 topographic data is 10 m. White dots locate the  $^{36}\text{Cl}$  surface samples. R1 and R2 designate two wind-gaps on the eastern side of the fault trace.

To the east of the EFS trace, two well-preserved hanging channels (R1 and R2) are incised into the Neogene marls (Figures 5b and 6). These two paleochannels appear as wind-gaps as they have been beheaded by the EFS and further incised by the regressive erosion of some of the many small gullies draining the Neogene marls east of the fault zone. As seen in Figures 5 and 6, the R1 wind-gap is hanging 4-5 m higher than the younger, currently abandoned, alluvial surface to the west. The beheaded streambed of the R1 wind-gap is also a little higher and wider than the R2 wind-gap to the south. Obviously, the beheaded channels R1 and R2 are much too wide to

have been only carved by the small rills now incising them. None of the current intermittent channels standing to the west of the fault between R0 and the next southern major river appears large enough to have fed R1 (Figures 5 and 7). Allowing for dextral motion along the fault zone, the closest upstream river with an appropriate size to match downstream with R1 is R0. The offset between the course of the northern stream R0 on the western side of the fault zone and the course of the stream R1 on the eastern side of the fault zone, shown in Figure 7, amounts to  $195 \pm 15$  m (Figure 8).

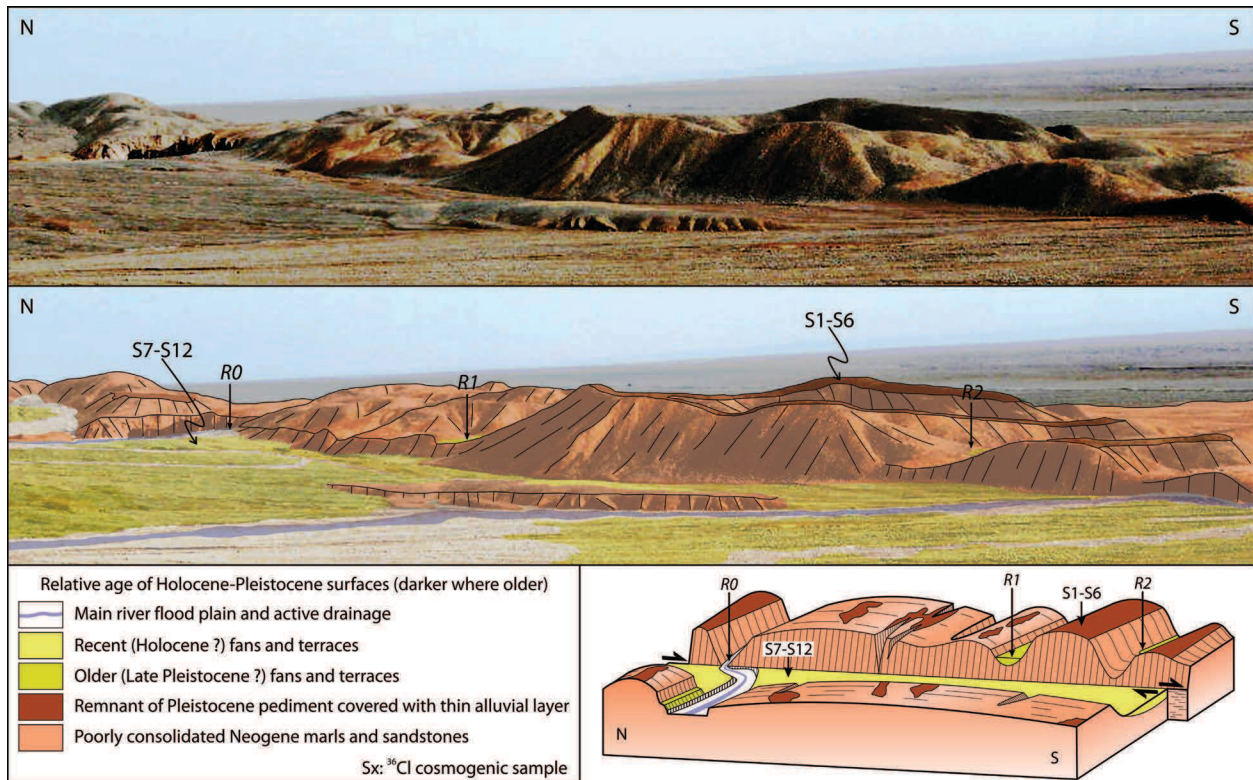


**Figure 6.** (a) A panoramic view of eastern part of site South, looking northeast (see Figure 5b for location). The fault trace runs nearby the base of a scarp between Neogene marls and Quaternary alluvial deposits. (b) Interpretative sketch shows remnants of Pleistocene alluvial surface (green shading) locally preserved on top of Neogene deposits (orange shading). The Neogene deposits are incised by two main channels (R1 and R2) on the eastern side of the fault trace. Recent alluvial fans and terraces (light-yellow shading) are incised by flood plain active rivers (white-blue shading). Locations of  $^{36}\text{Cl}$  surface samples are shown by black curvy-arrows. (c) Schematic diagram highlights two beheaded wind-gaps (R1 and R2) south of the ongoing incision of active river (R0).

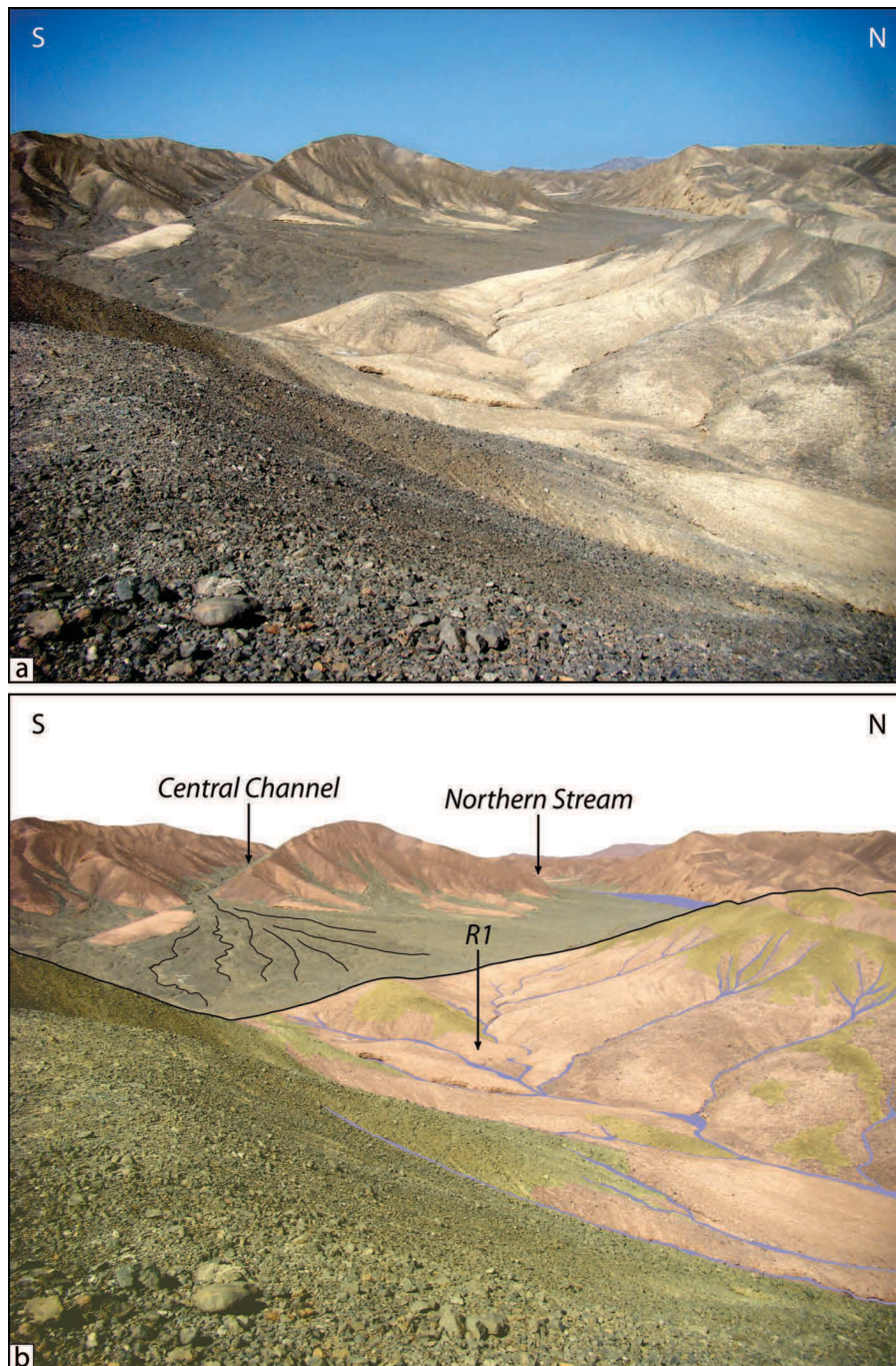


**Figure 7.** Field photograph (a) and interpretative sketch (b) of the northern stream (R0) west of the fault zone taken from R1 east of the fault zone. The central channel, west of the fault, is located almost in front of R1. Thick black line denotes the top of the scarp pointing to the trace of EFS. Pink and gray shadings are for Neogene marls and Quaternary alluvial fans, respectively. East of the fault, scarce remnants of late Pleistocene alluvial fan deposits (green shading) are preserved on top of the Neogene marls.

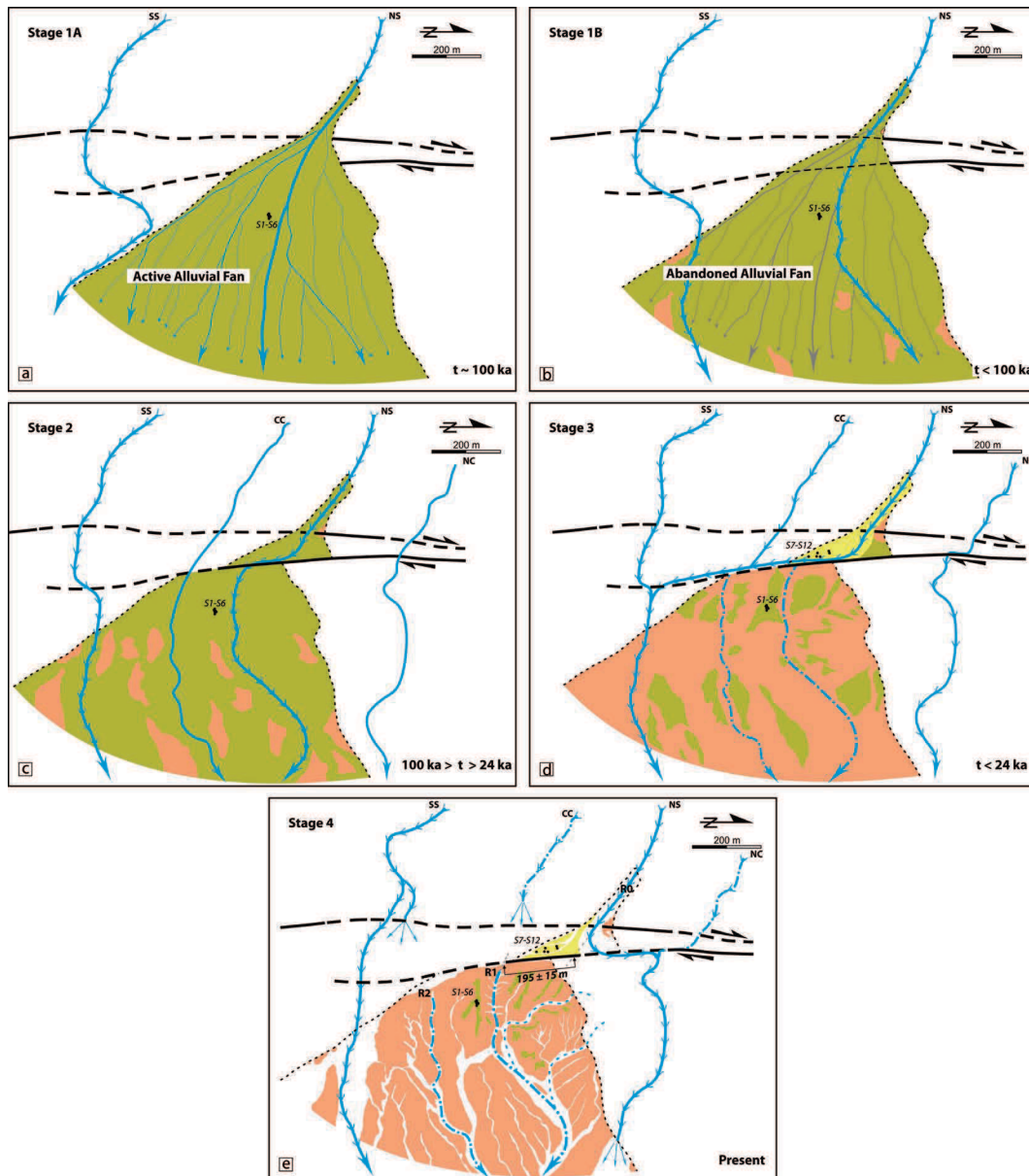


**Figure 8.** Late Pleistocene-Holocene morphotectonic evolution of the landform of site South. Stage (1A): Emplacement of a large alluvial fan at the outlet of a northern stream (NS), close to the fault zone. The fault traces are buried by the fan aggradation covering the uppermost layers of Neogene marls during a phase of sedimentary discharge ( $\sim 100$  ka, see section 3.3.1). A southern stream (SS) flows along the southern edge of the alluvial fan. Black dots (S1-S6) indicate the locations where the corresponding  $^{36}\text{Cl}$  samples will be collected. Stage (1B): By the end of the aggradation of the fan, an erosion phase coeval with incision of the northern stream, piracy of the southern stream, abandonment of the fan surface and progressive exposure of patches of Neogene marls (orange shading) due to regressive erosion within small rills and channels (gray lines). Stage (2): Ongoing erosion processes and regressive erosion coeval with the formation of central (CC) and northern (NC) channels and the increase of the cumulative right-

lateral offsets of the northern (NS) and southern (SS) stream courses. The progressive offset of the northern stream shifts the down-fault course towards the South. Stage (3): Further right-lateral slip and coeval incision produces larger cumulative offsets and the abandonment of the CC, NS and NC downstream from the fault zone (dashed blue lines). As the downstream courses of the central channel and northern stream are defeated, the remaining stream to the south (SS) captures the upstream courses of the defeated streams. A younger alluvial fan (yellow shading) has emplaced (after 24 ka, oldest possible age of the youngest pebble, sample S12, see section 3.3.1) in the small depression sited between the western and eastern fault strands. Black dots (S7-S12) indicate the locations where the corresponding  $^{36}\text{Cl}$  samples will be collected. Stage (4): Present-day situation. The northern stream has registered  $195 \pm 15$  m of right-lateral offset. Lowering of the local base level, coeval incision and right-lateral motion along the fault resulted in the piracy of its upstream course now flowing into the downstream course of NC. The erosion processes reduced the exposures of the older fan which scarce remnants cap the Neogene marls.

The following sections present and discuss the cosmogenic and luminescence dating results that constrain the ages of the displaced geomorphic features at the two sites described above.

### 3.3. Chronological Tools: Cosmic Ray Exposure and OSL Dating

Although geomorphic features in arid regions are well preserved and offer the possibility to document the amount of fault slip, the scarcity of organic material limits severely the use of radiocarbon dating (which in any case can only be used to date the last ~45 ka). In order to obtain ages for the offset geomorphic features, we undertook both  $^{36}\text{Cl}$  CRE and OSL dating of the abandoned alluvial surfaces. Cl-36 can be produced by two different mechanisms, cosmic ray interactions and radiogenic production by disintegration of U and Th. The analytical procedure and the calculations of cosmic ray exposure ages are identical to that extensively described in *Le Dortz et al.* [2011]. Following a methodology that proved efficient for the neighboring Dehshir and Anar faults in Central Iran [*Le Dortz et al.*, 2009, 2011, 2012], 24 surface samples were collected to determine the CRE ages of alluvial surfaces. Since Jurassic Limestone is the dominant source of material in the area, we collected calcite rich pebbles and measured their concentration of *in-situ* produced  $^{36}\text{Cl}$  cosmogenic nuclide. The basic information required for CRE age calculations is summarized in the captions to Tables 2 and 3; these tables provide the concentrations of *in-situ* produced  $^{36}\text{Cl}$  with the corresponding ‘no-erosion’ ages (Table 2) and the chemical composition of the carbonate samples (Table 3).

In addition, OSL is used to determine the time elapsed since the last exposure of sediments to sufficient sunlight to reset any latent luminescence signal, and so to determine the burial age of the target material. During subsequent burial, energy (dose) is absorbed from environmental ionising radiation, and some of this energy is stored in the form of electrons trapped in meta-stable states. This energy can be released by stimulation with visible light, and some of the released energy is emitted in turn as luminescence [e.g., *Aitken*, 1998]. By calibrating this luminescence in terms of dose using an artificial source of radiation it can be used as a measure of the dose, usually termed the equivalent dose,  $D_e$ . The rate of absorption of energy (dose rate) can be determined from a knowledge of the radioactivity of the surrounding sediment, the water content (water absorbs some energy and so reduces the dose rate), and from the burial depth (which affects the dose rate from cosmic rays). All these issues are discussed by *Aitken* [1985]. A review of the precision and accuracy of quartz OSL dating on various types of sediment (and using similar analytical protocols to those used here) is given by *Murray and Olley* [2002].

The samples were returned to the laboratory and opened under subdued red light. The light-exposed ends of each of tube samples were reserved for dose rate measurements using high resolution gamma spectrometry [*Murray et al.*, 1987]. The radionuclide activity concentrations were converted to dose rates using the factors given by *Guérin et al.* [2011] and the cosmic ray contribution to dose rate derived from *Prescott and Hutton* [1994]. The remainder of the sample was wet sieved (180-250 $\mu\text{m}$ ) and acid cleaned in the usual manner, finally using concentrated HF for 40 min to give a clean quartz-rich fraction.

All luminescence measurements used a Risø TLDA20 reader equipped with a blue LED (470 nm,  $\sim 80 \text{ mW}\cdot\text{cm}^{-2}$  at the sample) stimulation source and photon detection through  $\sim 7$  mm U-340 glass filter [*Bøtter-Jensen et al.*, 2010]. The reader was equipped with a calibrated beta source delivering  $\sim 0.1 \text{ Gy}\cdot\text{s}^{-1}$  to quartz mounted on stainless steel. Quartz was prepared for measurement by mounting as a  $\sim 8$  mm diameter monolayer of grains on stainless steel discs (9.7 mm diameter) using silicone oil. The luminescence purity of the quartz-rich fraction was confirmed using IR stimulation, and no significant IR luminescence (compared to the blue-stimulated quartz signal) was detected. Measurement of quartz dose used a SAR protocol [*Murray and Wintle* 2000, 2003] with a 260 $^{\circ}\text{C}$  preheat for 10 s, and a cut heat of 220 $^{\circ}\text{C}$ . The sample was held at 125 $^{\circ}\text{C}$  during optical stimulation. A standard dose recovery test was

undertaken on 14 samples here following blue light resetting room temperature; on average the ratio of measured to given dose (recycling ratio) was  $1.03 \pm 0.05$  ( $n=41$ ), confirming that using these samples our protocol is able to measure accurately a known dose given before any laboratory thermal treatment.

It is clearly important that any latent OSL signal be sufficiently well bleached before deposition that and apparent residual dose is small compared to the subsequent burial dose. Our equivalent doses were determined using large multi-grain aliquots; because of the inevitable effects of averaging, it is very unlikely that there is any useful information on the degree of bleaching available in an examination of the dose distributions of any particular sample [Li, 1994; Olley *et al.*, 1999; Wallinga, 2001]. However, some of the equivalent doses here are smaller than, or comparable to, the average of those found in non-aeolian sediments (typically  $2.4 \pm 0.6$  Gy;  $n=67$ , according to the recent summary in Murray *et al.* [2012]). This, coupled with the stratigraphic consistency and the agreement between paired samples (section 4.3), is taken as evidence that, in general, these samples are unusually well-bleached for water-lain material. One unit provides a pair of samples that are exceptions to this (section 4.3, unit 8w, samples NT-XV and NT-XXI) but this unit was identified as atypical in the field (see section 4.2) and does not invalidate our general conclusion. The relevant luminescence measurements are summarised in Table 4, together with sample depth and assumed average burial water contents.

### 3.3.1. $^{36}\text{Cl}$ CRE Dating

At the site North, two abandoned alluvial surfaces of the last fan system (see section 3.1) were targeted for  $^{36}\text{Cl}$  sampling (Figure 2, right panel). Six carbonate samples (S13 to S18, see Figure 3 for locations) were collected from the abandoned alluvial surface deposited by the northern stream, close to the piracy P1 along the valley that is offset by  $420 \pm 50$  m. These provide CRE ages ranging between  $15.9 \pm 1.4$  ka and  $80 \pm 7$  ka (Table 2 and NF on Figure 9). About 800 m farther south, 6 samples (S19 to S24) were collected on the surface emplaced by the southern stream that is offset by  $180 \pm 20$  m. They provide CRE ages ranging from  $24 \pm 2$  ka to  $221 \pm 23$  ka (Table 2 and SF on Figure 9). For both alluvial surfaces, the surface samples display scattered  $^{36}\text{Cl}$  concentrations, hence variable CRE ages. Such scatter suggests the alluvial sampled surfaces are young so that a variable inheritance component predominates over the *in-*

*situ*  $^{36}\text{Cl}$  concentrations, as already observed for alluvial terraces sampled in Central Iran, along the Anar and Dehshir faults [Le Dortz *et al.*, 2009, 2011]. At the Nayband sites, the limited thickness (1.5 m) of the fan conglomerates prevented the sampling of a depth profile deep enough ( $\geq 4$  m) to determine the denudation rate and to apply the rejuvenation profile procedure and so determine the range of inheritance and maximum exposure ages [Le Dortz *et al.*, 2012]. Notwithstanding the inheritance, the outliers (i.e., the oldest samples) can be discarded and weighted mean CRE ages calculated for each fan surface. In this case, weighted mean CRE ages are  $29 \pm 18$  ka (S14-17) and  $28 \pm 8$  ka (S19, S21, S22) for the northern and southern surfaces, respectively (Figure 10). Alternatively, accounting for the variable inheritance, one may favor the youngest sample on each surface as the best approximation for the abandonment age of the alluvial surface, as already suggested for work undertaken in Mongolia [e.g., Vassallo *et al.*, 2007] or Tibet [e.g., Mériaux *et al.*, 2005] and demonstrated in Central Iran [Le Dortz *et al.*, 2009, 2011]. This would yield abandonment ages of  $15.9 \pm 1.4$  ka for the northern surface and  $24 \pm 2$  ka for the southern one (Figure 9). Since the relative elevation above the active network and the surface roughness of the fans are similar, they are probably coeval. Assuming this to be the case, one may assume an abandonment age of  $\sim 16$  ka for both fans, and so postulate that the youngest of the sampled pebbles on the southern fan contains more inheritance than that on the northern one. Following this argument, the last fan system aggraded during the LGM (i.e., marine isotope stage 2, MIS-2).

At the site South, two alluvial surfaces deposited during the evolution of the drainage network (Figure 8) are preserved (Figure 5). Fragmentary remnants of the older surface overlie the Neogene marls, some 10-20 m above the active overbank surfaces (Figure 6). The younger surface is well preserved as a lower alluvial terrace and stands only 2-3 m above the active overbank surfaces.

Six samples (S7 to S12) were collected on this well-preserved lower surface. As for the site North, where the alluvial surfaces stand  $\sim 2$  m above the active streams, the scatter in  $^{36}\text{Cl}$  concentrations is significant. The corresponding CRE ages range from  $22.6 \pm 1.8$  ka to  $121 \pm 11$  ka (Table 2 and WF on Figure 9). It seems clear that the two highest  $^{36}\text{Cl}$  concentrations (S7 and S11) are outliers and these are discarded; the resulting weighted mean CRE age for the lower surface is  $29 \pm 13$  ka. If one allows for variable inheritance, one may rather assume that the

youngest pebble ( $22.6 \pm 1.8$  ka) provides the best estimate for the abandonment of the surface and so conclude this lower alluvial terrace also aggraded during the LGM.

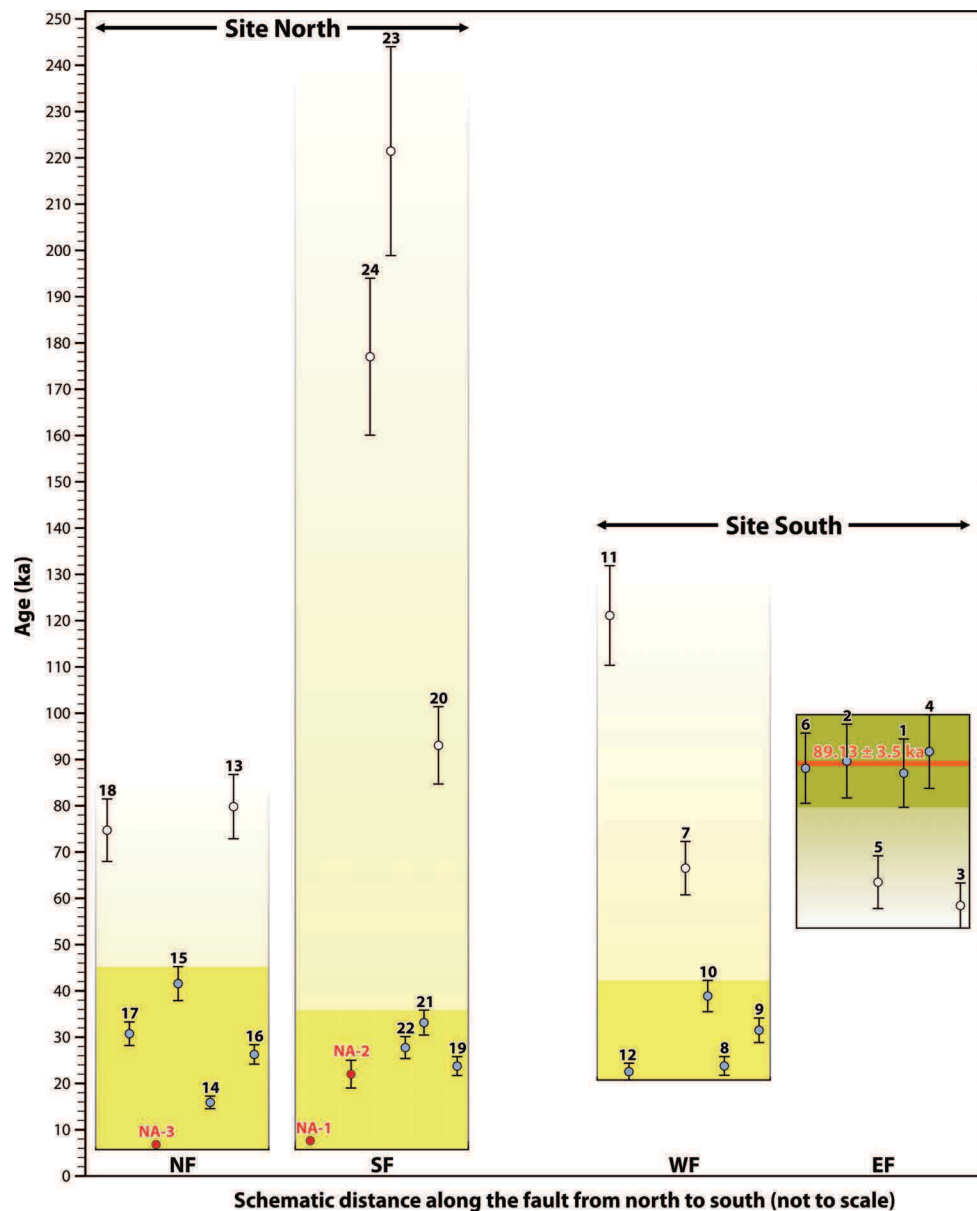


**Figure 9.** Plot of  $^{36}\text{Cl}$  and OSL ages for alluvial surfaces at the sites North and South, in schematic position from north to south. Dots and error bars are in blue and red for  $^{36}\text{Cl}$  and OSL, respectively. Dark shaded areas pointing the average standard deviation for  $^{36}\text{Cl}$  samples. Thick orange line represent the average age of eastern, older, surface at the site South after excluding outliers (white dots).

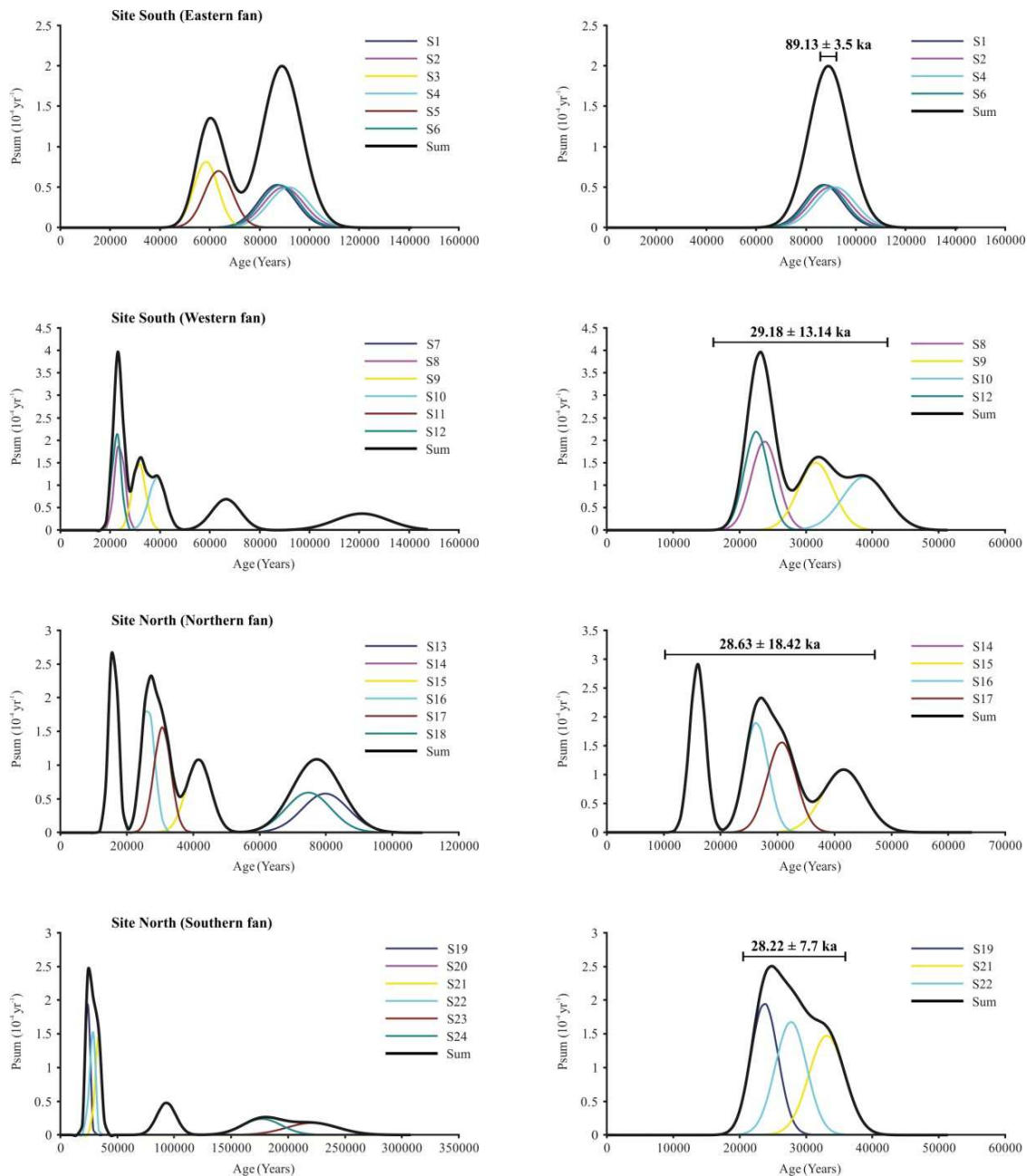


**Figure 10.** Distribution of *in-situ*  $^{36}\text{Cl}$  CRE ages, modeled with no erosion and no inheritance, for the surface samples collected on the alluvial fan surfaces at the sites North and South, including (left panel) and discarding (right panel) outlier samples. The thin colored curves represent the CRE age probability as Gaussian distribution for each sample while the thick black curves correspond to the summed Gaussian probability density function. The weighted mean CRE ages for each alluvial fan surface are obtained with errors equal to two standard deviations ( $2\sigma$ ).

The older fan stands on the Neogene marls; it was deposited by the northern stream R0 and subsequently abandoned when R0 started to incise within its alluviums (Figure 8, stages 1a and

1b). The present remnants of that old alluvial surface form a thin (~1-m thick) layer of cobbles and small boulders (50 cm in diameter) mainly derived from limestone. The material on the surface also includes a few boulders of sandstone and cobbles of reworked conglomerates from the Neogene deposits. We collected six limestone pebbles (S1-S6) from the best-preserved patches of the old alluvial surface (Figure 6) for the measurement of  $^{36}\text{Cl}$ . Assuming negligible denudation and no inheritance, the  $^{36}\text{Cl}$  CRE ages range from  $58 \pm 5$  ka to  $92 \pm 8$  ka (Table 2 and EF on Figure 9), these are less scattered than those measured on the lower surfaces at the sites North and South and do not suggest significant inheritance (Table 2). Assuming no inheritance and no erosion the two youngest pebbles (S3 and S5) are taken as outliers and the resulting weighted mean age of the surface is  $89 \pm 4$  ka. Alternatively, one may consider the possibility for erosion. Although previous CRE studies have demonstrated that denudation rates are very low ( $\leq 1\text{m/Ma}$ ) on well-preserved alluvial surfaces in Central Iran [*Le Dortz et al.*, 2011, 2012], erosion could be locally higher on less-preserved surfaces. Considering that the Neogene marls are poorly consolidated (and so prone to rapid erosion) and that the topography at the site South is significantly dissected due to the presence of a regional E-facing slope separating the Tabas block from the Lut block, erosion is likely to be locally significant. This has probably been the case for the few remaining outcrops of the higher terrace. Indeed, they result from an almost complete dissection of the old alluvial surface, the remains of which appear as narrow horizontal patches standing 10-20 m above the present-day network. Thus, it is possible that the initial surface of the higher terrace was significantly affected by erosion and subsequent rejuvenation; this would explain the presence of the two younger outliers. To allow for such rejuvenation, the age of the oldest pebble should be considered a proxy for the true age of the alluvial surface [e.g., *Brown et al.*, 2005]. In that case, the oldest possible age of the old surface should be about 100 ka (Figure 9).

Although the limited thickness of conglomerates at both sites precluded the sampling of a depth-profile and thus prevented the estimation of the minimum range of inheritance [*Le Dortz et al.*, 2012] comparing the surface CRE ages with near-surface OSL ages from the same alluvial surfaces would provide an estimate of the maximum possible range of inheritance for each surface sample. This is particularly useful if the abandonment age of young alluvial surfaces in arid environments is to be constrained; such surfaces in Mongolia [*Vassallo et al.*, 2007] and Central Iran [*Le Dortz et al.*, 2011] are known to have significant variable inheritance.

**Table 2.** Concentrations of *in-situ* produced  $^{36}\text{Cl}$  and corresponding CRE ages. The chemical extraction of chlorine by precipitation of silver chloride has been adapted from the protocol of *Stone et al.* [1996]. The samples were picked with a known quantity of stable chlorine carrier [e.g., *Desilets et al.*, 2006] to simultaneously determine  $^{36}\text{Cl}$  and chlorine concentrations by isotope dilution accelerator mass spectrometry (AMS). The chemical treatment of the samples and the measurements were performed at the CEREGE laboratory (Aix-en-Provence, France), using KNSTD1600 standard. The Excel spreadsheet provided by *Schimmelpfennig et al.* [2009] was used to calculate all  $^{36}\text{Cl}$  ages with a  $^{36}\text{Cl}$  spallation production rate of  $42 \pm 0.2 \text{ at.}^{36}\text{Cl} (\text{g Ca})^{-1} \cdot \text{a}^{-1}$  [*Braucher et al.*, 2011] similar to the one of *Schimmelpfennig et al.* [2011]. A  $^{36}\text{Cl}$  half-life of 301 ka [*Gosse and Phillips*, 2001], a density of  $2 \text{ g cm}^{-3}$ , and a neutron attenuation length of  $160 \text{ g.cm}^{-2}$  [*Gosse and Phillips*, 2001] are used.

Sample	Sample description	Latitude ( $^{\circ}\text{N}$ )	Longitude ( $^{\circ}\text{E}$ )	Elevation (m)	Cl (ppm)	Measured $^{36}\text{Cl}$ ( $10^6 \text{ at/g rock}$ )	$^{36}\text{Cl}$ CRE age (ka) no erosion
Site South							
<i>Eastern Fan</i>							
N09S1	Cobble (10 cm)	31.98406	57.52886	654	29	$2.28 \pm 0.05$	$87.05 \pm 7.53$
N09S2	Cobble (10 cm)	31.98407	57.52885	657	26	$2.28 \pm 0.05$	$89.65 \pm 7.97$
N09S3	Cobble (10 cm)	31.98405	57.52883	658	77	$1.72 \pm 0.05$	$58.44 \pm 4.88$
N09S4	Cobble (5 cm)	31.98406	57.5289	657	40	$2.42 \pm 0.07$	$91.71 \pm 8.06$
N09S5	Fragment of a cobble (25 cm)	31.98406	57.52882	657	36	$1.73 \pm 0.07$	$63.49 \pm 5.70$
N09S6	Cobble (10 cm)	31.98409	57.52887	658	29	$2.29 \pm 0.05$	$88.11 \pm 7.58$
<i>Western Fan</i>							
N09S7	Cobble (10 cm)	31.98592	57.52728	645	21	$1.73 \pm 0.05$	$66.52 \pm 5.77$
N09S8	Cobble (10 cm)	31.98585	57.52728	644	29	$0.66 \pm 0.02$	$23.78 \pm 2.02$
N09S9	Cobble (10 cm)	31.98564	57.52729	644	30	$0.87 \pm 0.03$	$31.49 \pm 2.65$
N09S10	Fragment of a boulder	31.98586	57.5272	645	27	$1.07 \pm 0.04$	$38.88 \pm 3.38$
N09S11	Cobble (10 cm)	31.98615	57.52719	645	31	$3.01 \pm 0.06$	$121.11 \pm 10.77$
N09S12	Cobble (5 cm)	31.98614	57.52714	645	45	$0.66 \pm 0.02$	$22.55 \pm 1.82$
Site North							
<i>Northern Fan</i>							
N09S13	Cobble (5 cm)	32.04174	57.52525	652	48	$2.15 \pm 0.07$	$79.81 \pm 6.94$
N09S14	Cobble (10 cm)	32.04186	57.52517	652	19	$0.45 \pm 0.02$	$15.91 \pm 1.36$
N09S15	Cobble (10 cm)	32.04191	57.5251	650	15	$1.10 \pm 0.04$	$41.57 \pm 3.67$
N09S16	Cobble (10 cm)	32.04171	57.52504	650	45	$0.73 \pm 0.02$	$26.27 \pm 2.09$
N09S17	Cobble (10 cm)	32.04222	57.52492	652	17	$0.84 \pm 0.02$	$30.74 \pm 2.55$
N09S18	Cobble (10 cm)	32.04238	57.5249	653	37	$1.99 \pm 0.07$	$74.72 \pm 6.75$
<i>Southern Fan</i>							
N09S19	Cobble (10 cm)	32.03525	57.52539	640	28	$0.65 \pm 0.02$	$23.75 \pm 2.04$
N09S20	Cobble (10 cm)	32.03531	57.52539	640	29	$2.32 \pm 0.07$	$93.05 \pm 8.35$
N09S21	Cobble (5 cm)	32.03533	57.52537	640	25	$0.87 \pm 0.02$	$33.14 \pm 2.70$
N09S22	Cobble (10 cm)	32.03537	57.52535	640	27	$0.75 \pm 0.03$	$27.75 \pm 2.37$
N09S23	Cobble (10 cm)	32.03539	57.52535	640	34	$4.88 \pm 0.12$	$221.45 \pm 22.56$
N09S24	Cobble (10 cm)	32.03548	57.52536	641	29	$4.06 \pm 0.09$	$177.03 \pm 16.96$

**Table 3.** Chemical composition of the samples collected for  $^{36}\text{Cl}$  dating. Measurements of the major elements were undertaken by ICP-OES technique at the CNRS SRM facility (CRPG Nancy). The radiogenic  $^{36}\text{Cl}$  contribution has been obtained by measuring the concentrations of U and Th in the target mineral [Zreda *et al.*, 1991; Stone *et al.*, 1996, 1998; Gosse and Phillips, 2001].

Sample	H <sub>2</sub> O (%)	Al <sub>2</sub> O <sub>3</sub> (%)	CaO (%)	Fe <sub>2</sub> O <sub>3</sub> (%)	K <sub>2</sub> O (%)	MgO (%)	MnO (%)	Na <sub>2</sub> O (%)	P <sub>2</sub> O <sub>5</sub> (%)	SiO <sub>2</sub> (%)	TiO <sub>2</sub> (%)	Th (%)	U (%)
Site South													
<i>Southern Fan</i>													
N09S1	0.32	0.14	54.45	0.16	0.01	0.49	0.01	0	0	0.49	0.00	0.14	1.67
N09S2	0.32	0.10	54.76	0.07	0.00	0.45	0.01	0	0	0.00	0.00	0.07	2.30
N09S3	0.32	0.14	54.45	0.16	0.01	0.49	0.01	0	0	0.49	0.00	0.14	1.67
N09S4	0.32	0.17	54.13	0.26	0.03	0.53	0.01	0	0	0.98	0.01	0.21	1.04
N09S5	0.32	0.14	54.45	0.16	0.01	0.49	0.01	0	0	0.49	0.00	0.14	1.67
N09S6	0.32	0.14	54.45	0.16	0.01	0.49	0.01	0	0	0.49	0.00	0.14	1.67
<i>Western Fan</i>													
N09S7	0.31	0.10	54.40	0.11	0.00	0.50	0.01	0	0	0.43	0.00	0.09	5.36
N09S8	0.27	0.09	54.48	0.06	0.00	0.34	0.01	0	0	0.86	0.00	0.05	1.25
N09S9	0.31	0.10	54.40	0.11	0.00	0.50	0.01	0	0	0.43	0.00	0.09	5.36
N09S10	0.31	0.10	54.40	0.11	0.00	0.50	0.01	0	0	0.43	0.00	0.09	5.36
N09S11	0.34	0.12	54.32	0.16	0.00	0.65	0.01	0	0	0.00	0.01	0.12	9.47
N09S12	0.31	0.10	54.40	0.11	0.00	0.50	0.01	0	0	0.43	0.00	0.09	5.36
Site North													
<i>Northern Fan</i>													
N09S13	0.29	0.12	53.96	0.08	0.02	0.99	0.01	0	0	0	0.00	0.10	3.06
N09S14	0.25	0.06	54.89	0.04	0.00	0.46	0.00	0	0	0	0.00	0.04	4.39
N09S15	0.29	0.12	53.96	0.08	0.02	0.99	0.01	0	0	0	0.00	0.10	3.06
N09S16	0.32	0.18	53.04	0.12	0.03	1.53	0.01	0	0	0	0.01	0.16	1.74
N09S17	0.29	0.12	53.96	0.08	0.02	0.99	0.01	0	0	0	0.00	0.10	3.06
N09S18	0.29	0.12	53.96	0.08	0.02	0.99	0.01	0	0	0	0.00	0.10	3.06
<i>Southern Fan</i>													
N09S19	0.38	0.12	53.63	0.05	0.01	1.09	0.01	0	0	0	0.00	0.09	1.65
N09S20	0.39	0.15	53.46	0.06	0.02	1.20	0.01	0	0	0	0.01	0.13	1.84
N09S21	0.38	0.12	53.63	0.05	0.01	1.09	0.01	0	0	0	0.00	0.09	1.65
N09S22	0.38	0.12	53.63	0.05	0.01	1.09	0.01	0	0	0	0.00	0.09	1.65
N09S23	0.36	0.09	53.80	0.04	0.00	0.98	0.00	0	0	0	0.00	0.06	1.46
N09S24	0.38	0.12	53.63	0.05	0.01	1.09	0.01	0	0	0	0.00	0.09	1.65

### 3.3.2. OSL Dating

At site North, three OSL samples were collected within the last alluvial fan system to better constrain the abandonment ages of the alluvial surfaces incised by young rills and gullies (Figure 2). The first sample, NA-1, was collected half a kilometer west of the fault trace within the upstream end of alluvial deposits, from a fan apex emplaced by the southern stream that fed the major fan east of the fault trace. The sample comes from the 3-m high riser of a young and still active intermittent channel associated with the piracy P2 by a south-flowing stream. This sample was extracted from a loose, fine sandy lens at 174 cm below the fan surface using stainless steel tube (6 cm x 25 cm); both ends were sealed and covered immediately after sample extraction, using both aluminum foil and black tape.

The second sample, NA-2, was collected some 15 m east of the fault trace, nearby an active channel, and close to the outlet of the southern abandoned alluvial fan (Figure 2). Because there was no suitable exposure by the riser of the young channel incising the abandoned fan surface, a pit was directly excavated into the surface of the fan. The sample was collected from the bulk of coarser sediments containing loose, fine-grained sediments following the procedure described below and designed specifically for the arid environments [e.g., *Rizza et al.*, 2011a, 2011b]. The material was extracted at 47-cm depth, within stratified, poorly compacted, sub-angular, fine to very coarse pebbles (1 to 5 cm) within a fine to coarse sandy matrix. To prevent light-induced effects on the OSL signal during the material extraction, we covered the pit with several layers of dark thick tarpaulins and plastics. Then, in complete darkness, the targeted sampling area (15 cm in diameter) was cleaned by removing around 10 cm of the materials exposed to the sunlight during the pit digging. About 1 kg of the bulk sediment, including silts to coarse pebbles (<3 cm) was collected from this cleaned sediment face. The sampled material is collected in a thick-black plastic bag, doubled by several additional black bags and wrapped with a black tape before exposing to light. This process avoided an unacceptable light exposure during sampling, and preserved as much as possible the field water content.

The third sample, NA-3, was collected close to the fault and nearby the piracy P1 adjacent to a recent and still active E-W flowing channel (Figure 2). As for the NA-2 extraction, a pit was excavated into the surface of the abandoned alluvial fan, some ten meters east of the fault trace.

Using the same procedure as above, the sample was extracted at 50-cm depth, within a stratified unit containing fine to coarse pebbles (0.5 to 3 cm) in a fine to coarse sandy matrix.

The NA-1 ( $7.7 \pm 0.5$  ka) and NA-3 ( $6.8 \pm 0.6$  ka) ages are indistinguishable and suggest the most recent aggradation of the last fan system ceased some 6 to 7 ka ago. In contrast, NA-2 has an OSL age of  $22 \pm 3$  ka; in the absence of any evidence for incomplete bleaching this would indicate that the aggradation of the last fan system occurred in at least two different episodes: an older one during the LGM, as suggested by the  $22 \pm 3$  ka age and a younger one during the mid-Holocene, as indicated by the  $6.8 \pm 0.6$  ka and  $7.7 \pm 0.5$  ka ages. Hence, the OSL results suggest that at least two channel incisions appear to have occurred: one at around the LGM and another in the mid-Holocene.

### 3.4. Interpretation and Possible Range of Slip Rate

Figure 11 displays the offsets smaller than 300 m documented along the 30-km-long stretch of the segment NA2 of the Nayband fault, south of the Dig-e Rostam hot springs (Figure 1b). 88 offsets of rills and stream channels were measured (i) on Quickbird imagery, (ii) on high-resolution topographic map obtained by Real-Time Kinematic (RTK) survey and (iii) where possible, by direct field measurements. The preserved offsets range from a few meters up to several hundred meters and are listed in Table A1. A large majority (80 per cent) of the preserved offsets are less than 25 m while the largest offsets are unevenly distributed over a much wider range (Figure 11). Assuming that such a distribution is comparable to that observed along the Kunlun strike-slip fault in Tibet, where 80 per cent of the offsets postdate the Last Glacial Maximum [*Van Der Woerd et al.*, 2002], one may divide 25 m by 19 ka (oldest possible period corresponding to the onset of the major deglaciation during the LGM [e.g., *Lambeck et al.*, 2002; *Clark et al.*, 2009]) and so infer a minimum right-slip rate of the order of  $1.3 \text{ mm yr}^{-1}$ . Alternatively, following *Meyer and Le Dortz* [2007] who assigned the recent regional incision widely recorded in Central Iran to the onset of Holocene (12 ka), one may postulate that the incised channels offset by up to 25 m postdate this recent regional incision, and suggest a larger rate in excess of  $2 \text{ mm yr}^{-1}$ .

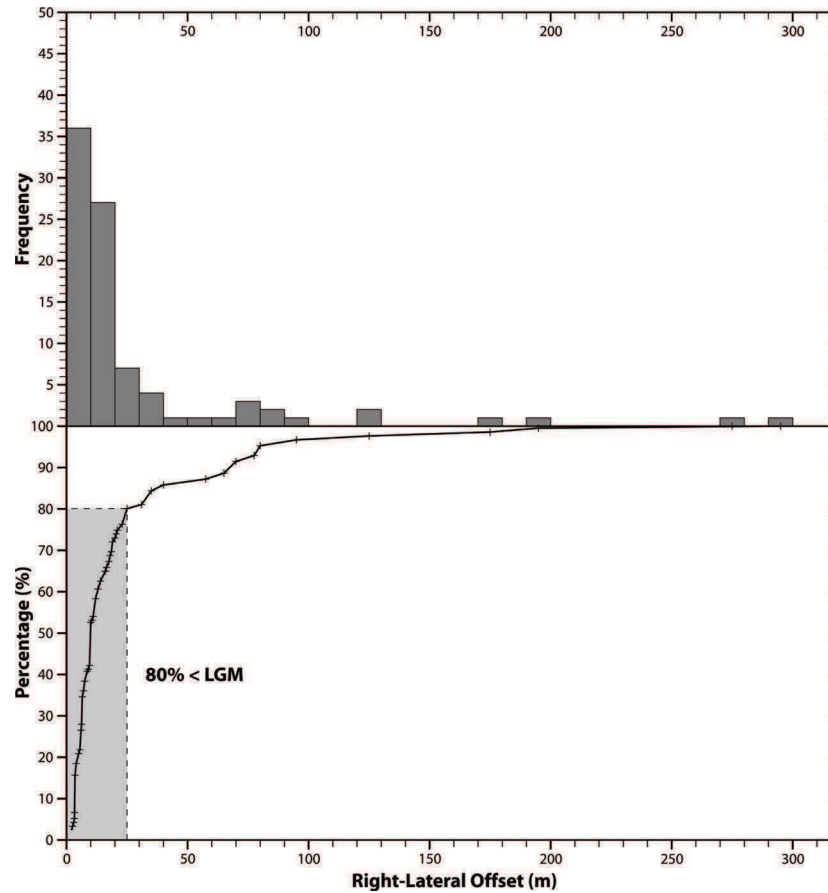


**Figure 11.** Frequency (top) and percentage (bottom) of the 88 right-lateral offsets smaller than 300 m measured along the 30-km long stretch of the segment NA2 of the Nayband fault. Close to 80 per cent of the preserved offsets are less than 25 m and are thought postdate the Last Glacial Maximum (LGM). See Table A1 for detail locations and corresponding measurements of the geomorphic offsets.

In any case, these estimates shall be examined in the context of the site North and the site South observations, where dating of offset features is available. At the site North, a  $25 \pm 5$  m right-lateral dogleg offset of two ephemeral gullies incised within Neogene marls (orange-shaded pedimented surfaces in Figure 2) has been preserved (see section 3.1). This  $25 \pm 5$  m offset is larger (and so hence older) than that observed 50 m to the south (of  $9 \pm 1$  m) in a narrow gully incised within the young alluvial fan surface nested within the Neogene marls. The  $9 \pm 1$  m offset has accumulated after the abandonment of that young alluvial surface and its subsequent incision. Therefore, this small offset cannot be older than NA-3 ( $6.8 \pm 0.6$  ka), the youngest possible age for the most recent alluvial aggradation. It is very unlikely that the next and larger  $25 \pm 5$  m offset would have accumulated during the same time span as a consequence of along-strike, slip variation. Rather, this larger offset should have accumulated over a longer time span

and one can derive a maximum bound on the slip rate of  $4.16 \text{ mm yr}^{-1}$ , by dividing the maximum amount (30 m) of the offset by the youngest possible age of the pedimented surfaces (7.2 ka, the youngest possible age of the sample NA-1, collected within the young inset alluvial sediment). Conversely, dividing the minimum amount (20 m) of that offset by the oldest possible age of the most recent alluvial fan (25 ka, oldest possible age of the sample NA-2) provides a minimum bound on the slip rate of  $0.80 \text{ mm yr}^{-1}$ .

The age of the young alluvial fan surface has also been estimated using  $^{36}\text{Cl}$  dating. Allowing for variable inheritance (see section 3.3.1) favors the youngest CRE age of  $15.9 \pm 1.4 \text{ ka}$  (sample S14) as a proxy for the age of abandonment of the surface. Assuming the incision of the pedimented surfaces is coeval with the emplacement of the young alluvial fan and combining the minimum of the  $25 \pm 5 \text{ m}$  offset with that CRE age provides a lower bound of slip rate of  $1.15 \text{ mm yr}^{-1}$ . This lower bound can also be compared with the one derived from the  $9 \pm 1 \text{ m}$  offset. Assuming this offset of  $9 \pm 1 \text{ m}$  has accrued since 7.4 ka, the oldest possible age of NA-3, provides another safe estimate of  $1.08 \text{ mm yr}^{-1}$  of the minimum slip rate. One has to retain the largest of the three determinations of the minimum slip rate (i.e.,  $1.15 \text{ mm yr}^{-1}$ ). This indicates that the  $9 \pm 1 \text{ m}$  offset and the incision of the youngest alluvial fan are a little younger than 7.4 ka.

At the site South, the right-lateral offset between the course of the active stream R0 to the west and the R1 wind-gap to the east of the fault zone amounts to  $195 \pm 15 \text{ m}$  (see section 3.2 and Figure 8). Assuming negligible denudation, combining the largest possible offset (210 m) with the youngest possible age of the weighted mean CRE age (86 ka) as a proxy for the abandonment age of the old alluvial surface at this site yields a maximum slip rate estimate of  $2.45 \text{ mm yr}^{-1}$ . Assuming noticeable denudation and that one would not find an older pebble than S4, one would consider the oldest CRE age possibility of S4 (100 ka) as the abandonment age of the alluvial surface and the smallest possible offset (180 m) to infer a minimum slip rate of  $1.80 \text{ mm yr}^{-1}$ . Because the small thickness of alluvial deposits did not allow the estimation of the amount of denudation by CRE depth-profiles, one cannot discard the possibility that the surface is older than sample S4 and so the former value cannot be taken as a safe estimate of the minimum slip rate.

In summary, the geomorphic offset markers and their corresponding possible ages indicate the slip rate ranges between  $1.15$  and  $2.45 \text{ mm yr}^{-1}$ , pointing to a mean slip rate of  $1.8 \pm 0.7 \text{ mm yr}^{-1}$  over the last  $100 \text{ ka}$  (Figure 12). As seen there, combining the right-lateral offset of  $40 \pm 5 \text{ m}$  preserved along the tributary incising within the poorly-consolidated, pedimented Neogene marls at the site North (Figures 2, 3a, 3b and 3c) with the oldest available age for the young alluvial surfaces ( $22 \pm 3 \text{ ka}$ , sample NA-2) would provide a slip rate of  $1.4$  to  $2.4 \text{ mm yr}^{-1}$ , consistent with the range of  $1.8 \pm 0.7 \text{ mm yr}^{-1}$ . All these considerations reinforce the suggestion of an overall minimum slip rate estimate of  $\sim 1.3 \text{ mm yr}^{-1}$ , assuming that the majority of the preserved offsets postdate the onset of the last major deglaciation.

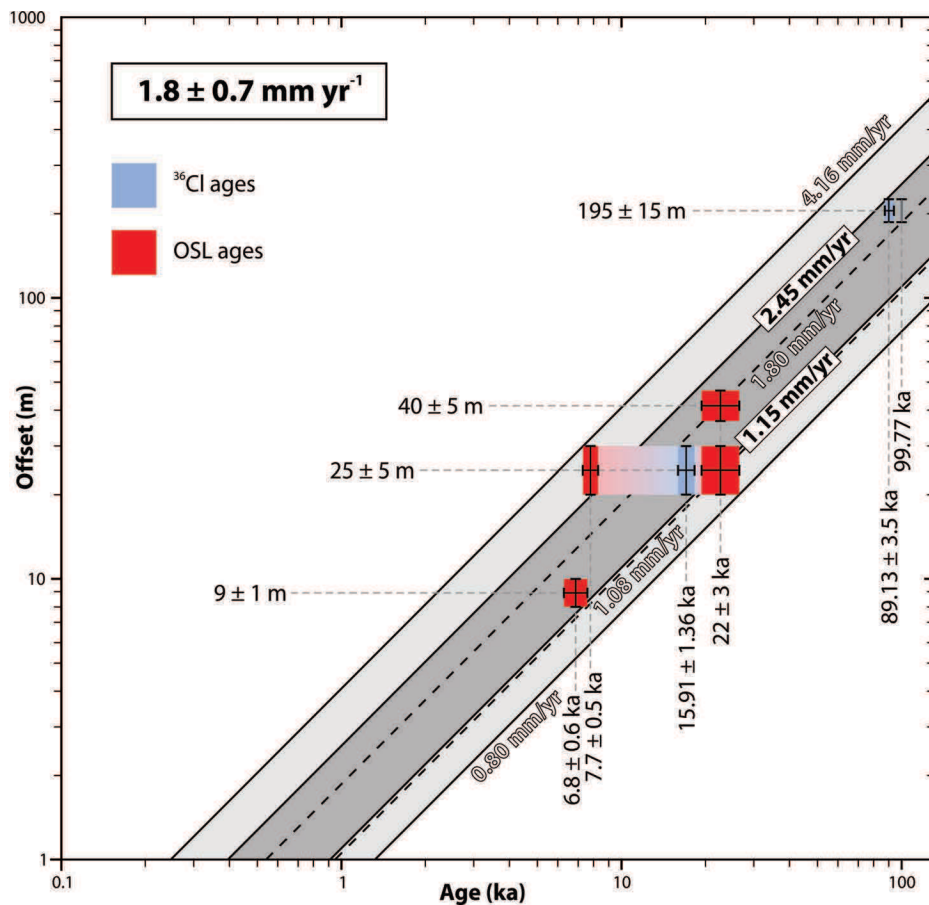


**Figure 12.** Summary of right-slip rates deduced from geomorphic offsets combined with cosmogenic and OSL dating at the sites North and South. Red and blue boxes based on the OSL and  $^{36}\text{Cl}$  CRE ages, respectively. The light gray domains denote maximum and minimum slip rates based on the OSL dating. The dark gray domain that refines the minimum and maximum rates is based on  $^{36}\text{Cl}$  CRE dating. The slip rate averaged over the last  $100 \text{ ka}$  is  $1.8 \pm 0.7 \text{ mm yr}^{-1}$  (see section 3.4 for discussion).

#### 4. Identification of Past Earthquakes on the Nayband Fault

Although the instrumental and historical seismic records [*Ambraseys and Melville*, 1982; *Ambraseys and Jackson*, 1998; *Berberian and Yeats*, 1999; *Engdahl et al.*, 2006] do not mention any destructive earthquake in the vicinity of the Nayband fault (Figure 1b), both the sharpness of the fault trace across the recent deposits, and the morphological evidence for recent cumulative dextral offset described above, make it worth seeking evidence for past earthquakes. The following sections document small dextral offsets and relate them to several paleoearthquakes evidenced within a paleoseismic trench.

##### 4.1. Geomorphic Setting of the Trench Site

South of 31° 57'N, the trace of the fault segment NA2 no longer follows the boundary between basement rocks and Neogene sediments (Figure 1c). The fault extends in a depression with subdued relief, cutting across late Pliocene-Pleistocene deposits as well as Holocene alluvial fans and recent ponds (Figures 1c and 13). The overall fault trace is linear with a few compressional step-overs and several right-stepping step-overs favoring local extension and sediment ponding. Thin layers of silts and clays that often cover the ponds are denoted by white hues on the Quickbird imagery. One such pond is located close to 31° 54'N at some 550 m asl and is positioned across a 80-m-wide releasing step-over (Figure 14a). The western and eastern borders of this depression are outlined by two fault scarps, facing each other (Figure 14b).

To the north, a compressional step-over within late Pliocene-Pleistocene alluvial fan conglomerates bounds two narrow ridges up to 604 m asl near 31° 56'N. The step-over is made of late Pliocene-Pleistocene deposits uplifted and folded. Along the western foothill of the ridges, well-exposed outcrops show layers dipping 15 degrees to the northwest. The uplifted alluvial fan conglomerates of the core of the ridge have been subsequently eroded and incised. The latest incision together with regressive erosion processes have resulted in the formation of small rills and gullies distributed along the fault (Figure 15). These recent channels are incised into older and abandoned alluvial surfaces and have recorded small amounts of right-lateral offset ranging from 3 to 16 m (Figure 16). The offset rills were measured both in the field with a tape and on the high-resolution topographic map obtained by a Real-Time Kinematic (RTK) survey devoted to a systematic survey of offset rills and gullies. The resulting high-resolution

topographic map allows one to restore the offset channels to simple linear patterns along the fault. As seen in Figure 16a, by extrapolating the recent channel thalwegs on both sides of the fault the offsets of channels A, B, C and D amount to 3, 3.5, 4 and 10 m, respectively. Furthermore, several other gullies and channels illustrate cumulative dextral offsets along the fault trace on the order of 6, 10, 13 and 16 m (Figures 16b-16d).

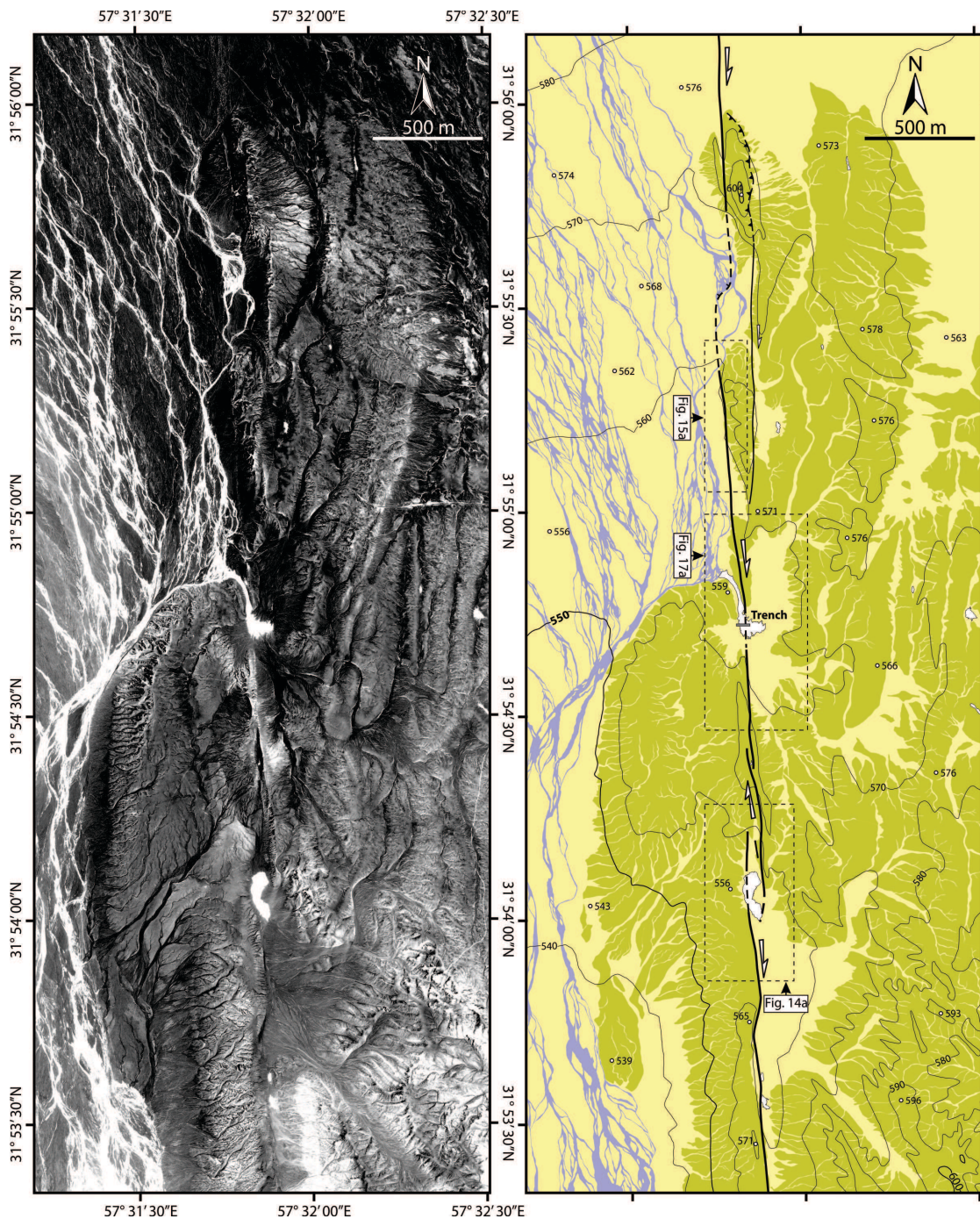
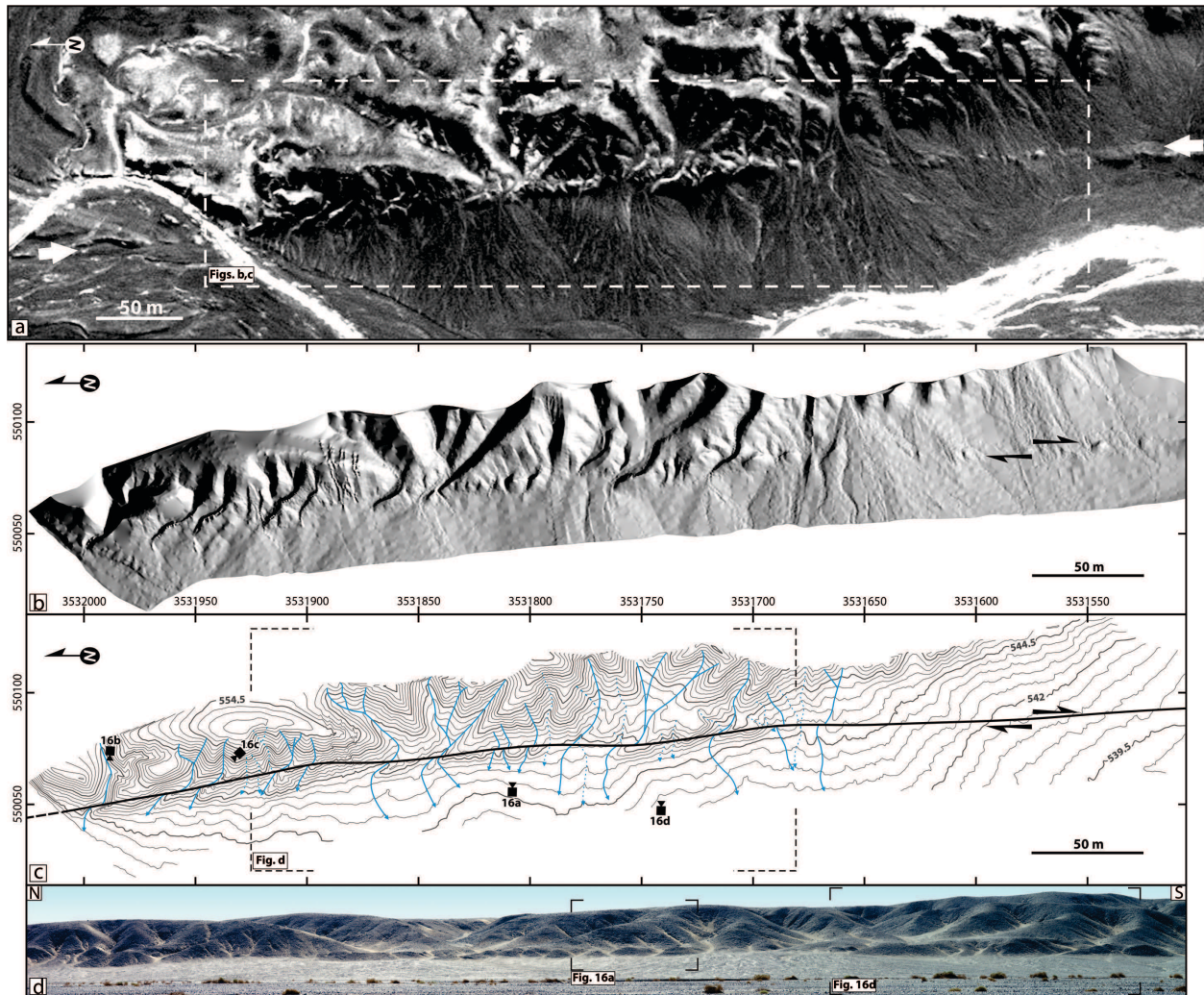


Figure 13. See next page.

**Figure 13.** Central portion of the Nayband fault. Raw Quickbird imagery (a) and interpretation (b) (see Fig. 1c for location). Regional geology adapted from field observations and geological map [*Alavi-Naini and Griffis, 1981b*]. Contour lines with 10-m-interval and elevation points in meters (asl) derived from 1:25,000 topographic map (National Cartographic Center of Iran; Sheet No. 7553-IV NW). Recent ponds (white areas) located across releasing bend and step-over geometries. A compressional step-over within older deposits (dark yellow) to the north delineates a narrow ridge towering of 604 m (asl). Boxes show the locations of Figures 14a, 15a and 17a.



**Figure 14.** (a) Raw Quickbird imagery of a local pull-apart within releasing step-over along the Nayband fault. See Figure 13b for location. Black arrows delineate the fault traces north and south of the step-over. (b) Photograph looking south along W-facing scarp in the foreground and E-facing scarp farther south. Pond area in between is denoted by whitish silts and clays.



**Figure 15.** Fault trace north of the trench site (see Figure 13b for location). (a) Raw Quickbird imagery showing fault scarp (white arrows) across the late Pliocene-Pleistocene (central part) and late Pleistocene-Holocene (northern and southern parts) deposits. Rectangle denotes the outline of (b) and (c). (b) High-resolution shaded relief map from a DGPS survey, illuminated under a SSW-oriented 40°-inclined sun. (c) Corresponding topographic map. Contour interval is 50 cm (survey data not tied to absolute elevation). The longest gullies (thick blue lines) display right-lateral offset ranging from several meters to more than 10 meters. The smallest gullies (dashed blue lines) cross the fault without detectable offset. Dashed corners correspond to the outline of (d). Locations of photographs in Figure 16 are indicated. (d) Photograph toward east. Panoramic view of the fault trace along the western flank of smoothed hills made of late Pliocene-Pleistocene deposits. Intermittent gullies are partly filled by aeolian sediments (whitish sands and silts). Black corners denote the outlines of Figures 16a and 16d.

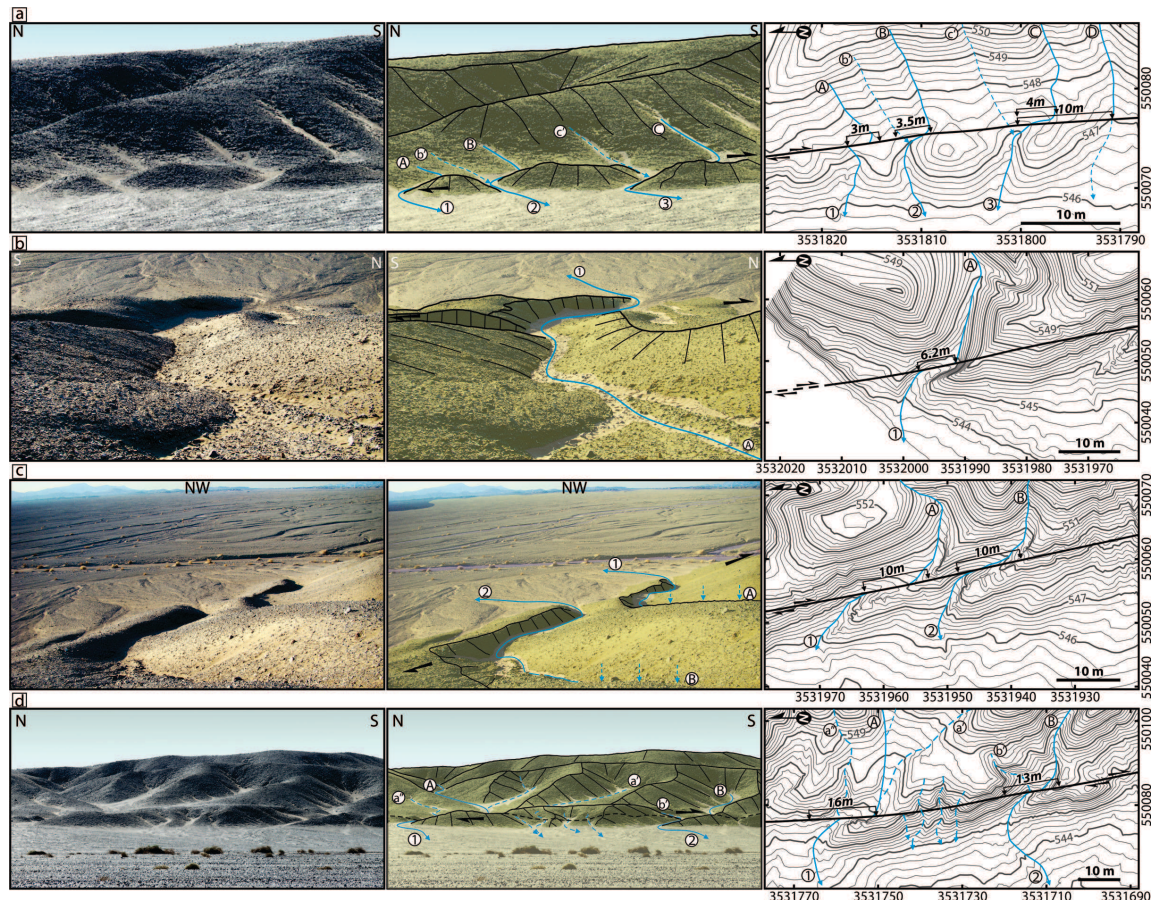


**Figure 16.** Recent right-lateral offsets north of the trench site. Field photographs (left panels), interpretative sketches (central panels) and corresponding topographic maps (right panels). See Figures 15c and 15d for locations. Contour interval is 20 cm (survey data not tied to absolute elevation). Lettered (A, B, C) gullies up-fault drain through outlets (1, 2, 3) down-fault and figure out the recent offsets. Small regressive gullies (a', b', c') show no recent offset.

Farther south, near  $31^{\circ} 55'N$ , a small channel has been right-laterally offset at the fault by 16 m (Figure 17). A larger though still ephemeral stream is incised into both the alluvial fan surface and the 2 m-high, east-facing scarp; this channel has been offset by  $35 \pm 5$  m. About 300 m farther south, a small dry pond, approximately 110-m long and 50-m wide, has formed along the fault (Figures 13 and 17). The ephemeral streams to the south and southeast of this dry pond are the primary sources of the sandy and pebbly material infilling this small depression. Smaller gullies surround the pond and collect surficial flows, as well as small drainages, effectively deliver the silt and clay materials mantling the pond during flood events. This pond is bounded to the west by older and higher alluvial fan surfaces as well as by the round-shaped termination of a fairly flat-topped ridge; this is gently inclined to the east and composed of late Pliocene-

Pleistocene gravelly alluvial deposits. This ridge, which is about 6 m higher than the pond may be interpreted as the northern part of a ~600-m wide shutter-ridge that has deflected the pond outlet northward by some 250 m (Figure 17c). This outlet extends northward along a narrow, 10-m-wide channel, and veers westward to bypass the shutter-ridge and reach the active flood plain. The location of the fault is well-constrained both on the Quickbird imagery and in the field by a clear single trace on both sides of the pond (Figure 18). Nonetheless, there is no detectable fault scarp within the part of the depression that is mantled by the pond deposits. Thus, it is probable that the latest fault rupture or scarplet has been sealed under the latest pond sediment aggradation. Given that the well-constrained fault morphology vanishes across the pond and the nature of the pond deposits, this location appeared to be a suitable place to conduct paleoseismic studies along this fault segment.

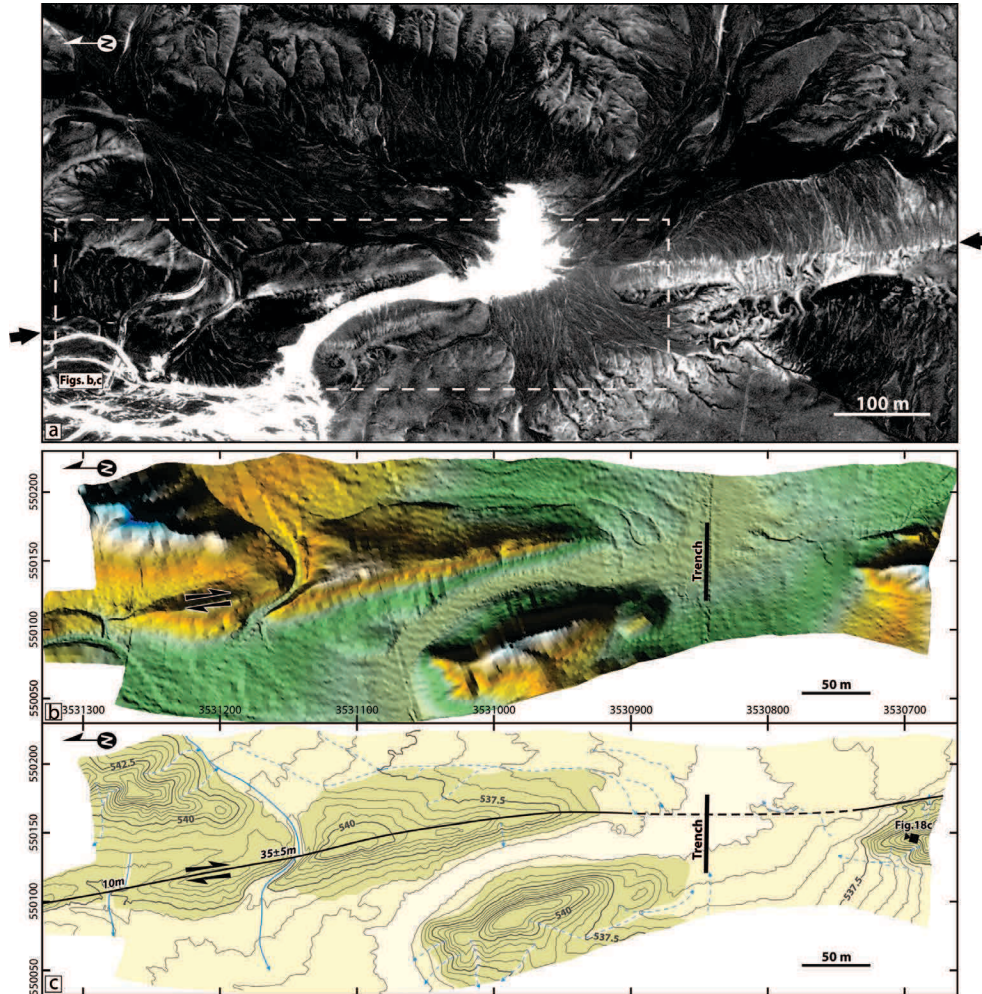


**Figure 17.** (a) Raw Quickbird satellite image showing the fault trace (black arrows) south of the trench site (see Figure 13b for location). Fault cuts across late Pliocene-Pleistocene (northern and

southern parts) and late Pleistocene-Holocene (central part) deposits. White pixels in the center of image indicate a local pond drained westwards. Rectangle denotes the outline of (b) and (c). (b) High-resolution colored shaded relief map extracted from the DGPS survey of the trench site. (c) Corresponding topographic map. Contour interval is 50 cm (survey data not tied to absolute elevation). Geology adapted from field observations and geological map [Alavi-Naini and Griffis, 1981b]. Fault scarp is clear on both sides of the local pond and not discernable within the pond. Fault trace is extrapolated towards the main fault strand in the trench (see Figure 19). Two gullies (thick blue lines) 300 and 400 m north of the trench display right-lateral offsets on the order of  $35 \pm 5$  and 16 m, respectively. Dashed blue lines denote small tributaries and regressive gullies.

## 4.2. Trench Stratigraphy

The south Dig-e Rostam (SDR) trench was excavated across the fault, within the dry pond (Figures 17 and 18). The trench strikes N90°E, has a length of 59 m, a depth of up to 4.3 m, and a width of some 1.5 m. Once the trench was excavated, the walls were cleaned to remove trench smears and gouges created by the trackhoe. A string grid, defining 1 m x 1 m panels, was strung along the length of the trench walls and each grid panel was then photographed by four slightly overlapping shots. The excavation exposes a succession of fine-grained well-bedded layers interbedded with few gravelly units. These deposits are mostly horizontal and composed of laminated silts, clays, and sands. Based on the grain size and the location of trench excavation within the dry pond, these sediments are presumed to have been deposited in a playa-type environment. Most of the exposed layers are distinctive and laterally continuous (and so easy to correlate) along most of the length of the trench and remain undisturbed away from the fault zone. Several steep fault strands highlight a 10-m-wide fault zone cutting through the exposed deposits. The central part of this zone, the main fault zone (MFZ), defines three distinctive sections (Figure 19a). The eastern section extends from the eastern tip of the trench up to meters 12-14, the MFZ extends between meters 12-14 and 16-17, and the western section is between meters 16-17 and the western tip of the trench near meter 58. At each section the stratigraphic units are numbered from oldest (smaller number) to youngest (larger number), but the unit designations do not imply correlation between sections. The stratigraphy of the three sections is summarized in the following paragraphs, and a detailed description of all the units is given in Table 5.

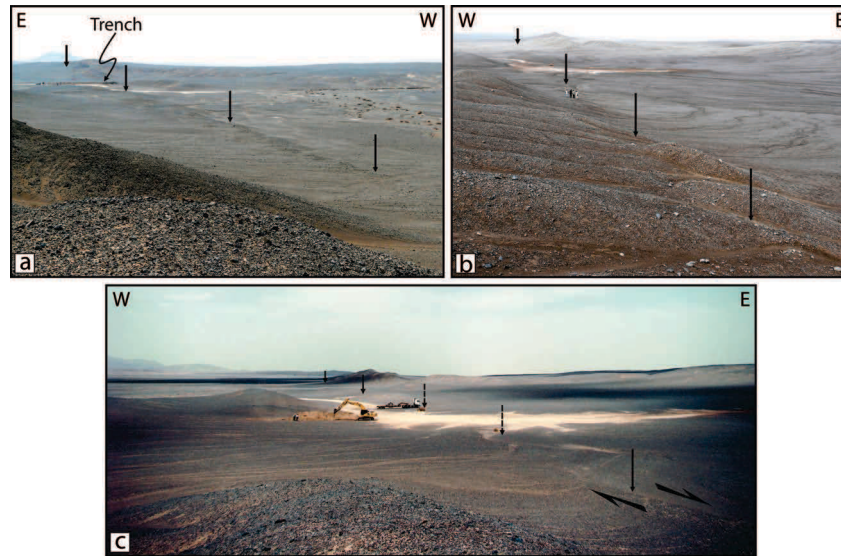


**Figure 18.** Field photographs of the fault showing clear scarps north (a) and south (b) of the pond and no discernable scarp (c) within the pond.

The eastern section is composed of a 4-m stack of sediment units, mostly fine-grained pond deposits, and can be subdivided into five sets. The deepest (oldest) set contains fine-grained sediments including compact clay and silt strata (units 1e to 4e; Figure 19b). The strata between and next to the fault strands are tilted by 15 to 25 degrees eastward so that the oldest unit (unit 1e) is only exposed to the west. These fine-grained sediments are overlain by untilted, coarse-grained alluvial deposits (unit 5e). Unit 5e has an erosive base into unit 4e and represents the second set of sediments. An abrupt change in sedimentary facies along an erosion surface, between the coarse-grained alluvial deposits (unit 5e) and the fine-grained pond sediments (unit 6e), defines onset of a new set. This third set is mainly composed of compact clays and silts. The lower part of unit 6e, however, incorporates a few cobbles, possible remnants of a desert pavement developed on the underlying alluvial unit. Unit 6e was later disturbed by liquefied sandy sediments (unit 7e), which likely originated from unit 5e. A younger set, the fourth set, is 1.0- to 1.2-m thick and begins with a conspicuous erosion surface subsequently sealed by a thin (few centimeters) sandy-gravelly, possibly sheet flood, layer (unit 8e). This unit 8e is covered by well-bedded clays, silts, and sandy strata (units 9e to 12e) corresponding to pond sediments that remain horizontal except near to the main fault zone. The uppermost set of sediments begins by a facies contact between sandy strata (unit 12e) and compact clays (unit 13e). This fifth set consists of laminated silts and compact clays (units 13e to 16e) capped by the most recent pond deposits (unit 26).



The main fault zone, as shown on Figure 19a, is 3-4 m wide with prominent fault strands defining its western and eastern limits. The MFZ deposits can be subdivided into four sets, where all but one (unit 26) units are cut by several steep fault strands (Figure 19b). The lowest set is composed of fine-grained pond sediments (units 1f to 3f). Bedding, where discernable, is horizontal (between meters 14 and 15) or tilted up to 25° westward. The second set begins with an erosion surface overlain by a 20-cm-thick layer of coarse-grained deposits (unit 4f). Unit 4f contains poorly sorted ungraded gravels with sparse cobbles embedded in clay and silt. This unit 4f is incised and filled by fining-upward alluvial strata (units 5f and 6f). An abrupt change in sedimentary facies between the coarse-grained alluvial strata (unit 6f) and fine-grained sediments (unit 7f) represents the onset of a new set. The third set, unit 7f, incorporates a few cobbles in the lower part similar to the lower part of unit 6e in the eastern section. The uppermost (youngest) set in the MFZ begins with a finely-laminated lens of sandy gravels (unit 10f) that pinches eastward. This fourth set ends up with unit 26, here unconformably on thin-bedded silts and clays (units 11f to 13f), as these later units are gently inclined to the east. Several narrow strips of sheared matrix-supported gravels (units 1s to 4s) are dislocated along the prominent fault strands and emplaced in the MFZ. They contain gravels that are oriented parallel to the fault planes and increasingly sheared as approaching the faults.

The western section is a stack of some 4-m-thick, well-bedded, fine-grained, sediments intercalated by few fanglomerate layers in the lower and upper parts (Figures 19a and 19c). The exposed sediments in this section can be subdivided into six distinctive sets. The oldest set is exposed only close to the western tip of the trench and dominated by loose fine-grained sediments containing scarce ungraded gravels (unit 1w), which likely correspond to mud flow deposit. The second set (unit 2w) consists in alluvial deposits (distal fanglomerates) overlying an erosion surface. The first two sets strata are gently (<5°) inclined eastward along the western half of the western section. The third set (units 3w, 4w, and 5w) is a fining upward sequence from coarse sands with some gravel lenses (transition alluvial fan-playa facies) to silt and clay layers (distal playa facies); this sequence corresponds to the development of a pond environment. Several liquefied sandy features, including sandy dikes and pillars (unit 6w), have injected into units 1w to 3w. A thin (<15 cm) layer of coarse sands (unit 7w) is exposed close to the MFZ (between meters 17 and 20) unconformable on top of the compact clays of unit 4w (Figure 19b). This coarser facies forms the fourth set represented by fining-upward alluvial deposits (unit 8w)

to the west. Both units 7w and 8w unconformably overly the older deformed deposits (units 3w, 4w, and 6w). The fifth set dominated by well-bedded, fine-grained strata (units 9w to 12w), aggraded on an erosion surface onlapping the previous units. This fifth set disappears westward by meter 56, at the western end of the trench. The uppermost, sixth set begins with a thin laminated sandy unit (unit 13w) that incorporates a very thin (few centimeters) layer of gravelly sands at the base with few sparse pebbles (<1 cm) in the middle of the unit. This unit 13w fills mud-cracks distributed on top of unit 12w and then, underlies a pile of ~2-m-thick, fine-grained sediments (units 14w to 20w). In the central part of the western section, between meters 35 and 44, unit 20w interfingers with ungraded gravelly alluvial deposits (unit 21w) coming from the west. The western part of the trench shows a transition between pond sediments (units 16w and 20w) and coarsening-upward gravelly deposits (units 21w to 25w) so that the maximum pond development occurred during the aggradation of unit 15w. The gravelly units have been covered by the topmost deposits (units 26 and 25w). Unit 26 represents the most recent pond sediments made of laminated clays emplaced in the centre of the pond. Unit 26 interfingers westward with poorly-sorted gravelly debris-flow deposits (unit 25w) coming from the shutter ridge to the west.

### 4.3. OSL Dating and Ages of Stratigraphic Units

The stratigraphic chronology of the deposits exposed in the trench is determined using 18 OSL ages combined with lateral correlation of units along the length of the trench walls. All but one OSL age are essentially consistent with the stratigraphic order of units (Figure 20). However, sample NT-XV from unit 8w yields an age ( $15.3 \pm 1.0$  ka) significantly older than the lower sample NT-XIV ( $6.4 \pm 0.5$  ka) from unit 3w (Figure 20). To solve this inconsistency, three further samples were collected from as near these two samples as possible and to sample NT-XII from unit 9w ( $6.7 \pm 0.5$  ka). The two samples located above (NT-XX) and below (NT-XXII) unit 8w yielded very similar ages of  $6.3 \pm 0.5$  ka and  $7.3 \pm 0.7$  ka, respectively, while sample NT-XXI from unit 8w yielded an age of  $8.3 \pm 0.6$  ka, again out of stratigraphic sequence although much less discrepant than before. This unit consists of gravely coarse sands with a significant content of clay, and appears to be mostly reworked material within a distal mudflow. The two unusually old ages (NT-XV and NT-XXI) from unit 8w, when considered together with these field observations suggest that unit 8w sediments were probably incompletely bleached at deposition. As a result, they are dismissed from further discussion.

**Table 4.** Summary of the OSL ages for the samples collected from the trench site (NT-samples) and the site North (NA-samples) along the Nayband fault. Burial depth, radionuclide concentrations and estimated water content used to calculate the dose rates are given. The number of multi-grain aliquots (grain size 180-250  $\mu\text{m}$ ) contributing to the equivalent dose is denoted by 'n'.

Sample	Risø code	Latitude (°N)	Longitude (°E)	Depth (cm)	Water content (%)	$^{238}\text{U}$ (Bq.kg $^{-1}$ )	$^{226}\text{Ra}$ (Bq.kg $^{-1}$ )	$^{232}\text{Th}$ (Bq.kg $^{-1}$ )	$^{40}\text{K}$ (Bq.kg $^{-1}$ )	Annual dose rate (Gy.ka $^{-1}$ )	n	Equivalent dose (Gy)	Age (ka)
NT-I	122910	31.91234	57.53061	31	0	16 ± 5	20.5 ± 0.4	23.6 ± 0.5	318 ± 8	2.06 ± 0.10	24	2.02 ± 0.14	0.98 ± 0.08
NT-II	112901	31.91234	57.53066	35	0	29 ± 8	25.9 ± 0.7	34.2 ± 0.8	510 ± 13	2.94 ± 0.14	22	2.18 ± 0.14	0.74 ± 0.06
NT-III	112902	31.91234	57.53066	103	0	24 ± 6	21.0 ± 0.5	25.5 ± 0.6	398 ± 10	2.30 ± 0.11	22	14.1 ± 0.4	6.1 ± 0.4
NT-IV	112903	31.91234	57.53066	121	0	19 ± 4	18.7 ± 0.4	22.1 ± 0.4	337 ± 8	2.00 ± 0.10	23	16.9 ± 0.7	8.4 ± 0.6
NT-V	112904	31.91234	57.53056	47	0	27 ± 5	17.9 ± 0.4	17.4 ± 0.4	258 ± 7	1.73 ± 0.08	24	9.7 ± 0.5	5.6 ± 0.4
NT-VI	112905	31.91234	57.53066	242	1	35 ± 5	22.3 ± 0.5	23.8 ± 0.6	388 ± 10	2.25 ± 0.11	23	39 ± 2	17.4 ± 1.3
NT-VII	112906	31.91234	57.53050	40	0	12 ± 5	21.8 ± 0.5	28.6 ± 0.6	423 ± 9	2.43 ± 0.11	26	1.92 ± 0.10	0.79 ± 0.06
NT-IX	112907	31.91234	57.53057	252	1	23 ± 4	23.2 ± 0.5	19.9 ± 0.4	218 ± 7	1.62 ± 0.08	18	114 ± 5	70 ± 5
NT-XI	112908	31.91234	57.53027	232	4	36 ± 8	29.1 ± 0.7	37.0 ± 0.8	659 ± 15	3.29 ± 0.15	22	13.4 ± 0.6	4.1 ± 0.3
NT-XII	112909	31.91234	57.53027	292	0	30 ± 6	22.9 ± 0.5	26.6 ± 0.6	440 ± 11	2.46 ± 0.12	26	16.6 ± 0.9	6.7 ± 0.5
NT-XIV	112910	31.91234	57.53027	322	0	16 ± 5	17.6 ± 0.4	18.3 ± 0.5	239 ± 7	1.56 ± 0.08	23	9.9 ± 0.5	6.4 ± 0.5
NT-XV	112911	31.91234	57.53027	314	0	25 ± 4	22.7 ± 0.4	20.7 ± 0.4	239 ± 6	1.70 ± 0.08	23	26.0 ± 1.0	15.3 ± 1.0
NT-XVIII	122911	31.91234	57.53066	197	1	32 ± 9	20.1 ± 0.7	22.4 ± 0.8	335 ± 11	2.06 ± 0.10	30	21.2 ± 1.3	10.3 ± 0.8
NT-XIX	122912	31.91234	57.53027	382	0	15 ± 5	17.0 ± 0.5	16.6 ± 0.4	212 ± 7	1.44 ± 0.07	36	28.4 ± 1.7	19.7 ± 1.6
NT-XX	132901	31.91234	57.53026	287	0	47 ± 6	26.6 ± 0.5	29.9 ± 0.5	470 ± 10	2.66 ± 0.13	15	16.8 ± 1.1	6.3 ± 0.5
NT-XXI	132902	31.91234	57.53028	308	0	19 ± 6	21.9 ± 0.6	22.0 ± 0.6	299 ± 9	1.83 ± 0.09	22	15.2 ± 0.7	8.3 ± 0.6
NT-XXII	132903	31.91234	57.53026	318	0	21 ± 5	18.0 ± 0.4	18.4 ± 0.5	240 ± 6	1.55 ± 0.08	28	11.3 ± 0.9	7.3 ± 0.7
NT-XXIII	132904	31.91234	57.53061	7	1	20 ± 6	21.1 ± 0.5	26.3 ± 0.6	379 ± 10	1.95 ± 0.09	12	0.13 ± 0.06	0.07 ± 0.03
NA-1	122905	32.03694	57.51797	170	0	16 ± 4	18.7 ± 0.4	20.2 ± 0.4	346 ± 9	2.00 ± 0.10	24	15.3 ± 0.6	7.7 ± 0.5
NA-2	122907	32.03638	57.52505	47	0	27 ± 5	24.1 ± 0.5	2.2 ± 0.4	35 ± 4	0.85 ± 0.05	39	18 ± 2	22 ± 3
NA-3	122906	32.04193	57.52502	50	0	26 ± 7	23.3 ± 0.6	15.0 ± 0.6	177 ± 7	1.50 ± 0.08	23	10.1 ± 0.8	6.8 ± 0.6

**Table 5.** Detailed description of stratigraphic units in Nayband trench. Units are designated from oldest (smaller number) to youngest (larger number); the letters e, f, w, and s refer to units exposed in the eastern section, the main fault zone, the western section, and sheared deposits, respectively.

Set	Unit	Eastern Section	Set	Unit	Main Fault Zone	Set	Unit	Western Section
26 Cream to buff laminated clays with sparse sub-angular pebbles (2 per cent, 1-3 cm), with distributed mud-cracks on top.								
V	16e	Light brown, stratified, compact laminated clays in the upper part, including a laminated silty layer (5-6 cm thick) at the base, with few sub-angular pebbles (2 per cent, 1-2 cm).	IV	13f	Grey, laminated loose sands and silts thinning westward, scattered millimeter-thick caliche fragments in the upper part.	VI	24w	Light brown, liquefied coarse sands, including sandy dikes, with scattered fine pebbles (<1 cm).
	15e	Light brown, stratified alternations of laminated loose silts and compact clays, with millimeter-thick caliche fragments as pale-colored fine grained calcite.		12f	Similar to 15e.		23w	Grey sandy dikes, with 1- to 7-cm width, containing coarse sands and scarce pebbles (<3 cm).
	14e	Similar to 13e but with caliche fragments in the upper part.		11f	Similar to 13e and 14e.		22w	Grey to light brown, stratified, sub-angular poorly-sorted pebbles and cobbles (75 per cent, 0.5-4 cm up to 12 cm), few inter-beds of laminated silts and clays in the middle, millimeter-thick caliche fragments in the upper 20 cm, loose clay, sand and silt matrix.
	13e	Buff to light grey, laminated silty layer (5-7 cm) at the base overlain by compact clays.		EROSION			21w	Light brown to beige, stratified, sub-rounded, poorly-to moderate-sorted pebbles and cobbles (60 per cent, 0.5-3 cm up to 7 cm), calcite cement underneath the pebbles, thin inter-beds of laminated silts and clays, including some caliche fragments.
	12e	Grey poorly- to well-laminated loose sands and silts, with few tiny-sub vertical clay-filled fractures.	III	9f	Similar to 7e.		20w	Light brown, compact silts and clays, fairly stratified, few sub-angular pebbles (2 per cent, 1-2 cm), with a laminated silty layer 5-6 cm (bottom) and compact laminated clays (top).
11e	Cream to buff, stratified, a very thin (3-5-cm thick) silty layer at the base overlain by compact clays.	8f		Grey, finely-laminated loose sands and silts with sparse pebbles (5 per cent, 0.5 cm).	19w	Undifferentiated units 9w, 10w, 11w, 14w, 15w, 16w and 20w.		
IV	10e	Light grey laminated sands and silts.	II	7f	Light brown compact clays and silts, fairly stratified, containing poorly-sorted scattered pebbles and cobbles (5 per cent, 0.5-2 cm up to 7 cm).	18w	Undifferentiated units 14w, 15w and 16w.	
	9e	Light brown laminated compact clays with thin inter-beds of silts.		6f	Similar to 5f, containing sub-angular poorly-sorted fining-upward pebbles and cobbles (60 per cent, 0.5-2 cm up to 8 cm), clasts decreasing upward (40 per cent), with loose clay and silt matrix.	17w	Undifferentiated units 9w, 10w, 11w, 14w, 15w and 16w.	
III	8e	Grey, very thin layer of sub-rounded poorly-sorted coarse sands to fine pebbles (30 per cent, 0.5-1 cm), with erosion surface at the base.	5f	Grey to light brown, stratified, alluvial deposits, with sub-angular, poorly-sorted, fine to coarse pebbles (80 per cent, 0.5-3 cm up to 6 cm), including a compact 3-5-cm thick carbonate caliche, with erosion surface at the base.	16w	Brown to beige, stratified, alternations of compact clays and laminated silts, with wavy lamination in the upper part, sub-angular, poorly-sorted pebbles (5-40 per cent, 0.5-2 cm up to 5 cm), pebbles increasing westward, 5-8-cm thick carbonate caliche at the base.		
	EROSION			7e	Grey to light grey liquefied sands, with scattered fine pebbles (<1 cm).	15w	Cream to light brown, stratified, compact clays with two inter-beds of 4-5-cm thick silty layers, wavy lamination in silty beds in the upper 10 cm.	
						14w	Light cream, stratified, alternations of silts and clays, with inter-beds of coarse sands to fine pebbles (<1 cm), sub-angular, poorly- to moderate-sorted pebbles (10 per cent, 0.5-2 cm up to 6 cm), grain size increasing westward (up to 12 cm), sparse caliche fragments in the upper part.	

Table 5. (continued)

Set	Unit	Eastern Section	Set	Unit	Main Fault Zone	Set	Unit	Western Section
III	6e	Light brown compact clays and silts, fairly stratified, containing poorly-sorted scattered pebbles and cobbles (5 per cent, 0.5-2 cm up to 7 cm), grains content as well as grains size increasing in the lower parts up to 30 per cent and 10 cm, respectively, with erosion surface at the base.	II	4f	Buff to light grey sheet flood deposit, fairly stratified, sub-rounded, poorly-sorted pebbles and cobbles (60 per cent, 0.5-2 cm up to 9 cm), loose sand and silt matrix, with erosion surface at the base.	VI	13w	Dark grey laminated sands filling open cracks on top of unit 12w, with few sparse pebbles (<1 cm).
	II	5e		Grey to buff alluvial deposits, fairly stratified to stratified, sub-angular, poorly- to moderate-sorted pebbles (70 per cent, 0.5-2 cm up to 6 cm), with silt and clay matrix and some carbonate cement, with erosion surface at the base.	2f		Cream to light brown, stratified, alternations of silts and clays, laminated in silty beds, few scattered coarse pebbles (2-4 cm) in the middle part, compact 5-6-cm thick carbonate caliche on top.	V
I		4e	Cream to light brown alternations of poorly-laminated loose silts and compact clays.	I	1f	Cream to light brown, fairly stratified, very compact clays.	11w	
	I	3e	Cream, laminated loose silts.		Sheared Deposits	4s	Light brown to cream, including pieces of units 1f to 5f and 1e to 6e, sub-angular pebbles and cobbles (10 percent, 0.5-1 cm up to 8 cm), oriented thin lenses of clay and silt parallel to the fault planes, with compact clay, silt and sand matrix.	10w
2e		Cream to light brown, stratified, alternations of silts and clays, laminated in silty parts, with few scattered coarse pebbles (2-4 cm).	IV	9w				Cream to buff, compact beds of silts (6-8-cm thick in the lower part) and clays.
I	1e	Cream to light brown, fairly stratified, very compact clays, few sparse sub-angular coarse pebbles (up to 5 cm) in the lower part.		I	2s	Similar to 1s, with poorly- to moderate-sorted pebbles (10-15 per cent, 0.5-1 cm up to 3cm).	III	8w
	3e	Cream, laminated loose silts.	II					7w
I	2e	Cream to light brown, stratified, alternations of silts and clays, laminated in silty parts, with few scattered coarse pebbles (2-4 cm).		I	1s	Beige, including sub-rounded, poorly-sorted pebbles (20-30 per cent, 0.5-2 cm up to 5 cm), oriented clasts parallel to the bounding fault planes compact sand, clay and silt matrix.	II	5w
	1e	Cream to light brown, fairly stratified, very compact clays, few sparse sub-angular coarse pebbles (up to 5 cm) in the lower part.	I					4w
I	1e	Cream to light brown, fairly stratified, very compact clays, few sparse sub-angular coarse pebbles (up to 5 cm) in the lower part.		I	1s	Beige, including sub-rounded, poorly-sorted pebbles (20-30 per cent, 0.5-2 cm up to 5 cm), oriented clasts parallel to the bounding fault planes compact sand, clay and silt matrix.	I	2w
	1e	Cream to light brown, fairly stratified, very compact clays, few sparse sub-angular coarse pebbles (up to 5 cm) in the lower part.	I					1w

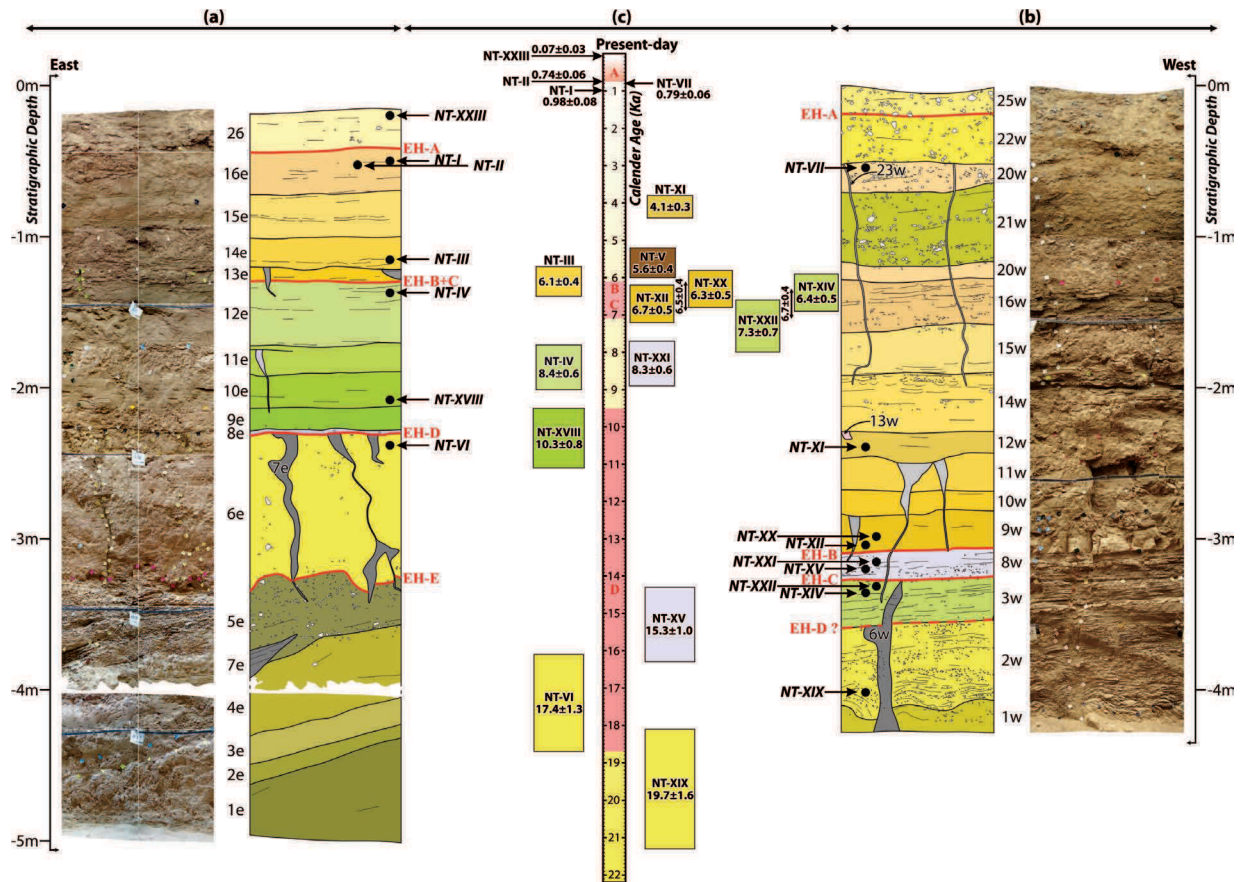


**Figure 20.** Photo mosaics and corresponding stratigraphic logs of the sediments exposed in the trench excavation, with vertical positions of dated OSL samples (see exact locations in Figures 19b and 19c) and event horizons of five past earthquakes (see section 4.4). (a) Section east of the MFZ, near meters 8 (top 4 m) and 12 (bottom 1 m). (b) Section west of the MFZ, between meters 42-43. (c) Corresponding OSL ages (colored boxes) are given in thousands of years before present (ka B.P.). Pink colored intervals denote the maximum time windows for the last four paleoearthquakes (see section 4.4). Two vertical arrows denote weighted mean ages of the samples collected from units 3w and 9w. Note the ages of samples NT-XV and NT-XXI, which are older than the immediate below samples (NT-XIV and NT-XXII).

The available OSL ages indicate that the oldest sediments in the trench are seen within the MFZ. The lower, hence older, units (units 1f to 3f) are older than  $70 \pm 5$  ka (sample NT-IX) while the upper units (units 11f to 26) are younger than  $5.6 \pm 0.4$  ka (sample NT-V). The time interval of  $64 \pm 5$  ka between these samples and the sediment thickness between them (<2 m) indicates that the MFZ exposes a discontinuous record of sediments between the end of MIS-5 (~75 ka, [e.g., Grootes and Stuiver, 1997; Cutler et al., 2003]) and the late Holocene. The

depositional environment of the oldest trench units (units 1f to 3f) is similar to that of the youngest deposits (units 11f to 26 in the MFZ, units 20w and 26 in the western section, and units 13e to 26 in the eastern section); all appear to be pond sediments (Table 5). The oldest OSL age,  $70 \pm 5$  ka (sample NT-IX) indicates the pond environment corresponds to long lasting depositional conditions at the trench site. Moreover, the pond outlet exhibits a  $\sim 250$  m northward deflection (see section 4.1 and Figure 17c) that results from cumulative right-lateral motion along the Nayband fault. Given the estimated slip rate of  $1.8 \pm 0.7$  mm yr<sup>-1</sup> (see section 3.4), the now dry pond should have been formed against the shutter-ridge at least some  $160 \pm 60$  ka ago.

Two stratigraphic columns with the OSL age constraints, on each side of the MFZ, are given in Figure 20. These OSL ages indicate that the emplacement of nearly all the sediments exposed both to the west and to the east of the MFZ are consistent with MIS-1 and MIS-2 (11-24 ka [e.g., *Phillips et al.*, 2000]). Indeed, to the west of the MFZ, the  $\sim 4$ -m-thick stack of sediments was deposited at least within the last 20 ka (sample NT-XIX) while to the east of the MFZ, the upper 2.4 m of the sediment pile were deposited during the last 17 ka (sample NT-VI). These yield average sedimentation rates of 0.14 and 0.20 mm yr<sup>-1</sup>, respectively east and west of the MFZ (Figure 21).

The deposits in the western section (units 3w to 26) reach a maximum thickness of 4.2 m (near meter 19) and were aggraded within the last  $6.7 \pm 0.4$  ka (weighted average age of samples NT-XIV and NT-XII). Comparing this age with that of a sample collected some 60 cm below (NT-XIX,  $19.7 \pm 1.6$  ka) argues for a significant lack of stratigraphic record covering about 13 ka. Although shorter, a similar significant lack of stratigraphic record is also found to the east of the MFZ, where ages of  $10.3 \pm 0.8$  ka (sample NT-XVIII) and  $17.4 \pm 1.3$  ka (sample NT-VI) suggest  $\sim 7$  ka of sediments are missing. In the MFZ, unit 7f is a lateral equivalent of unit 6e (Figure 19b and Table 5); the upper part of unit 6e yields  $17.4 \pm 1.3$  ka and a comparison with the age of  $5.6 \pm 0.4$  ka (sample NT-V within the MFZ) also indicates a lack of stratigraphic record of  $\sim 12$  ka. Thus, sediment appears to be missing along the whole length of the trench. This missing sediment package in the eastern section represents at least 5 ka and at most 9.2 ka. It is thus completely included within the longer time gap of both the MFZ and the western section. This long gap is based on the two older OSL ages of  $17.4 \pm 1.3$  ka and  $19.7 \pm 1.6$  ka

(samples NT-VI and NT-XIX) in the eastern and western sections, respectively. If these two samples were partially bleached (as were samples from unit 8w) this could lead to an erroneously long gap in the sediment deposits. However, neither of these sedimentary units contains any evidence for reworking (in contrast to unit 8w) and we so reject this hypothesis, and conclude that there is no sediment record for approximately the upper half of MIS-2 and the early Holocene. This absence may result either from a prominent gap of sedimentation or from removal of the sediments by a subsequent erosion. The second option is less likely, assuming the nearly continuous aggradation during the sediment gap needs at least two erosion phases (Figure 21): one before the deposition of unit 8e and another one after unit 12e. As the tops of units 12e (sample NT-IV) and 3w (samples NT-XIV and NT-XXII) appear nearly coeval, the duration of the younger of the two erosion phases would hardly fit between units 12e and 3w. In fact, the difference in gap duration between the eastern and western sections is mainly explained by the fact that aggradation resumes earlier to the east of the fault (before  $10.3 \pm 0.8$  ka) than to the west of it (before  $6.7 \pm 0.4$  ka). Therefore, a prominent gap of sedimentation appears simpler and hence more likely; it suggests that climatic conditions favored sediment transport and erosion rather than aggradation at the end of MIS-2 and beginning of MIS-1.

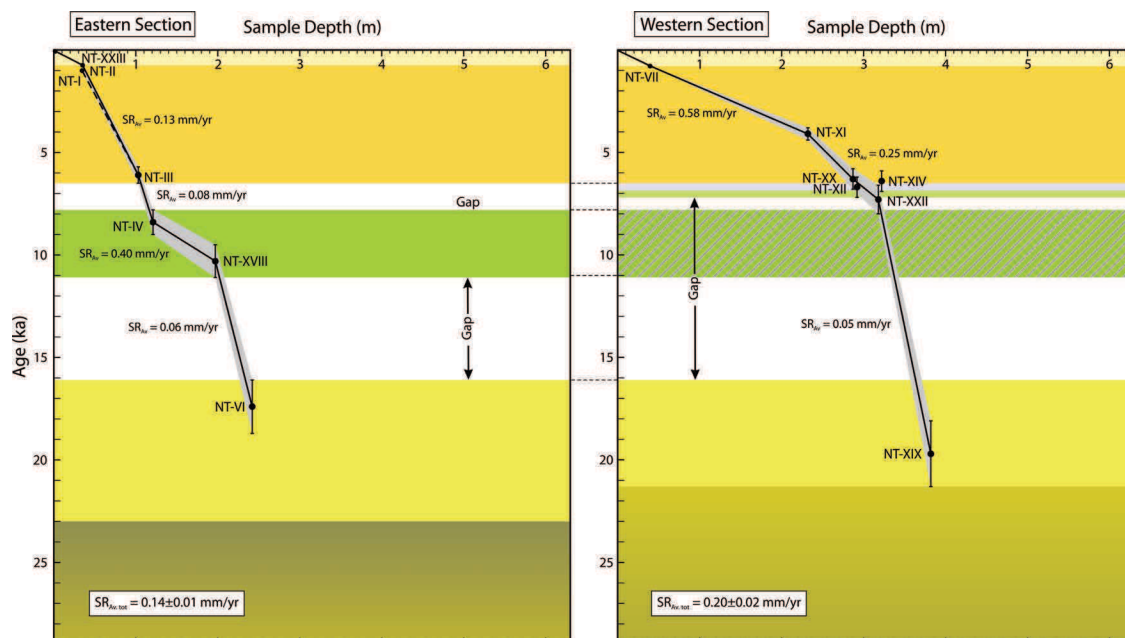


**Figure 21.** Sedimentation rates calculated for the eastern and western stratigraphic logs. Colors are as for units displayed on Figures 19 and 20 and figure out the duration of the preserved units (hatched where extrapolated). Note the pile of sediments younger than 7 ka is much thicker in the western section than in

the eastern one. Very low ( $<0.1 \text{ mm yr}^{-1}$ ) sedimentation rates characterize sediment gaps. The single gap evidenced in the western section splits into two gaps flanking units 9e to 12e (green color) in the eastern section.

Comparing the thicknesses of the units younger than  $\sim 7 \text{ ka}$  on both sides of the MFZ indicates a much thicker pile of deposits in the western section than in the eastern one. Indeed, the samples NT-XII and NT-XX (weighted average of  $6.5 \pm 0.4 \text{ ka}$ ) collected from the base of unit 9w and the sample NT-III ( $6.1 \pm 0.4 \text{ ka}$ ) collected above unit 13e indicate that units 9w and 13e are indistinguishable in age. In addition, the two OSL samples that were collected from the upper parts of unit 16e (sample NT-I,  $0.98 \pm 0.08 \text{ ka}$  and sample NT-II,  $0.74 \pm 0.06 \text{ ka}$ ) are in the same age range that the one obtained from the upper part of unit 20w (sample NT-VII,  $0.79 \pm 0.06 \text{ ka}$ ). These well-constrained and similar ages acquired from these three samples indicate that the deposition of unit 16e to the east of the MFZ occurred at about the same time as the deposition of the upper part of unit 20w to the west of the MFZ. Up to 0.9 m of sediment (units 13e to 16e) was deposited east of the MFZ essentially at the same time a 3.3 m (units 9w to 20w) were deposited on the west side (Figure 19). This difference probably results from the initial position of the western section closer to the center of the pond. In addition, renewing of eastward tilting would have occurred between units 8w and 9w to produce sagging to the west of the Main Fault Zone, hence increasing the accommodation space and allowing more aggradation in this section.

#### 4.4. Seismic Event Identification

The recognition of seismic events in the SDR trench is based on direct (structural observations) as well as secondary (earthquake-induced sedimentary features) evidence of paleoearthquakes. There is evidence for at least four surface faulting events within the last  $17.4 \pm 1.3 \text{ ka}$  and two older earthquakes, one before  $\sim 23 \text{ ka}$  and another before  $70 \pm 5 \text{ ka}$ . The identification of these six seismic events, designated as A, B, C, D, E and F from the youngest to the oldest (Figure 19) is reported below.

The recognition of the most recent earthquake, **event (A)**, is based on three independent lines of evidence. First, the abrupt upward terminations of several fault strands, sealed by the most recent pond deposit (unit 26, Figures 19a and 19b), provide the primary line of evidence. One

such clear fault termination is exposed near meter 20, where the well-bedded deposits resting below unit 26 are vertically offset by 20-25 cm. Two other fault strands, one near meter 12 and another one near meter 15, resulted in the offset of several layers by 10-15 cm (units 13e to 16e in the eastern section corresponding to units 11f to 13f in the MFZ section) lying below the undisturbed unit 26 (Figure 22). Second, locally tilted units 10f to 13f (between meters 12 and 16) are unconformably covered by flat-lying unit 26. Additionally, the drag folding of unit 20w against a prominent steep fault strand near meter 16.5 is also unconformably overlain by unit 26, testifying for event A (Figure 23). Third, the occurrence of several sandy dikes (units 23w and 24w) disrupting the upper strata are sealed by unit 25w (Figures 19c and 24), testifying for the same event in the western section of the trench. These dikes have apparent widths ranging from a few up to 40 cm and consist of loose, unsorted, sands injected from the underlying strata containing scarce pebbles from the host layers.

Although the upward termination of a fault strand is sometimes difficult to relate with a given seismic event of a series of paleoearthquakes [*Bonilla and Lienkaemper, 1990*], the fact that displacements of several centimeters occur just below the abrupt truncation of the fault by the sealing horizon provides confidence for the interpretation of event A. Similarly, the narrow fault zone near meter 20, with vertical displacements almost constant through the four-meter-thick pile of units 3w to 20w, sealed by unit 26, indicates that the base of unit 26 must correspond to an event horizon. Furthermore, the dragged layers and sandy dikes are sealed by the same stratigraphic horizon (units 26 and 25w) as the fault terminations. Therefore, event A has occurred after the deposition of units 16e, 13f, 20w, 22w and prior to the deposition of the most recent sediments (units 26 and 25w). Consequently the lower limit of units 26 and 25w represents the event horizon of the most recent earthquake. The layers from which samples NT-I ( $0.98 \pm 0.08$  ka), NT-II ( $0.74 \pm 0.06$  ka) and NT-VII ( $0.79 \pm 0.06$  ka) were collected define the lower bound of the event-A horizon (EH-A in Figures 19b and 19c). The reliability of these ages is supported by sample NT-XXIII collected 7 cm below the ground surface. This gives an age of  $0.07 \pm 0.03$  ka, confirming that these sediments are likely to have been well-bleached at deposition. Thus, the minimum time interval for event A stands between 0.68 ka (youngest possible age of sample NT-II) and  $\sim 0.1$  ka (oldest possible age of sample NT-XXIII). Therefore, the most recent earthquake (event A) occurred more recently than eight hundred years ago, i.e.,

after circa AD 1200 (oldest possible age of the youngest sample, NT-II, located below the event horizon).

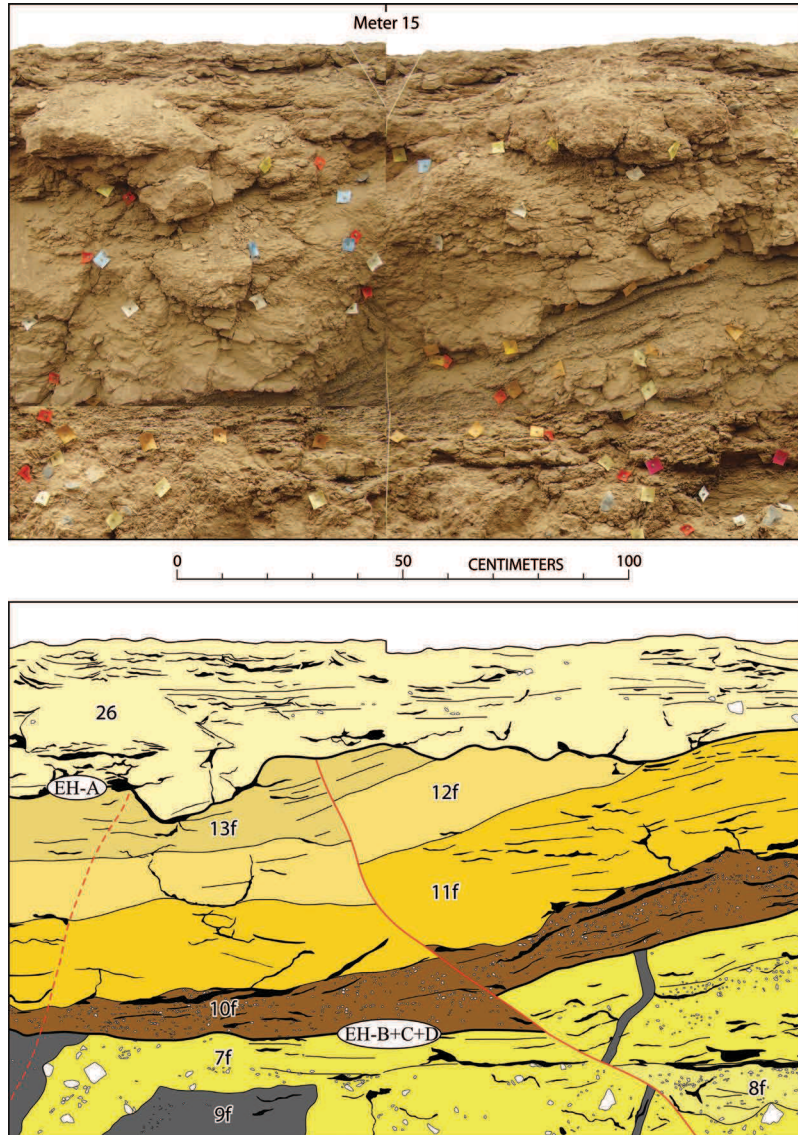


**Figure 22.** Evidence for the most recent earthquake (event A). Photomosaic (top) and interpretation (bottom) showing a west-dipping fault strand near meter 15 offsetting units 7f and 10f to 13f as well as the older event horizon (EH-B+C+D), which abruptly terminates upward, at the base of the most recent undisturbed deposits (unit 26).

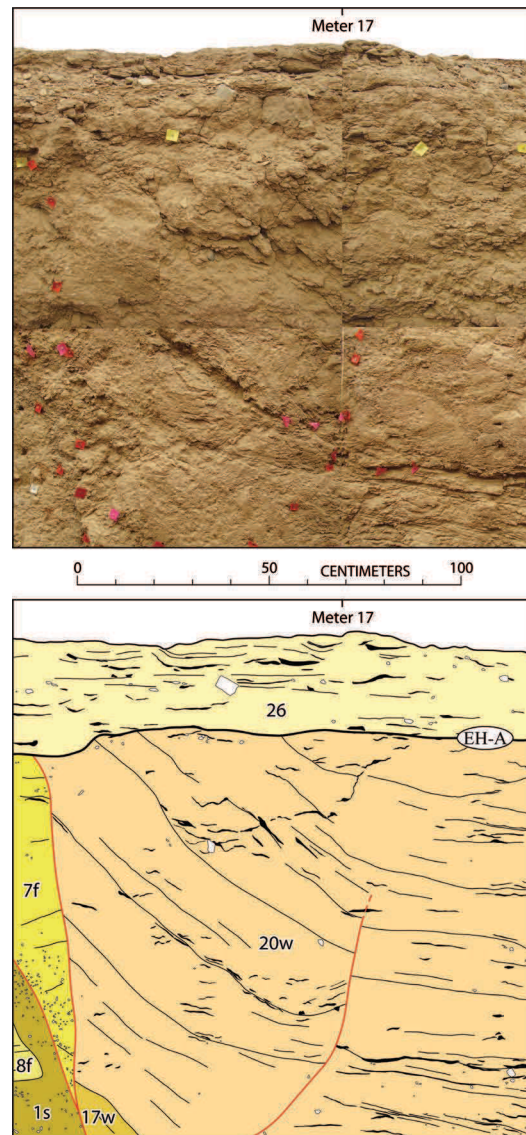


**Figure 23.** Photomosaic (top) and interpretive sketch (bottom) close to the western limit of the MFZ. The young fine-grained sediments of units 20w are dragged up against a prominent steep fault near meter 16.5 and unconformably overlain by the flat-lying unit 26. An east-dipping secondary fault displaces the lower part of unit 20w along the hinge of folded strata and gradually terminates upward as folding is less effective away from the prominent fault strand.

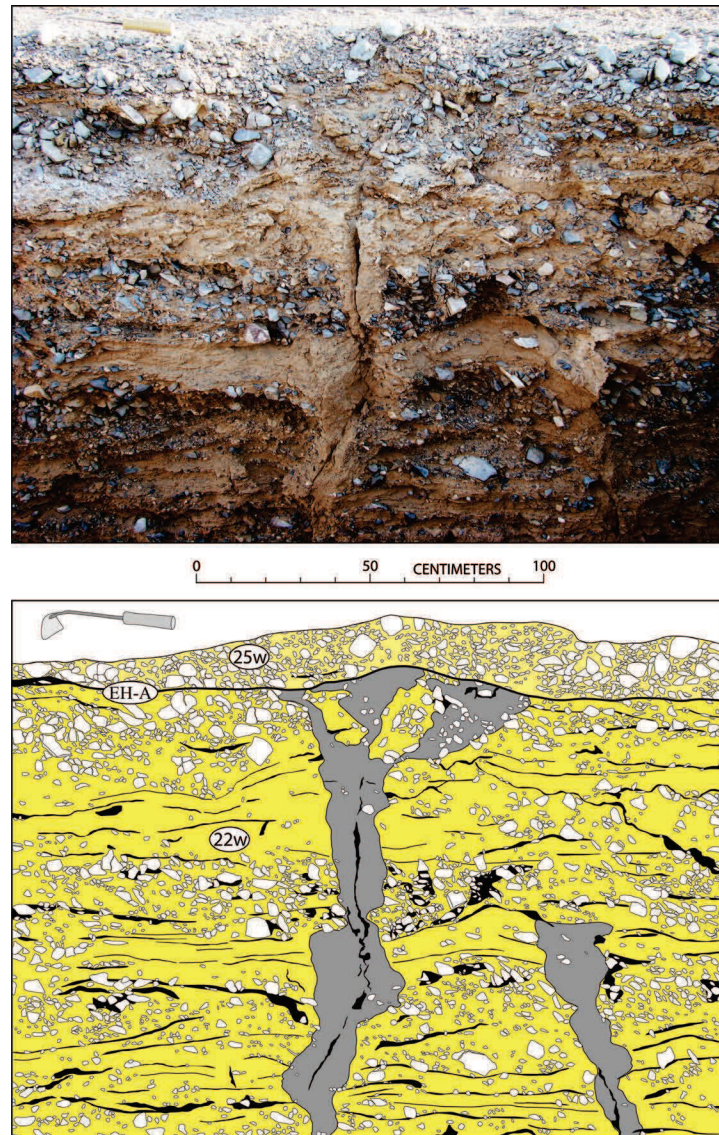


**Figure 24.** Oblique photograph (top) and interpretive sketch (bottom) of two sandy dikes formed during event A, at the western end of the trench. These steep sandy dikes are made of loose sandy material with scarce pebbles from the host layers (unit 22w) and cut through the flat-lying, coarse-grained strata with fine-grained inter-beds of unit 22w. The cone-shaped larger dike is covered by gravelly deposits (unit 25w) while the smaller one abutting against a coarse-grain layer of the host unit did not reach the ground surface at the time of the most recent earthquake (EH-A).

The penultimate and antepenultimate earthquakes, **event B** and **event C**, are less easy to identify because they are closely related in time. Their respective event horizons are only separated in the western section of the trench where preserved evidence allows us to distinguish

unambiguously two unconformable erosion boundaries that should correspond to two earthquakes and to date them very precisely.

To the west of the MFZ, the most conclusive evidence for **event B** is subtle. Its event horizon, EH-B, corresponds mainly to an erosion surface prior to the deposition of unit 9w, which overlies unit 8w and its eastward lateral equivalent unit 7w as well as older units (4w, 3w, and 1w). All these older units dip eastward while unit 9w is horizontal, and so stands unconformably and onlapping westward onto underlying units. Locally, event B also produced small vertical faults affecting units 3w to 7w (meters 19 to 20) that are sealed by unit 9w (Figure 20b).

Unambiguous evidence for **event C** is also seen in the western section of the trench. From meter 42 westward, several liquefaction features (unit 6w) disrupt units 1w to 3w and are covered by undisturbed alluvial deposits of unit 8w (Figures 19c and 25). The liquefied features range in width from a few centimeters to as much as 180 cm, and in height up to more than 110 cm, they consist of sand-filled feeder dikes and pillars. These liquefied features are sealed by unit 8w indicating an event horizon below this unit. Unit 7w a lateral equivalent of unit 8w seals small faults (near meter 17.5) disrupting the underlying units. Consequently, the lower limit of units 7w and 8w also delineates the event horizon, EH-C, of the third paleoearthquake. EH-C corresponds to an unconformable erosion boundary between unit 8w and underlying east-dipping units 4w, 3w, 2w, and 1w.

To constrain accurately the respective ages of events B and C, a total of six OSL samples were taken from units 3w (NT-XIV and NT-XXII), 8w (NT-XV and NT-XXI), and 9w (NT-XII and NT-XX) so that each unit sampling was duplicated (see section 4.3). Unit 8w yielded quite different ages and these are discarded for the reasons discussed earlier. Unit 3w yielded overlapping ages of  $6.4 \pm 0.5$  ka and  $7.3 \pm 0.7$  ka from which a weighted average age of  $6.7 \pm 0.4$  ka was calculated. Unit 9w also yielded very similar ages of  $6.7 \pm 0.5$  and  $6.3 \pm 0.5$  ka which give a weighted average of  $6.5 \pm 0.4$  ka. Thus, the ages of units 3w and 9w are indistinguishable. As the ~25-cm thick unit 8w stands between these two units, the weighted average age of the two bounding units,  $6.6 \pm 0.3$  ka, provides the age of unit 8w. Therefore, events B and C occurred between  $6.7 \pm 0.4$  and  $6.5 \pm 0.4$  ka, suggesting that in a very short period of at most ~1 ka the following events occurred: the end of the aggradation of unit 3w, event C and its

subsequent erosion, the deposition of unit 8w, event B and its subsequent erosion, and finally the onset of accumulation of unit 9w. This short timing remains possible because aggradation and erosion may be very rapid under desert conditions. The occurrence of two seismic events within a short time interval may indicate that the seismic behavior of the Nayband fault can be characterized by clustering earthquakes.

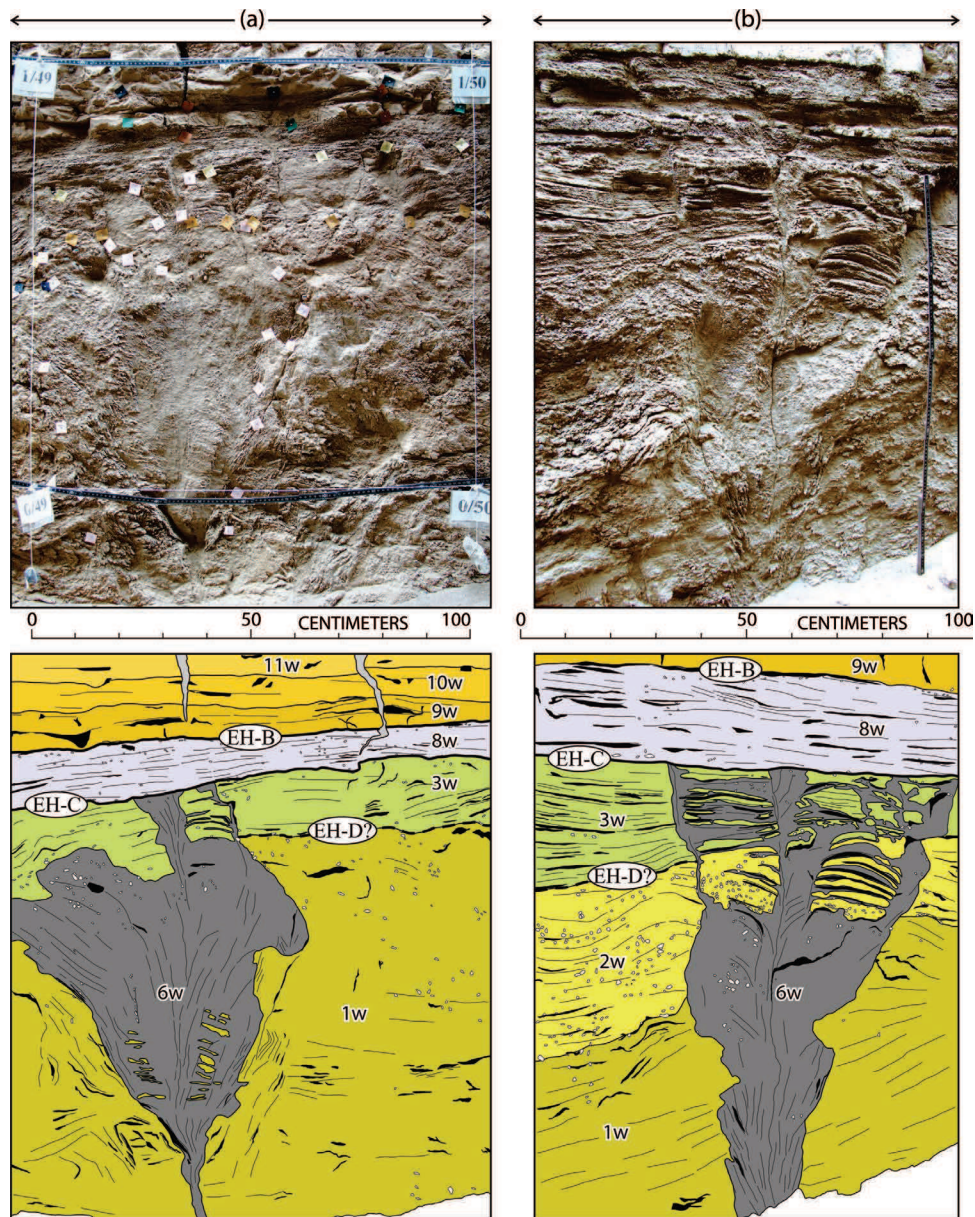


**Figure 25.** Liquefaction features on the southern (left) and the northern (right) walls in the western section of the trench exposure deposits giving evidence for event C. (Left) Photomosaic and interpretive sketch of a sand blow (unit 6w) between meters 49 and 50. The sandy material coming from older layer(s) than 1w, and the intruded materials are overlain by an undisturbed alluvial layer (unit 8w). Some

remnants of the host sediments (units 1w and 3w) remain away from the central pillar. (Right) Oblique photograph and interpretative sketch of another sand blow (unit 6w) between meters 47 and 48. The base of unit 9w corresponds to a lateral equivalent of the event horizon of the penultimate earthquake (EH-B).

In the eastern section of the trench and the MFZ, events B and C cannot be distinguished separately. The contact between units 12e and 13e defines the mixed event horizon (EH-B+C) of the penultimate and antepenultimate events. There, two fault strands, one near meter 9 and another near meter 11, terminate upward at the same stratigraphic horizon, at the base of unit 13e (Figures 19b and 26). The sealed faults cut through units 1e to 12e, offsetting the entire sequence by more than 15 cm, at the base of unit 12e. The fine-grained sediments of unit 13e overlie these fault strands. Using OSL samples collected below (NT-IV) and above (NT-III) the EH-B+C, the age of these two earthquakes on this vertical section is bracketed between  $8.4 \pm 0.6$  ka and  $6.1 \pm 0.4$  ka. Interestingly, the short time span for the occurrence of events B and C, which is determined in the western section, fits within the time interval determined for the sealing of these faults. Units 9e to 12e have been preserved only to the east of the MFZ and they abruptly disappear against the eastern prominent fault strand of the MFZ (around meter 12). It is likely that a thick (more than 1 m), fine-grained, and flat-lying sequence was eroded in the MFZ after earthquakes B and C and before the deposition of unit 10f, i.e., prior to  $5.6 \pm 0.4$  ka (NT-V; Figures 20 and 21, see section 4.3).

The recognition of a fourth paleoearthquake, **Event D**, is based on several abrupt upward fault terminations and earthquake-induced sedimentary features that are only seen in the eastern part of the trench. Several distinct upward terminations of fault splays, of which the ones observed close to meters 9 and 10 are the most demonstrative, provide evidence for event D (Figures 19b and 27). To the east of the MFZ (Figure 27), two west-dipping faults cut up through units 1e to 6e, abruptly terminating at the same stratigraphic horizon, at the base of unit 8e. Units 1e-6e are tilted ( $\sim 25^\circ$ ) eastward between the fault strands and associated with vertical displacements along the eastern fault strand that range from 120 cm (at the base of unit 6e) to 140 cm (at the base of unit 2e). Unit 6e is much thicker to the east than to the west of the eastern fault (near meter 9), where its upper part has been removed by erosion after event D. Additional evidence for event D comes from the recognition of liquefaction features emplaced within units 6e and 7f. These features, to the east of the MFZ, consist of rather loose sands that originate from

the lower sandy-gravelly strata, mainly from unit 5e, and are sealed by unit 8e. The liquefied features are sealed by the same stratigraphic horizon as the abrupt fault terminations; this makes the possibility of a site effect caused by a remote earthquake unlikely. Therefore, the event horizon of the fourth paleoearthquake (EH-D) has to be set at the base of unit 8e (Figure 27). This event D occurred after the deposition of unit 6e; hence it postdates  $17.4 \pm 1.3$  ka (sample NT-VI, collected from the top of unit 6e). Since the units immediately above EH-D consist of a very thin sandy-pebbly layer (unit 8e) topped by compact clays (unit 9e), unsuitable for OSL dating, sample NT-XVIII ( $10.3 \pm 0.8$  ka) was collected from sandy layers at the base of unit 10e. Thus, the fourth event on this vertical section occurred between  $10.3 \pm 0.8$  and  $17.4 \pm 1.3$  ka.

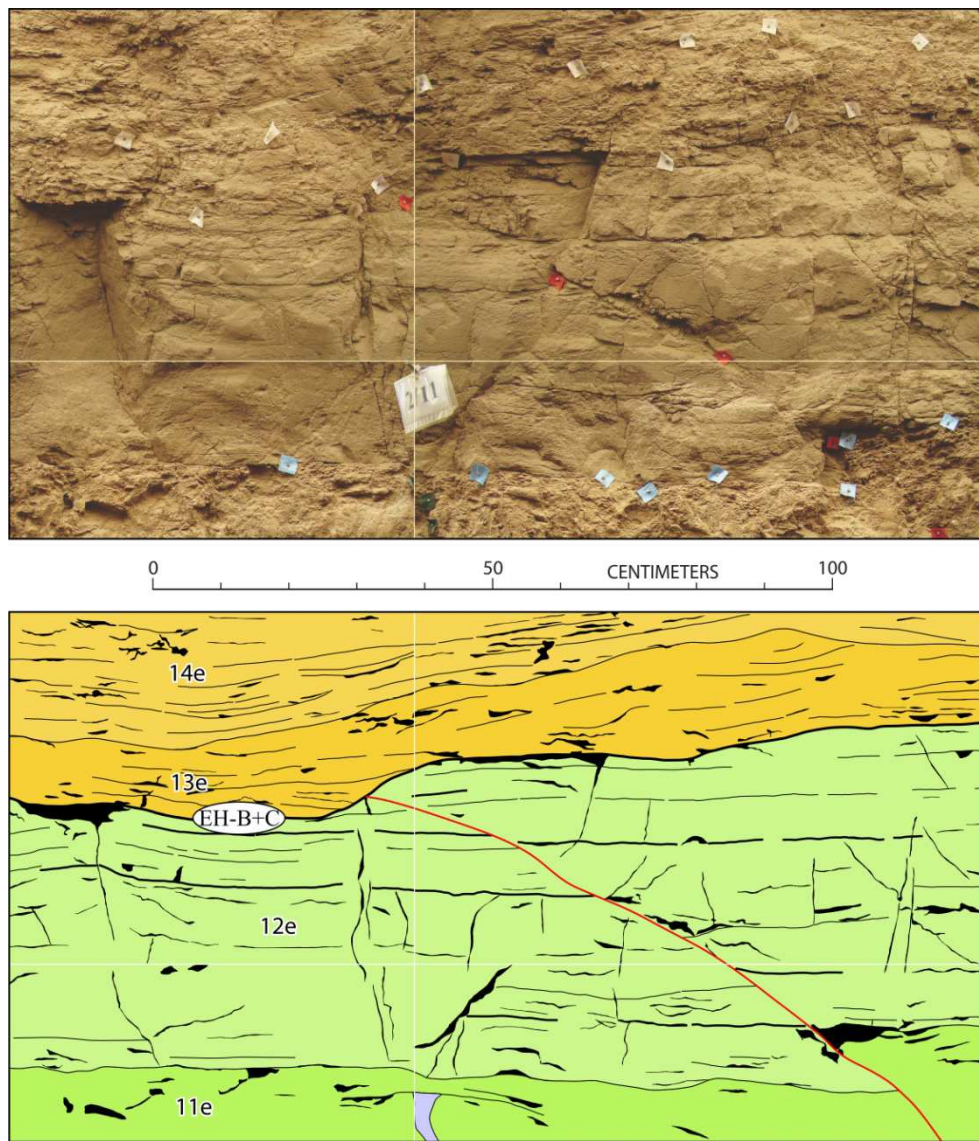
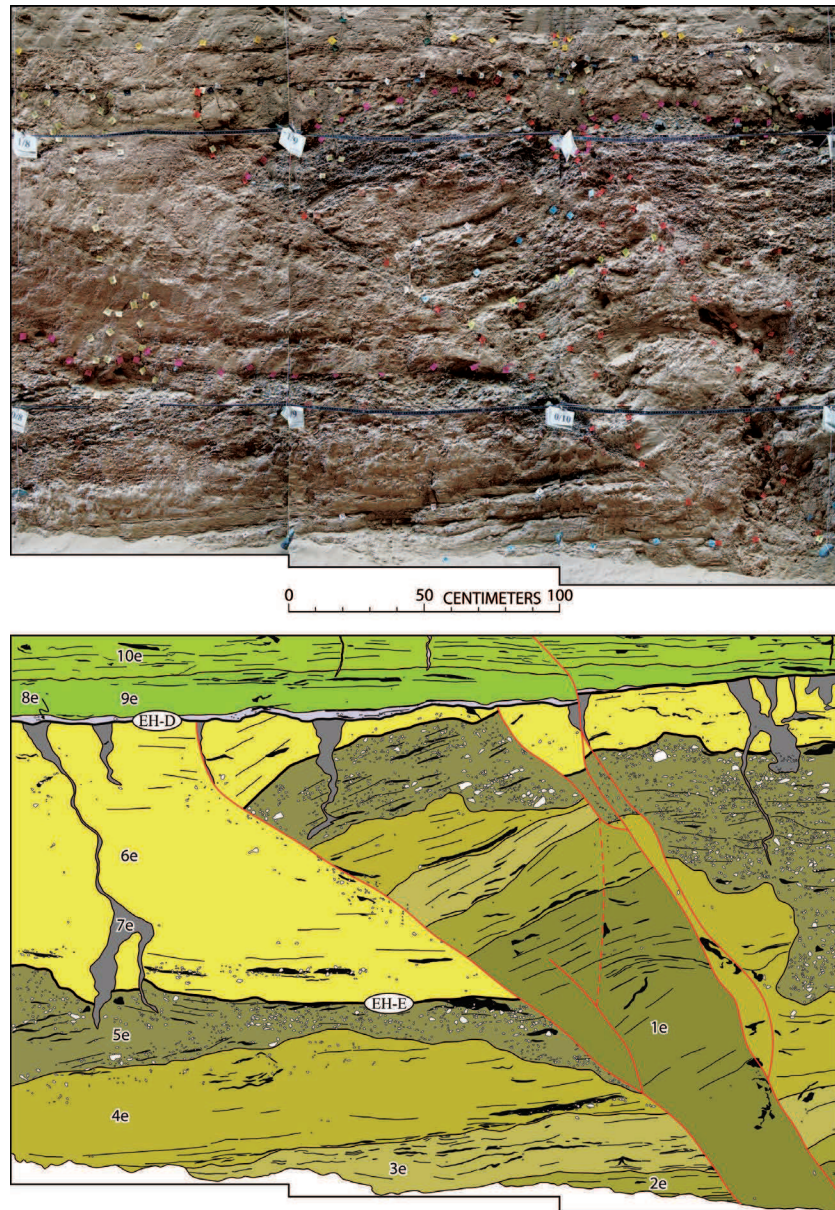


Figure 26. See next page.

**Figure 26.** Evidence for the penultimate and antepenultimate earthquakes (events B+C), east of the main fault zone around meter 11. A west-dipping fault strand displaces the well-bedded, fine-grained pond sediments (units 11e and 12e) and forms a 10-15-cm high E-facing buried scarplet. Note the similar vertical displacements (15 cm) across the strata from the base of unit 12e up to the event horizon (EH-B+C). Both the fault and the scarplet are overlain by unit 13e. The base of unit 13e also corresponds to a lateral equivalent of EH-C.

Liquefaction features in the MFZ (unit 9f) are unconformably covered by a sandy lens (unit 10f) that yielded an OSL age of  $5.6 \pm 0.4$  ka (sample NT-V). The long time span between units 10f and 7f (corresponding to the lower part of unit 6e) overlaps the occurrence of events B, C, and D and hence does not permit to determine what are the respective contributions of these three earthquakes within the MFZ.

The recognition of a fifth paleoearthquake, **event E**, is based on several abrupt upward terminations of fault strands located within the MFZ and a fissure fill localized at the base of unit 6e to the east of the MFZ. In the MFZ, near meter 15, a nearly vertical fault strand cut through sediments up as far as unit 6f, for which the lower limit is downthrown westward by  $\sim 50$  cm (Figure 19b). Upwards, this fault is sealed both by unit 7f and the liquefied feature (unit 9f) produced by event D, indicating a fault displacement occurred between deposition of units 6f and 7f. Similarly, two superposed, low-dipping fault strands, close to meter 13, offset the entire sequence up to unit 6f. The upper one is sealed by unit 7f while the lower one, which shows a vertical throw of  $\sim 1$  m at the base of unit 6f, is characterized by a steeper upward prolongation that displaces the base of unit 7f by less than 10 cm. This difference indicates that there should be a faulting event between units 6f and 7f. Additionally, to the east of the MFZ near meter 10, the western strand of a west-dipping faulted wedge shows different vertical displacements between units 6e and lower units (Figure 19b). Indeed, the lower units are displaced by  $\sim 140$  cm (measured at the base of unit 4e) while the base of unit 6e is displaced by only 35 cm. As the displacement of the base of unit 6e must have occurred during event D, the remaining vertical displacement of  $\sim 1$  m is presumably associated with an older faulting event. This later displacement, and all the upward fault terminations discussed above, occurred before the deposition of unit 6e or its lateral equivalent, unit 7f. Thus, the lower limit of these two units must correspond to an event horizon (EH-E on Figure 19b).



**Figure 27.** Evidence for the fourth paleoearthquake (event D), eastern section of the trench exposure deposits between meters 8 and 11. Photomosaic (top) and interpretive sketch (bottom) showing two west-dipping faults displacing units 1e to 6e, abruptly terminating at the same stratigraphic level, and overlain by a thin layer of sandy-gravelly material (unit 8e). All the layers between these two faults are tilted  $25^\circ$  eastward and unconformably sealed by flat-lying units 8e to 10e. Several liquefied sandy features (unit 7e), likely originated from unit 5e, are injected upward into the fine-grained pond sediments (unit 6e) and covered by a same stratigraphic level that the fault terminations, at the base of unit 8e (EH-D). Note also

the small displacements of EH-D, unit 8e, and subsequent layers by a fault splay reactivated during a younger event (Event B).

Additional evidence for event E comes from the fact that the oldest units exposed in the eastern section (units 1e to 5e) have been tilted eastward by  $\sim 15^\circ$  between meters 10 and 14 whereas these older units are unconformably covered by the horizontal unit 6e (Figure 19b). Moreover, a fissure, with a depth of 40 cm, between meters 4 and 5 (Figure 19a) has affected unit 5e and was subsequently filled with the fine-grained sediments of unit 6e, consistent with a fifth paleoearthquake before deposition of unit 6e. The age of this event E is poorly constrained as there is no direct age control below the EH-E. However, one can combine the estimated average sedimentation rate of the eastern section ( $0.14 \text{ mm yr}^{-1}$ , Figure 21) with the sediment thickness between sample NT-VI and EH-E to suggest that event E should have occurred before some 23 ka.

There is also evidence for an older paleoearthquake, **event F**, in the MFZ. Several sub-vertical fault strands, between meters 13.5 and 15.5, offset units 1f to 3f by  $\sim 40$  cm and are sealed by unit 4f. This implies the occurrence of a paleoearthquake (event F) prior to the deposition of unit 4f (Figure 19b), hence before  $70 \pm 5$  ka (sample NT-IX).

## 5. Discussion and conclusions

### 5.1. Slip Rate Constraints and Paleearthquakes along the Nayband Fault

Combining the geomorphic offset markers with their corresponding  $^{36}\text{Cl}$  CRE and OSL ages provides a long-term slip rate averaged over the last 100 ka of  $1.8 \pm 0.7 \text{ mm yr}^{-1}$  for NA2 fault segment (Figure 12). This rate is consistent with that to the south, averaged over a longer time span ( $1.5 \text{ mm yr}^{-1}$  [Walker and Jackson, 2002] further refined to  $1.4 \pm 0.5 \text{ mm yr}^{-1}$  [Walker et al., 2009]) by using 2-4 km geomorphic offsets postdating the lavas flow of the Gandom Berian basaltic plateau ( $^{40}\text{Ar}/^{39}\text{Ar}$  ages of 2.15-2.31 Ma, Walker et al. [2009]). These results suggest that the slip rate remained constant through the entire Quaternary.

As documented in section 4.4 the strain release on the Nayband fault has produced at least four earthquakes within the last  $17.4 \pm 1.3$  ka (OSL sample NT-VI). From the age of the fourth

earthquake, event D, bracketed between 18.7 ka (maximum age of sample NT-VI) and 9.5 ka (minimum age for sample NT-XVIII), a rough recurrence interval of 3-6 ka for surface rupturing earthquakes can be derived. However, this approximate recurrence interval may be biased as there is a lack of sediment record between  $10.3 \pm 0.8$  ka (NT-XVIII) and  $17.4 \pm 1.3$  ka, hence the paleoseismic record may be incomplete. It is probably better to focus on the last  $\sim 7$  ka, which provides a relatively continuous sediment record in the western section of the trench. It should be noted that, between event B and event A, there is a set of small fissures observed below the base of units 12w and 14w, where 12w is lacking. These fissures, which are filled by an aeolian sandy deposit, could be interpreted either as desiccation cracks or tentatively as features induced by an additional earthquake. This set of fissures occurred before  $4.1 \pm 0.3$  ka (sample NT-XI in unit 12w). Nevertheless, these small fissures are evenly distributed and at least some must correspond to desiccation cracks produced during one of the late Holocene drought cycles following 4.2 ka [Staubwasser *et al.*, 2003]. It is thus very unlikely that an earthquake postdating event B and predating event A would have taken place before  $4.1 \pm 0.3$  ka. We conclude that three major events, A, B, and C occurred in a time span between 5.3 ka (minimum time interval between events A and C) and 7 ka (maximum time interval between events A and C). This 5.3-7 ka interval contains thus two earthquake cycles yielding a recurrence interval between two successive events ranging between 2.7 and 3.5 ka. However, this estimate does not account for the actual record of seismic events as seen in the trench. Three earthquakes are identified during the last  $\sim 7$  ka, but the two older events occurred around  $6.6 \pm 0.5$  ka while the younger one occurred more recently than 0.8 ka. Thus, time intervals between successive earthquakes appear highly variable; it is at most 1 ka, probably less, between events B and C whereas it is  $6.2 \pm 0.9$  ka between events A and B. Therefore, the available record of paleoearthquakes suggests the seismic behavior of the Nayband fault is characterized by event clustering. In such a case, a mean recurrence interval of earthquake occurrence is of little use in assessing seismic hazard; what is most relevant is a well-constrained history of past earthquakes with as accurate as possible estimates of their respective magnitudes.

The smallest right-lateral offsets preserved less than 1 km to the north of the trench site are on the order of 3-4 m (Figure 16a). Considering these smallest right-lateral displacements occurred during the most recent earthquake, the magnitude of event A should be on the order of  $M_w \sim 7$ . The right-lateral offsets ranging between 6 and 16 meters (Figures 16b-16d) must

incorporate the displacements of former events, including the events B, C, and possible older events. The distribution of the 67 measured right-lateral offsets smaller than 30 m (see Table A1 and section 3.4) is plotted as a summed Gaussian probability density function in Figure 28; this shows multiple peaks with a maximum density around offsets of 10 m. The next three most important density peaks correspond to offsets of 3-4 m, 6 m, and 16 m, while the remaining lower density peaks correspond to 2 m, 12 m, 13 m, and 25 m. Considering these peaks in ascending offsets, the 2 m and 3-4 m offset peaks should correspond to the most recent earthquake (event A) indicating the youngest event is characterized by displacements between ~2 and 4 m. The 6 m peak is approximately twice that of the younger event, suggesting the penultimate event B is characterized by displacements similar to those of event A. The 10 m peak corresponds approximately to three times the displacement of event A and should sum events A, B, and C displacements. The 12 m and 13 m peaks are very close and should correspond to the addition of an older fourth earthquake (possibly event D?). The 16 m peak would correspond to adding the displacements of a fifth earthquake. The next peak, which would be expected for some 20 m offsets, is not observed, there is only a subdued wide bump that could figure a sixth event, and then the last peak is for 25 m offsets, it may correlate with adding the displacement of a seventh earthquake. Thus, this plot suggests an average displacement per event of ~3 m. It is noteworthy that the denser peaks correspond to the best-preserved offsets of the three younger events. For peaks with offsets >10 m, the densities decrease significantly. The three younger earthquakes, events A, B, and C, occurred within the last ~7 ka; more specifically, the oldest event, C, which is younger than  $6.5 \pm 0.4$  ka, postdates, or could be approximately coeval with, the youngest regional incision event that represents the last landscape modification of the Holocene. This last incision is more recent than 7.4 ka (oldest possible age of sample NA-3 at site North) and was completed before 6.1 ka (youngest possibility for the base of unit 9w in the western section of the trench). Thus, the offsets related to earthquakes older than event C predate the last incision that modified the drainage network by ~7 ka, consequently, they should be much less well preserved than those of the younger events. We conclude that the ~3 m displacement per event for earthquakes A, B, and C (Figure 28) indicates that the magnitudes of these events were of at least  $M_w \sim 7$ .

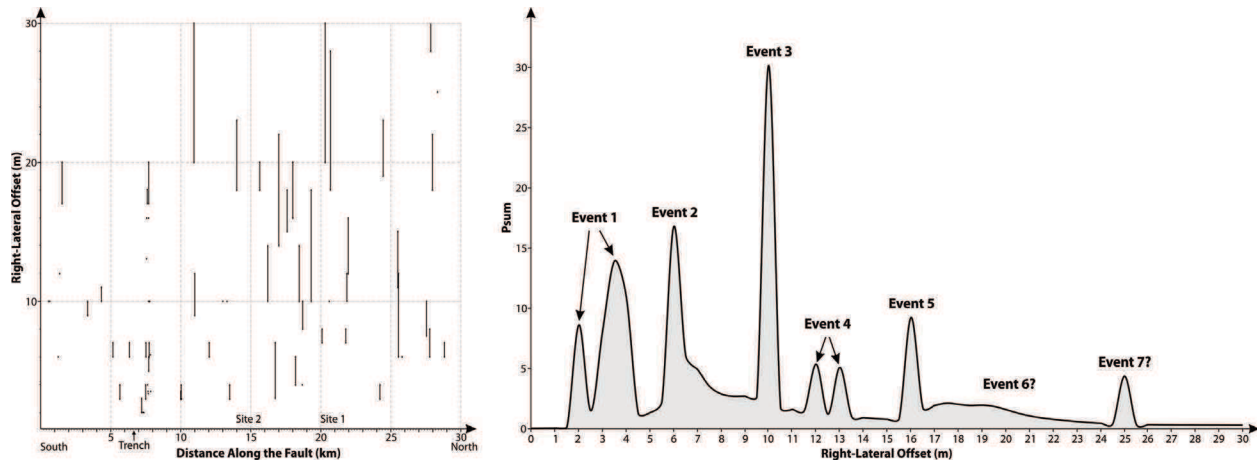


**Figure 28.** (Left) Distribution of the 67 measured right-lateral offsets smaller than 30 m extracted from database of Table A1 and plotted as a function of latitude along the 30-km-long stretch of the segment NA2 of the Nayband fault. Locations of the trench site and the sites North and South are indicated. (Right) Summed Gaussian probability density function of the plotted measured offset in (left) shows multiple peaks with a maximum density around 10 m. Each of the isolated peaks may correspond to a large paleoearthquake while the “bimodal” ones may result from a single seismic event (see text).

Although the amount of lateral displacement during an event is not accessible in a single trench, there are some additional indicators that one can use to estimate the magnitudes of the identified earthquakes. The event horizon of the penultimate and antepenultimate earthquakes (EH-B+C), near meter 12 is downthrown to the west by 20 cm during the most recent earthquake (event A; Figure 19b). Restoration of this vertical throw suggests a vertical displacement on the event horizon of the fourth paleoearthquake (EH-D) of more than a meter during events B+C. Taking into consideration that the Nayband fault is a primary strike-slip fault, one meter of vertical displacement should be associated with several meters of right-lateral displacement. Thus, the magnitude of the penultimate and antepenultimate earthquakes (events B and C) should be also on the order of  $M_w \sim 7$ , in agreement with their respective 3 m average displacement that can be proposed from geomorphic offset analysis (see previous paragraph).

The vertical displacement associated with event D is even larger than the ones for events B and C. Indeed, on the fault strand close to meter 9, the vertical throw of event D is on the order of 120 cm (Figures 19b and 27). This vertical displacement would also be compatible with several meters of right-lateral slip during event D and a magnitude of  $M_w \sim 7$  or greater. Such a magnitude would be in agreement with the prominent sand-filled feeder dikes and pillars

observed along the eastern trench exposures and sealed by event horizon D. If one takes into account the estimated vertical throws during events A, B, C, and D, this implies a total vertical displacement of approximately 200 cm during event E, distributed on several fault strands between meters 10 and 15 (see section 4.4). These observations suggest a magnitude  $M_w \sim 7$  or greater for the fifth paleoearthquake.

The estimates of the magnitude of events A, B, C, D, and E all suggest that the 65-km-long NA2 strike-slip fault segment can be expected to produce  $M_w \sim 7$  earthquakes, in agreement with the empirical relationships linking surface rupture lengths and moment magnitudes for strike-slip faults [*Wells and Coppersmith, 1994*].

## 5.2. The Most Recent Earthquake on the Nayband Fault Versus the Historical Records

The most recent of the paleoearthquakes found on the Nayband fault occurred during the last 800 years (i.e., after AD 1200) in a remote and uninhabited desert land. Although this event occurred during the time span covered by the historical seismic records [*Ambraseys and Melville, 1982; Ambraseys and Jackson, 1998; Berberian and Yeats, 1999*], none of the available catalogs provides evidence for an historical earthquake on the Nayband fault.

Either the earthquake has been unnoticed or it was reported with an inaccurately located epicenter, perhaps because of the anarchy prevailing during and after the Mongol invasions (from AD 1220 by the end of the Saljuq Empire until the fall of Baghdad in AD 1258 [e.g., *Boyle, 1968*]). The historical catalogs indicate that several large earthquakes occurred after AD 1200, to the north and northeast of the Nayband fault. To the north, five earthquakes occurred in AD 1209, AD 1251, AD 1270, AD 1389 and AD 1405, all located close to the city of Neyshabur, 400 km to the north of the Nayband fault. To the northeast, two earthquakes occurred in AD 1336 and AD 1549, in the cities of Khaf and Qa'en, 300 and 180 km to the northeast of the Nayband fault, respectively. All these events can be associated with active faults (Neyshabur fault system, Doruneh fault, and Sistan fault system) in the vicinity of their epicentral regions. The AD 1549 (Qa'en) earthquake, that closest to the Nayband fault, is related either to the Abiz fault [*Berberian and Yeats, 1999*] or to the North Birjand fault [*Berberian and Yeats, 2001*]. Thus, it is very unlikely that one of the known historical earthquakes in Central Iran can be associated to the Nayband fault; rather it is more likely that the earthquake that took place on the

fault within the last 800 years went unnoticed. This conclusion, combined with the fact that there are other strike-slip faults known to have produced destructive earthquakes with recurrence interval of several thousands of years in Central Iran [Nazari *et al.*, 2009; Fattahi *et al.*, 2010; Foroutan *et al.*, 2012] challenges the reliability of assessing the regional seismic hazard using historical seismic catalogs alone.

### 5.3. Implications for Seismic Hazard and Kinematics in Central and Eastern Iran

The first paleoseismic investigation ever conducted along the Nayband fault demonstrates the occurrence of several large, infrequent, and irregular earthquakes during MIS-1, and possibly part of MIS-2. Indeed, the fault hosted at least four large ( $M_w \sim 7$ ) earthquakes within the last  $17.4 \pm 1.3$  ka and two older earthquakes one probably before some 23 ka and another before  $70 \pm 5$  ka. The occurrences of three large earthquakes during the last  $\sim 7$  ka suggest that the Nayband fault can be characterized by a clustering of events; two events occurred close to  $6.6 \pm 0.3$  ka, separated by a maximum time interval of 1 ka, and the youngest earthquake (after AD 1200) is separated from the penultimate one by  $\sim 6$  ka. Although the most recent earthquake occurred less than 800 years ago, the long seismic cycle of some 6 ka preceding this most recent event may indicate the imminent threat of another large earthquake along the Nayband fault. This is compatible with the seismic clustering recorded over the last decades along the prolongation of the Nayband fault to the south. Indeed, overlapping segments of the Gowk fault hosted two destructive earthquakes within seventeen years by the end of the 20th century (the 1998 March 14,  $M_w$  6.6, Fandoqa earthquake [Berberian *et al.*, 2001; Fielding *et al.*, 2004] and the 1981 July 28,  $M_s$  7.1, Sirch earthquake [Berberian *et al.*, 1984]).

The data for the Nayband fault complement the paleoseismic information already available for the Central Iran Plateau (Figure 29). For the Dehshir fault [Nazari *et al.*, 2009], the most recent earthquake (EH-A) occurred shortly before  $2.0 \pm 0.2$  ka [Fattahi *et al.*, 2010]; the available historical seismic catalogs provide no evidence for an historical earthquake in the vicinity of the Dehshir fault. The revised OSL ages (green numbers on Figure 29b) indicate the Dehshir fault hosted at least three earthquakes within the last  $20.2 \pm 0.8$  ka. Considering of the age of the most recent event ( $2.0 \pm 0.2$  ka) yields an average recurrence interval of large earthquakes at most between 5700 and 6400 years. Similarly, the paleoseismic records of the Anar fault document the occurrence of at least three large earthquakes (EH-A, EH-B and EH-C

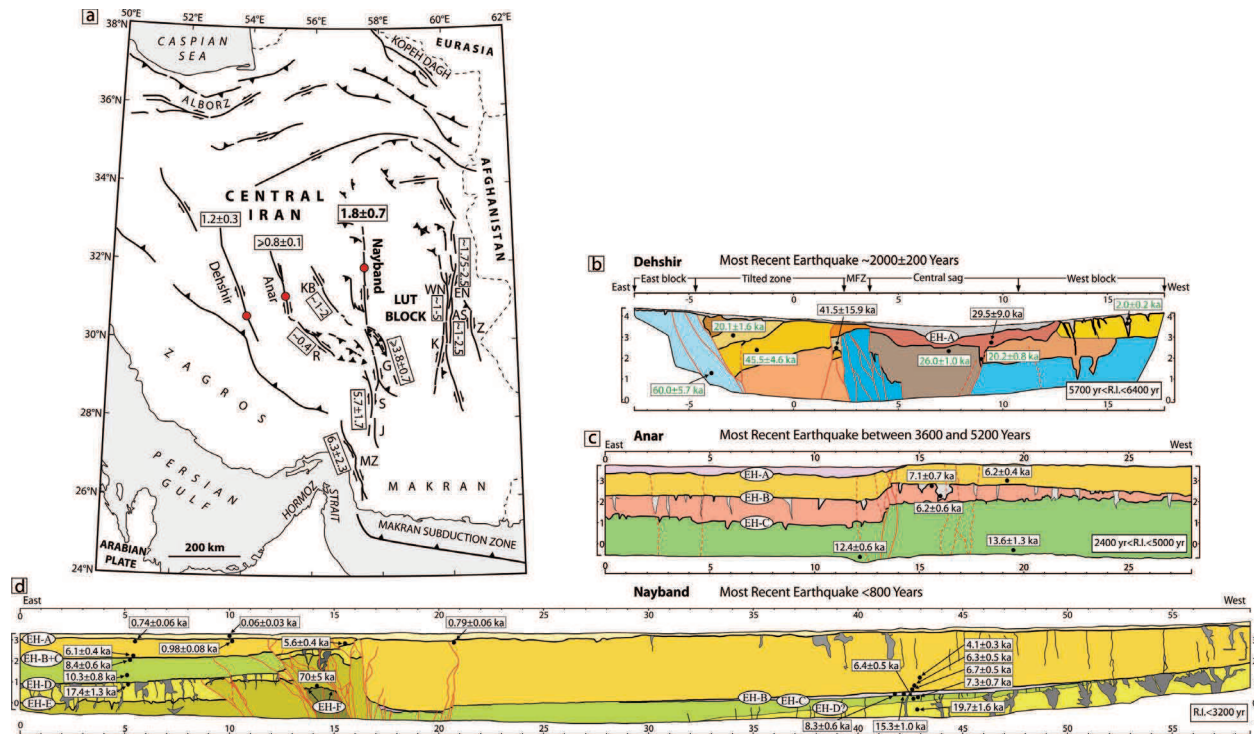


**Figure 29.** Summary of late Quaternary slip rates and paleoseismic data presently available across Central Iran. (a) Map of the major active faults in Central and Eastern Iran. AS, Assaghi fault; EN, East Neh fault; G, Gowk fault; J, Jiroft fault; K, Kahourak fault; KB, Kuh Banan fault; MZ, Minab-Zendan fault system; R, Rafsanjan fault; S, Sabzevaran fault; WN, West Neh fault; and Z, Zahedan fault. Numbers in boxes refer to right-slip rates averaged over the last 270 ka for the Dehshir fault [Le Dortz *et al.*, 2011], ~120 ka for the Rafsanjan fault [Fattahi *et al.*, 2011], ~120 ka for the Minab-Zandan fault system [Regard *et al.*, 2005], 100 ka for the Nayband fault [this study], ~42 ka for the Sabzevaran and Jiroft fault system [Regard *et al.*, 2005], 10 ka for the Anar fault [Le Dortz *et al.*, 2009; Foroutan *et al.*, 2012], ~8 ka for the Gowk [Walker *et al.*, 2010b], and estimated over the Holocene for the Kuh Banan [Allen *et al.*, 2011; Walker and Allen, 2012], West Neh, East Neh, and Assaghi [Meyer and Le Dortz, 2007] faults. Red circles locate paleoseismic sites along the Dehshir (b, modified from Nazari *et al.* [2009] with refined OSL ages indicated in green, see Table 3 of Le Dortz *et al.* [2011] for the OSL age parameters), Anar (c, Foroutan *et al.* [2012]), and Nayband faults (d, [this study]). Age of the most recent earthquake as well as the average recurrence interval of large earthquakes is indicated for each fault.

on Figure 29b) within the last 15 ka [Foroutan *et al.*, 2012]. There, the most recent earthquake occurred sometime between 3.6 and 5.2 ka ago, and the average recurrence interval of the large earthquakes ranges between 2.4 and 5 ka. It seems that large and infrequent earthquakes appear to typify the seismic behavior of the slow-slipping, intracontinental, strike-slip fault systems slicing Central and Eastern Iran. The limited data available, however, fail to document any distance interactions between the seismic behavior of the neighboring fault systems. Both the fact that the recurrence intervals on these faults exceed the time span covered by historical catalogs and the fact that some of these faults have produced large unrecorded earthquakes during the time span covered by these catalogs suggests caution in the regional seismic hazard assessment.

The observed geomorphic offset markers and their corresponding  $^{36}\text{Cl}$  and OSL ages provide the long-term slip rate of the Nayband fault averaged over the last 100 ka. This short-term geologic estimated slip rate of  $1.8 \pm 0.7 \text{ mm yr}^{-1}$  is consistent with the long-term geologic slip rates previously reported ( $1.5 \text{ mm yr}^{-1}$  [Walker and Jackson, 2002] and  $1.4 \pm 0.5 \text{ mm yr}^{-1}$  [Walker *et al.*, 2009]).

This rate matches with an overall late Pleistocene and Holocene right-slip rate along the western margin of the Lut block and along the transfer zone between Zagros and Makran decreasing from south to north (Figure 29a). This northward decrease (Minab-Zendan fault system,  $4.7 \pm 2.0 \text{ mm yr}^{-1}$  or  $6.3 \pm 2.3 \text{ mm yr}^{-1}$ , depending on the age attributed to the offset markers on the Zendan fault [Regard *et al.*, 2010]; Sabzevaran-Jiroft fault system,  $5.7 \pm 1.7 \text{ mm yr}^{-1}$  [Regard *et al.*, 2005]); Gowk,  $\geq 3.8 \pm 0.7 \text{ mm yr}^{-1}$  [Walker *et al.*, 2010b]; and Nayband,  $1.8 \pm 0.7 \text{ mm yr}^{-1}$  faults) appears consistent with the general pattern of the GPS horizontal velocities related to stable Eurasia (Figure 1b) [Vernant *et al.*, 2004]. By contrast, the long-term slip rate across the Lut block appears more difficult to reconcile with the available GPS data indicating a dextral shear of  $16 \pm 2 \text{ mm yr}^{-1}$  at the latitude of  $\sim 30.5^\circ\text{N}$  (difference between the vectors KERM and ZABO, Figure 1a). Extrapolating the present-day differential motion over the late Pleistocene and Holocene timescales, and accounting for the slip rates determined along the Nayband ( $1.8 \pm 0.7 \text{ mm yr}^{-1}$  [this study]) or Gowk ( $3.8 \pm 0.7 \text{ mm yr}^{-1}$  [Walker *et al.*, 2010b]) faults, would imply that the right-lateral strike-slip faults at the same latitudes but east of the Lut block (the West Neh, Kahourak, Assaghi, and Zahedan faults) should accommodate a minimum

dextral shear of 9.5 or 11.5 mm yr<sup>-1</sup>. On that timescale, and assuming the estimate of ~1-5 and ~1-2.5 mm yr<sup>-1</sup> averaged over the Holocene along the West Neh and Assaghi faults [Meyer and Le Dortz, 2007] are meaningful, such dextral shear rates would require cumulated slip rates across the Kahourak and Zahedan faults of at least 2 to 4 mm yr<sup>-1</sup> and at most 7.5 to 9.5 mm yr<sup>-1</sup>. A comprehensive geomorphological study, an interseismic interferometric study or a dense GPS network across the Sistan faults is necessary to help unravel the strain distribution “puzzle” in Eastern Iran.

### Acknowledgments

This study, conducted in the frame of Mohammad Foroutan PhD thesis, benefited of the logistic and financial assistance of the Geological Survey of Iran. Université Pierre et Marie Curie provided complementary funding for the fieldwork and the <sup>36</sup>Cl measurements. The <sup>36</sup>Cl measurements were performed at the ASTER AMS national facility supported by the INSU/CNRS, the French Ministry of Research and Higher Education, IRD, and CEA. OSL dating has been performed at the Nordic Laboratory for Luminescence Dating of Aarhus University. MF acknowledges a grant from the French Embassy in Tehran for part of his PhD thesis and complementary support from UPMC-ISTeP. Pierre-André Lhôte, Attaché Scientifique et Culturel, is thanked for his continuing support to the cooperation between UPMC and GSI. We thank R. Sohbaty and the technical staff at the Nordic Laboratory for Luminescence Dating for helping with OSL-measurements and acknowledge E. R. Engdahl for giving us access to his updated EHB catalog. A. Rashidi and M. Nazem Zadeh from Kerman GSI office helped with the logistics of the fieldwork. We thank M. Adhami, H. Bani Assadi, and H. Mokhtari for their safe driving in the field.

### References

Agard, P., Omrani, J., Jolivet, L., Mouthereau, F. (2005), Convergence history across Zagros (Iran): constraints from collisional and earlier deformation, *Int. J. Earth Sci.*, 94, 401-419.

- Agard, P., Omrani, J., Jolivet, L., Whitechurch, H., Vrielynck, B., Spakman, W., Monié, P., Meyer, B., and R. Wortel (2011), Zagros orogeny: a subduction-dominated process, *Geol. Mag.*, 148(5-6), 692-725.
- Aghanabati, A. (1974), Geological map of Tabas, Quadrangle *I7*, scale 1:250,000, Geol. Surv. of Iran, Tehran.
- Aghanabati, A. (1993), Geological map of Bam, Quadrangle *J11*, scale 1:250,000, Geol. Surv. of Iran, Tehran.
- Aitken, M. J. (1985), *Thermoluminescence Dating*, 359 pp., Academic Press, London.
- Aitken, M. J. (1998), *An Introduction to Optical Dating*, 267 pp., Oxford Univ. Press, Oxford.
- Alavi, M. (1991), Sedimentary and structural characteristics of the Paleo-Tethys remnants in northeastern Iran, *Geol. Soc. Am. Bull.*, 103, 983-992.
- Alavi-Naini, M., and Griffis, R. (1981a), Geological map of Naybandan, Quadrangle *J8*, scale 1:250,000, Geol. Surv. of Iran, Tehran.
- Alavi-Naini, M., and Griffis, R. (1981b), Geological map of Lakar Kuh, Quadrangle *J9*, scale 1:250,000, Geol. Surv. of Iran, Tehran.
- Allen, M. B., and H. A. Armstrong (2008), Arabia-Eurasia collision and the forcing of mid-Cenozoic global cooling, *Palaeogeogr., Palaeoclimatol., Palaeoecol.*, 265, 52-58.
- Allen, M., Jackson, J., and R. Walker (2004), Late Cenozoic reorganization of the Arabia-Eurasia collision and the comparison of short-term and long-term deformation rates, *Tectonics*, 23, TC2008, doi:10.1029/2003TC001530.
- Allen, M. B., Kheirikhah, M., Emami, M. H., and S. J. Jones (2011), Right-lateral shear across Iran and kinematic change in the Arabia-Eurasia collision zone, *Geophys. J. Int.*, 184, 555-574.
- Ambraseys, N. N., and J. A. Jackson (1998), Faulting associated with historical and recent earthquakes in the Eastern Mediterranean region, *Geophys. J. Int.*, 133, 390-406.

- Ambraseys, N., and C. Melville (1982), *A History of Persian Earthquakes*, 219 pp., Cambridge Univ. Press, Cambridge.
- Baker, C. (1993), Active seismicity and tectonics of Iran, *PhD thesis*, University of Cambridge, UK.
- Berberian, M. (1979a), Tabas-e-Golshan (Iran) catastrophic earthquake of 16 September 1978; a preliminary field report, *Disasters*, 2, 207-219.
- Berberian, M. (1979b), Earthquake faulting and bedding thrust associated with the Tabas-e-Golshan (Iran) earthquake of September 16, 1978, *Bull. Seismol. Soc. Am.*, 69, 1861-1887.
- Berberian, M., and G. C. P. King (1981), Towards a paleogeography and tectonic evolution of Iran, *Can. J. Earth Sci.*, 18, 210-265.
- Berberian, M., and M. Qorashi (1994), Coseismic fault-related folding during the South Golbaf earthquake of November 20, 1989, in southeast Iran, *Geology*, 22, 531-534.
- Berberian, M., and R. S. Yeats (1999), Patterns of historical earthquake rupture in the Iranian plateau, *Bull. Seismol. Soc. Am.*, 89(1), 120-139.
- Berberian, M., and R. S. Yeats (2001), Contribution of archaeological data to studies of earthquake history in the Iranian Plateau, *J. Struct. Geol.*, 23, 563-584.
- Berberian, M., Jackson, J. A., Qorashi, M., and M. H. Kadjar (1984), Field and teleseismic observations of the 1981 Golbaf-Sirch earthquakes in SE Iran, *Geophys. J. R. astr. Soc.*, 77, 809-838.
- Berberian, M., Jackson, J. A., Fielding, E., Parsons, B. E., Priestly, K., Qorashi, M., Talebian, M., Walker, R., Wright, T. J., and C. Baker (2001), The 1998 March 14 Fandoqa earthquake ( $M_w$  6.6) in Kerman province, southeast Iran: re-rupture of the 1981 Sirch earthquake fault, triggering of slip on adjacent thrusts and the active tectonics of the Gowk fault zone, *Geophys. J. Int.*, 146, 371-398.

- Besse, J., Torcq, F., Gallet, Y., Ricou, L. E., Krystyn, L., and A. Saidi (1998), Late Permian to Late Triassic palaeomagnetic data from Iran: constraints on the migration of the Iranian block through the Tethyan Ocean and initial destruction of Pangaea, *Geophys. J. Int.*, *135*, 77-92.
- Bonilla, M. G., and J. J. Lienkaemper (1990), Visibility of fault strands in exploratory trenches and timing of rupture events, *Geology*, *18*, 153-156.
- Bøtter-Jensen, L., Thomsen, K. J., Jain, M. (2010), Review of optically stimulated luminescence (OSL) instrumental developments for retrospective dosimetry, *Radiat. Meas.*, *45*, 253-257.
- Boulin, J. (1988), Hercynian and Eocimmerian events in Afghanistan and adjoining regions, *Tectonophysics*, *148*, 253-278.
- Boyle, J. A., (1968), *The Cambridge History of Iran*, vol. 5: *The Saljuq and Mongol periods*, 763 pp., Cambridge Univ. Press, Cambridge.
- Braucher, R., Merchel, S., Borgomano, J., Bourlès, D. L. (2011), Production of cosmogenic radionuclides at great depth: A multi element approach, *Earth Planet. Sci. Lett.*, *309*, 1-9.
- Brown, E. T., Molnar, P., Bourlès, D. L. (2005), Comment on “Slip-rate measurements on the Karakorum fault may imply secular variations in fault motion”, *Science*, *309*, 1326, doi:10.1126/science.1112508.
- Camp, V. E., and R. J. Griffis (1982), Character, genesis and tectonic setting of igneous rocks in the Sistan suture zone, eastern Iran, *Lithos*, *3*, 221-239.
- Clark, P. U., Dyke, A. S., Shakun, J. D., Carlson, A. E., Clark, J., Wohlfarth, B., Mitrovica, J. X., Hostetler, S. W., McCabe, A. M. (2009), The Last Glacial Maximum, *Science*, *325*, 710-714.
- Cutler, K. B., Edwards, R. L., Taylor, F. W., Chen, H., Adkins, J., Gallup, C. D., Cutler, P. M., Burr, G. S., Bloom, A. L. (2003), Rapid sea-level fall and deep-ocean temperature change since the last interglacial period, *Earth Planet. Sci. Lett.*, *206*, 253-271.
- Dehghani, G. A., and J. Makris (1984), The gravity field and crustal structure of Iran, *N. Jb. Geol. Paläont. Abh.*, *168*, 215-229.

- Desilets, D., Zreda, M., Almasi, P. F., Elmore, D. (2006), Determination of cosmogenic  $^{36}\text{Cl}$  in rocks by isotope dilution: innovations, validation and error propagation, *Chem. Geol.*, 233, 185-195.
- Engdahl, E. R., van der Hilst, R., and R. Buland (1998), Global teleseismic earthquake relocation with improved travel times and procedures for depth determination, *Bull. Siesmol. Soc. Am.*, 88(3), 722-743.
- Engdahl, E. R., Jackson, J. A., Myers, A. C., Bergman, E. A., and K. Priestley (2006), Relocation and assessment of seismicity in the Iran region, *Geophys. J. Int.*, 167, 761-778.
- Fattahi, M., Nazari, H., Bateman, M. D., Meyer, B., Sébrier, M., Talebian, M., Le Dortz, K., Foroutan, M., Ahmadi Givi, F., Ghorashi, M. (2010), Refining the OSL age of the last earthquake ob the Dheshir fault, Central Iran, *Quat. Geochronol.*, 5, 286-292, doi:10.1016/j.quageo.2009.04.005.
- Fattahi, M., Walker, R. T., Talebian, M., Sloan, R. A., and A. Rashidi (2011), The structure and late Quaternary slip rate of the Rafsanjan strike-slip fault, SE Iran, *Geosphere*, 7(5), 1159-1174.
- Fielding, E. J., Wright, T. J., Muller, J., Parsons, B. E., Walker, R. (2004), Aseismic deformation of a fold-and-thrust belt imaged by synthetic aperture radar interferometry near Shahdad, southeast Iran, *Geology*, 32(7), 577-580.
- Foroutan, M., Sébrier, M., Nazari, H., Meyer, B., Fattahi, M., Rashidi, A., Le Dortz, k., and M. D. Bateman (2012), New evidence for large earthquakes on the Central Iran plateau: palaeoseismology of the Anar fault, *Geophys. J. Int.*, 189(1), 6-18, doi:10.1111/j.1365-246X.2012.05365.x.
- Frankel, K. L., and J. F. Dolan (2007), Characterizing arid region alluvial fan surface roughness with airborne laser swath mapping digital topographic data, *J. Geophys. Res.*, 112, F02025, doi:10.1029/2006JF000644.
- Gosse, J. C., Phillips, F. M. (2001), Terrestrial in situ cosmogenic nuclides: theory and application, *Quat. Sci. Rev.*, 20, 1475-1560.

- Groottes, P. M., and M. Stuiver (1997), Oxygen 18/16 variability in Greenland snow and ice with  $10^{-3}$ - to  $10^5$ -year time resolution, *J. Geophys. Res.*, *102*(C12), 24,455-26,470.
- Guérin, G., Mercier, N., and G. Adamiec (2011), Dose-rate conversion factors: update, *Ancient TL*, *29*(1), 5-8.
- Hollingsworth, J., Jackson, J., Walker, R., Nazari, H. (2008), Extrusion tectonics and subduction in the eastern South Caspian region since 10 Ma, *Geology*, *36*(10), 763-766, doi:10.1130/G25008A.1.
- Karagaranbafghi, F., Foeken, J. P. T., Guest, B., Stuart, F. M. (2012), Cooling history of the Chapedony metamorphic core complex, Central Iran: Implications for the Eurasia-Arabia collision, *Tectonophysics*, *524-525*, 100-107.
- Kluyver, H. M., Tirrul, R., Chance, P. N., Johns, G. W., and H. M., Meixner (1983), Explanatory text of the Naybandan Quadrangle map, Quadrangle *J8*, scale 1:250,000, Geol. Surv. of Iran, Tehran.
- Lambeck, K., Yokoyama, Y., Purcell, T. (2002), Into and out of the Last Glacial Maximum: sea-level change during Oxygen Isotope Stages 3 and 2, *Quat. Sci. Rev.*, *21*, 343-360.
- Le Dortz, K., Meyer, B., Sébrier, M., Nazari, H., Braucher, R., Fattahi, M., Benedetti, L., Foroutan, M., Siame, L., Bourlès, D., Talebian, M., Bateman, M. D., and M. Ghorraishi (2009), Holocene right-slip rate determined by cosmogenic and OSL dating on the Anar fault, Central Iran, *Geophys. J. Int.*, *179*, 700-710.
- Le Dortz, K., Meyer, B., Sébrier, M., Braucher, R., Nazari, H., Benedetti, L., Fattahi, M., Bourlès, D., Foroutan, M., Siame, L., Rashidi, A., and M. D. Bateman (2011), Dating inset terraces and offset fans along the Dehshir Fault (Iran) combining cosmogenic and OSL methods, *Geophys. J. Int.*, *185*, 1147-1174.
- Le Dortz, K., Meyer, B., Sébrier, M., Braucher, R., Bourlès, D., Benedetti, L., Nazari, H., Foroutan, M. (2012), Interpreting scattered *in-situ* produced cosmogenic nuclide depth-profile data, *Quat. Geochronol.*, *11*, 98-115.

- Li, S.-H. (1994), Optical dating: insufficiently bleached sediments, *Radiat. Meas.*, 23(2/3), 563-567.
- Mahdavi, M. A. (1996), Geological map of Ravar, Quadrangle 19, scale 1:250,000, Geol. Surv. of Iran, Tehran.
- Masson, F., Chéry, J., Hatzfeld, D., Martinod, J., Vernant, P., Tavakoli, F., and M. Ghafory-Ashtiani (2005), Seismic versus aseismic deformation in Iran inferred from earthquakes and geodetic data, *Geophys. J. Int.*, 160, 217-226.
- Masson, F., Anvari, M., Djamour, Y., Walpersdorf, A., Tavakoli, F., Daignières, M., Nankali, H., and S. Van Gorp (2007), Large-scale velocity field and strain tensor in Iran inferred from GPS measurements: new insight for the present-day deformation pattern within NE Iran, *Geophys. J. Int.*, 170, 436-440.
- McQuarrie, N., Stock, J. M., Verdel, C., and B. P. Wernicke (2003), Cenozoic evolution of Neotethys and implications for the causes of plate motions, *Geophys. Res. Lett.*, 30(20), 2036, doi:10.1029/2003GL017992.
- Mériaux, A.-S., Tapponnier, P., Ryerson, F. J., Xiwei, X., King, G., Van der Woerd, J., Finkel, R. C., Haibing, L., Caffee, M. W., Zhiqin, X., and C. Wenbin (2005), The Aksay segment of the northern Altyn Tagh fault: Tectonic geomorphology, landscape evolution, and Holocene slip rate, *J. Geophys. Res.*, 110, B04404, doi:10.1029/2004JB003210.
- Meyer, B., and K. Le Dortz (2007), Strike-slip kinematics in Central and Eastern Iran: Estimating fault slip-rates averaged over the Holocene, *Tectonics*, 26, TC5009, doi:10.1029/2006TC002073.
- Murray, A. S., and J. M. Olley (2002), Precision and accuracy in the optically stimulated luminescence dating of sedimentary quartz: a status review, *Geochronometria*, 21, 1-16.
- Murray, A. S. and A. G. Wintle (2000), Luminescence dating of quartz using an improved single-aliquot regenerative-dose protocol, *Radiat. Meas.*, 32, 57-73.
- Murray, A. S. and A. G. Wintle (2003), The single aliquot regenerative dose protocol: potential for improvements in reliability, *Radiat. Meas.*, 37, 377-381.

- Murray, A. S., Marten, R., Johnston, A., Martin, P. (1987), Analysis for naturally occurring radionuclides at environmental concentrations by gamma spectrometry, *J. Radioanal. Nucl. Chem. Art.*, 115(2), 263-288.
- Murray, A. S., Thomsen, K. J., Masuda, N., Buylaert, J. P., Jain, M. (2012), Identifying well-bleached quartz using the different bleaching rates of quartz and feldspar luminescence signals, *Radiat. Meas.*, 47, 688-696.
- Muttoni, G., Mattei, M., Balini, M., Zanchi, A., Gaetani, M., and F. Berra (2009), The drift history of Iran from the Ordovician to the Triassic, in *South Caspian to Central Iran Basins*, edited by Brunet., M. -F., Wilmsen, M., and J. W. Granath, *Geol. Soc. Lond. Spec. Publ.*, 312, 7-29.
- Nalbant, S. S., Steacy, S., and J. McCloskey (2006), Stress transfer relations among the earthquakes that occurred in Kerman province, southern Iran since 1981, *Geophys. J. Int.*, 167, 309-318, doi:10.1111/j.1365-246X.2006.03119.x.
- Nazari, H., Fattahi, M., Meyer, B., Sébrier, M., Talebian, M., Foroutan, M., Le Dortz, K., Bateman, M. D., and M. Ghorashi (2009), First evidence for large earthquakes on the Deshir Fault, Central Iran Plateau, *Terra Nova*, 21, 417-426, doi:10.1111/j.1365-3121.2009.00892.x.
- NIOC (1977), Geological map of Iran, *Sheet 6, south-east Iran*, scale 1:1,000,000, Natl. Iran. Oil Co., Explor. and Prod., Tehran.
- Olley, J. M., Caitcheon, G. G., Roberts, R. G. (1999), The origin of dose distributions in fluvial sediments, and the prospect of dating single grains from fluvial deposits using optically stimulated luminescence, *Radiat. Meas.*, 30, 207-217.
- Peltzer, G., Tapponnier, P., Gaudemer, Y., Meyer, B., Guo, S., Yin, K., Chen, Z., and H. Dai (1988), Offsets of late Quaternary morphology, rate of slip, and recurrence of large earthquakes on the Chang Ma fault (Gansu, China), *J. Geophys. Res.*, 93, 7793-7812.
- Phillips, W. M., Sloan, V. F., Shroder Jr., J. F., Sharma, P., Clarke, M. L., Rendell, H. M. (2000), Asynchronous glaciation at Nanga Parbat, northwestern Himalaya Mountains, Pakistan, *Geology*, 28(5), 431-434.

- Prescott, J. R., and J. T. Hutton (1994), Cosmic ray contributions to dose rates for luminescence and ESR dating: large depths and long-term time variations, *Radiat. Meas.*, 23(2/3), 497-500.
- Regard, V., Bellier, O., Thomas, J. -C., Bourlès, D., Bonnet, S., Abbassi, M. R., Braucher, R., Mercier, J., Shabanian, E., Soleymani, Sh., and Kh. Feghhi (2005), Cumulative right-lateral fault slip rate across the Zagros-Makran transfer zone: role of the Minab-Zendan fault system in accommodation Arabia-Eurasia convergence in southeast Iran, *Geophys. J. Int.*, 162, 177-203.
- Regard, V., Hatzfeld, D., Molinaro, M., Aubourg, C., Bayer, R., Bellier, O., Yamini-Fard, F., Peyret, M., and M. Abbassi (2010), The transition between Makran subduction and the Zagros collision: recent advances in its structure and active deformation, in *Tectonic and Stratigraphic Evolution of Zagros and Makran during the Mesozoic-Cenozoic*, edited by Leturmy, P., and Robin, C., *Geol. Soc. Lond. Spec. Publ.*, 330, 43-64.
- Rizza, M., Mahan, S., Ritz, J.-F., Nazari, H., Hollingsworth, J., Salamati, R. (2011a), Using luminescence dating of coarse matrix material to estimate the slip rate of the Astaneh fault, Iran, *Quat. Geochronol.*, 6, 390-406.
- Rizza, M., Ritz, J.-F., Braucher, R., Vassallo, R., Prentice, C., Mahan, S., McGill, S., Chauvet, A., Marco, S., Todbileg, M., Demberel, S., and D. Bourlès (2011b), Slip rate and slip magnitudes of past earthquakes along the Bogd left-lateral strike-slip fault (Mongolia), *Geophys. J. Int.*, 186, 897-927.
- Sahandi, M. R. (1992), Geological map of Kerman, Quadrangle *J10*, scale 1:250,000, Geol. Surv. of Iran, Tehran.
- Schimmelpfennig, I., Benedetti, L., Finkel, R., Pik, R., Blard, P.-H., Bourlès, D., Burnard, P., Williams, A. (2009), Sources of in-situ  $^{36}\text{Cl}$  in basaltic rocks. Implication for calibration of production rates, *Quat. Geochronol.*, 4, 441-461, doi:10.1016/j.quageo.2009.06.003.
- Schimmelpfennig, I., Benedetti, L., Garreta, V., Pik, R., Blard, P.-H., Burnard, P., Bourlès, D., Finkel, R., Ammon, K., Dunai, T. (2011), Calibration of cosmogenic  $^{36}\text{Cl}$  production rates from Ca and K spallation in lava flows from Mt. Etna (38°N, Italy) and Payun Matru (36°S, Argentina), *Geochim. Cosmochim. Acta*, 75, 2611-2632.

- Sieh, K. E., and Jahns, R. H. (1984), Holocene activity of the San Andreas fault at Wallace Creek, California, *Geol. Soc. Am. Bull.*, 95, 883-896.
- Soheili, M. (1995), Geological map of Sirjan, Quadrangle III, scale 1:250,000, Geol. Surv. of Iran, Tehran.
- Staubwasser, M., Sirocko, F., Grootes, P.M., and M. Segl (2003), Climate change at the 4.2 ka BP termination of the Indus valley civilization and Holocene south Asian monsoon variability, *Geophys. Res. Lett.*, 30(8), 1425, doi:10.1029/2002GL016822.
- Stöcklin, J., and Nabavi, M. H. (1969), Geological map of Boshruyeh, Quadrangle J7, scale 1:250,000, Geol. Surv. of Iran, Tehran.
- Stone, J. O., Allan, G. L., Fifield, L. K., and R. G. Cresswell (1996), Cosmogenic chlorine-36 from calcium spallation, *Geochim. Cosmochim. Acta*, 60(4), 679-692.
- Stone, J. O., Evans, J. M., Fifield, L. K., Allan, G. L., and R. G. Cresswell (1998), Cosmogenic chlorine-36 production in calcite by muons, *Geochim. Cosmochim. Acta*, 62(3), 433-454.
- Talebian, M., Biggs, J., Bolourchi, M., Copley, A., Ghassemi, A., Ghorashi, M., Hollingsworth, J., Jackson, J., Nissen, E., Oveisi, B., Parsons, B., Priestley, K., and A. Saiidi (2006), The Dahuiyeh (Zarand) earthquake of 2005 February 22 in central Iran: reactivation of an intramountain reverse fault, *Geophys. J. Int.*, 164, 137-148.
- Tirrul, R., Bell, I. R., Griffis, R. J., and V. E. Camp (1983), The Sistan suture zone of eastern Iran, *Geol. Soc. Am. Bull.*, 94, 134-150.
- Vahdati Daneshmand, F. (1992), Geological map of Rafsanjan, Quadrangle II0, scale 1:250,000, Geol. Surv. of Iran, Tehran.
- Van Der Woerd, J., Tapponnier, P., Ryerson, F. J., Meriaux, A.-S., Meyer, B., Gaudemer, Y., Finkel, R. C., Caffee, M. W., Guoguang, Z., and X. Zhiqin (2002), Uniform postglacial slip-rate along the central 600 km of the Kunlun Fault (Tibet), from  $^{36}\text{Al}$ ,  $^{10}\text{Be}$ , and  $^{14}\text{C}$  dating of riser offsets, and climatic origin of the regional morphology, *Geophys. J. Int.*, 148, 356-388.

- Vassallo, R., Ritz, J.-F., Braucher, R., Jolivet, M., Carretier, S., Larroque, C., Chauvet, A., Sue, C., Todbileg, M., Bourlès, D., Arzhannikova, A., and S. Arzhannikov (2007), Transpressional tectonics and stream terraces of the Gobi-Altay, Mongolia, *Tectonics*, 26, TC5013, doi:10.1029/2006TC002081.
- Vernant, Ph., Nilforoushan, F., Hatzfeld, D., Abbassi, M. R., Vigny, C., Masson, F., Nankali, H., Martinod, J., Ashtiani, A., Bayer, R., Tavakoli, F., and J. Chéry (2004), Present-day crustal deformation and plate kinematics in the Middle East constrained by GPS measurements in Iran and northern Oman, *Geophys. J. Int.*, 157, 381-398.
- Walker, F., and M. B. Allen (2012), Offset rivers, drainage spacing and the record of strike-slip faulting: The Kuh Banan Fault, Iran, *Tectonophysics*, 530-531, 251-263.
- Walker, R., and J. Jackson (2002), Offset and evolution of the Gowk fault, S.E. Iran: a major intra-continental strike-slip system, *J. Struct. Geol.*, 24, 1677-1698.
- Walker, R., and J. Jackson (2004), Active tectonics and late Cenozoic strain distribution in central and eastern Iran, *Tectonics*, 23, TC5010, doi:10.1029/2003TC001529.
- Walker, R., Jackson, J., and C. Baker (2003), Surface expression of thrust faulting in eastern Iran: source parameters and surface deformation of the 1978 Tabas and 1968 Ferdows earthquake sequences, *Geophys. J. Int.*, 152, 749-765.
- Walker, R. T., Gans, P., Allen, M. B., Jackson, J., Khatib, M., Marsh, N., and M. Zarrinkoub (2009), Late Cenozoic volcanism and rates of active faulting in eastern Iran, *Geophys. J. Int.*, 177, 783-805.
- Walker, R. T., Talebian, M., Saiffori, S., Sloan, R. A., Rashidi, A., MacBean, N., Ghassemi, A. (2010a), Active faulting, earthquakes, and restraining bend development near Kerman city in southeastern Iran, *J. Struct. Geol.*, 32, 1046-1060.
- Walker, R. T., Talebian, M., Sloan, R. A., Rashidi, A., Fattahi, M., and C. Bryant (2010b), Holocene slip-rate on the Gowk strike-slip fault and implications for the distribution of tectonic strain in eastern Iran, *Geophys. J. Int.*, 181, 221-228.

- Walker, R. T., Khatib, M. M., Bahroudi, A., Rodés, A., Schnabel, C., Fattahi, M., Talebian, M., Bergman, E. (2013), Co-seismic, geomorphic, and geologic fold growth associated with the 1978 Tabas-e-Golshan earthquake fault in eastern Iran, *Geomorphology*, <http://dx.doi.org/10.1016/j.geomorph.2013.02.016>.
- Wallinga, J. (2001), The Rhine-Meuse system in a new light: optically stimulated luminescence dating and its application to fluvial deposits, *PhD thesis*, 180 pp., Faculty of Geographical Sciences, Utrecht University, Utrecht, Netherlands.
- Weldon, R. J., and Sieh, K. E. (1985), Holocene rate of slip and tentative recurrence interval for large earthquakes on the San Andreas fault, Cajon Pass, southern California, *Geol. Soc. Am. Bull.*, *96*, 793-812.
- Wellman, H. W., (1966), Active wrench faults of Iran, Afghanistan and Pakistan, *Geol. Rundsch.*, *55*(3), 716-735.
- Wells, D. L., and K. J. Coppersmith (1994), New empirical relationships among magnitude, rupture length, rupture width, rupture area, and surface displacement, *Bull. Seismol. Soc. Am.*, *84*(4), 974-1002.
- Zanchi, A., Zanchetta, S., Garzanti, E., Balini, M., Berra, F., Mattei, M., and G. Muttoni (2009), The Cimmerian evolution of the Nakhlak-Anarak area, Central Iran, and its bearing for the reconstruction of the history of the Eurasian margin, in *South Caspian to Central Iran Basins*, edited by Brunet, M.-F., Wilmsen, M., and J. W. Granath, *Geol. Soc. Lond. Spec. Publ.*, *312*, 261-286.
- Zreda, M. G., Phillips, F. M., Elmore, D., Kubik, P. W., Sharma, P., and R. I. Dorn (1991), Cosmogenic chlorine-36 production rates in terrestrial rocks, *Earth Planet. Sci. Lett.*, *105*, 94-109.

**Table A1.** Locations and corresponding measurements of geomorphic offsets marked by black crosses in Figure 11, arranged sequentially by latitude from north to south. The minimum and maximum bounds of the offsets denote uncertainties in the measurements. The uncertainties are mostly due to definition of the piercing points and to the resolution of Quickbird imagery (pixel size 60 x 60 cm), when the smallest offsets were not accessible in the field and measured on the imagery.

No.	Latitude	Longitude	Dextral Offset Minimum (m)	Dextral Offset Maximum (m)	No.	Latitude	Longitude	Dextral Offset Minimum (m)	Dextral Offset Maximum (m)
1	32.11182	57.51995	6	7	45	31.98376	57.52771	275	315
2	32.10752	57.52063	25	25	46	31.97815	57.52655	18	23
3	32.10430	57.52093	18	22	47	31.97359	57.52788	3	4
4	32.10294	57.52108	28	34	48	31.97197	57.52806	10	10
5	32.10250	57.52118	6	8	49	31.96970	57.52824	10	10
6	32.10030	57.52132	7	10	50	31.96127	57.52867	6	7
7	32.09710	57.52163	30	40	51	31.95131	57.52915	9	12
8	32.08464	57.52211	6	6	52	31.95089	57.52915	20	30
9	32.08453	57.52212	6	6	53	31.94250	57.52955	3	3
10	32.08238	57.52221	6	12	54	31.94233	57.52956	3	4
11	32.08194	57.52218	11	15	55	31.94207	57.52956	3	3.5
12	32.07233	57.52263	19	23	56	31.92264	57.53121	160	190
13	32.07021	57.52212	3	4	57	31.92256	57.52937	3.5	3.5
14	32.06887	57.52288	110	140	58	31.92241	57.52939	6.2	6.2
15	32.06844	57.52217	80	110	59	31.92213	57.52944	10	10
16	32.06760	57.52277	60	80	60	31.92198	57.52947	10	10
17	32.05249	57.52389	65	75	61	31.92174	57.52948	6	7
18	32.05003	57.52392	12	16	62	31.92161	57.52951	5	6
19	32.04905	57.52400	10	12	63	31.92127	57.52957	18	20
20	32.04830	57.52402	7	8	64	31.92112	57.52957	16	16
21	32.04743	57.52408	70	85	65	31.92106	57.52961	10	10
22	32.04157	57.52441	35	45	66	31.92087	57.52963	3.3	3.3
23	32.03842	57.52467	20	30	67	31.92081	57.52963	3.5	3.5
24	32.03778	57.52466	8	10	68	31.92067	57.52966	4	4
25	32.03521	57.52492	20	30	69	31.92046	57.52971	17	18
26	32.03305	57.52496	7	8	70	31.92026	57.52968	16	16
27	32.02610	57.52548	10	18	71	31.91992	57.52970	13	13
28	32.02062	57.52561	8	10	72	31.91967	57.52975	3	4
29	32.02039	57.52562	4	4	73	31.91949	57.52975	6	7
30	32.01831	57.52547	10	14	74	31.91840	57.52979	2	2
31	32.01796	57.52555	70	90	75	31.91761	57.52981	2	2
32	32.01662	57.52565	50	65	76	31.91696	57.52989	2	3
33	32.01599	57.52561	4	6	77	31.91474	57.53021	30	40
34	32.01498	57.52558	16	20	78	31.91279	57.53050	250	300
35	32.01067	57.52591	15	18	79	31.90890	57.53072	6	7
36	32.00900	57.52594	70	90	80	31.90255	57.53112	3	4
37	32.00525	57.52633	14	22	81	31.89846	57.53099	6	7
38	32.00427	57.52641	30	40	82	31.89109	57.53126	9	10
39	32.00294	57.52659	3	7	83	31.88214	57.53201	8	9
40	31.99816	57.52693	10	14	84	31.86579	57.53491	17	20
41	31.99299	57.52715	18	20	85	31.86410	57.53522	12	12
42	31.99101	57.52737	60	70	86	31.86321	57.53540	6	6
43	31.98540	57.52743	115	135	87	31.85796	57.53670	10	10
44	31.98469	57.52752	180	210	88	31.85736	57.53679	10	10



## CHAPTER 5

# GENERAL DISCUSSION,

# CONCLUSIONS & PERSPECTIVES

---

This dissertation has investigated the role of major active, N-striking, strike-slip faults slicing Central Iran. The right-slip rates and the seismic behavior of these right-lateral strike-slip faults have been investigated over the late Pleistocene and Holocene timescales. The results of this study provide a better understanding of the patterns of strain accumulation and strain release along these major strike-slip faults. The main results are summarized and their implications are discussed throughout this chapter with emphasis on the timing of the latest alluvial fan emplacement and the most recent regional incision in Central Iran (section 5.1), the geologic slip rates of the Dehshir, Anar, and Nayband strike-slip faults over the late Pleistocene and Holocene (section 5.2), the seismic behavior of these strike-slip faults over the last seismic cycles (section 5.3), the paleoseismic records versus the available historical seismic catalogs (section 5.4), and the geologic slip rates of these faults versus the geodetic rates of deformation (section 5.5). Finally, studies in progress and some perspectives are given at the end of this chapter (section 5.6).

### 5.1. Timing of latest alluvial fan emplacement and most recent incision in Central Iran

The most recent regional alluvial aggradation and the subsequent incision form young geomorphic markers which can be offset by fault motions and record slip history of a given fault over several seismic cycles. Knowledge of the timing of such climatic events has important implication for estimating slip rate along active faults. The timing of the regional phases of alluvial fan emplacements is often related to global climate changes as alternations of glacial and interglacial periods. This tuning between regional alluviations and climate evolution has been extensively investigated in North America, the Andes, Alps, Himalayas, Tibet, and Mediterranean regions (e.g., *Armijo et al.*, 1986, 1991; *Wells et al.*, 1987; *Knox*, 1993, 2000; *Goodbred Jr and Kuehl*, 2000; *Owen et al.*, 2002; *Pratt et al.*, 2002; *Van Der Woerd et al.*, 2002; *Zheng et al.*, 2002; *Pan et al.*, 2003; *Mayewski et al.*, 2004; *Bookhagen et al.*, 2005; *Bridgland and Westaway*, 2008; *Lu et al.*, 2010; *Mueller et al.*, 2012). In most cases, the latest phase of regional incision has been related to the shift between the last glacial period and the onset of the Holocene global warming. This is also the case in Iran where several geomorphic studies attempted to relate the recent incision of the latest generation of alluvial fans to the onset of Holocene ( $12 \pm 2$  ka) (*Walker and Jackson*, 2004; *Meyer et al.*, 2006; *Meyer and Le Dortz*, 2007). This first-order reasoning has been further tested using absolute dating of alluvial fans in several places across the Central Iran Plateau. Cosmogenic  $^{10}\text{Be}$  and OSL dating of alluvial fans in the regions of Anar and Dehshir have shown that the most recent alluvial aggradation is a little younger than the onset of Holocene and that these alluvial fans have been further incised. In the Anar (*Le Dortz et al.*, 2009) and Dehshir (*Le Dortz et al.*, 2011) regions, aggradation of the recent alluvial fans was still active at least until 9.4 and 10.6 ka, respectively, and these authors concluded that the last regional incision occurred after 9.4 ka. Moreover, comparing these ages with the onset of the regional pluvial episodes of the early-middle Holocene evidenced in Northern Oman (*Burns et al.*, 2001) they suggested that the regional incision in Central Iran has more likely occurred between 6 and 10.5 ka. *Walker and Fattahi* (2011) by reviewing the geomorphic and chronologic data available in Central and Eastern Iran proposed a late Pleistocene and Holocene regional climate scenario. In this model, the most recent alluvial fan systems have been emplaced during the early Holocene between  $\sim 7$  and 9 ka, which was later followed by a regional incision  $\sim 5$  ka.

The results presented in this dissertation help to place more robust constraints on the regional climate scenario using refined and additional OSL ages in the Anar region and additional dating along the Nayband fault. Along the Anar fault, the major phase of aggradation of the last generation of alluvial fans has been confirmed to be still active until 9.5 ka, but a secondary phase of alluviation postdating 7.8 ka has been characterized (*Foroutan et al.*, 2012). This latter alluviation in the Anar region is coincident with the emplacement of the youngest alluvial fan surfaces some 230-km farther east along the Nayband fault. There, the aggradation of the most recent alluvial fans lasted at most until 7.4 ka (the oldest possible age of the youngest sample collected from the most recent fans,  $6.8 \pm 0.6$  ka). This last aggradation was later followed by a regional incision that should have started at most 7.4 ka and at least 6.2 ka ago. The latter age is also compatible with the onset of the latest continuous record of sediments ponded nearby the Nayband trench by 6.1 ka.

The time range between the last alluvial fans aggradation (7.4 ka) and the youngest possibility for the most recent incision (6.1 ka) is comparable with the ages of earthquake-induced liquefaction features (e.g., sand blow, sandy dike, and pillar; ~6-7 ka) both in the Anar and Nayband trenches. In the Anar trench, the liquefaction features associated with the penultimate earthquake are dated between  $6.2 \pm 0.6$  and  $7.1 \pm 0.7$  ka. In the Nayband trench, the age of the liquefied features that correspond to the third paleoearthquake is bracketed between  $6.5 \pm 0.4$  and  $6.7 \pm 0.4$  ka. These features testify for the presence of shallow water table at the time of the corresponding earthquakes (e.g., *Obermeier*, 1996), likely as a consequence of maximum precipitations during the Holocene optimum (e.g., *Wen et al.*, 2010). These ages are also compatible with the last aggradation of the South Golbaf lake deposits, where youngest dated sediments yielded an age of  $6.3 \pm 0.2$  ka (*Fattahi et al.*, 2013). One can also notice that the distributed desiccation cracks in the Nayband trench occurred just before  $4.1 \pm 0.3$  ka and might relate to very low level of annual average precipitation most likely as a result of the late Holocene drought cycles following 4.2 ka (*Staubwasser et al.*, 2003).

In addition, the offset distribution pattern of the young geomorphic features along the Nayband fault provides another line of evidence for the timing of the most recent incision. Plotting the summed Gaussian probability density function (pdf) of preserved offset rills and stream channels along the second segment of the Nayband fault highlights multiple peaks of

which three peaks smaller than 10 m offsets have pronounced densities (see Figure 4.28). These three prominent peaks correspond to the preserved offsets of the last three earthquakes which have occurred at most during the last 7.1 ka. The most pronounced of the three last peaks corresponds to the 10 m offsets. For peaks with offsets larger than 10 m, the densities decrease significantly. Indeed, the offsets larger than 10 m are much less preserved than the ones cumulating the offsets of the three younger seismic events only. The marked transition between subdued peaks and more pronounced ones may result from the shift between aggradation and erosion associated with the formation of many rills and channels. Thus, the latest major phase of incision has probably occurred before the third earthquake, which the occurrence time is bracketed between 6.1 and 7.1 ka.

The time span of the latest regional alluviation and the onset of the most recent incision (6.1 to 7.4 ka) determined in Central Iran can be also compared with the abandonment age of the most recent alluvial fans previously proposed to the north and south of Central Iran (*Regard et al.*, 2005; *Fattahi et al.*, 2007; *Shabanian et al.*, 2012). To the south, *Regard et al.* (2005) using cosmogenic  $^{10}\text{Be}$  dating of the youngest alluvial fan surfaces along the Minab-Zendan fault system proposed that the latest alluvial deposits should have been emplaced between  $5.7 \pm 0.6$  and  $9.2 \pm 1.0$  ka. To the north, *Fattahi et al.* (2007) suggested that the latest alluvial terraces along the central part of the Doruneh fault has been deposited within the last  $7.9 \pm 3.1$  ka. Recently, *Shabanian et al.* (2012) using cosmogenic  $^{10}\text{Be}$  dating of the youngest alluvial fan surfaces at the piedmont of the Binalud mountain front suggested an abandonment age of  $4.8 \pm 1.7$  ka for the most recent surfaces. All the proposed ages are concordant within uncertainties with the time range of 6.1 to 7.4 ka.

In summary, all these considerations indicate that the latest regional alluvial fan aggradation in Central Iran lasted until  $\sim 7$  ka during the Holocene optimum, and this latest widespread alluviation was later followed by a major phase of incision that began before  $\sim 6$  ka.

## 5.2. Late Pleistocene and Holocene slip rates of major strike-slip faults in Central Iran

Knowledge of the geologic rate of deformation is a key point to assess the contribution of individual strike-slip faults to the regional strain field in Central Iran. Although the general

picture is far from being complete, so far several studies have addressed part of this question by estimating the short-term geologic ( $10^3$ - $10^5$  yr) slip rates on several of these strike-slip faults (*Meyer et al.*, 2006; *Le Dortz et al.*, 2009; *Walker et al.*, 2010b; *Allen et al.*, 2011; *Fattahi et al.*, 2011; *Jamali et al.*, 2011; *Le Dortz et al.*, 2011; *Foroutan et al.*, 2012; *Walker and Allen*, 2012). The late Pleistocene and Holocene slip rate studies indicate that most of the strike-slip faults in Central Iran are slipping at average rates  $\leq 2$  mm yr<sup>-1</sup> with the noticeable exception of the Gowk fault, 3.8-5.7 mm yr<sup>-1</sup> (*Walker et al.*, 2010b; *Fattahi et al.*, 2013), which lies along the southwestern border of the Lut block.

For the easternmost N-striking strike-slip fault in Central Iran, several observations gathered along the Nayband fault and presented in this study (Chapter 4) provide a short-term geologic slip rate over the late Pleistocene and Holocene. The distribution of the right-lateral geomorphic features smaller than several hundred meters along the fault indicates that a large majority (80 per cent) of the preserved offsets is less than 25 m. Comparing such a distribution to that observed along the Kunlun strike-slip fault in Tibet, where 80 per cent of the preserved offsets postdate the LGM (*Van Der Woerd et al.*, 2002), and dividing 25 m by 19 ka (oldest possible age of the onset of the major deglaciation during the LGM, *Lambeck et al.*, 2002; *Clark et al.*, 2009) provides a minimum slip rate of 1.3 mm yr<sup>-1</sup>. This rough reasoning has also been tested using <sup>36</sup>Cl CRE and OSL dating of cumulative geomorphic offsets along the Nayband fault. Indeed, combining several geomorphic offset features ranging between  $9 \pm 1$  and  $195 \pm 15$  m with corresponding ages spanning from  $6.8 \pm 0.6$  to  $\sim 100$  ka brackets the minimum and maximum bounds of slip rate between 1.15 and 2.45 mm yr<sup>-1</sup>. This yields a short-term geologic ( $10^3$ - $10^5$  yr) slip rate of  $1.8 \pm 0.7$  mm yr<sup>-1</sup> averaged over the late Pleistocene and Holocene, reinforcing the qualitative reasoning done when assuming the majority of the preserved offsets postdate the onset of the last major deglaciation. The short-term geologic slip rate of  $1.8 \pm 0.7$  mm yr<sup>-1</sup> agrees within uncertainties with the long-term geologic slip rates previously reported on the order of 1.5 mm yr<sup>-1</sup> (*Walker and Jackson*, 2002) and  $1.4 \pm 0.5$  mm yr<sup>-1</sup> (*Walker et al.*, 2009). This may suggest that there is no significant temporal slip variation along the Nayband fault during the Quaternary period.

For the westernmost N-striking strike-slip fault in Central Iran, the Dehshir fault, additional observations given in this study (Chapter 2) provide right-slip rate of  $1.2 \pm 0.3$  mm yr<sup>-1</sup> averaged

over the late Pleistocene and Holocene. North of the Marvast river, two alluvial fans with extreme lower and upper bounds of right-lateral offset between 25 and 55 m have been reported. Combining this offset range with an estimate of the abandonment age of the respective alluvial surfaces ( $39.7 \pm 2.6$  ka, OSL sample AB-I) provides minimum and maximum slip rate of 0.6 and  $1.48 \text{ mm yr}^{-1}$ , respectively. Alternatively, assuming the emplacement of these alluvial surfaces are coeval with the equivalent terrace tread nearby the Marvas River ( $<28.2$  ka, *Le Dortz et al.*, 2011) provides another set of lower and upper bounds of the slip rate of 0.88 and  $1.95 \text{ mm yr}^{-1}$ , respectively. From these two upper bounds ( $1.48$  and  $1.95 \text{ mm yr}^{-1}$ ) one has to retain the smaller value. Similar reasoning indicates that the larger value of the minimum slip rates ( $0.9 \text{ mm yr}^{-1}$ ) defines a safe estimate of the minimum slip rate. This estimated slip rate of  $0.9$  to  $1.48 \text{ mm yr}^{-1}$  agrees well with the previously reported right-slip rate of the Dehshir fault. Indeed, *Le Dortz et al.* (2011) combining several right-laterally offset streams and terraces along the southern part of the fault with respective cosmogenic  $^{10}\text{Be}$ ,  $^{36}\text{Cl}$ , and OSL ages documented a right-slip rate of  $1.2 \pm 0.3 \text{ mm yr}^{-1}$  averaged over the last 270 ka.

The right-slip rate of the Anar fault has also been estimated over the Holocene. *Le Dortz et al.* (2009) combining a cumulative right-lateral offset riser of  $8 \pm 0.5$  m preserved along the southern part of the fault with the corresponding surface  $^{10}\text{Be}$  CRE and near surface OSL ages proposed a minimum slip rate of  $0.8 \text{ mm yr}^{-1}$ . There, the significant spread of  $^{10}\text{Be}$  concentrations and hence CRE ages (range from  $18 \pm 1.1$  to  $77.8 \pm 4.9$  ka) indicates a variable inheritance; i.e., a noticeable cosmogenic nuclide concentrations prior emplacement of the sampled pebbles. Since the  $^{10}\text{Be}$  CRE ages indicate significant and variable inheritance, the OSL age ( $11.8 \pm 6.5$  ka) of the sample collected from 80 cm below the same surface has been used to bracket the abandonment age of the alluvial surface, and hence to estimate the right-slip rate of the fault. In this study (Chapter 3), this OSL age is refined to  $10.1 \pm 0.6$  ka using finite mixture model (*Roberts et al.*, 2000). Combining the cumulative offset of  $8 \pm 0.5$  m postdating the fan aggradation with the refined age of the fan abandonment ( $10.1 \pm 0.6$  ka) yields a minimum slip rate of  $0.8 \pm 0.1 \text{ mm yr}^{-1}$  on the Anar fault and confirms the previously proposed minimum rate of  $0.8 \text{ mm yr}^{-1}$ . This low rate of slip is comparable with the right-slip rate proposed along the prolongation of the Anar fault to the south. Indeed, *Fattahi et al.* (2011) using OSL dating of an offset alluvial fan proposed the right-slip rate of the Rafsanjan fault on the order of  $0.4 \text{ mm yr}^{-1}$  over the last  $\sim 120$  ka.

In summary, apart from the noticeable exception of the Gowk fault, the major N-striking strike-slip faults slicing Central Iran are characterized by slip rates smaller than  $2.5 \text{ mm yr}^{-1}$ . In this frame, the estimated slip rates from the western to eastern border of Central Iran are indistinguishable, within uncertainties, suggesting that the active deformation is evenly distributed across the major strike-slip faults inside Central Iran. The next section summarizes how these rather slow-slipping faults release the accumulated strains through the late Pleistocene and Holocene timescales.

### 5.3. Seismic behavior of major strike-slip faults in Central Iran

Ambiguities in the seismic behavior of the N-striking strike-slip faults in Central Iran arise mainly because of the lack of instrumental and historical seismic and also paleoseismic records (e.g., *Ambraseys and Melville, 1982; Ambraseys and Jackson, 1998; Berberian and Yeats, 1999; Engdahl et al., 2006*) along these active faults. The way these seismically quiescent, but active faults release the accumulated strain through time has long been a matter of debate. Either these faults release the accumulated strain by aseismic creep, as previously suggested by *Berberian (1976)* as a possible behavior for the Dehshir fault, or they generate large earthquakes, which went unnoticed in the historical records. Although no detailed geodetic profiles are available across these strike-slip faults to provide evidence for aseismic creep, the lack of significant microseismicity right along the faults makes the creep assumption very unlikely. In addition, the sharpness of the cumulative horizontal offsets preserved along the strike-slip faults suggests that these right-lateral offsets could have accrued during large and infrequent earthquakes rather than by steady creeping. Thus, performing paleoseismic studies was the only way to solve these ambiguities and document the seismic behavior of these slow-slipping strike-slip faults over their last seismic cycles. However, none of the previous paleoseismic studies in Iran has been conducted in Central Iran. Indeed, these studies have been performed in northwest Iran (*De Martini et al., 1998; Hessami et al., 2003; Solaymani Azad, 2009*), the Zagros (*Bachmanov et al., 2004*), and the Alborz (*Nazari, 2005; Ritz et al., 2006, 2012; Nazari et al., 2009b, 2010; Solaymani Azad et al., 2011*).

The first paleoseismic study in Central Iran was performed along the Dehshir fault and provided evidence of several large and infrequent earthquakes (*Nazari et al.*, 2009a). Using OSL dating of the sediments exposed in a trench excavated across the southern part of the fault, they showed that the Dehshir fault hosted at least three large-magnitude earthquakes during the last  $21.1 \pm 11.2$  ka. However, due to the large uncertainties associated with most of the OSL ages, the occurrence times of the identified earthquakes were poorly constrained.

Refining the analytical procedure used by *Nazari et al.* (2009a) at the site North, the error bars of six out of the eight ages have been reduced and the OSL ages been recalculated (see section 2.3.1). The revised OSL ages provide better constraints for the occurrence times of the paleoearthquakes. Accordingly, refining the age of a sample collected from one of the fissure fills associated with the most recent earthquake indicates that this latest earthquake occurred shortly before  $2.0 \pm 0.2$  ka (*Fattahi et al.*, 2010; see Appendix A.1). In addition, the occurrence time of the third earthquake is well bracketed between 19.4 and 21.7 ka. This time range is comparable with that of the penultimate event identified between 18.7 and 21.3 ka at the site South (see section 2.3.2). This suggests the surface rupture associated with the third earthquake exceeded some 30-km length, extending at least from the site North to the site South. Using empirical relationships linking surface rupture lengths and moment magnitudes for strike-slip faults, as proposed by *Wells and Coppersmith* (1994), this would yield to a magnitude of  $M_w \approx 7$  for the third earthquake.

The refined OSL ages also provide a better constraint for the recurrence interval of large earthquakes along the Dehshir fault. Accounting for the age of the most recent earthquake ( $2.0 \pm 0.2$  ka) and considering the occurrence of a fourth seismic event just before  $20.1 \pm 1.6$  ka (see Figure 2.2 and Table 2.1) provides a time duration of  $18.2 \pm 1.0$  kyr for the three seismic cycles. This yields an average recurrence interval of large-magnitude earthquakes by  $6.1 \pm 0.4$  ka. However, due to the incomplete record of sediments and hence seismic events demonstrated at the trench site, between MIS-3 and the late Holocene, this estimated recurrence interval is more likely overestimated. In other words, combining the overestimated recurrence interval of  $6.1 \pm 0.4$  ka with the elapsed time since the most recent earthquake ( $2.0 \pm 0.2$  ka) does not rule out the possibility of occurrence of the next large earthquake along the southern part of the Dehshir fault in the near future. Accounting for the average slip rate of  $1.2 \text{ mm yr}^{-1}$  and considering the

elapsed time since the most recent earthquake ( $2.0 \pm 0.2$  ka) would imply that the southern part of the fault is theoretically capable at present to produce a large-magnitude ( $M_w > 7$ ) earthquake with an average horizontal slip of  $\sim 2.5$  m.

The paleoseismic study performed on the Anar fault also demonstrates that this slow-slipping fault releases the accumulated strains by large and infrequent earthquakes (*Foroutan et al.*, 2012). The paleoseismic data obtained from a trench excavated across the fault trace indicate that this presently quiescent fault hosted at least three large-magnitude earthquakes during the late Pleistocene and Holocene. The timing of these three paleoearthquakes is constrained using OSL dating at  $4.4 \pm 0.8$ ,  $6.8 \pm 1.0$ , and  $9.8 \pm 2.0$  ka. Restoration of the youngest warped layers to their respective positions before occurrence of the most recent earthquake shows a vertical displacement of 60 cm associated with the latest surface faulting event. Taking into consideration that the Anar fault is a primary strike-slip fault, such a vertical displacement should have been associated with at least a couple of meters of right-lateral displacement. Interestingly, the smallest right-lateral offset preserved along the Anar fault is on the order of 3 m, which most likely occurred during the most recent earthquake. Using the empirical relationships linking coseismic slip and moment magnitude for strike-slip faults (*Wells and Coppersmith*, 1994), the average horizontal offset of 3 m would yield a magnitude of  $M_w \approx 7$  for the most recent earthquake.

The three recognized seismic events on the Anar fault have occurred within a sedimentary succession that is not older than 15 ka. This yields an average recurrence interval of large earthquakes at most 5 ka, which exceeds the time span covered by historical seismic catalogs (e.g., *Ambraseys and Melville*, 1982; *Ambraseys and Jackson*, 1998; *Berberian and Yeats*, 1999). The occurrence time of these three earthquakes indicate that the time interval between two successive earthquakes is on the order of 2400 and 2900 yr between the most recent-penultimate events and the penultimate-third events, respectively. Then, combining these time intervals with the elapsed time since the most recent earthquake, which is 3600 yr at least and 5200 yr at most, suggests that the Anar fault is getting close to the end of its seismic cycle and may anticipate an imminent destructive earthquake for the city of Anar.

The paleoseismic study conducted along the Nayband fault also document large and infrequent earthquakes (Chapter 4). The paleoseismic data demonstrate that this historically

silent fault produced several large-magnitude earthquakes during the late Pleistocene and Holocene. The trench that was excavated across the second segment of the Nayband fault (NA2), within a dry pond, provides evidence of at least four large-magnitude ( $M_w \sim 7$ ) earthquakes during the last  $17.4 \pm 1.3$  ka and of two older earthquakes one probably before some 23 ka and another before  $70 \pm 5$  ka.

The ages of the identified surface-rupturing events have been well constrained using 18 OSL ages. All but one (NT-XV,  $15.3 \pm 1.0$  ka) OSL age of a first sampling were consistent with the stratigraphic order of the units. In order to understand and interpret the cause of that inconsistency, three additional samples were collected to duplicate the inconsistent sample as well as the immediately above and below samples. The sample that was collected from a same stratigraphic unit that the sample NT-XV yielded an age older than the immediately below sample; confirming the sampled sediments are likely to have been partially bleached at deposition. Indeed, this second set of sampling helped to solve for that inconsistency and emphasized the usefulness of a multiple sampling strategy to investigate the existence of incompletely bleached sediments at deposition. The seismic history of the Nayband fault is well-established and the most interesting feature concerns the most recent earthquake.

The timing of the most recent earthquake is well constrained by three OSL samples that were collected from the units immediately below the corresponding event horizon. These three samples yielded ages of  $0.74 \pm 0.06$ ,  $0.79 \pm 0.06$ , and  $0.98 \pm 0.08$  ka. To investigate the possibility of partial bleaching that would have aged the most recent earthquake, an additional sample was collected very near to the ground surface as a modern bleached analog of the topmost samples. This sample yields an age of  $0.07 \pm 0.03$  ka, indicating that the three sampled sediments collected immediately below the event horizon of the most recent earthquake are likely to have been well-bleached at deposition. Thus, the youngest ( $0.74 \pm 0.06$  ka) of the three OSL ages defines a safe lower bound for the occurrence time of the most recent earthquake. Therefore, the most recent earthquake on the Nayband fault occurred during the last 800 years. This important conclusion challenges the completeness of the historical seismic catalogs (see next section).

The magnitudes of the surface faulting events have been estimated both by measuring the preserved right-lateral offsets along the second segment of the Nayband fault and by restoring

the vertical displacements associated with the recognized paleoearthquakes in the trench exposure. Plotting summed Gaussian probability density function of the measured right-lateral offsets smaller than 30 m along the NA2 fault segment displays multiple peaks ranging from 3 to 25 m. The most important density peaks correspond to dextral offsets of 3-4 m, 6 m, 10 m, and 16 m while the remaining lower density peaks correspond to 2 m, 12 m, 13 m, and 25 m (Figure 4.28). Considering the smallest of these dextral offsets (i.e., 2 m and 3-4 m) occurred during the most recent earthquake, the magnitude of this surface faulting event should be on the order of  $M_w \sim 7$ . Then, the cumulative right-lateral offsets of 6 m, 10 m, 12-13 m, and 16 meters should incorporate the displacements of the former four earthquakes. Interestingly, such a pattern of right-lateral offsets, ranging between 3 and 16 m, is preserved less than 1 km north of the trench site (Figure 4.16). This plot and the preserved small geomorphic offsets near the trench site suggest an average displacement per event of  $\sim 3$  m. In addition, the restoration of the vertical throws associated with the fourth and the fifth paleoearthquakes in the trench exposure indicates that  $\sim 1$  m of vertical displacement has occurred during each of these events. This would be compatible with several meters of right-lateral slip per event. Therefore, the magnitudes of the last five earthquakes were probably on the order of  $M_w 7$ .

Although the average slip per event along the Nayband fault appears similar over the last seismic cycles, the temporal pattern of strain release seems irregular. The relatively continuous sediment record during the last  $\sim 7$  kyr provides evidence for the last three earthquakes. The two older events have occurred around  $6.6 \pm 0.5$  ka while the younger one occurred more recently than 0.8 ka. Thus, the time interval between two successive earthquakes appears variable, which is at most of 1 kyr between two older events whereas it is of  $6.2 \pm 0.9$  kyr between two younger ones. The available paleoseismic record suggests that the seismic behavior of the Nayband fault should be characterized by irregular recurrence intervals and clustering strain release. Combining such an irregularity with the fact that the amount of slip per event appears to be similar and on the order of 3 m, suggests that the Nayband fault may not necessarily release the whole strain accumulated during each interseismic period by a single large-magnitude earthquake at the end of seismic cycle. Then, from this and accounting for the occurrence of the most recent earthquake within the last 800 years, the possibility for occurrence of an impending earthquake along the Nayband fault cannot be excluded. Furthermore, combining the minimum time duration between the penultimate and the most recent earthquakes (5300 years) with the

minimum slip rate of  $1.15 \text{ mm yr}^{-1}$  suggests that at least some 6 m of lateral slip could have been released during the most recent earthquake. While the average lateral slip associated with this earthquake is on the order of 3 m. This suggests that the Nayband fault is capable at present to produce a large-magnitude ( $M_w > 7$ ) earthquake with an average horizontal slip of at least  $\sim 3$  m.

The clustering strain release on the Nayband fault is compatible with the recent seismic activities along its southern continuation. There, the Gowk fault hosted three destructive earthquakes with magnitudes greater than  $M_w$  6.6 over a seventeen-year period since 1981 (*Berberian et al.*, 1984; *Berberian et al.*, 2001; *Fielding et al.*, 2004; *Nalbant et al.*, 2006). Two of these events, the 1981 July 28,  $M_s$  7.1, Sirch earthquake and the 1998 March 14,  $M_w$  6.6, Fandoqa earthquake, occurred in overlapping segments of the northern part of the fault, indicating that strain release on the Gowk fault can also be characterized by clustering earthquakes.

In summary, the first paleoseismic studies performed along the N-striking, Dehshir, Anar, and Nayband faults in Central Iran demonstrate that these active faults generated large and infrequent earthquakes (Figure 5.1); despite the lack of instrumental and historical seismic records in the fault vicinity. Some of these earthquakes were unnoticed in the historical seismic catalogs while some of them have occurred during a time span beyond that imperfectly covered by the historical records. The paleoseismic data available across Central Iran indicate that the two westernmost low-slipping, seismogenic strike-slip faults, the Dehshir and Anar faults, have long recurrence intervals of several thousands of years. It is noteworthy that such long recurrence intervals could have been overestimated by incomplete sediment records in the trench exposures, leading to underestimate the true number of paleoearthquakes, particularly, in the two paleoseismic sites along the Dehshir fault (Chapter 2). By contrast, the rather continuous record of sediments over the last  $\sim 7$  ka in the Nayband trench indicates that the seismic behavior of the fault appears to be characterized by irregular recurrence intervals and clustering earthquakes. The seismic histories of the Dehshir, Anar, and Nayband faults documented over their last seismic cycles suggest that these seismogenic faults are capable of producing large-magnitude ( $M_w > 7$ ) earthquakes in the near future. All these considerations highlight that Central Iran is not totally a rigid block and the moderate internal deformation is responsible for significant seismic hazard.

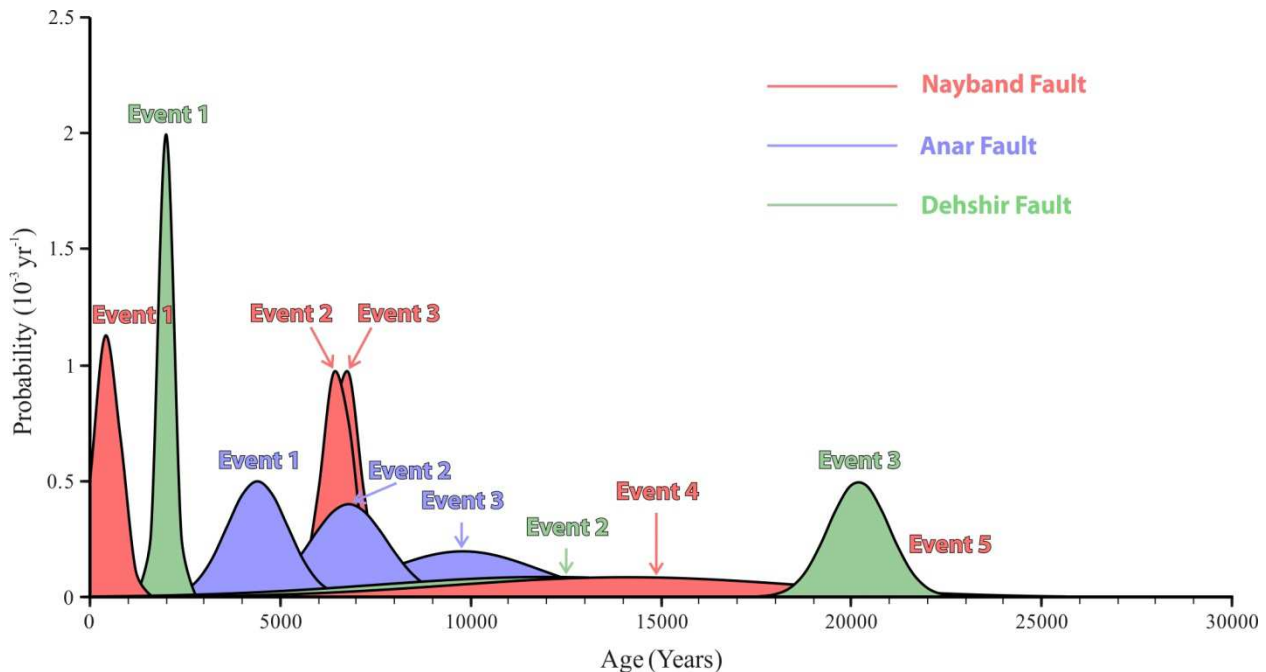


**Figure 5.1.** Probability density functions of the identified paleoearthquakes in this study along the Dehshir, Anar, and Nayband faults. Each of the peaks correspond to a large paleoearthquake and represent the error in the age assessment of each event. Note the occurrence of the most recent earthquakes on the Dehshir and Nayband faults during the last 2200 years (see section 5.4).

#### 5.4. Historical seismic catalogs versus paleoseismic data

Several paleoseismic studies in regions with long historical seismic records, as Italy (*Pantosti et al.*, 1996; *Galli et al.*, 2008) and Lebanon (*Daëron et al.*, 2005, 2007), provide evidence for occurrence of several large-magnitude earthquakes which have not been recorded in historical sources. There are also examples of slow-slipping strike-slip faults that have generated large and devastating instrumental earthquakes without known historical earthquake. For instance, the 2008,  $M_w$  7.9, Sichuan/Wenchuan earthquake with 69,000 dead (e.g., *Wang et al.*, 2009; *de Michele et al.*, 2010) in the eastern Tibet Plateau occurred on the Longmen Shan fault zone. There, individual faults are characterized by slip rate of less than  $1 \text{ mm yr}^{-1}$  over the late Pleistocene and Holocene (*Densmore et al.*, 2007; *Godard et al.*, 2009); this part of the Longmen Shan fault zone had not experienced a large earthquake for at least 2700 years (*Zhang*, 2013). Another example occurred in Iran, the 2003,  $M_w$  6.6, Bam earthquake in southeast Iran with

40,000 dead (e.g., *Talebian et al.*, 2004; *Jackson et al.*, 2006). This devastating event occurred on the slow-slipping Bam fault without record of historical earthquake over the last 2400 years.

Overall, the historical seismic catalogs suggest that the N-striking, right-lateral strike-slip faults slicing Central Iran are quiescent. However, the available paleoseismic records demonstrate several of these faults generated large and infrequent earthquakes over the last thousands of years. As seen in the previous section some of these earthquakes occurred in a time span beyond the historical catalogs while some of them occurred during the last two millennia. The historical seismic record in the Iranian Plateau covers a long time period spanning some 2400 years (e.g., *Ambraseys and Melville*, 1982). Although there is no available historical seismic source before the 4th century BC, several archeological studies provide evidence for the occurrence of at least six devastating earthquakes across the Iranian Plateau between 2700 and 6000 years ago. These earthquakes should have occurred in 700 BC at the Godin mound, 1000-800 BC at the Marlik mound, 1650-1600 BC at the Godin mound, 2000 BC at the Aq Tapeh mound, 2000-1500 BC at the Sagzabad mound, and 3800 BC at the Sialk mounds (Figure 5.2) (*Ambraseys and Melville*, 1982; *Berberian and Yeats*, 2001 and references therein; *Berberian et al.*, 2012). Although these earthquakes occurred within a time period during which there were at least some administrative temple records written in Elamite hieroglyphics from the beginning of the 3rd millennium BC at the Sialk and Yahya mounds in the Central Iran Plateau near Kashan and south of Kerman, respectively (*Gershevitch*, 1985), there is no contemporary written report of these events. The recognition of these paleoearthquakes, which is based only on archeoseismic evidence, suggests that some of these events might have been reported until the end of the Achaemenid Empire by 330 BC but the corresponding records were presumably destroyed during the Alexander's invasion (334-323 BC).

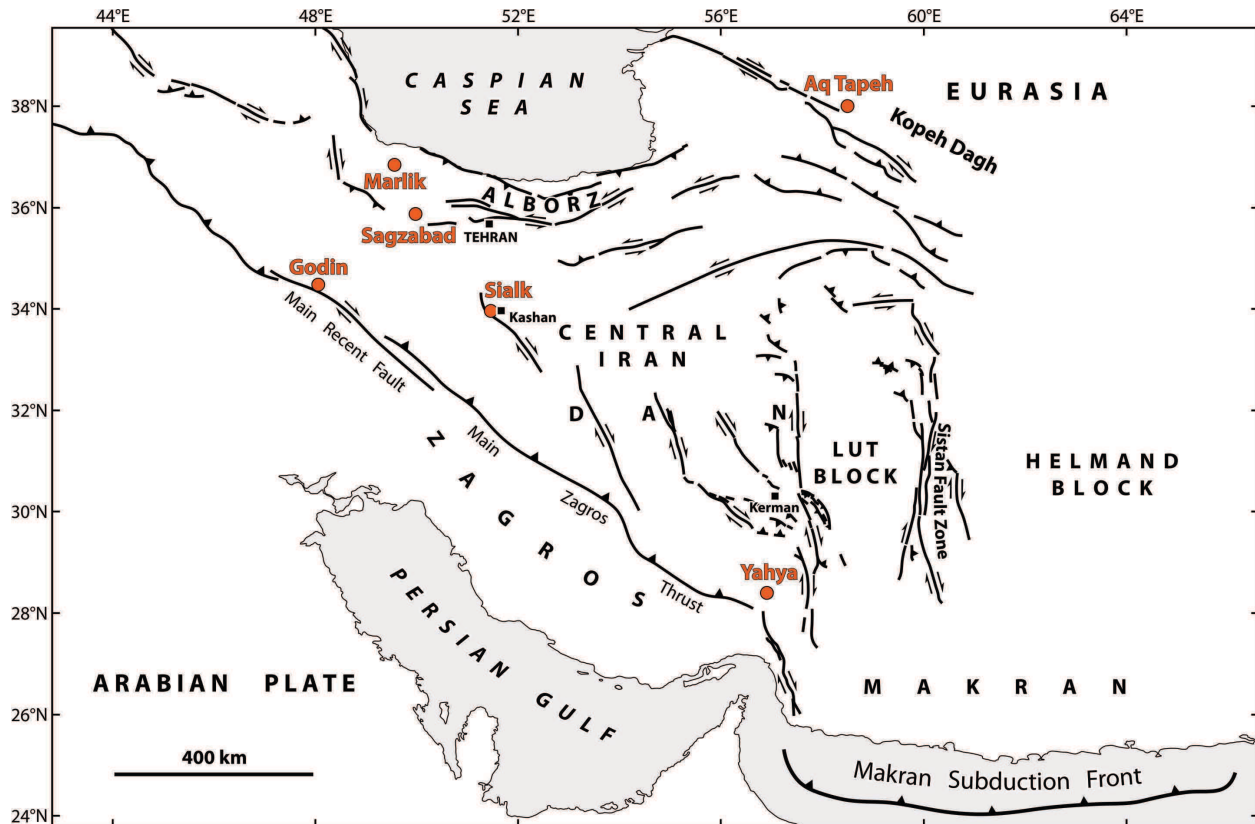


**Figure 5.2.** Archaeological sites with evidence of destructive earthquakes beyond the 4th century BC on the Iranian Plateau. Orange circles delineate the location of archaeological mounds from *Lambergkarlovsky (1970)*, *Berberian and Yeats (2001)*, *Frame (2010)*, *Quigley et al. (2011)*, and *Berberian et al. (2012)*. A, Anar fault; D, Dehshir fault; and N, Nayband fault.

Therefore, the most recent earthquake on the Anar fault (3600-5200 years ago) occurred in a time span beyond the available historical catalogs, whereas the most recent earthquakes along the Dehshir (shortly before  $2000 \pm 200$  years ago) and Nayband faults (within the last 800 years) occurred during a time span covered by the historical records. However, these two latter large-magnitude earthquakes have been reported by none of the available catalogs (*Ambraseys and Melville, 1982*; *Ambraseys and Jackson, 1998*; *Berberian and Yeats, 1999*). Either these seismic events, which occurred in remote and uninhabited desert lands, went unnoticed or they have been reported with mislocated epicenters.

Considering the occurrence time of the most recent earthquake on the Dehshir fault, none of the available historical seismic records testifies for the occurrence of a seismic event in the Iranian Plateau between 200 BC and AD 200; indicating that this latest earthquake on the

Dehshir fault went more likely unnoticed. In the case of the most recent earthquake on the Nayband fault, the historical catalogs indicate that several large earthquakes occurred after AD 1200, to the north and northeast of the Nayband fault. However, all the seismic events are recorded far (180-400 km) from the Nayband fault and can be associated with other active faults in the vicinity of their epicentral regions (see section 4.5.2). Thus, both the most recent earthquakes on the Dehshir and Nayband faults went unnoticed in the available historical data. The occurrence of these two earthquakes along the western and eastern borders of Central Iran provides outstanding examples for the incompleteness of the historical seismic catalogs in Central Iran.

In summary, the record of large-magnitude earthquakes along the slow-slipping strike-slip faults in Central Iran within the last two millennia poses a great challenge for the assessment of the regional seismic hazard using historical seismic catalogs alone. In addition, a possible clustering of paleoearthquakes along the Nayband fault as well as the recent burst of instrumental earthquakes along the Gowk fault demonstrates the importance of using geological information to unravel the regional seismic hazard.

### 5.5. Geologic versus geodetic slip rates in Central and Eastern Iran

The right-lateral shear induced by the differential accommodation of the Arabia-Eurasia convergence between the Zagros collision domain to the west and the active Makran subduction zone to the east is mostly taken up by right-lateral slip along the major strike-slip faults in Central and Eastern Iran. The rates of deformation along the strike-slip faults in Eastern Iran are poorly constrained, whereas the short-term geologic ( $10^3$ - $10^5$  yr) slip rates are well constrained along most of the major strike-slip faults in Central Iran (Figure 5.3).

The geologic slip rates of the Dehshir and Anar faults have been constrained to  $1.2 \pm 0.3$  and  $\geq 0.8 \pm 0.1$  mm yr<sup>-1</sup> over the last 270 and 10 ka, respectively (*Le Dortz et al.*, 2009, 2011; *Foroutan et al.*, 2012). The late Quaternary right-slip rate of the Rafsanjan strike-slip fault is limited to 0.4 mm yr<sup>-1</sup> over the last ~120 ka (*Fattahi et al.*, 2011). The dextral slip-rate of the more easterly trending Kuh Banan fault is estimated between 1-2 mm yr<sup>-1</sup> (*Allen et al.*, 2011; *Walker and Allen*, 2012). For the Nayband fault, a right-slip rate of  $1.8 \pm 0.7$  mm yr<sup>-1</sup> is averaged

over the last 100 ka (see Chapter 4). This latter slip rate matches with an overall northward decrease of the dextral shear from the Minab-Zendan fault system up to the northernmost part of the western margin of the Lut block, as a consequence of the transfer zone required between the Zagros collision domain and the Makran subduction zone.

That pronounced northward decrease in slip rate involves several N- and NW-striking active faults. Indeed, part of the right-lateral deformation along the Minab-Zendan fault system ( $6.3 \pm 2.3 \text{ mm yr}^{-1}$ ) is transferred through a right step on to the Sabzevaran-Jiroft fault system ( $5.7 \pm 1.7 \text{ mm yr}^{-1}$ , *Regard et al.*, 2005). At the northern termination of the Sabzevaran-Jiroft fault system, the Sabzevaran strike-slip motion is transferred northward through a right step on to the Gowk fault slipping at a rate of  $3.8\text{-}5.7 \text{ mm yr}^{-1}$ . Part of the difference between the dextral motions of the Sabzevaran-Gowk faults is taken up by several E-striking thrust faults and by the NW-striking right-lateral Rafsanjan fault. Farther north, the remaining portion of the dextral shear ( $3.8\text{-}5.7 \text{ mm yr}^{-1}$ ) on the Gowk fault is transferred northward on to the NW-striking Kuh Banan, the N-striking Lakar kuh, and the Nayband ( $1.8 \pm 0.7 \text{ mm yr}^{-1}$ ) faults. This northward decrease in slip rates appears broadly consistent with the general pattern of the GPS horizontal velocities relative to stable Eurasia (Figure 5.3).

By contrast, west of the Lut block, the E-W summation of the available individual geologic slip rates across the major strike-slip faults in Central Iran yields a cumulative right-lateral rate of  $\sim 3.7\text{-}6.9 \text{ mm yr}^{-1}$ , challenging a present-day coherent motion with limited internal deformation documented by two years (*Vernant et al.*, 2004) and six years (*Masson et al.*, 2007) of GPS campaigns. Either the rates of slip along these right-lateral strike-slip faults have decreased since inception of dextral faulting or the scarce GPS data available do not give access to steady interseismic loading of the locked faults. A denser GPS network or interseismic interferometric studies should help to further investigate that problem.

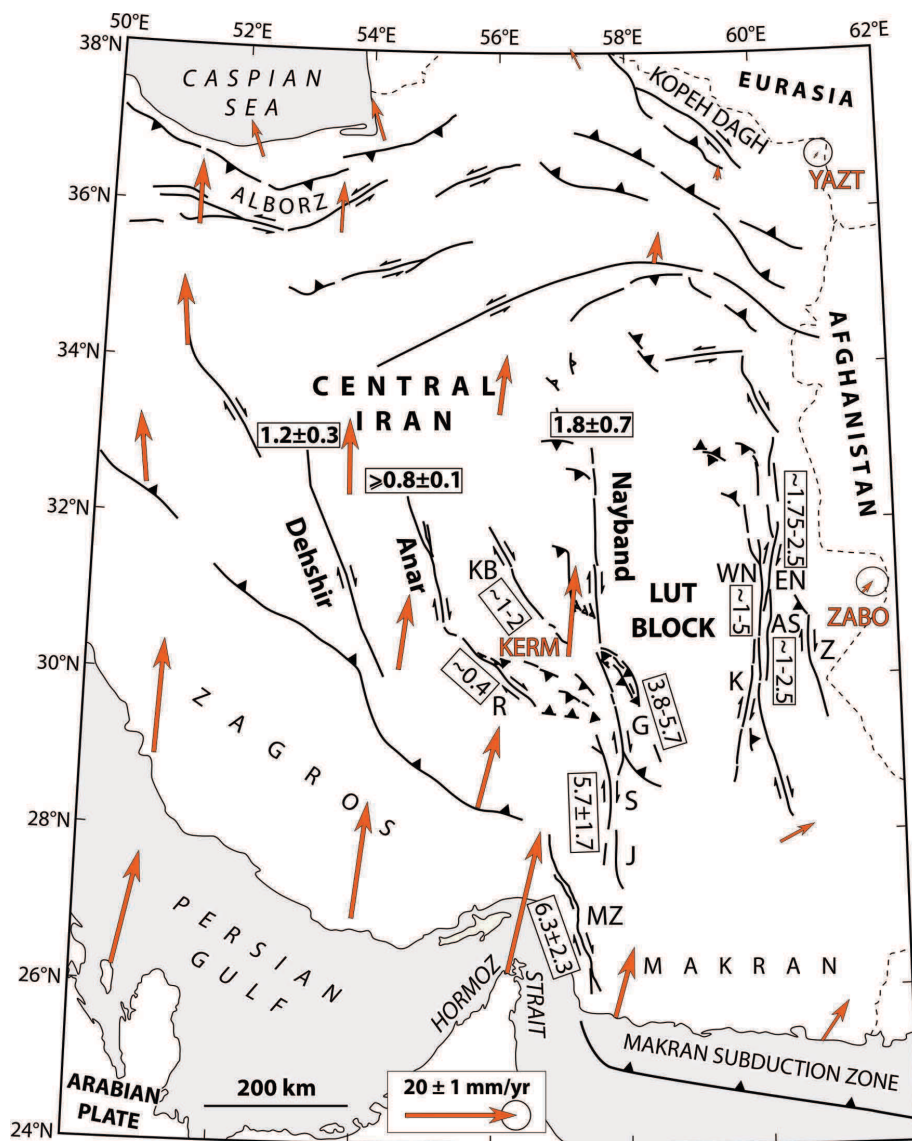


**Figure 5.3.** Summary of late Quaternary slip rates available across Central and Eastern Iran. GPS velocities (orange arrows) in Eurasian-fixed reference frame with 95 per cent confidence ellipse for ZABO and YAZT sites from *Vernant et al. (2004)* and *Masson et al. (2007)*. A, Anar fault; B, Bam fault; D, Dehshir fault; DR, Doruneh fault; G, Gowk fault; J, Jiroft fault; KB, Kuh Banan fault; L, Lakar Kuh fault; MZ, Minab-Zendan fault system; MZT, Main Zagros Thrust fault; N, Nayband fault; QZ, Qom-Zefreh fault; R, Rafsanzan fault; S, Sabzevaran fault; and SFZ, Sistan Fault Zone.

The available GPS data reveal an overall differential motion of  $16 \pm 2 \text{ mm yr}^{-1}$  between Central and Eastern Iran (between the vectors KERM and ZABO) that is accounted for by N-S dextral shear at  $\sim 30.5^\circ\text{N}$  (Figure 5.3). *Walker and Jackson (2004)* accounting for a  $\sim 70 \text{ km}$  of total offset across the eastern side of the Lut block, and assuming a 5 Ma for the onset of strike-

slip faulting proposed a cumulative slip rate of  $\sim 15 \text{ mm yr}^{-1}$  along the Sistan fault zone. Considering the  $16 \pm 2 \text{ mm yr}^{-1}$  of the present-day dextral shear between Central and Eastern Iran and accounting for the absence of active faulting inside the Lut block, *Walker and Jackson's* (2004) model postulates a total right-lateral shear of less than  $3 \text{ mm yr}^{-1}$  along the western margin of the Lut block, on the Nayband-Gowk fault system. Although the right-slip rate of  $1.8 \pm 0.7 \text{ mm yr}^{-1}$  averaged over the last 100 ka along the Nayband fault agrees with this model, the slip rate of  $3.8\text{-}5.7 \text{ mm yr}^{-1}$  averaged over the Holocene along the Gowk fault (*Walker et al.*, 2010b; *Fattahi et al.*, 2013) exceeds the model prediction.

Extrapolating the present-day differential motion over the late Pleistocene and Holocene timescales, and accounting for the right-slip rates determined along the Nayband ( $1.8 \pm 0.7 \text{ mm yr}^{-1}$ ) or Gowk ( $3.8\text{-}5.7 \text{ mm yr}^{-1}$ ) faults would imply that the right-lateral strike-slip faults east of the Lut block at  $\sim 30.5^\circ\text{N}$  (the West Neh, Kahourak, Assaghi, and Zahedan faults) should accommodate a minimum dextral shear of  $8.3$  or  $11.5 \text{ mm yr}^{-1}$ . Although there is no available direct Quaternary dating of geomorphic offset features along these active faults, *Meyer and Le Dortz* (2007), hypothesizing the recent regional incision in Eastern Iran occurred by the onset of Holocene ( $12 \pm 2 \text{ ka}$ ), proposed right-slip rates of  $\sim 1\text{-}5$  and  $\sim 1\text{-}2.5 \text{ mm yr}^{-1}$  for the West Neh and Assaghi faults, respectively. If these estimated slip rates are meaningful, accounting for the minimum dextral shear of  $8.3$  or  $11.5 \text{ mm yr}^{-1}$  across the West Neh, Kahourak, Assaghi, and Zahedan faults would require cumulated slip rates across the Kahourak and Zahedan faults of at least  $\sim 1$  to  $4 \text{ mm yr}^{-1}$  and at most  $\sim 6.5$  to  $9.5 \text{ mm yr}^{-1}$ .

The higher rates appear difficult to reconcile with both the morphological trace and the size of the Kahourak and Zahedan faults. Such rates may suggest another geodynamic process or a transitory deformation is influencing the regional GPS strain field. For instance, the relaxation processes associated with a great subduction earthquake in the Makran subduction zone (the 1945,  $M_w$  8.1 earthquake; *Page et al.*, 1979), such as those still resulting from the 1960,  $M_w$  9.5 subduction earthquake in Chile (*Khazaradze et al.*, 2002; *Khazaradze and Klotz*, 2003). Indeed, a postseismic relaxation lasting for several decades after the occurrence of the event could significantly reduce the velocity of the ZABO site and hence bias the interpretation of the velocity field in terms of dextral shear alone. Consequently, this may result in an apparent increase of the overall differential motion between Central and Eastern Iran. In addition, an

overestimation of the observed velocity of the KERM site mentioned by *Tavakoli* (2007) may also result in an increased differential motion between the KERM and ZABO sites. Overall, the uncertainties associated with the available GPS data across Central and Eastern Iran as well as with the geologic slip rates in Eastern Iran are large enough to allow alternative interpretations. In any case, a comprehensive geomorphic study, an interseismic interferometric study or a dense GPS network across the Sistan fault zone should help unraveling the strain distribution “puzzle” in Eastern Iran.

In summary, the available geologic and geodetic rates of deformation in Central and Eastern Iran may remain difficult to match.

## 5.6. Studies in progress and perspectives

### 5.6.1. Paleoseismology of the Gowk fault

So far, the geologic slip rate along the strike-slip faults slicing Central Iran is rather well constrained over the late Quaternary timescales. The available data demonstrate that these active faults slip at a rate of less than  $2.5 \text{ mm yr}^{-1}$  with an exception, the Gowk fault, which slips at a rate of  $3.8$  to  $5.7 \text{ mm yr}^{-1}$  over the Holocene (*Walker et al.*, 2010b; *Fattahi et al.*, 2013). At present our understanding of the seismic behavior of these strike-slip faults is limited to the first paleoseismic studies ever conducted along the slow-slipping N-striking ones. In contrast to these slow-slipping faults, which produced large and infrequent earthquakes, the northern segments of the Gowk fault have generated several destructive earthquakes during the last decades (Figure 5.4). These segments caused three consecutive, destructive earthquakes with magnitudes larger than  $M_w$  6.6 during the seventeen-year period between 1981 and 1998. These are the 1981 June 11 Golbaf event of  $M_s$  6.7, the 1981 July 28 Sirch event of  $M_s$  7.1, and the 1998 March 14 Fandoqa event of  $M_w$  6.6 (*Berberian et al.*, 1984, 2001; *Fielding et al.*, 2004; *Nalbant et al.*, 2006). Two of these events, the Sirch and Fandoqa earthquakes, occurred in overlapping segments of the northern part of the fault, indicating that the strain release at least along the northern segments is characterized by earthquake clustering. Furthermore, several smaller instrumental and historical earthquakes with magnitudes ranging between 5 and 6 have occurred

along the northern parts of the fault. Noteworthy, there is no record of significant instrumental and historical earthquakes along the southern segments of the Gowk fault (Figure 5.4).

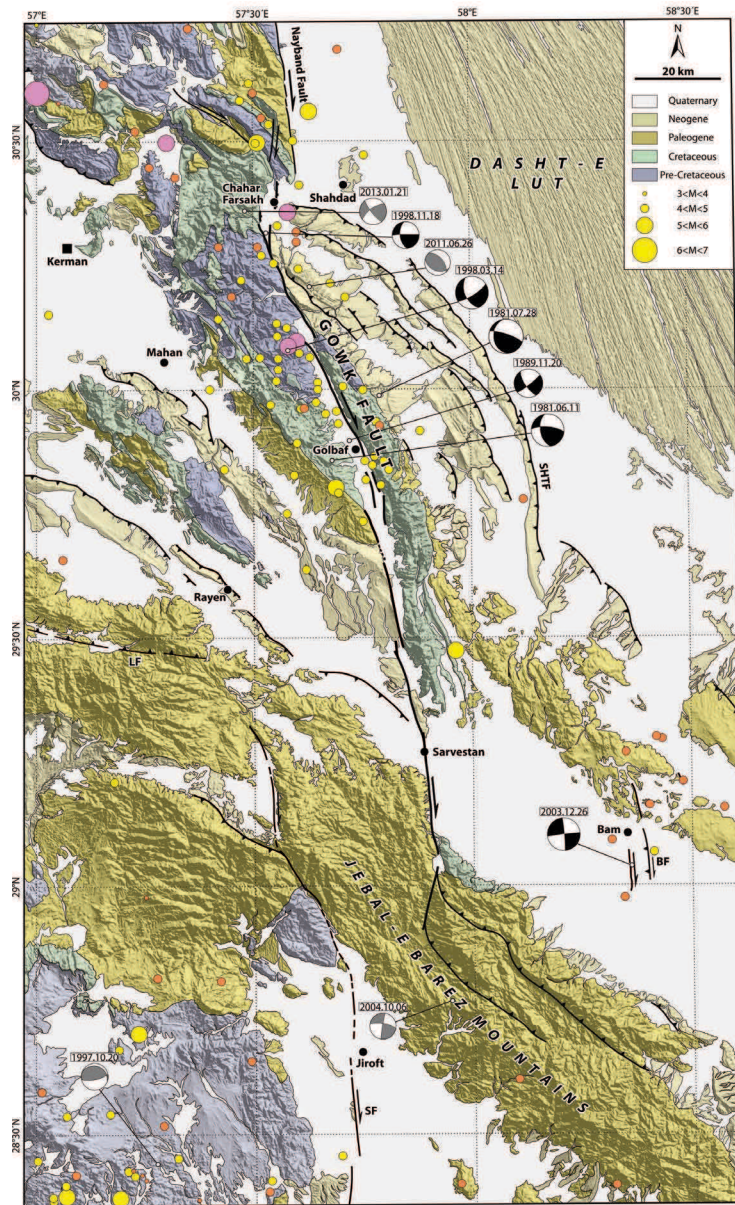


**Figure 5.4.** Simplified seismotectonic map of southwestern Lut Block. Regional geology compiled from Babakhani and Kholghi (1989), Babakhani and Alavi Tehrani (1992), Sahandi (1992), Vahdati Daneshmand (1992), Aghanabati (1992, 1993a, 1993b), Sabzehei (1993), and Soheili (1995), overlain on shaded relief 90-m SRTM topography. Active fault traces (dashed where inferred) from Landsat, SPOT, Quickbird imageries and field observations. BF, Bam fault; LF, Lalehzar fault; SF, Sabzevaran fault; and SHTF, Shahdad Thrust faults. Orange circles are epicenters of most recent (2004-2013) earthquakes ( $m_b > 3$ ) from the NEIC catalog. Yellow circles are epicenters of recent (1918-2004) earthquakes from

*Engdahl et al.* (2006). Violet circles are historical epicenters (before 1918) from *Ambraseys and Melville* (1982). Well-constrained fault-plane solutions are indicated in black (see Table 5.1 for source parameters). Grey solutions are from the CMT catalog.

**Table 5.1.** Source parameters of the well-constrained fault-plane solutions of instrumental earthquakes in southwestern Lut Block. The fault-plane solutions are shown on Figure 5.4.

Event	Region	Lat. (°N)	Long. (°E)	Strike	Dip	Rake	Depth (km)	M <sub>w</sub>	Fault	Source
1981 Jun. 11	Golbaf	29.86	57.68	169	52	156	20	6.58	Gowk	<i>Berberian et al.</i> (2001)*
1981 Jul. 28	Sirch	29.99	57.79	177	69	184	18	6.98	Gowk	<i>Berberian et al.</i> (2001)*
1989 Nov. 20	South Golbaf	29.90	57.72	145	69	188	10	5.83	Gowk	<i>Berberian et al.</i> (2001)*
1997 Oct. 20	SW Jiroft	28.44	57.28	077	72	78	33	5.4	—	Harvard CMT*
1998 Mar. 14	Fandoqa	30.08	57.58	156	54	195	5	6.57	Gowk	<i>Berberian et al.</i> (2001)*
1998 Nov. 18	Chahar Farsakh	30.32	57.53	174	55	173	15	5.34	Gowk	<i>Berberian et al.</i> (2001)*
2003 Dec. 26	Bam	29.04	58.36	355	86	-178	5.5	6.6	Bam	<i>Jackson et al.</i> (2006)
2004 Oct. 06	Jebal-e Barez	28.77	57.95	189	86	165	49	5.2	Gowk?	Harvard CMT*
2011 Jun. 26	Sirch	30.21	57.63	317	56	103	22	5.1	Gowk	Harvard CMT**
2013 Jan. 21	Chahar Farsakh	30.36	57.48	141	78	160	12	5.3	Gowk	Harvard CMT**

\* Epicenters from *Engdahl et al.* (1998) or subsequent updates to their catalog.

\*\* Epicenters from *NEIC* catalog (<http://earthquake.usgs.gov/earthquakes/eqarchives/epic/>).

The records of several instrumental and historical seismic events along the northern segments of the Gowk fault testify for the rather high level of seismicity on these segments during the last centuries. However, performing paleoseismic investigations is essential to extend the available seismic history back through the Holocene and to better understand how such a higher slip rate (3.8-5.7 mm yr<sup>-1</sup>) along the Gowk fault releases the accumulated strain over the last seismic cycles. Indeed, such a study also permits one to compare the seismic behavior of this faster slipping strike-slip fault with the slow-slipping ones in Central Iran.

To assess the seismic history of the Gowk fault, two paleoseismic trenches were excavated across the northern part of the fault. The exposed sediments are cut and displaced by many steep fault strands and preserved evidence of several past earthquakes. The work is very preliminary but the methodology we will apply is similar to that yet performed for the other paleoseismic

sites in Central Iran. The fifteen OSL samples collected from the Gowk trenches have been sent to the Nordic Laboratory for Luminescence Dating of Aarhus University in Denmark.

### **5.6.2. Slip rate along the Sistan fault system**

At present our understanding of the distribution of active deformation east of the Lut block, along the Sistan fault system, remains poorly constrained. In fact, little is known of the slip rate on the active strike-slip faults to the east of the Lut block mostly due to the lack of tectonic-geomorphic studies combined with the Quaternary chronological dating methods. In addition, the present-day slip rates along the individual active faults in the Sistan fault system are still to be assessed; so far no geodetic study had tackled this question. However, determining the geologic and geodetic slip rates along the Sistan fault system: the Kahourak, W-Neh, E-Neh, Assaghi, and Zahedan right-lateral strike-slip faults are key points to assess the active deformation pattern of Eastern Iran.

Therefore, performing comprehensive geomorphic studies, a dense GPS network or interseismic interferometric studies remain an essential study to unravel the strain distribution across the Sistan fault system.



## REFERENCES

- Adamic, G., and M. Aitken (1998), Dose-rate conversion factors: update, *Ancient TL*, 16(2), 37-50.
- Adams, J. (1980), Paleoseismicity of the Alpine fault seismic gap, New Zealand, *Geology*, 8, 72-76.
- Agard, P., Omrani, J., Jolivet, L., Mouthereau, F. (2005), Convergence history across Zagros (Iran): constraints from collisional and earlier deformation, *Int. J. Earth Sci.*, 94, 401-419.
- Agard, P., Omrani, J., Jolivet, L., Whitechurch, H., Vrielynck, B., Spakman, W., Monié, P., Meyer, B., and R. Wortel (2011), Zagros orogeny: a subduction-dominated process, *Geol. Mag.*, 148(5-6), 692-725.
- Aghanabati, A. (1974), Geological map of Tabas, Quadrangle *I7*, scale 1:250,000, Geol. Surv. of Iran, Tehran.
- Aghanabati, A. (1992), Geological map of Jahanabad, Quadrangle *K12*, scale 1:250,000, Geol. Surv. of Iran, Tehran.
- Aghanabati, A. (1993a), Geological map of Bam, Quadrangle *J11*, scale 1:250,000, Geol. Surv. of Iran, Tehran.
- Aghanabati, A. (1993b), Geological map of Allahabad, Quadrangle *K11*, scale 1:250,000, Geol. Surv. of Iran, Tehran.
- Aitken, M. J. (1985), *Thermoluminescence Dating*, 359 pp., Academic Press, London.
- Aitken, M. J. (1998), *An introduction to optical dating*, Oxford Univ. Press, Oxford, UK.
- Aitken, M. J., and B. W. Smith (1988), Optical dating: recuperation after bleaching, *Quat. Sci. Rev.*, 7, 387-393.
- Aitken, M. J., Zimmerman, D. W., Fleming, S. J. (1968), Thermoluminescent dating of ancient pottery, *Nature*, 219, 442-445.
- Akyüz, H. S., Hartleb, R., Barka, A., Altunel, E., Sunal, G., Meyer, B., and R. Armijo (2002), Surface rupture and slip distribution of the 12 November 1999 Düzce earthquake (*M* 7.1), North Anatolian Fault, Bolu, Turkey, *Bull. Seismol. Soc. Am.*, 92(1), 61-66.
- Alavi, M. (1991), Sedimentary and structural characteristics of the Paleo-Tethys remnants in northeastern Iran, *Geo. Soc. of Am. Bull.*, 103, 983-992.

- Alavi-Naini, M., and Griffis, R. (1981a), Geological map of Naybandan, Quadrangle *J8*, scale 1:250,000, Geol. Surv. of Iran, Tehran.
- Alavi-Naini, M., and Griffis, R. (1981b), Geological map of Lakar Kuh, Quadrangle *J9*, scale 1:250,000, Geol. Surv. of Iran, Tehran.
- Allen, C. R. (1968), The tectonic environments of seismically active and inactive areas along the San Andreas fault system, in *Conference on Geologic Problems of San Andreas Fault System*, edited by Dickinson, W. R., and A. Grantz, *Stanford Univ. Publ., Geol. Sci., 11*, 70-82.
- Allen, M. B., and H. A. Armstrong (2008), Arabia-Eurasia collision and the forcing of mid-Cenozoic global cooling, *Palaeogeogr., Palaeoclimatol., Palaeoecol.*, *265*, 52-58.
- Allen, M., Jackson, J., and R. Walker (2004), Late Cenozoic reorganization of the Arabia-Eurasia collision and the comparison of short-term and long-term deformation rates, *Tectonics*, *23*, TC2008, doi:10.1029/2003TC001530.
- Allen, M. B., Kheirkhah, M., Emami, M. H., and S. J. Jones (2011), Right-lateral shear across Iran and kinematic change in the Arabia-Eurasia collision zone, *Geophys. J. Int.*, *184*, 555-574.
- Ambraseys, N. N., and J. A. Jackson (1998), Faulting associated with historical and recent earthquakes in the Eastern Mediterranean region, *Geophys. J. Int.*, *133*, 390-406.
- Ambraseys, N., and C. Melville (1982), *A history of Persian Earthquakes*, Cambridge Univ. Press, Cambridge.
- Amidi, S. M. (1975), Contribution à l'étude stratigraphique, pétrologique et pétrochimique des roches Magmatiques de la région Natanz-Nain-Surk (Iran Central), *PhD thesis*, 316 pp., Université Scientifique et Médicale de Grenoble, France.
- Argus, D. F., and R. G. Gordon (2001), Present tectonic motion across the Coast Ranges and San Andreas fault system in central California, *Geol. Soc. Am. Bull.*, *113*(12), 1580-1592.
- Armijo, R., Tapponnier, P., Mercier, J. L., Tong-Lin, H. (1986), Quaternary extension in southern Tibet: field observations and tectonic implications, *J. Geophys. Res.*, *91*(B14), 13,803-13,872.
- Armijo, R., Lyon-Caen, H., and D. Papanastassiou (1991), A possible normal-fault rupture for the 464 BC Sparta earthquake, *Nature*, *351*, 137-139.

- Avouac, J.-P., and P. Tapponnier (1993), Kinematic model of active deformation in central Asia, *Geophys. Res. Lett.*, 20(10), 895-898.
- Avouac, J.-P., Ayoub, F., Leprince, S., Konca, O., Helmberger, D. V. (2006), The 2005,  $M_w$  7.6 Kashmir earthquake: Sub-pixel correlation of ASTER images and seismic waveform analysis, *Earth Planet. Sci. Lett.*, 249, 514-528.
- Babakhani, A. R., and M. H. Kholghi (1989), Geological map of Nakhilab (Ab-E-Sard), Quadrangle *K10*, scale 1:250,000, Geol. Surv. of Iran, Tehran.
- Babakhani, A. R., and N. Alavi Tehrani (1992), Geological map of Sabzevaran, Quadrangle *J12*, scale 1:250,000, Geol. Surv. of Iran, Tehran.
- Bachmanov, D. M., Trifonov, V. G., Hessami, K. T., Kozhurin, A. I., Ivanova, T. P., Rogozhin, E. A., Hademi, M. C., Jamali, F. H. (2004), Active faults in the Zagros and central Iran, *Tectonophysics*, 380, 221-241.
- Bailey, R. M., Smith, B. W., and E. J. Rhodes (1997), Partial bleaching and the decay from characteristics of quartz OSL, *Radiat. Meas.*, 27(2), 123-136.
- Baker, C. (1993), Active seismicity and tectonics of Iran, *PhD thesis*, University of Cambridge, UK.
- Barka, A. (1996), Slip distribution along the North Anatolian Fault associated with the large earthquakes of the period 1939 to 1967, *Bull. Seismol. Soc. Am.*, 86(5), 1238-1254.
- Barka, A., Akyüz, H. S., Altunel, E., Sunal, G., Çakir, Z., Dikbas, A., Yerli, B., Armijo, R., Meyer, B., de Chabalier, J. B., Rockwell, T., Dolan, J. R., Hartleb, R., Dawson, T., Christofferson, S., Tucker, A., Fumal, T., Langridge, R., Stenner, H., Lettis, W., Bachhuber, J., and W. Page (2002), The surface rupture and slip distribution of the 17 August 1999 İzmit earthquake ( $M$  7.4), North Anatolian Fault, *Bull. Seismol. Soc. Am.*, 92(1), 43-60, doi:10.1785/0120000841.
- Bateman, M. D., and J. A. Catt (1996), An absolute chronology for the raised beach and associated deposits at Seweby, East Yorkshire, England, *J. Quatern. Sci.*, 11(5), 389-395.
- Bateman, M. D., Boulter, C. H., Carr, A. S., Frederick, C. D., Peter, D. Wilder, M. (2007), Preserving the palaeoenvironmental record in Drylands: Bioturbation and its significance for luminescence-derived chronologies, *Sedim. Geol.*, 195, 5-19.

- Bayer, R., Chery, J., Tatar, M., Vernant, Ph., Abbassi, M., Masson, F., Nilforoushan, F., Doerflinger, E., Regard, V., and O. Bellier (2006), Active deformation in Zagros-Makran transition zone inferred from GPS measurements, *Geophys. J. Int.*, *165*, 373-581.
- Becker, A., Davenport, C. A., Eichenberger, U., Gilli, E., Jeannin, P. -Y., Lacave, C. (2006), Speleoseismology: A critical perspective, *J. Seismol.*, *10*, 371-388.
- Berberian, M. (1976), Contribution to the seismotectonics of Iran (part II), *39*, 517 pp., Geol. Surv. of Iran, Tehran.
- Berberian, M. (1979a), Tabas-s-Golshan (Iran) catastrophic earthquake of 16 September 1978; a preliminary field report, *Disasters*, *2*, 207-219.
- Berberian, M. (1979b), Earthquake faulting and bedding thrust associated with the Tabas-e-Golshan (Iran) earthquake of September 16, 1978, *Bull. Seismol. Soc. Am.*, *69*, 1861-1887.
- Berberian, M. (1981), Active faulting and tectonics of Iran, in *Zagros-Hindu Kush-Himalaya Geodynamic Evolution, Geodynamic Series*, edited by Gupta, H., and F. Delany, *3*, 33-69.
- Berberian, M. (2005), The 2003 Bam urban earthquake: a predictable seismotectonic pattern along the western margin of the rigid Lut block, southeast Iran, *Earthq. Spectra*, *21*(S1), 35-99.
- Berberian, F. and M. Berberian (1981), Tectono-Plutonic episodes in Iran, in *Zagros, Hindu Kush, Himalaya: geodynamic evolution*, edited by Gupta, H. K., and F. M. Delany, *Geodyn. Ser.*, *3*, 5-32.
- Berberian, M., and G. C. P. King (1981), Towards a paleogeography and tectonic evolution of Iran, *Can. J. Earth Sci.*, *18*, 210-265.
- Berberian, M., and M. Qorashi (1994), Coseismic fault-related folding during the South Golbaf earthquake of November 20, 1989, in southeast Iran, *Geology*, *22*, 531-534.
- Berberian, M., and R. S. Yeats (1999), Patterns of historical earthquake rupture in the Iranian plateau, *Bull. Seismol. Soc. Am.*, *89*(1), 120-139.
- Berberian, M., and R. S. Yeats (2001), Contribution of archaeological data to studies of earthquake history in the Iranian Plateau, *J. Struct. Geol.*, *23*, 563-584.

- Berberian, M., Jackson, J. A., Qorashi, M., and M. H. Kadjar (1984), Field and teleseismic observations of the 1981 Golbaf-Sirch earthquakes in SE Iran, *Geophys. J. R. astr. Soc.*, 77, 809-838.
- Berberian, M., Qorashi, M., Jackson, J. A., Priestley, K., and T. Wallace (1992), The Rudbar-Tarom earthquake of 20 June 1990 in NW Persia: preliminary field and seismological observations, and its tectonic significance, *Bull. Seismol. Soc. Am.*, 82(4), 1726-1755.
- Berberian, M., Jackson, J. A., Qorashi, M., Khatib, M., Priestley, K., Talebian, M., and M. Ghafari-Ashtiani (1999), The 1997 May 10 Zirkuh (Qa'emat) earthquake ( $M_w$  7.2): faulting along the Sistan suture zone of eastern Iran, *Geophys. J. Int.*, 136, 671-694.
- Berberian, M., Jackson, J. A., Qorashi, M., Talebian, M., Khatib, M., and K. Priestley (2000), The 1994 Sefidabeh earthquakes in eastern Iran: blind thrusting and bedding-plane slip on a growing anticline, and active tectonics of the Sistan suture zone, *Geophys. J. Int.*, 142, 283-299.
- Berberian, M., Jackson, J. A., Fielding, E., Parsons, B. E., Priestly, K., Qorashi, M., Talebian, M., Walker, R., Wright, T. J., and C. Baker (2001), The 1998 March 14 Fandoqa earthquake ( $M_w$  6.6) in Kerman province, southeast Iran: re-rupture of the 1981 Sirch earthquake fault, triggering of slip on adjacent thrusts and the active tectonics of the Gowk fault zone, *Geophys. J. Int.*, 146, 371-398.
- Berberian, M., Shahmirzadi, S. M., Nokandeh, J., Djamali, M. (2012), Archeoseismicity and environmental crises at the Sialk Mounds, Central Iranian Plateau, since the Early Neolithic, *J. Arch. Sci.*, 39, 2845-2858.
- Berger, G. W. (1990), Effectiveness of natural zeroing of the thermoluminescence in sediments, *J. Geophys. Res.*, 95(B8), 12, 375-12, 397.
- Besse, J., Torcq, F., Gallet, Y., Ricou, L. E., Krystyn, L., and A. Saidi (1998), Late Permian to Late Triassic palaeomagnetic data from Iran: constraints on the migration of the Iranian block through the Tethyan Ocean and initial destruction of Pangaea, *Geophys. J. Int.*, 135, 77-92.
- Biasi, G. P., Weldon II, R. J., Fumal, T. E., and G. G. Seitz (2002), Paleoseismic event dating and the conditional probability of large earthquakes on the southern San Andreas fault, California, *Bull. Seismol. Soc. Am.*, 92(7), 2761-2781.
- Bilham, R. (2010), Lessons from the Haiti earthquake, *Nature*, 463, 878-879.

- Bonilla, M. G., and J. J. Lienkaemper (1990), Visibility of fault strands in exploratory trenches and timing of rupture events, *Geology*, *18*, 153-156.
- Bookhagen, B., Thiede, R. C., Strecker, M. R. (2005), Late Quaternary intensified monsoon phases control landscape evolution in the northwest Himalaya, *Geology*, *33*(2), 149-152.
- Borrero, J. C. (2005), Field survey of Northern Sumatra and Banda Aceh, Indonesia after the tsunami and earthquake of 26 December 2004, *Seism. Res. Lett.*, *76*(3), 312-320.
- Bøtter-Jensen, L. (1988), The automated Risø TL dating reader system, *Nucl. Tracks Radiat. Meas.*, *14*(1/2), 177-180.
- Bøtter-Jensen, L. (1997), Luminescence techniques: instrumentation and methods, *Radiat. Meas.*, *27*(5/6), 749-768.
- Bøtter-Jensen, L., Thomsen, K. J., Jain, M. (2010), Review of optically stimulated luminescence (OSL) instrumental developments for retrospective dosimetry, *Radiat. Meas.*, *45*, 253-257.
- Boulin, J. (1988), Hercynian and Eocimmerian events in Afghanistan and adjoining regions, *Tectonophysics*, *148*, 253-278.
- Boyle, J. A. (1968), *The Cambridge History of Iran*, vol. 5: *The Saljuq and Mongol periods*, 763 pp., Cambridge Univ. Press, Cambridge.
- Braucher, R., Merchel, S., Borgomano, J., Bourlès, D. L. (2011), Production of cosmogenic radionuclides at great depth: A multi element approach, *Earth Planet. Sci. Lett.*, *309*, 1-9.
- Bridgland, D., Westaway, R. (2008), Climatically controlled river terrace staircases: A worldwide Quaternary phenomenon, *Geomorphology*, *98*, 285-315.
- Brown, E. T., Molnar, P., Bourlès, D. L. (2005), Comment on "Slip-rate measurements on the Karakorum fault may imply secular variations in fault motion", *Science*, *309*, 1326, doi:10.1126/science.1112508.
- Bull, W. B. (1996), Dating San Andreas fault earthquakes with lichenometry, *Geology*, *24*(2), 11-114.
- Bull, W. B. (2007), *Tectonic geomorphology of mountains: a new approach to paleoseismology*, Blackwell Publishing, Oxford, UK.
- Burns, S. J., Fleitmann, D., Matter, A., Neff, U., Mangini, A. (2001), Speleothem evidence from Oman for continental pluvial events during interglacial periods, *Geology*, *29*(7), 623-626.

- Calais, E., Freed, A., Mattioli, G., Amelung, F., Jónsson, S., Jansma, P., Hong, S.-H., Dixon, T., Prépetit, C., and R. Momplaisir (2010), Transpressional rupture of an unmapped fault during the 2010 Haiti earthquake, *Nat. Geosci.*, *3*, 794-799.
- Camp, V.E., and R. J. Griffis (1982), Character, genesis and tectonic setting of igneous rocks in the Sistan suture zone, eastern Iran, *Lithos*, *3*, 221-239.
- Chevalier, M.-L., Ryerson, F. J., Tapponnier, P., Finkel, R. C., Van Der Woerd, J., Haibing, L., Qing, L. (2005), Slip-rate measurements on the Karakorum fault may imply secular variations in fault motion, *Science*, *307*, 411-414, doi:10.1126/science.1105466.
- Clark, P. U., Dyke, A. S., Shakun, J. D., Carlson, A. E., Clark, J., Wohlfarth, B., Mitrovica, J. X., Hostetler, S. W., McCabe, A. M. (2009), The Last Glacial Maximum, *Science*, *325*, 710-714.
- Cutler, K. B., Edwards, R. L., Taylor, F. W., Chen, H., Adkins, J., Gallup, C. D., Cutler, P. M., Burr, G. S., Bloom, A. L. (2003), Rapid sea-level fall and deep-ocean temperature change since the last interglacial period, *Earth Planet. Sci. Lett.*, *206*, 253-271.
- Daëron, M., Benedetti, L., Tapponnier, P., Sursock, A., Finkel, R. C. (2004), Constraints on the post ~25-ka slip rate of the Yammoûneh fault (Lebanon) using in situ cosmogenic <sup>36</sup>Cl dating of offset limestone-clast fans, *Earth Planet. Sci. Lett.*, *227*, 105-119.
- Daëron, M., Klinger, Y., Tapponnier, P., Elias, A., Jaques, E., Sursock, A. (2005), Sources of the large A.D. 1202 and 1759 Near East earthquakes, *Geology*, *33*(7), 529-532, doi:10.1130/G21352.1.
- Daëron, M., Klinger, Y., Tapponnier, P., Elias, A., Jaques, E., and A. Sursock (2007), 12,000-year-long record of 10 to 13 paleoearthquakes on the Yammoûneh fault, Levant fault system, Lebanon, *Bull. Seismol. Soc. Am.*, *97*(3), 749-771, doi:10.1785/0120060106.
- Daniels, J. M. (2003), Floodplain aggradation and pedogenesis in a semiarid environment, *Geomorphology*, *56*, 225-242.
- Dehghani, G. A., and J. Makris (1984), The gravity field and crustal structure of Iran, *N. Jb. Geol. Palaeont. Abh.*, *168*, 215-229.
- De Martini, P. M., Hessami, K., Pantosti, D., D'Addezio, G., Alinaghi, H., Ghafory-Ashtiani, M. (1998), A geologic contribution to the evaluation of the seismic potential of the Kahrizak fault (Tehran, Iran), *Tectonophysics*, *287*, 187-199.

- de Michele, M., Raucoules, D., de Sigoyer, J., Pubellier, M., and N. Chamot-Rooke (2010), Three-dimensional surface displacement of the 2008 May 12 Sichuan earthquake (China) derived from Synthetic Aperture Radar: evidence for rupture on a blind thrust, *Geophys. J. Int.*, *183*, 1097-1103.
- Densmore, A. L., Ellis, M. A., Li, Y., Zhou, R., Hancock, G. S., and N. Richardson (2007), Active tectonics of the Beichuan and Pengguan faults at the eastern margin of the Tibetan Plateau, *Tectonics*, *26*, TC4005, doi:10.1029/2006TC001987.
- Desilets, D., Zreda, M., Almasi, P. F., Elmore, D. (2006), Determination of cosmogenic  $^{36}\text{Cl}$  in rocks by isotope dilution: innovations, validation and error propagation, *Chem. Geol.*, *233*, 185-195.
- Devès, M., King, G. C. P., Klinger, Y., Agnon, A. (2011), Localised and distributed deformation in the lithosphere: Modelling the Dead Sea region in 3 dimensions, *Earth Planet. Sci. Lett.*, *308*, 172-184.
- Dixon, T. H., Norabuena, E., Hotaling, L. (2003), Paleoseismology and Global Position System: earthquake-cycle effects and geodetic versus geologic fault slip rates in the Eastern California shear zone, *Geology*, *31*(1), 55-58.
- Dolan, J. F., Sieh, K., Rockwell, T. K., Guphill, P., Miller, G. (1997), Active tectonics, paleoseismology, and seismic hazards of the Hollywood fault, northern Los Angeles basin, California, *Geol. Soc. Am. Bull.*, *109*(12), 1595-1616.
- Dolan, J. F., Bowman, D. D., Sammis, C. G. (2007), Long-range and long-term fault interactions in Southern California, *Geology*, *35*(9), 855-858.
- Duller, G. A. T. (1991), Equivalent dose determination using single aliquots, *Nucl. Tracks Radiat. Meas.*, *18*(4), 371-378.
- Duller, G. A. T. (1995), Luminescence dating using single aliquots: methods and applications, *Radiat. Meas.*, *24*(3), 217-226.
- Emami, M. H., Sadeghi, M. M., Omrani, S. J. (1993), Magmatic map of Iran, scale 1:1,000,000, Geol. Surv. of Iran, Tehran.
- Engdahl, E. R., van der Hilst, R., and R. Buland (1998), Global teleseismic earthquake relocation with improved travel times and procedures for depth determination, *Bull. Seismol. Soc. Am.*, *88*(3), 722-743.

- Engdahl, E. R., Jackson, J. A., Myers, A. C., Bergman, E. A., and K. Priestley (2006), Relocation and assessment of seismicity in the Iran region, *Geophys. J. Int.*, *167*, 761-778.
- England, P., and P. Molnar (1997), Active deformation of Asia: from kinematics to dynamics, *Science*, *278*, 647, doi:10.1126/science.278.5338.647.
- Farbod, Y. (2012), Active tectonics of the Doruneh fault: seismogenic behavior and geodynamic role, *PhD thesis*, Univ. of Aix-Marseille, Aix-en-Provence, France.
- Farbod, Y., Bellier, O., Shabaniyan, E., and M. R. Abbassi (2011), Geomorphic and structural variations along the Doruneh Fault System (central Iran), *Tectonics*, *30*, TC6014, doi:10.1029/2011TC002889.
- Fattahi, M., Walker, R., Hollingsworth, J., Bahroudi, A., Nazari, H., Talebian, M., Armitage, S., Stokes, S. (2006), Holocene slip-rate on the Sabzevar thrust fault, NE Iran, determined using optically stimulated luminescence (OSL), *Earth Planet. Sci. Lett.*, *254*, 673-684, doi:10.1016/j.epsl.2006.03.027.
- Fattahi, M., Walker, R. T., Khatib, M. M., Dolati, A., and A. Bahroudi (2007), Slip-rate estimate and past earthquakes on the Doruneh fault, eastern Iran, *Geophys. J. Int.*, *168*, 691-709.
- Fattahi, M., Nazari, H., Bateman, M. D., Meyer, B., Sébrier, M., Talebian, M., Le Dortz, K., Foroutan, M., Ahmadi Givi, F., Ghorashi, M. (2010), Refining the OSL age of the last earthquake on the Dheshir fault, Central Iran, *Quat. Geochronol.*, *5*, 286-292, doi:10.1016/j.quageo.2009.04.005.
- Fattahi, M., Walker, R. T., Talebian, M., Sloan, R. A., and A. Rashidi (2011), The structure and late Quaternary slip rate of the Rafsanjan strike-slip fault, SE Iran, *Geosphere*, *7*(5), 1159-1174.
- Fattahi, M., Walker, R. T., Talebian, M., Sloan, R. A., Rasheedi, A. (2013), Late Quaternary active faulting and landscape evolution in relation to the Gowk Fault in the South Golbaf Basin, S.E. Iran, *Geomorphology*, <http://dx.doi.org/10.1016/j.geomorph.2013.08017>.
- Fielding, E. J., Wright, T. J., Muller, J., Parsons, B. E., Walker, R. (2004), Aseismic deformation of a fold-and-thrust belt imaged by synthetic aperture radar interferometry near Shahdad, southeast Iran, *Geology*, *32*(7), 577-580.
- Foroutan, M., Sébrier, M., Nazari, H., Meyer, B., Fattahi, M., Rashidi, A., Le Dortz, k., and M. D. Bateman (2012), New evidence for large earthquakes on the Central Iran plateau:

- palaeoseismology of the Anar fault, *Geophys. J. Int.*, 189(1), 6-18, doi:10.1111/j.1365-246X.2012.05365.x.
- Forti, P. (2001), Seismotectonic and paleoseismic studies from speleothems: The state of the art, *Geol. Belg.*, 4/3-4, 175-185.
- Frame, L. (2010), Metallurgical investigations at Godin Tepe, Iran, Part I: the metal finds, *J. Archaeol. Sci.*, 37, 1700-1715.
- Frankel, K. L., and J. F. Dolan (2007), Characterizing arid region alluvial fan surface roughness with airborne laser swath mapping digital topographic data, *J. Geophys. Res.*, 112, F02025, doi:10.1029/2006JF000644.
- Frankel, K. L., Brantley, K. S., Dolan, J. F., Finkel, R. C., Klinger, R. E., Knott, J. R., Machette, M. N., Owen, L. A., Phillips, F. M., Slate, J. L., and B. P. Wernicke (2007a), Cosmogenic  $^{10}\text{Be}$  and  $^{36}\text{Cl}$  geochronology of offset alluvial fans along the northern Death Valley fault zone: Implications for transient strain in the eastern California shear zone, *J. Geophys. Res.*, 112, B06407, doi:10.1029/2006JB004350.
- Frankel, K. L., Dolan, J. F., Finkel, R. C., Owen, L. A., and J. S. Hoefft (2007b), Spatial variations in slip rate along the Death Valley-Fish Lake Valley fault system determined from LiDAR topographic data and cosmogenic  $^{10}\text{Be}$  geochronology, *Geophys. Res. Lett.*, 34, L18303, doi:10.1029/2007GL030549.
- Frankel, K. L., Dolan, J. F., Owen, L. A., Ganev, P., Finkel, R. C. (2011), Spatial and temporal constancy of seismic strain release along an evolving segment of the Pacific-North America plate boundary, *Earth Planet. Sci. Lett.*, 304, 565-576.
- Freund, R. (1970), Rotation of strike slip faults in Sistan, southeast Iran, *J. Geol.*, 78, 188-200.
- Friedrich, A. M., Wernicke, B. P., and N. A. Niemi (2003), Comparison of geodetic and geologic data from the Wasatch region, Utah, and implications for the spectral character of Earth deformation at periods of 10 to 10 million years, *J. Geophys. Res.*, 108(B4), 2199, doi:10.1029/2001JB000682.
- Fürsich, F. T., Wilmsen, M., Seyed-Emami, K., and M. R., Majidifard (2009), Lithostratigraphy of the Upper Triassic-Middle Jurassic Shemshak Group of Northern Iran, in *South Caspian to Central Iran Basins*, edited by Brunet, M.-F., Wilmsen, M., and J. W. Granath, *Geol. Soc. Lond. Spec. Publ.*, 312, 129-160.

- Galbraith, R. F., and P. F. Green (1990), Estimating the component ages in a finite mixture, *Nucl. Tracks Radiat. Meas.*, 17(3), 197-206.
- Galbraith, R. F., and G. M. Laslett (1993), Statistical models for mixed fission track ages, *Nucl. Tracks Radiat. Meas.*, 21(4), 459-470.
- Galbraith, R. F., Roberts, R. G., Laslett, G. M., Yoshida, H., and J. M. Olley (1999), Optical dating of single and multiple grains of quartz from Jinmium rock shelter. northern Australia: Part I, Experimental design and statistical models, *Archaeometry*, 41(2), 339-364.
- Galli, P., Galadini, F. Pantosti, D. (2008), Twenty years of paleoseismology in Italy, *Earth-Sci. Rev.*, 88, 89-117.
- Ganev, P. N., Dolan, J. F., McGill, S. F., and K. L. Frankel (2012), Constancy of geologic slip rate along the central Garlock fault: implications for strain accumulation and release in southern California, *Geophys. J. Int.*, 190, 745-760.
- Gershevitch, I. (1985), *The Cambridge History of Iran*, vol. 2: *The Median and Achaemenian periods*, 929 pp., Cambridge Univ. Press, Cambridge.
- Godard, V., Pik, R., Lavé, J., Cattin, R., Tibari, B., de Sigoyer, J., Pubellier, M., and J. Zhu (2009), Late Cenozoic evolution of the central Longmen Shan, eastern Tibet: Insight from (U-Th)/He thermochronometry, *Tectonics*, 28, TC5009, doi:10.1029/2008TC002407.
- Godfrey-Smith, D. I., Huntley, D. J., and W. -H. Chen (1988), Optical dating studies of quartz and feldspar sediment extracts, *Quat. Sci. Rev.*, 7, 373-380.
- Gold, R., dePolo, C., Briggs, R., Crone, A., and J. Gosse (2013), Late Quaternary slip-rate variations along the Warm Springs Valley fault system, Northern Walker Lane, California-Nevada border, *Bull. Seismol. Soc. Am.*, 103(1), 542-558, doi:10.1785/0120120020.
- Goodbred Jr, S. L., Kuehl, S. A. (2000), The significance of large sediment supply, active tectonism, and eustasy on margin sequence development: Late Quaternary stratigraphy and evolution of the Ganges-Brahmaputra delta, *Sediment. Geol.*, 133, 227-248.
- Gosse, J. C., Phillips, F. M. (2001), Terrestrial in situ cosmogenic nuclides: theory and application, *Quat. Sci. Rev.*, 20, 1475-1560.

- Grant, L. B., and K. Sieh (1994), Paleoseismic evidence of clustered earthquakes on the San Andreas fault in the Carrizo Plain, California, *J. Geophys. Res.*, *99*(B4), 6819-6841.
- Grootes, P. M., and M. Stuiver (1997), Oxygen 18/16 variability in Greenland snow and ice with  $10^{-3}$ - to  $10^5$ -year time resolution, *J. Geophys. Res.*, *102*(C12), 24,455-26,470.
- Guérin, G., Mercier, N., and G. Adamiec (2011), Dose-rate conversion factors: update, *Ancient TL*, *29*(1), 5-8.
- Guralnik, B., Matmon, A., Avni, Y., Porat, N., Fink, D. (2011), Constraining the evolution of river terraces with integrated OSL and cosmogenic nuclide data, *Quat. Geochronol.*, *6*, 22-32.
- Hartleb, R. D., Dolan, J. F., Kozacı, Ö., Akyüz, H. S., Seitz, G. (2006), A 2500-yr-long paleoseismologic record of large, infrequent earthquakes on the North Anatolian fault at Çukurçimen, Turkey, *Geol. Soc. Am. Bull.*, *118*(7/8), 823-840, doi:10.1130/B25838.1.
- Hassanzadeh, J., Stokli, D. F., Horton, B. K., Axen, G. J., Stockli, L. D., Grove, M., Schmitt, A. K., Walker, J. D. (2008), U-Pb zircon geochronology of late Neoproterozoic-Early Cambrian granitoids in Iran: Implication for paleogeography, magmatism, and exhumation history of Iranian basement, *Tectonophysics*, *451*, 71-96.
- Hayes, G. P., Briggs, R. W., Sladen, A., Fielding, E. J., Prentice, C., Hudnut, K., Mann, P., Taylor, F. W., Crone, A. J., Gold, R., Ito, T., and M. Simons (2010), Complex rupture during the 12 January 2010 Haiti earthquake, *Nat. Geosci.*, *3*, 800-805.
- Henshilwood, C. S., d'Errico, F., Yates, R., Jacobs, Z., Tribolo, C., Duller, G. A. T., Mercier, N., Sealy, J. C., Valladas, H., Watts, I., Wintle, A. G. (2002), Emergence of modern human behavior: Middle Stone Age engravings from South Africa, *Science*, *295*, 1278-1280.
- Hessami, K., Pantosti, D., Tabassi, H., Shabanian, E., Abbassi, M. R., Fegghi, K., and S. Solaymani (2003), Paleoearthquakes and slip rates of the North Tabriz Fault, NW Iran: preliminary results, *Ann. Geophys.*, *46*(5), 903-915.
- Hollingsworth, J., Jackson, J., Walker, R., Gheitanchi, M. R., and M. J. Bolourchi (2006), Strike-slip faulting, rotation, and along-strike elongation in the Kopeh Dag mountains, NE Iran, *Geophys. J. Int.*, *166*, 1161-1177, doi:10.1111/j.1365-246X.2006.02983.x.
- Hollingsworth, J., Jackson, J., Walker, R., Nazari, H. (2008), Extrusion tectonics and subduction in the eastern South Caspian region since 10 Ma, *Geology*, *36*(10), 763-766, doi:10.1130/G25008A.1.

- Holzer, T. L., and M. M. Clark (1993), Sand boils without earthquakes, *Geology*, *21*, 873-876.
- Huber, H. (1977), Geological map of Iran, sheets no. *I-6*, scale 1:1,000,000, with explanatory notes, National Iranian Oil Company, Exploration and Production Affairs, Tehran.
- Hubert-Ferrari, A., Armijo, R., King, G., Meyer, B., Barka, A. (2002), Morphology, displacement, and slip rates along the North Anatolian fault, Turkey, *J. Geophys. Res.*, *107*(B10), 2235, doi:10.1029/2001JB000393.
- Huntley, D. J., and Lian, O. B. (1999), Determining when a sediment was last exposed to sunlight by optical dating, in *Holocene climate and environmental changes in the Palliser Triangle, Southern Canadian prairies*, edited by Lemmen, D. S., and R. E. Vance, *Geol. Surv. Can. Bull.*, *534*, 211-222.
- Huntley, D. J., Godfrey-Smith, D. I., and M. L. W. Thewalt (1985), Optical dating of sediments, *Nature*, *313*, 105-107.
- Jackson, J., and D. McKenzie (1984), Active tectonics of the Alpine-Himalayan Belt between western Turkey and Pakistan, *Geophys. J. R. astr. Soc.*, *77*, 185-264.
- Jackson, J., Haines, J., Holt, W. (1995), The accommodation of Arabia-Eurasia plate convergence in Iran, *J. Geophys. Res.*, *100*(B8), 15205-15219.
- Jackson, J., Bouchon, M., Fielding, E., Funning, G., Ghorashi, M., Hatzfeld, D., Nazari, H., Parson, B., Priestley, K., Talebian, M., Tatar, M., Walker, R. and T. Wright (2006), Seismotectonic, rupture process, and earthquake-hazard aspects of the 26 December 2003 Bam, Iran, earthquake, *Geophys. J. Int.*, *166*, 1270-1292.
- Jamali, F., Hessami, K., Ghorashi, M. (2011), Active tectonics and strain partitioning along dextral fault system in Central Iran: Analysis of geomorphological observations and geophysical data in the Kashan region, *J. Asian Earth Sci.*, *40*, 1015-1025.
- Karagaranbafghi, F., Foeken, J. P. T., Guest, B., Stuart, F. M. (2012), Cooling history of the Chapedony metamorphic core complex, Central Iran: Implications for the Eurasia-Arabia collision, *Tectonophysics*, *524-525*, 100-107.
- Khazaradze, G., and J. Klotz (2003), Short- and long-term effects of GPS measured crustal deformation rates along the south central Andes, *J. Geophys. Res.*, *108*(B6), 2289, doi:10.1029/2002JB001879.

- Khazaradze, G., Wang, K., Klotz, J., Hu, Y., and J. He (2002), Prolonged post-seismic deformation of the 1960 great Chile earthquake and implications for mantle rheology, *Geophys. Res. Lett.*, 29(22), 2050, doi:10.1029/2002GL015986.
- King, G., Oppenheimer, D., Amelung, F. (2004), Block versus continuum deformation in the Western United States, *Earth Planet. Sci. Lett.*, 19, 101-112., 128, 55-64.
- Klinger, Y., Sieh, K., Altunel, S. E., Akoglu, A., Barka, A., Dawson, T., Gonzalez, T., Meltzner, A., and T. Rockwell (2003), Paleoseismic evidence of characteristic slip on the western segment of the North Anatolian fault, Turkey, *Bull. seismol. Soc. Am.*, 93(6), 2317-2332.
- Kluyver, H. M., Tirrul, R., Chance, P. N., Johns, G. W., and H. M., Meixner (1983), Explanatory text of the Naybandan Quadrangle map, Quadrangle J8, scale 1:250,000, Geol. Surv. of Iran, Tehran.
- Knox, J. C. (1993), Large increases in flood magnitude in response to modest changes in climate, *Nature*, 361, 430-432.
- Knox, J. C. (2000), Sensitivity of modern and Holocene floods to climate change, *Quat. Sci. Rev.*, 19, 439-457.
- Lambeck, K., Yokoyama, Y., Purcell, T. (2002), Into and out of the Last Glacial Maximum: sea-level change during Oxygen Isotope Stages 3 and 2, *Quat. Sci. Rev.*, 21, 343-360.
- Lamberg-Karlovsky, C. C. (1970), *Excavations at Tepe Yahya, Iran, 1967-1969, Progress Report 1*, 134 pp., American School of Prehistoric Research, Peabody Museum, Harvard Univ., Cambridge, Mass.
- Le Dortz, K., Meyer, B., Sébrier, M., Nazari, H., Braucher, R., Fattahi, M., Benedetti, L., Foroutan, M., Siame, L., Bourlès, D., Talebian, M., Bateman, M. D., and M. Ghoraishi (2009), Holocene right-slip rate determined by cosmogenic and OSL dating on the Anar fault, Central Iran, *Geophys. J. Int.*, 179, 700-710.
- Le Dortz, K., Meyer, B., Sébrier, M., Braucher, R., Nazari, H., Benedetti, L., Fattahi, M., Bourlès, D., Foroutan, M., Siame, L., Rashidi, A., and M. D. Bateman (2011), Dating inset terraces and offset fans along the Dehshir Fault (Iran) combining cosmogenic and OSL methods, *Geophys. J. Int.*, 185, 1147-1174.
- Le Dortz, K., Meyer, B., Sébrier, M., Braucher, R., Bourlès, D., Benedetti, L., Nazari, H., Foroutan, M. (2012), Interpreting scattered *in-situ* produced cosmogenic nuclide depth-profile data, *Quat. Geochronol.*, 11, 98-115.

- Lee, J., Spencer, J., Owen, L. (2001), Holocene slip rates along the Owens Valley fault, California: Implications for the recent evolution of the Eastern California Shear Zone, *Geology*, 29(9), 819-822.
- Li, C., Zhang, P.-Z., Yin, J., and W. Min (2009), Late Quaternary left-lateral slip rate of the Haiyuan fault, northeastern margin of the Tibetan Plateau, *Tectonics*, 28, TC5010, doi:10.1029/2008TC002302.
- Li, S.-H. (1994), Optical dating: insufficiently bleached sediments, *Radiat. Meas.*, 23(2/3), 563-567.
- Lindsey, E. O., and Y. Fialko (2013), Geodetic slip rates in the southern San Andreas Fault system: Effects of elastic heterogeneity and fault geometry, *J. Geophys. Res.*, 118, 689-697, doi:10.1029/2012JB009358.
- Liu, J., Klinger, Y., Sieh, K., Rubin, C. (2004), Six similar sequential ruptures of the San Andreas fault, Carrizo Plain, California, *Geology*, 32(8), 649-652.
- Lu, H., Burbank, D. W., Li, Y. (2010), Alluvial sequence in the north piedmont of the Chinese Tian Shan over the past 550 kyr and its relationship to climate change, *Palaeogeogr. Palaeoclimat. Palaeoecol.*, 285, 343-353.
- Machette, M. N., Personius, S. F., Nelson, A. R., Schwartz, D. P., and W. R. Lund (1991), The Wasatch fault zone, Utah—segmentation and history of Holocene earthquakes, *J. Struct. Geol.*, 13(2), 137-149.
- Mahdavi, M. A. (1996), Geological map of Ravar, Quadrangle 19, scale 1:250,000, Geol. Surv. of Iran, Tehran.
- Masson, F., Chéry, J., Hatzfeld, D., Martinod, J., Vernant, P., Tavakoli, F., and M. Ghafory-Ashtiani (2005), Seismic versus aseismic deformation in Iran inferred from earthquakes and geodetic data, *Geophys. J. Int.*, 160, 217-226.
- Masson, F., Anvari, M., Djamour, Y., Walpersdorf, A., Tavakoli, F., Daignières, M., Nankali, H., and S. Van Gorp (2007), Large-scale velocity field and strain tensor in Iran inferred from GPS measurements: new insight for the present-day deformation pattern within NE Iran, *Geophys. J. Int.*, 170, 436-440.
- Matmon, A., Schwartz, D. P., Haeussler, P. J., Finkel, R., Lienkaemper, J. J., Stenner, H. D., Dawson, T. E. (2006), Denali fault slip rates and Holocene-late Pleistocene kinematics of central Alaska, *Geology*, 34(8), 645-648, doi:10.1130/G22361.1.

- Mayewski, P. A., Rohling, E. E., Stager, J. C., Karlén, W., Maasch, K. A., Meeker, L. D., Meyerson, E. A., Gasse, F., van Kreveld, S., Holmgren, K., Lee-Thorp, J., Rosqvist, G., Rack, F., Staubwasser, M., Schneider, R. R., Steig, E. (2004), Holocene climate variability, *Quat. Res.*, *62*, 243-255.
- McCalpin, J. P. (2009), *Paleoseismology*, 2nd ed., Academic, San Diego, Calif.
- McGill, S. F., Wells, S. G., Fortner, S. K., Kuzma, H. A., McGill, J. D. (2009), Slip rate of the western Garlock fault, at Clark Wash, near Lone Tree Canyon, Mojave Desert, California, *Geol. Soc. Am. Bull.*, *121*(3/4), 536-554.
- McQuarrie, N., Stock, J. M., Verdel, C., and B. P. Wernicke (2003), Cenozoic evolution of Neotethys and implications for the causes of plate motions, *Geophys. Res. Lett.*, *30*(20), 2036, doi:10.1029/2003GL017992.
- Meade, B. J. (2007), Present-day kinematics at the India-Asia collision zone, *Geology*, *35*(1), 81-84, doi:10.1130/G22924A.1.
- Mejdahl V. and L. Bøtter-Jensen (1994), Luminescence dating of archaeological materials using a new technique based on single aliquot measurements, *Quat. Geochronol. (Quat. Sci. Rev.)*, *13*, 551-554.
- Mériaux, A.-S., Tapponnier, P., Ryerson, F. J., Xiwei, X., King, G., Van der Woerd, J., Finkel, R. C., Haibing, L., Caffee, M. W., Zhiqin, X., and C. Wenbin (2005), The Aksay segment of the northern Altyn Tagh fault: Tectonic geomorphology, landscape evolution, and Holocene slip rate, *J. Geophys. Res.*, *110*, B04404, doi:10.1029/2004JB003210.
- Meyer, B., and K. Le Dortz (2007), Strike-slip kinematics in Central and Eastern Iran: Estimating fault slip-rates averaged over the Holocene, *Tectonics*, *26*, TC5009, doi:10.1029/2006TC002073.
- Meyer, B., Mouthereau, F., Lacombe, O., and P. Agard (2006), Evidence of Quaternary activity along the Deshir Fault: implication for the Tertiary tectonics of Central Iran, *Geophys. J. Int.*, *164*, 192-201.
- Meisling, K. E., and K. E. Sieh (1980), Disturbance of trees by the 1857 Fort Tejon earthquake, California, *J. Geophys. Res.*, *85*(B6), 3225-3238.
- Mohajjel, M. (2009), Thin-skinned deformation near Shahdad, southeast Iran, *J. Asian Earth Sci.*, *36*, 146-155.

- Molnar, P., Fitch, T. J., Wu, F. T. (1973), Fault plane solutions of shallow earthquakes and contemporary tectonic in Asia, *Earth Planet. Sci. Lett.*, *19*, 101-112.
- Mouthereau, F., Lacombe, O., Vergés, J. (2012), Building the Zagros collisional orogen: Timing, strain distribution and the dynamics of Arabia/Eurasia plate convergence, *Tectonophysics*, *532-535*, 27-60.
- Mueller, R. G., Joyce, A. A., Borejsza, A. (2012), Alluvial archives of the Nochixtlan valley, Oaxaca, Mexico: Age and significance for reconstructions of environmental change, *Palaeogeogr. Palaeoclimat. Palaeoecol.*, *321-322*, 121-136.
- Murray, A. S., and V. Mejdahl (1999), Comparison of regenerative-dose single-aliquot and multiple-aliquot (SARA) protocols using heated quartz from archaeological sites, *Quat. Geochronol.*, *18*, 223-229.
- Murray, A. S., and J. M. Olley (2002), Precision and accuracy in the optically stimulated luminescence dating of sedimentary quartz: a status review, *Geochronometria*, *21*, 1-16.
- Murray, A. S., and R. G. Roberts (1997), Determining the burial time of single grains of quartz using optically stimulated luminescence, *Earth Planet. Sci. Lett.*, *252*, 163-180.
- Murray, A. S., and A. G. Wintle (2000), Luminescence dating of quartz using an improved single-aliquot regenerative-dose protocol, *Radiat. Meas.*, *32*, 57-73.
- Murray, A. S. and A. G. Wintle (2003), The single aliquot regenerative dose protocol: potential for improvements in reliability, *Radiat. Meas.*, *37*, 377-381.
- Murray, A. S., Marten, R., Johnston, A., Martin, P. (1987), Analysis for naturally occurring radionuclides at environmental concentrations by gamma spectrometry, *J. Radioan. Nucl. Chem.*, *115(2)*, 263-288.
- Murray, A. S., Olley, J. M., and G. G. Caitcheon (1995), Measurement of equivalent doses in quartz from contemporary water-lain sediments using optically stimulated luminescence, *Quat. Sci. Rev.*, *14*, 365-371.
- Murray, A. S., R. G. Roberts and A. G. Wintle (1997), Equivalent dose measurement using a single aliquot of quartz, *Radiat. Meas.*, *27(2)*, 171-184.
- Murray, A. S., Thomsen, K. J., Masuda, N., Buylaert, J. P., Jain, M. (2012), Identifying well-bleached quartz using the different bleaching rates of quartz and feldspar luminescence signals, *Radiat. Meas.*, *47*, 688-696.

- Muttoni, G., Mattei, M., Balini, M., Zanchi, A., Gaetani, M., and F. Berra (2009), The drift history of Iran from the Ordovician to the Triassic, in *South Caspian to Central Iran Basins*, edited by Brunet, M.-F., Wilmsen, M., and J. W. Granath, *Geol. Soc. Lond. Spec. Publ.*, 312, 7-29.
- Nabavi, M. H. (1970), Geological quadrangle map of Iran, Yazd sheet (H9), scale 1:250,000, Geol. Surv. of Iran, Tehran.
- Nabavi, M. H. (1977), *Introduction to the geology of Iran* (in Farsi), Geol. Surv. of Iran, Tehran.
- Nalbant, S. S., Steacy, S., and J. McCloskey (2006), Stress transfer relations among the earthquakes that occurred in Kerman province, southern Iran since 1981, *Geophys. J. Int.*, 167, 309-318, doi:10.1111/j.1365-246X.2006.03119.x.
- Nazari, H. (2005), Analyse de la tectonique récente et active dans l'Alborz Central et la région de Téhéran: Approche morphotectonique et paléosismologique, *PhD thesis*, 247 pp., Univ. of Montpellier II, Montpellier, France.
- Nazari, H., Fattahi, M., Meyer, B., Sébrier, M., Talebian, M., Foroutan, M., Le Dortz, K., Bateman, M. D., and M. Ghorashi (2009a), First evidence for large earthquakes on the Deshir Fault, Central Iran Plateau, *Terra Nova*, 21, 417-426, doi:10.1111/j.1365-3121.2009.00892.x.
- Nazari, H., Ritz, J.-F., Salamati, R., Shafei, A., Ghassemi, A., Michelot, J.-L., Massault, M., and M. Ghorashi (2009b), Morphological and palaeoseismological analysis along the Taleghan fault (Central Alborz, Iran), *Geophys. J. Int.*, 178, 1028-1041.
- Nazari, H., Ritz, J.-F., Salamati, R., Shahidi, A., Habibi, H., Ghorashi, M., and A. Karimi Bavandpur (2010), Distinguishing between fault scarps and shorelines: the question of the nature of the Kahrizak, North Rey and South Rey features in the Tehran plain (Iran), *Terra Nova*, 22, 227-237, doi:10.1111/j.1365-3121.2010.00938.x.
- Niemi, N. A., Wernicke, B. P., Friedrich, A. M., Simons, M., Bennett, R. A., and J. L. Davis (2004), BARGEN continuous GPS data across the eastern Basin and Range province, and implications for fault system dynamics, *Geophys. J. Int.*, 159, 842-862.
- NIOC (1977), Geological map of Iran, *Sheet 6, south-east Iran*, scale 1:1,000,000, Natl. Iran. Oil Co., Explor. and Prod., Tehran.

- Obermeier, S. F. (1996), Use of liquefaction-induced features for paleoseismic analysis- An overview of how seismic liquefaction features can be distinguished from other features and how their regional distribution and properties of source sediment can be used to infer the location and strength of Holocene paleo-earthquakes, *Eng. Geol.*, 44, 1-76.
- Olley, J. M., Murray, A., and R. G. Roberts (1996), The effects of disequilibrium in the uranium and thorium decay chains on burial dose rates in fluvial sediments, *Quat. Sci. Rev. (Quat. Geochronol.)*, 15, 751-760.
- Olley, J. M., Caitcheon, G. G., Roberts, R. G. (1999), The origin of dose distributions in fluvial sediments, and the prospect of dating single grains from fluvial deposits using optically stimulated luminescence, *Radiat. Meas.*, 30, 207-217.
- Olley, J. M., Pietsch, T., Roberts, R. G. (2004), Optical dating of Holocene sediments from a variety of geomorphic settings using single grains of quartz, *Geomorphology*, 60., 337-358.
- Oskin, M., Perg, L., Shelef, E., Strane, M., Gurney, E., Singer, B., Zhang, X. (2008), Elevated shear zone loading rate during an earthquake cluster in eastern California, *Geology*, 36(6), 507-510.
- Owen, G. (1987), Deformation processes in unconsolidated sands, in *Deformation of Sediments and Sedimentary Rocks*, Jones, M. E., and R. M. F. Preston, *Geol. Soc. Spec. Publ.*, 29, 11-24.
- Owen, L. A., Kamp, U., Spencer, J. Q., Haserodt, K. (2002), Timing and style of Late Quaternary glaciation in the eastern Hindu Kush, Chitral, northern Pakistan: a review and revision of the glacial chronology based on new optically stimulated luminescence dating, *Quat. Int.*, 97-98, 41-55.
- Page, W. D., Alt, J. N., Cluff, L. S., and G. Plafker (1979), Evidence for the recurrence of large-magnitude earthquakes along the Makran coast of Iran and Pakistan, *Tectonophysics*, 52, 533-547.
- Pan, B., Burbank, D., Wang, Y., Wu, G., Li, J., Guan, Q. (2003), A 900 k.y. record of strath terrace formation during glacial-interglacial transitions in northwest China, *Geology*, 31(11), 957-960.

- Pantosti, D., D'Addezio, G., and F. R. Cinti (1996), Paleoseismology of the Ovindoli-Pezza fault, central Apennines, Italy: A history including a large, previously unrecorded earthquake in the Middle Ages (860-1300 A.D.), *J. Geophys. Res.*, *101*(B3), 5937-5959.
- Pathier, E., Fielding, E. J., Wright, T. J., Walker, R., Parson, B. E., and S. Hensley (2006), Displacement field and slip distribution of the 2005 Kashmir earthquake from SAR imagery, *Geophys. Res. Lett.*, *33*, L20310, doi:10.1029/2006GL027193.
- Peltzer, G., and P. Tapponnier (1988), Formation and evolution of strike-slip faults, rifts, and basins during the India-Asia collision: an experimental approach, *J. Geophys. Res.*, *93*(B12), 15,085-15,117.
- Peltzer, G., and F. Saucier (1996), Present-day kinematics of Asia derived from geologic fault rates, *J. Geophys. Res.*, *101*(B12), 27,943-27,956.
- Peltzer, G., Tapponnier, P., Gaudemer, Y., Meyer, B., Guo, S., Yin, K., Chen, Z., and H. Dai (1988), Offsets of late Quaternary morphology, rate of slip, and recurrence of large earthquakes on the Chang Ma fault (Gansu, China), *J. Geophys. Res.*, *93*, 7793-7812.
- Phillips, W. M., Sloan, V. F., Shroder Jr., J. F., Sharma, P., Clarke, M. L., Rendell, H. M. (2000), Asynchronous glaciation at Nanga Parbat, northwestern Himalaya Mountains, Pakistan, *Geology*, *28*(5), 431-434.
- Porat, N., Duller, G. A. T., Amit, R., Zilberman, E., Enzel, Y. (2009), Recent faulting in the southern Arava, Dead Sea Transform: Evidence from single grain luminescence dating, *Quat. Int.*, *199*, 34-44.
- Pratt, B., Burbank, D. W., Heimsath, A., Ojha, T. (2002), Impulsive alluviation during early Holocene strengthened monsoons, central Nepal Himalaya, *Geology*, *30*(10), 911-914.
- Prentice, C. S., Kendrick, K., Berryman, K., Bayasgalan, A., Ritz, J. F., and Q. Spencer (2002), Prehistoric ruptures of the Gurvan Bulag fault, Gobi Altay, Mongolia, *J. Geophys. Res.*, *107*(B12), doi:10.1029/2001JB000803.
- Prentice, C. S., Mann, P., Crone, A. J., Gold, R. D., Hudnut, K. W., Briggs, R. W., Koehler, R. D., and P. Jean (2010), Seismic hazard of the Enriquillo-Plantain Garden fault in Haiti inferred from palaeoseismology, *Nat. Geosci.*, *3*, 789-793.
- Prescott, J. R., and J. T. Hutton (1988), Cosmic ray and gamma ray dosimetry for TL and ESR, *Nucl. Tracks Radiat. Meas.*, *14*(1/2), 223-227.

- Prescott, J. R., and J. T. Hutton (1994), Cosmic ray contributions to dose rates for luminescence and ESR dating: large depths and long-term time variations, *Radiat. Meas.*, 23(2/3), 497-500.
- Quigley, M., Fattahi, M., Sohbati, R., Schmidt, A. (2011), Palaeoseismicity and pottery: Investigating earthquake and archaeological chronologies on the Hajiarab alluvial fan, Iran, *Quat. Int.*, 242, 185-195.
- Regard, V. (2003), Variations temporelle et spatiale de la transition subduction-collision: Tectonique de la transition Zagros-Makran (Iran) et modélisation analogique, *PhD thesis*, 336 pp., Univ. d'Aix-Marseille III, Aix-en-Provence, France.
- Regard, V., Bellier, O., Thomas, J. -C., Bourlès, D., Bonnet, S., Abbassi, M. R., Braucher, R., Mercier, J., Shabanian, E., Soleymani, Sh., and Kh. Fegghi (2005), Cumulative right-lateral fault slip rate across the Zagros-Makran transfer zone: role of the Minab-Zendan fault system in accommodation Arabia-Eurasia convergence in southeast Iran, *Geophys. J. Int.*, 162, 177-203.
- Regard, V., Hatzfeld, D., Molinaro, M., Aubourg, C., Bayer, R., Bellier, O., Yamini-Fard, F., Peyret, M., and M. Abbassi (2010), The transition between Makran subduction and the Zagros collision: recent advances in its structure and active deformation, in *Tectonic and Stratigraphic Evolution of Zagros and Makran during the Mesozoic-Cenozoic*, edited by P. Leturmy and C. Robin, *Geol. Soc. Lond. Spec. Publ.*, 330, 43-64.
- Reilinger, R., McClusky, S., Vernant, P., Lawrence, S., Ergintav, S., Cakmak, R., Ozener, H., Kadirov, F., Guliev, I., Stepanyan, R., Nadariya, M., Hahubia, G., Mahmoud, S., Sakr, K., ArRajehi, A., Paradissis, D., Al-Aydrus, A., Prilepin, M., Guseva, T., Evren, E., Dmitrova, A., Filikov, S. V., Gomez, F., Al-Ghazzi, R., and G. Karam (2006), GPS constraints on continental deformation in the Africa-Arabia-Eurasia continental collision zone and implications for the dynamics of plate interactions, *J. Geophys. Res.*, 111, B05411, doi:10.1029/2005JB004051.
- Rhodes, E. J. (2011), Optically stimulated luminescence dating of sediments over the past 200,000 years, *Annu. Rev. Earth Planet. Sci.*, 39, 461-488.
- Rhodes, E. J., Fanning, P. C., Holdaway, S. J. (2010), Developments in optically stimulated luminescence age control for geoarchaeological sediments and hearths in western New South Wales, Australia, *Quat. Geochronol.*, 5, 348-352.

- Rittenour, T. M. (2008), Luminescence dating of fluvial deposits: applications to geomorphic, palaeoseismic and archaeological research, *Boreas*, 37, 613-635.
- Ritz, J.-F., Nazari, H., Ghassemi, A., Salamati, R., Shafei, A., Solaymani, S., Vernant, P. (2006), Active transtension inside central Alborz: A new insight into northern Iran-southern Caspian geodynamics, *Geology*, 34(6), 477-480, doi:10.1130/G22319.1.
- Ritz, J.-F., Nazari, H., Balescu, S., Lamothe, M., Salamati, R., Ghassemi, A., Shafei, A., Ghorashi, M., and A. Saidi (2012), Paleoearthquakes of the past 30,000 years along the North Tehran Fault (Iran), *J. Geophys. Res.*, 117, B06305, doi:10.1029/2012JB009147.
- Rizza, M., Mahan, S., Ritz, J.-F., Nazari, H., Hollingsworth, J., Salamati, R. (2011a), Using luminescence dating of coarse matrix material to estimate the slip rate of the Astaneh fault, Iran, *Quat. Geochronol.*, 6, 390-406.
- Rizza, M., Ritz, J.-F., Braucher, R., Vassallo, R., Prentice, C., Mahan, S., McGill, S., Chauvet, A., Marco, S., Todbileg, M., Demberel, S., and D. Bourlès (2011b), Slip rate and slip magnitudes of past earthquakes along the Bogd left-lateral strike-slip fault (Mongolia), *Geophys. J. Int.*, 186, 897-927.
- Roberts, R. G., Galbraith, R. F., Yoshida, H., Laslett, G. M., Olley, J. M. (2000), Distinguishing dose populations in sediment mixtures: a test of single-grain optical dating procedures using mixtures of laboratory-dosed quartz, *Radiat. Meas.*, 32, 459-465.
- Roberts, R. G., Flannery, T. F., Ayliffe, L. K., Yoshida, H., Olley, J. M., Prideaux, G. J., Laslett, G. M., Baynes, A., Smith, M. A., Jones, R., Smith, B. L. (2001), New ages for the last Australian megafauna: continent-wide extinction about 46,000 years ago, *Science*, 292, 1888-1892, doi:10.1126/science.1060264.
- Rockwell, T., Ragona, D., Seitz, G., Landgridge, R., Aksoy, M. E., Ucar, G., Ferry, M., Meltzner, A. J., Klinger, Y., Meghraoui, M., Satir, D., Barka, A., and B. Akbalik (2009), Palaeoseismology of the North Anatolian Fault near the Marmara Sea: implications for segmentation and seismic hazard, in *Palaeoseismology: Historical and Prehistorical Records of Earthquake Ground Effects for Seismic Hazard Assessment*, edited by Reicherter, K., Michetti, A. M., and P. G. Silva, *Geol. Soc. Lond. Spec. Publ.*, 316, 31-54.
- Rodnight, H. (2008), How many equivalent dose values are needed to obtain a reproducing distribution?, *Ancient TL*, 26(1), 3-9.

- Rossetti, F., Nasrabady, M., Vignaroli, G., Theye, T., Gerdes, A., Razavi, M. H., and H. Moin Vaziri (2010), Early Cretaceous migmatitic mafic granulites from the Sabzevar range (NE Iran): implications for the closure of the Mesozoic peri-Tethyan oceans in central Iran, *Terra Nova*, 22, 26-34.
- Sabzehei, M. (1993), Geological map of Hadjiabad, Quadrangle *I12*, scale 1:250,000, Geol. Surv. of Iran, Tehran.
- Sahandi, M. R. (1992), Geological map of Kerman, Quadrangle *J10*, scale 1:250,000, Geol. Surv. of Iran, Tehran.
- Scharer, K. M., G. P. Biasi., and R. J. Weldon II (2011), A reevaluation of the Pallett Creek earthquake chronology based on new AMS radiocarbon dates, San Andreas fault, California, *J. Geophys. Res.*, 116, B12111, doi:10.1029/2010JB008099.
- Schimmelpfennig, I., Benedetti, L., Finkel, R., Pik, R., Blard, P.-H., Bourlès, D., Burnard, P., Williams, A. (2009), Sources of in-situ  $^{36}\text{Cl}$  in basaltic rocks. Implication for calibration of production rates, *Quat. Geochronol.*, 4, 441-461, doi:10.1016/j.quageo.2009.06.003.
- Schimmelpfennig, I., Benedetti, L., Garreta, V., Pik, R., Blard, P.-H., Burnard, P., Bourlès, D., Finkel, R., Ammon, K., Dunai, T. (2011), Calibration of cosmogenic  $^{36}\text{Cl}$  production rates from Ca and K spallation in lava flows from Mt. Etna (38°N, Italy) and Payun Matru (36°S, Argentina), *Geochim. Cosmochim. Acta*, 75, 2611-2632.
- Schmidt, A., Quigley, M., Fattahi, M., Azizi, G., Maghsoudi, M., and H. Fazeli (2011), Holocene settlement shifts and palaeoenvironments on the Central Iranian Plateau: investigating linked systems, *The Holocene*, 21(4), 583-595, doi:10.1177/0959683610385961.
- Schwartz, D. P., and K. J. Coppersmith (1984), Fault behavior and characteristic earthquakes: examples from the Wasatch and San Andreas fault zone, *J. Geophys. Res.*, 89(B7), 5681-5698.
- Schwartz, D. P., Haeussler, P. J., Seitz, G. G., and T. E. Dawson (2012), Why the 2002 Denali fault rupture propagated onto the Totschunda fault: implications for fault branching and seismic hazards, *J. Geophys. Res.*, 117, B11304, doi:10.1029/2011JB008918.
- Shabaniyan, E., Siame, L., Bellier, O., Benedetti, L., and M. R. Abbassi (2009), Quaternary slip rates along the northeastern boundary of the Arabia-Eurasia collision zone (Koppeh Dagh Mountains, Northeast Iran), *Geophys. J. Int.*, 178, 1055-1077, doi:10.1111/j.1365-246X.2009.04183.x.

- Shabanian, E., Bellier, O., Siame, L., Abbassi, M. R., Bourlès, D., Braucher, R., and Y. Farbod (2012), The Binalud Mountains: A key piece for the geodynamic puzzle of NE Iran, *Tectonics*, *31*, TC6003, doi:10.1029/2012TC003183.
- Sieh, K. E. (1978), Prehistoric large earthquakes produced by slip on the San Andreas fault at Pallett Creek, California, *J. Geophys. Res.*, *83*(B8), 3907-3939.
- Sieh, K. E. (1981), A review of geological evidence for recurrence times of large earthquakes, in *Earthquake Prediction: An International Review*, edited by D. W. Simpson and P. G. Richards, *Maurice Ewing Ser.*, *4*, 181-207.
- Sieh, K. E. (1996), The repetition of large-earthquake ruptures, *Proc. Natl. Acad. Sci.*, *93*(9), 3764-3771.
- Sieh, K. (2006), Sumatran megathrust earthquakes: from science to saving lives, *Phil. Trans. R. Soc. A.*, *364*, 1947-1963.
- Sieh, K., Stuiver, M., Brillinger, D. (1989), A more precise chronology of earthquakes produced by the San Andreas fault in Southern California, *J. Geophys. Res.*, *94*(B1), 603-623.
- Sieh, K. E., and Jahns, R. H. (1984), Holocene activity of the San Andreas fault at Wallace Creek, California, *Geol. Soc. Am. Bull.*, *95*, 883-896.
- Smith, B. W., Aitken, M. J., Rhodes, E. J., Robinson, P. D., and D. M. Geldard (1986), Optical dating: methodological aspects, *Radiat. Prot. Dosim.*, *17*, 229-233.
- Soheili, M. (1995), Geological map of Sirjan, Quadrangle *III*, scale 1:250,000, Geol. Surv. of Iran, Tehran.
- Solaymani Azad, S. (2009), Evaluation de l'aléa sismique pour les villes de Téhéran, Tabriz et Zandjan dans le NW de l'Iran: Approche morphotectonique et paléosismologique, *PhD thesis*, 150 pp., Univ. of Montpellier II, Montpellier, France.
- Solaymani Azad, S., Ritz, J.-F., Abbassi, M. R. (2011), Left-lateral active deformation along the Mosha-North Tehran fault system (Iran): Morphotectonics and paleoseismological investigations, *Tectonophysics*, *497*, 1-14, doi:10.1016/j.tecto.2010.09.013.
- Spinler, J., Bennett, R. A., Anderson, M. L., McGill, S. F., Hreinsdóttir, S., and A. McCallister (2010), Present-day strain accumulation and slip rates associated with southern San Andreas and eastern California shear zone faults, *J. Geophys. Res.*, *115*(B11407), doi:10.1029/2010JB007424.

- Staubwasser, M., Sirocko, F., Grootes, P. M., and M. Segl (2003), Climate change at the 4.2 ka BP termination of the Indus valley civilization and Holocene south Asian monsoon variability, *Geophys. Res. Lett.*, *30*(8), 1425, doi:10.1029/2002GL016822.
- Stevens, T., Armitage, S. J., Lu, H., Thomas, D. S. G. (2007), Examining the potential of high sampling resolution OSL dating of Chinese loess, *Quat. Geochronol.*, *2*, 15-22.
- Stöcklin, J. (1974), Northern Iran: Alborz Mountains, *Geol. Soc. Lond. Spec. Publ.*, *4*, 213-234.
- Stöcklin, J., and Nabavi, M. H. (1969), Geological map of Boshruyeh, Quadrangle *J7*, scale 1:250,000, Geol. Surv. of Iran, Tehran.
- Stone, J. O., Allan, G. L., Fifield, L. K., and R. G. Cresswell (1996), Cosmogenic chlorine-36 from calcium spallation, *Geochim. Cosmochim. Acta*, *60*(4), 679-692.
- Stone, J. O., Evans, J. M., Fifield, L. K., Allan, G. L., and R. G. Cresswell (1998), Cosmogenic chlorine-36 production in calcite by muons, *Geochim. Cosmochim. Acta*, *62*(3), 433-454.
- Talebian, M., Fielding, E. J., Funning, G. J., Ghorashi, M., Jackson, J., Nazari, H., Parson, B., Priestley, K., Rosen, P. A., Walker, R., and T. J. Wright (2004), The 2003 Bam (Iran) earthquake: Rupture of a blind strike-slip fault, *Geophys. Res. Lett.*, *31*, L11611, doi:10.1029/2004GL020058.
- Talebian, M., Biggs, J., Bolourchi, M., Copley, A., Ghassemi, A., Ghorashi, M., Hollingsworth, J., Jackson, J., Nissen, E., Oveisi, B., Parsons, B., Priestley, K., and A. Saiidi (2006), The Dahuiyeh (Zarand) earthquake of 2005 February 22 in central Iran: reactivation of an intramountain reverse fault, *Geophys. J. Int.*, *164*, 137-148.
- Tapponnier, P., Ryerson, F. J., Van der Woerd, J., Mériaux, A.-S., Lasserre, C. (2001), Long-term slip rates and characteristic slip: keys to active fault behaviour and earthquake hazard, *C. R. Acad. Sci., Ser. II*, *333*(9), 483-494.
- Tavakoli, F. (2007), Present-day deformation and kinematics of the active faults observed by GPS in the Zagros and east of Iran, *PhD thesis*, Univ. of Joseph Fourier, Grenoble, France.
- Thatcher, W., Foulger, G. R., Julian, B. R., Svarc, J., Quilty, E., Bawden, G. W. (1999), Present-day deformation across the Basin and Range Province, Western United States, *Science*, *283*, 1714-1718, doi:10.1126/science.283.5408.1714.
- Tirrul, R., Bell, I. R., Griffis, R. J., and V. E. Camp (1983), The Sistan suture zone of eastern Iran, *Geol. Soc. Am. Bull.*, *94*, 134-150.

- Vahdati Daneshmand, F. (1992), Geological map of Rafsanjan, Quadrangle *II0*, scale 1:250,000, Geol. Surv. of Iran, Tehran.
- Van Der Woerd, J., Ryerson, F. J., Tapponnier, P., Meriaux, A-S., Gaudemer, Y., Meyer, B., Finkel, R. C., Caffee, M. W., Guoguang, Z., Zhiqin, X. (2000), Uniform slip-rate along the Kunlun fault: Implications for seismic behaviour and large-scale tectonics, *Geophys. Res. Lett.*, 27(16), 2353-2356.
- Van Der Woerd, J., Tapponnier, P., Ryerson, F. J., Meriaux, A-S., Meyer, B., Gaudemer, Y., Finkel, R. C., Caffee, M. W., Guoguang, Z., and X. Zhiqin (2002), Uniform postglacial slip-rate along the central 600 km of the Kunlun Fault (Tibet), from  $^{36}\text{Al}$ ,  $^{10}\text{Be}$ , and  $^{14}\text{C}$  dating of riser offsets, and climatic origin of the regional morphology, *Geophys. J. Int.*, 148, 356-388.
- Vassallo, R., Ritz, J.-F., Braucher, R., Jolivet, M., Carretier, S., Larroque, C., Chauvet, A., Sue, C., Todbileg, M., Bourlès, D., Arzhannikova, A., and S. Arzhannikov (2007), Transpressional tectonics and stream terraces of the Gobi-Altay, Mongolia, *Tectonics*, 26, TC5013, doi:10.1029/2006TC002081.
- Vernant, Ph., Nilforoushan, F., Hatzfeld, D., Abbassi, M. R., Vigny, C., Masson, F., Nankali, H., Martinod, J., Ashtiani, A., Bayer, R., Tavakoli, F., and J. Chéry (2004), Present-day crustal deformation and plate kinematics in the Middle East constrained by GPS measurements in Iran and northern Oman, *Geophys. J. Int.*, 157, 381-398.
- Vittori, E., Labini, S. S., and L. Serva (1991), Palaeoseismology: review of the state-of-the-art, *Tectonophysics*, 193, 9-32.
- Walker, F., and M. B. Allen (2012), Offset rivers, drainage spacing and the record of strike-slip faulting: The Kuh Banan Fault, Iran, *Tectonophysics*, 530-531, 251-263.
- Walker, M. (2005), *Quaternary Dating Methods*, John Wiley & Sons, Chichester, UK.
- Walker, R. T. (2006), A remote sensing study of active folding and faulting in southern Kerman province, S.E. Iran, *J. Struct. Geol.*, 28, 654-668.
- Walker, R., and M. Fattahi (2011), A framework of Holocene and Late Pleistocene environmental change in eastern Iran inferred from the dating of periods of alluvial fan abandonment, river terracing, and lake deposition, *Quat. Sci. Rev.*, 30, 1256-1271, doi:10.1016/j.quascirev.2011.03.004.

- Walker, R., and J. Jackson (2002), Offset and evolution of the Gowk fault, S.E. Iran: a major intra-continental strike-slip system, *J. Struct. Geol.*, *24*, 1677-1698.
- Walker, R., and J. Jackson (2004), Active tectonics and late Cenozoic strain distribution in central and eastern Iran, *Tectonics*, *23*, TC5010, doi:10.1029/2003TC001529.
- Walker, R., Jackson, J., and C. Baker (2003), Surface expression of thrust faulting in eastern Iran: source parameters and surface deformation of the 1978 Tabas and 1968 Ferdows earthquake sequences, *Geophys. J. Int.*, *152*, 749-765.
- Walker, R., Jackson, J., and C. Baker (2003), Active faulting and seismicity of the Dasht-e-Bayaz region, eastern Iran, *Geophys. J. Int.*, *157*, 265-282, doi:10.1111/j.1365-2966.2004.02179.x.
- Walker, R. T., Gans, P., Allen, M. B., Jackson, J., Khatib, M., Marsh, N., and M. Zarrinkoub (2009), Late Cenozoic volcanism and rates of active faulting in eastern Iran, *Geophys. J. Int.*, *177*, 783-805.
- Walker, R. T., Talebian, M., Saiffori, S., Sloan, R. A., Rashidi, A., MacBean, N., Ghassemi, A. (2010a), Active faulting, earthquakes, and restraining bend development near Kerman city in southeastern Iran, *J. Struct. Geol.*, *32*, 1046-1060.
- Walker, R. T., Talebian, M., Sloan, R. A., Rasheedi, A., Fattahi, M., and C. Bryant (2010b), Holocene slip-rate on the Gowk strike-slip fault and implications for the distribution of tectonic strain in eastern Iran, *Geophys. J. Int.*, *181*, 221-228.
- Walker, R. T., Bergman, E. A., Elliott, J. R., Fielding, E. J., Ghods, A.-R., Ghoraiishi, M., Jackson, J., Nazari, H., Nemati, M., Oveisi, B., Talebian, M., and R. J. Walters (2013a), The 2010-2011 South Rigan (Baluchestan) earthquake sequence and its implications for distributed deformation and earthquake hazard in southeast Iran, *Geophys. J. Int.*, doi:10.1093/gji/ggs109.
- Walker, R. T., Khatib, M. M., Bahroudi, A., Rodés, A., Schnabel, C., Fattahi, M., Talebian, M., Bergman, E. (2013b), Co-seismic, geomorphic, and geologic fold growth associated with the 1978 Tabas-e-Golshan earthquake fault in eastern Iran, *Geomorphology*, <http://dx.doi.org/10.1016/j.geomorph.2013.02.016>.
- Wallinga, J. (2001), The Rhine-Meuse system in a new light: optically stimulated luminescence dating and its application to fluvial deposits, *PhD thesis*, 180 pp., Faculty of Geographical Sciences, Utrecht University, Utrecht, Netherlands.

- Walpersdorf, A., Hatzfeld, D., Nankali, H., Tavakoli, F., Nilforoushan, F., Tatar, M., Vernant, P., Chéry, J., and F. Masson (2006), Difference in the GPS deformation pattern of North and Central Zagros (Iran), *Geophys. J. Int.*, 167, 1077-1088.
- Wang, Z., Fukao, Y., Pei, S. (2009), Structural control of rupturing of the Mw7.9 2008 Wenchuan earthquake, China, *Earth Planet. Sci. Lett.*, 279, 131-138.
- Wallace, R. E. (1981), Active faults, paleoseismology, and earthquake hazards in the western United States, in *Earthquake Prediction: An International Review*, edited by W. Simpson and G. Richards, *Maurice Ewing Ser., AGU*, Washington, D. C., 4, 209-216, doi:10.1029/ME004p0209.
- Weldon, R. J., and Sieh, K. E. (1985), Holocene rate of slip and tentative recurrence interval for large earthquakes on the San Andreas fault, Cajon Pass, southern California, *Geol. Soc. Am. Bull.*, 96, 793-812.
- Wellman, H. W. (1966), Active wrench faults of Iran, Afghanistan and Pakistan, *Geol. Rundsch.*, 55(3), 716-735.
- Wells, D. L., and K. J. Coppersmith (1994), New empirical relationships among magnitude, rupture length, rupture width, rupture area, and surface displacement, *Bull. Seismol. Soc. Am.*, 84(4), 974-1002.
- Wells, S. G., McFadden, L. D., and J. C. Dohrenwend (1987), Influence of late Quaternary climatic changes on geomorphic and pedogenic processes on a desert piedmont, eastern Mojave desert, California, *Quat. Res.*, 27, 130-146.
- Wen, R., Xiao, J., Chang, Z., Zhai, D., Xu, Q., Li, Y., and S. Itoh (2010), Holocene precipitation and temperature variations in the East Asian monsoonal margin from pollen data from Hulun Lake in northeastern Inner Mongolia, China, *Boreas*, 39, 262-272.
- Wesnousky, S. G., Seeber, L., Rockwell, T. K., Thakur, V., Briggs, R., Kumar, S., and D. Ragona (2001), Eight days in Bhuj: field report bearing on surface rupture and genesis of the 26 January 2001 earthquake in India, *Seism. Res. Lett.*, 72(5), 514-524.
- Wesnousky, S. G., Aranguren, R., Rengifo, M., Owen, L. A., Caffee, M. W., Murari, K. M., Pérez, O. (2012), Toward quantifying geomorphic rates of crustal displacement, landscape development, and the age of glaciation in the Venezuelan Andes, *Geomorphology*, 141-142, 99-113.

- Wintle, A. G. (1997), Luminescence dating: laboratory procedures and protocols, *Radiat. Meas.*, 27(5/6), 769-817.
- Wintle, A. G. (2008), Luminescence dating: where it has been and where it is going, *Boreas*, 37, 471-482, doi:10.1111/j.1502-3885.2008.00059.x.
- Wright, T. J., Parsons, B., England, P., Fielding, E. J. (2004), InSAR observations of low slip rates on the major faults of western Tibet, *Science*, 305, 236-239.
- Yeats, R. S., and C. S. Prentice (1996), Introduction to special section: Paleoseismology, *J. Geophys. Res.*, 101(B3), 5847-5853.
- Zanchetta, S., Zanchi, A., Villa, I., Poli, S., and G. Muttoni (2009), The Shanderman eclogites: a Late Carboniferous high-pressure event in the NW Talesh Mountains (NW Iran), in *South Caspian to Central Iran Basins*, edited by Brunet, M.-F., Wilmsen, M., and J. W. Granath, *Geol. Soc. Lond. Spec. Publ.*, 312, 57-78.
- Zanchi, A., Zanchetta, S., Garzanti, E., Balini, M., Berra, F., Mattei, M., and G. Muttoni (2009), The Cimmerian evolution of the Naxhlak-Anarak area, Central Iran, and its bearing for the reconstruction of the history of the Eurasian margin, in *South Caspian to Central Iran Basins*, edited by Brunet, M.-F., Wilmsen, M., and J. W. Granath, *Geol. Soc. Lond. Spec. Publ.*, 312, 261-286.
- Zhang, P.-Z. (2013), Beware of slowly slipping faults, *Nature Geosci.*, 6, 323-324.
- Zhang, P.-Z., Shen, Z., Wang, M., Gan, W., Bürgmann, R., Molnar, P., Wang, Q., Niu, Z., Sun, J., Wu, J., Hanrong, S., Xinzhao, Y. (2004), Continuous deformation of the Tibetan Plateau from global positioning system data, *Geology*, 32(9), 809-812, doi:10.1130/G20554.1.
- Zheng, B., Xu, Q., Shen, Y. (2002), The relationship between climate change and Quaternary glacial cycles on the Qinghai-Tibetan Plateau: review and speculation, *Quat. Int.*, 97-98, 93-101.
- Zreda, M. G., Phillips, F. M., Elmore, D., Kubik, P. W., Sharma, P., and R. I. Dorn (1991), Cosmogenic chlorine-36 production rates in terrestrial rocks, *Earth Planet. Sci. Lett.*, 105, 94-109.



## Appendix A.1

# **Refining the OSL age of the last earthquake on the Dehshir fault, Central Iran**

---



## Research Paper

## Refining the OSL age of the last earthquake on the Dheshir fault, Central Iran

M. Fattahi<sup>a,b,c,\*</sup>, H. Nazari<sup>d</sup>, M.D. Bateman<sup>c</sup>, B. Meyer<sup>e</sup>, M. Sébrier<sup>e</sup>, M. Talebian<sup>d</sup>,  
K. Le Dortz<sup>e</sup>, M. Foroutan<sup>d</sup>, F. Ahmadi Givi<sup>a</sup>, M. Ghorashi<sup>d</sup>

<sup>a</sup>The Institute of Geophysics, University of Tehran, Kargar Shomali, Tehran, Iran

<sup>b</sup>Sheffield Centre for International Drylands Research, Department of Geography, University of Sheffield, Winter Street, Sheffield S10 2TN, UK

<sup>c</sup>School of Geography, University of Oxford, Mansfield Road, Oxford OX1 3TB, UK

<sup>d</sup>Research Institute for Earth Sciences, Geological Survey of Iran, Po Box: 13185-1494, Teheran, Iran

<sup>e</sup>UPMC Univ Paris 06, Laboratoire de Tectonique (UMR 7072 CNRS), F75005 Paris, 23, France

## ARTICLE INFO

## Article history:

Received 30 October 2008

Received in revised form

31 March 2009

Accepted 20 April 2009

Available online 3 May 2009

## Keywords:

Luminescence dating

Fault slip rate

Iran

Earthquake

Seismic hazard

## ABSTRACT

In Central Iran there are several cities along the Dehshir fault, which have similar geological conditions to that of the city of Bam prior to the 2003 earthquake (Mw 6.5), during which more than 30,000 lives were lost. Optical stimulated luminescence (OSL) samples were collected from the Dehshir fault in order to place constraints on its seismic history. The single aliquot regenerative (SAR) dose measurement protocol on coarse grained quartz extracts was used for this study. This SAR protocol had to be optimized for the low OSL sensitivity by varying both the preheat temperatures and test doses used. Dose recovery tests showed that given laboratory dose could be successfully recovered. However, replicate palaeodose ( $D_e$ ) data were scattered and consequently ages based on mean  $D_e$ 's had large uncertainties. As this is thought to largely reflect poor bleaching conditions prior to sediment burial at the site, various statistical procedures were employed in conjunction with the stratigraphic knowledge of the site to try and extract more refined burial ages from the samples. From this the timing of the last earthquake was estimated around  $2.0 \pm 0.2$  kyr. This refined age suggests that the earthquake catalogue of Iran is incomplete and more paleoseismological investigation is required to recognize and date the previous events of Dheshir fault.

© 2009 Elsevier B.V. All rights reserved.

## 1. Introduction

Iran is one of the most seismically active regions along the Alpine Himalayan belts, with numerous destructive earthquakes recorded both historically and instrumentally. Active tectonics in Zagros and Central Iran involves a combination of strike-slip and thrust faulting (e.g. Jackson and McKenzie, 1984; Berberian and Yeats, 1999). The Dehshir fault is the westernmost strike-slip of a series of N-striking dextral faults that slice Central and Eastern Iran (Fig. 1). This right-lateral fault is around 380 km long and trends NNW–SSE between  $29.5^\circ\text{N}$  and  $33^\circ\text{N}$  (e.g. Berberian, 1981; Walker and Jackson, 2004; Meyer and Le Dortz, 2007; Fig. 1). Meyer et al. (2006) estimated the slip rate ( $\#2 \text{ mm yr}^{-1}$ ) of the right-lateral Dheshir fault using geological and geomorphologic offsets.

Despite of the above mentioned works, there is little information about the timing of past earthquakes and the recurrence interval produced by individual faults in the region. Luminescence

dating is one of the most suitable dating methods for arid zones like Iran. Worldwide, it has been successfully applied to earthquake related sediments (e.g. Pucci et al., 2008; Porat et al., 2007; Vandenberghe et al., 2007; Mathew et al., 2006; Fattahi, 2009 and references there in). In Iran, whilst previous work in the north east of the country has shown that infrared stimulated luminescence (IRSL) from feldspar can provide reliable ages (e.g. Fattahi et al., 2006 and 2007; Fattahi and Walker, 2007) the application of optically stimulated luminescence (OSL) dating has been limited and problematic due to limited quartz, weakness of OSL signal, unconventional signal behaviour and partial bleaching. This study builds on the work of Nazari et al. (submitted for publication) who collected OSL samples from the Dehshir fault for seismic hazard risk assessment. They suggested a minimum slip rate of  $0.7\text{--}2.6 \text{ mm yr}^{-1}$ ; found evidence for several paleoearthquakes; and estimated a rough return period of several thousands years for earthquakes; with a magnitude of  $M \geq 6.5$ . However, the OSL ages presented by Nazari et al. were based on a weighted (by inverse variance) mean calculated from a scatter palaeodose ( $D_e$ ) distribution and consequently had large uncertainties. As a result Nazari et al. could only conclude that the last earthquake occurred

\* Corresponding author at: The Institute of Geophysics, Tehran University, Kargar Shomali, Tehran, Iran. Fax: +98 21 8009560/+44 1865271929.

E-mail addresses: [morteza.fattahi@ouce.ox.ac.uk](mailto:morteza.fattahi@ouce.ox.ac.uk), [m.fattahi@ut.ac.ir](mailto:m.fattahi@ut.ac.ir) (M. Fattahi).

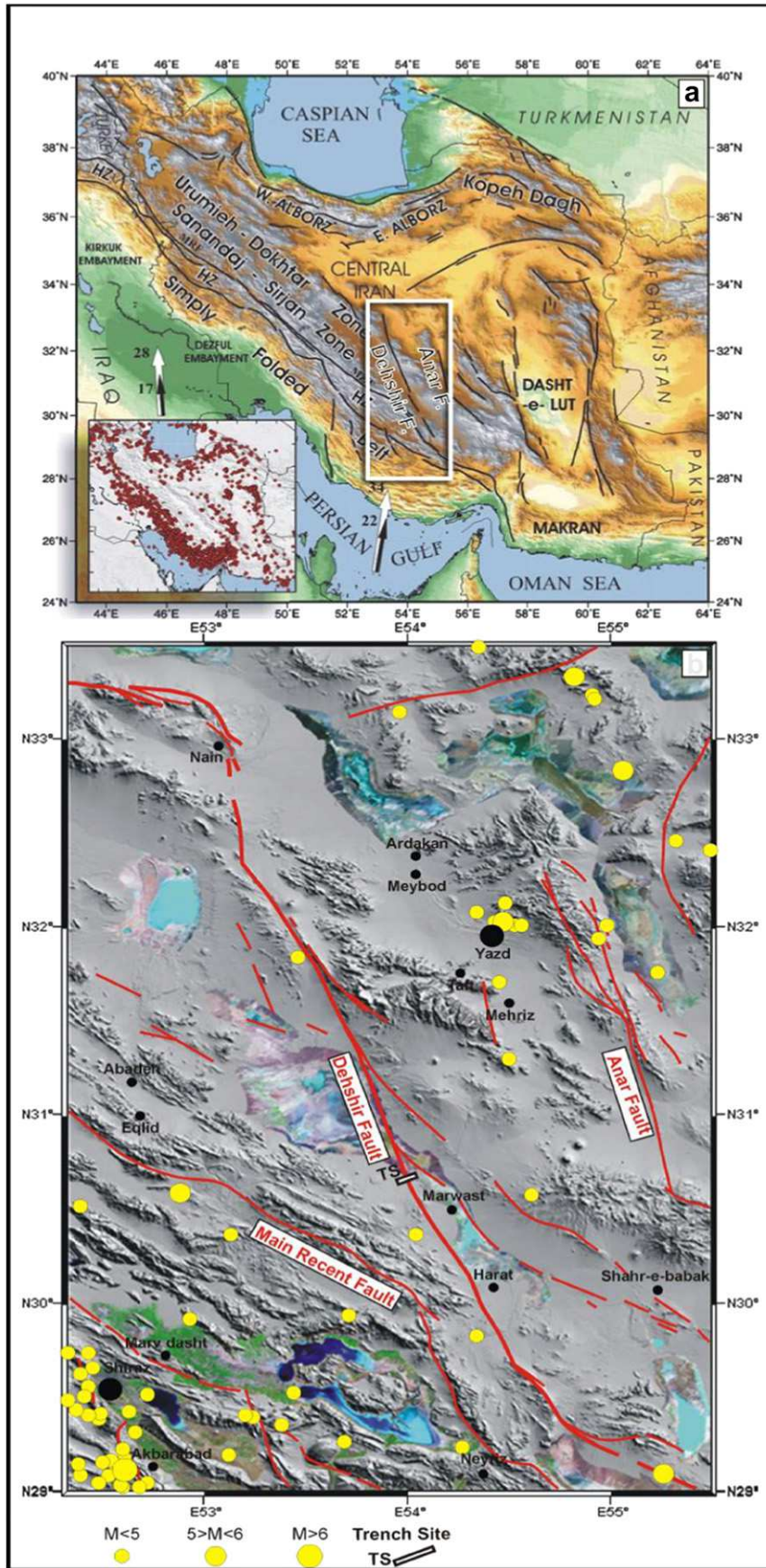


**Fig. 1.** (a) Simplified map of active faults of Iran from Talebian (2003). Inset shows the instrumental seismicity from Engdahl et al. (1998) ( $m_b > 5$ ). Black and white arrows are velocity vectors in a Eurasian fixed frame from REVEL (Sella et al., 2002) and NUVEL1A (DeMets et al., 1994) global plate models, respectively. (b) Seismotectonic map of Dehshir fault shown by rectangle in (a) with 1973–2008 seismicity from NEIC (<http://neic.usgs.gov/neis/epic/>). Background image is from SRTM data (<http://edcsgs9.cr.usgs.gov/pub/data/srtm/>) supplemented with Landsat images.

sometime between 1.4 and 4.2 kyr. This study aims at refining the analytical procedure used by Nazari et al. (submitted for publication, Terra Nova) to narrow the large errors on calculated ages. This appears critical for a better assessment of the seismic hazard and allows developing a protocol appropriate to date fluvial and colluvial material from Iran.

## 2. Study site

Following each surface rupturing earthquake, material eroding from fault scarps supplies colluvial deposits which fill open fissures or mantle the fault scarps. A trench excavated through the Dehshir fault at 30:38:28N 54:01:17E revealed clear evidence for recent faulting of young alluvial fan conglomerates and subsequent colluvial units (see Nazari et al., submitted for publication for details). The uppermost layer, a silty sandy colluvial deposit, fills a set of open fissures which were caused by the last earthquake (Fig. 2). Therefore, the age of this colluvial sediment provides a valuable constraint on the last seismic activity of the Dehshir fault, which, when combined with estimates of the likely interval between large earthquakes, provides critical information on the earthquake hazard level for the region. One sample (Hi2006II) was collected for OSL dating from the uppermost layer of this colluvium which should have been completely reset if deposition of this post faulting sediment was sufficiently slow (Fig. 2). Two other samples (Hi2006I, Hi2006VI) were collected for OSL dating from two other layers for stratigraphic and technical control. The samples were collected using stainless steel tubes (5 cm by 25 cm) and both ends were sealed and covered using both aluminium foil and black tape.

## 3. Experimental details

All samples were prepared in the Sheffield Centre for International Drylands Research luminescence laboratory. Samples were opened in the laboratory under red light conditions. Five centimetres of each end, which was presumably exposed to light during sampling, were used to determine sample moisture content and for inductively coupled plasma mass spectrometer (ICP-MS) analysis of uranium, thorium and potassium concentrations carried out at SGS laboratories, Ontario Canada. Annual dose was estimated from these data and was attenuated for grain-size measured, palaeo-moisture (based on present-day values) and cosmic contribution (see Fattahi et al., 2007).

The middle part (light unexposed) of each tube was used for the  $D_e$  determination. The single aliquot regenerative (SAR) dose protocol of quartz (Murray and Wintle, 2000, 2003) was applied to

aliquots of 90–150  $\mu\text{m}$  quartz, which were prepared by sieving, HCl and  $\text{H}_2\text{O}_2$  treatment, followed by heavy liquid separation ( $<2.7 \text{ g/cm}^3$ ), HF for 60 min, HCl retreatment, resieving and finally a check with IR stimulation for feldspar contamination. All the experiments reported here were carried out using a Risø automated TL/OSL system (Model TL/OSL-DA-15; fitted with a  $^{90}\text{Sr}/^{90}\text{Y}$  beta source delivering  $\sim 3.2 \text{ Gy min}^{-1}$ ) equipped with an IR laser diode and blue LED as stimulation sources. OSL was detected using an Electron Tube bialkaline PMT. Luminescence was measured through a 7 mm Hoya U-340 filter.

## 4. Luminescence characteristics

The suitability of the samples for the SAR protocol was tested by examining its luminescence characteristics such as thermal transfer and dose sensitivity, through quality control procedures on the SAR data and via dose recovery tests (Murray and Wintle, 2003).

### 4.1. OSL responses

The samples used for this study were very insensitive to dose and suffered from a weak OSL signal (between 30 and 250 counts per Gy per sec for a 9.6 mm diameter aliquot). Initial attempts to measure OSL at the single grain level therefore proved futile and as a consequence measurements were made on 9.6 mm diameter aliquots. Only at this level was it found that there was sufficient natural OSL to measure above background. Normally the test dose within SAR is kept to where it is only a small proportion ( $\sim 10\%$ ) of the dose naturally acquired during burial. However, the low OSL sensitivity precluded this approach for these samples. As a result we also applied a range of different doses to the samples and analysed the OSL response levels to choose a test dose. Selection tried to minimize the size of the test dose to avoid any impact on subsequent regeneration points within SAR whilst providing sufficient OSL to properly monitor sensitivity changes. This resulted in a test dose of 6 Gy being used for all measurements.

### 4.2. Thermal transfer

To test if there were problems from the thermal transfer of charge into the OSL trap as a result of preheating, natural aliquots were stimulated at room temperature without any prior preheating and OSL was measured for 100 s. After more than 4 h delay the OSL was measured again. No significant OSL signal was observed for the second measurement. Then, SAR was applied to measure the  $D_e$  at different preheat temperatures (expected to be zero in ideal

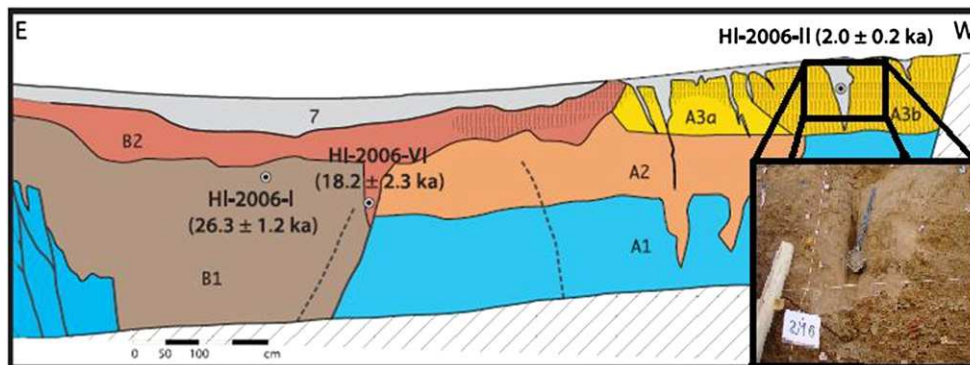


Fig. 2. Western part of the Gerdab trench logs on the Dehshir fault with the position and the dates of the OSL samples. Sedimentary units are indicated by different colours and labelled numerically. Units A and B are young alluvial and colluvial units. Unit 7 denotes the sandy silty unit infilling open fissures and mantling the ground surface after occurrence of the last surface rupturing earthquake. Inset shows where Hi2006II sample was collected.

scenario). All subsequently measured apparent values of  $D_e$  were less than 0.5 Gy for preheat temperatures from 160 °C to 300 °C. This is small compared with typical natural  $D_e$  and suggests that the samples do not suffer from significant thermal transfer.

4.3. Dose recovery preheat plateaus

Dose recovery preheat tests (as per Murray and Wintle, 2003) were carried out to provide a method to determine whether the overall effects of sensitivity changes had been properly corrected for and test whether known laboratory doses can be recovered by the modified SAR protocol. Three aliquots were used for each preheat temperature. After depleting the natural signal by light (OSL at room temperature for 200 s), each aliquot was given (~11.6 and 96.5 Gy for samples Hi2006II and Hi2006VI, respectively) beta doses and this dose was measured using the SAR protocol. The results are shown in Fig. 3 together with recycling ratios.

Thermal treatments (conventionally called preheat) are needed to empty any light sensitive unstable/shallow traps, particularly those filled by laboratory irradiations. Thermal treatments are a function of heating rate, the temperature to which the preheating is conducted to and the time at which the sample is held at this temperature. To determine the appropriate thermal treatments in the SAR protocol, two different heating rates (2 and 5 °C/s) were tested for preheat temperature ranges from 160 to 260 °C on sample Hi2006II. This sample showed no apparently constant  $D_e$  in the temperature interval 180–260 °C for heating rate 5 °C/s. The given dose could not be recovered to within 20% and the relevant recycling ratios were not close to unity (Fig. 3a). In contrast, the same sample with a heating rate of 2 °C/s greatly improved the ability to both recover a given dose and in terms of recycling meeting the SAR requirements (0.93, 1.0 and 1.05 for three aliquots, respectively) especially for temperatures below 220 °C (Fig. 3b). Recuperation was also noted to be smaller. The requirement of a slower heating rate was confirmed with results from sample Hi2006VI (Fig. 3c). As a result a preheat temperature of 200 °C or 220 °C with a heating rate of 2 °C/s was used for samples Hi2006II and Hi2006VI respectively for  $D_e$  determination.

5.  $D_e$  determination and age calculation

Up to forty-eight 9.6 mm diameter aliquots for each sample were prepared and measured using the optimised SAR protocol. Following measurement of the naturally acquired dose, a dose-response curve was constructed from five dose points including three regenerative doses (8, 16 and 26 Gy), and a zero dose (Fig. 4). A replicate measurement of the lowest regenerative dose was carried out at the end of each SAR cycle. The first 2 s of OSL decay curve was used for signal, and the final 10 s of OSL decay curve was used as a background for all measurements. The result of aliquots that created no significant recuperation signals and produced recycling ratios between 0.90 and 1.10 was chosen for further  $D_e$  analysis and age determination. These quality control criteria resulted in the rejection of 54%, 21% and 12% of aliquots for samples Hi2006I, Hi2006II and Hi2006VI, respectively. Results from the replicate  $D_e$  measurements for these samples can be seen in Table 1 and Fig. 5. From this it is apparent that Hi2006I has both a low overdispersion (OD; a calculation of the level of  $D_e$  variability in a data set which exceeds that which would be expected from a well-bleached sample) of 8% and low level of skewing (0.58). In contrast sample Hi2006VI has an OD value of 21% and sample Hi2006II shows a high OD value (47%). Both show skewing with a hint of a low  $D_e$  shoulders and some high  $D_e$  outliers (Table 1, Fig. 5d & f). Whilst not as convincingly skewed as reported for poorly bleached samples elsewhere (e.g. Rodnight et al., 2005; Olley et al., 1999),

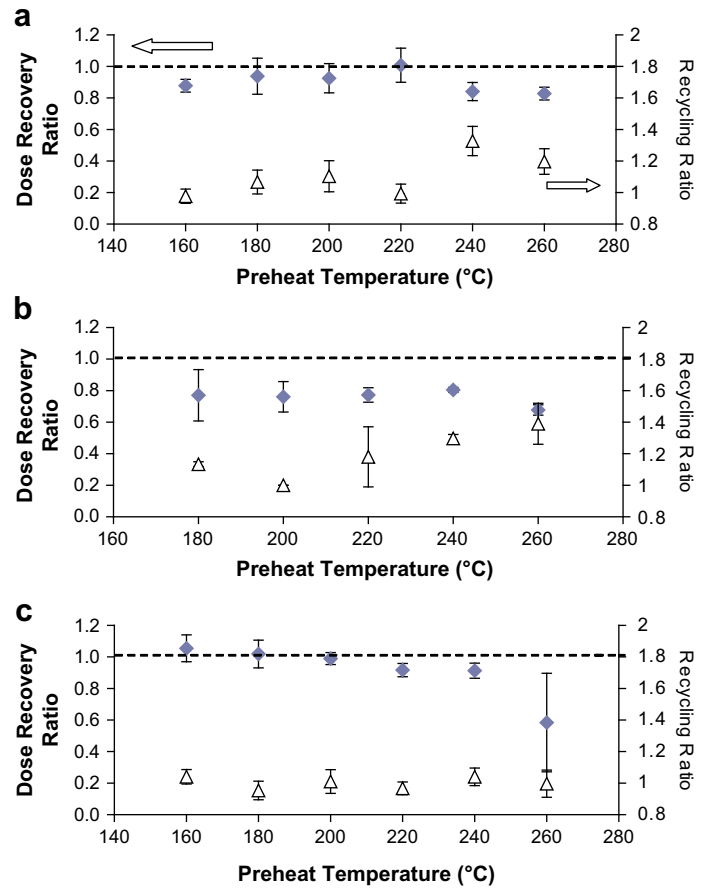


Fig. 3. Recycling ratio (open triangles) and preheat plateau for dose recovery test (solid diamonds) using different preheat temperatures and heating rates. (a) Heating rate of 2 °C/s for sample Hi2006II; (b) heating rate of 5 °C/s for sample Hi2006II and (c) heating rate of 2 °C/s for sample Hi2006VI. Note: dashed line denotes the given laboratory dose.

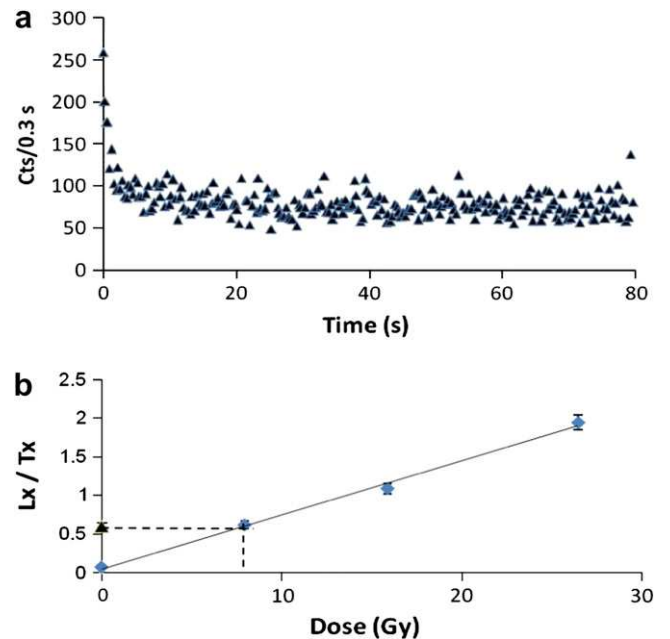
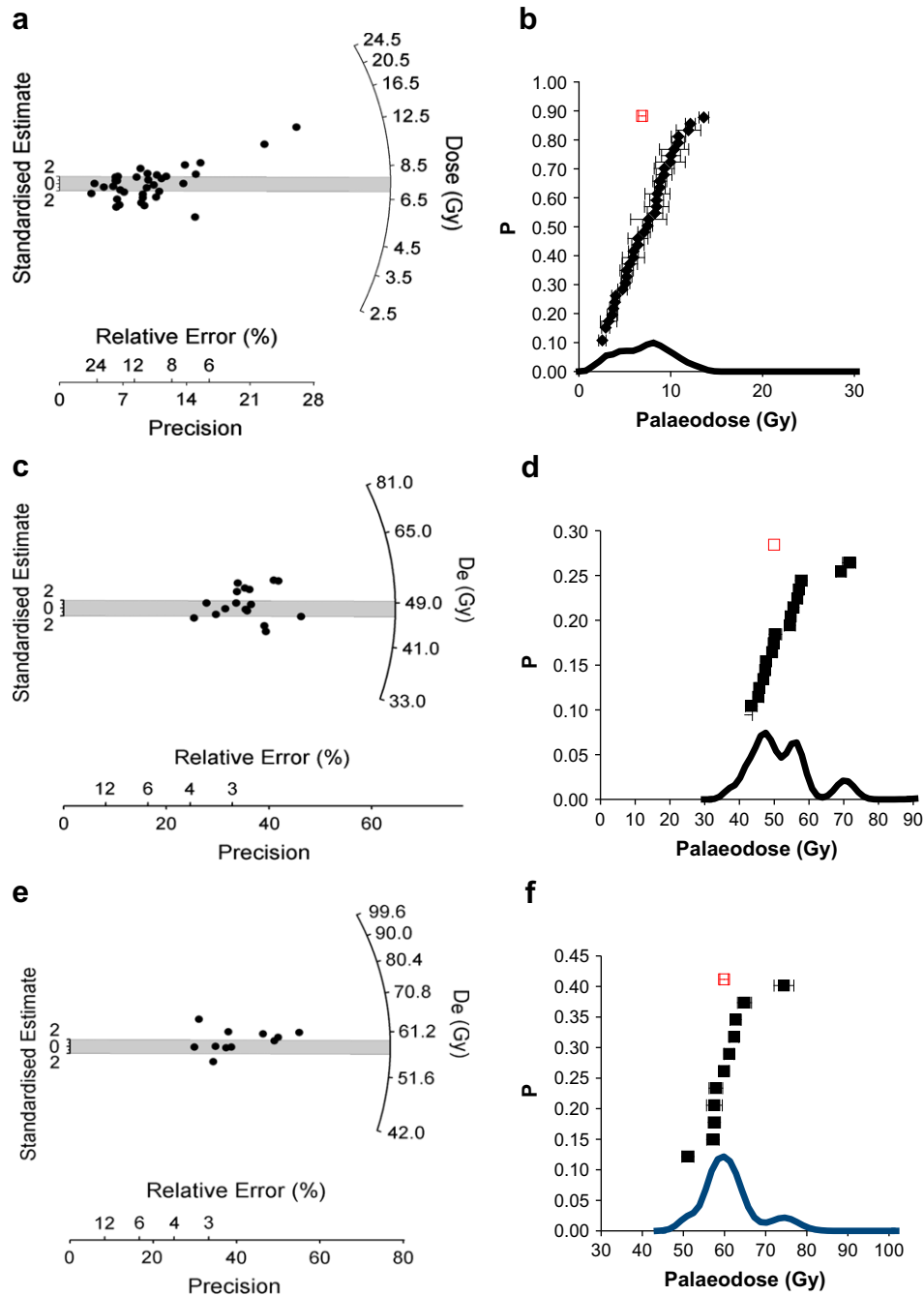


Fig. 4. An example of the OSL decay and SAR growth curve for sample Hi2006II showing (a) the weak natural OSL signal and (b) despite this, a good SAR growth curve could be measured.



**Fig. 5.**  $D_e$  distributions for samples Hi2006II (a, b), Hi2006VI (c, d) and Hi2006I (e, f). Showing radial plots on the left and probability ( $P$ ) density plots on the right with individual aliquot  $D_e$  plotted above (closed square) and the arithmetic mean of the data (open square).

given the depositional setting and the  $D_e$  distributions shown in Fig. 5, there is likelihood that the samples were incompletely bleached prior to deposition. As measurements are at the multi-grain level with an unknown number of grains contributing to OSL signal from each aliquot, multiple  $D_e$  populations within a sample (particularly ones with lower  $D_e$  values) may be largely masked (e.g. Bateman et al., 2003, 2008). Thus, slight low  $D_e$  shoulders on distributions when plotted as a combined probability plot may be significant as an indicator of partial bleaching problems. If this is the case then basing age calculations on an assumption that all the data were from a single population (as done in Nazari et al., submitted for publication), would lead to an over-estimation of true

burial age and high uncertainties. In response to these concerns, we have excluded aliquot data which fell outside 2 standard deviations of the mean as statistical outliers and then have applied different statistical approaches in order to calculate a suitable single  $D_e$  value for age determinations. By calculating the OD and skewness of the data it was possible to apply the Bailey and Arnold (2006) decision making test to determine which statistical model might best be used to minimize the inclusion of partially bleached data. This recommended the adoption of the Central Age Model (CAM; Galbraith et al., 1999) from which was derived a  $D_e$  value of  $60.24 \pm 0.28$  Gy,  $6.79 \pm 0.08$  Gy and  $48.78 \pm 0.33$  Gy for samples Hi2006I, Hi2006II and Hi2006VI, respectively. For comparison, data

**Table 1**

Dose rates, equivalent dose and calculated ages for quartz (size range between 90 and 250  $\mu\text{m}$ ) from the 3 samples. CAM and FMM are the Central Age Model and the Finite Mixture Model, respectively.

Sample	Lab code	Depth (m)	U (ppm)	Th (ppm)	K (%)	Cosmic (Gy/ka)	Dose rate (Gy/ka) <sup>c</sup>	N <sup>a</sup>	Over-dispersion	Skewness	CAM $D_e$ (Gy)	FMM $D_e$ (Gy)	$P^b$	CAM age (kyr)	FMM age (kyr)
Hi2006II	Shfd07043	0.45	1.67	5.5	0.73	0.24	1.79 $\pm$ 0.06	38	47%	1.56	6.79 $\pm$ 0.08	3.63 $\pm$ 0.28	19	3.8 $\pm$ 0.1	2.0 $\pm$ 0.2
Hi2006VI	Shfd07044	1.5	2.04	6	1.27	0.21	2.43 $\pm$ 0.09	21	21%	1.52	48.78 $\pm$ 0.33	48.84 $\pm$ 1.22	86	20.2 $\pm$ 0.8	20.2 $\pm$ 0.9
Hi2006I	Shfd07042	1.2	1.79	6	1.22	0.22	2.29 $\pm$ 0.09	11	8%	0.58	60.24 $\pm$ 0.28			26.0 $\pm$ 1.0	–

<sup>a</sup> N is the number of aliquots out of the 24 (48 for Hi2006II) not rejected using the quality control parameters and falling within two standard deviations of the mean  $D_e$ .

<sup>b</sup> P is percent of the data which fell in the lowest  $D_e$  cluster.

<sup>c</sup> A standard palaeo moisture content of 1.1% was applied to all samples.

were also analysed with the Finite Mixture Model (FMM; Galbraith and Green, 1990) with a sigma  $b$  of 0.1 and a  $k$  value between 4 and 2 (dependant of which minimized Bayesian information criterion or BIC in the model; see Galbraith and Green, 1990). Results from data for sample Hi2006II showed that 19% of the data fell in  $D_e$  cluster around  $3.6 \pm 0.3$  Gy, 25% of the data had a  $D_e$  cluster of  $5.7 \pm 0.5$  Gy and 44% of the data had a  $D_e$  value of  $9.4 \pm 0.5$  Gy, and 12% of data had a  $D_e$  cluster of  $15.5 \pm 1.2$  Gy. For sample Hi2006VI, 86% of the data fell in  $D_e$  cluster around  $48.8 \pm 1.2$  Gy and 14% of data had a  $D_e$  cluster of  $79.5 \pm 5.0$  Gy. Finite mixture modelling was not necessary for sample Hi2006I as this, after the outlier removal, had a normal distribution with only a single mode (Table 1).

As sample Hi2006II is from the stratigraphically youngest sediment, it must have a true burial  $D_e$  less than the minimum  $D_e$  measured for samples Hi2006VI (min =  $37.4 \pm 1.3$  Gy), assuming similar dose rates for the samples. Both statistical approaches appear to meet this requirement, however, using the lowest  $D_e$  identified by FMM (assuming this has the highest proportion of well-bleached grains) a much younger age is calculated for sample Hi2006II. This sample has a CAM age of  $3.8 \pm 0.1$  kyr compared to an FMM age of  $2.0 \pm 0.2$  kyr. Application of FMM to sample Hi2006VI makes little difference to the final age as it has a CAM age of  $20.2 \pm 0.8$  kyr compared to an FMM age of  $20.2 \pm 0.9$  kyr. Using FMM for samples Hi2006II and Hi2006VI and CAM for sample Hi2006I to calculate ages it can be seen that ages increase in antiquity with depth and that they confirm to stratigraphy so that sample Hi2006II, relating to the most recent movement on the fault, gives the youngest age. The age of Hi2006VI might correspond to the penultimate event provided that the sedimentation record is complete.

Irrespective of which statistical approach is adopted, the OSL results show that the last fault movement has definitely occurred within the Late Holocene. However, in the absence of any independent age control, it is not possible to be absolutely sure which of the statistical approaches undertaken to derive a single  $D_e$  for age calculation, gives the most accurate burial age for this fault related sample. The high level of OD and skewing of the sample would suggest that some partially bleached material has been incorporated within the single aliquot measurements. Thus, whilst both statistical approaches reduce uncertainties when compared to the work of Nazari et al. (submitted for publication), using the  $D_e$  derived from CAM to calculate an age would probably lead to an overestimate of the true burial age for sample Hi2006II. Based on the FMM derived  $D_e$ , the last earthquake which caused fault movement, occurred around  $2.0 \pm 0.2$  kyr. The age of sample Hi2006VI might correspond to a previous earthquake event at around  $20.2 \pm 0.9$  kyr.

## 6. Conclusions

Applying OSL for dating quartz extracted from colluvial samples from Iran is usually difficult and time consuming. The samples used for this study suffered from weak OSL signal and initially a lack of

a preheat plateau even for dose recovery tests. The performance of the SAR protocol was improved by experimentally determining an appropriate test dose and adjusting both the preheat temperature and the ramp-time. Despite this, for  $D_e$  determination many aliquots per samples had to be rejected as they did not satisfy the quality control SAR requirements. As the depositional context had a high probability of inclusion of partially bleached sediment, an understanding of the  $D_e$  distributions of mixed dose populations at the aliquot level was needed. Accordingly, whilst CAM was suggested on the basis of samples'  $D_e$  distributions and skewness, FMM was preferred as the most likely to minimize the impact of age over-estimation due to partial bleaching. Ages calculated for this study therefore show that the most recent earthquake causing slippage in the Dhesir fault appears to be around  $2.0 \pm 0.2$  kyr. This refines considerably the age window of 1.4–4.2 kyr reported by Nazari et al. (submitted for publication) in which the last earthquake could have taken place. It also demonstrates that the historical record of earthquakes may be incomplete for the Iranian antiquity, because an  $M \geq 6.5$  event is not mentioned in the region located around the Dshir fault. This result is critical for seismic hazard assessment and strengthens the urgent need for thorough palaeoseismic investigations in Central and Eastern Iran.

## Acknowledgement

We appreciate the constructive comments and suggestions of the anonymous reviewer which improved the quality of this paper. We would like to thank Rob Ashurst for his assistance in OSL sample preparation. The first author appreciate the support of the research department of the university of Tehran.

Editorial handling by: R. Grün

## References

- Bailey, R.M., Arnold, L.J., 2006. Statistical modelling of single grain quartz  $D_e$  distributions and an assessment of procedures for estimating burial dose. *Quaternary Science Reviews* 25, 2475–2502.
- Bateman, M.D., Frederick, C.D., Jaiswal, M.K., Singhvi, A.K., 2003. Investigations into the potential effects of pedoturbation on luminescence dating. *Quaternary Science Reviews* 22, 1169–1176.
- Bateman, M.D., Carr, A.S., Murray-Wallace, C.V., Roberts, D.L., Holmes, P.J., 2008. A dating intercomparison study on Late Stone Age coastal midden deposits, South Africa. *Geoarchaeology* 23, 715–741.
- Berberian, M., 1981. Active faulting and tectonics of Iran. In: Gupta, H.K., Delany, F.M. (Eds.), *Zagros-Hindu Kush-Himalaya Geodynamic Evolution*. Geodynamics Series, vol. 3. AM. Geophys. Union, pp. 33–69.
- Berberian, M., Yeats, R.S., 1999. Patterns of historical earthquake rupture in the Iranian plateau. *Bulletin of the Seismological Society of America* 89, 120–139.
- DeMets, C., Gordon, R.G., Argus, D.F., Stein, S., 1994. Effect of recent revisions to the geomagnetic reversal time scale on estimates of current plate motions. *Geophysical Research Letters* 21, 2191–2194.
- Engdahl, E.R., van der Hilst, R., Buland, R., 1998. Global teleseismic earthquake relocation with improved travel times and procedures for depth determination. *Bulletin of the Seismological Society of America* 88, 722–743.
- Fattahi, M., 2009. Dating past earthquakes and related sediments by thermoluminescence methods: a review. *Quaternary International* 199 (1–2), 104–146.
- Fattahi, M., Walker, R., 2007. Luminescence dating of the last earthquake of the Sabzevar thrust fault, NE Iran. *Quaternary Geochronology* 2 (1–7), 284–289.

- Fattahi, M., Walker, R., Hollingsworth, J., Bahroudi, A., Talebian, M., Armitage, S., Stokes, S., 2006. Holocene slip-rate on the Sabzevar thrust fault, NE Iran, determined using Optically-stimulated Luminescence (OSL). *Earth and Planetary Science Letters* 245, 673–684.
- Fattahi, M.R., Walker, M.M., Khatib, A., DolatiBahroudi, J., 2007. Slip-rate estimates and past earthquakes on the Doruneh fault, eastern Iran. *Geophysical Journal International* 168, 691–709.
- Galbraith, R.F., Green, P.F., 1990. Estimating the component ages in a finite mixture. *Radiation Measurements* 17, 197–206.
- Galbraith, R.F., Roberts, R.G., Laslett, G.M., Yoshida, H., Olley, J.M., 1999. Optical dating of single and multiple grains of quartz from Jinmium rock shelter, northern Australia. Part I, experimental design and statistical models. *Archaeometry* 41, 339–364.
- Jackson, J.A., McKenzie, D., 1984. Active tectonics of the Alpine–Himalayan Belt between western Turkey and Pakistan. *Geophysical Journal of the Royal Astronomical Society* 77, 185–264.
- Mathew, G., Singhvi, A.K., Karanth, R.V., 2006. Luminescence chronometry and geomorphic evidence of active fold growth along the Kachchh Mainland Fault (KMF), Kachchh, India: seismotectonic implications. *Tectonophysics* 422, 71–87.
- Meyer, B., Mouthereau, F., Lacombe, O., Agard, P., 2006. Evidence of Quaternary activity along the Dehshir fault: implication for the Tertiary tectonics of Central Iran. *Geophysical Journal International* 164, 192–201.
- Meyer, B., Le Dortz, K., 2007. Strike-slip kinematics in Central and Eastern Iran: estimating fault slip-rates averaged over the Holocene. *Tectonics* 26, TC5009. doi:10.1029/2006TC002073.
- Murray, A.S., Wintle, A.G., 2000. Luminescence dating of quartz using an improved single-aliquot regenerative-dose protocol. *Radiation Measurements* 32 (1), 57–73.
- Murray, A.S., Wintle, A.G., 2003. The single aliquot regenerative dose protocol: potential for improvements in reliability. *Radiation Measurements* 37, 377–381.
- Nazari, H., Fattahi, M., Meyer, B., Sebrier, M., Talebian, M., Foroutan, M., Le Dortz, K., Bateman, M.D., Ghoreishi, M. First evidence for large earthquakes on the Dehshir Fault, Central Iran plateau. *Terra Nova*, submitted for publication.
- Olley, J.M., Caitcheona, G.G., Roberts, R.G., 1999. The origin of dose distributions in fluvial sediments, and the prospect of dating single grains from fluvial deposits using optically stimulated luminescence. *Radiation Measurements* 30, 207–217.
- Porat, N., Levi, T., Weinberger, R., 2007. Possible resetting of quartz OSL signals during earthquakes – evidence from late Pleistocene injection dikes, Dead Sea basin, Israel. *Quaternary Geochronology* 2 (1–4), 272–277.
- Pucci, S., De Martini, P.M., Pantosti, D., 2008. Preliminary slip rate estimates for the Düzce segment of the North Anatolian Fault Zone from offset geomorphic markers. *Geomorphology* 97 (3–4), 538–554.
- Rodnight, H., Duller, G.A.T., Tooth, S., Wintle, A.G., 2005. Optical dating of a scroll-bar sequence on the Klip River, South Africa, to derive the lateral migration rate of a meander bend. *The Holocene* 15, 802–811.
- Sella, G.F., Dixon, T.H., Mao, A., 2002. REVEL: a model for recent plate velocities from space geodesy. *Journal of Geophysical Research* 107. doi:10.1029/2000JB000033.
- Talebian, 2003. Active Faulting in the Zagros Mountains of Iran. King's College D. Phil. thesis. University of Cambridge, Cambridge.
- Vandenberghe, D., Vanneste, K., Verbeeck, K., Paulissen, E., Buylaert, J.-P., De Corte, F. & Van den haute, P. (2007). Late Weichselian and Holocene earthquake events along the Geleen fault in NE Belgium: OSL age constraints. *Quaternary International*, doi:10.1016/j.quaint.2007.11.017.
- Walker, R., Jackson, J., 2004. Tectonics of Central and Eastern Iran. *Tectonics* 23, TC5010. doi:10.1029/2003TC001529. 309.

## Appendix A.2

# **Dating inset terraces and offset fans along the Dehshir fault (Iran) combining cosmogenic and OSL methods**

---

## Dating inset terraces and offset fans along the Dehshir Fault (Iran) combining cosmogenic and OSL methods

K. Le Dortz,<sup>1,2,\*</sup> B. Meyer,<sup>1,2</sup> M. Sébrier,<sup>1,2</sup> R. Braucher,<sup>3</sup> H. Nazari,<sup>4</sup> L. Benedetti,<sup>3</sup> M. Fattahi,<sup>5,6</sup> D. Bourlès,<sup>3</sup> M. Foroutan,<sup>4</sup> L. Siame,<sup>3</sup> A. Rashidi<sup>7</sup> and M. D. Bateman<sup>6</sup>

<sup>1</sup>UPMC Univ Paris 06, ISTEP, UMR 7193, F-75005, Paris, France. E-mail: bertrand.meyer@upmc.fr

<sup>2</sup>CNRS, ISTEP, UMR 7193, F-75005, Paris, France

<sup>3</sup>CEREGE UMR6635, Aix-en-Provence, France

<sup>4</sup>Research Institute for Earth Sciences, Geological Survey of Iran, P.O. Box 13185-1494 Tehran, Iran

<sup>5</sup>Institute of Geophysics, University of Tehran, Iran

<sup>6</sup>Sheffield Centre for International Drylands Research, University of Sheffield, Sheffield S10 2TN, UK

<sup>7</sup>Geological Survey of Iran, P.O. Box 7615736841 Kerman, Iran

Accepted 2011 March 7. Received 2011 March 7; in original form 2010 July 15

### SUMMARY

<sup>10</sup>Be and <sup>36</sup>Cl cosmic ray exposure (CRE) and optically stimulated luminescence (OSL) dating of offset terraces have been performed to constrain the long-term slip rate of the Dehshir fault. Analysis of cosmogenic <sup>10</sup>Be and <sup>36</sup>Cl in 73 surface cobbles and 27 near-surface amalgams collected from inset terraces demonstrates the occurrence of a low denudation rate of 1 m Ma<sup>-1</sup> and of a significant and variable inheritance from exposure prior to the aggradation of these alluvial terraces. The significant concentrations of cosmogenic nuclides measured in the cobbles collected within the riverbeds correspond to 72 ± 20 ka of inheritance. The mean CRE age of the surface samples collected on the older terrace T3 is 469 ± 88 ka but the analysis of the distribution of <sup>10</sup>Be concentration in the near-surface samples discard ages older than 412 ka. The mean CRE age of the surface samples collected on terrace T2 is 175 ± 62 ka but the <sup>10</sup>Be depth profile discard ages older than 107 ka. For each terrace, there is a statistical outlier with a younger age of 49.9 ± 3.3 and 235.5 ± 35.4 ka on T2 and T3, respectively. The late sediments aggraded before the abandonment of T2 and inset levels, T1 b and T1a, yielded OSL ages of, respectively, 26.9 ± 1.3, 21.9 ± 1.5 and 10.0 ± 0.6 ka. For a given terrace, the OSL ages, where available, provide ages that are systematically younger than the CRE ages. These discrepancies between the CRE and OSL ages exemplify the variability of the inheritance and indicate the youngest cobble on a terrace, that minimizes the inheritance, is the most appropriate CRE age for approaching that of terrace abandonment. However, the upper bound on the age of abandonment of a terrace that is young with respect to the amount of inheritance is best estimated by the OSL dating of the terrace material. For such terraces, the CRE measurements are complementary of OSL dating and can be used to unravel the complex history of weathering and transport in the catchment of desert alluvial fans. This comprehensive set of dating is combined with morphological offsets ranging from 12 ± 2 to 380 ± 20 m to demonstrate the Dehshir fault slips at a rate in the range 0.9 mm yr<sup>-1</sup>–1.5 mm yr<sup>-1</sup>. The variable inheritance exemplified here may have significant implications for CRE dating in arid endorheic plateaus such as Tibet and Altiplano.

**Key words:** Geomorphology; Seismicity and tectonics; Continental tectonics: strike-slip and transform; Tectonics and landscape evolution.

### 1 INTRODUCTION

The Dehshir fault is a 380-km-long, strike-slip fault cutting through the Central Iran plateau, north of the Zagros. It is located be-

tween 29.5°N–54.6°E and 33°N–53.1°E and is part of a series of N-striking dextral faults slicing Central and Eastern Iran (e.g. Berberian 1981). The total offset of the fault, denoted by the geological offsets of the Nain Baft suture and the Urumieh Doktor magmatic arc, amounts to 65 ± 15 km (inset Fig. 1, Walker & Jackson 2004; Meyer *et al.* 2006). The southern portion of the Dehshir fault that runs across a series of Quaternary alluvial fans shows clear

\*Now at: Laboratoire de géologie, Ecole Normale Supérieure, UMR 8538, 75252 Paris, France. E-mail: ledortz@geologie.ens.fr

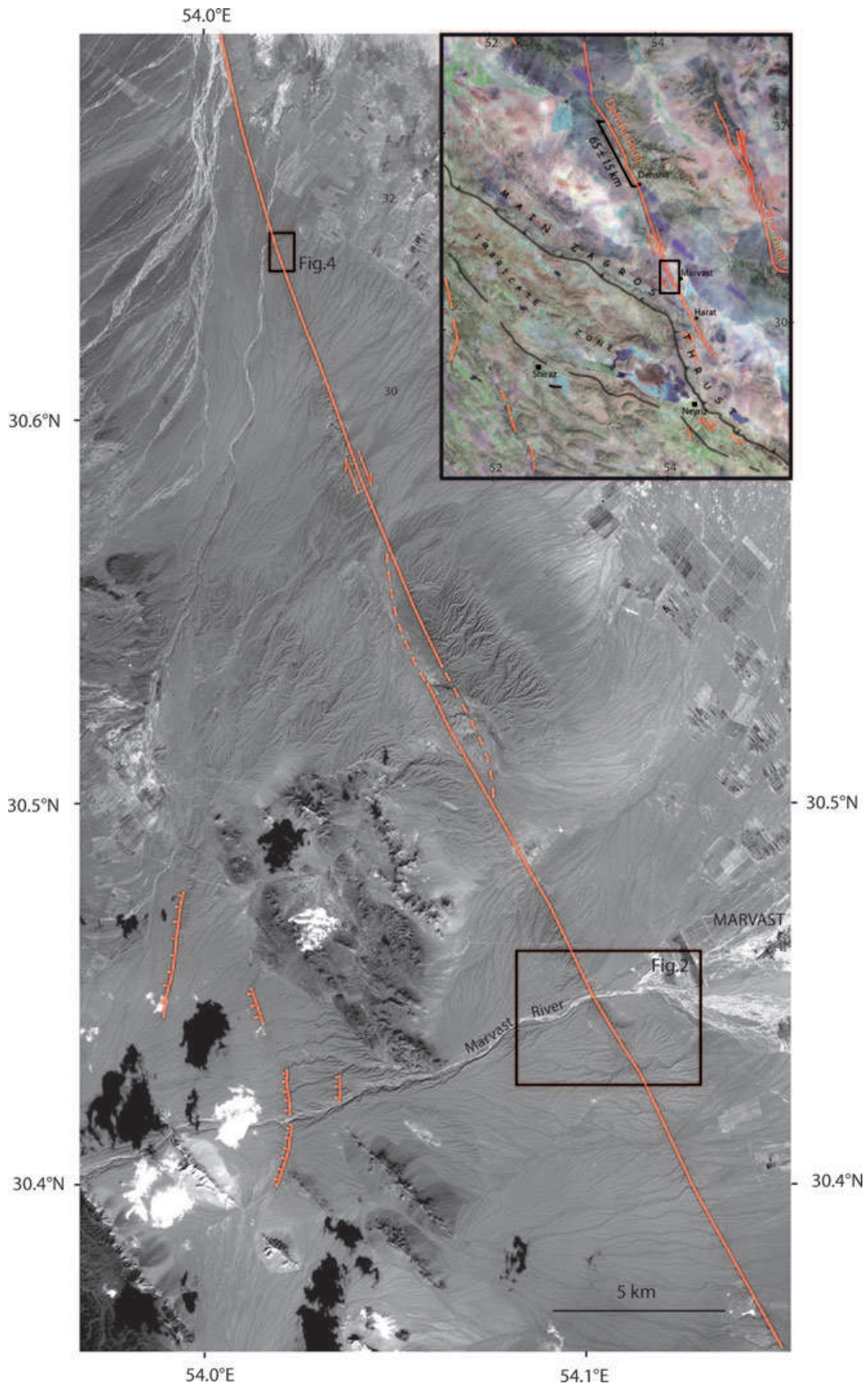


**Figure 1.** Spot imagery of the southern part of the Dehshir Fault, near Marvast Town. The fault cuts across abandoned alluvial fan systems and active rivers. Boxes indicate locations of Figs 2 and 4. The inset is a Landsat mosaic of the Dehshir fault and surroundings. The Nain Baft ophiolite outcrops are stylized in purple. The total dextral offset of the fault ( $65 \pm 15$  km) is outlined by the displacement of the suture.

evidence of recent right-lateral motion (Fig. 1). Geomorphologic studies have been performed to estimate the slip rate of the fault. Combining cumulative offsets of gullies and terrace risers with their inferred Holocene age, Meyer *et al.* (2006) and Meyer & Le Dortz (2007) suggested the fault slips at  $2 \text{ mm yr}^{-1}$ . This initial estimate has been further investigated by dating of optically stimulated luminescence (OSL) samples collected within colluviums thought to predate the incision of an abandoned fan. Nazari *et al.* (2009) derived a minimum slip rate of  $0.8\text{--}2.5 \text{ mm yr}^{-1}$  by combining the offset of two gullies incised within the fan with the weighted mean OSL age of the colluviums. However, neither the offset-gullies nor the surface of the abandoned fan have been dated directly. Nazari *et al.* (2009) collected primarily the OSL samples for palaeoseismic purpose, within the fault zone where fanglomerate layers have been disrupted and/or warped.

To date the surface of the fan and provide further constraints on the slip rate, we have sampled the surface to estimate its cosmic ray exposure (CRE) age and the sediments below the surface for OSL dating of their emplacement. Although these two dating techniques are commonly used separately, a few recent studies have combined luminescence dating with cosmogenic data. In some cases the two methods yielded comparable ages though the CRE ages are always slightly older than the OSL ones (e.g. Owen *et al.* 2003, 2006; DeLong & Arnold 2007). Other studies yielded to significant differences, CRE ages being as much as twice older than the OSL ones (Hetzl *et al.* 2004; Le Dortz *et al.* 2009; Nissen *et al.* 2009). Some authors favoured the CRE ages whether they used surface samples only (Hetzl *et al.* 2004) or near-surface samples only (Nissen *et al.* 2009). Others (Le Dortz *et al.* 2009) that used both surface and near-surface samples concluded to a variable inheritance for the CRE ages and favoured the OSL ages for dating the abandonment of alluvial surfaces.

We performed the sampling at two sites on the southern portion of the fault where Meyer *et al.* (2006) documented right-lateral offsets of imbricate fan surfaces and riser cuts (Fig. 1). To constrain the age of the abandoned fan surfaces and the age of the subsequent incision, we collected 100 samples (73 surface samples and 27 near-surface samples along three profiles) to determine their CRE age by measuring the accumulation of  $^{10}\text{Be}$  and  $^{36}\text{Cl}$  cosmogenic nuclides. Using two isotopes with markedly different half-lives offered the opportunity to better constrain the erosion rate and evaluate the trade-off between erosion and CRE age of the studied surfaces. We also collected six additional samples within quartz-rich sandy layers located below alluvial surfaces to measure by OSL the time elapsed since the last sunlight exposure of the sediment.

First, we describe the detailed morphology of the two sites with emphasis on inset terrace levels imbricate within successive alluvial fan systems. Then, we present the results of the CRE and OSL dating and discuss how far they help constraining the abandonment age of the terrace treads and the age of the riser cuts that bound the treads. Finally, we discuss the slip rate of the Dehshir fault and the morphoclimatic chronology of the area.

## 2 OFFSET QUATERNARY FANS ALONG THE SOUTHERN PORTION OF THE DEHSHIR FAULT

### 2.1 Site Dehshir South: Marvast River

The Marvast River is the largest and the most active of the intermittent rivers draining the study area, a dryland part of endorheic

Central Iran Plateau. The river course is about 70 km long from its source within the High Zagros to the South of the Marvast City. The incision of the Marvast River is limited because it vanishes into the Marvast salt flat, whose base level stands at the elevation of 1520 m. The drainage basin of the Marvast River is about 1100 km<sup>2</sup>, and the upstream catchment drains several distinctive rock units including cover (Zagros platform lithologies) and basement (Sanandaj Sirjan metamorphics). The river and its former tributaries have emplaced the vast Quaternary piedmont made of coalescent fans that cover most of the surface on the satellite imagery of Fig. 1. The recent incision of the piedmont has resulted in a narrow channel supplying water to the city of Marvast, the formation of inset terraces and the fan head entrenchment. The Dehshir fault cuts across the Marvast River, the active fans and the abandoned fan systems (Fig. 2). To the west of Marvast City, several inset terraces are distinguished (T0, T1a, T1b, T2 and T3) and their relative age can be assessed by their relative elevation (Fig. 3). The material of each terrace, well layered, is of fluvial-torrential origin and contains polygenic cobbles (Fig. 3). The lower terrace T0 corresponds to the present-day overflowing flood channel of the Marvast River. Many braided channels up to 0.5–0.8 m deep incise T0. Very loose conglomerates alternate with silty–sandy layers. The pebbles and the cobbles, either in the riverbed or on the surface of T0 are well rounded and have not experienced cryoclasty. T1 is a terrace located 1–3 m above T0. T1 is made of two distinctive levels, T1b is slightly older and 1 m above T1a. Both T1a and T1b levels have been probably emplaced during the same climatic period. They contain pebbles and well-rounded cobbles with diameters up to 30 cm. The material is poorly cemented and some sandy layers are found intercalated within the slightly indurate conglomeratic layers. Cobbles on the T1 surface display bar and swell morphology, most of them are well rounded; very few have been fragmented suggesting a very limited cryoclasty. T2 is an older terrace standing about 4–5 m above T1 upstream of the Dehshir fault and 2–4 m above the present streambed downstream. Several indurate sandy layers alternate with coarse conglomerates. T2 surface is flat and many fragmented cobbles are found on it, suggesting that the terrace underwent low temperatures and contrasted seasons during long period of times associated with strong wind deflation, as under glacial climates. The upper part of the terrace is fairly cemented by a discontinuous calcrete up to 1 m thick at some places. T3 is the top surface of the highest alluvial fan system. It stands more than 5 m above T2. Where exposed upstream, by the Marvast incision, T3 contains many cryoclasted cobbles and a few large cobbles. The conglomerate levels are strongly indurate and the upper part of T3 is cemented by a continuous, 0.4–0.8 m thick, reddish calcrete. Numerous gelifRACTED cobbles can be found on its surface. Many gullies incise T3; they are deeper and wider than the shallow immature rills incising T2. The overall terrace has a characteristic striped-morphology on the satellite imagery with flat strips separated by narrow intervening intermittent gullies (Fig. 2).

There are also a few remnants of older fanglomerates cropping out close to the fault (Fig. 2). These older conglomerates are assigned to the Pliocene according to the geological mapping by GSI (1981). The layers are mostly tilted to the west and squeezed within the fault zone, but the orientation of the cobbles indicates an eastward palaeocurrent direction (Meyer *et al.* 2006). The successive fans have been all emplaced by the Marvast River and progressively deformed through time. The most recent riser cut of the Marvast River stands between T1 tread and the river course (T1b/T0) West of the fault and between T2 tread and the river course (T2/T0) East of the fault. This T2/T0 riser, deflected in a right-lateral sense by

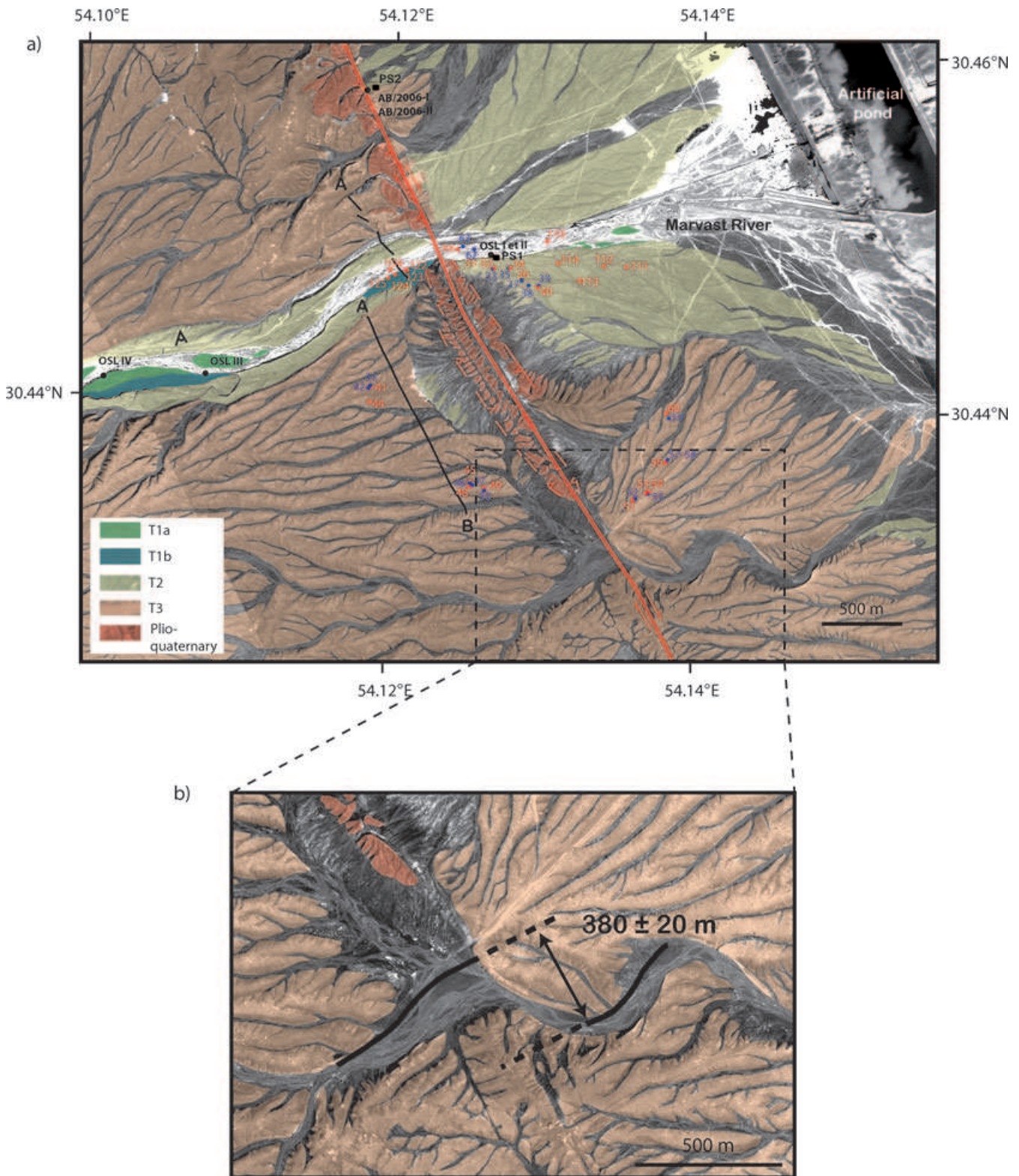


**Figure 2.** Site Dehshir South. (a) Quickbird imagery. The fault trace cuts across the Marvast River, intermittent channels and successive abandoned fans and terraces (T3 in orange, T2 in yellow, T1 a and b in green). The numbered dots show the position of the surface samples collected for  $^{10}\text{Be}$  and  $^{36}\text{Cl}$  CRE dating (red and blue dots, respectively). The black squares show the position of the near-surface samples collected along depth profiles PS1 and PS2 (Figs 11, 12). The black dots locate the OSL samples taken below the ground surface. AB locates the topographic profile of Fig. 3. (b) Close up on the  $380 \pm 20$  m dextral offset of a river course, incised within the oldest (T3) fan surface.

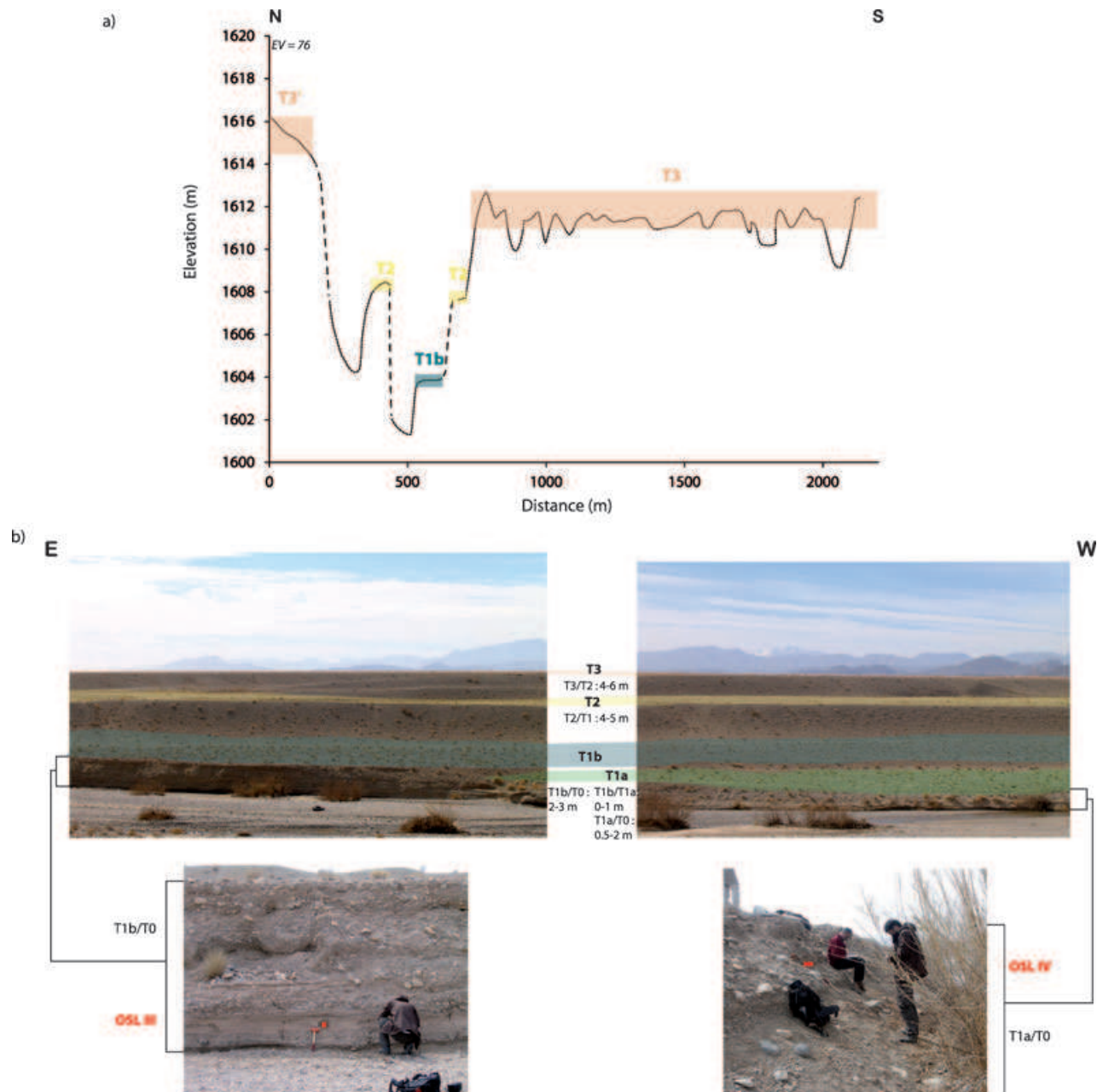


**Figure 3.** (a) Topographic profile across the abandoned fan system (see location on Fig. 2) highlights the relative elevation of the terraces and their degree of incision by the Marvast river. The profile is worked out from a differential GPS survey. (b) Field photograph of the inset terraces. Location of OSL III and IV are indicated on the close up pictures of the risers T1b/T0 and T1a/T0, respectively.

an amount of  $25 \pm 5$  m, is not a passive marker and might have been rejuvenated by lateral erosion (Fig. 2a). Several larger offsets occur further to the South. About 2 km south of the Marvast River, a large dry river, deeply incised within the oldest fan T3, is right-laterally offset by  $380 \pm 20$  m (Fig. 2b). This offset is higher than the 180–200 m offset streams described by Meyer *et al.* (2006) a little further to the South. The latter offsets correspond to streams that are narrower and less incised than for the former. Consequently, the value of  $380 \pm 20$  m corresponds to the largest dextral offset observed among the many rivers incising T3 and provides a minimum bound of the fault motion since the abandonment of T3 tread.

## 2.2 Site Dehshir North

The site Dehshir North is located about 25 km north of the Marvast River (Fig. 1). The site lies close to a 30-km-long, north–south trending, intermittent stream in which present-day drainage is mostly restricted to the northern part of the piedmont. The stream is disconnected from the Marvast River but it grades almost back to the Marvast River outlet from the Sanandaj Sirjan Mountains and drains a significant area of the Quaternary piedmont. At site Dehshir North, the piedmont mainly consists of the distal part of the abandoned fan T3 (Fig. 4). Similarly to the site Dehshir South, several lower levels (T2, T1b and T1a) with limited extension are nested within

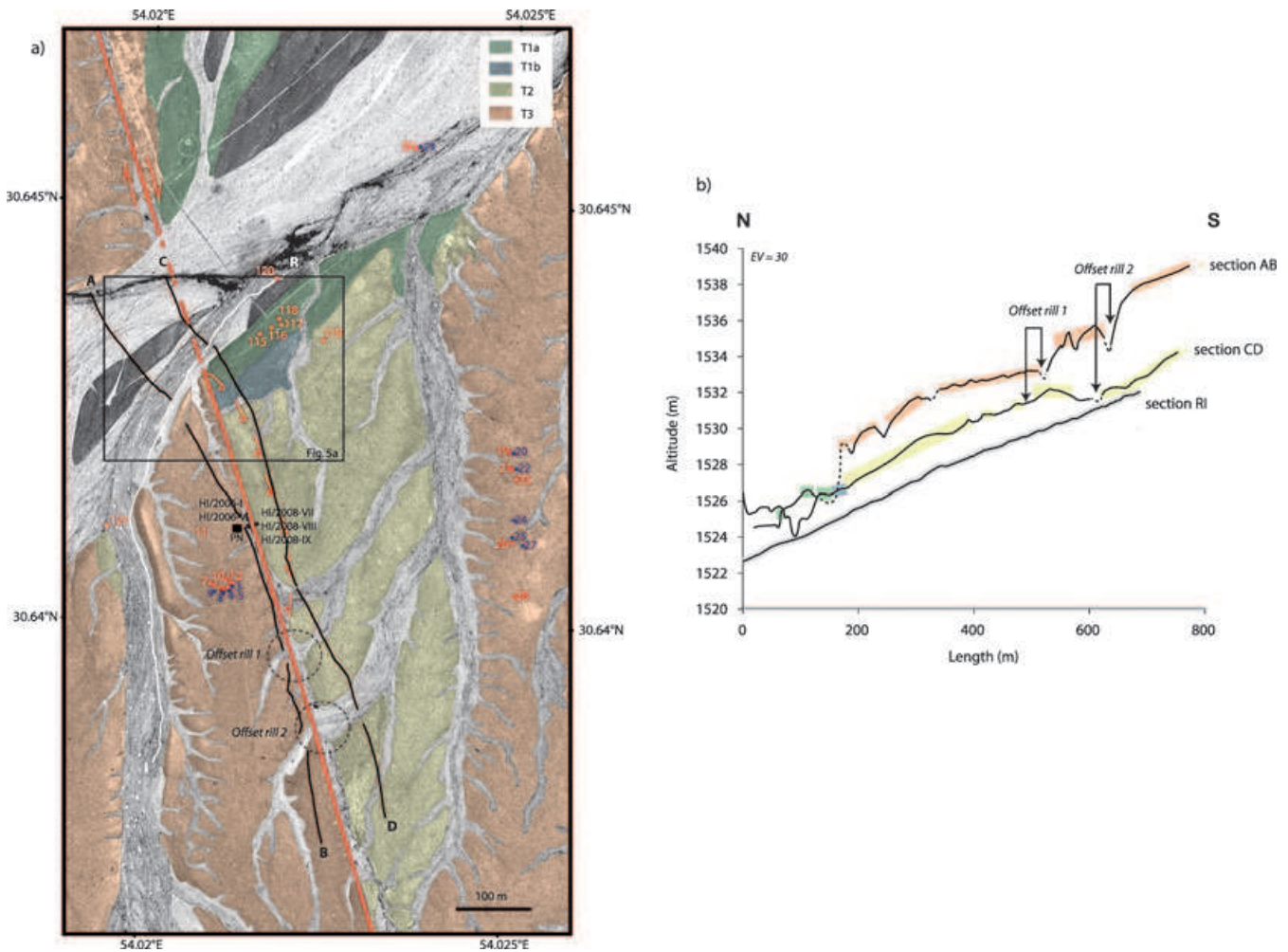


**Figure 4.** Site Dehshir North. (a) Quickbird imagery. Different coloured shading denotes the successive abandoned fans (same code as for Fig. 2). Numbered dots show the position of the surface samples collected for  $^{10}\text{Be}$  and  $^{36}\text{Cl}$  CRE dating (red and blue dots, respectively). The black square shows the position of the near-surface samples collected along the depth profiles PN (Figs 7 and 8). Rectangle denotes the close up on the offset riser on Fig. 5. Dotted circles indicate location of 20–30 m right-lateral offset gullies. Black (AB and CD) and white (RI) lines locate topographic sections on each side of the fault and on the riverbed, respectively. (b) Topographic profiles, achieved from differential GPS survey and projected along fault strike, highlight the amount of stream incision upstream and downstream of the fault. The offset gullies are indicated.

the alluvial fan T3. The material of each terrace is also of fluvial-torrential origin but the gravel sizes are smaller than at site Dehshir South. Fine content is higher and the coarser levels are void of boulders.

The higher level T3, although much resembling that along the Marvast River on the SPOT Imagery, has been a little less incised and dissected by the rivers than at Dehshir South. At Dehshir North, T3 stands about 4 m only above the active riverbed (Fig. 4b) and its surface displays many cryoclasted cobbles. T3 is incised upstream by many short gullies regularly spaced every 20–30 m. Such gullies probably formed as a result of regressive erosion after the abandonment of the terrace T3 and the cutting of the risers. T2 has a very limited extension with respect to T3. It is a lateral fan sloping down gently northwards that was aggraded by small local tributaries that are incised within T3 terrace and rework its alluvial material. T2 surface stands 2–4 m below T3 and is much less incised than the old terrace; only a few short gullies irregularly spaced are distinguished on the Quickbird Imagery (Fig. 4a). As T3, the surface of T2 dis-

plays cryoclastic material. The emplacement of the lateral fan T2 is partly controlled by the local development of the Dehshir fault. The terrace T1 lies 1 m at most below the terrace T2 and stands 1 m above the riverbed T0. Most of the gullies that incise T3 and T2 merge downstream with T1 and their incision is probably synchronous with the emplacement of T1. The surface of T1 displays only very few cryoclasted cobbles. Similarly to the site Dehshir South, two levels (T1a and T1b) can be distinguished, with T1b being older and standing 0.5–1 m above T1a. Both the terrace T1 and the lateral fan T2 are nested in the highest terrace T3 and have a very limited extent.

Some small gullies that incise T3 and T2 cross the fault zone at a right angle. Two of these gullies are clearly offset in a right-lateral sense by 20–30 m (Fig. 4), an amount similar to the deflection of the Marvast River at the site Dehshir South. These gullies post-date the emplacement of T3 and T2 and might have formed as a result of regressive erosion since the last significant incision of the network. Their incision is probably coeval with the emplacement of

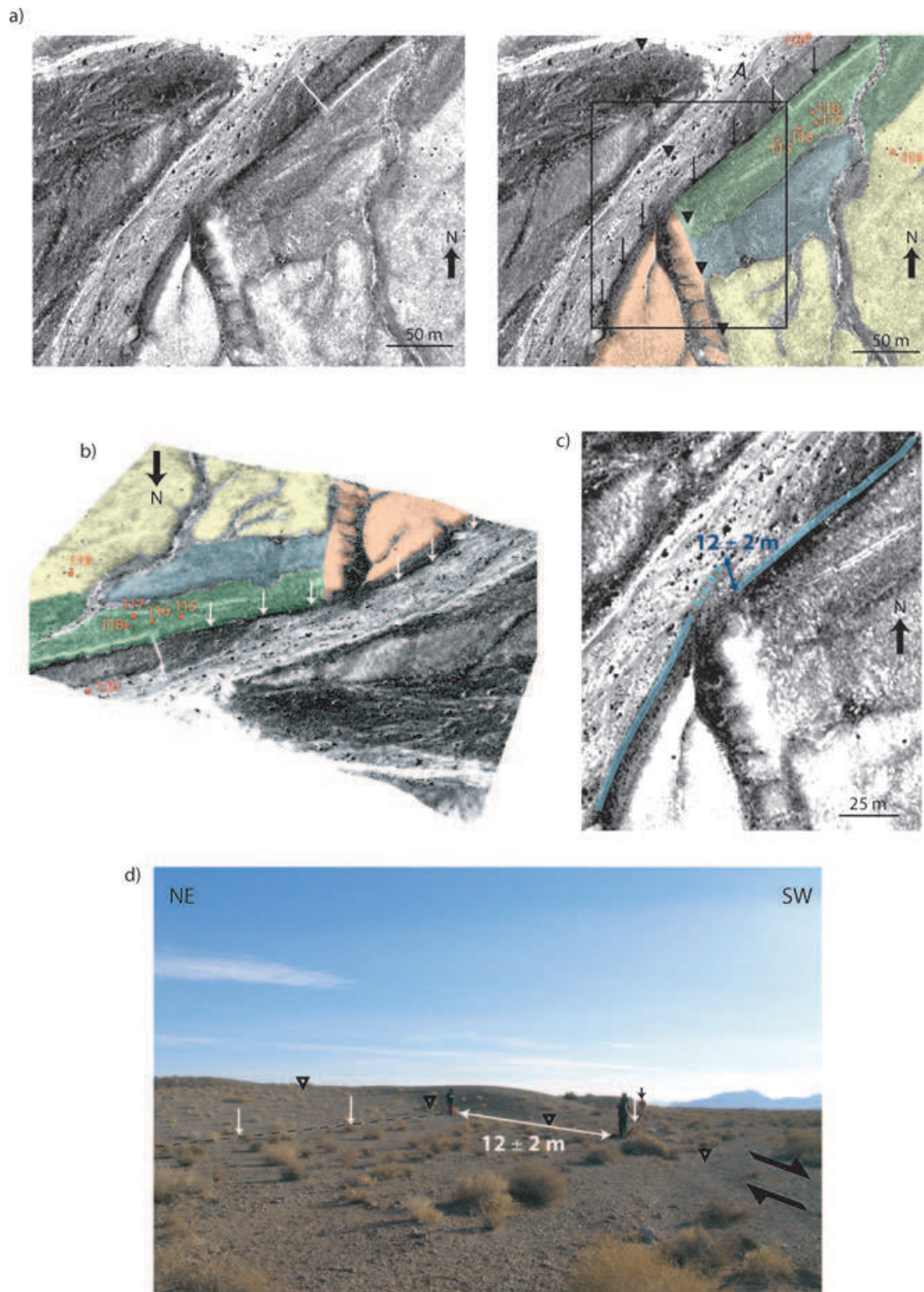


**Figure 5.** (a) Raw (left panel) and interpreted (right panel) images of the dextral offset of the recent riser (T1a/T0). Open triangles point to the fault trace and arrows to the foot of the riser. Rectangle denotes the enlargement on the offset-riser. (b) Quickbird image wrapped on the digital elevation model worked out from a DGPS survey. (c) Enlargement on the  $12 \pm 2$  m offset riser (T1a/T0 downstream, T3/T0 upstream). The blue line denotes the base of the riser. (d) Field photograph of the offset riser with vertical arrows pointing to the foot of the riser.

the terrace T1 with which they merge downstream, and the gullies, according to weighted mean OSL dating in a trench within the fault zone, are supposed to be younger than  $21.1 \pm 11.2$  ka (Nazari *et al.* 2009). There is also an offset of the right bank of the main river flood channel (Fig. 5). Upstream, the most recent riser cut (T3/T0) stands

between T3 tread and the riverbed. Downstream, T1 is protected from erosion because of the right-lateral motion of the fault and the most recent riser stands between T1 tread and the riverbed (T1a/T0). The riser that post-dates the terrace T1a is offset by  $12 \pm 2$  m (Fig. 5).

### 3 CHRONOLOGY OF THE REGIONAL FANS

The dating of the alluvial surfaces and inset terraces at both sites is required to establish the chronology of the fans and constrain the age of the offset-risers. Two complementary dating methods, CRE and OSL, have been performed to estimate the age of abandonment of alluvial surfaces. OSL relies on natural background radioactivity of the material with a small contribution of cosmogenic radiation and measures the time elapsed since the last sunlight exposure of a sediment layer. CRE provides the time of exposure of superficial material to cosmic rays.

#### 3.1 Sampling strategy and analytical procedures for cosmogenic and OSL dating

All the terraces (T0, T1, T2 and T3) were sampled at each site for cosmogenic dating.

For some surfaces (T3 at sites Dehshir North and Dehshir South, T2 at site Dehshir South) and taking advantage of the occurrence of polygenic cobbles, both the  $^{10}\text{Be}$  and  $^{36}\text{Cl}$  cosmogenic nuclides dating techniques have been applied. We measured the concentrations of *in situ* produced  $^{10}\text{Be}$  and  $^{36}\text{Cl}$  accumulated, respectively, in quartz-rich and carbonates samples exposed to cosmic rays. Surface samples were collected to estimate the CRE ages (Table 1). Most of the surface samples, 67 over the 73 collected, consist of individual cobbles, four correspond to two fragments of the same gelifRACTED cobbles, and two only are amalgams of many (about 25) pieces of small pebbles. Near-surface samples were also collected along three profiles to estimate the inheritance, that is, the concentrations of cosmogenic nuclides accumulated in the cobbles prior to their deposition. Each near-surface sample is an amalgam of pebbles or fragments of cobbles collected at the same depth. Provided that the sediment emplaced in a short period of time and that the pre-exposure is homogeneous, the exponential decrease of concentrations with depth provides an estimate of the homogeneous inheritance (e.g. Anderson *et al.* 1996; Repka *et al.* 1997). The inherited concentration is determined from the asymptotic value that the profile tends to at depth, and a chi-square inversion is often used to minimize the differences between measured and modelled concentrations (e.g. Siame *et al.* 2004; Braucher *et al.* 2009). Collecting pebbles from the active streambed also helps to estimate the inherited component (e.g. Brown *et al.* 1998). However, this method relies on the questionable assumption that the pre-depositional history of the pebbles collected in the present-day streambed is comparable to that of the pebbles collected on abandoned fan surfaces during aggradation stages.

Three main types of secondary particles are involved in the *in situ* production of  $^{10}\text{Be}$ : fast nucleons (essentially neutrons), stopping (or negative) muons and fast muons. Each of them has its own effective attenuation length. We used in this paper the same parameters as Heisinger *et al.* (2002) and Braucher *et al.* (2003) for the muonic attenuation lengths that are  $1500\text{ g cm}^{-2}$  for stopping muons and  $5300\text{ g cm}^{-2}$  for fast muons. For fast neutron, an attenuation length of  $160\text{ g cm}^{-2}$  (Gosse & Phillips 2001) is used. Samples were prepared at the CEREGE laboratory in Aix-en-Provence for  $^{10}\text{Be}$  concentration measurements following chemical procedures adapted from Brown *et al.* (1991) and Merchel & Herpers (1999). After addition in each sample of  $\sim 100\ \mu\text{l}$  of an in-house  $3.10^{-3}\text{ g g}^{-1}$  ( $^9\text{Be}$ ) carrier solution is prepared from deep-mined phenakite (Merschel *et al.* 2008), all  $^{10}\text{Be}$  concentrations were normalized to  $^{10}\text{Be}/^9\text{Be}$  SRM 4325 NIST standard with an assigned

value of  $(2.79 \pm 0.03) 10^{-11}$ . This standardization is equivalent to 07KNSTD within rounding error. All  $^{10}\text{Be}$  data reported in this study (Table 1) have been measured at ASTER (CEREGE, Aix-en-Provence). Analytical uncertainties (reported as  $1\sigma$ ) include uncertainties associated with accelerator mass spectrometry (AMS) counting statistics, AMS external error (0.5 per cent) and chemical blank measurement. Long-term measurements of chemically processed blank yield ratios on the order of  $(3.0 \pm 1.5) 10^{-15}$  (Arnold *et al.* 2010). Cosmocalc add-in for excel (Vermeesch 2007) has been used to calculate sample scaling and standard atmospheric pressures. Stone (2000) polynomial has been used to determine surficial production rate assuming a Sea Level High Latitude (SLHL) production rate of  $4.49\text{ at g}^{-1}\text{ yr}^{-1}$  for  $^{10}\text{Be}$ .

$^{36}\text{Cl}$  can be produced by two mechanisms in superficial rocks, cosmic ray interactions (spallation reactions of Ca, K, Ti and Fe, capture of low-energy epithermal and thermal neutrons by  $^{35}\text{Cl}$  and direct capture of slow negative muons by K and Ca) and radiogenic production by disintegration of U and Th. To determine the proportion of radiogenic  $^{36}\text{Cl}$  requires measuring the concentrations of U and Th in the target mineral (Zreda *et al.* 1991; Stone *et al.* 1996, 1998; Gosse & Phillips 2001; Schimmelpfennig *et al.* 2009). Major elemental compositions of rock samples were determined by the Inductively Coupled Plasma – Optical Emission Spectrometry technique by the Centre National de la Recherche Scientifique (CNRS) service for rocks and minerals analysis at Centre de Recherches Pétrographiques et Géochimiques (CRPG) Nancy. For the  $^{36}\text{Cl}$  measurements, the chemical extraction of chlorine by precipitation of silver chloride has been adapted from the protocol of Stone *et al.* (1996). The samples were spiked with a known quantity of stable chlorine carrier (e.g. Desilets *et al.* 2006) to simultaneously determine  $^{36}\text{Cl}$  and chlorine concentrations by isotope dilution AMS. The chemical treatment of the samples was carried out at the CEREGE laboratory in Aix-en-Provence and the measurements were performed at the Lawrence Livermore National Laboratory, using KNSTD1600 standard. The excel spreadsheet provided by Schimmelpfennig *et al.* (2009) was used to calculate all  $^{36}\text{Cl}$  production rates and to model  $^{36}\text{Cl}$  data. Accordingly, a surface spallation rate of  $48.8 \pm 3.4\text{ at g}^{-1}(\text{Ca})\text{ yr}^{-1}$  (Stone *et al.* 1996) is used. However, we use a neutron attenuation length of  $160\text{ g cm}^{-2}$  (Gosse & Phillips 2001) instead of  $177\text{ g cm}^{-2}$  (Farber *et al.* 2008) to be self-consistent with the  $^{10}\text{Be}$  model age calculations. The concentrations of *in situ* produced  $^{10}\text{Be}$  and  $^{36}\text{Cl}$  are given in Table 1 and the chemical composition of the carbonate samples in Table 2.

OSL was used to date the alluvial layers emplaced during the aggradation of the fans. Lenses of fine sandy-silts intercalated between conglomerates at various depths below the surface were sampled for OSL in opaque tubes. The Single Aliquot Regeneration (SAR) protocol (e.g. Murray & Wintle 2000) was employed for the Equivalent dose ( $D_e$ ) measurement once quartz had been extracted and cleaned from each sample. The analytical procedures employed are identical to that applied to similar samples from the neighbouring Anar, Sabzevar and Doruneh areas (Fattahi *et al.* 2006; 2007; Le Dortz *et al.* 2009).

Initial attempts to use single grains for  $D_e$  determination failed due to the dimness of OSL signal. As a result  $D_e$  measurements were undertaken on 9.6 mm diameter aliquots containing approximately 1500–2000 grains. Although normally this might result in averaging out of any multiple dose component within a sample, here it is assumed that for these dim samples the luminescence signal from each aliquot was produced by a relatively few number of bright grains and thus may be considered as almost measuring at single grain

**Table 1.** The  $^{10}\text{Be}$  and  $^{36}\text{Cl}$  nuclide concentrations and CRE modelled ages for surface and near-surface samples along the Dehshir fault. Propagated analytical uncertainties include error blank, carrier and counting statistics. Zero erosion model ages are calculated for surface samples with propagated analytical uncertainties, including error blank, carrier and counting statistics; corresponding geographic correction factors and without shielding in agreement with site topography.  $^{10}\text{Be}$  and  $^{36}\text{Cl}$  half-life are, respectively, 1.387 Ma (Chmeleff *et al.* 2010; Korschinek *et al.* 2010) and 301 ka (Gosse & Phillips 2001). For surface samples, a density of  $2.2\text{ g cm}^{-3}$  and  $2\text{ g cm}^{-3}$  have been used for quartz and carbonates samples, respectively. An attenuation length of  $160\text{ g cm}^{-2}$  (Gosse & Phillips 2001) has been used. Stone (2000) polynomial has been used to determine surficial production rate assuming a SLHL production rate of  $4.49\text{ at g}^{-1}\text{ yr}^{-1}$  for  $^{10}\text{Be}$  with 6 per cent of uncertainty. The  $^{36}\text{Cl}$  production rate of  $48.8 \pm 3.4\text{ at g}^{-1}\text{ yr}^{-1}$  is from Stone *et al.* (1996).  $^{10}\text{Be}$  ages have been calculated using Cosmocalc (Vermeesch 2007).  $^{36}\text{Cl}$  ages have been calculated using Excel spreadsheet of Schimmelpennig *et al.* (2009). N.M means no or incoherent measure. Maximum erosion rates have been calculated for the surface cobbles collected on T3 tread, with an infinite time of exposure hence at the steady-state equilibrium. About 20–30 pebbles with centimetre size have been generally collected for the amalgamated samples of the profiles. For the T2/T0 riser profile, the amalgams are made of a dozen of larger cobbles.

Samples	Sample description	Density ( $\text{g cm}^{-3}$ )	Thickness (cm)	Latitude ( $^{\circ}\text{N}$ )	Longitude ( $^{\circ}\text{E}$ )	Elevation (m)	$^{10}\text{Be}$			$^{36}\text{Cl}$				
							Stone scaling factor	Measured $^{10}\text{Be}$ ( $10^5\text{ at g}^{-1}\text{ SiO}_2$ )	$^{10}\text{Be}$ model age (ka) no erosion	maximum erosion rate ( $\text{m Ma}^{-1}$ )	$^{36}\text{Cl}$ Cl (ppm)	Measured $^{36}\text{Cl}$ ( $10^7\text{ at g}^{-1}\text{ rock}$ )	$^{36}\text{Cl}$ model age (ka) no erosion	maximum erosion rate ( $\text{m Ma}^{-1}$ )
Dehshir North	–	–	–	–	–	–	–	–	–	–	–	–	–	–
T0	–	–	–	–	–	–	–	–	–	–	–	–	–	–
DN06S30	Cobble (15 cm) in the river bed	2.2	6	30.6457	54.0236	1539	2.64	$9.23 \pm 0.22$	$79.42 \pm 5.14$	8.98	–	–	–	–
DN08S120	Cobble (10 cm) in the river bed	2.2	8	30.64414	54.02172	1548	2.65	$27.16 \pm 0.71$	$241.55 \pm 15.80$	3.16	–	–	–	–
DN08S121	Cobble (15 cm) in the river bed	2.2	7	30.64111	54.01947	1547	2.65	$7.18 \pm 0.19$	$61.15 \pm 4.03$	14.30	–	–	–	–
DN06S29	Cobble (15 cm) in the river bed	2	7	30.64571	54.02366	1539	–	–	–	–	52	$0.32 \pm 0.005$	$56.40 \pm 5.16$	17.16
T1	–	–	–	–	–	–	–	–	–	–	–	–	–	–
DN08S115	Cobble (10 cm)	2.2	6	30.64343	54.02151	1550	2.66	$43.06 \pm 1.17$	$397.28 \pm 26.16$	1.79	–	–	–	–
DN08S116	Cobble (10 cm)	2.2	6	30.64351	54.02167	1549	2.65	$10.30 \pm 0.28$	$88.19 \pm 5.81$	9.62	–	–	–	–
DN08S117	Cobble (10 cm)	2.2	7	30.64355	54.0218	1550	2.66	$14.42 \pm 0.39$	$124.44 \pm 8.19$	6.60	–	–	–	–
DN08S118	Cobble (15 cm)	2.2	6	30.64362	54.02177	1549	2.65	$14.55 \pm 0.39$	$125.69 \pm 8.26$	6.53	–	–	–	–
T2	–	–	–	–	–	–	–	–	–	–	–	–	–	–
DN08A119	Amalgam (25 pluricentimetric clasts)	2.2	–	30.64337	54.02239	1550	2.66	$43.97 \pm 1.11$	$406.54 \pm 26.47$	1.74	–	–	–	–
T3	–	–	–	–	–	–	–	–	–	–	–	–	–	–
DN06S1	Cobble (10 cm)	2.2	3	30.64068	54.01913	1550	2.72	N.M	–	–	–	–	–	–
DN06S2	2 fragments of the same gelyfracted cobble	2.2	3	30.64065	54.01907	1550	2.66	$26.55 \pm 3.66$	$235.55 \pm 35.38$	2.91	–	–	–	–
DN06S6	Cobble (10 cm)	2.2	5	30.640361	54.021083	1550	2.66	$51.88 \pm 0.72$	$489.51 \pm 30.15$	1.31	–	–	–	–
DN06S7	Cobble (15 cm)	2.2	4	30.64045	54.02092	1550	2.66	$48.78 \pm 1.19$	$456.66 \pm 29.58$	1.42	–	–	–	–
DN06S10	Cobble (10 cm)	2.2	5	30.6405	54.020917	1550	2.66	$49.21 \pm 0.69$	$461.15 \pm 28.42$	1.40	–	–	–	–
DN06A11	Amalgam (20 pluricentimetric clasts)	2.2	–	30.6405	54.020917	1550	2.66	$48.37 \pm 0.66$	$452.25 \pm 27.83$	1.43	–	–	–	–
DN06S19	Cobble (10 cm)	2.2	4	30.64208	54.02502	1550	2.66	$46.84 \pm 0.65$	$436.33 \pm 26.88$	1.49	–	–	–	–
DN06S21	Cobble (10 cm)	2.2	4	30.64189	54.02503	1550	2.66	$54.60 \pm 0.75$	$518.71 \pm 31.93$	1.23	–	–	–	–
DN06S23	Cobble (10 cm)	2.2	7	30.64177	54.0251	1550	2.66	$50.72 \pm 2.12$	$477.09 \pm 34.88$	1.35	–	–	–	–

**Table 1.** (Continued.)

Samples	Sample description	Density (g cm <sup>-3</sup> )	Thickness (cm)	Latitude (°N)	Longitude (°E)	Elevation (m)	<sup>10</sup> Be Stone scaling factor	Measured <sup>10</sup> Be (10 <sup>5</sup> at g <sup>-1</sup> SiO <sub>2</sub> )	<sup>10</sup> Be model age (ka) no erosion	<sup>10</sup> Be maximum erosion rate (m Ma <sup>-1</sup> )	<sup>36</sup> Cl Cl (ppm)	Measured <sup>36</sup> Cl (10 <sup>7</sup> at g <sup>-1</sup> rock)	<sup>36</sup> Cl model age (ka) no erosion	<sup>36</sup> Cl maximum erosion rate (m Ma <sup>-1</sup> )
DN06S26	Cobble (10 cm)	2.2	8	30.64101	54.02506	1550	2.66	46.99 ± 1.02	437.88 ± 27.94	1.49	–	–	–	–
DN06S28	Cobble (20 cm)	2.2	9	30.64038	54.02512	1550	2.66	45.92 ± 0.99	426.74 ± 27.23	1.53	–	–	–	–
DN06S3	Cobble (10 cm)	2	8	30.640417	54.021222	1554	–	–	–	–	16	1.21 ± 0.011	291.88 ± 37.60	1.80
DN06S4	Cobble (10 cm)	2	5	30.640333	54.021083	1556	–	–	–	–	18	1.18 ± 0.014	268.43 ± 33.33	2.10
DNS06S5	2 fragments of the same gelyfracted cobble	2	4	30.640333	54.021083	1556	–	–	–	–	26	N.M	–	–
DNS06S8	Cobble (15 cm)	2	3	30.640389	54.021055	1555	–	–	–	–	28	N.M	–	–
DNS06S9	Cobble (10 cm)	2	5	30.640361	54.020972	1552	–	–	–	–	13	1.30 ± 0.018	351.98 ± 48.07	1.33
DN06S20	Cobble (10 cm)	2	5	30.64208	54.02504	1550	–	–	–	–	24	1.36 ± 0.013	345.97 ± 45.90	1.48
DN06S22	Cobble (10 cm)	2	3	30.64189	54.0251	1550	–	–	–	–	19	1.25 ± 0.019	297.22 ± 37.59	1.79
DN06S24	Cobble (10 cm)	2	3	30.64129	54.02508	1549	–	–	–	–	18	1.31 ± 0.014	307.95 ± 39.30	1.68
DN06S25	Cobble (10 cm)	2	3	30.64108	54.02507	1550	–	–	–	–	40	1.53 ± 0.024	383.59 ± 53.46	1.40
DN06S27	Cobble (10 cm)	2	4	30.64099	54.02521	1550	–	–	–	–	38	1.41 ± 0.02	354.70 ± 47.24	1.57
Dehshir South T0	–	–	–	–	–	–	–	–	–	–	–	–	–	–
DS06S64	Cobble (15 cm) in the river bed	2.2	7	30.44864	54.12418	1620	2.77	7.11 ± 0.15	57.78 ± 3.68	12.41	–	–	–	–
DS08S109	Cobble (15 cm) in the river bed	2.2	5	30.44742	54.11986	1626	2.79	7.63 ± 0.21	61.83 ± 4.08	14.13	–	–	–	–
DS08S110	Cobble (15 cm) in the river bed	2.2	6	30.44926	54.13	1613	2.76	10.97 ± 0.29	90.34 ± 5.94	9.37	–	–	–	–
DS06S62	Cobble (10 cm) in the river bed	2	4	30.44866	54.12527	1615	–	–	–	–	60	0.45 ± 0.007	72.83 ± 6.82	12.94
DN06S63	Cobble (10 cm) in the river bed	2	5	30.44881	54.12454	1615	–	–	–	–	52	0.40 ± 0.012	65.04 ± 6.54	14.45
T1	–	–	–	–	–	–	–	–	–	–	–	–	–	–
DS08S122	Cobble (10 cm)	2.2	4	30.44743	54.12096	1626	2.79	34.77 ± 0.93	298.60 ± 19.60	2.48	–	–	–	–
DS08S123	Cobble (15 cm)	2.2	7	30.44741	54.12083	1626	2.79	19.96 ± 0.52	165.94 ± 10.87	4.80	–	–	–	–
DS08S124	Cobble (10 cm)	2.2	6	30.44716	54.12017	1627	2.79	3.99 ± 0.11	32.07 ± 2.12	28.42	–	–	–	–
DS08S125	Cobble (15 cm)	2.2	6	30.44695	54.11975	1627	2.79	16.28 ± 0.44	134.22 ± 8.83	6.07	–	–	–	–
T2	–	–	–	–	–	–	–	–	–	–	–	–	–	–
DS06S31	Cobble (10 cm)	2.2	4	30.4476	54.12655	1622	2.78	N.M	–	–	–	–	–	–
DS06S32	Cobble (10 cm)	2.2	5	30.4476	54.12655	1622	2.78	21.01 ± 0.52	175.57 ± 11.39	3.96	–	–	–	–
DS06S34	Cobble (20 cm)	2.2	6	30.44765	54.12751	1619	2.77	21.95 ± 0.32	184.19 ± 11.38	3.77	–	–	–	–
DS06S36	Cobble (20 cm)	2.2	6	30.447	54.1284	1620	2.77	15.08 ± 0.24	124.58 ± 7.73	5.66	–	–	–	–
DS06S40	Cobble (10 cm)	2.2	5	30.44663	54.12945	1620	2.77	N.M	–	–	–	–	–	–
DS08S111	Cobble (10 cm)	2.2	6	30.44792	54.13517	1612	2.76	18.52 ± 0.49	154.99 ± 10.15	5.18	–	–	–	–
DS08S112	Cobble (10 cm)	2.2	7	30.44793	54.13371	1615	2.76	22.12 ± 0.60	186.22 ± 12.26	4.22	–	–	–	–
DS08S113	Cobble (10 cm)	2.2	7	30.44708	54.13213	1618	2.77	26.61 ± 0.68	225.76 ± 14.73	3.41	–	–	–	–

**Table 1.** (Continued.)

Samples	Sample description	Density (g cm <sup>-3</sup> )	Thickness (cm)	Latitude (°N)	Longitude (°E)	Elevation (m)	<sup>10</sup> Be Stone scaling factor	Measured <sup>10</sup> Be (10 <sup>5</sup> at g <sup>-1</sup> SiO <sub>2</sub> )	<sup>10</sup> Be model age (ka) no erosion	<sup>10</sup> Be maximum erosion rate (m Ma <sup>-1</sup> )	<sup>36</sup> Cl Cl (ppm)	Measured <sup>36</sup> Cl (10 <sup>7</sup> at g <sup>-1</sup> rock)	<sup>36</sup> Cl model age (ka) no erosion	<sup>36</sup> Cl maximum erosion rate (m Ma <sup>-1</sup> )
DS08S114	Cobble (10 cm)	2.2	6	30.44803	54.13074	1623	2.78	6.16 ± 0.17	49.87 ± 3.29	17.80	–	–	–	–
DS06S33	Cobble (15 cm)	2	7	30.44759	54.1265	1620	–	–	–	–	24	0.97 ± 0.009	190.26 ± 20.80	3.38
DS06S35	Cobble (20 cm)	2	5	30.44764	54.12754	1621	–	–	–	–	52	0.76 ± 0.009	135.85 ± 13.57	6.01
DS06S37	Cobble (10 cm)	2	4	30.44695	54.1284	1620	–	–	–	–	23	0.87 ± 0.009	170.02 ± 18.11	3.92
DS06S38	Cobble (10 cm)	2	4	30.44669	54.12885	1615	–	–	–	–	43	0.67 ± 0.098	123.50 ± 12.49	6.50
DS06S39	Cobble (10 cm)	2	4	30.44663	54.12946	1620	–	–	–	–	11	0.57 ± 0.009	104.41 ± 10.51	6.89
T3	–	–	–	–	–	–	–	–	–	–	–	–	–	–
DS06S41	2 fragments of the same gelyfracted cobble	2.2	6	30.4408	54.11883	1632	2.80	52.28 ± 0.75	465.68 ± 28.72	1.39	–	–	–	–
DS06S44	Cobble (15 cm)	2.2	8	30.43993	54.11873	1636	2.80	57.81 ± 0.81	520.28 ± 32.06	1.22	–	–	–	–
DS06S45	Cobble (15 cm)	2.2	5	30.43552	54.12536	1632	2.80	52.76 ± 0.84	470.58 ± 29.21	1.37	–	–	–	–
DS06S48	Cobble (15 cm)	2.2	8	30.43532	54.12533	1630	2.79	N.M	–	–	–	–	–	–
DS06S49	Cobble (20 cm)	2.2	9	30.43518	54.1263	1630	2.79	N.M	–	–	–	–	–	–
DS06S51	2 fragments of the same gelyfracted cobble	2.2	6	30.43475	54.13594	1620	2.77	N.M	–	–	–	–	–	–
DS06S53	Cobble (10 cm)	2.2	5	30.43517	54.13687	1623	2.78	49.22 ± 0.66	438.32 ± 26.95	1.48	–	–	–	–
DS06S54	Cobble (15 cm)	2.2	6	30.43521	54.13694	1618	2.77	N.M	–	–	–	–	–	–
DS06S56	Cobble (10 cm)	2.2	8	30.4369	54.138	1620	2.77	63.71 ± 0.90	589.48 ± 36.34	1.06	–	–	–	–
DS06S60	Cobble (15 cm)	2.2	7	30.43971	54.13797	1620	2.77	45.77 ± 0.65	405.18 ± 24.98	1.62	–	–	–	–
DS06S42	1 fragment of a gelyfracted Cobble (15 cm)	2	5	30.4407	54.11863	1630	–	–	–	–	17	1.51 ± 0.022	384.20 ± 54.50	1.19
DS06S43	Cobble (15 cm)	2	4	30.44082	54.11877	1632	–	–	–	–	17	1.55 ± 0.015	396.25 ± 56.62	1.13
DS06S46	Cobble (10 cm)	2	3	30.43548	54.12536	1630	–	–	–	–	14	1.54 ± 0.014	371.29 ± 52.05	1.21
DS06S47	Cobble (15 cm)	2	6	30.43538	54.12553	1630	–	–	–	–	26	1.46 ± 0.034	361.52 ± 50.52	1.40
DS06S50	Cobble (15 cm)	2	4	30.4351	54.12631	1631	–	–	–	–	18	1.45 ± 0.016	363.29 ± 49.85	1.03
DS06S52	Cobble (10 cm)	2	4	30.43482	54.13612	1625	–	–	–	–	16	1.24 ± 0.014	287.11 ± 35.74	1.84
DS06S55	Cobble (15 cm)	2	5	30.43515	54.13692	1626	–	–	–	–	17	1.27 ± 0.020	294.57 ± 37.25	1.79
DS06S57	Cobble (10 cm)	2	5	30.43708	54.13814	1627	–	–	–	–	10	1.44 ± 0.013	352.98 ± 48.02	1.29
DS06S58	Cobble (15 cm)	2	8	30.43708	54.13814	1627	–	–	–	–	10	1.19 ± 0.023	271.00 ± 33.83	1.92
DS06S59	Cobble (10 cm)	2	6	30.43941	54.13816	1625	–	–	–	–	8	1.41 ± 0.011	362.38 ± 49.94	1.22
Dehshir North <sup>10</sup> Be														
Pit in the surface T3														
PN	–	–	–	–	–	1550	–	–	–	–	–	–	–	–
DN06P12Q	Amalgam 25 cm below ground surface	2.2	–	30.64114	54.02133	–	2.66	33.77 ± 0.85	–	–	–	–	–	–

Table 1. (Continued.)

Samples	Sample description	Density (g cm <sup>-3</sup> )	Thickness (cm)	Latitude (°N)	Longitude (°E)	Elevation (m)	<sup>10</sup> Be Stone scaling factor	Measured <sup>10</sup> Be (10 <sup>5</sup> at g <sup>-1</sup> SiO <sub>2</sub> )	<sup>10</sup> Be model age (ka) no erosion	<sup>10</sup> Be maximum erosion rate (m Ma <sup>-1</sup> )	<sup>36</sup> Cl Cl (ppm)	Measured <sup>36</sup> Cl (10 <sup>7</sup> at g <sup>-1</sup> rock)	<sup>36</sup> Cl model age (ka) no erosion	<sup>36</sup> Cl maximum erosion rate (m Ma <sup>-1</sup> )
DN06P13Q	Amalgam 55 cm below ground surface	2.2	–	30.64114	54.02133	–	2.66	25.80 ± 0.66	–	–	–	–	–	–
DN06P14Q	Amalgam 95 cm below ground surface	2.2	–	30.64114	54.02133	–	2.66	22.12 ± 0.45	–	–	–	–	–	–
DN06P15Q	Amalgam 165 cm below ground surface	2.2	–	30.64114	54.02133	–	2.66	13.60 ± 0.34	–	–	–	–	–	–
DN06P16Q	Amalgam 230 cm below ground surface	2.2	–	30.64114	54.02133	–	2.66	6.89 ± 0.17	–	–	–	–	–	–
DN06P17Q	Amalgam 270 cm below ground surface	2.2	–	30.64114	54.02133	–	2.66	4.37 ± 0.07	–	–	–	–	–	–
DN06P18Q	Amalgam 305 cm below ground surface	2.2	–	30.64114	54.02133	–	2.66	9.68 ± 0.24	–	–	–	–	–	–
Dehshir North <sup>36</sup> Cl Pit in the surface T3	–	–	–	–	–	1550	–	–	–	–	–	–	–	–
DN06P12C	Amalgam 25 cm below ground surface	2.2	–	30.64114	54.02133	–	–	–	–	–	29	1.78 ± 0.018	–	–
DN06P13C	Amalgam 55 cm below ground surface	2.2	–	30.64114	54.02133	–	–	–	–	–	32	1.30 ± 0.015	–	–
DN06P14C	Amalgam 95 cm below ground surface	2.2	–	30.64114	54.02133	–	–	–	–	–	20	1.10 ± 0.011	–	–
DN06P15C	Amalgam 165 cm below ground surface	2.2	–	30.64114	54.02133	–	–	–	–	–	38	0.63 ± 0.024	–	–
DN06P16C	Amalgam 230 cm below ground surface	2.2	–	30.64114	54.02133	–	–	–	–	–	26	0.34 ± 0.007	–	–
DN06P18C	Amalgam 305 cm below ground surface	2.2	–	30.64114	54.02133	–	–	–	–	–	22	0.18 ± 0.004	–	–
Dehshir South <sup>10</sup> Be Riser T2/T0 PS1	–	–	–	–	–	1645	–	–	–	–	–	–	–	–
DS08P126	Amalgam 30 cm below ground surface	2.2	–	30.44823	54.12648	–	2.82	11.23 ± 0.30	–	–	–	–	–	–

**Table 1.** (Continued.)

Samples	Sample description	Density (g cm <sup>-3</sup> )	Thickness (cm)	Latitude (°N)	Longitude (°E)	Elevation (m)	<sup>10</sup> Be Stone scaling factor	Measured <sup>10</sup> Be (10 <sup>5</sup> at g <sup>-1</sup> SiO <sub>2</sub> )	<sup>10</sup> Be model age (ka) no erosion	<sup>10</sup> Be maximum erosion rate (m Ma <sup>-1</sup> )	<sup>36</sup> Cl Cl (ppm)	Measured <sup>36</sup> Cl (10 <sup>7</sup> at g <sup>-1</sup> rock)	<sup>36</sup> Cl model age (ka) no erosion	<sup>36</sup> Cl maximum erosion rate (m Ma <sup>-1</sup> )
DS08P127	Amalgam 60 cm below ground surface	2.2	–	30.44823	54.12648	–	2.82	6.10 ± 0.17	–	–	–	–	–	–
DS08P128	Amalgam 100 cm below ground surface	2.2	–	30.44823	54.12648	–	2.82	5.82 ± 0.16	–	–	–	–	–	–
DS08P129	Amalgam 150 cm below ground surface	2.2	–	30.44823	54.12648	–	2.82	5.91 ± 0.16	–	–	–	–	–	–
DS08P130	Amalgam 210 cm below ground surface	2.2	–	30.44823	54.12648	–	2.82	8.86 ± 0.24	–	–	–	–	–	–
DS08P131	Amalgam 270 cm below ground surface	2.2	–	30.44823	54.12648	–	2.82	3.62 ± 0.10	–	–	–	–	–	–
DS08P132	Amalgam 370 cm below ground surface	2.2	–	30.44823	54.12648	–	2.82	4.31 ± 0.12	–	–	–	–	–	–
Pit in the surface T2														
PS2	–	–	–	–	–	1628								
DS06P65	Amalgam 20 cm below ground surface	2.2	–	30.45705	54.11839	–	2.79	16.67 ± 0.24	–	–	–	–	–	–
DS06P66	Amalgam 50 cm below ground surface	2.2	–	30.45705	54.11839	–	2.79	30.80 ± 0.60	–	–	–	–	–	–
DS06P67	Amalgam 80 cm below ground surface	2.2	–	30.45705	54.11839	–	2.79	N.M	–	–	–	–	–	–
DS06P68	Amalgam 155 cm below ground surface	2.2	–	30.45705	54.11839	–	2.79	12.72 ± 0.33	–	–	–	–	–	–
DS06P69	Amalgam 200 cm below ground surface	2.2	–	30.45705	54.11839	–	2.79	10.33 ± 0.25	–	–	–	–	–	–
DS06P70	Amalgam 280 cm below ground surface	2.2	–	30.45705	54.11839	–	2.79	6.51 ± 1.17	–	–	–	–	–	–
DS06P71	Amalgam 300 cm below ground surface	2.2	–	30.45705	54.11839	–	2.79	2.32 ± 0.10	–	–	–	–	–	–

**Table 2.** Mean chemical composition of the samples collected for  $^{36}\text{Cl}$  dating. Measurements of the major elements were undertaken at the SARM facility (Nancy, France).

Samples	H <sub>2</sub> O (per cent)	Al <sub>2</sub> O <sub>3</sub> (per cent)	CaO (per cent)	Fe <sub>2</sub> O <sub>3</sub> (per cent)	K <sub>2</sub> O (per cent)	MgO (per cent)	MnO (per cent)	Na <sub>2</sub> O (per cent)	P <sub>2</sub> O <sub>5</sub> (per cent)	SiO <sub>2</sub> (per cent)	TiO <sub>2</sub> (per cent)	Th (per cent)	U (per cent)
DN06S3	0.30	0.04	54.38	0.15	0	0.59	0.01	0	0.02	0.11	0.00	0.020	0.763
DN06S4	0.35	0.15	53.85	0.08	0	0.90	0.02	0	0.02	0.21	0.01	0.113	2.740
DN06S5	0.29	0.09	54.39	0.10	0	0.68	0.01	0	0.02	0.11	0.00	0.064	1.295
DN06S8	0.22	0.07	54.92	0.08	0	0.57	0.01	0	0.02	0.00	0.01	0.058	0.382
DNS06S9	0.29	0.09	54.39	0.10	0	0.68	0.01	0	0.02	0.11	0.00	0.064	1.295
DN06P12C	0.41	0.40	52.75	0.33	0.09	0.92	0.02	0	0	1.99	0.03	0.309	1.164
DN06P13	0.41	0.40	52.75	0.33	0.09	0.92	0.02	0	0	1.99	0.03	0.309	1.164
DN06P14C	0.41	0.40	52.75	0.33	0.09	0.92	0.02	0	0	1.99	0.03	0.309	1.164
DN06P15C	0.41	0.40	52.75	0.33	0.09	0.92	0.02	0	0	1.99	0.03	0.309	1.164
DN06P16C	0.41	0.40	52.75	0.33	0.09	0.92	0.02	0	0	1.99	0.03	0.309	1.164
DN06P18C	0.41	0.40	52.75	0.33	0.09	0.92	0.02	0	0	1.99	0.03	0.309	1.164
DNO6S20	0.31	0.08	53.74	0.15	0	1.20	0.03	0	0	0.12	0.00	0.048	0.861
DN06S22	0.26	0.02	54.28	0.04	0	1.10	0.00	0	0	0.00	0.00	0.000	1.330
DNO6S24	0.31	0.08	53.74	0.15	0	1.20	0.03	0	0	0.12	0.00	0.048	0.861
DN06S25	0.36	0.14	53.20	0.26	0	1.31	0.05	0	0	0.24	0.01	0.095	0.392
DNO6S27	0.31	0.08	53.74	0.15	0	1.20	0.03	0	0	0.12	0.00	0.048	0.861
DNO6S29	0.31	0.08	53.74	0.15	0.00	1.20	0.03	0	0.00	0.12	0.00	0.048	0.861
DS06S33	0.245	0.022	54.39	0.06	0	0.652	0.0035	0	0.008	0	0	0.025	1.433
DS06S35	0.245	0.022	54.39	0.06	0	0.652	0.0035	0	0.008	0	0	0.025	1.433
DS06S37	0.245	0.022	54.39	0.06	0	0.652	0.0035	0	0.008	0	0	0.025	1.433
DS06S38	0.27	0.02	54.08	0.05	0	0.87	0.01	0	0.02	0.00	0.00	0.028	0.370
DS06S39	0.22	0.02	54.71	0.08	0	0.44	0.00	0	0.00	0.00	0.00	0.021	2.495
DS06S42	0.27	0.05	54.89	0	0	0.55	0	0	0	0	0.00	0.096	3.010
DSO6S43	0.27	0.05	54.89	0	0	0.55	0	0	0	0	0.00	0.096	3.010
DS06S46	0.27	0.05	54.89	0	0	0.55	0	0	0	0	0.00	0.096	3.010
DSO6S47	0.27	0.05	54.89	0	0	0.55	0	0	0	0	0.00	0.096	3.010
DS06S50	0.27	0.05	54.89	0	0	0.55	0	0	0	0	0.00	0.096	3.010
DNO6S52	0.28	0	54.60	0.12	0	0.38	0	0	0	0	0.00	0.020	2.995
DSO6S55	0.28	0	54.60	0.12	0	0.38	0	0	0	0	0.00	0.020	2.995
DS06S57	0.28	0	54.60	0.12	0	0.38	0	0	0	0	0.00	0.020	2.995
DSO6S58	0.28	0	54.60	0.12	0	0.38	0	0	0	0	0.00	0.020	2.995
DSO6S59	0.28	0	54.60	0.12	0	0.38	0	0	0	0	0.00	0.020	2.995
DS06S62	0.22	0.04	54.16	0.16	0.00	0.90	0.03	0.00	0.00	0.00	0.00	0.045	0.675
DS06S63	0.22	0.04	54.16	0.16	0.00	0.90	0.03	0.00	0.00	0.00	0.00	0.045	0.675

level. Therefore, the  $D_e$  distribution of the single aliquot  $D_e$  measurements is considered to be almost a true reflection of the actual  $D_e$  distribution within a sample. For some samples the depositional setting, field sedimentary logs and the scatter of the replicate aliquot  $D_e$  data indicated that prior to burial, full resetting (bleaching) of the OSL signal had not taken place and/or that the sediments had undergone some post-depositional disturbance (Bateman *et al.* 2007). As a result of this, Finite Mixture Model (FMM, Roberts *et al.* 2000) was used where samples showed skewed, scattered or multimodal distributions. We used the dominant FMM component for samples displaying multimodal  $D_e$  distributions and the lowest FMM component of  $D_e$  for samples whose  $D_e$  distributions were skewed (assuming partially bleached without significant bioturbation) samples (Bateman *et al.* 2007; Boulter *et al.* 2007). Where samples had a low overdispersion and unimodal, normally distributed  $D_e$ s then the Central Age Model (CAM, Galbraith *et al.* 1999)  $D_e$  was used for age calculation purposes. The relevant information for OSL ages are presented in Table 3 in years from present with  $1\sigma$  errors.

### 3.2 CRE ages

Fig. 6 displays the results for the site Dehshir North, and Fig. 7 for the site Dehshir South. The concentrations are given in Table 1 with the corresponding CRE ages modelled assuming erosion and inheritance are negligible.

#### 3.2.1 Surface T3

For T3, both the  $^{10}\text{Be}$  and  $^{36}\text{Cl}$  zero-erosion, zero-inheritance ages of surface samples are overall consistent and suggest that the terrace tread is old.

At Dehshir North (Fig. 6), the CRE ages range between 235 and 519 ka for the  $^{10}\text{Be}$  measurements, and between 268 and 383 ka for the  $^{36}\text{Cl}$  measurements. For the  $^{10}\text{Be}$  concentrations, all but one surface sample provide CRE ages greater than 400 ka. The younger  $^{10}\text{Be}$  exposure age (DN06S2,  $235.5 \pm 35.4$  ka) might be considered as an outlier and excluded from the statistics. Then, the weighted mean of the zero-erosion zero-inheritance  $^{10}\text{Be}$  model age of T3 is  $462 \pm 55$  ka while the  $^{36}\text{Cl}$  one is  $325 \pm 74$  ka (Fig. 6b).

At site Dehshir South (Fig. 7), the scattering of the concentrations is greater. The weighted means of the zero-erosion zero-inheritance  $^{10}\text{Be}$  and  $^{36}\text{Cl}$  ages are  $481 \pm 119$  and  $344 \pm 83$  ka, respectively (Fig. 7b). The results are nonetheless similar at both sites and confirm the qualitative inference of the synchronism of levels T3 drawn from the resemblance of their surface at distant sites on the Quickbird imagery. They indicate T3 is a rather old surface (several hundred thousand years old) and that  $^{36}\text{Cl}$  surface ages are a little younger than  $^{10}\text{Be}$  ages. The slight difference between the  $^{10}\text{Be}$  and  $^{36}\text{Cl}$  weighted mean ages may either result from a statistical bias due to the limited number of samples or be meaningful. The  $^{36}\text{Cl}$  half-life (301 ka, e.g. Gosse & Phillips 2001) being lower than that of  $^{10}\text{Be}$  ( $1.387 \pm 0.12$  Ma, Chmeleff *et al.* 2010; Korshinek *et al.* 2010) and T3 an old terrace, the difference may suggest the carbonates have reached the steady-state equilibrium for which the production of  $^{36}\text{Cl}$  is balanced by the loss due to radioactive decay and the loss due to erosion, if there is any.

Because there is a trade-off between denudation rate and exposure age, it is important to estimate the erosion. Assuming an infinite age for the emplacement of T3 allows estimating a maximum erosion rate for each of the surface samples, both for  $^{36}\text{Cl}$  and  $^{10}\text{Be}$  isotopes (Table 1). For the carbonates, none of the surface samples provides a  $^{36}\text{Cl}$  maximum denudation rate greater than  $2.1 \text{ m Ma}^{-1}$ , and the

averaged value is  $1.5 \text{ m Ma}^{-1}$ . Discarding the outlier DN06S2, the quartz surface samples indicate a  $^{10}\text{Be}$  maximum denudation rate smaller than  $1.6 \text{ m Ma}^{-1}$  with an averaged value of  $1.4 \text{ m Ma}^{-1}$ . This is further strengthened by modelling the depth-distribution of the  $^{36}\text{Cl}$  concentrations in the amalgamated carbonate samples collected along a 3 m depth profile excavated in T3 at the site Dehshir North (Fig. 8). The profile shows an overall exponential decrease of concentrations with depth allowing for modelling the erosion rate. The  $^{36}\text{Cl}$  concentration depth profile is modelled with assigning a surface age of 3 Ma; old enough to ascertain the equilibrium between production and disintegration has been reached. Letting the erosion rate and the inheritance free to vary, the profile is modelled for three density values (between 2 and  $2.4 \text{ g cm}^{-3}$ ) within the range of that measured for the samples of the profile (Fig. 8). For all the densities tested, the model converges towards zero inheritance solutions and low erosion rates. The solutions with zero inheritance are not surprising because the assigned surface age of 3 Ma makes a homogeneous inheritance of several tens of thousands of years ago undetectable. By contrast, the solutions with low maximum erosion rates are meaningful. The greatest erosion rate of  $1.90 \text{ m Ma}^{-1}$  is obtained for a density value of  $2 \text{ g cm}^{-3}$ . Smaller erosion rates of 1.48 and  $1.18 \text{ m Ma}^{-1}$  corresponding to densities of 2.2 and  $2.4 \text{ g cm}^{-3}$  are closer to the erosion rate calculated for each of the carbonate surface samples (Table 1).

Whatever the method applied (surface sample, near-surface samples and depth-profile modelling) and whatever the isotope considered, the estimates of the maximum erosion rate are very low. They are close to that found in hyperarid regions ( $<1 \text{ m Ma}^{-1}$ , Matmon *et al.* 2009) and in good agreement with the pristine morphology of the flat-topped surface of T3. The  $^{10}\text{Be}$  depth profile can be theoretically modelled with erosion rates ranging between 0 and  $1.4 \text{ m Ma}^{-1}$ , maximum erosion rate averaged from the  $^{10}\text{Be}$  surface samples. Accounting for the trade-off between erosion rate and exposure age (the higher the erosion rate, the older the exposure age), the  $^{10}\text{Be}$  depth profile has been modelled under the assumption of no erosion to minimize the exposure age. We hence tested a range of inheritance values to solve for the zero erosion exposure age (Fig. 9). The best fit is obtained for a surface age of 464 ka and a homogeneous inheritance of  $3.8 \cdot 10^5 \text{ g}^{-1}(\text{SiO}_2)$ . This inheritance, if acquired at the surface and prior to the emplacement of the terrace, would correspond to a period of pre-exposure of about 32 ka, small with respect to the exposure age. Accounting for the trade-off between inheritance and age, several other solutions remain acceptable (Fig. 9b). Assuming a homogeneous inherited concentration of  $7.6 \cdot 10^5 \text{ g}^{-1}(\text{SiO}_2)$ , twice that obtained for the best fit and close to the concentration measured for the deepest sample of the profile, provides an age of 327 ka. Hypothesizing zero inheritance yields an older age of 686 ka that does not match with the concentrations of surface samples, demonstrating the usefulness of combining both surface and near-surface sampling.

In summary, T3 is a rather old and well-preserved alluvial surface, in which cobbles have incorporated a poorly constrained inheritance of several tens of thousands of years. This amount of inheritance, though limited with respect to the CRE age of T3, contributes to the  $469 \pm 88$  ka weighted mean age of all the quartz cobbles collected on the terrace tread at sites Dehshir North and Dehshir South (Fig. 10).

#### 3.2.2 Surface T2

At Dehshir North, only one amalgam quartz-rich surface sample has been dated on T2 fan surface. The zero-erosion zero-inheritance

**Table 3.** Equivalent dose ( $D_e$ ), annual dose rate ( $D_a$ ) and calculated OSL ages for each sample. The weighted mean ages published in Nazari *et al.* (2009) have been refined following the statistical analysis used by Fattahi *et al.* (2010) to account for partial bleaching. Ages have been calculated for Quartz grains with size ranging between 90 and 150 microns.

Sample	Latitude (°N)	Longitude (°E)	Depth (m)	Water (per cent)	K (per cent)	U (per cent)	Th (per cent)	Equivalent dose CAM (Gy)	Equivalent dose FMM <sup>a</sup> (Gy)	Annual dose rate (Gy ka <sup>-1</sup> )	Age (ka)
Site Dehshir North											
Trench (alluviums coeval with T1 aggradation)											
HI/2006-VI	30.64121	54.02127	1.5	1.3	1.27 ± 0.01	2.04 ± 0.05	6.0 ± 0.1	48.8 ± 0.3	29.3 ± 2.0	2.43 ± 0.09	20.2 ± 0.8 <sup>b</sup>
HI/2008-VIII	30.64123	54.02148	0.95	0.9	0.66 ± 0.01	1.13 ± 0.05	4.6 ± 0.1	45.3 ± 7.1		1.45 ± 0.03	20.1 ± 1.6 <sup>c</sup>
HI/2006-I	30.64118	54.02131	1.2	0.9	1.22 ± 0.01	1.79 ± 0.05	6.0 ± 0.1	60.2 ± 0.28		2.29 ± 0.09	26.0 ± 1.0 <sup>b</sup>
Trench (alluviums coeval with T2 aggradation)											
HI/2008-VII	30.64123	54.02145	1.6	1.1	0.61 ± 0.01	1.1 ± 0.05	4.3 ± 0.1	62.0 ± 6.0	83.0 ± 7.3	1.36 ± 0.03	45.5 ± 4.6 <sup>b</sup>
HI/2008-IX	30.64123	54.02150	2.8	1.2	0.66 ± 0.01	1.12 ± 0.05	4.5 ± 0.1	83.0 ± 7.3		1.40 ± 0.03	60.0 ± 5.7 <sup>b</sup>
Site Dehshir South											
Riser T2/T0											
OSL I	30.44823	54.12632	0.8	1.1 ± 0.2	0.78 ± 0.01	1.52 ± 0.05	4.8 ± 0.1	46.5 ± 1.4	45.6 ± 7.7	1.73 ± 0.04	26.9 ± 1.3 <sup>b</sup>
OSL II	30.84823	54.12658	3.4	1.05 ± 0.2	0.85 ± 0.01	1.05 ± 0.05	4.2 ± 0.1	45.6 ± 7.7		1.55 ± 0.04	29.4 ± 5.1 <sup>b</sup>
Riser T1b/T0											
OSL III	30.44132	54.10805	2.64	0.35 ± 0.2	0.67 ± 0.01	0.95 ± 0.05	3.4 ± 0.1	28.9 ± 1.7	15.7 ± 0.8	1.32 ± 0.04	21.9 ± 1.5 <sup>b</sup>
Riser T1a/T0											
OSL IV	30.44116	54.10173	0.8	0.2 ± 0.2	0.71 ± 0.01	1.15 ± 0.05	5.0 ± 0.1	23.4 ± 2.6	15.7 ± 0.8	1.57 ± 0.04	10.0 ± 0.6 <sup>c</sup>
Pit in the surface T2											
AB/2006-I	30.45719	54.11822	0.9	1.1 ± 0.2	0.86 ± 0.01	1.78 ± 0.05	4.2 ± 0.1	73.3 ± 3.7	72.9 ± 3.8	1.83 ± 0.05	39.7 ± 2.6 <sup>c</sup>
AB/2006-II	30.45719	54.11831	0.7	1.1 ± 0.2	1.1 ± 0.01	1.64 ± 0.05	5.9 ± 0.1	57.4 ± 7.6	43.2 ± 2.3	2.16 ± 0.05	20.0 ± 1.3 <sup>c</sup>

<sup>a</sup>Finite Mixture Modelling (Roberts *et al.* 2000) of replicate  $D_e$  values only undertaken where  $D_e$  distributions were multimodal, skewed and/or scattered (see text for details).

<sup>b</sup>Age based on  $D_e$  determined using Central age Model (CAM; Galbraith *et al.* 1999).

<sup>c</sup>Age based on  $D_e$  determined using Finite mixture Modelling (FMM, Roberts *et al.* 2000).

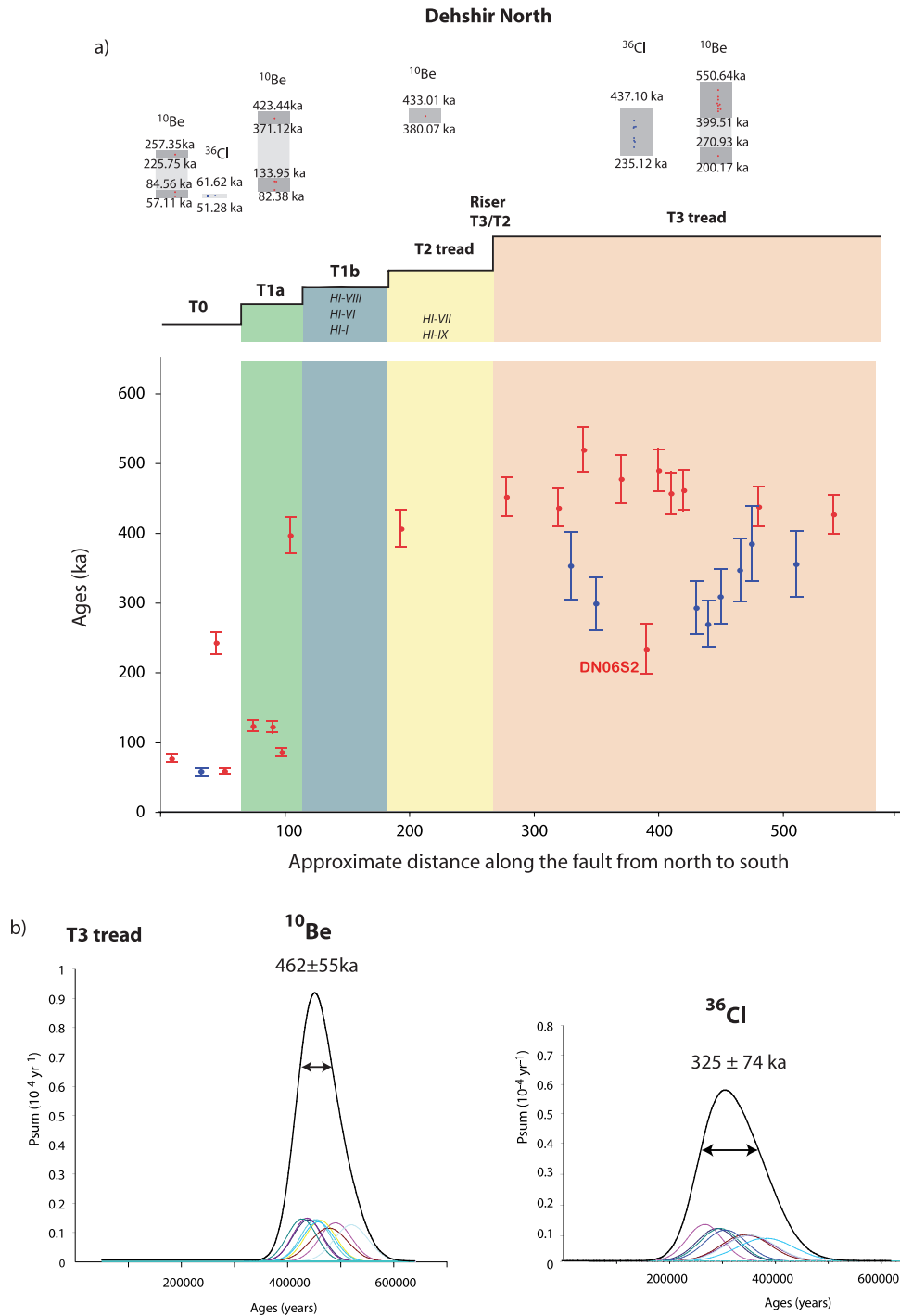


**Figure 6.** Summary of observations at site Dehshir North. (a)  $^{10}\text{Be}$  and  $^{36}\text{Cl}$  CRE ages of surface samples modelled without erosion and without inheritance are indicated by red and blue dots above each surface. The shaded columns extend from the minimum age to the maximum age given by the error bars of the samples. The OSL samples collected beneath each surface are indicated in stratigraphic order (see text for discussion). The plot of CRE ages is given for each surface sample, in relative position from north to south. Dots and errors bars are in red and blue for  $^{10}\text{Be}$  and  $^{36}\text{Cl}$ , respectively. (b) Distribution of *in situ* produced  $^{10}\text{Be}$  (left panel) and  $^{36}\text{Cl}$  (right panel) CRE ages modelled without erosion and without inheritance for the surface samples collected on T3 tread. The thin curves represent the CRE age probability as Gaussian distribution for each individual sample and the thick curves correspond to the summed Gaussian density probability function. The weighted mean CRE age is obtained with errors equal to two standard deviations ( $2\sigma$ ). Outlier sample DN06S2 ( $235.5 \pm 35.4$  ka) has not been included in the  $^{10}\text{Be}$  statistics.

CRE age is  $406.5 \pm 26.5$  ka (Table 1, Fig. 6a). This age is a little younger than of the weighted mean age of T3 and agrees with the assumption that T2 aggradation at this site results from reworking of T3 material. Indeed, T2 CRE age is older than several

ages that have been used to estimate the weighted mean age of T3 and much older than that of the T3 outlier. At Dehshir South, 12 samples collected on T2 have been analysed (Figs 2a and 7). The  $^{10}\text{Be}$  and  $^{36}\text{Cl}$  concentrations, hence the corresponding CRE ages

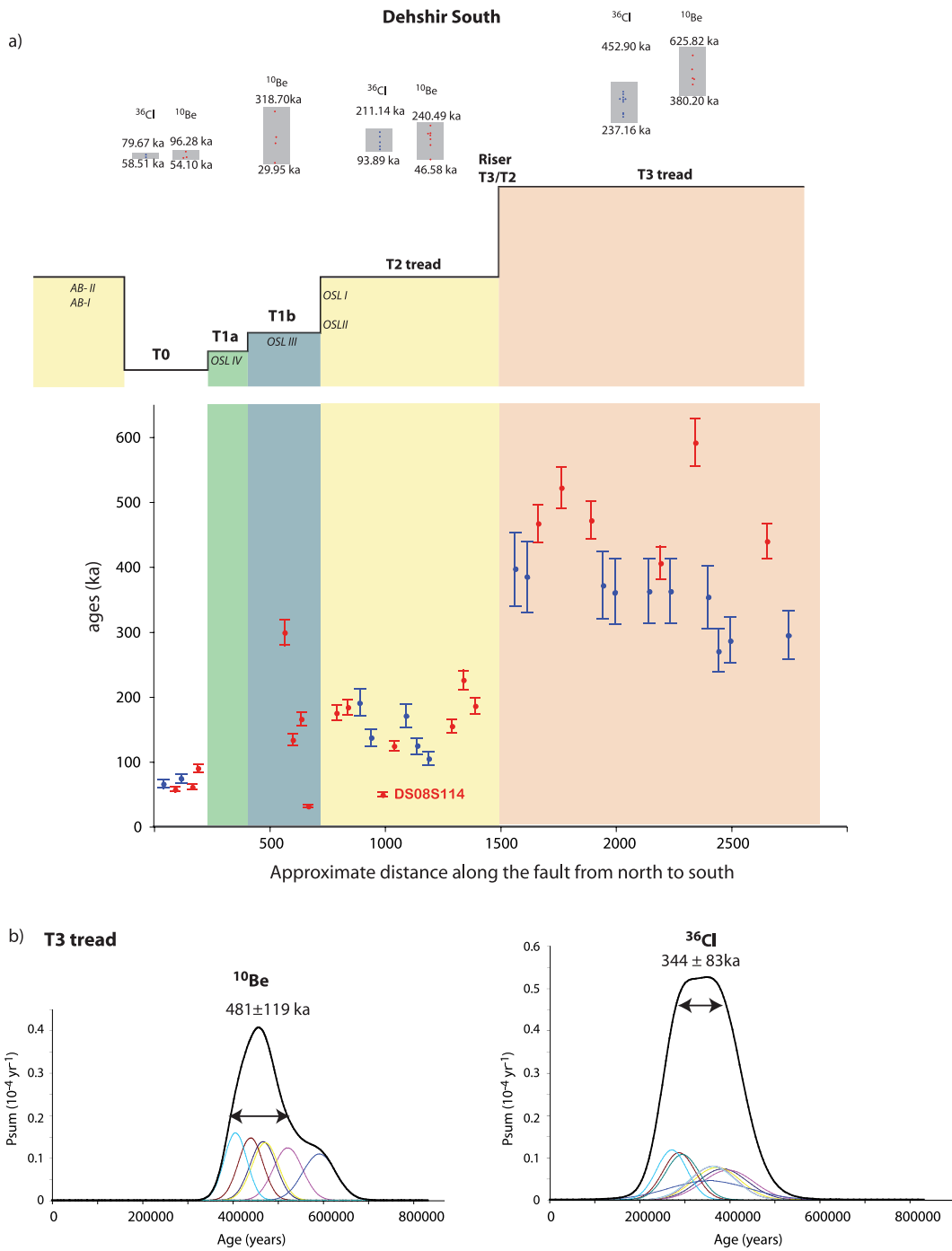


**Figure 7.** Summary of observations at site Dehshir South. (a) <sup>10</sup>Be and <sup>36</sup>Cl CRE ages of surface samples modelled without erosion and without inheritance are indicated by red and blue dots above each surface. The shaded columns extend from the minimum age to the maximum age given by the error bars of the samples. The OSL samples collected beneath each surface are indicated in stratigraphic order (see text for discussion). The plot of CRE ages is given for each surface sample, in relative position from north to south. Dots and errors bars are in red and blue for <sup>10</sup>Be and <sup>36</sup>Cl, respectively. (b) Distribution of *in situ* produced <sup>10</sup>Be (left-hand side) and <sup>36</sup>Cl (right-hand side) CRE ages modelled without erosion and without inheritance for the surface samples collected on T3 Tread. The thin curves represent the CRE age probability as Gaussian distribution for each individual sample and the thick curves correspond to the summed Gaussian density probability function. The weighted mean age is obtained with errors equal to two standard deviations (2σ).

calculated assuming zero-erosion and zero-inheritance are scattered (Table 1, Fig. 7a). The CRE ages of the surface samples range between  $49.9 \pm 3.3$  and  $225.8 \pm 14.7$  ka for the <sup>10</sup>Be and between  $104.4 \pm 10.5$  and  $190.3 \pm 20.8$  ka for the <sup>36</sup>Cl. The youngest <sup>10</sup>Be CRE age on T2 (DS08S114,  $49.9 \pm 3.3$  ka) might be con-

sidered as an outlier and excluded from the statistics. Discarding the outlier and keeping in mind the limited number of samples, the ages remain scattered without significant differences between <sup>10</sup>Be and <sup>36</sup>Cl ages. The distribution is multimodal with a weighted mean CRE age of  $175 \pm 62$  ka (Fig. 11a). This average is

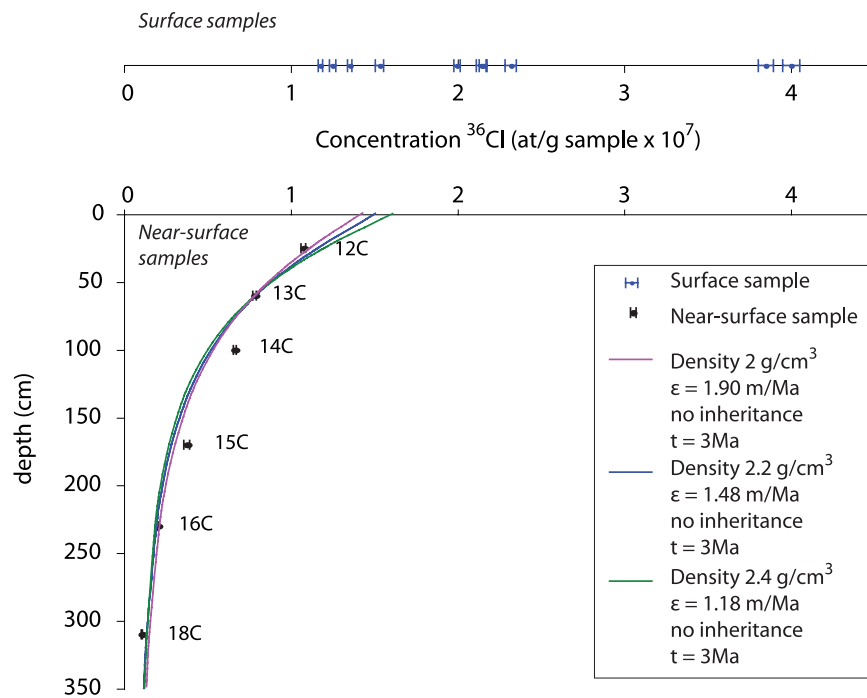


**Figure 8.** Plot of the near-surface, measured  $^{36}\text{Cl}$  concentrations (black dots) as a function of depth at profile PN (location on Fig. 4). Surface samples (blue dots) are shown but not included in the modelling. The erosion rate  $\epsilon$  is modelled for a 3-Ma-old surface to ensure that the steady-state equilibrium between production and disintegration has been reached. For the three different densities tested (obtained from the near-surface samples), the best-fit erosion rate–inheritance is indicated.

consistent with the intermediate elevation of T2 terrace and its surface characteristics as well as the fact that none of the CRE ages obtained for T2 is older than the youngest age calculated for T3.

Amalgamated samples have also been collected along two depth profiles at site Dehshir South. The  $^{10}\text{Be}$  concentrations are listed in Table 1. The profile PS1 was collected by the riser between T2 and the Marvast riverbed, 300 m east of the fault zone (Figs 2 and 11). The profile PS2 has been collected 1.5 km NE of PS1, close to the fault scarp in a pit dug within the T2 surface and nearby remnants of T3 (Figs 2 and 12). For both profiles, the uneven distribution of the  $^{10}\text{Be}$  concentrations dismisses a uniform pre-exposure prior to the emplacement of T2 material and precludes any appropriate modelling of a homogeneous inheritance. As for the study of alluvial surfaces in the Anar neighbouring area (Le Dortz *et al.* 2009), the profile data, together with the scattering of the concentrations of the surface cobbles, suggest the occurrence of a variable inheritance.

### 3.2.3 Surface T1 and T0

At site Dehshir North, the four surface samples collected on T1a provide CRE ages ranging between 82 and 424 ka (Figs 4 and 6a). The sample with the oldest age might be considered an outlier and the CRE age of the terrace would be better determined by the three youngest samples and bracketed between 82 and 134 ka. The T1a outlier has an age close to that of the amalgam on T2 fan surface and close to that of the surface samples collected on T3. This suggests that the T1a outlier is a T2 or T3 cobble reworked by the small gullies incising the surface of T2 and T3 treads and which incision is coeval with the emplacement of T1.

At site Dehshir South, the four surface samples have been collected on T1b. They provide  $^{10}\text{Be}$  exposure ages ranging between 30 and 318 ka (Figs 2 and 7a). The oldest sample, even older than the

samples collected on T2 tread, is as an outlier. Either it is a former cobble of T3 locally reworked by the small gullies incising T3 or a cobble exposed to cosmic rays for a long time in the upstream catchment of the Marvast River. In any case, such an outlier indicates that the inheritance of individual cobbles collected on T1 tread can be very important. Of the three remaining samples collected on T1b, two provide CRE ages that are not distinguishable from the CRE weighted mean age ( $175 \pm 62$  ka) of T2, the terrace immediately above. Only one sample (DS08S124,  $32.1 \pm 2.1$  ka) provides an age significantly younger than the ages on T2. This CRE age on T1b surface is significantly younger than the CRE ages on the T1a surface at site Dehshir North, suggesting that at this latter location, the surface cobbles of the T1a terrace contain an important amount of inherited  $^{10}\text{Be}$ .

At site Dehshir South, five samples have been collected in the present-day streambed of the Marvast River. Whatever the isotope considered, all provide non-zero CRE ages ranging between 54 and 96 ka, suggesting the occurrence of a significant inheritance. The CRE ages of T0 are younger than the CRE ages of T1b except for the youngest sample of T1b (DS08S124,  $32.1 \pm 2.1$  ka). At site Dehshir North, four samples have been collected in the main river flood plain T0. Discarding the outlier, three samples (two  $^{10}\text{Be}$  ages and one  $^{36}\text{Cl}$  age) provide non-zero CRE ages ranging between 57 and 84 ka, confirming the occurrence of a significant inheritance averaging some 70 ka. When including the outlier corresponding to the oldest sample collected in the river, the scattering of the concentrations increases and suggests the pre-exposure history of a cobble before the abandonment of an alluvial surface is highly variable.

To summarize (Fig. 13a), the observed average inheritance in the present stream beds of some 70 ka, as well as the distribution of CRE ages for the inset levels T1 and T2, suggest that T1 and T2 treads are likely to be younger than their CRE weighted mean age.

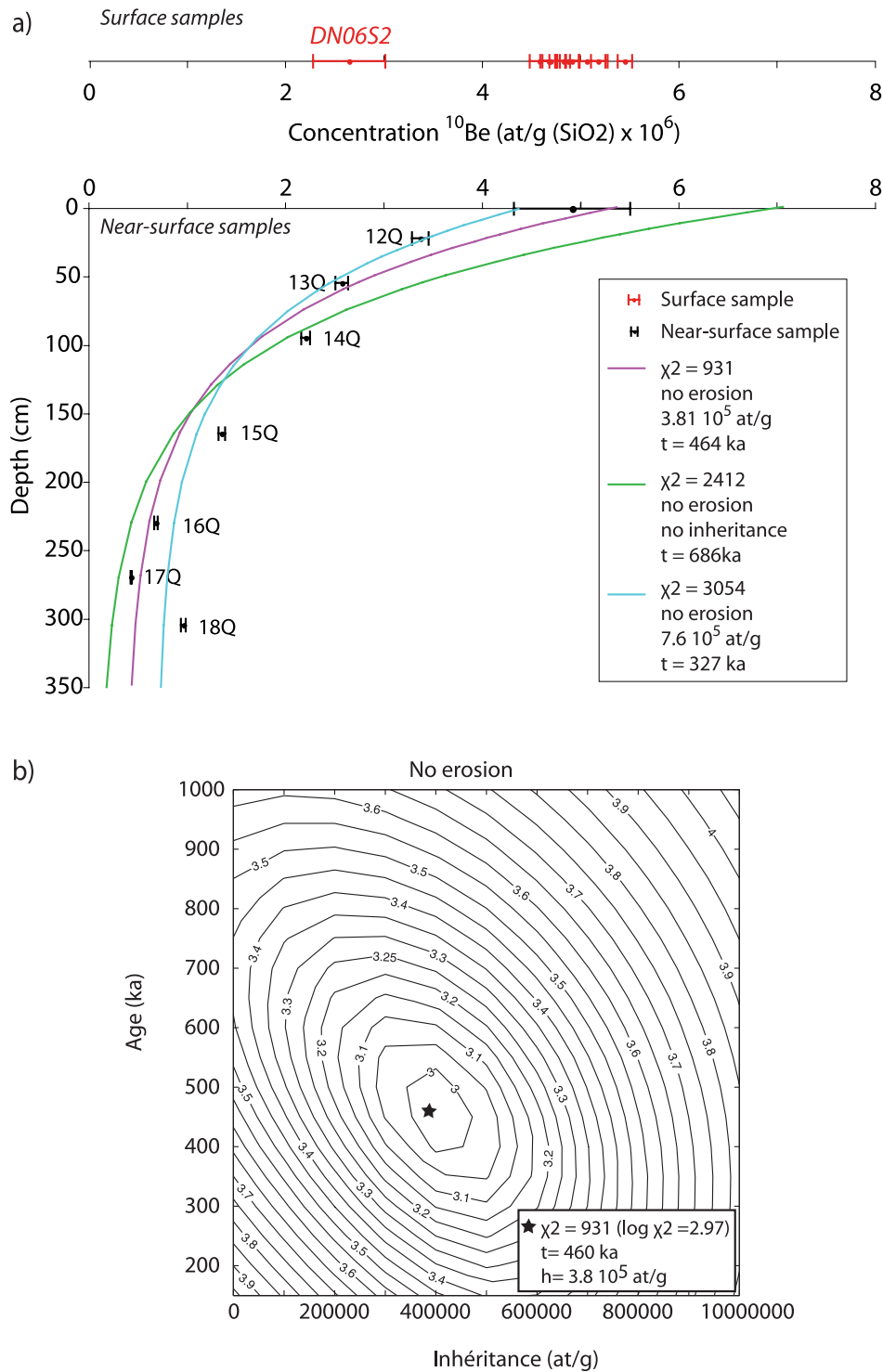


**Figure 9.** (a) Plot of the near-surface, measured  $^{10}\text{Be}$  concentrations (black dots) as a function of depth at profile PN (location on Fig. 4). Surface samples are indicated as red dots. The modelled curves fit distributions of concentrations, without erosion, and for three assigned inheritances. The modelling includes both the near-surface samples and the weighted mean age of the surface samples (DN06S2 excluded). (b)  $\text{Log}(\chi^2)$  values for a range of inheritance and CRE ages modelled without erosion are plotted below. The modelling converges towards a best-fit age of 460 ka and inheritance  $3.8 \times 10^5$  at  $\text{g}^{-1}(\text{SiO}_2)$  (star).

Thus, the ages of abandonment of the terrace treads may be better approximated by the CRE age of the youngest sample found on each surface. Such a conclusion has already been drawn for alluvial fan surfaces in the neighbouring region of Anar (Le Dortz *et al.* 2009).

### 3.3 OSL ages

OSL dating was performed to better constrain the chronology of alluvial terraces at the two studied sites. Five OSL samples initially sought to determine the ages of faulted deposits for palaeoseismology purposes were sampled at site Dehshir North (Nazari *et al.*

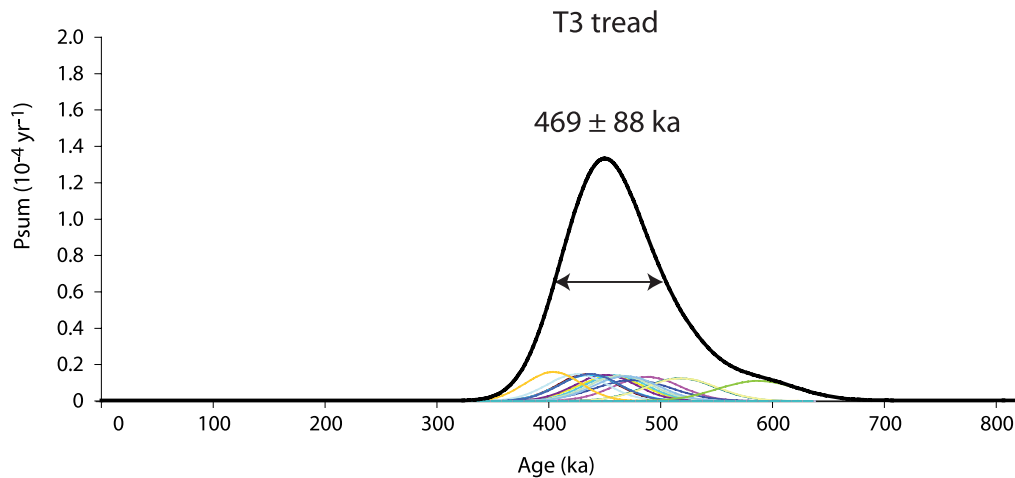


**Figure 10.** Weighted mean  $^{10}\text{Be}$  CRE age of T3 tread including the surface sample exposure ages of North and South sites and excluding outlier sample DN06S2. The thin curves represent the CRE age probability as Gaussian distribution for each individual sample and the thick curves correspond to the summed Gaussian density probability function. The weighted mean age is obtained with errors equal to two standard deviations ( $2\sigma$ ).

2009). Then, six new OSL samples were collected at site Dehshir South. As no suitable material was found within old terrace T3, OSL ages help only constraining the aggradation timing of terraces T2 and T1; they also permit comparison with CRE ages. The ages of all the OSL samples, including those previously published by Nazari *et al.* (2009), have been recalculated in Section 3.1 using CAM or FMM techniques to account for the scatter of the  $D_e$  distributions.

OSL samples were collected at site Dehshir North, in a trench excavated within T3 and T2 (fig. 4 in Nazari *et al.* 2009). Within this trench, the distal alluvial and colluvial deposits corresponding to the T2 and subsequent levels provide refined OSL ages of  $60.0 \pm 5.7$ ,  $45.5 \pm 4.6$  and  $20.1 \pm 1.6$  ka in accord with the stratigraphic succession (Table 3, sample HI/2008-IX in unit E1, sample HI/2008-VII in unit D3b, sample HI/2008-VIII in unit D4, Nazari *et al.* 2009). In addition, recent colluviums incised by small streams flowing through the Dehshir fault zone and which base level matches with the tread of T1 yielded two OSL ages of  $26.0 \pm 1.0$  ka for the lower colluviums and  $20.2 \pm 0.8$  for the upper ones (Table 3, sample HI/2008-I in unit B1 and sample HI/2008-VI in unit B2, Fattahi *et al.* 2010). These two latter OSL ages, which post-date the incision of T2, are coeval with the emplacement of T1. They imply that the T1b tread, all the more the T1a tread, is at most 21 ka (oldest possible age of the most superficial sample). Notwithstanding that the OSL samples have not been directly collected under the terrace treads sampled for CRE dating, the data available at site Dehshir North indicate large discrepancies between the CRE and OSL ages. The cannibalism of the old T3 terrace by subsequent alluvial deposits may explain such discrepancies by locally recycling T3 cobbles during the aggradation of the lower terraces T2 and T1. This possibility is further examined at site Dehshir South for which OSL samples have been taken right below the terrace treads T2 and T1 where sampled for CRE dating.

For T2 at Dehshir South, two OSL samples, OSL I and OSL II, have been collected from the riser between T2 and the active riverbed, very close to the profile PS1 (Figs 2a and 11b). OSL I has been collected 15 m to the West of PS1 and at a depth of 0.8 m (OSL I) and OSL II, 10 m to the East of PS1 and at a depth of 3.4 m. The samples OSL I and II yielded ages of  $26.9 \pm 1.3$  ka and  $29.4 \pm 5.1$  ka, respectively (Table 3). These similar OSL ages suggest that the material of the terrace T2 emplaced rapidly and that its tread is at most 28.2 ka. The OSL samples of the riser T2/T0 provide ages

much younger than the weighted mean  $^{10}\text{Be}$  and  $^{36}\text{Cl}$  CRE age of T2,  $175 \pm 62$  ka (Fig. 11a), but closer to  $49.9 \pm 3.3$  ka, the youngest CRE age on T2 tread (DS08S114 in Table 1). Two additional OSL samples (AB/2006-I and II in Table 3) were collected within a colluvium pediment topping T2 in the pit of profile PS2 (Figs 2a and 12b). These samples yielded OSL ages of  $39.7 \pm 2.6$  and  $20.0 \pm 1.3$  which confirm this desert pediment was formed both by the end of the emplacement of terrace T2 and after its abandonment. To summarize, the OSL ages obtained for T2 indicate its aggradation occurred during the time-interval 25.6–65.7 ka. This suggests that the samples collected on T2 tread, providing exposure ages older than 66 ka, contain an inherited CRE component. For T1, two OSL samples, OSL III and IV, were collected at Dehshir South in fine sands, respectively, below the surface of T1b and T1a (Fig. 3b). The error bars on sample OSL III, taken by the riser T1b/T0, provide minimum and maximum OSL ages of 20.4 ka and 23.4 ka for the T1b tread. The sample OSL IV, taken by the riser T1a/T0, provides minimum and maximum OSL ages of 9.4 ka and 10.6 ka for the T1a tread. These ages are in agreement with the relative elevation of the terraces, the samples from the riser T2/T0 being older than the sample from the riser T1b/T0, itself older than the sample from the riser T1a/T0. Similarly to the terrace T2, the OSL age of T1b is younger than the  $^{10}\text{Be}$  CRE ages of the samples collected on the T1b tread. This OSL age is almost one order of magnitude younger than the three oldest  $^{10}\text{Be}$  samples and 30 per cent younger than the youngest  $^{10}\text{Be}$  sample (DS08S114). There is no direct comparison available between OSL and CRE ages for T1a because this surface has not been sampled for cosmogenic dating.

At the two studied sites along the Dehshir fault, the OSL ages on terraces T2 and T1 are systematically younger than the CRE ones on the same terrace. For a given terrace, the CRE statistical outlier, which is the youngest CRE age and has been consequently removed from the calculation of the weighted mean CRE age, remains slightly older than, but closer to the OSL ages. Two extreme options may be contemplated: either OSL ages have been rejuvenated or CRE concentrations include a high percentage of inheritance. Most of the physical processes that are known to affect the OSL method, such as partial bleaching, incorporate an antecedent signal leading to overestimation of the age of sediment burial. This has been accounted for the studied samples by the statistical processing of the  $D_e$  distributions. Conversely, OSL signal is sensitive to the

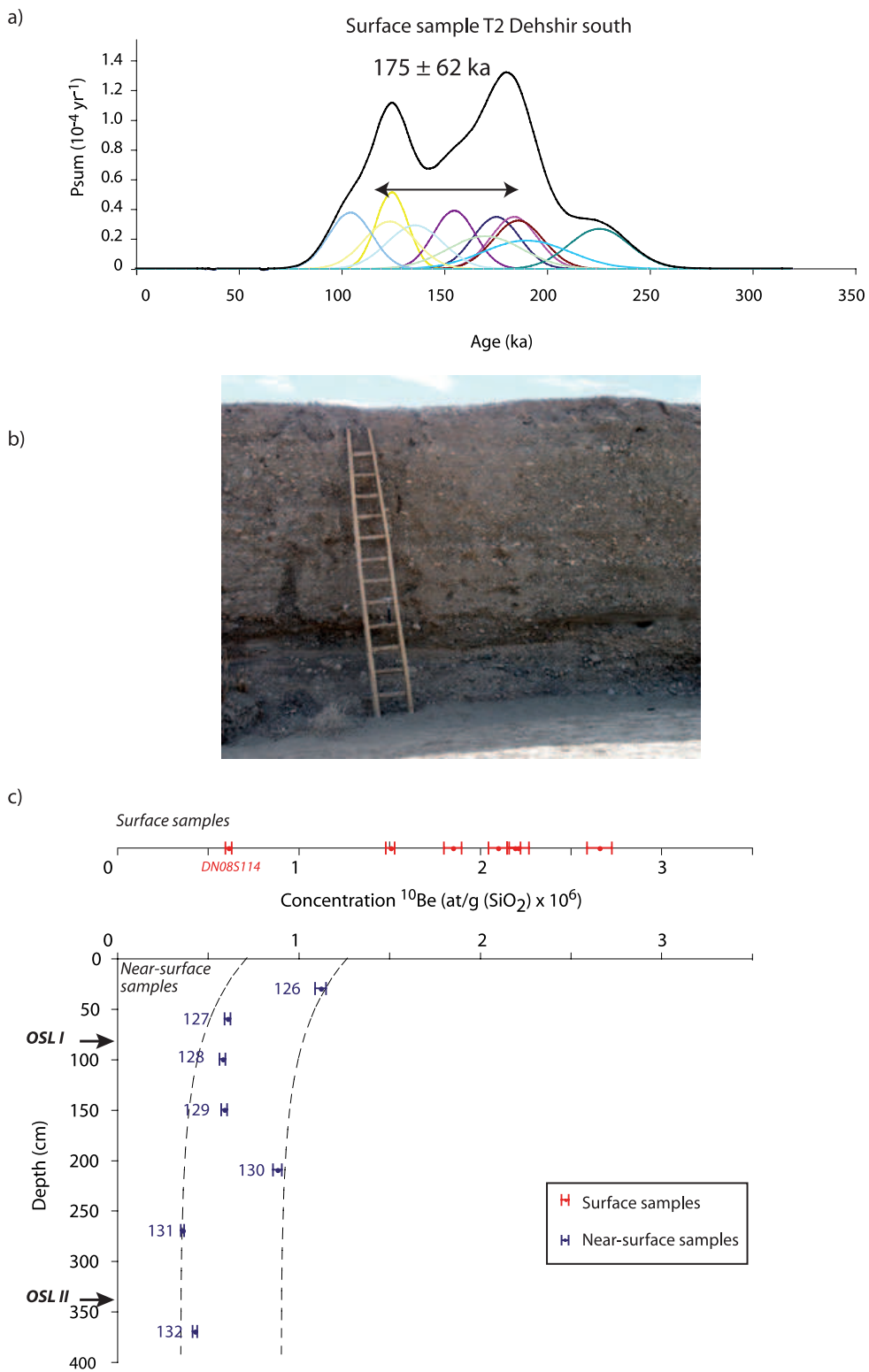


**Figure 11.** (a) Weighted mean CRE age for the <sup>10</sup>Be and <sup>36</sup>Cl surface samples collected on T2 tread at Dehshir South site. The ages have been calculated assuming no erosion and no inheritance and the sample DS08S114 (49.9 ± 3.3 ka) has not been included in the statistics. The thin curves represent the CRE age probability as Gaussian distribution for each individual sample and the thick curves correspond to the summed Gaussian density probability function. The weighted mean age is obtained with errors equal to two standard deviations (2σ). (b) Field photograph showing the 4-m-high T2/T0 riser sampled for profile PS1 (see Fig. 2 for location). (c) Profile of <sup>10</sup>Be concentrations through the terrace T2 at site PS1. Red and blue dots are surface and near-surface samples, respectively. The two OSL samples collected by the same riser along strike within sandy lenses are indicated. Dashed curves represent the forward models of theoretical <sup>10</sup>Be near-surface concentration for a 30 ka abandonment age assuming homogeneous inheritances of 3.5 10<sup>5</sup> at g<sup>-1</sup>(SiO<sub>2</sub>) (left-hand side) and 9 10<sup>5</sup> at g<sup>-1</sup>(SiO<sub>2</sub>) (right-hand side).

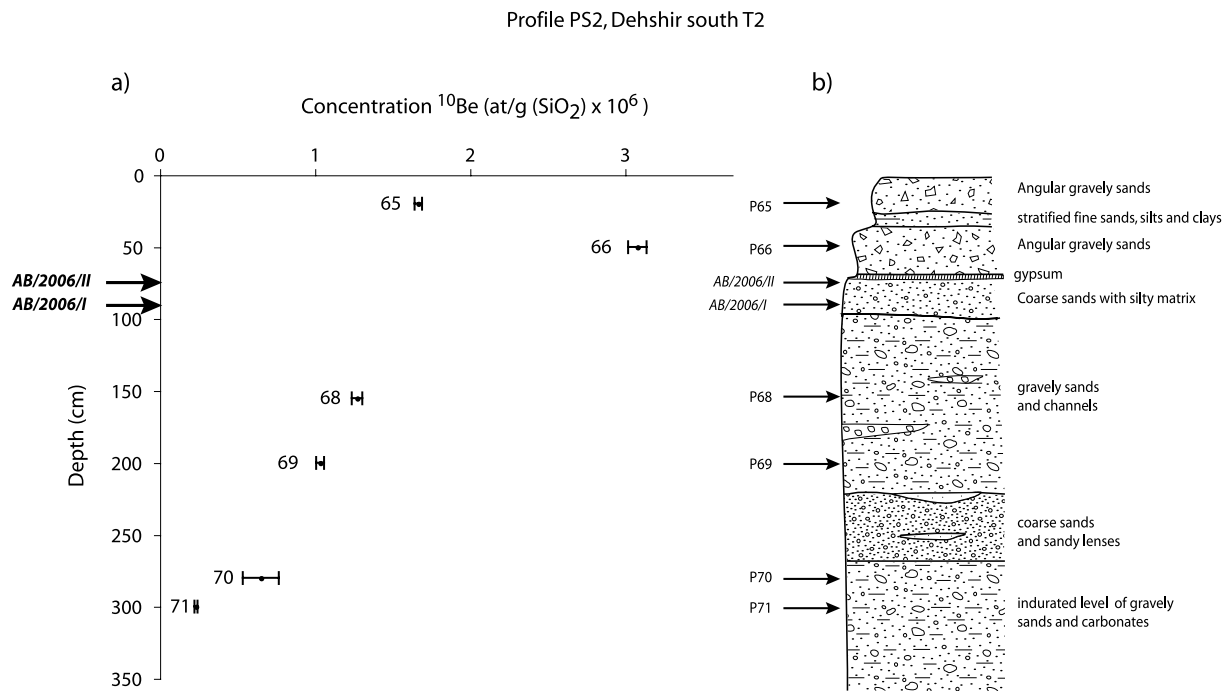


**Figure 12.** Plot of the measured  $^{10}\text{Be}$  concentrations as a function of depth (left panel) and simplified stratigraphy (right panel) through profile PS2. Depth profile PS2 has been excavated within T2 tread, North of the Marvast River (see location on Fig. 2). Relative positions of OSL samples AB/2006/I and II and CRE near-surface amalgams are shown (black arrows).

temperature and a loss of luminescence might occur at temperatures above 50–60°C. Such temperatures may occur on the Iran plateau during summertime so that OSL ages could be theoretically rejuvenated. Nevertheless, to account for gamma rays shielding, OSL samples were taken at least at 0.7 m below the ground surface (Table 3), a depth large enough to prevent strong variations of temperature. In addition, if temperature had affected the OSL signal, such effect would decrease with increasing sampling depth. However, no trade-off is observed between the OSL ages and the sampling depth (Table 3). On the contrary, OSL ages, whatever the depth, appear similar for the same terrace and in agreement with the relative elevation of the terraces. As a consequence, the variable inheritance of CRE concentrations should chiefly explain the discrepancy with OSL ages.

### 3.4 Discussion on the abandonment age of the alluvial surfaces

The overall chronology of the fan surfaces crossed by the Dehshir fault has been established but the abandonment age of each surface is not easily assigned for several reasons (Fig. 13). First, the scattering of CRE concentrations on a given surface, the occurrence of more concentrated samples on younger surfaces than on older ones, the occurrence of significant concentrations in active riverbeds, indicate there is a variable inheritance uneasy to account for. Secondly, where CRE and OSL data are available for the same terrace, the OSL ages of the late sediments of the terrace are always much younger than the CRE ages of the cobbles abandoned on its tread. Such disparities between OSL and CRE ages appear to result from the high variability of the CRE inheritance that needs further consideration. Previous works already faced variable inheritance (Ryerson *et al.* 2006); nevertheless, they show decreases of amalgamated concentrations with depth, which permit finally to model

an average inheritance. In our case, a limiting isochron (Mériaux *et al.* 2004) cannot be modelled as sample amalgamations exhibit high variability of depth concentrations (e.g. Figs 11 and 12).

#### 3.4.1 Variable CRE inheritance and maximum abandonment ages of alluvial treads

A rough estimate of the variable inheritance is provided by the CRE weighted mean of  $72 \pm 20$  ka obtained from eight of the nine samples collected in the riverbeds once the oldest outlier discarded. Moreover, amalgam sample DS08P130 from profile PS1 (Fig. 11c) has a measured concentration (Table 1) of  $8.86 \times 10^5$  at  $\text{g}^{-1}(\text{SiO}_2)$ , even though it is located at 2.1 m below the T2 surface whose surface samples yielded a weighted mean CRE age of  $175 \pm 62$  ka. Assuming 175 ka represents the actual age of T2 tread and subtracting the concentration acquired *in situ*, at 2.1 m depth, by sample DS08P130 during these 175 ka of exposure would yield to a remaining, hence inherited, concentration of  $7.25 \times 10^5$  at  $\text{g}^{-1}(\text{SiO}_2)$ . Most of the sample concentration would therefore result from inheritance. Such inherited concentration would have been acquired in about 60 ka, if accumulated at the surface. Then, the 70 ka ages of riverbed samples appear to give a good estimate of the amount of inheritance carried by T2 material. Consequently, T2 mean age should be reduced to  $105 \pm 62$  ka. These 70 ka inheritance estimates are larger than the 32 ka of inheritance age-equivalent obtained for T3 by conventional modelling of the  $^{10}\text{Be}$  profile (Fig. 9). We have therefore investigated another method to use the inheritance. Assuming each terrace formed during a short-lived aggradation coeval with a single climatic crisis, the near-surface concentrations have been used to fix the maximum abandonment age of the terrace (Fig. 14). The principle is simple and rests on the impossibility for any sample to be incorporated into the sediment of the terrace with a negative concentration. Accounting for the depth of each near-surface sample

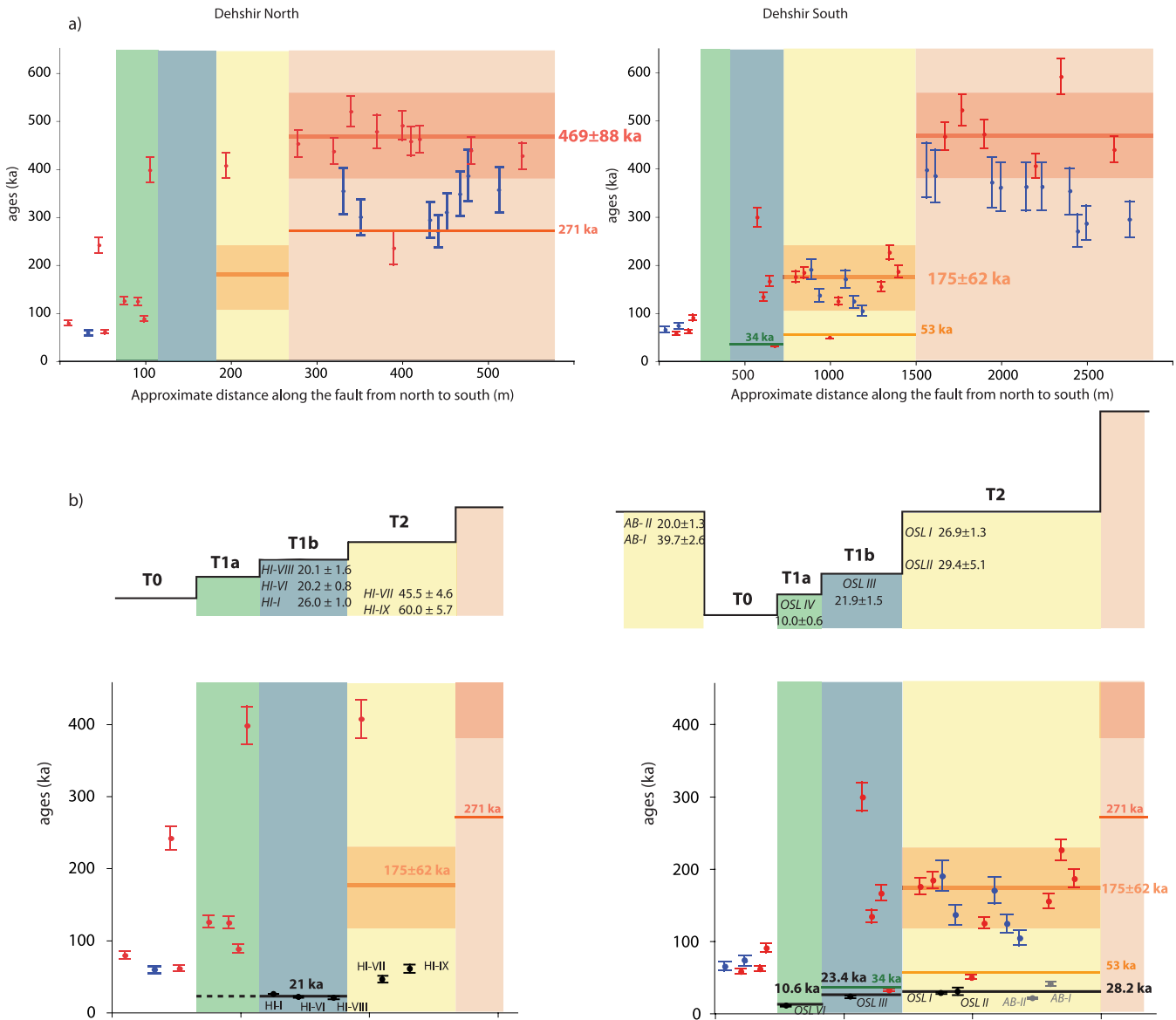


**Figure 13.** Synthesis of observations and plot of sample ages in relative position from north to south for site Dehshir North (left panels) and site Dehshir South (right panels). Dots and errors bars are in red, blue and black for  $^{10}\text{Be}$ ,  $^{36}\text{Cl}$  and OSL dating, respectively. (a) The thick lines and shaded regions are the weighted mean with  $2\sigma$  confidence interval for the CRE surface age. Samples DN06S2 and DN08S114 have been omitted for the T3 and T2 statistics, respectively. The thin lines are the oldest possible CRE age of the youngest CRE sample collected on the terrace treads. (b) Upper part, relative positions and OSL ages of the samples collected below the terrace treads of T2, T1b and T1a. Samples HI (Nazari *et al.* 2009; Fattahi *et al.* 2010) and AB have been collected within trenches excavated for palaeoseismic purposes and samples OSL I-IV by the terrace risers. Lower part, CRE and OSL ages available for terraces T2 and T1. The thick black line is the oldest possible age of the most surficial OSL sample collected below each terrace tread.

and assuming its measured concentration results only from *in situ* exposure; that is, assuming no inheritance for the sample, it is possible to calculate for any sample of a profile the time required to bring it back from its measured concentration to a null concentration. The maximum abandonment age of the terrace is then obtained from the near-surface sample of a given profile for which the concentration is restored to zero without bringing back any other sample of the profile to a negative concentration. For the profile PS1 across T2 (Fig. 14a), this is obtained for the sample DS08P127 with 107 ka of *in situ* exposure. This indicates that T2 was abandoned at most 107 ka ago and that for this maximum time of exposure the concentration remaining in the other samples of the profile corresponds to a minimum inheritance. Therefore, this method figures out the variability of the inheritance that amounts, for such an exposure time, to

$7.86 \cdot 10^5$  at  $\text{g}^{-1}(\text{SiO}_2)$  for the near-surface amalgam collected at 2.1 m depth; such concentration would correspond to a minimum exposure of 66 ka if acquired at the surface prior to the emplacement of the terrace (Fig. 14a). It is worth noting that this rejuvenation would bring back only one of the surface samples to a negative concentration. This remains acceptable, as this sample is the statistical outlier DS08S114. All the other such 107-ka-rejuvenated surface samples would keep positive concentrations. Whereas older depth-profile determined CRE ages of T2 are not possible because they would bring, at least one of the near-surface amalgams, the amalgam 127 (Fig. 14a), back to a negative concentration, younger exposure ages remain possible. Theoretically, all exposure ages ranging between 0 and 107 ka are possible. On the one hand, exposure ages ranging between 53 ka (oldest possible age of the youngest sample,

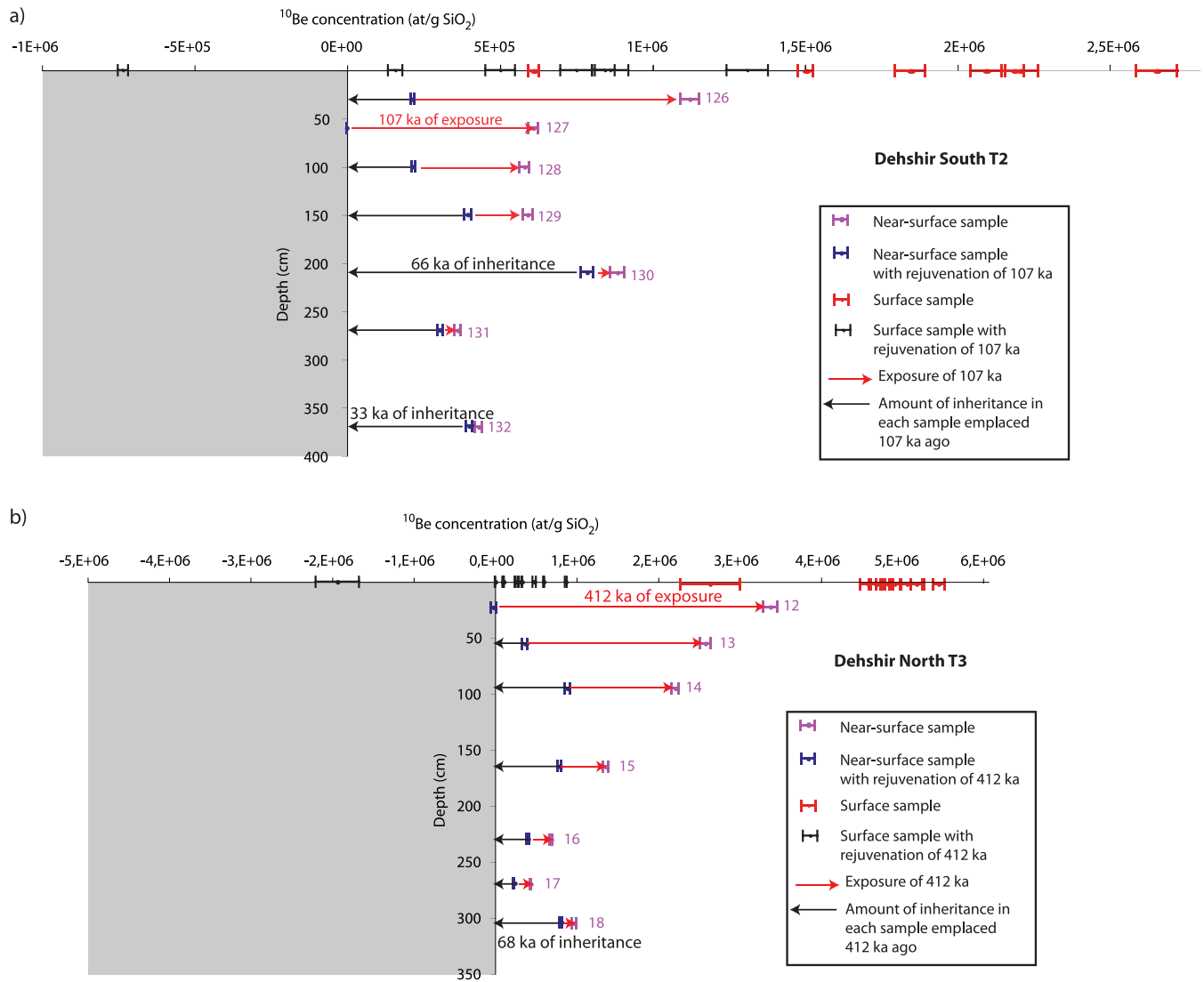


**Figure 14.** Depth-profile PS1 and PN of  $^{10}\text{Be}$  concentrations respectively through terrace T2 (a) and T3 (b). Violet and red dots are the measured concentrations of the near-surface amalgams and surface samples, respectively. Blue dots and black dots are the respective concentrations of the near-surface amalgams and surface samples once one near-surface amalgam is restored to a null concentration without bringing back any other near-surface sample to a negative concentration (see text for discussion). The time of *in situ* exposure to bring that near-surface sample to its measured concentration is indicated in red, and the residual concentrations remaining in the other near-surface samples by black arrows materializing the sample inheritance for such duration of exposure. The only rejuvenated surface sample displaying a negative concentration is the sample DN06S2 on T3, therefore a statistical and physical outlier for a 412 ka exposure age. This race to zero-concentration for the near-surface amalgams indicates that T2 and T3 have to be younger than 107 ka and 412 ka, respectively. Shaded area corresponds to physically unrealistic domains of negative  $^{10}\text{Be}$  concentrations.

DS08S114, on T2) and 107 ka would make that statistical outlier younger than the age of the terrace. On the other hand, exposure ages ranging between zero and 53 ka would be compatible with the occurrence of the statistical outlier as well as the other surface samples collected on T2.

The same method applied to the depth profile PN across T3 (Fig. 14b) demonstrates the terrace was abandoned at most 412 ka ago, confirms the occurrence of a significant inheritance which minimum amounts to 68 ka for the deepest amalgam collected at more than 3 m depth, and exemplifies its variability. It is nonetheless important to note that this is an uppermost bound of exposure duration. This leaves open all the possibilities ranging between the time of abandonment of T2 and 412 ka, hence at least the possibilities between 107 and 412 ka.

### 3.4.2 Abandonment age of terrace treads

The age of abandonment of the uppermost level T3 is to be discussed with the only data available, the CRE ages (Figs 13 and 15). One may rest on the statistical analysis of the surface samples and retains the weighted mean age of  $469 \pm 88$  ka. To account for the inheritance incorporated in the former estimate, it is possible to subtract to that weighted mean age the 32 ka of inheritance age-equivalent obtained from the modelling of the  $^{10}\text{Be}$  profile. It is nonetheless worth noting that this average inheritance has been modelled under the incorrect assumption that the inheritance is homogeneous. Accounting for the variability of the inheritance, the near-surface profile data are incompatible with an age older than 412 ka (Fig. 14b) and the large uncertainties of the former estimate

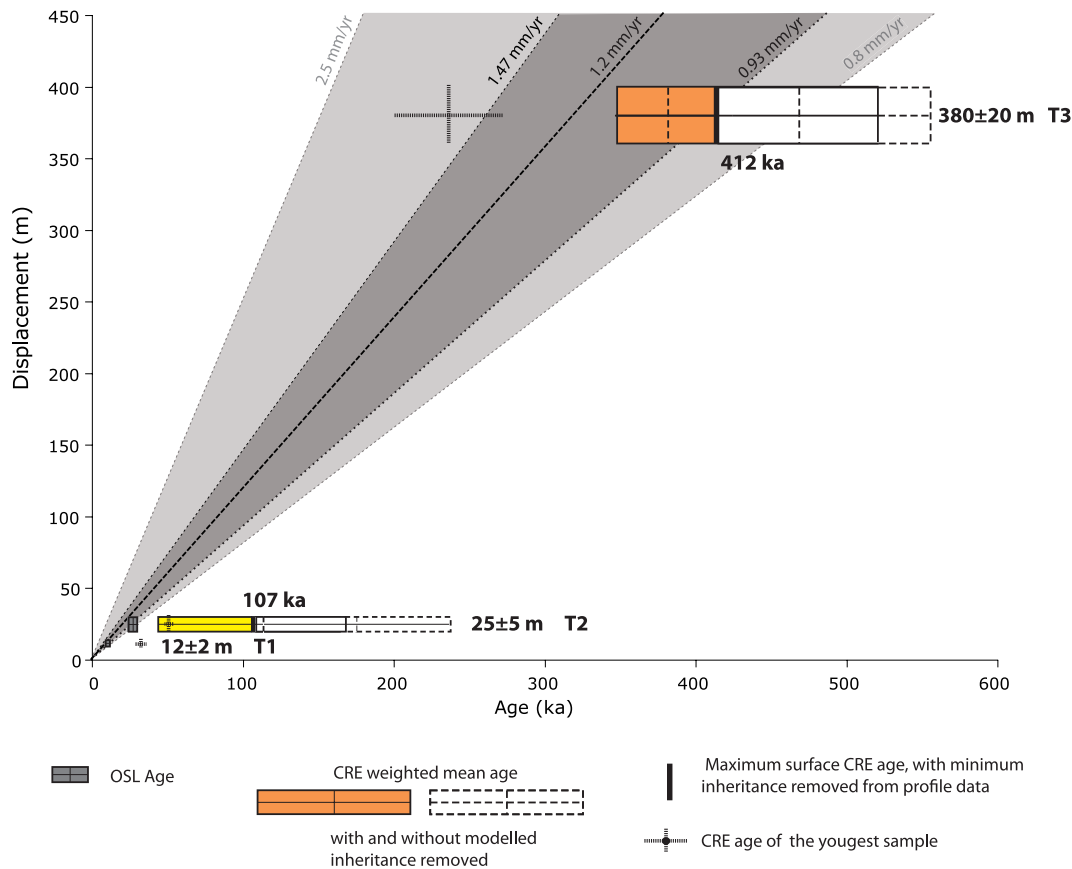


**Figure 15.** Summary of offsets and ages available to assess the slip rate of the Dehshir fault. Dashed boxes and boxes correspond to weighted mean CRE age with and without removal of the estimated inheritance (see text for discussion). The oldest possible abandonment ages of T3 and T2 (thick vertical black lines) are determined from the near-surface concentrations (Fig. 14). The exposure age of the youngest sample (black cross) on each terrace is also indicated. Grey boxes correspond to the OSL age domains of the late sediments emplaced below the treads of T2 and T1. Light grey slip rate domain is the range of minimum slip rate of Nazari *et al.* (2009). The dark grey domain narrows the uncertainties and demonstrates the Dehshir fault slips faster than  $0.93 \text{ mm yr}^{-1}$  but slower than  $1.47 \text{ mm yr}^{-1}$ .

( $437 \pm 88 \text{ ka}$ ) can be reduced to the interval 349–412 ka (Fig. 15). Alternatively, retaining the youngest sample and allowing for the occurrence of a greater amount of inheritance would provide a much younger abandonment age of 271 ka (oldest possible CRE age of the youngest sample). As there is ample evidence for a large variability of the inheritance on the younger surfaces, one cannot rule out the later hypothesis and may consider an age of 271 ka for the abandonment of T3.

The age of abandonment of the intermediate level T2 is easier to estimate because both OSL and CRE ages are available. The weighted mean of the zero-erosion CRE age ( $175 \pm 62 \text{ ka}$ ) is of little use for constraining the age of abandonment because of the variable inheritance. Subtracting a possible inheritance of 70 ka (Fig. 14a), a value similar to the average obtained for the cobbles collected in the active riverbed, takes back the former estimate to  $105 \pm 62 \text{ ka}$ . Although limiting the uncertainties to the range 43–107 ka, the upper bound on the abandonment age (Fig. 14a) allows for a wide range of possibilities, including the oldest possible CRE age (53 ka) of the youngest surface cobble. Accounting for the occurrence of a variable inheritance, this latter solution is a better estimate of the maximum age of abandonment of the surface although the youngest cobble may also bear an inherited component. This inherited component may correspond to the difference with the oldest possible age of the youngest OSL collected below the tread of T2. The surface of T2 is younger than the oldest possible age of

the superficial OSL sample and is at most 28.2 ka at site Dehshir South (Fig. 13b). Assuming this OSL age is close to the actual abandonment age of T2 tread, a forward modelling of near-surface concentrations of PS1 profile (Fig. 11c) can be calculated with zero erosion and different choices of inheritance. Whatever the selected value of homogeneous inheritance, none permits to account correctly for the uneven distribution with depth of the measured near-surface concentrations. Nevertheless, two limiting curves appear to bracket these measured concentrations, they correspond to  $3.5 \cdot 10^5$  and  $9 \cdot 10^5$  at  $\text{g}^{-1}(\text{SiO}_2)$  of homogeneous inheritances (Fig. 11c). These values of inherited concentrations would correspond to pre-exposure, if acquired at the surface prior to the emplacement of the terrace, of 30 ka and 75 ka, respectively. Although these values of inherited concentrations result from forward modelling based on the assumption that the inheritance is homogeneous, they indicate the inheritances carried by the amalgam samples of T2 sediments may be nearly as high as  $10^6$  at  $\text{g}^{-1}(\text{SiO}_2)$ . It is worth noting that all but one measured surface samples have  $^{10}\text{Be}$  concentrations that are higher than  $10^6$  at  $\text{g}^{-1}(\text{SiO}_2)$ . Interestingly, subtracting to the near-surface samples the concentrations corresponding to 30 ka of *in situ* exposure makes the residual concentrations, which correspond to inheritance, noteworthy. This inherited concentration amounts to  $8.57 \cdot 10^5$  at  $\text{g}^{-1}(\text{SiO}_2)$  for sample DS08P130 at 2.1 m depth and corresponds to pre-exposure time at the surface of 71 ka. Thus considering 70 ka of inheritance for T2 gravels is

a reasonable estimate that can be proposed to average the variable inheritance.

Finally, the OSL ages of the risers T1b/T0 and T1a/T0 indicate their respective tread are at most 23.4 ka and 10.6 ka, respectively. Given the uncertainties associated to the OSL ages of the risers and considering that partial bleaching has been accounted, the youngest possible ages of T2, T1b and T1a treads are, respectively, 25.6 ka, 20.4 ka and 9.4 ka.

#### 4 SLIP RATE ESTIMATE AND CONCLUSIONS

The former chronology and offset-risers provide estimates on the minimum and maximum slip rate of the Dehshir fault. At site Dehshir South, the river course displaced by  $380 \pm 20$  m is incised within the terrace T3. Combining the offset of  $380 \pm 20$  m with the maximum exposure age of 412 ka yields a minimum slip rate of  $0.92 \pm 0.05$  mm yr<sup>-1</sup>. Assuming that the regional level T3 is coeval at both sites and that the oldest possible age of the youngest sample collected on T3 (i.e. 271 ka) may approximate its abandonment, the slip rate would be at least  $1.40 \pm 0.08$  mm yr<sup>-1</sup>. The 25-m-deflection of the Marvast River might also be used to estimate the slip rate on a shorter period of time, but this deflection probably overestimates the true tectonic offset because T1 tread is no longer observed downstream. The offset of the gullies incising both T3 and T2 treads at site Dehshir North is a true tectonic offset. This 20–30 m offset provides reliable estimates of the upper and lower bounds of the slip rate. The offset cannot be older than the OSL age collected below the tread of T2 (OSL1  $26.9 \pm 1.3$  ka) and accounts for a minimum slip rate greater than  $0.71$  mm yr<sup>-1</sup> (20 m in the last 28.2 ka). The offset cannot be younger than the infilling of T1b and allows determining the upper and lower bounds of the maximum slip rate. The infilling of T1b being younger than  $21.9 \pm 1.5$  ka, the lower and upper bounds of the maximum slip rate are, respectively,  $0.85$  mm yr<sup>-1</sup> (20 m in the last 23.4 ka) and  $1.47$  mm yr<sup>-1</sup> (30 m in the last 20.4 ka). The  $12 \pm 2$  m offset of the riser T1a/T0 at Dehshir North is also an estimate of the actual tectonic offset post-dating the emplacement of T1a, which is at most 10.6 ka according to sample OSL IV (Table 3, Fig. 13). The  $12 \pm 2$  m offset yields a lower bound of the minimum slip rate of  $1.13 \pm 0.2$  mm yr<sup>-1</sup>. The early estimate of Nazari *et al.* (2009) can therefore be refined and the actual slip rate ranges between  $0.93$  mm yr<sup>-1</sup>, largest of the conservative estimates of the minimum slip rate, and  $1.47$  mm yr<sup>-1</sup>, safe estimate of the maximum slip rate. Therefore, the slip rate of the Dehshir fault is well determined at  $1.2 \pm 0.3$  mm yr<sup>-1</sup> (Fig. 15).

This study demonstrates the usefulness of combining CRE and OSL data to unravel the abandonment ages of alluvial fans and inset terraces in the desert environment of Central Iran. On the one hand, the use of <sup>10</sup>Be and <sup>36</sup>Cl cosmogenic isotopes with different half-lives allows constraining a very low denudation rate of  $0.001$  mm yr<sup>-1</sup> for the terrace treads and alluvial fan surfaces of Central Iran. On the other hand, the combination of surface and near-surface sampling exemplifies the occurrence and the variability of inheritance in the cosmogenic isotope concentrations and emphasizes the difficulty in assessing abandonment ages of young alluvial surfaces with CRE measurements in such arid environment (e.g. Le Dortz *et al.* 2009). The scattering of the CRE surface and near-surface concentrations indicates that the cobbles have not been uniformly exposed to cosmic rays prior to their emplacement. This variable inheritance may originate from a differential exhumation and weath-

ering of the bedrock catchments, or more likely for Dehshir sites, from reworking of cobbles originating from different levels of upper, hence older, fans. The abandonment age of an alluvial surface is thus better estimated by the CRE age of the youngest surface sample than by the weighted mean CRE age of many samples, as already formulated in Mongolia (Vassallo *et al.* 2007) and along the southern rim of the Tarim basin (Mériaux *et al.* 2005). However, the youngest sample on a surface may also incorporate inheritance and still overestimate the abandonment age. The amount of CRE inheritance potentially remaining in the youngest sample of a given surface may be obtained by comparing with the OSL age of the late sediments aggraded before the abandonment of the surface. For alluvial surfaces that are young with respect to the considerable amount of inheritance, up to 70 ka in the desert environment of Central Iran, the upper bound on the abandonment age of an alluvial surface appears best estimated by the OSL dating of the late sediment aggraded. For such young surfaces, the CRE measurements are complementary of OSL dating and can be used to unravel the complex history of weathering and transport in the catchment of desert alluvial fans. Finally, such variable CRE inheritance, typifying arid endorheic regions without incision rates, may require more consideration than hitherto drawn for the Andes and Tibet plateaus.

#### ACKNOWLEDGMENTS

This study would have been impossible without financial assistance from INSU-CNRS (PNTS and 3F programs) and CNES-SPOT Image (ISIS program contracts ISIS0403-622 and ISIS0510-812). Université Pierre et Marie Curie (UPMC) and Geological survey of Iran (GSI) provided complementary funding and logistic assistance. KL received a Ministry of Research and Education scholarship granted by the President of UPMC. MF acknowledges support from the research institute of Tehran University. The <sup>10</sup>Be measurements were performed at the ASTER AMS national facility (CEREGE, Aix-en-Provence) that is supported by the INSU/CNRS, the French Ministry of Research and Higher Education, IRD and CEA. The <sup>36</sup>Cl measurements were performed at the LLNL-CAMS. We thank L. Leanni, K. Pou, B. Finkel, F. Chauvet, M. Arnold and G. Aumaître for their help during chemistry and measurements at CEREGE and acknowledge B. Oveisi and M. Nazemzadeh for efficient organization and help during fieldwork. We acknowledge thorough reviews by Richard Walker and Anne-Sophie Mériaux. We are very thankful to Anne-Sophie Mériaux for her acute verification of the cosmogenic calculations.

#### REFERENCES

- Anderson, R.S., Repka, J.L. & Dick, G.S., 1996. Explicit treatment of inheritance in dating depositional surfaces using in situ <sup>10</sup>Be and <sup>26</sup>Al, *Geology*, **24**, 47–51.
- Arnold, M. *et al.*, 2010. The French accelerator mass spectrometry facility ASTER: improved performance and developments, *Nucl. Instrum. Methods Phys. Res. B*, **268**, 1954–1959.
- Bateman, M.D., Boulter, C.H., Carr, A.S., Frederick, C.D., Peter, D. & Wilder, M., 2007. Detecting post-depositional sediment disturbance in sandy deposits using optical luminescence, *Quat. Geochron.*, **2**(1–4), 57–64.
- Berberian, M., 1981. Active faulting and tectonics of Iran, in Gupta, H.K. & Delaney, F.M. (eds), *Zagros-Hindu Kush-Himalaya Geodynamic Evolution*, *Am. Geophys. Union, Geodynamics Series*, **3**, 33–69.
- Boulter, C., Bateman, M.D. & Frederick, C.D., 2007. Developing a protocol for selecting and dating sandy sites in East Central Texas: preliminary results, *Quat. Geochron.*, **2**, 45–50.

- Braucher, R., Brown, E.T., Bourlès, D.L. & Colin F., 2003. In situ produced  $^{10}\text{Be}$  measurements at great depths: implications for production rates by fast muons, *Earth planet. Sci. Lett.*, **211**, 251–258.
- Braucher, R., Del Castillo, P., Siame, L., Hidy, A.J. & Bourlès, D.L., 2009. Determination of both exposure time and denudation rate from an in situ-produced  $^{10}\text{Be}$  depth profile: a mathematical proof of uniqueness. Model sensitivity and applications to natural cases, *Quat. Geochron.*, **4**(1), 1–82.
- Brown, E.T., Edmond, J.M., Raisbeck, G.M., Yiou, F., Kurz, M.D. & Brook, E.J., 1991. Examination of surface exposure ages of Antarctic moraines using in situ produced  $^{10}\text{Be}$  and  $^{26}\text{Al}$ , *Geochim. Cosmochim. Acta.*, **55**, 2699–2703.
- Brown, E.T., Bourlès, D.L., Raisbeck, G.M., Yiou, F., Burchfiel, B.C., Molnar, P., Deng, Q. & Li, J., 1998. Estimation of slip rates in the southern Tien Shan using cosmic ray exposure dates of abandoned alluvial fans, *Geol. Soc. Am. Bull.*, **110**(3), 377–386.
- Chmeleff, J., von Blackenburg, F., Kossert, K. & Jakob, D., 2010. Determination of the  $^{10}\text{Be}$  half-life by multicollector ICP-MS and liquid scintillation counting, *Nucl. Instrum. Methods Phys. Res. B*, **268**, 192–199.
- DeLong, S.B. & Arnold, L.J., 2007. Dating alluvial deposits with optically stimulated luminescence, AMS  $^{14}\text{C}$  and cosmogenic techniques, western Transverse Ranges, California, USA, *Quat. Geochron.*, **2**, 129–136.
- Desilets, D., Zreda, M., Almasi, P.F. & Elmore, D., 2006. Determination of cosmogenic  $^{36}\text{Cl}$  in rocks by isotope dilution: innovations, validation and error propagation, *Chem. Geol.*, **233**, 185–195.
- Farber, D., Mériaux, A.-S. & Finkel, R., 2008. Attenuation length for fast nucleon production of  $^{10}\text{Be}$  derived from near-surface production profiles, *Earth planet. Sci. Lett.*, **274**, 295–300.
- Fattahi, M., Walker, R., Hollingsworth, J., Bahroudi, A., Talebian, M., Armitage, S. & Stokes, S., 2006. Holocene slip-rate on the Sabzevar thrust fault, NE Iran, determined using Optically-stimulated Luminescence (OSL), *Earth planet. Sci. Lett.*, **245**, 673–684.
- Fattahi, M., Walker, R., Khatib, M.M., Dolati, A. & Bahroudi, J., 2007. Slip-rate estimates and past earthquakes on the Doruneh fault, eastern Iran, *Geophys. J. Int.*, **168**, 691–709.
- Fattahi, M. et al., 2010. Refining the OSL age of the last earthquake on the Dheshir fault, Central Iran, *Quat. Geochron.*, **5**, 286–292, doi:10.1016/j.quageo.2009.04.005.
- Galbraith, R.F., Roberts, R.G., Laslett, G.M., Yoshida, H. & Olley, J.M., 1999. Optical dating of single and multiple grains of quartz from Jinmium rock shelter, northern Australia, part 1, Experimental design and statistical models, *Archaeometry*, **41**, 339–364.
- Gosse, J.C. & Phillips, F.M., 2001. Terrestrial in situ cosmogenic nuclides: theory and application, *Quat. Sci. Rev.*, **20**, 1475–1560.
- Geological Survey of Iran, 1981. Geological Map of Iran, Ministry of Industry and Mines, scale 1:250 000, Anar quadrangle map.
- Heisinger, B. et al., 2002. Production of selected cosmogenic radionuclides by muons: 1. Fast muons, *Earth planet. Sci. Lett.*, **200**, 345–355.
- Hetzl, R., Tao, M., Stokes, S., Niedermann, S., Ivy-Ochs, S., Gao, B., Strecker, M.R. & Kubik, P.W., 2004. Late pleistocene/holocene slip rate of the Zhangye thrust (Qilian Shan, China) and implications for the active growth of the northeastern Tibetan Plateau, *Tectonics*, **23**(6), TC6006, doi:10.1029/2004TC001653.
- Korschinek, G. et al., 2010. A new value for the  $^{10}\text{Be}$  half-life by heavy-ion elastic recoil detection and liquid scintillation counting, *Nucl. Instrum. Methods Phys. Res. B*, **268**, 187–191.
- Le Dortz, K. et al., 2009. Holocene right-slip rate determined by cosmogenic and OSL dating on the Anar fault, Central Iran, *Geophys. J. Int.*, **179**, 700–710 doi:10.1111/j.1365-246X.2009.04309.x.
- Matmon, O. et al., 2009. Desert pavement-coated surfaces in extreme deserts present the longest-lived landforms on Earth, *Geol. Soc. Am. Bull.*, **121**, 688–697.
- Merchel, S. & Hergers, U., 1999. An update on radiochemical separation techniques for the determination of long-lived radionuclides via accelerator mass spectrometry, *Radiochimica Acta*, **84**, 215–219.
- Merchel, S. et al., 2008. Towards more precise  $^{10}\text{Be}$  and  $^{36}\text{Cl}$  data from measurements at the 10–14 level: influence of sample preparation, *Nucl. Instrum. Methods Phys. Res. B*, **266**, 4921–4926.
- Mériaux, A.-S., Ryerson, F.J., Tapponnier, P., Van Der Woerd, J., Finkel, R.C., Xu, X., Xu, Z. & Caffè, M.W., 2004. Rapid slip along the central Altn Tagh Fault: morphochronologic evidence from Cherchen He and Sulamu Tagh, *J. geophys. Res.*, **109**, B06401, doi:10.1029/2003JB002558.
- Mériaux, A.-S. et al., 2005. The Aksay segment of the northern Altn Tagh fault: tectonic geomorphology, landscape evolution, and Holocene slip rate, *J. geophys. Res.*, **110**, B04404, doi:10.1029/2004JB003210.
- Meyer, B. & Le Dortz, K., 2007. Strike-slip kinematics in Central and Eastern Iran: estimating fault slip-rates averaged over the Holocene, *Tectonics*, **6**, TC5009, doi:10.1029/2006TC002073, 2007.
- Meyer, B., Mouthereau, F., Lacombe, O. & Agard, P., 2006. Evidence of quaternary activity along the Deshir Fault, *Geophys. J. int.*, **164**, 192–201.
- Murray, A.S. & Wintle, A.G., 2000. Luminescence dating of quartz using an improved single-aliquot regenerative-dose protocol, *Radiat. Meas.*, **32**, 57–73.
- Nazari, H. et al., 2009. First evidence for large earthquakes on the Deshir fault, Central Iran Plateau, *Terra Nova*, **21**, 417–426.
- Nissen, E. et al., 2009. The late Quaternary slip-rate of the Har-Us-Nuur fault (Mongolian Altai) from cosmogenic  $^{10}\text{Be}$  and luminescence dating, *Earth planet. Sci. Lett.*, **286**, 467–478, doi:10.1016/j.epsl.2009.06.048.
- Owen, L.A., Finkel, R.C., Ma, H., Spencer, J.Q., Derbyshire, E., Banard, P. & Caffè, M.W., 2003. Timing and style of late Quaternary glaciation in northeastern Tibet, *Geol. Soc. Am. Bull.*, **115**, 1356–1364.
- Owen, L.A., Finkel, R.C., Haizhou, M. & Barnard, P.M., 2006. Late Quaternary landscape evolution in the Kunlun Mountains and Qaidam Basin, Northern Tibet: a framework for examining the links between glaciation, lake level changes and alluvial fan formation, *Quat. Int.*, **154–155**, 73–86.
- Repka, J.L., Anderson, R.S. & Finkel, R.C., 1997. Cosmogenic dating of fluvial terraces, Fremont River, Utah, *Earth planet. Sci. Lett.*, **152**, 59–73.
- Roberts, R.G., Galbraith, R.F., Yoshida, H., Laslett, G.M. & Olley, J.M., 2000. Distinguishing dose populations in sediment mixtures: a test of single-grain optical dating procedures using mixtures of laboratory-dosed quartz, *Radiat. Meas.*, **32**, 459–465.
- Ryerson, F.J. et al., 2006. Applications of morphochronology to the active tectonics of Tibet. *GSA, Special Papers*, **415**, 61–86, doi:10.1130/2006.2415(05).
- Schimmelpfennig, I., Benedetti, L., Finkel, R., Pik, R., Blard, P.-H., Bourlès, D., Burnard, P. & Williams, A., 2009. Sources of in-situ  $^{36}\text{Cl}$  in basaltic rocks. Implications for calibration of production rates, *Quat. Geoch.*, **4**(6), 441–461.
- Siame, L. et al., 2004. Local erosion rates versus active tectonics: cosmic ray exposure modelling in Provence (south-east France), *Earth planet. Sci. Lett.*, **220**(3–4), 345–364.
- Stone J.O., 2000. Air pressure and cosmogenic isotope production, *J. geophys. Res.*, **105**(B10), 23 753–23 759.
- Stone, J.O.H., Allan, G.L., Fifield, L.K. & Cresswell, R.G., 1996. Cosmogenic chlorine-36 from calcium spallation, *Geochim. Cosmochim. Acta.*, **60**, 679–692.
- Stone, J.O., Evans, J.M., Fifield, L.K., Allan, G.L. & Cresswell, R.G., 1998. Cosmogenic chlorine-36 production in calcite by muons, *Geochim. Cosmochim. Acta.*, **62**, 433–454.
- Vassallo, R. et al., 2007. Transpressional tectonics and stream terraces of the Gobi-Altay, Mongolia, *Tectonics*, **26**, TC5013, doi:10.1029/2006TC002081.
- Vermeesch, P., 2007. CosmoCalc: an Excel add-in for cosmogenic nuclide calculations, *Geochem. Geophys. Geosyst.*, **8**, Q08003, doi:10.1029/2006GC001530.
- Walker, R. & Jackson, J., 2004. Active tectonics and late Cenozoic strain distribution in central and eastern Iran, *Tectonics*, **23**, TC5010, doi:10.1029/2003TC001529.
- Zreda, M.G., Phillips, F.M., Elmore, D., Kubik, P.W., Sharma, P. & Dorn, R.I., 1991. Cosmogenic chlorine-36 production rates in terrestrial rocks, *Earth planet. Sci. Lett.*, **105**, 94–109.



Appendix A.3

**Holocene right-slip rate determined by  
cosmogenic and OSL dating on  
the Anar fault, Central Iran**

---

# Holocene right-slip rate determined by cosmogenic and OSL dating on the Anar fault, Central Iran

K. Le Dortz,<sup>1,2</sup> B. Meyer,<sup>1,2</sup> M. Sébrier,<sup>1,2</sup> H. Nazari,<sup>3</sup> R. Braucher,<sup>4</sup> M. Fattahi,<sup>5,6</sup> L. Benedetti,<sup>4</sup> M. Foroutan,<sup>3</sup> L. Siame,<sup>4</sup> D. Bourlès,<sup>4</sup> M. Talebian,<sup>3</sup> M. D. Bateman<sup>5</sup> and M. Ghoraishi<sup>3</sup>

<sup>1</sup>UPMC Univ Paris 06, ISTEP, UMR 7193, F-75005, Paris, France. E-mail: kristell.le\_dortz@upmc.fr

<sup>2</sup>CNRS, ISTEP, UMR 7193; F-75005, Paris, France

<sup>3</sup>Geological Survey of Iran, Teheran, Iran

<sup>4</sup>CEREGE UMR6635, Aix-En-provence, France

<sup>5</sup>The Institute of geophysics, University of Tehran, Kargar Shomali, Tehran, Iran

<sup>6</sup>Sheffield Centre for International Drylands Research, Department of geography, University of Sheffield, Winter Street, Sheffield S10 2TN, UK

Accepted 2009 June 24. Received 2009 June 24; in original form 2008 October 22

## SUMMARY

<sup>10</sup>Be cosmic ray exposure (CRE) and optically stimulated luminescence (OSL) dating of cumulative offset of alluvial fan surfaces have been performed to derive the long-term slip-rate of the Anar fault. At two sites, the comparison between OSL ages obtained within the latest sediments emplaced during the aggradation of the fan and cosmogenic exposure ages of the pebbles abandoned on the surface before its incision and subsequent dextral offset indicates a significant and variable CRE inheritance. Combining offset risers with CRE and OSL dating implies the southern Anar fault slips at a minimum rate of 0.8 mm yr<sup>-1</sup>, a little faster than formerly estimated by assuming the incision, which created the risers, was coeval with the onset of the Holocene (12 ± 2 ka). The latest regional incision in the Anar area appears rather coeval with the onset of the early-middle Holocene pluvial episode (6–10.5 ka) evidenced in the neighbouring region of Northern Oman.

**Key words:** Geomorphology; Seismicity and tectonics; Continental tectonics: strike-slip and transform; Tectonics and landscape evolution; Tectonics and climate interactions.

## INTRODUCTION

The Anar fault is a 200-km-long strike-slip fault located within the Central Iran plateau between 30.6°N–55.3°E and 32.3°N–54.8°E, north of the Zagros (Fig. 1). It is the shortest of a series of northerly trending, right-lateral fault system slicing Central and Eastern Iran. The overall fault zone, from the Deshir fault to the west to the Sistan fault zone along the eastern margin of the Lut desert, is 700 km wide (e.g. Walker & Jackson 2004; Meyer *et al.* 2006). The whole system accounts for a NS right-lateral shear that absorbs the differential motion between the widespread Iran collision zone to the west, and the narrow Makran subduction zone to the east. Although the relative contributions of individual fault zones remain unknown, the overall dextral shear amounts to 16 mm yr<sup>-1</sup> according to GPS measurements and appears to be accounted for mostly by the edges of the Lut (Vernant *et al.* 2004), to the east of the Anar fault. Despite the absence of resolvable GPS deformation for Central Iran over time-periods of 2 yr (Vernant *et al.* 2004) and 6 yr (Masson *et al.* 2007), and despite the lack of seismicity in the vicinity of the Anar fault, there is clear morphological evidence that the Anar fault is active (Meyer & Le Dortz 2007). A slip-rate of 0.5–0.75 mm yr<sup>-1</sup> has been inferred through a morphoclimatic scenario

that assigns offset-risers an age of 12 ± 2 ka (Meyer & Le Dortz 2007).

We combine here results of offset measurements with ages of geomorphic markers to derive a direct measurement of the rate of slip on the Anar Fault. First, we summarize the regional tectonic setting and the overall morphology of the Anar fault zone. Then, we describe the detailed morphology of two sites recognized by Meyer & Le Dortz (2007) and for which cosmic ray exposure (CRE) and optically stimulated luminescence (OSL) dating of offset-risers allows determination of the slip-rate. Finally, we revisit the slip-rates inferred for other dextral faults slicing Central and Eastern Iran in the light of that now determined for the Anar fault.

## GEOLOGICAL SETTING AND OVERALL MORPHOLOGY OF THE ANAR FAULT ZONE

The Anar fault zone is a strike-slip fault involving two distinctive portions that disrupt the morphology and the structure of the Central Iran Plateau (Fig. 1). The northern portion is located within the mountains with several closely spaced splays cutting across the

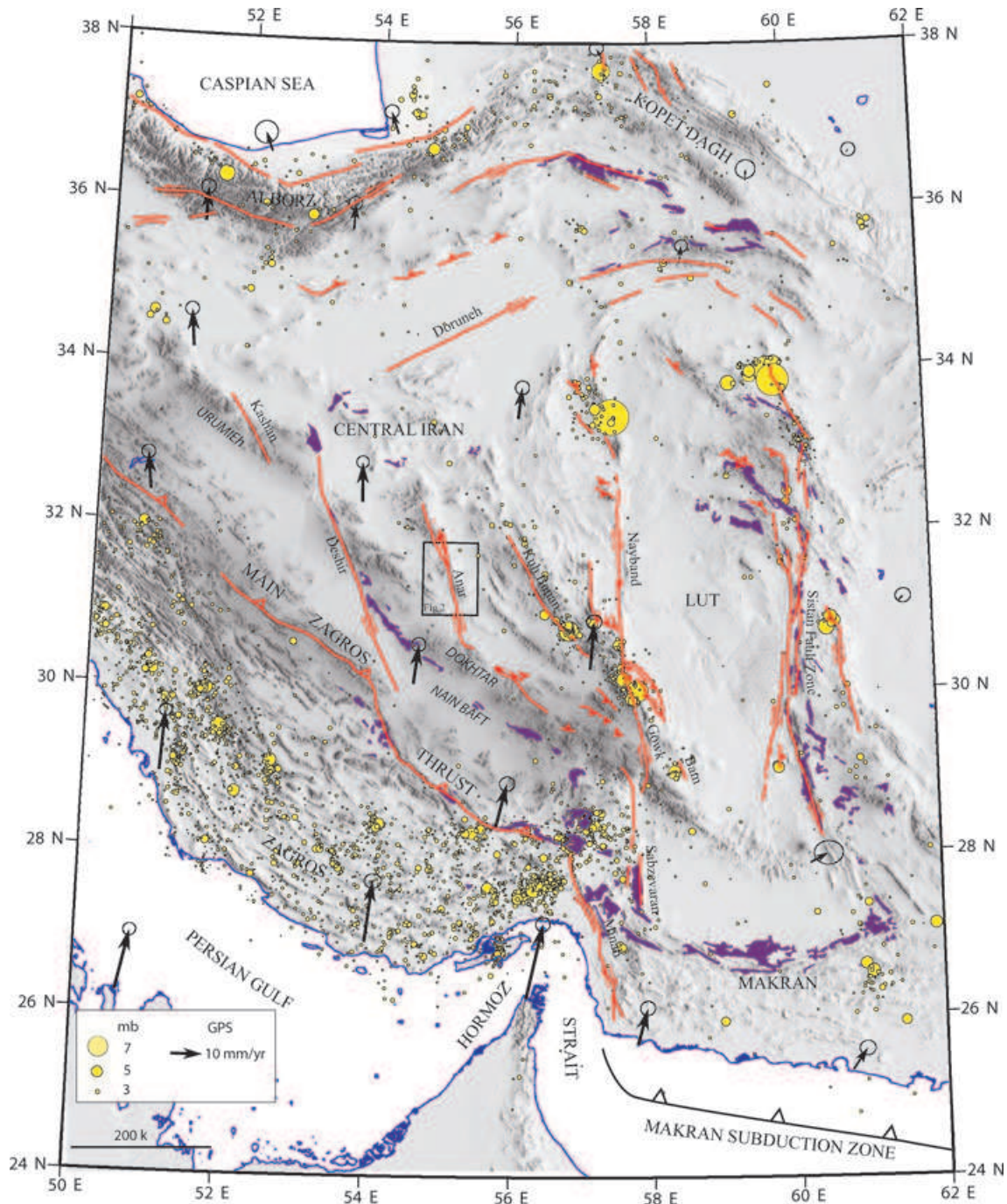


**Figure 1.** Map of the major active faults of Central and Eastern Iran. The background DEM image is from SRTM data. GPS velocities (black arrows) in Eurasian-fixed reference frame from Vernant *et al.* (2004). The 1973–2007 earthquake distribution (yellow dots) is from NEIC ([http://neic.usgs.gov/neis/epic/epic\\_rect.html](http://neic.usgs.gov/neis/epic/epic_rect.html)). Ophiolite outcrops and sutures are shown as purple patches. The box locates Fig. 2.

relief of the Kuh-e-Kharanaq range (Fig. 2). The splays merge southward extending into a single fault trace. The southern fault strand runs along the Kuh-e-Bafq range over a 20-km-long distance, and cuts right across the western piedmont of the range and across the Anar Salt flat. Further south, the fault bends eastwards, to reactivate a thrust fault to the north of the Urumieh Dokhtar magmatic arc. The total dextral offset is outlined by the displacement on the order of 20–30 km of a Lower Cretaceous sandstone unit (Fig. 2, Walker & Jackson 2004; Meyer & Le Dortz 2007). The ongoing strike-slip tectonics initiated after a widespread Palaeogene shortening stage

associated with the emplacement of the Kerman conglomerate. The shortening followed the Late Cretaceous–Early Tertiary closure of the Nain Baft suture and lasted until the final emplacement of the Main Zagros Thrust, probably by the early Neogene. It is nonetheless unlikely that the difference in height between the Kuh-e-Bafq range and its piedmont is entirely inherited from the Palaeogene shortening. Motion on several active thrusts that run across the eastern piedmont of the range might have contributed, even modestly, to the present elevation of the range (Fig. 2). In the case of the neighbouring Gowk strike-slip fault, such thrusts, sub parallel to

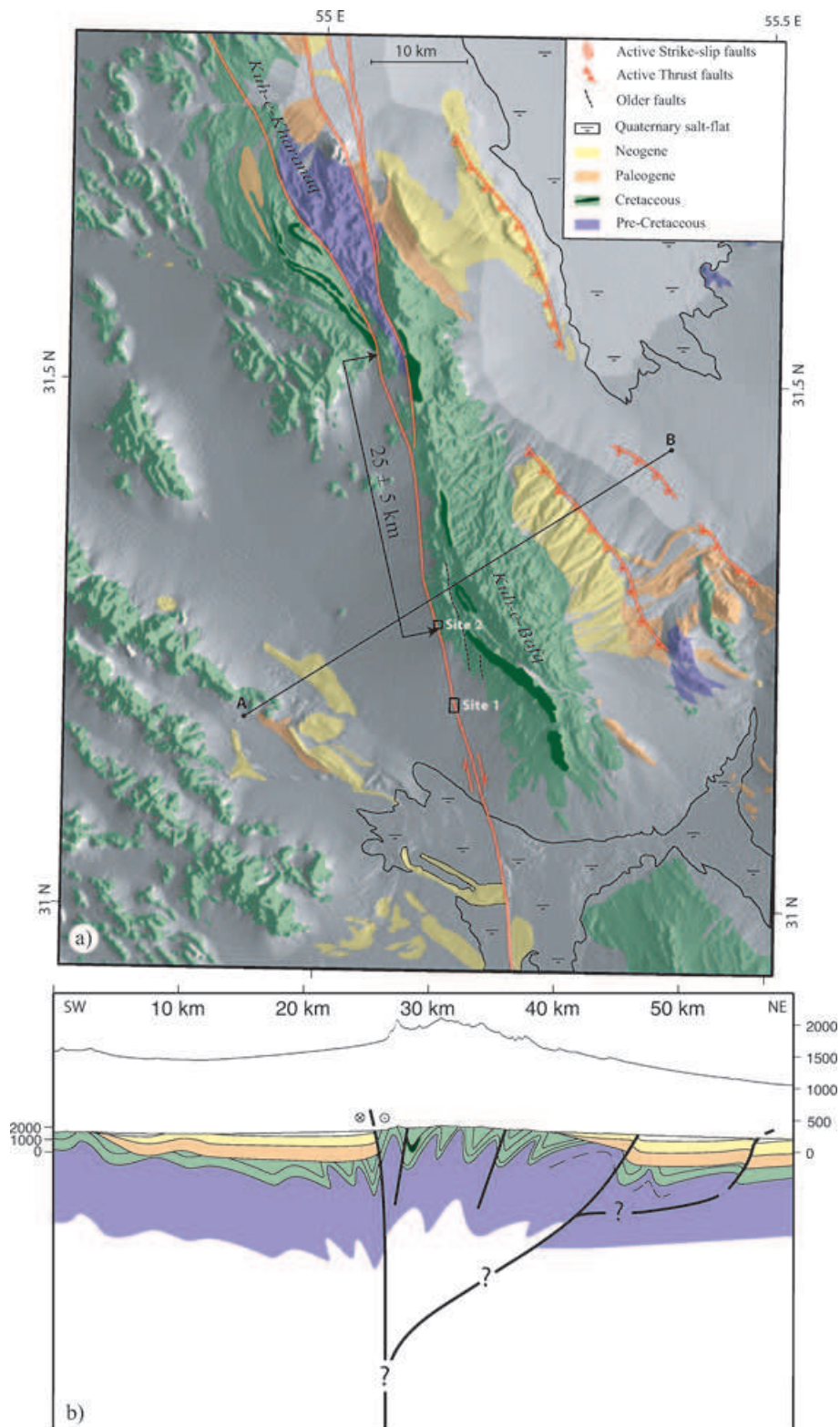


**Figure 2.** Simplified geological and morphotectonic map of the central part of the Anar fault zone (top panel). Geology is adapted from Yazd (Nabavi 1970) and Anar (Soheili 1981) geological maps and the Landsat and SPOT imagery available. Note the Lower Cretaceous sandstone unit delineating the  $25 \pm 5$  km geological offset. Boxes outline the frames of the Quickbird enlargements in Figs 3 and 4. AB locates the position of the simplified geological cross-section (bottom panel). Topography is also shown with a vertical exaggeration of 5.

the strike-slip, have contributed to the incremental growth of the relief during the 1998  $M_w = 6.6$  Fandoqa strike-slip event (Berberian *et al.* 2001). Similarly to the Gowk fault zone, the Anar strike-slip fault and the faint sub parallel thrust faults, 20 km apart, may root into a single slightly transpressive fault zone at depth (Fig. 2). For the Anar fault zone, however, the lack of documented coeval coseismic motion on the strike-slip and the thrust faults leaves open the possibility of other fault geometries. In any event, the morphological offsets investigated in the next section indicate prevalent dextral motion on a primary strike-slip fault.

### OFFSETS MARKERS AND SAMPLING STRATEGY

Morphological evidence of recent motion is clear along the southern strand of the fault where it cuts across coalescent fans fed by intermittent streams flowing west from the 2200-m-high Kuh-e-Bafq mountains. The surface of the fans, further abandoned by the streams as they continued to incise their deposits, stands a few metres above the present streambed that mark the active parts of

the fans. At two sites 8 km apart, risers resulting from the incision of ancient streambeds by present ones show dextral offsets. Site 1 locates in the middle of the piedmont where aggradation has been significant and incision has been limited. Numerous small rills and ephemeral streams have incised a few tens of cm into the abandoned fan surface. Longer streams have incised deeper and their wider streambed lie 1–2 m below the surface of the inactive parts of the fans (yellow shading, Fig. 3a). The fault cuts obliquely across the ancient and present streambeds. The scarp, less than a metre high, faces east and disrupts the drainage. Many of the small intermittent rills do not flow through the scarp. They have been isolated from their downstream courses and channelled south-eastwards along the scarp. A few larger streams cut through the scarp. The left bank of the largest stream visible in the northern part of the Quickbird extract shows a clear dextral offset. Either in the field or on the imagery, the offset is well constrained and consistent with  $8 \pm 0.5$  m of right-lateral fault motion (Figs 3b and c). Site 2 locates close to the Kuh-e-Bafq Mountains at the faulted contact between recent alluviums and abraded bedrock, where aggradation has been limited and incision has been more significant (Fig. 4a).

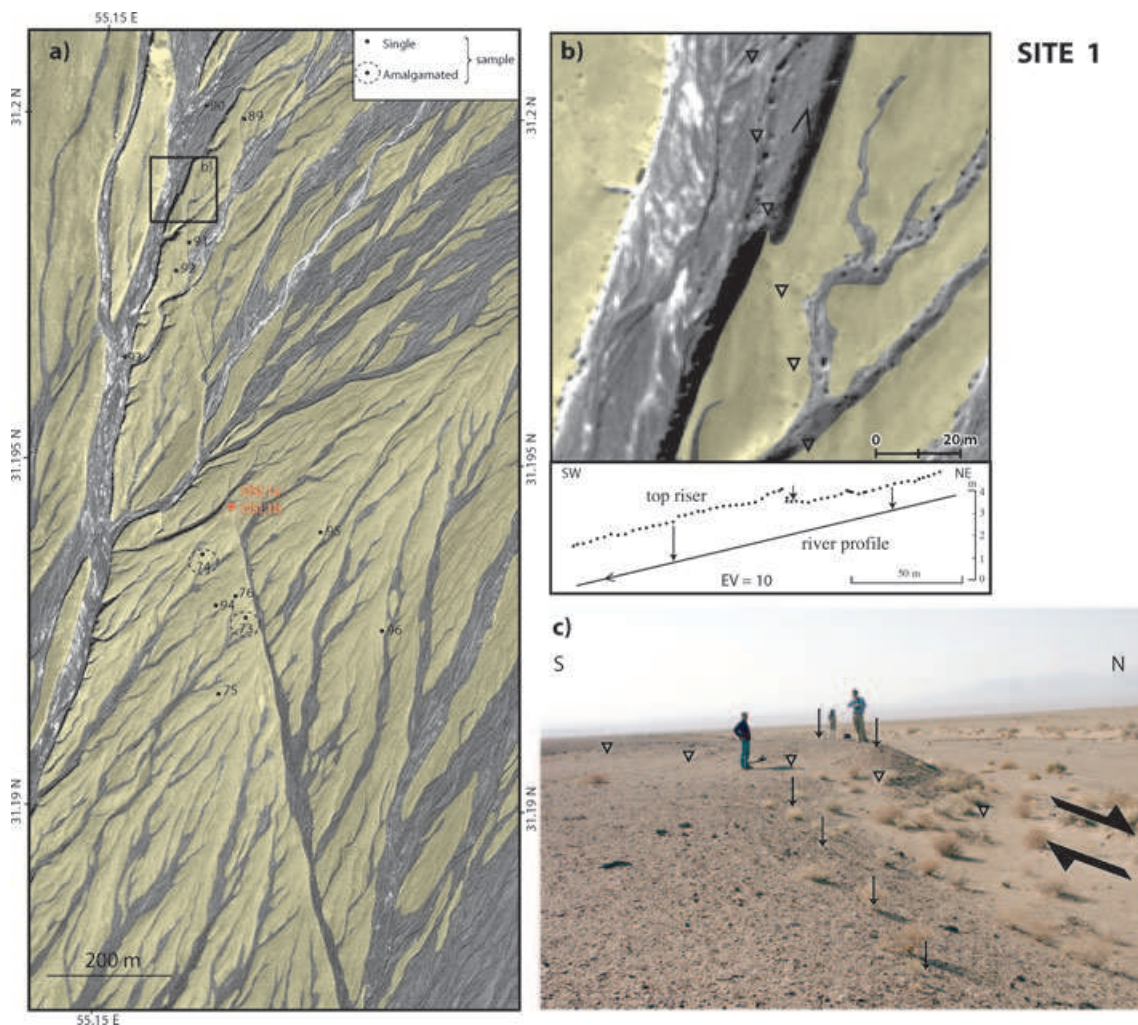


**Figure 3.** Site 1. (a) Quickbird imagery. The abandoned fan system, yellow shaded, is incised by channels and river streambeds. Numbered dots show position of surface samples collected for cosmogenic dating and dashed circle indicate the sampling area for amalgams. Red square locates position of the subsurface samples collected along the depth-profile in Fig. 5 and the OSL samples taken below the ground surface. (b) Close up on coeval 8 m dextral (top panel) and 0.7 m vertical (bottom panel) offsets of the riser. Open triangles point to the fault trace. Topographic profile (dots for density of the GPS survey) highlights the amount of stream incision up and down scarp. (c) Field photograph of the offset-riser with vertical arrows pointing to the top of the riser.

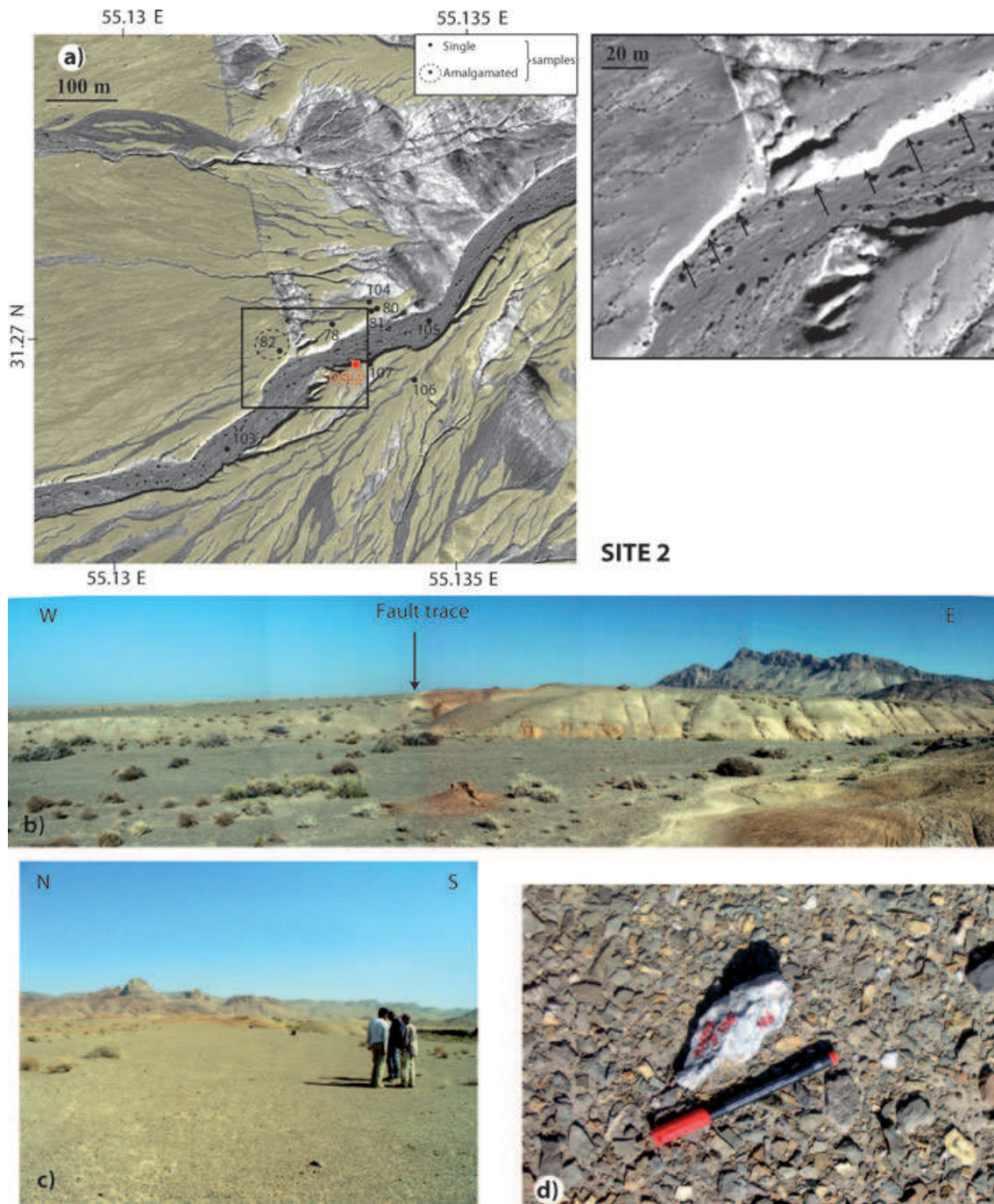


**Figure 4.** Site 2. (a) Quickbird imagery. Yellow shading denotes the abandoned fan. Numbered dots show position of surface samples collected for cosmogenic dating and dashed circle indicate the sampling area for amalgamated samples. Red square locates the OSL sample collected within the riverbank, 80 cm below the ground surface. Rectangle denotes the close up on the offset riser. Arrows point to the base of the lighted riser. (b) Panoramic view of the right bank of the stream. (c) Overview of the abandoned fan surface, downstream of the fault trace. (d) Close-up of cobbles paving the surface. White cobble is sample AS06S-106 ( $^{10}\text{Be}$  age of 22 ka).

To the north of the main stream, recent fans crop out west of the fault zone and further to the east where they are unconformable on the abraded bedrock. To the south of the main stream, the fans cover most of the area and the bedrock is no longer discernible. The fault zone cuts entirely across recent sediments and is distinguished by a subdued west-facing scarp. The scarp height is less than a metre and decreases southward. On both sides of the fault, the surface of the fan stands a few metres above the bed of the main

intermittent stream. The steep riser cuts provide natural sections of the alluvial deposits typifying the stratigraphy of floodplains and braided channels (Fig. 4b). The sequence starts with coarse conglomerates grading into pebbly-sandy material, and terminates by sandy-silty lenses alternating with conglomeratic layers. East of the fault, the riser is  $\sim 4.5$  m high and the erosive contact between the strath deposits and the steeply dipping basement locates close to the base of the riser. West of the fault, the riser is  $\sim 3.5$  m high

and cut within the alluvial deposits only. The right-lateral offset measured along the right bank of the stream is  $7.5 \pm 0.5$  m, similar to that at site 1.

At both sites, the offsets have formed since the rivers incised their older floodplains and abandoned the fan surface. Assuming these offsets date from the onset of the Holocene ( $12 \pm 2$  ka), Meyer & Le Dortz (2007) hypothesized a slip-rate of  $0.5\text{--}0.75$  mm yr<sup>-1</sup> that requires further investigation. To constrain the age of incision and abandonment of the fan surface, we sampled quartz-rich sandy layers below the surface for OSL dating and collected quartz-rich pebbles on the surface for measuring the accumulation of cosmogenic nuclides. Both methods are complementary. OSL relies on natural background radioactivity of the material with a small contribution of cosmogenic radiation and measures the time elapsed since the last sunlight exposure of a sediment layer by determining the radiation dose accumulated since its burial and the dose rate due to cosmic radiation. The cosmogenic nuclides, which production decreases rapidly with depth, provide the exposure time resulting from *in situ* interactions between the cosmic rays and the material while exposed at the earth surface.

We collected surface pebbles to estimate their <sup>10</sup>Be CRE ages, following a technique pioneered to study erosion-rates (Nishiizumi *et al.* 1984), date alluvial surfaces (e.g. Bierman *et al.* 1995;

Anderson *et al.* 1996; Repka *et al.* 1997), and helpful to estimate fault-slip rates (e.g. Ritz *et al.* 1995; Siame *et al.* 1997; Brown *et al.* 1998; Van der Woerd *et al.* 1998). At both sites, the surface of the fans forms a loose desert pavement of varnished clasts separated by a sandy-silty matrix. The clasts are made of locally derived shales, sandstone and conglomerates of the Kuh-e-Bafq Lower Cretaceous formations. The clasts reach in diameter up to tens of centimetres. A few are well rounded, many are angular, and some fragments result from cryoclastic weathering of cobbles and boulders. Very few boulders are unevenly distributed on the abandoned fan surface. We have collected quartz samples from single surface pebbles mainly. In a few cases, small pebbles were amalgamated. For one sample (AS06S-76), we extracted the pebbles from the exposed side of a big boulder of conglomerate. We collected 20 samples on the abandoned fan surface, seven amalgamated samples at increasing depth in a pit dug into the surface and four samples in the present streambeds (Figs 3a and 4a). For the depth profile, each sample corresponds to the amalgamation of ten centimetre-sized clasts, at least.

## DATING RESULTS AND DISCUSSIONS

To determine the exposure age of the surface, we measured the concentration of *in situ* produced <sup>10</sup>Be that accumulated in the collected

**Table 1.** The <sup>10</sup>Be nuclide concentrations and modelled age for surface and depth-profile samples along the Anar fault.

Sample	Sample description	Latitude (°N)	Longitude (°E)	Altitude (m)	Stone scaling factor	Measured <sup>10</sup> Be (10 <sup>5</sup> at/g SiO <sub>2</sub> )	<sup>10</sup> Be model age (ka)
Site 1							
AS06S-73	Amalgam-pluricentimetric fragment	31.19474	55.15243	1574	2.73	7.86 ± 0.18	64.85 ± 4.15
AS06S-74	Amalgam-pluricentimetric fragment	31.19404	55.15357	1562	2.71	3.93 ± 0.12	32.11 ± 2.19
AS06S-75	3 fragments of the same gelyfracted pebble	31.19263	55.15304	1571	2.73	2.20 ± 0.05	18.00 ± 1.15
AS06S-76	Conglomerate with pebbles of quartz (cm)	31.19405	55.15330	1559	2.71	2.55 ± 0.06	20.99 ± 1.34
AS08S-89	Fragment of a cobble	31.20095	55.15331	1571	2.73	3.53 ± 0.086	28.91 ± 1.87
AS08S-91	Several fragments of the same gelyfracted pebble	31.19915	55.15242	1571	2.73	3.47 ± 0.08	28.41 ± 1.84
AS08S-92	Amalgam-pluricentimetric fragment	31.19874	55.15221	1570	2.73	3.96 ± 0.10	32.50 ± 2.11
AS08S-94	Two fragments of the same gelyfracted pebble	31.19391	55.15297	1570	2.73	5.20 ± 0.12	42.75 ± 2.77
AS08S-95	Pebble (10 cm)	31.19499	55.15471	1570	2.73	2.70 ± 0.067	22.06 ± 1.43
AS08S-96	Pebble (10 cm)	31.19358	55.15577	1570	2.73	3.83 ± 0.10	31.46 ± 2.08
AS08S-90	Pebble (10 cm) in the river bed	31.20113	55.15268	1571	2.73	1.62 ± 0.06	13.22 ± 0.94
AS08S-93	Pebble (10 cm) in the river bed	31.19748	55.15137	1570	2.73	2.25 ± 0.06	18.38 ± 1.20
Site 2							
AS06S-78	Pebble (15 cm)	31.27033	55.13313	1748	3.09	7.36 ± 0.25	53.60 ± 3.71
AS06S-80	Several fragments of the same gelyfracted pebble	31.27052	55.13378	1751	3.10	5.22 ± 0.12	37.82 ± 2.42
AS06S-81	Fragment of a cobble	31.27046	55.13368	1754	3.09	N.M.	–
AS06S-82	Amalgam	31.26986	55.13239	1743	3.08	10.6 ± 0.23	77.81 ± 4.97
AS08S-104	Two fragments of the same gelyfracted pebble	31.27056	55.13367	1746	3.09	4.49 ± 0.12	32.55 ± 2.15
AS08S-106	Pebble (10 cm)	31.26959	55.13435	1750	3.10	2.99 ± 0.08	21.59 ± 1.42
AS08S-107	Pebble (10 cm)	31.26978	55.1337	1751	3.10	4.3 ± 0.017	31.09 ± 2.05
AS08S-103	Fragment of a big pebble in the river bed	31.26868	55.13163	1741	3.08	0.853 ± 0.06	6.16 ± 0.56
AS08S-105	Pebble (15 cm) in the river bed	31.27033	55.13455	1742	3.08	1.72 ± 0.05	12.45 ± 0.84
Profile <sup>a</sup>							
AS08P-97	Amalgam 370 cm below ground surface	31.19526	55.15340	1567	2.72	4.29 ± 0.12	
AS08P-98	Amalgam 270 cm below ground surface	31.19527	55.15341	1567	2.72	3.48 ± 0.09	
AS08P-99	Amalgam 170 cm below ground surface	31.19527	55.15341	1567	2.72	4.21 ± 0.11	
AS08P-100	Amalgam 100 cm below ground surface	31.19527	55.15341	1567	2.72	2.24 ± 0.06	
AS08P-101	Amalgam 70 cm below ground surface	31.19527	55.15341	1567	2.72	5.15 ± 0.14	
AS08P-102	Amalgam 30 cm below ground surface	31.19527	55.15341	1567	2.72	3.8 ± 0.10	
AS08P-108	Amalgam 150 cm below ground surface	31.19527	55.15341	1567	2.72	1.8 ± 0.05	

Notes: Blank sample with a mean <sup>10</sup>Be/<sup>9</sup>Be ratio of  $3 \times 10^{-15}$ , equivalent to  $6 \times 10^4$  atoms of <sup>10</sup>Be, was used to correct the measured isotopes ratios. Propagated analytical uncertainties include error blank, carrier and counting statistics. Zero erosion model ages are calculated for surface samples with propagated analytical uncertainties and corresponding geographic correction factors. N.M. means no measure.

<sup>a</sup>About 10 pebbles with centimetric size were sampled for each amalgam.

quartz-rich samples exposed to cosmic rays. Samples were prepared following chemical procedures adapted from Brown *et al.* (1991). All samples are crushed and sieved before chemical procedures. Extraction method for  $^{10}\text{Be}$  consists in isolation and purification of quartz and elimination of atmospheric  $^{10}\text{Be}$ .  $100\ \mu\text{l}$  of a  $3 \times 10^{-3}\ \text{gg}^{-19}\text{Be}$  solution are added to the decontaminated quartz. Beryllium was separated from the spiked solution obtained after its dissolution in HF by anion and cation exchanges and precipitations. The final precipitate is dried, and heated at  $900^\circ\ \text{C}$  to obtain BeO. Measurements were performed at the new French AMS National Facility, ASTER, located at CEREGE in Aix-en-Provence. The presented data were calibrated directly against the National Institute of Standards and Technology standard reference material 4325 by using the values recently determined by Nishiizumi *et al.* (2007) which are a  $^{10}\text{Be}/^9\text{Be}$  ratio of  $(2.79 \pm 0.03) \times 10^{-11}$  and a  $^{10}\text{Be}$  half-life of  $(1.36 \pm 0.07) \times 10^6$  yr. A modern  $^{10}\text{Be}$  production rate at sea-level and high-latitude of  $4.5 \pm 0.3\ \text{atoms}\ \text{g}^{-1}\ \text{yr}$ , computed for internal consistency from the data of Stone (2000) according

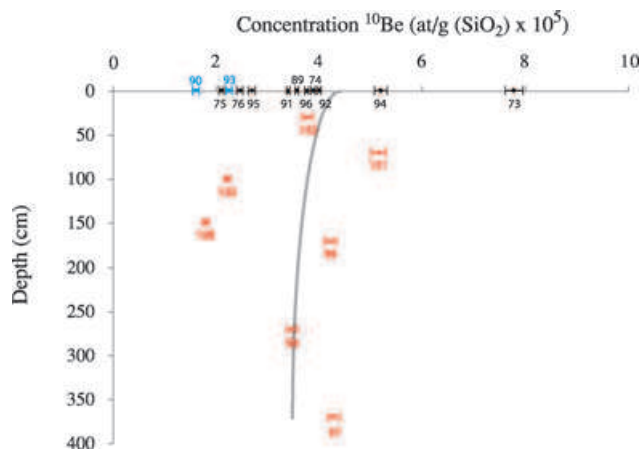


**Figure 5.** Plot of the measured  $^{10}\text{Be}$  concentrations as a function of depth for site 1. Black, red and blue dots are surface, depth-profile and modern stream samples, respectively. The uneven distribution of concentrations for the surface samples and the absence of depth-decreasing concentrations for the subsurface amalgams indicate heterogeneous exposure history and variable inheritance of the fanglomerate material. Forward model of  $^{10}\text{Be}$  concentration with depth for a 10 ka surface with no erosion and inheritance of 350,000 atoms per gram is shown for comparison.

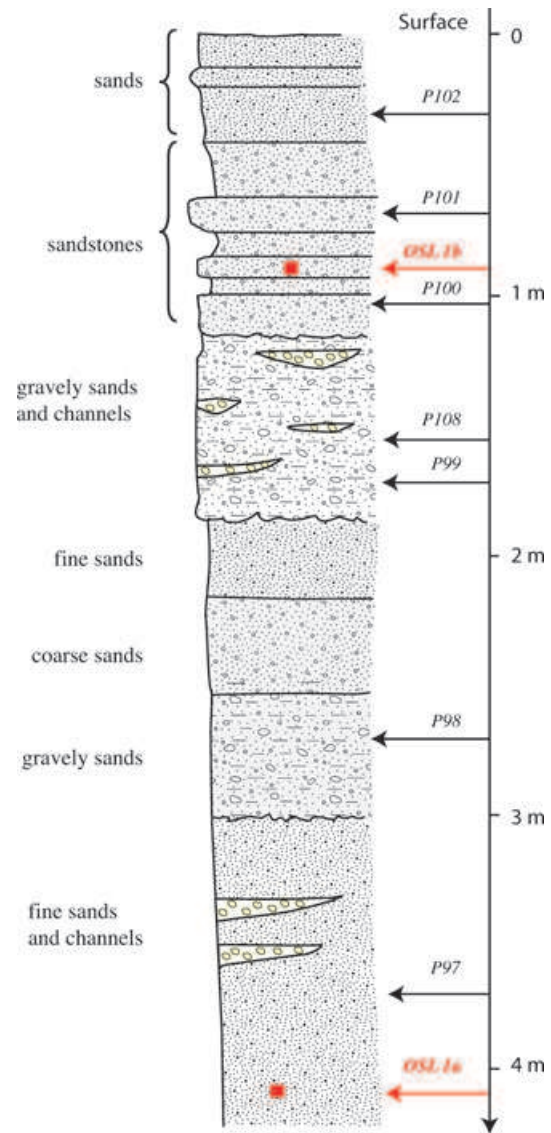


**Figure 6.** Simplified stratigraphy observed within the pit dug at site 1. Relative position of samples OSL-1a, 1b (red arrows) and CRE subsurface amalgams (black arrows) is shown.

**Table 2.** Equivalent dose ( $D_e$ ), annual dose rate ( $D_a$ ) and calculated ages for each sample.

Sample <sup>a</sup>	Sheffield codes	Equivalent dose $D_e$ (Grays) <sup>b</sup>	$N^c$	Depth (m)	Water (per cent)	$K^d$ (per cent)	$U^d$ (ppm)	$Th^d$ (ppm)	Annual dose rate $D_a$ (Grays $\text{ka}^{-1}$ ) <sup>e</sup>	Age (ka) <sup>f</sup>
Site 1 (Pit in the surface)										
OSL1a	Shfd08243	$12.78 \pm 7.97$	21	0.8	2	$1.21 \pm 0.01$	$1.6 \pm 0.05$	$5.9 \pm 0.1$	$2.20 \pm 0.05$	$5.8 \pm 3.6$
OSL1b	Shfd08244	$23.62 \pm 6.30$	10	4.1	0.6	$0.93 \pm 0.01$	$1.16 \pm 0.05$	$4 \pm 0.1$	$1.64 \pm 0.05$	$14.4 \pm 3.9$
Site 2 (Riser)										
OSL2	Shfd08245	$22.50 \pm 12.29$	16	0.8	1.1	$1.06 \pm 0.01$	$1.33 \pm 0.05$	$4 \pm 0.1$	$1.90 \pm 0.05$	$11.8 \pm 6.5$

Note: Ages have been calculated for Quartz grains with size ranging between 90 and  $250\ \mu\text{m}$ .

<sup>a</sup>The samples were collected using stainless steel tubes ( $5\ \text{cm} \times 25\ \text{cm}$ ) and both ends were sealed and covered using both aluminium foil and black tape.

Quartz was extracted from all samples using standard methods in the Sheffield Centre for International Drylands Research Centre Luminescence Laboratory

<sup>b</sup>Luminescence measured through 7 mm Hoya U-340 filters in a Risø (Model TL/OSL-DA-15) automated TL/OSL system. The equivalent dose ( $D_e$ ) was obtained using the conventional quartz single aliquot regeneration method (Murray & Wintle 2000). 24 aliquots have been processed for each sample.

<sup>c</sup> $N$  is the number of aliquots out of the 24 not rejected using the quality control parameters and falling within two standard deviations of the mean  $D_e$ .

<sup>d</sup>Uranium, thorium and potassium concentrations were measured using inductively coupled plasma mass spectrometer (ICP-MS).

<sup>e</sup>The annual dose ( $D_a$ ) was estimated from ICP-MS data and the cosmic ray contributions as described in Fattahi *et al.* (2006, 2007).

<sup>f</sup>Errors are  $1\sigma$ .

to the conclusions of the recently published study on absolute calibration of  $^{10}\text{Be}$  AMS standards by Nishiizumi *et al.* (2007), was used. This sea level and high-latitude production rate has then been scaled for the sampling altitudes and latitudes using the scaling factors proposed by Stone (2000) because, using the atmospheric pressure as a function of altitude, they take into account the physical properties of cosmic ray particle propagation in the atmosphere and include an improved account for the muonic component in the total cosmogenic production. Exposure ages were finally calculated with the estimates of the contribution of the nuclear particles given by Braucher *et al.* (2003) and assuming erosion as negligible during the involved time period, they are thus minimum exposure ages (Table 1).

The spread of concentrations, hence CRE calculated ages, is large and testifies for noticeable accumulation of nuclides prior deposition of the pebbles (Table 1). The inheritance is also attested by the significant concentrations measured for the few pebbles (number 90, 93, 103 and 105) collected in the modern streambeds. Depth distribution profiles of cosmogenic nuclide concentrations are sometimes performed to evaluate the inheritance (Anderson *et al.* 1996; Oskin *et al.* 2008). Provided the sediments emplaced in a short period of time (i.e. the same climatic crisis), an exponential decrease of the concentrations helps estimating a homogeneous pre-exposure. The uneven distribution of the concentrations retrieved from a 4 m depth profile within the abandoned fan surface (Fig. 5), together with the scattering of concentrations of the fan surface pebbles as well as of the stream pebbles, dismisses an homogeneous pre-exposure prior to the emplacement of the fan material. The inheritance is variable and may have taken place either during exhumation or transport. The small size of the drainage areas, less than 20 km<sup>2</sup> at both sites, is indicative of a rapid transport before the emplacement of the fans. The scattered surface pebble cosmogenic nuclide concentrations, therefore, indicates the observed inheritance more likely reflects variability of bedrock exhumation rates in the upper catchments rather than a long and complex history of successive burials and exposures during transport by the streams (e.g. Repka *et al.* 1997). The ages on the abandoned alluvial surface range between  $18 \pm 1.1$  and  $77.8 \pm 4.9$  kyr, and indicate the whole process of exhumation, transport, and sedimentation occurred during the last glacial period (Fig. 8). By contrast, the few pebbles collected in the present-day streambeds display lower concentrations, hence younger age equivalents. The ages of the river samples range between 6.2 and 18.4 kyr with all but one yielding post-glacial ages. This indicates that the fans likely emplaced until the end of the Last Glacial Stage and have been subsequently incised. Notwithstanding the inheritance, the youngest samples on the surface (samples 75 and 106 with zero erosion model age of  $18.0 \pm 1.1$  and  $21.6 \pm 1.4$  kyr, respectively) provide bounds on the abandonment of the surface, the cutting of the risers, and then on the minimum slip-rate. The minimum value for the slip-rate is  $0.45 \pm 0.06$  mm yr<sup>-1</sup> at site 1 assuming the age of the  $8 \pm 0.5$  m offset is at most  $18 \pm 1.1$  kyr, and  $0.34 \pm 0.04$  mm yr<sup>-1</sup> at site 2 assuming the age of the  $7.5 \pm 0.5$  m offset is at most  $21.6 \pm 1.4$  kyr.

To refine the former estimate and place independent constraints on the time the incision took place, we aimed at dating the uppermost alluvial layers that were emplaced during the aggradation of the fans. At both sites, we sampled lenses of fine sands at shallow depth below the surface of the fans and applied luminescence dating techniques (Table 2). At site 1, samples OSL1a and OSL1b have been, respectively, collected at 80 cm down and 410 cm down within a pit dug in the middle of the fan surface (Figs 3 and 6). At site 2, sample OSL2 has been directly taken at a depth of 80 cm from the riser of the river

(Figs 4 and 7). The OSL age determinations were carried out at the Sheffield Centre for International Dryland research luminescence laboratory (Table 2). Equivalent dose ( $D_e$ ) values were measured on extracted and cleaned quartz using the Single Aliquot Regeneration (SAR) protocol (e.g. Murray & Wintle 2000). Dose rates received by each samples were based on elemental analysis carried out using ICP at SGS laboratories Ontario, Canada with conversion to annual dose rate using Adamiec & Aitken (1998), Marsh *et al.* (2002) and Aitken (1998) taking into account attenuation factors relating to sediment grain sizes used, density and palaeo moisture. The contribution to dose rates from cosmic sources were calculated using the expression published in Prescott & Hutton (1994). The analytical procedures employed for the Anar samples is similar to that applied to samples from neighbouring Sabzevar and Doruneh areas (Fattahi *et al.* 2006, 2007). Ages were calculated using a mean  $D_e$  for each sample (Fig. 9) and ages are presented in Table 2 in years from present (2008) with  $1\sigma$  errors. For samples OSL1b and OSL2, there were only a few aliquots which met the quality assurance criteria (10 and 16 aliquots, respectively) precluding any meaningful examination of the  $D_e$  replicates in terms of establishing whether the samples were partially bleached prior to burial (Fig. 9). In order to counter this, ages for these two samples have been calculated in a very conservative manner using the standard deviation of the weighted (by inverse variance) mean  $D_e$  rather than the standard error, which would be normally adopted. As a result, the reported uncertainties on these ages are large (3.6 and 6.5 ka, respectively) and the mean  $D_e$  may incorporate an element of over-estimation if partial bleaching has occurred. As Fig. 9 shows, OSL1a has a broad  $D_e$  distribution centred around the mean  $D_e$  value. For consistency with the other samples and in order to take into account the breadth of  $D_e$  distribution, the age for this sample has also been calculated conservatively using the standard deviation of the mean  $D_e$ . Based on this, the ages for the samples are  $14.4 \pm 3.9$  kyr (OSL1a),  $5.8 \pm 3.6$  kyr (OSL1b) and  $11.8 \pm 6.5$  kyr (OSL2). Whether there has been incomplete resetting of the OSL samples or not, the samples collected 80 cm down at each site (OSL1a at site 1; OSL2 at site 2) provide temporal limits on the cutting of the risers and on the minimum value of the slip-rate. Using the oldest ages, determined by combining the mean age plus the associated  $1\sigma$  uncertainty, the minimum slip-rate is  $0.85 \pm 0.06$  mm yr<sup>-1</sup> at site 1 and  $0.41 \pm 0.03$  mm yr<sup>-1</sup> at site 2. This accounts for  $8 \pm 0.5$  and  $7.5 \pm 0.5$  m offsets at site 1 and 2, respectively and assumes that site 1 is at most 9.4 kyr old and site 2 at most 18.3 kyr old. The difference of slip-rates between the two sites might be due either to incomplete solar resetting of the older OSL sample or to difference in the sedimentation rate. The constancy of offset riser at both sites rather favours the latter as site 2 is located closer to the mountain and site 1 stands in the middle of the piedmont. The value of  $0.85$  mm yr<sup>-1</sup> is therefore a safe lower bound of the slip-rate on the southern segment of the Anar fault.

Finally, it is useful combining OSL and CRE results to discuss the inheritance (Fig. 8a). The risers postdate both the sediments they have incised and the abandonment of the fans. The surface of the fan being younger than the underlying sediments, the oldest possible age of a shallow OSL sample retrieved from these sediments provides a maximum age for the time of surface abandonment, hence an upper bound for the age of surface pebbles without inheritance (9.4 kyr at site 1 and 18.3 kyr at site 2). This confirms there has been a significant accumulation of nuclides before the emplacement of the pebbles and allows calculating the minimum proportion of pre-exposure for CRE age of each surface pebble (arrows, Fig. 8b).

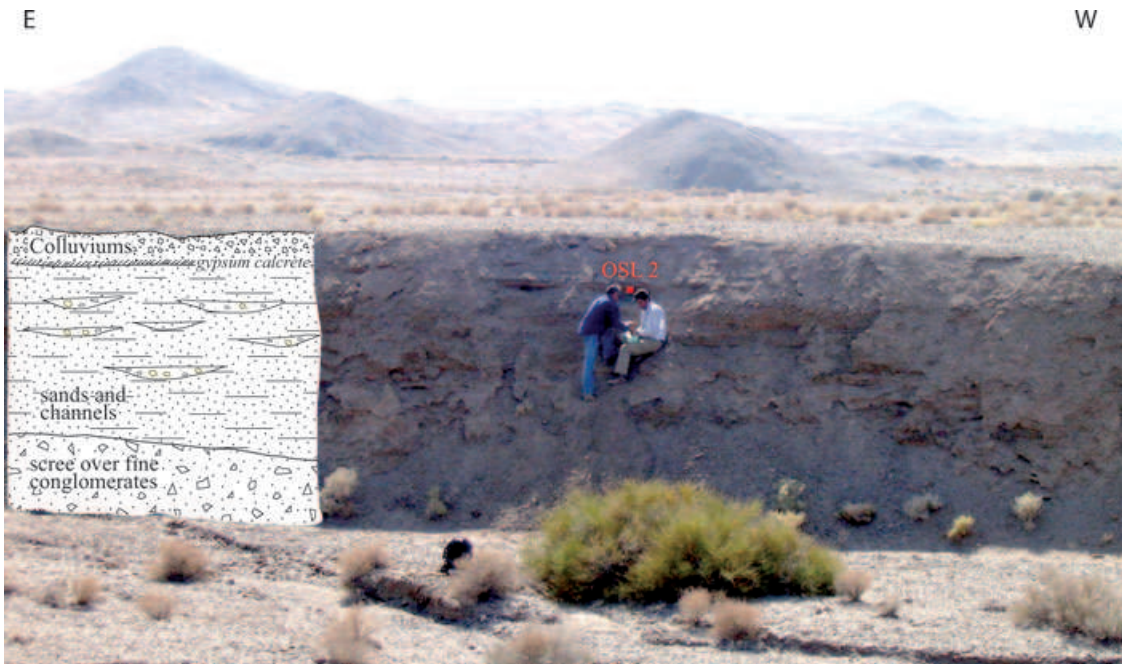


**Figure 7.** Photograph of the left bank of the river at site 2. Stratigraphy of the riser cut is schematized. The sample OSL-2 has been collected in a sandy layer just above the geologists.

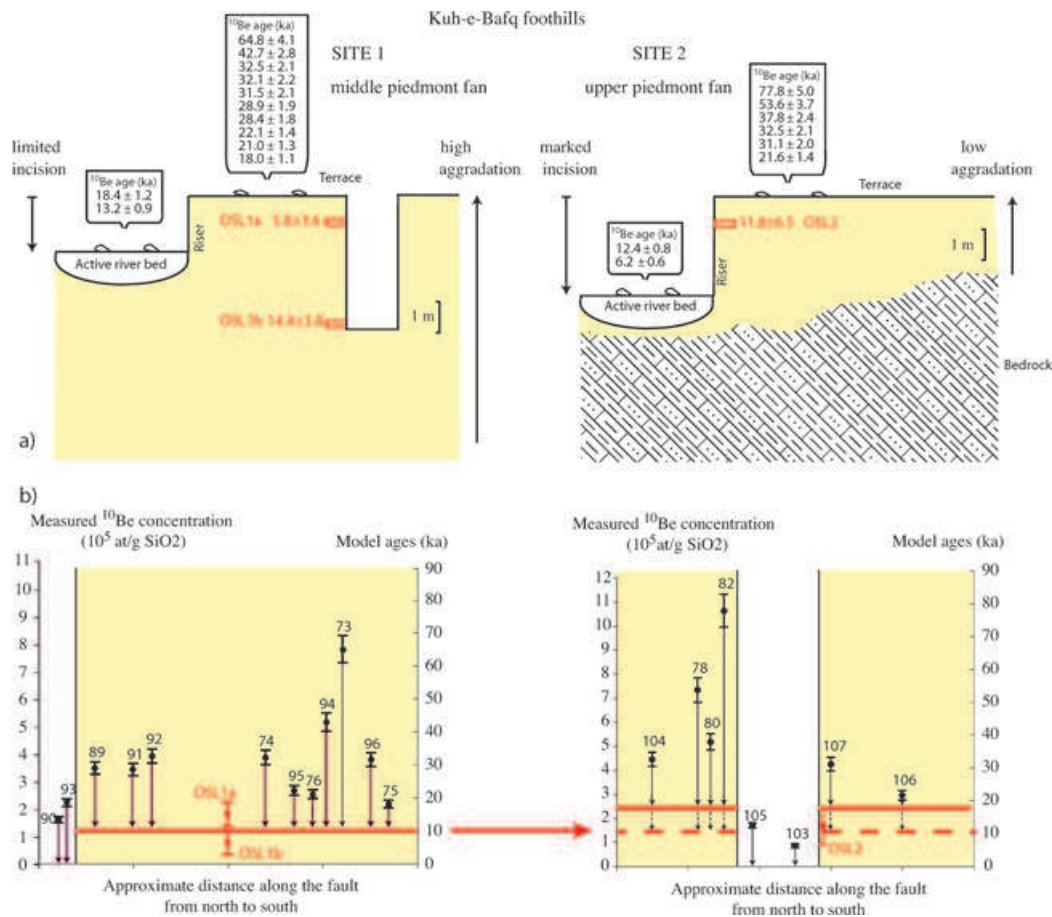


**Figure 8.** Summary of observations (top) and plot of sample ages in relative position from north to south (bottom) at sites 1 and 2. OSL and CRE surface ages are indicated in red and black, respectively. <sup>10</sup>Be concentrations and model ages are indicated by black dots, OSL ages by red squares. Data are tabulated in Tables 1 and 2. Red line is the oldest possible age of the surface strictly compatible at each site with the OSL results. Thick dashed line at site 2 is an extrapolation with the youngest OSL of site 1, see text for discussion. Vertical arrows figure the variable inheritance of individual pebbles.

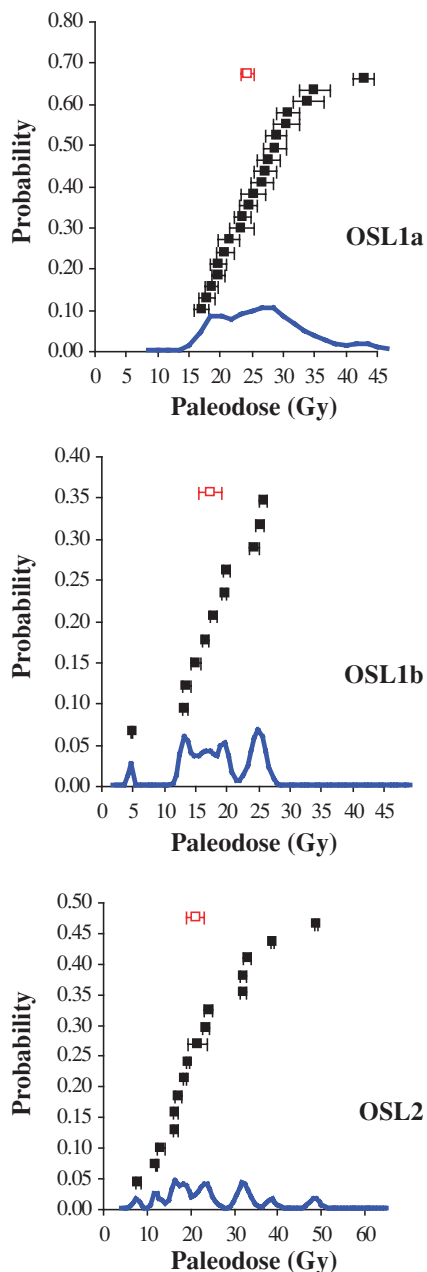


**Figure 9.** Equivalent dose distribution diagrams from SAR OSL for each of the samples. The equivalent dose distributions are displayed as a combined probability density function (blue curve) with individual aliquot  $D_e$  plotted above (filled black squares) and the arithmetic mean of the data (open red square).

## CONCLUSION

OSL dating indicates the Anar fans emplaced at the end of the Last Glacial Stage, most probably after the Last Glacial Maximum and during the beginning of the Holocene. The older and scattered CRE ages calculated for the surface and subsurface pebbles indicate that the material eventually incorporated in the fanglomerates has not been uniformly exposed to cosmic rays prior to both fan emplacement and abandonment. The variable CRE inheritance likely originated from a progressive exhumation and alteration of bedrock in the upper catchments of the streams during the Last Glacial Stage.

Accounting for the inheritance appears difficult (e.g. Hetzel *et al.* 2006; Oskin *et al.* 2008) and there is no straightforward modelling solution to retrieve the age of the surface. Using CRE ages alone may lead to significant overestimate (50–60 per cent) of the age of a fan surface abandonment, specifically when depth profiles of  $^{10}\text{Be}$  concentrations do not help modelling the inheritance.

Considering the Anar region, the incision of the fans is likely younger than the onset of the Holocene ( $12 \pm 2$  ka) as proposed by Meyer & Le Dortz (2007). Although relying on a single OSL sample, incision appears younger than 9.4 kyr and allows deriving a safe minimum slip-rate of  $\sim 0.8 \text{ mm yr}^{-1}$  on the Anar fault. The incision of the Anar fans appears to correspond to the early-middle Holocene (6–10.5 ka) pluvial period that Burns *et al.* (2001) evidenced by rapid speleothem growth phase in Northern Oman. Burns *et al.* (2001) correlate this pluvial episode and older ones with a significant northward shift of monsoon rainfall during peaks of interglacial periods. It is therefore possible that the regional incision in Central Iran has been driven by the onset of the early-middle Holocene pluvial episode (6–10.5 ka), which has been correlated with lower terraces in Southeastern Iran (Regard *et al.* 2006). This implies that the slip-rates inferred on the strike-slip faults slicing Central and Eastern Iran (Fig. 1) by Meyer & Le Dortz (2007) from the restoration of offset-risers of assumed Holocene age ( $12 \pm 2$  kyr) could be underestimated by up to 30 per cent.

## ACKNOWLEDGMENTS

This study would have been impossible without financial assistance from INSU-CNRS (PNTS and 3F programs) and from CNES-SPOT Image (ISIS program contracts ISIS0403–622 and ISIS0510–812). KL received a Ministry of Research and Education scholarship granted by the President of University Pierre and Marie Curie. This study benefited from logistic and financial assistance from Geological Survey of Iran. We acknowledge A. Rashidi and B. Oveisi for efficient organization and help during fieldwork. The  $^{10}\text{Be}$  measurements were performed at the ASTER AMS national facility (CEREGE, Aix en Provence), which is supported by the INSU-CNRS, the French Ministry of Research and Higher Education, IRD and CEA. We thank L. Leanni, F. Chauvet, M. Arnold and G. Aumaitre for their help during chemistry and measurements at CEREGE. MF acknowledges support from the research department of the University of Tehran. We acknowledge reviews by Vincent Regard and Richard Walker. We are grateful to R. Walker for suggesting improvements to the discussion of the OSL results.

## REFERENCES

- Adamiec, G. & Aitken, M.J., 1998. Dose-rate conversion factors: update, *Ancient TL*, **16**, 37–50.
- Aitken, M.J., 1998. *An Introduction to Optical Dating: The Dating of Quaternary Sediments by the Use of Photon-Stimulated Luminescence*, Oxford University Press, Oxford.
- Anderson, R.S., Repka, J.L. & Dick, G.S., 1996. Explicit treatment of inheritance in dating depositional surfaces using in situ  $^{10}\text{Be}$  and  $^{26}\text{Al}$ , *Geology*, **24**, 47–51.
- Berberian, M. *et al.*, 2001. The 1998 March 14 Fandoqa earthquake Mw6.6 in Kerman, southeast Iran: re-rupture of the 1981 Sirch earthquake fault, triggering of slip on adjacent thrusts, and the active tectonics of the Gowk fault zone, *Geophys. J. Int.*, **146**(2), 371–398.
- Bierman, P.R., Gillespie, A.R. & Caffee, M.W., 1995. Cosmogenic ages for earthquake recurrence intervals and debris flow fan deposition, Owens Valley, California, *Science*, **270**, 447–450.

- Braucher, R., Brown, E.T., Bourlès, D.L. & Colin, F., 2003. In situ produced  $^{10}\text{Be}$  measurements at great depths: implications for production rates by fast muons, *Earth planet. Sci. Lett.*, **211**, 251–258.
- Brown, E.T., Edmond, J.M., Raisbeck, G.M., Yiou, F., Kurz, M.D. & Brook, E.J., 1991. Examination of surface exposure ages of Antarctic moraines using in situ produced  $^{10}\text{Be}$  and  $^{26}\text{Al}$ , *Geochim. Cosmochim. Acta*, **55**, 2699–2703.
- Brown, E.T., Bourlès, D.L., Burchfiel, B.C., Deng, Q., Li, J., Molnar, P., Raisbeck, G.M. & You, F., 1998. Estimation of slip rates in the southern Tien Shan using cosmic ray exposure dates of abandoned alluvial fans, *Geol. Soc. Am. Bull.*, **110**, 377–386.
- Burns, S.J., Fleitmann, D., Matter, A., Neff, U. & Mangini, A., 2001. Speleothem evidence from Oman for continental pluvial events during interglacial periods, *Geology*, **29**, 623–626.
- Fattahi, M., Walker, R., Hollingsworth, J., Bahroudi, A., Talebian, M., Armitage, S. & Stokes, S., 2006. Holocene slip-rate on the Sabzevar thrust fault, NE Iran, determined using optically-stimulated luminescence (OSL), *Earth planet. Sci. Lett.*, **245**, 673–684.
- Fattahi, M., Walker, R., Khatib, M.M., Dolati, A. & Bahroudi, J., 2007. Slip-rate estimates and past earthquakes on the Doruneh fault, eastern Iran, *Geophys. J. Int.*, **168**, 691–709.
- Hetzel, R., Niedermann, S., Tao, M., Kubik, P.W. & Strecker, M.R., 2006. Climatic versus tectonic control on river incision at the margin of NE Tibet:  $^{10}\text{Be}$  exposure dating of river terraces at the mountain front of the Qilian Shan, *J. geophys. Res.*, **111**, F03012.
- Marsh, R.E., Prestwich, W.V., Rink, W.J. & Brennan, B.J., 2002. Monte Carlo determinations of the beta dose rate to tooth enamel, *Radiat. Measur.*, **35**, 609–616.
- Masson, F., Anvari, M., Djamour, Y., Walpersdorf, A., Tavakoli, F., Daignières, M., Nankali, H. & Van Gorp, S., 2007. Large-scale velocity field and strain tensor in Iran inferred from GPS measurements: new insight for the present-day deformation pattern within NE Iran, *Geophys. J. Int.*, **170**(1), 436–440. doi:10.1111/j.1365-246X.2007.03477.x
- Meyer, B. & Le Dortz, K., 2007. Strike-slip kinematics in Central and Eastern Iran: estimating fault slip-rates averaged over the Holocene, *Tectonics*, **26**, TC5009, doi:10.1029/2006TC002073.
- Meyer, B., Mouthereau, F., Lacombe, O. & Agard, P., 2006. Evidence of Quaternary activity along the Deshir fault: implication for the Tertiary tectonics of Central Iran, *Geophys. J. Int.*, **164**, 192–201.
- Murray, A.S. & Wintle, A.G., 2000. Luminescence dating of quartz using an improved single-aliquot regenerative-dose protocol, *Radiat. Measur.*, **32**, 57–73.
- Nabavi, M.H., 1970. Geological Map of Yazd sheet (H9), scale 1:250,000, Geol. Surv. of Iran, Teheran.
- Nishiizumi, K., Lal, D., Klein, J., Middleton, L. & Arnold, J.R., 1984. Production of  $^{10}\text{Be}$  and  $^{26}\text{Al}$  by cosmic rays in terrestrial quartz and implications for erosion rates, *Nature*, **319**, 134–136.
- Nishiizumi, K., Imamura, M., Caffee, M.W., Southon, J.R., Finkel, R.C., & McAninch, J., 2007. Absolute calibration of  $^{10}\text{Be}$  AMS standards, *Nucl. Instrum. Methods Phys. Res., B Beam Interact. Mater. Atoms*, **258**(2), 403–413.
- Oskin, M., Perg, L., Shelef, E., Strane, M., Gurney, E., Singer, B. & Zhang, X., 2008. Elevated shear-zone loading rate during an earthquake cluster in eastern California, *Geology*, **36**(6), 507–510, doi:10.1130/G24814A.1
- Prescott, J.R. & Hutton, J.T., 1994. Cosmic ray contributions to dose rates for luminescence and ESR dating: large depths and long-term time variations, *Radiat. Measur.*, **23**, 497–500.
- Regard, V. et al., 2006.  $^{10}\text{Be}$  dating of alluvial deposits from South-eastern Iran (The Hormoz Strait area), *Palaeogeogr., Palaeoclimatol., Palaeoecol.*, **242**, 36–53.
- Repka, J.L., Anderson, R.S. & Finkel, R.C., 1997. Cosmogenic dating of fluvial terraces, Fremont River, Utah, *Earth planet. Sci. Lett.*, **152**, 59–73.
- Ritz, J.F., Brown, E.T., Bourlès, D.L., Philip, H., Schlupp, A., Raisbeck, G.M., Yiou, F. & Enkhtuvshin, B., 1995. Slip-rates along active faults estimated with cosmic-ray-exposure dates: application to the Bogd Fault, Gobi-Altai, Mongolia, *Geology*, **23**, 1019–1022.
- Soheili, M., 1981. Geological Map of Anar sheet (H10), scale 1:250,000, Geol. Surv. of Iran, Teheran.
- Siame, L. et al., 1997. Cosmogenic dating ranging from 20 to 700 ka of a series of alluvial fan surfaces affected by the El Tigre fault, Argentina, *Geology*, **25**, 975–978.
- Stone, J.O., 2000. Air pressure and cosmogenic isotope production, *J. geophys. Res.*, **105**(B10), 23 753–13 759.
- Van Der Woerd, J. et al., 1998. Holocene left slip-rate determined by cosmogenic surface dating on the Xidatan segment of the Kunlun fault (Qinghai, China), *Geology*, **26**, 695–698.
- Vernant, P.H. et al., 2004. Present-day crustal deformation and plate kinematics in the Middle East constrained by GPS measurements in Iran and Northern Oman, *Geophys. J. Int.*, **157**, 381–398.
- Walker, R. & Jackson, J., 2004. Active tectonics and late Cenozoic strain distribution in central and eastern Iran, *Tectonics*, **23**, TC5010, doi:10.1029/2003TC001529.

# Erratum

**Le Dortz, K. et al., 2009. Holocene right-slip rate determined by cosmogenic and OSL dating on the Anar fault, Central Iran, *Geophys. J. Int.*, 179, 700–710, doi: 10.1111/j.1365-246X.2009.04309.x**

In Fig. 6 published in Le Dortz *et al.* (2009), the labels OSL1a and OSL1b have been unfortunately inverted. Such an inversion has also occurred in a sentence on page 8 of the article. The correct sentence is ‘Based on this, the ages for the samples are  $14.4 \pm 3.9$  kyr (OSL1b),  $5.8 \pm 3.6$  kyr (OSL1a) and  $11.8 \pm 6.5$  kyr (OSL2).’

We apologize to the readers for these inversions and we thank Jérôme Van der Woerd for bringing these typographical errors to our attention. For clarity the correct Fig. 6 is given here.

## REFERENCES

Le Dortz, K. et al., 2009. Holocene right-slip rate determined by cosmogenic and OSL dating on the Anar fault, Central Iran, *Geophys. J. Int.*, 179, 700–710, doi: 10.1111/j.1365-246X.2009.04309.x.

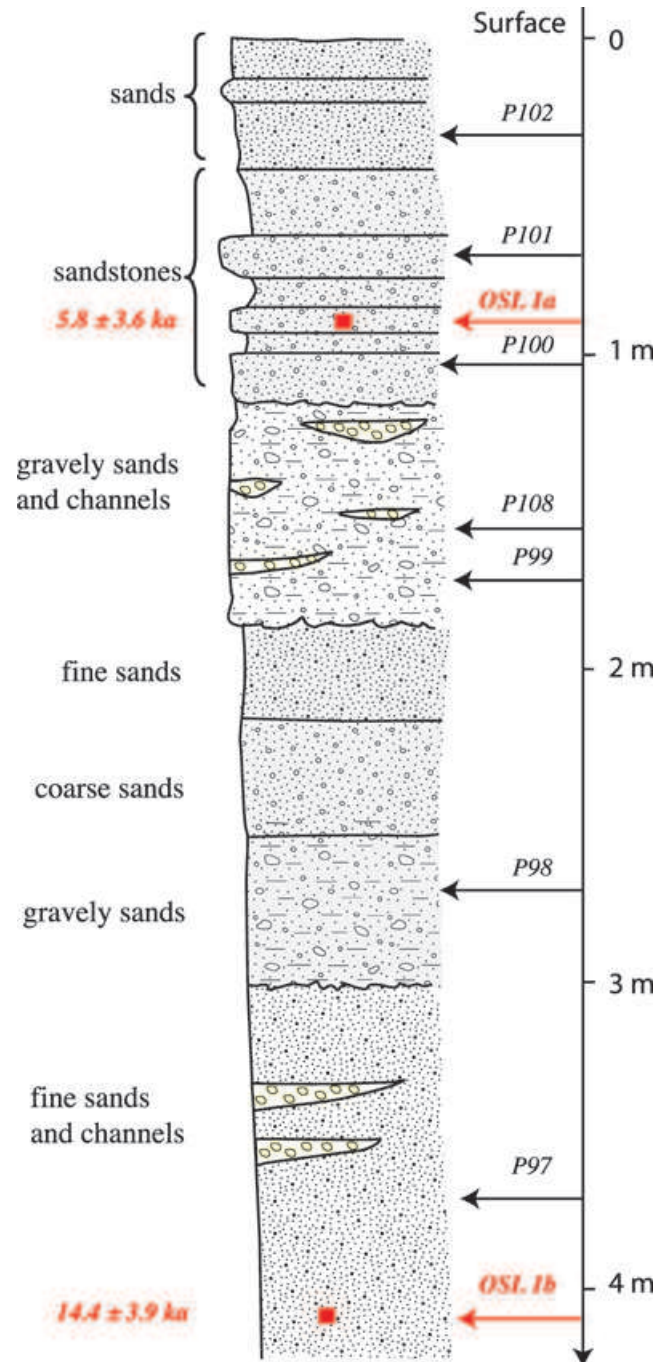


**Figure 6.** Simplified stratigraphy observed within the pit dug at site 1. Relative position of samples OSL-1a, 1b (red arrows) and CRE subsurface amalgams (black arrows) is shown.